frontiers | Research Topics

Organ microenvironment in vascular formation, homeostasis and engineering

Edited by
Akiko Mammoto, Tadanori Mammoto and Jonathan W. Song

Published in
Frontiers in Bioengineering and Biotechnology

ISSN 1664-8714
ISBN 978-2-83251-414-6
DOI 10.3389/978-2-83251-414-6

About Frontiers

Frontiers is more than just an open access publisher of scholarly articles: it is a pioneering approach to the world of academia, radically improving the way scholarly research is managed. The grand vision of Frontiers is a world where all people have an equal opportunity to seek, share and generate knowledge. Frontiers provides immediate and permanent online open access to all its publications, but this alone is not enough to realize our grand goals.

Frontiers journal series

The Frontiers journal series is a multi-tier and interdisciplinary set of open-access, online journals, promising a paradigm shift from the current review, selection and dissemination processes in academic publishing. All Frontiers journals are driven by researchers for researchers; therefore, they constitute a service to the scholarly community. At the same time, the *Frontiers journal series* operates on a revolutionary invention, the tiered publishing system, initially addressing specific communities of scholars, and gradually climbing up to broader public understanding, thus serving the interests of the lay society, too.

Dedication to quality

Each Frontiers article is a landmark of the highest quality, thanks to genuinely collaborative interactions between authors and review editors, who include some of the world's best academicians. Research must be certified by peers before entering a stream of knowledge that may eventually reach the public - and shape society; therefore, Frontiers only applies the most rigorous and unbiased reviews. Frontiers revolutionizes research publishing by freely delivering the most outstanding research, evaluated with no bias from both the academic and social point of view. By applying the most advanced information technologies, Frontiers is catapulting scholarly publishing into a new generation.

What are Frontiers Research Topics?

Frontiers Research Topics are very popular trademarks of the *Frontiers journals series*: they are collections of at least ten articles, all centered on a particular subject. With their unique mix of varied contributions from Original Research to Review Articles, Frontiers Research Topics unify the most influential researchers, the latest key findings and historical advances in a hot research area.

Find out more on how to host your own Frontiers Research Topic or contribute to one as an author by contacting the Frontiers editorial office: frontiersin.org/about/contact

Organ microenvironment in vascular formation, homeostasis and engineering

Topic editors

Akiko Mammoto — Medical College of Wisconsin, United States

Tadanori Mammoto — Medical College of Wisconsin, United States

Jonathan W. Song — The Ohio State University, United States

Citation

Mammoto, A., Mammoto, T., Song, J. W., eds. (2023). *Organ microenvironment in vascular formation, homeostasis and engineering*. Lausanne: Frontiers Media SA. doi: 10.3389/978-2-83251-414-6

Table of contents

frontiers | Frontiers in Bioengineering and Biotechnology

TYPE Editorial
PUBLISHED 10 January 2023
DOI 10.3389/fbioe.2022.1130851

OPEN ACCESS

EDITED AND REVIEWED BY
Ranieri Cancedda,
Independent researcher, Italy

*CORRESPONDENCE
Akiko Mammoto,
amammoto@mcw.edu

SPECIALTY SECTION
This article was submitted to Tissue Engineering and Regenerative Medicine, a section of the journal Frontiers in Bioengineering and Biotechnology

RECEIVED 23 December 2022
ACCEPTED 28 December 2022
PUBLISHED 10 January 2023

CITATION
Mammoto A, Mammoto T and Song JW (2023), Editorial: Organ microenvironment in vascular formation, homeostasis and engineering.
Front. Bioeng. Biotechnol. 10:1130851.
doi: 10.3389/fbioe.2022.1130851

Editorial: Organ microenvironment in vascular formation, homeostasis and engineering

Akiko Mammoto[1,2]*, Tadanori Mammoto[1,3] and Jonathan W. Song[4,5]

[1]Department of Pediatrics, Medical College of Wisconsin, Milwaukee, WI, United States, [2]Department of Cell Biology, Neurobiology and Anatomy, Medical College of Wisconsin, Milwaukee, WI, United States, [3]Department of Pharmacology and Toxicology, Medical College of Wisconsin, Milwaukee, WI, United States, [4]Department of Mechanical and Aerospace Engineering, The Ohio State University, Columbus, OH, United States, [5]Comprehensive Cancer Center, The Ohio State University, Columbus, OH, United States

KEYWORDS

angiogenesis, microcirculation, vascular engineering, stem cell, mechanical force

Editorial on the Research Topic
Organ microenvironment in vascular formation, homeostasis and engineering

The expansion of blood vessel networks by angiogenesis plays key roles in organ morphogenesis and physiological function. Well-organized and functional blood vessels are necessary for transporting nutrients and gas exchange. In addition to these passive roles, endothelial cells (ECs) that line blood vessels secrete angiocrine factors and dictate tissue structures to control organ development, regeneration and repair from injury. Deregulated angiogenesis contributes to various pathologies, including cancer, retinopathy, diabetes, and arthritis (Carmeliet, 2003). Spatiotemporal changes in organ-specific chemical and mechanical microenvironment control vascular formation (Carmeliet, 2005; Mammoto et al., 2013), which is required for organ morphogenesis and homeostasis. Despite recent progress in our understanding of the molecular mechanisms that regulate angiogenesis, the role of organ-specific microenvironment in angiogenesis is not fully understood partly due to complexity of cellular and non-cellular components in the tissues. To further uncover the mechanisms of organ-specific angiogenesis and vascular functions, we need to use interdisciplinary techniques and technologies including organoid system, organ-on-chip system, *ex vivo* approach, omics approach, computational modeling, and advanced imaging system.

This Research Topic "*Organ Microenvironment in Vascular Formation, Homeostasis and Engineering*" has assembled a Research Topic of original research and review articles that integrate biomedical and bioengineering research to address key questions on how organ-specific microenvironments control angiogenesis in physiology and pathology. Enhanced understanding of the mechanisms by which organ-specific microenvironments control vascular formation using these advanced technologies will promote new strategies for organ and tissue regeneration and repair.

Tissue microenvironment in angiogenesis in health and disease

It is becoming more evident that ECs provide instructive cues that mediate tissue morphogenesis and differentiation. Asrar and Tucker reviewed the origin and migration of

craniofacial ECs and how these cells influence the development of craniofacial tissues such as salivary glands, teeth and jaw. In addition to organ development, angiogenesis constitutes an essential part of organ regeneration (Ding et al., 2011; Mammoto and Mammoto, 2019). Mechanical factors such as extracellular matrix (ECM) stiffness, shear stress, and stretching forces control angiogenesis and vascular function (Mammoto and Mammoto, 2019). Among these mechanical factors, Mammoto et al. have focused on the pulmonary artery (PA) pressure that transiently increases during regenerative lung growth after unilateral pneumonectomy (PNX) and demonstrated that increases in PA pressure following PNX control angiogenesis through mechanosensitive transcriptional co-activator, YAP1. Extracellular vesicles (EVs) that contain cargo such as nucleic acids, miRNAs, proteins, and lipids play key roles in autocrine and paracrine signaling and promote tissue regeneration (Kourembanas, 2015). The authors also show that blood vessel formation is stimulated in the fibrin gel containing EVs isolated from post-PNX mouse lung ECs or pressurized ECs, while YAP1 knockdown inhibits the effects, suggesting that increases in PA pressure stimulate angiogenesis through the YAP1 pathway during lung regeneration and EC-derived EVs have potential to stimulate angiogenesis.

Tissue microenvironment also contributes to various pathologies. For example, the crosstalk of tumor cells and non-cancerous cells within the tumor microenvironment is a crucial part of the tumor angiogenesis. Guarino et al. have demonstrated that tumor-derived EVs, which play a key role in autocrine and paracrine signaling involved in tumor angiogenesis (Asare-Werehene et al., 2020), downregulate TRPV4 expression and induce abnormal angiogenesis by activating Rho/Rho kinase/YAP/VEGFR2 pathways. Their results suggest that tumor-derived EVs and TRPV4 are novel targets for vascular normalization and cancer therapy. Holter et al. utilized microscale engineering technology to model and investigate stromal fibroblast cell-EC interactions within the tumor microenvironment. Here they showed that fibroblast secreted CXCL12 can reprogram the tumor microenvironment by potently inducing a leakier endothelium that is hospitable to angiogenesis and tumor cell intravasation.

Strategies for bioengineered blood vessels leverage the factors derived from the tissue microenvironment for creating prevascularized tissue constructs. Shafiee et al.review the cell-based co-culture strategies for tissue engineering prevascularized constructs. Here they emphasize co-culture strategies with endothelial lineage cells with different supporting cells, such as mesenchymal stem cells (MSCs), fibroblasts, and perivascular cells, towards the formation of organized and functional vascular networks. Mykuliak et al. extend this concept by comparing the effects of bone marrow-derived mesenchymal stem/stromal cells (BMSCs) and adipose tissue-derived mesenchymal stem/stromal cells (ASCs) in supporting the formation of mature and interconnected networks in a microfluidic chip. Here they show differences in blood vessel function and morphometrics due to differences in tissue origin of the MSCs. Luo et al. have demonstrated that hyaluronic acid (HA), one of the major ECM components constituting tissue microenvironment, promotes angiogenesis induced by human umbilical-derived MSCs and endothelial colony forming cells (ECFCs) in Matrigel plugs and increases blood perfusion of the ischemic mouse limb; HA supported cell proliferation and migration, and enhanced CD44 expression by downregulating microRNA-139-5p in ECFCs.

One of the primary goals of vascular tissue engineering is to address the mortality and morbidity associated with ischemic diseases. Two papers developed novel experimental models to gain insights into specific aspects of tissue ischemia and reperfusion injury. Willi et al. developed an *ex vivo* intestine tissue-based microfluidic model to investigate acute post-ischemic effects on microvascular stability, remodeling, and collateral flow formation. This model uses intact tissue such that one can readily study the responses of perivascular cells, such as pericytes, due to altered flow conditions and vascular occlusion. Optical tweezers is one of the most widely used approaches for single-molecule and single-cell biophysics. Shao et al. used infrared optical tweezers for a novel application in controlling dynamic reperfusion in subdermal capillaries in mice. Here they demonstrate the capacity of optical tweezers as a non-invasive strategy for manipulating blood flow conditions.

Advanced *in vitro* systems to mimic tissue microenvironments

Lampejo et al. discuss the role of biomimetic tissue engineered models for advancing our understanding of microvascular physiology. They emphasize the importance of widely adopted biomimetic modeling approaches in incorporating the necessary physiological complexity that reconstitute native environments for investigating microvascular dynamics. They examine the application and future opportunities of biomimetic microvascular models for enabling basic science discoveries and therapeutic evaluation studies by collaborating tissue engineers, physiologists, and vascular biologists.

Anti-angiogenesis agents have been used as anti-cancer drugs due to their combined mode of action in preventing neovascularization and disruption of existing vasculatures in the tumor microenvironment. However, it is challenging to validate the anti-angiogenic properties of these drugs due to lack of proper *in vitro* angiogenesis models comprised of mature and long-lived vascular networks. Yavvari et al. developed a three-dimensional drug-testable *in vitro* angiogenesis system in which human umbilical vein ECs are embedded and sandwiched in the collagen scaffold and co-cultured with human dermal fibroblasts. Using this system, authors have demonstrated that single or combinational anti-angiogenic drugs can be tested to predict the effects of these drugs on the vasculatures *in vivo*.

Recent advances in the organoid systems make them promising models for regenerative medicine, drug testing and developmental biology (Gupta et al., 2021). Induced pluripotent stem cells can be differentiated into kidney organoids that develop nephrons, resembling cellular and architectural complexity in the developing kidney (Takasato et al., 2016). However, these organoid systems have several limitations, such as the limited culture duration, loss of nephrogenic potential, immaturity and lack of vasculature (Nishinakamura, 2019), partly due to the lack of mimicking an *in vivo* microenvironment (Rossi et al., 2018). Since kidneys develop in hypoxia *in vivo*, to make more clinically applicable kidney organoids, Schumacher et al. cultured kidney organoids under physiological hypoxia and found that this condition initiates angiogenesis, leading to enhanced angiocrine factor secretion and improved endothelial patterning. Recapitulating the physiological environment in the organoid systems is important to improve the

vascularization of organoids and extend their potential for tissue engineering and drug discovery.

In conclusion, the papers in this Research Topic "*Organ Microenvironment in Vascular Formation, Homeostasis and Engineering*" cover a broad area of research from fundamental understanding of the role of tissue microenvironment in angiogenesis to advancements in the technology that can be leveraged for improved strategies for tissue engineering and development of new treatments for various diseases.

Author contributions

AM, TM, and JS drafted and edited the manuscript. All authors contributed to the article and approved the submitted version.

Conflict of interest

The authors declare that the research was conducted in the absence of any commercial or financial relationships that could be construed as a potential conflict of interest.

Publisher's note

All claims expressed in this article are solely those of the authors and do not necessarily represent those of their affiliated organizations, or those of the publisher, the editors and the reviewers. Any product that may be evaluated in this article, or claim that may be made by its manufacturer, is not guaranteed or endorsed by the publisher.

References

Asare-Werehene, M., Nakka, K., Reunov, A., Chiu, C. T., Lee, W. T., Abedini, M. R., et al. (2020). The exosome-mediated autocrine and paracrine actions of plasma gelsolin in ovarian cancer chemoresistance. *Oncogene* 39 (7), 1600–1616. doi:10.1038/s41388-019-1087-9

Carmeliet, P. (2003). Angiogenesis in health and disease. *Nat. Med.* 9 (6), 653–660. doi:10.1038/nm0603-653

Carmeliet, P. (2005). Angiogenesis in life, disease and medicine. *Nature* 438 (7070), 932–936. doi:10.1038/nature04478

Ding, B. S., Nolan, D. J., Guo, P., Babazadeh, A. O., Cao, Z., Rosenwaks, Z., et al. (2011). Endothelial-derived angiocrine signals induce and sustain regenerative lung alveolarization. *Cell* 147 (3), 539–553. doi:10.1016/j.cell.2011.10.003

Gupta, N., Dilmen, E., and Morizane, R. (2021). 3D kidney organoids for bench-to-bedside translation. *J. Mol. Med. Berl.* 99 (4), 477–487. doi:10.1007/s00109-020-01983-y

Kourembanas, S. (2015). Exosomes: Vehicles of intercellular signaling, biomarkers, and vectors of cell therapy. *Annu. Rev. Physiol.* 77, 13–27. doi:10.1146/annurev-physiol-021014-071641

Mammoto, A., and Mammoto, T. (2019). Vascular niche in lung alveolar development, Homeostasis, and regeneration. *Front. Bioeng. Biotechnol.* 7, 318. doi:10.3389/fbioe.2019.00318

Mammoto, T., Mammoto, A., and Ingber, D. E. (2013). Mechanobiology and developmental control. *Annu. Rev. Cell Dev. Biol.* 29, 27–61. doi:10.1146/annurev-cellbio-101512-122340

Nishinakamura, R. (2019). Human kidney organoids: Progress and remaining challenges. *Nat. Rev. Nephrol.* 15 (10), 613–624. doi:10.1038/s41581-019-0176-x

Rossi, G., Manfrin, A., and Lutolf, M. P. (2018). Progress and potential in organoid research. *Nat. Rev. Genet.* 19 (11), 671–687. doi:10.1038/s41576-018-0051-9

Takasato, M., Er, P. X., Chiu, H. S., and Little, M. H. (2016). Generation of kidney organoids from human pluripotent stem cells. *Nat. Protoc.* 11 (9), 1681–1692. doi:10.1038/nprot.2016.098

frontiers in Bioengineering and Biotechnology

REVIEW
published: 25 November 2021
doi: 10.3389/fbioe.2021.745314

Recent Advances on Cell-Based Co-Culture Strategies for Prevascularization in Tissue Engineering

Sepehr Shafiee[†], *Siavash Shariatzadeh*[†], *Ali Zafari, Alireza Majd and Hassan Niknejad* *

Department of Pharmacology, School of Medicine, Shahid Beheshti University of Medical Sciences, Tehran, Iran

Currently, the fabrication of a functional vascular network to maintain the viability of engineered tissues is a major bottleneck in the way of developing a more advanced engineered construct. Inspired by vasculogenesis during the embryonic period, the *in vitro* prevascularization strategies have focused on optimizing communications and interactions of cells, biomaterial and culture conditions to develop a capillary-like network to tackle the aforementioned issue. Many of these studies employ a combination of endothelial lineage cells and supporting cells such as mesenchymal stem cells, fibroblasts, and perivascular cells to create a lumenized endothelial network. These supporting cells are necessary for the stabilization of the newly developed endothelial network. Moreover, to optimize endothelial network development without impairing biomechanical properties of scaffolds or differentiation of target tissue cells, several other factors, including target tissue, endothelial cell origins, the choice of supporting cell, culture condition, incorporated pro-angiogenic factors, and choice of biomaterial must be taken into account. The prevascularization method can also influence the endothelial lineage cell/supporting cell co-culture system to vascularize the bioengineered constructs. This review aims to investigate the recent advances on standard cells used in in vitro prevascularization methods, their co-culture systems, and conditions in which they form an organized and functional vascular network.

Keywords: co-culture, pre-vascularization, tissue engineering, endothelial cells, mesenchymal stem cells, fibroblast, perivascular cells, endothelial progenitor cells

OPEN ACCESS

Edited by:
Jonathan W. Song, The Ohio State University, United States

Reviewed by:
Valarmathi Mani Thiruvanamalai, University of Illinois at Urbana-Champaign, United States
Hidetoshi Masumoto, RIKEN Center for Biosystems Dynamics Research (BDR), Japan

***Correspondence:**
Hassan Niknejad
niknejad@sbmu.ac.ir

[†]*These authors have contributed equally to this work and share first authorship*

Specialty section:
This article was submitted to Tissue Engineering and Regenerative Medicine, a section of the journal Frontiers in Bioengineering and Biotechnology

Received: *21 July 2021*
Accepted: *02 November 2021*
Published: *25 November 2021*

Citation:
Shafiee S, Shariatzadeh S, Zafari A, Majd A and Niknejad H (2021) Recent Advances on Cell-Based Co-Culture Strategies for Prevascularization in Tissue Engineering. Front. Bioeng. Biotechnol. 9:745314. doi: 10.3389/fbioe.2021.745314

1 INTRODUCTION

The concept of tissue engineering and regenerative medicine originates from the idea of replacing damaged or dysfunctional organs with new regenerated ones. As the tissue grows, oxygen and nutrient supply as well as wastes elimination cannot be achieved by simple diffusion. Therefore, vascular or vascular-like networks are crucial for proper function and survival of any tissue. Central necrosis will happen in engineered tissues thicker than 100–250 μm if there is no efficient vascular bed (Fu et al., 2021). Therefore, developing approaches to form adequate and functional vasculature within artificial tissues and organs and prevascularization of engineered constructs prior to implantation are considered as a promising concept in tissue engineering field (Yazdanpanah et al., 2015). The survival of incorporated stem cells in scaffolds depends on the efficiency and efficacy of networks developed by prevascularization. In order to mimic the physiological structure of the capillaries, some efforts have been dedicated to design perfusable micro-channels in scaffolds

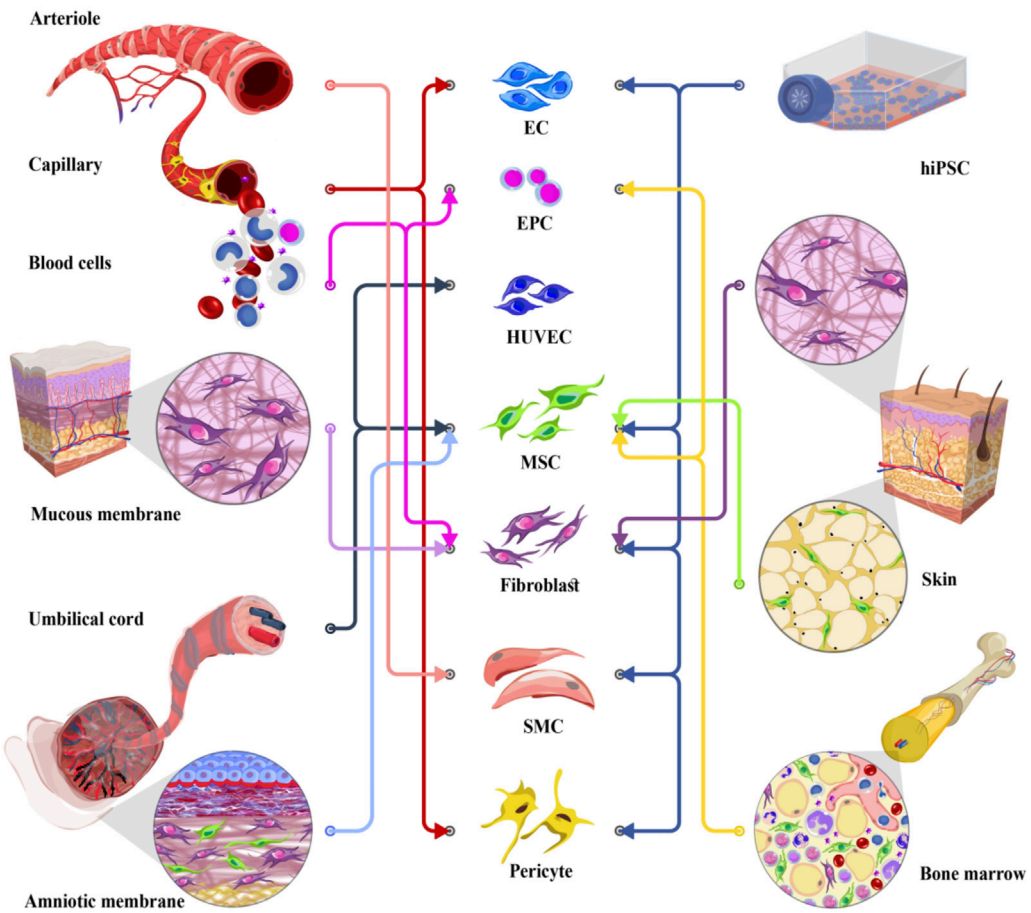

FIGURE 1 | Common cells for prevascularization and their isolation sites. EC (Endothelial cells), EPC (Endothelial progenitor cells), HUVEC (Human umbilical vein endothelial cells), MSC (Mesenchymal stem cells), fibroblast, SMC (Smooth muscle cells), and pericyte have been used for prevascularization of different tissues. Endothelial and supporting cells can be obtained from various cell sources, including skin, mucosal membrane, bone, and peripheral blood, or differentiated from hiPSCs (human induced pluripotent stem cells). Recently, particular attention has been given to the umbilical cord and amniotic membrane as easy to access cell sources. These cells show lower immunogenicity than the other cell lineages, introducing them as excellent candidates in the prevascularization process.

(Farhadihosseinabadi et al., 2018; Figueiredo et al., 2020; Liu et al., 2020). Many studies have tried to use the physiological capability of stem cells for developing a vascular network *de novo*, known as vasculogenesis which can be usually seen in the embryonic period. To induce vasculogenesis, many *in vitro* strategies such as cell sheet engineering, cell spheroid and cell encapsulation, bio-printing and micro-fluid techniques have been introduced. The other methods of prevascularization take advantage of physiological process of angiogenesis, when new blood vessels are developed from the existing vessels (Farhadihosseinabadi et al., 2018). To date, several *in vitro*, *in vivo* and *in situ* prevascularization strategies have been employed to compose functional engineered tissues. *In vivo* prevascularization techniques such as prevascularization via AV-loop, subcutaneous implantation and flaps mostly recruit the angiogenesis process, counting on the ability of host vessels to invade the implanted scaffold (Kiaie et al., 2020; Vidal et al., 2020; Redenski et al., 2021). *In situ* methods employ a combination of *in vitro* and *in vivo* approaches. In all of these methods, endothelial lineage cells are the key part of developing a proper vascular network. Moreover, cell-to-cell interactions, biomaterials, and growth factors profoundly influence *in vitro* prevascularization. Although formation of capillary-like networks can be initiated by endothelial lineage cells, interactions of endothelial and supporting cells are essential for developing a functional vascular network (**Figure 1**).

2 ENDOTHELIAL LINEAGE CELLS

Producing a lumenized endothelial cell network is one of the main milestones of prevascularization (Kiaie et al., 2020; Später

et al., 2020). Endothelial cells (ECs) which form the interior lining of blood vessels, can be obtained from various tissues including umbilical vein, aorta and different micro vessels such as micro vessels in adipose tissue or foreskin (Krüger-Genge et al., 2019). These cells can be differentiated from human induced pluripotent stem cells (hiPSCs) and pluripotent stem cells. (Natividad-Diaz et al., 2019) Furthermore, endothelial progenitor cells (EPCs) can be isolated from peripheral blood and bone marrow (**Figure 1**) (Sun et al., 2020). Appropriate ECs should be selected based on its isolation process and angiogenic properties. ECs are mainly identified by expressing cluster of differentiation (CD) 31 and von Willebrand factor (vWf) in co-cultures, while they express a variety of biomarkers including, Fli-1 (friend leukemia integration-1), CD13, CD29, CD36, CD34, CD39, CD44, CD47, ICAM-1 (intercellular adhesion molecule-1), CD61, CD62, CD80, CD102, CD105, CD106, CXCL16, CD143, CD144, CD146, ADAMTS13 (a disintegrin and metalloproteinase with thrombospondin motifs-13), ADAMTS18, and VE-cadherin (vascular endothelial cadherin). However, it must be taken into account that the ratio of expressed markers can be different in specialized endothelial cell networks (Goncharov et al., 2020). In recent years, different sources of endothelial cells have been used alone or in a co-culture system to form capillary network *in vitro*. In this section, we discuss the most applicable endothelial lineage cells used in prevascularization.

2.1 Human Umbilical Vein Endothelial Cells

Human umbilical vein endothelial cells (HUVECs), well-known for their angiogenic features, are harvested from the endothelium of the umbilical cord veins. Their angiogenic capabilities could be attributed to the existence of a progenitor cell subpopulation within HUVECs (Ingram et al., 2005; Kocherova et al., 2019). These cells express many common EC markers such as CD31, vWf, CD34, CD54, ICAM-1, CD62-E, CD106, VCAM-1 (vascular cell adhesion protein-1), and CD143 (Ma et al., 2014a; Kuss et al., 2018). HUVECs have been used in various prevascularization strategies such as bioprinting. For instance, HUVEC spheroids encapsulated in fibrin and collagen were printed with high rate of viability on scaffolds with tuned surface topological features to control the alignment of the developed capillary-bed (Benning et al., 2018). Considering their simple and low-cost isolation methods, they have been widely used in co-culture systems with a wide variety of supporting and target tissue cells. HUVECs can be co-cultured with mesenchymal stem cells (MSCs) derived from different origins. Adipose tissue mesenchymal stem cells (AD-MSCs) and bone marrow mesenchymal stem cells (BM-MSCs) are known as commonly used MSCs that are frequently co-cultured with HUVECs for prevascularization of various target tissues. BM-MSCs and AD-MSCs show similar vasculogenic capabilities. However, the isolation process of AD-MSCs is more accessible than BM-MSCs (Ma et al., 2014b). In addition to AD-MSCs and BM-MSCs, HUVECs co-culture with amniotic membrane derived mesenchymal cells have shown successful results with a ratio of 1:1 for developing prevascularized micro-tissues (Zhang S. et al., 2017).

Different factors influence the prevascularization of engineered tissues via HUVECs/MSCs co-culture systems including seeding density ratio, growth media and culture conditions. The optimal HUVECs/MSCs ratio recommended by some studies is 5:1 (Kaully et al., 2009; Rao et al., 2012; Ma et al., 2014a). Au et al. reporeted that vascular networks created by cell suspension of HUVECs with the HUVECs/BM-MSCs ratio of 5:1 in a collagen/fibronectin hydrogel remained functional for 130 days after implantation *in vivo* (Au et al., 2008).

Different studies focusing on angiogenesis within bone regeneration have used HUVECs and MSCs co-culture systems. HUVECs/MSCs co-culture can reduce mineralization of the engineered bone tissues. In this matter, subsequent seeding of endothelial cells after reaching proper confluency of MSCs can be a potent solution (Kim et al., 2019). MSCs from different origins support both network formation and osteogenic differentiation of engineered bone constructs. Human umbilical cord mesenchymal stem cells, BM-MSCs, hiPSCs derived mesenchymal stem cells (hiPSC-MSCs) and embryonic stem cell differentiated mesenchymal cells in separate cultures with HUVECs developed vessel-like network on a calcium phosphate cement (CPC) scaffold. In that study, no significant difference in capillary development and mineralization was detected between different type of MSCs which were co-cultured with HUVECs (Chen et al., 2018). Moreover, HUVECs co-cultured with hiPSC-MSCs developed capillary-like structures and promoted mineralization on CPC scaffold, so that a complex and well-organized capillary network was successfully formed at 21 days post-culture. (Liu et al., 2017).

HUVEC/BM-MSC spheroids encapsulated within collagen/fibrin hydrogels showed more favorable capillary-like structure formation and osteogenic differentiation than the cell suspension form (Heo et al., 2019). HUVEC/AD-MSC spheroids with 1:1 ratio encapsulated in hyaluronic acid/gelatin bioactive hydrogels were successfully used for prevascularizing a 3D-bioprinted Polycaprolactone/Hydroxyapatite scaffold. A significant cell migration and sprouting was observed in the co-culture system after 7 days (Kuss et al., 2018). HUVEC/AD-MSC spheroids with a ratio of 1:9 have been bio-printed to make a prevascularized adipose micro-tissue. The cell spheroids formed capillary-like structure within 7–14 days (Benmeridja et al., 2020). HUVEC/BM-MSC spheroids can develop a capillary-like network in fibrin scaffold. The optimal vessel development was achieved in the HUVEC/MSC spheroids with a 1:1 ratio. It is worth noting that there may be less chance of capillary-like developments in HUVEC spheroids alone. Furthermore, MSCs migration always happens after HUVECs migration (Roux et al., 2018)

Different models of cell sheet engineering have been applied for developing prevascularized structures in bone tissue engineering. Zhang et al. developed a prevascularized natural nanofibrous extracellular matrix sheet with high mechanical strength using HUVECs/MSCs (Zhang et al., 2018). Likewise, HUVECs/AD-MSCs magnetic responsive sheets have been used for developing an engineered bone tissue by internalizing iron oxide nanoparticles in the cells (Silva et al., 2020). Furthermore, osseous cell sheets created by osteo-induction of AD-MSCs have

been applied as a bio-paper for bio-printing HUVECs via laser-assisted bioprinting (Kawecki et al., 2018).

Dynamic co-culture and physical tension could enhance both angiogenic and osteogenic differentiation. Culturing HUVECs with BM-MSCs within a dynamic condition of tubular perfusion system bioreactor showed an increase in production of bone morphogenic protein 2 (BMP-2) and development of CD31 network indicating osteogenesis and vasculogenesis (Nguyen et al., 2017). It was concluded that tension could promote osteogenic properties of HUVECs/BM-MSCs cultures (Jiang et al., 2018).

HUVECs/MSCs have been also used for developing a prevascularized engineered cardiac constructs. In a study conducted by Sharma et al. a confluent culture of MSCs on a fibroblast-derived nanoscale extracellular matrix (ECM) scaffold formed a CD166 tracks aligned with ECM nano-fibers. Subsequent seeding of HUVECs on the developed scaffold resulted in formation of a well-organized capillaries aligned with CD166 tracks (Qian et al., 2019). Culturing HUVECs and fibroblasts on a micro-patterned polyethersulfone/polyvinylpyrrolidone membranes also formed an aligned network with topological features of membranes (Skrzypek et al., 2018). It seems that the origin of MSCs profoundly affect the vascularization capability of HUVECs. HUVECs in culture with dermal fibroblast, AD-MSCs, BM-MSCs and Wharton's jelly-MSCs were used to prevascularize both agarose-collagen and fibrin hydrogels. Particularly, capillary networks were more noteworthy in co-cultures on fibrin hydrogels as well as HUVECs/fibroblasts and AD-MSCs co-culture, while co-cultures containing BM-MSCs developed less significant capillary-like structures (Kniebs et al., 2020).

2.2 Endothelial Progenitor Cells

Endothelial Progenitor Cells (EPCs), which are circulating in the peripheral blood, play a crucial part in regeneration of vasculature bed endothelial lining. EPCs are also more proliferative and potent than the adult endothelial cells, where their pro-angiogenic properties are more noteworthy than that of non-progenitor endothelial cells (Asahara et al., 1997; Aicher et al., 2006). They can be derived from bone marrow, peripheral blood, umbilical cord blood and also can be harvested by differentiation of the hiPSCs (Garikipati and Kishore, 2017; Huizer et al., 2017). Endothelial colony-forming cells (ECFCs) are adult EPCs that take part in vasculogenesis and regenerating endothelial lining. The EPCs derived from human cord blood (human cord blood endothelial colony-forming cells or hCB-ECFCs) show much greater proliferative and angiogenic abilities compared with EPCs isolated from human peripheral blood (hPB-ECFCs) (Peters, 2018). Until now, EPCs have been used for vascularizing common scaffolds such as decellularized scaffolds (Guo et al., 2018), Poly-Ethylene Glycol Hydrogel (Peters et al., 2016), and Matrigel (Iqbal et al., 2017; Rosca et al., 2018). With all the controversies over the EPCs and their applications, they show promising potentials for scaffold vascularization (Peters, 2018). EPCs ability to develop capillary-like networks in culture with osteoblasts (Fuchs et al., 2007), fibroblasts (Dai et al., 2018) and mesenchymal stem cells (Liu H. et al., 2018) has been demonstrated in several studies.

In spite of many encouraging results obtained from using EPCs for prevascularization, some concerns still remain regarding their origin and classification. In fact, there is variation in definition of EPCs phenotype and their distinctive features in the literature (**Table 1**). Some authors divided EPCs into two categories, including hematopoietic EPCs which are stem cells originated from bone marrow with pro-vasculogenic properties, and non-hematopoietic EPCs which have ECs phenotype with less potency for pro-vasculogenic features (Garikipati and Kishore, 2017). In another classification, these cells have been categorized into two subpopulations including early EPCs and late EPCs with different angiogenic features. Early EPCs are spindle shaped and possess extensive proliferative abilities in the second and third week after isolation; however, their proliferative potential is limited after 6 weeks. It has been reported that they are also involved in innate immunity and inflammation. As a result, their application is limited because they may raise inflammatory responses and consequently cause graft rejection (Cheng et al., 2013). Late EPCs are cobblestone shaped that form primitive colonies after 3 weeks and are far more proliferative than early EPCs (Fedorovich et al., 2010). There is an agreement now that late EPCs contribute in angiogenesis and the early EPCs may indirectly join in endothelial network formation (Medina et al., 2010). Although there are many controversies surrounding the specific biomarkers for EPCs isolation, some markers such as CD34, CD133, and VEGFR2 (vascular endothelial growth factor receptor-2) have been frequently used for identification of these cells (Sen et al., 2011).

Recently, EPCs co-cultured with different supporting cells have been successfully used for prevascularization. Growth factors released from MSCs, including VEGF (vascular endothelial growth factor) and bFGF (basic fibroblast growth factor), enhance angiogenic capability of EPCs (Fauza et al., 2018). EPCs from peripheral blood combined with peripheral blood MSCs were used for prevascularizing a 3D biphasic calcium phosphate bio-ceramic. In that study, the expression of VEGF, PDGF (platelet-derived growth factor) and alkaline phosphatase significantly increased in EPCs/MSCs co-culture (Chen et al., 2019). It has been reported that the optimal angiogenic and osteogenic value were observed in in PB-EPCs/BM-MSCs cultures within 1:3 or 2:1 ratio (Peng et al., 2019). Moreover, a prevascularized patch with antifibrotic properties have been developed by bioprinting EPCs and BM-MSCs on a decellularized liver scaffold (Wonil et al., 2018).

EPCs isolated from cord blood in culture with fibroblasts developed a capillary-like network in 7 days with a similar morphology to HUVECs/fibroblasts co-culture. Interestingly, EPCs/fibroblasts made anastomosis with the host vasculature earlier than HUVECs/fibroblasts and signs of blood perfusion was appeared after 1 day of implantation. It was observed that higher ratio of fibroblasts can result in stronger anastomosis to the host vasculature (Chen et al., 2010). Lee et al. used a co-culture system by peripheral blood isolated EPCs and human mucosal fibroblasts and keratinocytes to develop a skin tissue construct.

TABLE 1 | Common markers used for isolation of endothelial cells and supporting cells.

Cell type	Specific cell category		Markers used for isolation		References
			Positive	Negative	
Endothelial lineage cells	HUVECs		CD31, CD34, CD40, CD54, CD62-E, CD106, CD143, vWf, ICAM-1, VCAM-1, VE-cadherin, ADAMTS13, ADAMTS18	-	Chopra et al. (2018)
	EPCs				Bouïs et al. (2001)
		Early EPCs	CD14, CD31, CD45, CD133, vWF	-	Peters (2018)
		Late EPCs(OECs)	CD31, CD34, CD133, vWF, VEGFR-2, VE-cadherin	CD14, CD45, CD115	Jang et al. (2019)
		Non-hematopoietic EPCs	CD31, CD34, CD105, CD146, VEGFR-2, VE-cadherin	CD133	Hofmann et al. (2009)
		Hematopoietic EPCs	CD31, CD34, CD105, CD133, VEGFR-2, CXCR-4, c-Kit	-	Garikipati and Kishore, (2017)
		ECFCs	CD31, CD34, CD44, vWF, VEGFR-2, VE-cadherin	CD14, CD45, CD115, CD133	Khaki et al. (2018)
		CECs	CD31, CD34, CD44, CD146, vWF, VEGFR-2, VE-cadherin	CD45	Oswald et al. (2004)
	Microvascular and differentiated endothelial cells				Müller et al. (2002)
		hDMECs	CD31, CD36, CD40, CD144, vWF	-	Mukai et al. (2008)
		hiPSC-ECs	CD31, CD49d, CD105, CD144, vWF, VEGFR-2, VE-cadherin	-	Sukmawati and Tanaka, (2015)
		MSC-ECs	CD31, CD44, CD73, CD105, CD144, vWF, VCAM-1, FLT-1, VEGFR-2, VE-cadherin	-	Swerlick et al. (1992)
					Xing et al. (2020)
Supporting cells	MSCs		CD11, CD44, CD73, CD90, CD105, CD106, CD166, Integrin-α1, IGF-2	CD11b, CD19, CD34, CD45, HLA-DR	De Souza et al. (2016a)
	Fibroblasts		CD9, CD29, CD44, CD73, CD90, CD105, CD166, MMP-1, MMP-3	CD146	Lynch and Watt, (2018)
	Pericytes		CD73, CD90, CD105, CD146, PDGFRβ, α-SMA, NG2, Desmin, RGS5	-	Owens and Wise (1997), Xueyong et al. (2008)
	VSMCs		CD73, CD90, CD105, α-SMA, PDGFRβ, H-caldesmon, Smoothelin, Calponin	-	Viswanathan et al. (2019)

HUVECs, Human umbilical vein endothelial cells; EPCs, Endothelial progenitor cells; OECs, Outgrowth endothelial cells; ECFCs, Endothelial colony forming cells; CECs, Circulating endothelial cells; hDMECs, Human dermal microvascular endothelial cells; hiPSC-ECs, Human induced pluripotent stem cells derived endothelial cells; MSC-EC, Mesenchymal stem cell-derived endothelial cells; MSCs, Mesenchymal stem cells; VSMCs, Vascular smooth muscle cells; CD, Cluster of differentiation; vWF, von Willebrand factor; ICAM-1, Intercellular adhesion molecule-1; VCAM-1, Vascular cell adhesion molecule-1; ADAMTS, A disintegrin and metalloproteinase with thrombospondin motifs;VEGFR-2, Vascular endothelial growth factor receptor 2;VE-cadherin, Vascular endothelial cadherin;CXCR-4, C-X-C chemokine receptor type 4; FLT-1, FMS-like tyrosine kinase-1; IGF-2, Insulin-like growth factor-2; HLA-DR, Human leukocyte antigen-DR; MMP, Matrix metalloproteinase; PDGFRβ, Platelet-derived growth factor receptor β; α–SMA, α-Smooth muscle actin; NG-2, Neuron-glial antigen 2; RGS-5, Regulator of G-protein signaling 5.

They seeded EPCs on a fibroblast-incorporated fibrin layer. Then, keratinocytes were seeded subsequently on the developed scaffold. It was showed that their co-cultured system formed a prevascularized construct whit successful results in the excisional wound of a nude mice (Lee et al., 2019).

2.3 Microvascular and Adult Endothelial Cells

Adult endothelial cells have limited proliferation. These cells are highly specialized and exhibit unique morphology and characteristics in tissues like liver and kidney, which limit their potential application in prevascularization (Bale et al., 2015). However, microvascular endothelial cells such as human dermal microvascular endothelial cells (hDMECs), adult human cardiac endothelial cells (hCECs), adult human pulmonary artery endothelial cells (hPAECs), and aortic endothelial cells have been successfully used for prevascularization of engineered tissue constructs (Jiang et al., 2018; Manikowski et al., 2018). For instance, aortic endothelial cells in co-culture with BM-MSCs developed microvasculature after 14 days of culture (Pekozer et al., 2016).

MSCs co-culture with other adult endothelial cells such as human cardiac microvascular endothelial cells (hCMVECs) has been found to be effective to produce a functional prevascularized 3D cardiac graft (Valarmathi et al., 2018). hCMVECs in the present of MSCs could successfully form a capillary-like network in a 3D collagen cell carrier (CCC) within 7 days under vasculogenic conditions. Later, hiPSC-derived embryonic cardiomyocytes were cultured on the prevascularized CCC

under myogenic conditions for another week to achieve myogenic differentiation (Valarmathi et al., 2017). Human adipose tissue microvascular endothelial cells (hAMECs) are potent candidates for prevascularization of skin and soft tissue substitutes. Promising results have been reported in co-seeding of hAMECs and adult normal human dermal fibroblasts to form a well-organized vascular network. The optimal mechanical strength and capillary development are achieved in ECs/fibroblasts ratio of 4:1. It is observed that modifying the ECs/fibroblasts ratio can change the pattern of vascular network, giving researchers more choices for prevascularization of different tissues (Czajka and Drake, 2014). For instance, human dermal microvessel endothelial cells isolated from foreskin in culture with gingival fibroblasts and gingival epithelial cells, by an ECs/fibroblasts ratio of 1:1 were used to develop a prevascularized buccal mucosa substitute, with the potential application in urethral defects (Heller et al., 2016). In another example, a complex capillary-like network was developed by human dermal fibroblasts (hDFs) co-cultured with hDMECs with ratio 1:1 in thermoresponsive biomimetic polyisocyanopeptide (PIC) with pore diameters of 100–150 μm (Zimoch et al., 2018). In another study Sasagawa et al. created a construct using human aortic endothelial cells entrapped between two hDFs cell sheets that successfully developed a $CD31^+$ network within 3 days (Sasagawa et al., 2014).

2.4 Stem Cell-Derived Endothelial Cells

Finding an autologous endothelial cell source is one of the main challenges of prevascularization. Endothelial cells can be differentiated from different stem cell sources such as MSCs, hiPSCs, and also from embryonic stem cells, fetal pluripotent stem cells, and totipotent embryo stem cells (Xu et al., 2019). Several strategies have been employed for the endothelial differentiation of stem cells. Most of these strategies use an endothelial differentiation medium that contains growth factors such as VEGF (Oswald et al., 2004; Wu et al., 2007; Wang et al., 2018). A 2D monolayer or a 3D embryoid body of hiPSCs or embryonic stem cells can be differentiated into endothelial lineage cells using an endothelial differentiation medium (Kim et al., 2007; Zhang J. et al., 2017; Suresh and West, 2020). Furthermore, the pluripotent stem cells can be co-cultured with OP9 stromal cells that produce endothelial differentiating factors (Figueiredo et al., 2015). As another strategy, genetic modification can be used for endothelial differentiation of the embryonic stem cells and hiPSCs. For Instance, Wang et al. differentiated endothelial cells from hiPSCs by altering the transcription factor E26 transformation-specific variant 2 or ETV2 gene (Wang K. et al., 2020). Lindgren et al. also modified the expression of ETV2 for endothelial differentiation of embryonic stem cells (Lindgren et al., 2015). In addition to ETV2, alteration of the other transcriptional factors such as GATA-2, LMO-2, and TAL-1 have been proposed as a strategy for endothelial differentiation of stem cells (Elcheva et al., 2014; Lange et al., 2020). After endothelial differentiation, endothelial-specific markers such as CD31, CD34, CD144, VEGFR-2, and vWF have been used for confirming the endothelial differentiation of stem cells (Kennedy et al., 2021). There are still several questions regarding the functionality of endothelial cells differentiated from hiPSCs. Li et al. observed that endothelial cells derived from hiPSC have a significantly decreased proliferation rate than those derived from embryonic stem cells, and they can lose their endothelial phenotype and markers through passages (Li et al., 2011). Although ECs differentiated from hiPSCs have been used to develop functional capillary beds, it has been shown that the vascular network developed by hiPSCs had less density than the vascular network created by HUVECs (Bezenah et al., 2018). Further investigations are required on the effect of various endothelial differentiation strategies on network forming ability of stem cell-derived endothelial cells.

Several studies used stem cell-derived endothelial cells for prevascularization. Culture of various ECs, such as hCECs, hPAECs, hiPSCs derived endothelial cells (hiPSC-ECs) with adipose-derived stromal cells successfully developed a well-formed capillary-like network (Calderon et al., 2017; Manikowski et al., 2018). However, it was observed that without external growth factors, the developed network collapsed, and ECs mono-culture could not complete the capillary-like network (Manikowski et al., 2018). In another study, co-culture of ECs differentiated from BM-MSCs of Witsar rat with BM-MSCs have been used for developing a scaffold-free cell sheet. Accordingly, the development of a capillary-like network and lumen formation was observed within a week that eventually promoted repair of the rat cranial bone defects (Xu et al., 2019). Moreover, MSC-derived $CD31^+$ endothelial cells in culture with AD-MSCs and MSC-derived fibroblasts were successfully used for prevascularizing a fibroblast niche coated tissue engineered dermal graft (TEDG) scaffold, which was developed as a skin substitute (Ajit et al., 2020). In another study, Masuda et al. developed a cardiac cell sheet using rat embryonic stem cell-derived ECs, dermal fibroblasts and embryonic stem cell-derived cardiomyocytes. It was reported that cardiomyocytes could promote endothelial cell differentiation and sprouting (Masuda et al., 2015). Overall, stem cell-differentiated endothelial cells represent a valid and promising cell source for prevascularization. However, prior to clinical application of these cells in prevascularized constructs, it is important to resolve concerns regarding the efficiency of these cells in fabricating endothelial networks, and their teratogenicity.

3 SUPPORTING CELLS

To achieve proper perfusion in engineered tissue constructs, the quality of vessels is as vital as their length and sprout numbers. Development of these functional networks can be achieved using supporting cells along with endothelial cells. Combination of endothelial lineage cells with target tissue cells and supporting cells like fibroblasts (Sorrell et al., 2007), smooth muscle cells (Fillinger et al., 1997), mesenchymal stem cells (Aguirre et al., 2010), pericyte cells (Antonelli-Orlidge et al., 1989), epithelial cells (Kim et al., 2002), and osteoblasts (Hofmann et al., 2008) seems to be a potential solution for vascularization of engineered tissue constructs. Supporting cells affect the formation and

organization of capillary networks directly, while target tissue cells such as cardiomyocytes, osteoblasts, epithelial cells, keratinocytes, and neural cells have an indirect effect (Grellier et al., 2009). Supporting cells facilitate inosculation to the host vasculature in addition to their ability to improve ECs viability and proliferation and they also stabilize newly formed vessels by inhibiting uncontrolled angiogenesis. The effectiveness and supportive role of supporting cells are owing to the production of growth factors and ECM, resulting in stabilizing the capillary-like formations. In fact, these cells not only support and stabilize newly formed capillaries, but also act as a source of pro-angiogenic growth factors such as VEGF and bFGF.

3.1 Mesenchymal Stem Cells

Mesenchymal stem cells, as the first group of supporting cells, are able to differentiate into various cell types such as pericytes, adipocytes, chondrocytes, myocytes and osteoblasts (Caplan, 1991; Abbasi-Kangevari et al., 2019). They can be harvested from different tissues including bone marrow (BM-MSCs), adipose tissue (AD-MSCs), placenta, umbilical cord, amniotic fluid, peripheral blood (PB-MSC), dental pulp, limbal stroma as well as differentiated hiPSCs (Funderburgh et al., 2016). They express various surface markers including CD11, CD44, CD73, CD90, CD105, CD106, and CD166. However, these cells do not express CD14, CD34, and CD45 (Avolio et al., 2017; Valarmathi et al., 2018) (**Table 1**). The angiogenic ability of MSCs is differ from each other, so that they morphologically form different vessel networks depending on their origins. For example, the morphology of vessels induced by umbilical artery, umbilical vein and "Wharton's jelly" mesenchymal cells are different (Xu et al., 2017).

AD-MSCs are preferred in many studies due to their simple isolation and their ability to induce angiogenesis (Chen et al., 2015; Freiman et al., 2016). The umbilical-derived mesenchymal cells have a great angiogenic ability, while the placenta-derived MSCs show a higher proliferation rate, multi-lineage differentiation capability and lower immunogenicity (Kargozar et al., 2018). It is worth to mention that the hiPSC-MSCs and BM-MSCs both promote vascularization, even though telomerase activity is 10-fold greater in hiPSC-MSCs than in BM-MSCs (Chen et al., 2018).

MSCs have been used in many studies due to their abilities to promote vessel formation and maturation by different mechanisms (Navone et al., 2014; Oki et al., 2018). The MSCs produce pro-angiogenic cytokines such as hypoxia-inducible factor 1α (HIF-1α), angiogenin, angiopoietin I, angiopoietin II, angiopoietin IV, interleukin-1β (IL-1β), interleukin-6 (IL-6), interleukin-8 (IL-8), insulin-like growth factor 1 (IGF-1), VEGF, bFGF, PDGF, transforming growth factor-β (TGF-β), monocyte chemoattractant protein-1 (MCP-1), and as well as by triggering the VEGF-A signaling cascade. They are also capable of producing anti-angiogenic factors such as angiostatin and vasohibin (Bandara et al., 2017; Rezaie et al., 2019; Maacha et al., 2020). Therefore, the balance between autocrine and paracrine secretion of pro-angiogenic and anti-angiogenic factors is responsible for promoting vasculogenesis and stabilizing the newly formed vessels by adjusting the permeability of new vessels through manipulation of cell-to-cell junctions (Ghajar et al., 2006; Sorrell et al., 2009; Bussche and Van De Walle, 2014). Origin of MSCs, culture environment, culture growth factors, scaffold, and co-culture ratio can contribute to the ability of MSCs for utilization for prevascularization.

In recent years, several studies suggested the potential use of MSCs exosomes for inducing angiogenesis (Moghadasi et al., 2021). Moreover, mesenchymal exosomes extracted from the placenta and adipose tissue can be a promising tool for prevascularization (Liang et al., 2016; Komaki et al., 2017). However, there are contradictory findings regarding the angiogenic effect of BM-MSC derived exosomes. Lee et al. showed BM-MSCs' exosomes could suppress angiogenesis (Lee et al., 2013).

MSCs can be differentiated into the endothelial lineage cells. Du et al. induced MSCs in culture with osteogenic MSCs prevascularized mesoporous bioactive glass (MBG) scaffold where they used 10 ng/ml of bFGF and 40 ng/ml of VEGF to induce endothelial differentiation in AD-MSCs. MSC-EC were positive for CD31 and vWF (Du et al., 2018). It is also reported that BM-MSCs can differentiate into ECs in a non-direct co-culture with ECs. It was observed that ECs induced differentiation of BM-MSCs into CD31 positive cells (Li et al., 2018).

3.2 Fibroblasts

Fibroblasts, as the main producers of ECM collagen, have an essential role in angiogenesis and wound healing process. These cells have been utilized in co-culture with endothelial cell lines such as HUVECs, EPCs, and microvascular endothelial cells (MVECs) to develop a prevascularized skin substitute (Sorrell et al., 2007; Dai et al., 2018). Fibroblasts are mostly isolated from skin, mucosal membrane and other soft tissues. Both the method and the site of isolation are considered as the important factors for the angiogenic ability of fibroblasts (Bishop et al., 1999). It was reported that formation of a capillary-like network was only observed in the culture of endothelial lineage cells with human dermal fibroblasts, not in culture with neonatal human foreskin fibroblasts 1 (hFF-1) (Costa-Almeida et al., 2014).

Since fibroblasts have mesenchymal origins, no significant marker has been identified for distinction of MSCs and fibroblasts. Markers like CD9, CD29, CD44, CD90, CD105, CD166, and CD73 are expressed in both MSCs and fibroblasts. However, there is a slight difference between the expression levels of some markers in MSCs and fibroblasts. The expression of CD106, integrin alpha 1, and IGF-2 (insulin-like growth factor 2) are high in MSCs, while MMP-1(matrix metalloproteinase-1), and MMP-3 are highly expressed by fibroblasts. Moreover, fibroblasts show a lower expression of CD146 compared with MSCs (Costa-Almeida et al., 2018).

Paracrine interactions between fibroblasts and ECs would regulate angiogenesis (Montesano et al., 1993). Physical stimulation can affect paracrine signaling, which induces angiogenesis. For instance, mechanical strain helps to stabilize capillary network assembly, and electrical stimulation can promote angiogenesis by ECs/fibroblasts interaction (Landau et al., 2018; Geng et al., 2019). In a study conducted by

Asakawa et al., HUVECs cell sheet stacked with two hDFs cell sheets on a fibrin layer in five different orders. The best network formation with the highest relative vascular network lumen area was observed when HUVECs sheets directly placed on the fibrin layer and under the two fibroblast sheets (Asakawa et al., 2010). Using layer by layer assembly, Miyazaki et al. developed a prevascularized skin substitute by HUVECs and neonatal hDFs co-culture. In that study, HUVECs showed elongation at days 4 and 7 post-culture, where the vessel-like lumenized structures were clearly observed (Miyazaki et al., 2019).

HUVECs/fibroblast's co-culture have been frequently used alongside another supporting cells or target tissue cells in different tri-culture methods. Using self-assembly and re-seeding methods, Jakubowska et al. constructed a prevascularized vaginal mucosa substitute through tri-culture of HUVECs/fibroblasts/epithelial cells, with a HUVECs/fibroblasts ratio of 2:1 (Jakubowska et al., 2020). In another study, in a tri-culture system, HUVECs and human respiratory epithelial cell were cultured with hDFs or human nasal fibroblasts in a fibrin gel and agarose-collagen type 1 scaffold which successfully formed a prevascularized respiratory mucosa.

Adding small molecules can alter network formation and morphology in an ECs/fibroblasts co-culture system. For instance, adding trehalose in a HUVECs/human normal dermal fibroblasts co-culture with a growth media containing VEGF can inhibit network formation and altering endothelial cell morphology through inhibition of VEGFR2 receptor in a dose-dependent manner. Moreover, fibroblasts in this co-culture system showed myofibroblasts' phenotype and supported endothelial vessel network which was identified by presentation of α-smooth muscle actin (α-SMA) (Takeuchi et al., 2011). Recently, we used lacto-n-neotetraose to improve the healing process of full-thickness wounds in the mice models. Our results showed that subcutaneously injection of this oligosaccharide significantly increased the expression of VEGF in the wound bed. These findings highlight the great potential of natural materials to induce secretion of angiogenic factors within the implant sites (Farhadihosseinabadi et al., 2020).

3.3 Perivascular Cells

Perivascular cells including vascular smooth muscle cells (VSMCs) and pericytes regulate many features of natural vessels (Kerkar et al., 2006). VSMCs surround larger arteries, while pericytes wrap around capillaries to stabilize the newly formed vessel. VSMCs can be differentiated from mesenchymal stem cells, human embryonic stem cells, skin fibroblasts, hiPSCs or isolated from vascular tissues such as aortic ring and human umbilical cord (Montezano et al., 2017; Pang and Thomas, 2018; Perry et al., 2019). VSMCs show two different major phenotypes: synthetic and contractile. Synthetic phenotype, which is usually observed near sites of vascular remodeling, has more remarkable proliferative ability than the spindle-shaped contractile type which has less proliferative capacity and more contractile fibers (Metz et al., 2012). VSMCs isolated from microvessels and their native environment initially show spindle-shaped phenotype with a hill and valley morphology of synthetic type after growing in culture media (Kwartler et al., 2016). VSMCs in angiogenesis models are identified by α-SMA. The contractile phenotype of these smooth muscle cells is characterized by smooth muscle myosin heavy chain, smoothelin, calponin, and SM22α (Owens and Wise, 1997).

ECs and VSMCs act as a coupled system for transmission of signals from receptors localized on the endothelium surface and vice versa. Angiogenic growth factors expression will be higher when cell-to-cell interactions exist in this co-culture system (Heydarkhan-Hagvall et al., 2003). In a bilayer co-culture system, provoked by ECs-SMCs physical contacts, ECs influence SMCs' morphology, proliferation rate, and protein production (Fillinger et al., 1993). It has been demonstrated that down regulation of PDGF expression in a spheroidal co-culture system of ECs and SMCs can inhibit apoptosis of ECs, resulting in longer viability of the vessels (Korff et al., 2001). In a study, pre-culturing of SMCs on decellularized native bone scaffold and subsequent seeding of HUVECs induced tubulogenesis. Moreover, higher vascular density and lumen formation was observed after using this method by dynamic culturing in a bio-reactor (Liu X. et al., 2018).

SMC spheroids have been used for stabilizing a mono-layer of HUVECs for developing a double-layered vascular-like structures. In that study, HUVECs were seeded around a golden needle and the encapsulated SMC spheroid were added subsequently. After 4 days of HUVECs/SMCs incubation, the bi-layer structure was separated from the needle where they showed a well-formed network vessels (Shimazu et al., 2019).

Pericytes are attached to the abluminal side of ECs, where they are around the basement membrane. These cells show excellent pro-angiogenic capabilities (Avolio et al., 2017). These cells can be harvested from umbilical cord, adipose tissue, human heart, skeletal muscle, dental pulp, saphenous vein and also from differentiation of hiPSCs (Sims, 1986; Geevarghese and Herman, 2014). Pericytes express markers such as α-SMA, NG2 (neuron-glial antigen 2), desmin, and RGS5 (regulator of G-protein signaling 5). Additionally, they represent CD73, CD90, CD105, CD146, and PDGFRβ, which are also produced by MSCs. It seems that some MSCs can be differentiated into pericytes. These differentiated cells express pericyte markers with pericyte-like morphology in ECs/MSCs co-culture, which support the endothelial network (De Souza et al., 2016a). When EPCs and MSCs were seeded on 3D polyurethane, the constructed vessels were positive for common pericytes' markers, supporting the hypothesis that MSCs in co-culture with EPCs can be differentiated into pericytes. Furthermore, MSCs can be differentiated into pericytes after subsequent addition into a pre-formed capillary-like network (McFadden et al., 2013). Similarly, pericytes have the ability to be differentiated to the other mesenchymal-originated cells such as SMCs, fibroblasts and osteoblasts that can significantly alter metabolic and mechanical properties of these supporting cells as well as signaling cascades of ECs (Armulik et al., 2005; Bergers and Song, 2005; Blocki et al., 2013; Orlova et al., 2014).

While ECs/pericytes in a 3D co-culture can result in tube-like formations, a 2D co-culture with ECs/pericytes direct contact does not form such structures (Darland and D'amore, 2001).

Several studies indicated that pericytes might act as inhibitors of ECs proliferation. It has been suggested that pericytes prevent proliferation of ECs via contact inhibition. Although, they inhibit proliferation of ECs, they stabilize the forming vessels and alter tube length lumen diameter and sprouting (Orlidge and D'amore, 1987; Waters et al., 2013).

Pericytes have been used in tri-culture system in the presence of HUVECs and hiPSC-MSCs with a HUVECs/pericytes ratio of 4:1 for prevascularizing a calcium-phosphate scaffold. In that investigation, both angiogenesis and osteogenesis were significantly promoted after implantation the developed construct in the rat cranial bone defect (Zhang C. et al., 2017).

Pericyte-like MSCs and SMCs can support the newly formed endothelial cell network in culture with EPCs (Loibl et al., 2014). Cell sheets engineered by EPCs and SMCs differentiated from MSCs improved ejection fraction of infarcted cardiac muscles (Shudo et al., 2017). It is reported that prevascularization of a polystyrene scaffold was achieved by co-culture of EPCs and SMCs with a 6:1 ratio (Jia et al., 2018a).

3.4 Differentiated Cells in Target Tissues

The native cells of the target tissue can indirectly affect differentiation and proliferation of ECs and development of the capillary-like networks. Besides, vascular development can affect the tissue-resident cells behaviors. These reciprocal interactions can influence the formation of prevascularized target tissues such as neural networks. HUVECs in co-culture with Witsar rat neural cells by a ratio of 1:2.5 were used for prevascularization of a poly (L-lactide) (PLLA)/poly (lactide-co-glycolide) (PLGA) scaffold. It was observed that interaction between endothelial cell network and neural cells lead to development of a more complex neural network and morphologies (Shor et al., 2018). Vascular growth can interfere with development of myotubules formations. HUVECs in culture with skeletal muscle cells isolated from fresh human muscle tissue were used for prevascularization of skeletal muscle constructs. In that study, two methods have been evaluated. In the first method, direct co-culture of HUVECs and skeletal muscle cells were considered for developing a prevascularized construct, while in the second method myotubules differentiated in a HUVECs free environment and endothelial cells in a fibril hydrogel were subsequently added. The findings indicated that in the first method, myotubules development was suboptimal and endothelial network development interfered with myotubules differentiation. However, subsequent addition of endothelial cells resulted in better capillary network development without interfering with myotubule differentiation (Gholobova et al., 2020).

The development of vascular network does not always hinder differentiation of target tissue cells and even sometimes endothelial cell differentiation can enhance capabilities of target tissue cells and promote target tissue cell proliferation. Using layer by layer assembly, HUVECs in culture with human hepatocytes and fibroblasts were used for developing a 3D liver engineered tissue construct. After implantation, prevascularized construct produced more albumin, which indicates that prevascularization can enhance performance of hepatocytes (Sasaki et al., 2017). In another study, a sub-population of EPCs, outgrowth endothelial cells (OECs) from peripheral blood, cultured with human primary osteoblasts were used for prevascularization of platelet-rich fibrin (PRF). It was reported that capillary-like structures were developed 7 days post-culture and primary osteoblasts promoted angiogenic abilities of EPCs (Dohle et al., 2018).

Several strategies such as adding small molecules, culturing under hypoxic condition and subsequent seeding of endothelial cells have been considered to promote ECs/target tissue cells interactions. Co-culture of HUVECs and human endometrial epithelial cells with a 1:1 ratio in a 3D collagen scaffold was successfully used for developing an endothelial network. It was showed that adding estradiol could not influence endothelial cell behaviors directly, however, estradiol increased endogenous VEGF levels of endometrial epithelial cells which promoted endothelial network formation (Pence et al., 2015).

Short term hypoxia improves development of a capillary-like network in an ECs/primary osteoblasts co-culture. However, prolonged hypoxia is considered as a cytotoxic parameter that shows negative effect on capillary network formation. (Gholobova et al., 2020) Sometimes, ECs can be used with heterogeneous populations of stem cells for fabricating a capillary-like network. HUVECs in co-culture with amniotic fluid stem cells were utilized for prevascularization of a collagen chondroitin sulfate scaffold. Culturing under hypoxic conditions did not result in better capillary formation development. It was revealed that hypoxia increased VEGF, PDGF, and VEGR1, but reduced expression of VEGFR2 (Lloyd-Griffith et al., 2015). In some studies, instead of using an isolated cell line, cellular extract or isolated heterogeneous cell population or isolated microvessels were used for prevascularizing scaffolds. For instance, stromal vascular fraction (SVF) (isolated from adipose tissue which contains mesenchymal cells, endothelial progenitor cells, hematopoietic lineage cells and stromal cells, fibroblast and pericytes) and micro vascular fraction (MVF-microvascular fragments that are usually isolated from adipose tissue) can be used for prevascularization of engineered tissue constructs. It has been shown that wound healing can be promoted by encapsulating SVF cells in a collagen-fibrin hydrogel (Nilforoushzadeh et al., 2019). In another study, a prevascularized adipose tissue was constructed by using MVF (Acosta et al., 2020). Furthermore, a prevascularized skin substitute was developed utilizing MVF and SVF via *in vivo* prevascularization methods (Später et al., 2018). In another study amniotic fluid stem cells cultured with HUVECs with a ratio of 4:1 resulted in prevascularization of a collagen chondroitin sulphate scaffold in 7 days (Lloyd-Griffith et al., 2015).

4 CO-CULTURE SYSTEM OPTIMIZATION

Providing a proper environment for proliferation and migration of endothelial cells, and development of a capillary-like network assembly with the help of supporting cells can be somewhat challenging since many considerations including the following

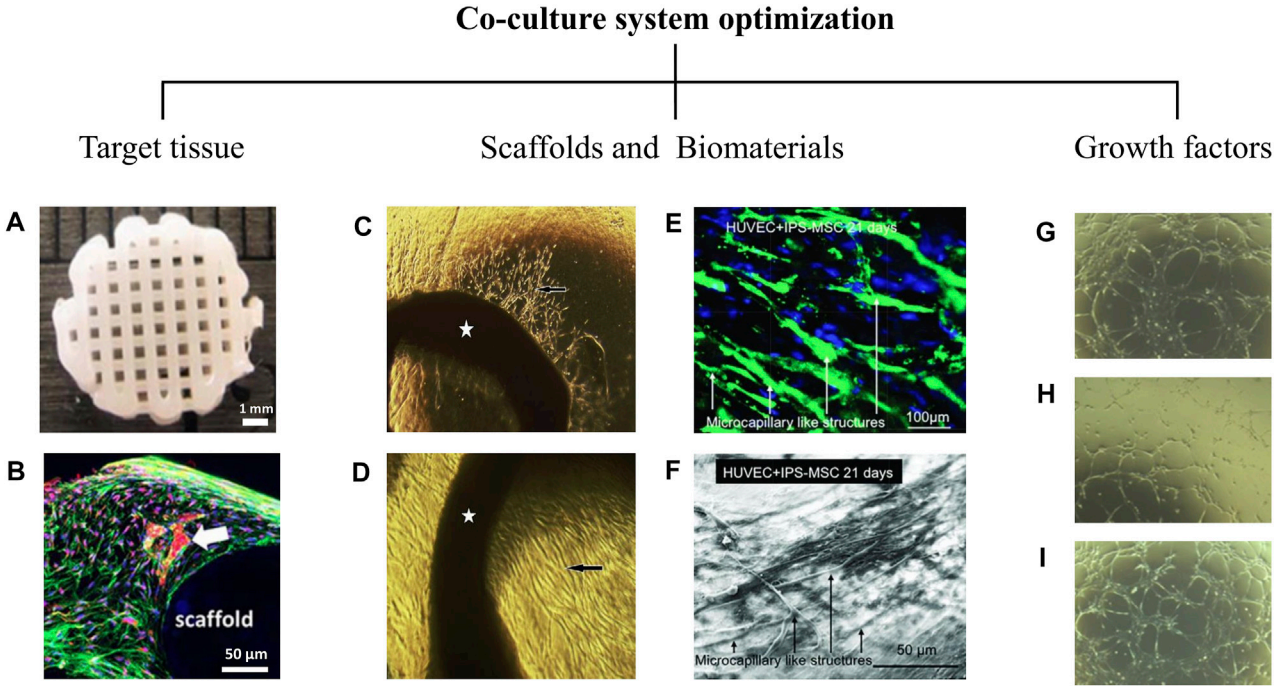

FIGURE 2 | Co-culture system optimization. Co-culture system optimization depends on critical factors that profoundly alter cell behaviors. Target tissue is a decisive factor in the vascularization process. The cellular microenvironment is another critical factor that influences prevascularization. As shown in the **(A,B)**, co-culture of AD-MSCs (Adipose tissue derived mesenchymal stem cells) and HUVECs (Human umbilical vein endothelial cells) in a 3D printed polycaprolactone/hydroxyapatite scaffold coated with cell-laden hydrogels leads to the formation of an appropriate capillary network (white arrow) at day 21 (Kuss et al., 2018). It is evident that topographical and physicochemical properties and even the type of biomaterial used in scaffolds affect prevascularization. **(C,D)** Aortic rings (pointed by stars) cultured on the mesenchymal side **(C)** and epithelial side **(D)** of a decellularized amniotic membrane developed in our laboratory. After 7 days of culture, capillary-like structures and endothelial-like penetrations (black arrows) have been identified on both sides of the amniotic membrane (original magnification X40) (Niknejad et al., 2013). **(E,F)** HUVECs and hiPSC-MSC (human induced pluripotent stem cell derived mesenchymal stem cells) co-culture on a calcium phosphate cement (CPC) scaffold. Microcapillary formations was formed at day 21 (Liu et al., 2017). The prevascularization process is also influenced by growth factors used in cell culture media. **(G–I)** The formation of cord-like structures by endothelial cells in response to FGF2 **(G)**, VEGF **(H)**, and the combination of both **(I)** has shown at day 10 (original magnification X20) (Khan et al., 2017).

parameters must be taken into account (**Supplementary Table S1**).

4.1 Target Tissue

Since blood perfusion and vascular network of most of the tissues are different, it is evident that target tissue can play a significant role in determining the best types of endothelial and supporting cells for the co-culture system as well as methods and the other co-culture factors (**Figures 2A,B**). The structure of target tissues is a decisive factor in choosing the method of prevascularization. For instance, 2D co-culture systems and cell sheet engineering can be used for developing the prevascularized 2D constructs such as cardiac patch, skin graft, or lumenized structures including vascular or urethral grafts. In contrast, cell spheroids and cell encapsulations can be used for developing a 3D bone constructs. Moreover, since formation of a vascular network can change the biomechanical properties of scaffolds, many studies have been conducted to develop prevascularized scaffolds without reducing their biomechanical properties. Considering the biomechanical properties of target tissues, an appropriate scaffold can be selected to limit the uncontrolled formation of vascular-like structures.

The formation of a vascular network can impact some unique features of target tissues. For example, it has been shown that although the optimal vascular network development was seen in HUVECs/MSCs co-culture systems, the mineralization of the scaffolds was decreased in the co-culture group compared with MSCs monoculture (Ma et al., 2014b). In another example, increasing the cell seeding density of fibroblasts enhanced the mechanical properties of a prevascularized cardiac patch, while it decreased cardiac conductivity. Furthermore, the target tissue cells can significantly impact the formation of vessels by either promoting or inhibiting vasculogenesis and interacting with endothelial cells (Ong et al., 2017).

4.2 Scaffolds and Biomaterials

The crosstalk between ECM components and ECM composition such as collagen type I and IV, laminin, fibrin, and hyaluronic acid have a direct effect on ECs migration and elongation, length and number of sprouts as well as the alignment of newly formed vessels in the natural process of angiogenesis and vasculogenesis. The scaffolds mimic ECM by providing an environment that can support endothelial attachment, sprout formation, lumenogenesis and tubulogenesis and finally regulate

vasculogenesis process (**Figures 2C–F**). Although, the currently designed 3D scaffolds are less suitable to be applied *in vivo* and the ideal strength is not achieved yet, there are many improvements in cell penetration and migration inside the tissues thanks to bioprinting technology. Factors influencing scaffold design vary from case to case. To design a prevascularized implantable and viable tissue, the scaffold should be permeable and able to excrete wastes out of the tissue. Moreover, scaffolds are needed to show appropriate biocompatibility and less toxicity. Natural biomaterials are derived from components found in extracellular matrix, such as collagen or other natural materials including those obtained from plants, insects, or animals. Natural biomaterials usually have superb biocompatibility with the binding sites for proteins and cells similar to ECM. We used a Gelatin Methacryloyl (GelMA)/ chitosan nanoparticles composite hydrogel to delivery bFGF angiogenic factor. According to our findings, the bFGF was released from the developed scaffold in a sustain manner and promoted proliferation of cultured fibroblasts. The GelMA/ chitosan nanoparticles scaffold exhibited an excellent biocompatibility with great potential to be used in prevascularization processes (Modaresifar et al., 2018). However, natural materials may be immunogen and suffer from limited physical and mechanical stability. Major advantages of synthetic biomaterials include control over the bio-chemical and physical characteristics, and degradation rate of these constructs. Besides, these polymers are highly tunable and their pore size can be controlled for enhancing angiogenesis. To come up with a scaffold that take advantage of both biomechanical properties of a synthetic scaffold and cell supporting abilities of natural scaffolds, synthetic biomaterials are frequently coated with natural ones (Yu et al., 2015).

4.3 Growth Factors and Culture Conditions

Adding angiogenic factors to tissue-engineered constructs can enhance their vascularization process (**Figures 2G–I**) (Patel et al., 2008). Pro-angiogenic growth factors are used to initiate different steps of angiogenesis. Formation of new vessels can be increased by direct or indirect role of growth factors. VEGF and bFGF show direct effect on angiogenesis (Choi et al., 2018; Kawecki et al., 2021). They stimulate mobilization of EPCs that speed up the initiation of angiogenesis. For instance, it has been reported that genipin cross-linked electrospun gelatin mats loaded with VEGF can stimulate and induce angiogenesis for tissue engineering applications (Del Gaudio et al., 2013). However, the concentration of angiogenic factors must be firmly controlled because severe vascular leakage or hemangioma may occur in high concentrations of VEGF.

In addition to main angiogenic factors, there are some growth factors that indirectly increase angiogenesis process. These products including sonic hedgehog homolog (SHH) (Weyers et al., 2020), HIF-1 (Chai et al., 2020; Coyle et al., 2020), and BMP (Samee et al., 2008; Yang et al., 2021), which recruit cells in the vascularization area to secret angiogenic factors. PDGF, angiopoietin 1, and ephrinB2 also show an indirect role on angiogenesis (Harel et al., 2020; Hosaka et al., 2020; Yoon et al., 2020). They may help to stabilize the newly formed capillaries by recruiting smooth muscle cells. VEGF initiate angiogenesis but cannot induce blood vessel maturation, while PDGF induce blood vessel stability and maturation. Furthermore, combined administration of growth factors such as VEGF/bFGF (He et al., 2012) and VEGF/PDGF (Lutton et al., 2012) have shown an effective way to generate more stable capillary bed (Wang B. et al., 2020). However, further studies on the combined use of angiogenic agents help to identify the optimal angiogenic environment used in various fields of tissue engineering.

Hypoxic conditions can enhance the angiogenic ability of MSCs in the culture media. The MSCs cultured under hypoxic condition showed higher expression of pro-angiogenic factors including VEGF, vWF, FGF, and Flk-1, which significantly improved vascularization of PLGA scaffold compared with MSCs cultured under normal conditions (Kim et al., 2019). Confirmed by another study, MSCs sheet engineered under hypoxic conditions (2% O_2) had greater capillary network development compared to those cultured under normal condition (20% O_2) (Zhang et al., 2016).

4.4 Prevascularization Strategy

One of the critical elements determining the quality of prevascularization is choosing the most suitable method. The most important consideration for selecting the most suitable method is the target tissue. 2D prevascularization methods can be used for prevascularizing tissues like skin, gastrointestinal and urethral tract. Direct cell seeding on a 2D scaffold is one of the most common, yet inefficient methods for the prevascularization of 2D engineered constructs since random incorporation of endothelial lineage cells and supporting cells does not result in an aligned, maintainable, and functional vascular-like network. Co-culture of cells on highly aligned microfibers or using bioprinting for the patterned culture of endothelial cells and supporting cells on the scaffold have been proposed as potential solutions for this issue (Bourget et al., 2016; Qian et al., 2019).

Cell culture in two dimensions has been routinely performed during past decades in many labs. Although this approach was considered suitable, it does not properly mimic that of natural tissues function (Jensen and Teng, 2020). There are different cell responses in two and three-dimensional cultures. Prevascularization of 3D tissues can be much more challenging since it requires the endothelial network assembly to be aligned in a three-dimensional space. Some cells will immediately lose their normal physiologic features after they are taken out of the body and placed in 2D cell culture, while they might not be affected in a 3D culture medium (Duval et al., 2017). Both *in vivo* and *in vitro* strategies have been employed to achieve a functional 3D endothelial network assembly.

In-Vivo prevascularization methods such as AV-loop use the angiogenesis ability of host vessels to penetrate and vascularize the scaffold. In the AV-loop method, an arteriovenous shunt is surgically incorporated into the scaffold in order to prevascularize the construct (Wu et al., 2017; Weigand et al., 2018). Another *in vivo* strategy is implantation of the scaffold in a highly vascular pouch or flap in the body of the host (Lee et al., 2021). After the prevascularization of the scaffold, the final scaffold can be

implanted in the defected tissue. However, these methods are time-consuming and invasive and are not ideal for translation in clinical practice.

Over the years, direct injection of endothelial cell suspensions has been the most frequent strategy applied in regenerative medicine. This simple method has many weaknesses, including rapid diffusion of cells, low engraftment efficiency by loss of ECM interactions, and shear-induced cell death (Kito et al., 2013). Although random seeding of endothelial cells with supporting cells in a 3D scaffold with an optimal ratio in a biomaterial with optimal pore size can result in an endothelial network assembly, this method requires a lot of trial and error, and usually, the fabricated network is not organized. Furthermore, another issue is survival, differentiation, and migration of incorporated cells in a 3D environment. Encapsulating endothelial lineage cells and supporting cells in hydrogels containing essential factors for survival and differentiation of cells such as VEGF can ensure the survival of incorporated cells (Phelps et al., 2015; Kuss et al., 2018). Furthermore, it has been shown that using bioreactors for a dynamic culture environment with chemical and mechanical stimuli or growth factors gradient can direct the alignment of endothelial network assembly formed by encapsulated endothelial lineage cells/supporting cells (Tocchio et al., 2015; Nguyen et al., 2017).

Using cell spheroids as a prevasculrizing unit is an option to overcome the limitations of routine cell suspension methods. The endothelial cell spheroid system was first established as an *in vitro* model to study endothelial cell differentiation (Korff and Augustin, 1998). The spheroid sprouting method has also been applied as one of the *in vitro* models of angiogenesis. However, investigations on its ability to create a prevascularized tissue are in progress (Blacher et al., 2014). One study investigated bone regeneration using the co-culture of endothelial cells and osteoblasts for vascular sprouting and angiogenesis initiation. It was demonstrated that this co-culture system is likely to control the angiogenic properties of the ECs and also has a role in the optimization of osteoblast differentiation (Stahl et al., 2004). Encapsulation of cell spheroids has also been used for prevascularization. It has been shown that encapsulation of cell spheroid can result in more intricate and organized vascular network development compared to routine cell encapsulation (De Moor et al., 2021; Roux et al., 2021). However, it is worth noting that optimal EC/supporting cell ratio and EC/supporting cell interactions can be quite different in the spheroidal environment compared to the 2D and 3D co-culture systems (Benmeridja et al., 2020).

Scaffold-free cell sheet engineering has been widely used to achieve prevascularized 2D and 3D tissue constructs. Cell sheet engineering is a method of developing tissue constructs in which cell sheets are usually harvested on temperature-sensitive culture dishes (Yamato and Okano, 2004). These dishes are made by covalent grafting of a temperature-responsive polymer to ordinary culture plates. Changing the temperature modifies the surface characteristics from hydrophilic to hydrophobic allowing many cells to attach or detach. Alternatively, instead of thermal fluctuation, electromagnetic force can be utilized for attaching and detaching magnetic responsive sheets (Silva et al., 2020). In both methods, the formed cell sheets can keep their ECM and thus freely stick to other surfaces, including host tissues and another cell sheet. Several, tissues and organs such as the skin, the cornea, urothelium, and cardiac muscle are reconstructed by this method (Ng and Hutmacher, 2006; Umemoto et al., 2013; Song et al., 2020). One of the drawbacks of cell sheet engineering is ischemia or hypoxia of cells in the core. It has also been demonstrated that the location of the endothelial cell sheet compared to sheets composed of supporting cells could be crucial for developing an organized endothelial network and preventing hypoxia (Asakawa et al., 2010).

Recent advances in 3D-bioprinting, micro-molding, and microfluidic enabled researchers to micro-design the scaffold. As mentioned, micro-designing of the scaffold and micro-patterning of the surface topography has been used as one of the leading solutions to achieve an aligned network. Currently, lab-on-a-chip technologies have been widely used as angiogenesis and vasculogenesis models *in vitro* (Ko et al., 2019). These strategies focus on fabricating microchannels that will be later cellularized by endothelial and supporting cells to achieve a prevascularized construct. Several techniques such as microfluidics, laser degradation, photolithography, layer by layer assembly, micro-molding, and biodegradable sacrificial-template have been used to make microchannels mimicking the natural vascular network.

Microfluidic techniques have been widely used for simulating vasculogenesis and angiogenesis (Rambøl et al., 2020). One of the main challenges regarding the use of the microfluidic technique is finding the correct factors to maintain the optimal flow for cellularizing channels with endothelial and supporting cells. Furthermore, the microfluidic techniques are not scalable, and currently, most of their application remains limited to angiogenesis models. A common method for micropatterning is lithography which uses a particular electromagnetic wavelength to fabricate specific patterns on a scaffold incorporated with photosensitive biomaterials (Michna et al., 2018). An aligned microchannels network can be fabricated using this technique that will be used for the adhesion of endothelial cells to form an intricate and aligned endothelial network (Jiang and Luo, 2013). Another method of developing a microchannel network is using a biodegradable sacrificial template that can be degraded or washed after implantation and forming the microchannel network (Miller et al., 2012; Li et al., 2017; Hu et al., 2021). The microchannels can also be formed using laser biodegradation techniques (Pradhan et al., 2017). Another method is the layer-by-layer assembly technique which is used to form a thin scaffold with various patterns. In this technique, alternative charged layers will be deposited layer-by-layer to form microchannels (Sousa et al., 2021). These microchannels can be used as substrates for adhesion, proliferation, and network formation of endothelial cells (Miyazaki et al., 2019). These methods provide great control over the alignment of vascular-like networks. However, currently, the choice of biomaterials for designing the scaffold is limited, which means that the biomaterials used for creating these microchannels do not provide the ideal niche for endothelial cells. Also, we have yet to achieve 3D constructs with microchannels with desirable biomechanical properties using

these techniques. Furthermore, inosculation of microchannels formed by these techniques to the host vessels after implantation requires further *in vivo* investigations. Overall, these advances are promising, and further investigations in this area can pave the way for achieving a 3D engineered tissue with an organized and functional vascular network.

Another solution for fabricating a 3D prevascularized engineered construct is 3D bioprinting of endothelial and supporting cells or EC/supporting cell spheroid in a similar pattern to the vascular network (De Moor et al., 2021). This method can be used in combination with other techniques to achieve proper results (Nulty et al., 2021). However, one of the main obstacles of bioprinting is ensuring the survival of cells through the process of bio-printing. Benning et al. investigated the ability of various hydrogels including Matrigel, collagen, gelatin, gelatin/alginate, fibrin, agarose, and Pluronic F-127 for bioprinting of endothelial cells. They observed that endothelial cells that have been bioprinted using collagen and fibrin hydrogels were capable of proliferation and sprouting and maintained their endothelial phenotype. Although endothelial cells bioprinting in gelatin hydrogels were capable of proliferation, they were unable to initiate sprouting (Benning et al., 2018). Due to the promising results of bioprinting, developing more suitable hydrogels can be essential for using bioprinting in prevascularization.

5 FUTURE PERSPECTIVE

In vitro prevascularization strategies emphasize on optimization of the interactions between cells, biomaterials and culture conditions. To date, a wide variety of cells with diverse vasculogenic features have been studied to ensure survival of the engineered tissue. HUVECs, taking advantages of convenient and ethical isolation methods, are the most common endothelial cell lineage employed in prevascularization strategies and angiogenesis methods. Furthermore, efforts are being made to find a suitable cell source with high accessibility and angiogenesis capability. In this light, MSC-ECs and hiPSC-ECs have been suggested for the prevascularization of scaffolds since they can easily be isolated from various tissue, differentiated *in vitro*, and act as an autologous cell source. However, several inconsistencies exist in the reports regarding their pro-angiogenic abilities and their utilization for prevascularization. Further studies must be conducted to compare the pro-angiogenic capabilities of these cells, their markers, and their morphology to the current common endothelial lineage cells used in prevascularization. Moreover, amniotic-derived cells seem provide a reliable cell source that can be easily isolated and differentiated toward endothelial cells (Yazdanpanah et al., 2015; Abbasi-Kangevari et al., 2019). These cells also produce various angiogenic growth factors that candidate them as an appropriate supporting cell. Beside the cell sources, advances in biomaterial designs come up with positive results in prevascularization. Recent studies have focused on new strategies such as cell bioprinting and producing highly-tunable scaffolds with micro-patterning design to make further organized vessels similar to host vascular hierarchy. However, an important roadblock in achieving a sustainable vascularized construct is the interference of endothelial network development with the target tissue cells. To overcome this challenge, different ways are available including changing the ratio of endothelial cells and protective cells, applying genetic modifications to alter the signaling pathways in favor of angiogenesis, and using different growth factors and small molecule to facilitate anastomosis in the target tissue. Future studies provide more tools for achieving perfect prevascularization approaches to develop functional tissue engineered constructs.

AUTHOR CONTRIBUTIONS

HN contributed to the conception and design of the study. SeS, SiS, AZ, and AM organized the database. SeS, SiS, AZ wrote the first draft of the manuscript. SeS, SiS, AZ, and AM wrote sections of the manuscript. All authors contributed to manuscript revision, read, and approved the submitted version.

FUNDING

This work was supported by Vice-Chancellor's in Research Affairs, Shahid Beheshti University of Medical Sciences. Research reported in this publication was supported by the National Institutes for Medical Research Development (NIMAD), Tehran, Iran, under award number (963951).

ACKNOWLEDGMENTS

The authors would like to show their gratitude to Dr. Tahereh Tayebi for her precious assistance through this research.

SUPPLEMENTARY MATERIAL

The Supplementary Material for this article can be found online at: https://www.frontiersin.org/articles/10.3389/fbioe.2021.745314/full#supplementary-material

REFERENCES

Abbasi-Kangevari, M., Ghamari, S.-H., Safaeinejad, F., Bahrami, S., and Niknejad, H. (2019). Potential Therapeutic Features of Human Amniotic Mesenchymal Stem Cells in Multiple Sclerosis: Immunomodulation, Inflammation Suppression, Angiogenesis Promotion, Oxidative Stress Inhibition, Neurogenesis Induction, MMPs Regulation, and Remyelination Stimulation. *Front. Immunol.* 10, 238. doi:10.3389/fimmu.2019.00238

Acosta, F. M., Stojkova, K., Brey, E. M., and Rathbone, C. R. (2020). A Straightforward Approach to Engineer Vascularized Adipose Tissue Using Microvascular Fragments. *Tissue Eng. A* 26, 905–914. doi:10.1089/ten.tea.2019.0345

Aguirre, A., Planell, J. A., and Engel, E. (2010). Dynamics of Bone Marrow-Derived Endothelial Progenitor Cell/mesenchymal Stem Cell Interaction in Co-culture and its Implications in Angiogenesis. *Biochem. Biophysical Res. Commun.* 400, 284–291. doi:10.1016/j.bbrc.2010.08.073

Aicher, A., Heeschen, C., Sasaki, K.-I., Urbich, C., Zeiher, A. M., and Dimmeler, S. (2006). Low-Energy Shock Wave for Enhancing Recruitment of Endothelial Progenitor Cells. *Circulation* 114, 2823–2830. doi:10.1161/circulationaha.106.628623

Ajit, A., Ramakrishnan, R., Retnabai, S. T., Senan, M., and Krishnan, L. K. (2020). Generation of Niche Tuned Antifibrotic Fibroblasts and Non-viral Mediated Endothelial Commitment Using Adipose Stem Cells for Dermal Graft Development. *J. Biomed. Mater. Res. B: Appl. Biomater.* 108, 2807. doi:10.1002/jbm.b.34611

Antonelli-Orlidge, A., Saunders, K. B., Smith, S. R., and D'amore, P. A. (1989). An Activated Form of Transforming Growth Factor Beta Is Produced by Cocultures of Endothelial Cells and Pericytes. *Proc. Natl. Acad. Sci.* 86, 4544–4548. doi:10.1073/pnas.86.12.4544

Armulik, A., Abramsson, A., and Betsholtz, C. (2005). Endothelial/pericyte Interactions. *Circ. Res.* 97, 512–523. doi:10.1161/01.res.0000182903.16652.d7

Asahara, T., Murohara, T., Sullivan, A., Silver, M., Van Der Zee, R., Li, T., et al. (1997). Isolation of Putative Progenitor Endothelial Cells for Angiogenesis. *Science* 275, 964–966. doi:10.1126/science.275.5302.964

Asakawa, N., Shimizu, T., Tsuda, Y., Sekiya, S., Sasagawa, T., Yamato, M., et al. (2010). Pre-vascularization of *In Vitro* Three-Dimensional Tissues Created by Cell Sheet Engineering. *Biomaterials* 31, 3903–3909. doi:10.1016/j.biomaterials.2010.01.105

Au, P., Tam, J., Fukumura, D., and Jain, R. K. (2008). Bone Marrow-Derived Mesenchymal Stem Cells Facilitate Engineering of Long-Lasting Functional Vasculature. *Blood* 111, 4551–4558. doi:10.1182/blood-2007-10-118273

Avolio, E., Alvino, V. V., Ghorbel, M. T., and Campagnolo, P. (2017). Perivascular Cells and Tissue Engineering: Current Applications and Untapped Potential. *Pharmacol. Ther.* 171, 83–92. doi:10.1016/j.pharmthera.2016.11.002

Bale, S. S., Golberg, I., Jindal, R., Mccarty, W. J., Luitje, M., Hegde, M., et al. (2015). Long-term Coculture Strategies for Primary Hepatocytes and Liver Sinusoidal Endothelial Cells. *Tissue Eng. C: Methods* 21, 413–422. doi:10.1089/ten.tec.2014.0152

Bandara, N., Lim, S., Chen, H., Chen, S., Wang, L.-X., and Strappe, P. (2017). "The Proangiogenic Potential of Mesenchymal Stem Cells and Their Therapeutic Applications," in *Mesenchymal Stem Cells-Isolation, Characterization and Applications* (London, UK: IntechOpen). doi:10.5772/intechopen.68516

Benmeridja, L., De Moor, L., De Maere, E., Vanlauwe, F., Ryx, M., Tytgat, L., et al. (2020). High-throughput Fabrication of Vascularized Adipose Microtissues for 3D Bioprinting. *J. Tissue Eng. Regenerative Med.* 14, 840. doi:10.1002/term.3051

Benning, L., Gutzweiler, L., Tröndle, K., Riba, J., Zengerle, R., Koltay, P., et al. (2018). Assessment of Hydrogels for Bioprinting of Endothelial Cells. *J. Biomed. Mater. Res.* 106, 935–947. doi:10.1002/jbm.a.36291

Bergers, G., and Song, S. (2005). The Role of Pericytes in Blood-Vessel Formation and Maintenance. *Neuro-oncology* 7, 452–464. doi:10.1215/s1152851705000232

Bezenah, J. R., Kong, Y. P., and Putnam, A. J. (2018). Evaluating the Potential of Endothelial Cells Derived from Human Induced Pluripotent Stem Cells to Form Microvascular Networks in 3D Cultures. *Sci. Rep.* 8, 2671. doi:10.1038/s41598-018-20966-1

Bishop, E. T., Bell, G. T., Bloor, S., Broom, I., Hendry, N. F., and Wheatley, D. N. (1999). An *In Vitro* Model of Angiogenesis: Basic Features. *Angiogenesis* 3, 335–344. doi:10.1023/a:1026546219962

Blacher, S., Erpicum, C., Lenoir, B., Paupert, J., Moraes, G., Ormenese, S., et al. (2014). Cell Invasion in the Spheroid Sprouting Assay: a Spatial Organisation Analysis Adaptable to Cell Behaviour. *PloS one* 9, e97019. doi:10.1371/journal.pone.0097019

Blocki, A., Wang, Y., Koch, M., Peh, P., Beyer, S., Law, P., et al. (2013). Not all MSCs Can Act as Pericytes: Functional *In Vitro* Assays to Distinguish Pericytes from Other Mesenchymal Stem Cells in Angiogenesis. *Stem Cell Develop.* 22, 2347–2355. doi:10.1089/scd.2012.0415

Bouïs, D., Hospers, G. A. P., Meijer, C., Molema, G., and Mulder, N. H. (2001). Endothelium *In Vitro*: a Review of Human Vascular Endothelial Cell Lines for Blood Vessel-Related Research. *Angiogenesis* 4, 91–102. doi:10.1023/a:1012259529167

Bourget, J.-M., Kérourédan, O., Medina, M., Rémy, M., Thébaud, N. B., Bareille, R., et al. (2016). Patterning of Endothelial Cells and Mesenchymal Stem Cells by Laser-Assisted Bioprinting to Study Cell Migration. *Biomed. Research International* 2016, 3569843. doi:10.1155/2016/3569843

Bussche, L., and Van De Walle, G. R. (2014). Peripheral Blood-Derived Mesenchymal Stromal Cells Promote Angiogenesis via Paracrine Stimulation of Vascular Endothelial Growth Factor Secretion in the Equine Model. *Stem Cell translational Med.* 3, 1514–1525. doi:10.5966/sctm.2014-0138

Calderon, G. A., Thai, P., Hsu, C. W., Grigoryan, B., Gibson, S. M., Dickinson, M. E., et al. (2017). Tubulogenesis of Co-cultured Human iPS-Derived Endothelial Cells and Human Mesenchymal Stem Cells in Fibrin and Gelatin Methacrylate Gels. *Biomater. Sci.* 5, 1652–1660. doi:10.1039/c7bm00223h

Caplan, A. I. (1991). Mesenchymal Stem Cells. *J. Orthop. Res.* 9, 641–650. doi:10.1002/jor.1100090504

Chai, M., Gu, C., Shen, Q., Liu, J., Zhou, Y., Jin, Z., et al. (2020). Hypoxia Alleviates Dexamethasone-Induced Inhibition of Angiogenesis in Cocultures of HUVECs and rBMSCs via HIF-1α. *Stem Cel Res Ther* 11, 343. doi:10.1186/s13287-020-01853-x

Chen, L., Wu, J., Wu, C., Xing, F., Li, L., He, Z., et al. (2019). Three-Dimensional Co-culture of Peripheral Blood-Derived Mesenchymal Stem Cells and Endothelial Progenitor Cells for Bone Regeneration. *J. Biomed. Nanotechnol* 15, 248–260. doi:10.1166/jbn.2019.2680

Chen, L., Xing, Q., Zhai, Q., Tahtinen, M., Zhou, F., Chen, L., et al. (2017). Pre-vascularization Enhances Therapeutic Effects of Human Mesenchymal Stem Cell Sheets in Full Thickness Skin Wound Repair. *Theranostics* 7, 117–131. doi:10.7150/thno.17031

Chen, W., Liu, X., Chen, Q., Bao, C., Zhao, L., Zhu, Z., et al. (2018). Angiogenic and Osteogenic Regeneration in Rats via Calcium Phosphate Scaffold and Endothelial Cell Co-culture with Human Bone Marrow Mesenchymal Stem Cells (MSCs), Human Umbilical Cord MSCs, Human Induced Pluripotent Stem Cell-Derived MSCs and Human Embry. *J. Tissue Eng. Regen. Med.* 12, 191–203. doi:10.1002/term.2395

Chen, X., Aledia, A. S., Popson, S. A., Him, L., Hughes, C. C. W., and George, S. C. (2010). Rapid Anastomosis of Endothelial Progenitor Cell-Derived Vessels with Host Vasculature Is Promoted by a High Density of Cotransplanted Fibroblasts. *Tissue Eng. Part A* 16, 585–594. doi:10.1089/ten.tea.2009.0491

Chen, Y. L., Sun, C. K., Tsai, T. H., Chang, L. T., Leu, S., Zhen, Y. Y., et al. (2015). Adipose-derived Mesenchymal Stem Cells Embedded in Platelet-Rich Fibrin Scaffolds Promote Angiogenesis, Preserve Heart Function, and Reduce Left Ventricular Remodeling in Rat Acute Myocardial Infarction. *Am. J. Transl Res.* 7, 781–803.

Cheng, C.-C., Chang, S.-J., Chueh, Y.-N., Huang, T.-S., Huang, P.-H., Cheng, S.-M., et al. (2013). Distinct Angiogenesis Roles and Surface Markers of Early and Late Endothelial Progenitor Cells Revealed by Functional Group Analyses. *BMC genomics* 14, 182. doi:10.1186/1471-2164-14-182

Choi, S. M., Lee, K.-M., Kim, H. J., Park, I. K., Kang, H. J., Shin, H.-C., et al. (2018). Effects of Structurally Stabilized EGF and bFGF on Wound Healing in Type I and Type II Diabetic Mice. *Acta Biomater.* 66, 325–334. doi:10.1016/j.actbio.2017.11.045

Chopra, H., Hung, M., Kwong, D., Zhang, C., and Pow, E. (2018). Insights into Endothelial Progenitor Cells: Origin, Classification, Potentials, and Prospects. *Stem Cell Int.* 2018, 9847015. doi:10.1155/2018/9847015

Cipriano, J., Lakshmikanthan, A., Buckley, C., Mai, L., Patel, H., Pellegrini, M., et al. (2020). Characterization of a Prevascularized Biomimetic Tissue Engineered Scaffold for Bone Regeneration. *J. Biomed. Mater. Res.* 108, 1655–1668. doi:10.1002/jbm.b.34511

Costa-Almeida, R., Soares, R., and Granja, P. L. (2018). Fibroblasts as Maestros Orchestrating Tissue Regeneration. *J. Tissue Eng. regenerative Med.* 12, 240–251.

Costa-Almeida, R., Gomez-Lazaro, M., Ramalho, C., Granja, P. L., Soares, R., and Guerreiro, S. G. (2014). Fibroblast-endothelial Partners for Vascularization Strategies in Tissue Engineering. *Tissue Eng. Part. A.* 21, 1055–1065. doi:10.1089/ten.TEA.2014.0443

Coyle, R. C., Barrs, R. W., Richards, D. J., Ladd, E. P., Menick, D. R., and Mei, Y. (2020). Targeting HIF-α for Robust Prevascularization of Human Cardiac Organoids. *J. Tissue Eng. Regenerative Med.* 15, 3165. doi:10.1002/term.3165

Czajka, C. A., and Drake, C. J. (2014). Self-assembly of Prevascular Tissues from Endothelial and Fibroblast Cells under Scaffold-free, Nonadherent Conditions. *Tissue Eng. Part. A.* 21, 277–287. doi:10.1089/ten.TEA.2014.0183

Dai, N.-T., Huang, W.-S., Chang, F.-W., Wei, L.-G., Huang, T.-C., Li, J.-K., et al. (2018). Development of a Novel Pre-vascularized Three-Dimensional Skin Substitute Using Blood Plasma Gel. *Cel Transpl.* 27, 1535–1547. doi:10.1177/0963689718797570

Darland, D. C., and D'amore, P. A. (2001). TGFβ Is Required for the Formation of Capillary-like Structures in Three-Dimensional Cocultures of 10T1/2 and Endothelial Cells. *Angiogenesis* 4, 11–20. doi:10.1023/a:1016611824696

De Moor, L., Smet, J., Plovyt, M., Bekaert, B., Vercruysse, C., Asadian, M., et al. (2021). Engineering Microvasculature by 3D Bioprinting of Prevascularized Spheroids in Photo-Crosslinkable Gelatin. *Biofabrication* 13, 045021. doi:10.1088/1758-5090/ac24de

De Souza, L. E. B., Malta, T. M., Kashima Haddad, S., and Covas, D. T. (2016a). Mesenchymal Stem Cells and Pericytes: to what Extent Are They Related? *Stem Cell Develop.* 25, 1843–1852. doi:10.1089/scd.2016.0109

Deegan, A. J., Hendrikson, W. J., El Haj, A. J., Rouwkema, J., and Yang, Y. (2019). Regulation of Endothelial Cell Arrangements within hMSC - HUVEC Co-cultured Aggregates. *Biomed. J.* 42, 166–177. doi:10.1016/j.bj.2019.01.003

Del Gaudio, C., Baiguera, S., Boieri, M., Mazzanti, B., Ribatti, D., Bianco, A., et al. (2013). Induction of Angiogenesis Using VEGF Releasing Genipin-Crosslinked Electrospun Gelatin Mats. *Biomaterials* 34, 7754–7765. doi:10.1016/j.biomaterials.2013.06.040

Dohle, E., El Bagdadi, K., Sader, R., Choukroun, J., James Kirkpatrick, C., and Ghanaati, S. (2018). Platelet-rich Fibrin-based Matrices to Improve Angiogenesis in an *In Vitro* Co-culture Model for Bone Tissue Engineering. *J. Tissue Eng. Regen. Med.* 12, 598–610. doi:10.1002/term.2475

Du, J., Xie, P., Lin, S., Wu, Y., Zeng, D., Li, Y., et al. (2018). Time-Phase Sequential Utilization of Adipose-Derived Mesenchymal Stem Cells on Mesoporous Bioactive Glass for Restoration of Critical Size Bone Defects. *ACS Appl. Mater. Inter.* 10, 28340–28350. doi:10.1021/acsami.8b08563

Duval, K., Grover, H., Han, L.-H., Mou, Y., Pegoraro, A. F., Fredberg, J., et al. (2017). Modeling Physiological Events in 2D vs. 3D Cell Culture. *Physiology* 32, 266–277. doi:10.1152/physiol.00036.2016

Elcheva, I., Brok-Volchanskaya, V., Kumar, A., Liu, P., Lee, J. H., Tong, L., et al. (2014). Direct Induction of Haematoendothelial Programs in Human Pluripotent Stem Cells by Transcriptional Regulators. *Nat. Commun.* 5, 4372. doi:10.1038/ncomms5372

Fan, Z., Liao, X., Tian, Y., xuzhuzi, X., and Nie, Y. (2020). A Prevascularized Nerve Conduit Based on a Stem Cell Sheet Effectively Promotes the Repair of Transected Spinal Cord Injury. *Acta Biomater.* 101, 304–313. doi:10.1016/j.actbio.2019.10.042

Farhadihosseinabadi, B., Gholipourmalekabadi, M., Salimi, M., Abdollahifar, M. A., Bagheri, M., Samadikuchaksaraei, A., et al. (2020). The *In Vivo* Effect of Lacto-N-Neotetraose (LNnT) on the Expression of Type 2 Immune Response Involved Genes in the Wound Healing Process. *Sci. Rep.* 10, 997. doi:10.1038/s41598-020-57860-8

Farhadihosseinabadi, B., Farahani, M., Tayebi, T., Jafari, A., Biniazan, F., Modaresifar, K., et al. (2018). Amniotic Membrane and its Epithelial and Mesenchymal Stem Cells as an Appropriate Source for Skin Tissue Engineering and Regenerative Medicine. *Artif. Cell nanomedicine, Biotechnol.* 46, 431–440. doi:10.1080/21691401.2018.1458730

Fauza, D., Lagonda, C. A., Tjahjadi, F. B., and Kusnadi, Y. (2018). Mesenchymal Stem Cells-Derived Vascular Endothelial Growth Factor Improves Characteristics of Endothelial Progenitor Cells. *Cytotherapy* 20, S36–S37. doi:10.1016/j.jcyt.2018.02.090

Fedorovich, N. E., Haverslag, R. T., Dhert, W. J. A., and Alblas, J. (2010). The Role of Endothelial Progenitor Cells in Prevascularized Bone Tissue Engineering: Development of Heterogeneous Constructs. *Tissue Eng. Part A* 16, 2355–2367. doi:10.1089/ten.tea.2009.0603

Figueiredo, L., Le Visage, C., Weiss, P., and Yang, J. (2020). Quantifying Oxygen Levels in 3D Bioprinted Cell-Laden Thick Constructs with Perfusable Microchannel Networks. *Polymers* 12, 1260. doi:10.3390/polym12061260

Figueiredo, L. M., Costa, E. B. O., Orellana, M. D., Picanço-Castro, V., and Covas, D. T. (2015). OP9 Stromal Cells Proteins Involved in Hematoendothelial Differentiation from Human Embryonic Stem Cells. *Cell Reprogramming* 17, 338–346. doi:10.1089/cell.2015.0014

Fillinger, M. F., O'connor, S. E., Wagner, R. J., and Cronenwett, J. L. (1993). The Effect of Endothelial Cell Coculture on Smooth Muscle Cell Proliferation. *J. Vasc. Surg.* 17, 1058–1068. doi:10.1016/0741-5214(93)90676-d

Fillinger, M. F., Sampson, L. N., Cronenwett, J. L., Powell, R. J., and Wagner, R. J. (1997). Coculture of Endothelial Cells and Smooth Muscle Cells in Bilayer and Conditioned media Models. *J. Surg. Res.* 67, 169–178. doi:10.1006/jsre.1996.4978

Freeman, F. E., Allen, A. B., Stevens, H. Y., Guldberg, R. E., and Mcnamara, L. M. (2015). Effects of *In Vitro* Endochondral Priming and Pre-vascularisation of Human MSC Cellular Aggregates *In Vivo*. *Stem Cel Res Ther* 6, 218–18. doi:10.1186/s13287-015-0210-2

Freeman, F. E., Brennan, M. Á., Browe, D. C., Renaud, A., De Lima, J., Kelly, D. J., et al. (2020). A Developmental Engineering-Based Approach to Bone Repair: Endochondral Priming Enhances Vascularization and New Bone Formation in a Critical Size Defect. *Front. Bioeng. Biotechnol.* 8, 230. doi:10.3389/fbioe.2020.00230

Freiman, A., Shandalov, Y., Rozenfeld, D., Shor, E., Segal, S., Ben-David, D., et al. (2016). Adipose-derived Endothelial and Mesenchymal Stem Cells Enhance Vascular Network Formation on Three-Dimensional Constructs *In Vitro*. *Stem Cel Res Ther* 7, 5. doi:10.1186/s13287-015-0251-6

Fu, Q., Xia, B., Huang, X., Wang, F., Chen, Z., and Chen, G. (2021). Pro-angiogenic Decellularized Vessel Matrix Gel Modified by Silk Fibroin for Rapid Vascularization of Tissue Engineering Scaffold. *J. Biomed. Mater. Res. A* 109, 1701. doi:10.1002/jbm.a.37166

Fuchs, S., Hofmann, A., and Kirkpatrick, C. J. (2007). Microvessel-like Structures from Outgrowth Endothelial Cells from Human Peripheral Blood in 2-dimensional and 3-dimensional Co-cultures with Osteoblastic Lineage Cells. *Tissue Eng.* 13, 2577–2588. doi:10.1089/ten.2007.0022

Funderburgh, J. L., Funderburgh, M. L., and Du, Y. (2016). Stem Cells in the Limbal Stroma. *Ocul. Surf.* 14, 113–120. doi:10.1016/j.jtos.2015.12.006

Garikipati, V. N. S., and Kishore, R. (2017). "Endothelial Progenitor Cells: Procedure for Cell Isolation and Applications," in *Adult Stem Cells* (Berlin, Germany: Springer), 85–89. doi:10.1007/978-1-4939-6756-8_7

Geevarghese, A., and Herman, I. M. (2014). Pericyte-endothelial Crosstalk: Implications and Opportunities for Advanced Cellular Therapies. *Translational Res.* 163, 296–306. doi:10.1016/j.trsl.2014.01.011

Geng, K., Wang, J., Liu, P., Tian, X., Liu, H., Wang, X., et al. (2019). Electrical Stimulation Facilitates the Angiogenesis of Human Umbilical Vein Endothelial Cells through MAPK/ERK Signaling Pathway by Stimulating FGF2 Secretion. *Am. J. Physiology-Cell Physiol.* 317, C277. doi:10.1152/ajpcell.00474.2018

Ghajar, C. M., Blevins, K. S., Hughes, C. C. W., George, S. C., and Putnam, A. J. (2006). Mesenchymal Stem Cells Enhance Angiogenesis in Mechanically Viable Prevascularized Tissues via Early Matrix Metalloproteinase Upregulation. *Tissue Eng.* 12, 2875–2888. doi:10.1089/ten.2006.12.2875

Gholobova, D., Terrie, L., Mackova, K., Desender, L., Carpentier, G., Gerard, M., et al. (2020). Functional Evaluation of Prevascularization in One-Stage versus Two-Stage Tissue Engineering Approach of Human Bio-Artificial Muscle. *Biofabrication* 12, 035021. doi:10.1088/1758-5090/ab8f36

Goncharov, N. V., Popova, P. I., Avdonin, P. P., Kudryavtsev, I. V., Serebryakova, M. K., Korf, E. A., et al. (2020). Supplement Series A: MembraneMarkers of Endothelial Cells in Normal and Pathological Conditions. *Biochem. Mosc. Suppl. Ser. A* 14, 167–183. doi:10.1134/s1990747819030140

Grellier, M., Bordenave, L., and Amédée, J. (2009). Cell-to-cell Communication between Osteogenic and Endothelial Lineages: Implications for Tissue Engineering. *Trends Biotechnology* 27, 562–571. doi:10.1016/j.tibtech.2009.07.001

Guo, W., Xu, W., Wang, Z., Chen, M., Hao, C., Zheng, X., et al. (2018). Cell-Free Strategies for Repair and Regeneration of Meniscus Injuries through the Recruitment of Endogenous Stem/Progenitor Cells. *Stem Cell Int.* 2018, 1–10. doi:10.1155/2018/5310471

Gurel Pekozer, G., Torun Kose, G., and Hasirci, V. (2016). Influence of Co-culture on Osteogenesis and Angiogenesis of Bone Marrow Mesenchymal Stem Cells and Aortic Endothelial Cells. *Microvasc. Res.* 108, 1–9. doi:10.1016/j.mvr.2016.06.005

Harel, S., Sanchez-Gonzalez, V., Echavarria, R., Mayaki, D., and Hussain, S. N. (2020). Roles of miR-640 and Zinc Finger Protein 91 (ZFP91) in Angiopoietin-1-Induced *In Vitro* Angiogenesis. *Cells* 9, 1602. doi:10.3390/cells9071602

He, S., Xia, T., Wang, H., Wei, L., Luo, X., and Li, X. (2012). Multiple Release of Polyplexes of Plasmids VEGF and bFGF from Electrospun Fibrous Scaffolds towards Regeneration of Mature Blood Vessels. *Acta Biomater.* 8, 2659–2669. doi:10.1016/j.actbio.2012.03.044

Heller, M., Frerick-Ochs, E. V., Bauer, H.-K., Schiegnitz, E., Flesch, D., Brieger, J., et al. (2016). Tissue Engineered Pre-vascularized Buccal Mucosa Equivalents Utilizing a Primary Triculture of Epithelial Cells, Endothelial Cells and Fibroblasts. *Biomaterials* 77, 207–215. doi:10.1016/j.biomaterials.2015.10.073

Heo, D. N., Hospodiuk, M., and Ozbolat, I. T. (2019). Synergistic Interplay between Human MSCs and HUVECs in 3D Spheroids Laden in Collagen/fibrin Hydrogels for Bone Tissue Engineering. *Acta Biomater.* 95, 348. doi:10.1016/j.actbio.2019.02.046

Heydarkhan-Hagvall, S., Helenius, G., Johansson, B. R., Li, J. Y., Mattsson, E., and Risberg, B. (2003). Co-culture of Endothelial Cells and Smooth Muscle Cells Affects Gene Expression of Angiogenic Factors. *J. Cel Biochem* 89, 1250–1259. doi:10.1002/jcb.10583

Hofmann, A., Ritz, U., Verrier, S., Eglin, D., Alini, M., Fuchs, S., et al. (2008). The Effect of Human Osteoblasts on Proliferation and Neo-Vessel Formation of Human Umbilical Vein Endothelial Cells in a Long-Term 3D Co-culture on Polyurethane Scaffolds. *Biomaterials* 29, 4217–4226. doi:10.1016/j.biomaterials.2008.07.024

Hofmann, N. A., Reinisch, A., and Strunk, D. (2009). Isolation and Large Scale Expansion of Adult Human Endothelial colony Forming Progenitor Cells. *J. J. visualized experiments: JoVE* 32, 1524. doi:10.3791/1524

Hosaka, K., Yang, Y., Seki, T., Du, Q., Jing, X., He, X., et al. (2020). Therapeutic Paradigm of Dual Targeting VEGF and PDGF for Effectively Treating FGF-2 Off-Target Tumors. *Nat. Commun.* 11, 3704–3715. doi:10.1038/s41467-020-17525-6

Hu, Q., Tang, H., Yao, Y., Liu, S., Zhang, H., and Ramalingam, M. (2021). Rapid Fabrication of Gelatin-Based Scaffolds with Prevascularized Channels for Organ Regeneration. *Biomed. Mater.* 16, 045010. doi:10.1088/1748-605x/abef7b

Huizer, K., Mustafa, D. A. M., Spelt, J. C., Kros, J. M., and Sacchetti, A. (2017). Improving the Characterization of Endothelial Progenitor Cell Subsets by an Optimized FACS Protocol. *PloS one* 12, e0184895. doi:10.1371/journal.pone.0184895

Ingram, D. A., Mead, L. E., Moore, D. B., Woodard, W., Fenoglio, A., and Yoder, M. C. (2005). Vessel wall-derived Endothelial Cells Rapidly Proliferate Because They Contain a Complete Hierarchy of Endothelial Progenitor Cells. *Blood* 105, 2783–2786. doi:10.1182/blood-2004-08-3057

Iqbal, F., Szaraz, P., Wu, J., Gauthier-Fisher, A., Li, R., and Librach, C. (2017). Co-administration of First Trimester Umbilical Cord-Derived Perivascular Cells (FTM HUCPVCs) with Endothelial Progenitor Cells (EPCs) Leads to Enhanced Angiogenesis, Both *In Vitro* and *In Vivo*, Compared to Either Cell Type Alone. *Cytotherapy* 19, S160–S161. doi:10.1016/j.jcyt.2017.02.249

Jakubowska, W., Chabaud, S., Saba, I., Galbraith, T., Berthod, F., and Bolduc, S. (2020). Prevascularized Tissue-Engineered Human Vaginal Mucosa: *In Vitro* Optimization and *In Vivo* Validation. *Tissue Eng. Part A* 26, 811. doi:10.1089/ten.tea.2020.0036

Jang, S., Collin de l'Hortet, A., and Soto-Gutierrez, A. (2019). Induced Pluripotent Stem Cell-Derived Endothelial Cells. *Am. J. Pathol.* 189, 502–512. doi:10.1016/j.ajpath.2018.12.004

Jensen, C., and Teng, Y. (2020). Is it Time to Start Transitioning from 2D to 3D Cell Culture? *Front. Mol. Biosci.* 7, 33. doi:10.3389/fmolb.2020.00033

Jia, Z., Guo, H., Xie, H., Bao, X., Huang, Y., Yang, G., et al. (2018a). Harvesting Prevascularized Smooth Muscle Cell Sheets from Common Polystyrene Culture Dishes. *PloS one* 13, e0204677. doi:10.1371/journal.pone.0204677

Jiang, L.-Y., and Luo, Y. (2013). Guided Assembly of Endothelial Cells on Hydrogel Matrices Patterned with Microgrooves: a Basic Model for Microvessel Engineering. *Soft Matter* 9, 1113–1121. doi:10.1039/c2sm27126e

Jiang, Y. N., Zhao, J., Chu, F. T., Jiang, Y. Y., and Tang, G. H. (2018). Tension-loaded Bone Marrow Stromal Cells Potentiate the Paracrine Osteogenic Signaling of Co-cultured Vascular Endothelial Cells. *Biol. Open* 7, bio032482. doi:10.1242/bio.032482

Kargozar, S., Mozafari, M., Hashemian, S. J., Brouki Milan, P., Hamzehlou, S., Soleimani, M., et al. (2018). Osteogenic Potential of Stem Cells-Seeded Bioactive Nanocomposite Scaffolds: A Comparative Study between Human Mesenchymal Stem Cells Derived from Bone, Umbilical Cord Wharton's Jelly, and Adipose Tissue. *J. Biomed. Mater. Res.* 106, 61–72. doi:10.1002/jbm.b.33814

Kaully, T., Kaufman-Francis, K., Lesman, A., and Levenberg, S. (2009). Vascularization-The Conduit to Viable Engineered Tissues. *Tissue Eng. B: Rev.* 15, 159–169. doi:10.1089/ten.teb.2008.0193

Kawecki, F., Galbraith, T., Clafshenkel, W. P., Fortin, M., Auger, F. A., and Fradette, J. (2021). *In Vitro* Prevascularization of Self-Assembled Human Bone-like Tissues and Preclinical Assessment Using a Rat Calvarial Bone Defect Model. *Materials (Basel)* 14, 2023. doi:10.3390/ma14082023

Kawecki, F., Clafshenkel, W. P., Auger, F. A., Bourget, J.-M., Fradette, J., and Devillard, R. (2018). Self-assembled Human Osseous Cell Sheets as Living Biopapers for the Laser-Assisted Bioprinting of Human Endothelial Cells. *Biofabrication* 10, 035006. doi:10.1088/1758-5090/aabd5b

Kennedy, C. C., Brown, E. E., Abutaleb, N. O., and Truskey, G. A. (2021). Development and Application of Endothelial Cells Derived from Pluripotent Stem Cells in Microphysiological Systems Models. *Front. Cardiovasc. Med.* 8, 28. doi:10.3389/fcvm.2021.625016

Kerkar, S., Williams, M., Blocksom, J. M., Wilson, R. F., Tyburski, J. G., and Steffes, C. P. (2006). TNF-α and IL-1β Increase Pericyte/Endothelial Cell Co-culture Permeability. *J. Surg. Res.* 132, 40–45. doi:10.1016/j.jss.2005.06.033

Kérourédan, O., Hakobyan, D., Rémy, M., Ziane, S., Dusserre, N., Fricain, J.-C., et al. (2019). *In Situ* prevascularization Designed by Laser-Assisted Bioprinting: Effect on Bone Regeneration. *Biofabrication* 11, 045002. doi:10.1088/1758-5090/ab2620

Khaki, M., Salmanian, A. H., Abtahi, H., Ganji, A., and Mosayebi, G. (2018). Mesenchymal Stem Cells Differentiate to Endothelial Cells Using Recombinant Vascular Endothelial Growth Factor–A. *Rep. Biochem. Mol. Biol.* 6, 144.

Khan, S., Villalobos, M. A., Choron, R. L., Chang, S., Brown, S. A., Carpenter, J. P., et al. (2017). Fibroblast Growth Factor and Vascular Endothelial Growth Factor Play a Critical Role in Endotheliogenesis from Human Adipose-Derived Stem Cells. *J. Vasc. Surg.* 65, 1483–1492. doi:10.1016/j.jvs.2016.04.034

Kiaie, N., Gorabi, A. M., Tafti, S. H. A., and Rabbani, S. (2020). Pre-vascularization Approaches for Heart Tissue Engineering. *Regenerative Eng. Translational Med.* 2020, 1–10. doi:10.1007/s40883-020-00172-0

Kim, B.-S., Chen, J., Weinstein, T., Noiri, E., and Goligorsky, M. S. (2002). VEGF Expression in Hypoxia and Hyperglycemia: Reciprocal Effect on Branching Angiogenesis in Epithelial-Endothelial Co-cultures. *J. Am. Soc. Nephrol.* 13, 2027–2036. doi:10.1097/01.asn.0000024436.00520.d8

Kim, J.-S., Jung, Y., Kim, S. H., Shin, J.-S., Kim, S. H., and Park, C.-G. (2019). Vascularization of PLGA-Based Bio-Artificial Beds by Hypoxia-Preconditioned Mesenchymal Stem Cells for Subcutaneous Xenogeneic Islet Transplantation. *Xenotransplantation* 26, e12441. doi:10.1111/xen.12441

Kim, J., Moon, S.-H., Lee, S.-H., Lee, D.-R., Koh, G.-Y., and Chung, H.-M. (2007). Effective Isolation and Culture of Endothelial Cells in Embryoid Body Differentiated from Human Embryonic Stem Cells. *Stem Cell Develop.* 16, 269–280. doi:10.1089/scd.2006.0108

Kito, T., Shibata, R., Ishii, M., Suzuki, H., Himeno, T., Kataoka, Y., et al. (2013). iPS Cell Sheets Created by a Novel Magnetite Tissue Engineering Method for Reparative Angiogenesis. *Sci. Rep.* 3, 1418–8. doi:10.1038/srep01418

Kniebs, C., Kreimendahl, F., Köpf, M., Fischer, H., Jockenhoevel, S., and Thiebes, A. L. (2020). Influence of Different Cell Types and Sources on Pre-vascularisation in Fibrin and Agarose-Collagen Gels. *Organogenesis* 16, 14–26. doi:10.1080/15476278.2019.1697597

Ko, J., Ahn, J., Kim, S., Lee, Y., Lee, J., Park, D., et al. (2019). Tumor Spheroid-On-A-Chip: a Standardized Microfluidic Culture Platform for Investigating Tumor Angiogenesis. *Lab. Chip* 19, 2822–2833. doi:10.1039/c9lc00140a

Kocherova, I., Bryja, A., Mozdziak, P., Angelova Volponi, A., Dyszkiewicz-Konwińska, M., Piotrowska-Kempisty, H., et al. (2019). Human Umbilical Vein Endothelial Cells (HUVECs) Co-culture with Osteogenic Cells: from Molecular Communication to Engineering Prevascularised Bone Grafts. *J. Clin. Med.* 8, 1602. doi:10.3390/jcm8101602

Komaki, M., Numata, Y., Morioka, C., Honda, I., Tooi, M., Yokoyama, N., et al. (2017). Exosomes of Human Placenta-Derived Mesenchymal Stem Cells Stimulate Angiogenesis. *Stem Cel Res Ther* 8, 219. doi:10.1186/s13287-017-0660-9

Korff, T., and Augustin, H. G. (1998). Integration of Endothelial Cells in Multicellular Spheroids Prevents Apoptosis and Induces Differentiation. *J. Cel. Biol.* 143, 1341–1352. doi:10.1083/jcb.143.5.1341

Korff, T., Kimmina, S., Martiny-baron, G., and Augustin, H. G. (2001). Blood Vessel Maturation in a 3-dimensional Spheroidal Coculture Model: Direct Contact with Smooth Muscle Cells Regulates Endothelial Cell Quiescence and Abrogates VEGF Responsiveness. *FASEB j.* 15, 447–457. doi:10.1096/fj.00-0139com

Krüger-Genge, A., Blocki, A., Franke, R.-P., and Jung, F. (2019). Vascular Endothelial Cell Biology: an Update. *Int. J. Mol. Sci.* 20, 4411. doi:10.3390/ijms20184411

Kuss, M. A., Wu, S., Wang, Y., Untrauer, J. B., Li, W., Lim, J. Y., et al. (2018). Prevascularization of 3D Printed Bone Scaffolds by Bioactive Hydrogels and Cell Co-culture. *J. Biomed. Mater. Res.* 106, 1788–1798. doi:10.1002/jbm.b.33994

Kwartler, C., Zhou, P., Kuang, S.-Q., Duan, X.-Y., Gong, L., and Milewicz, D. (2016). Vascular Smooth Muscle Cell Isolation and Culture from Mouse Aorta. *Bio Protoc.* 6, e2045. doi:10.21769/bioprotoc.2045

Landau, S., Ben-Shaul, S., and Levenberg, S. (2018). Oscillatory Strain Promotes Vessel Stabilization and Alignment through Fibroblast YAP-Mediated Mechanosensitivity. *Adv. Sci.* 5, 1800506. doi:10.1002/advs.201800506

Lange, L., Hoffmann, D., Schwarzer, A., Ha, T.-C., Philipp, F., Lenz, D., et al. (2020). Inducible Forward Programming of Human Pluripotent Stem Cells to Hemato-Endothelial Progenitor Cells with Hematopoietic Progenitor Potential. *Stem Cel. Rep.* 14, 122–137. doi:10.1016/j.stemcr.2019.11.005

Lee, J., Shin, D., and Roh, J. L. (2019). Promotion of Skin Wound Healing Using Prevascularized Oral Mucosal Cell Sheet. *Head Neck* 41, 774–779. doi:10.1002/hed.25432

Lee, J.-K., Park, S.-R., Jung, B.-K., Jeon, Y.-K., Lee, Y.-S., Kim, M.-K., et al. (2013). Exosomes Derived from Mesenchymal Stem Cells Suppress Angiogenesis by Down-Regulating VEGF Expression in Breast Cancer Cells. *PloS one* 8, e84256. doi:10.1371/journal.pone.0084256

Lee, M., Choi, J. S., Eom, M. R., Jeong, E. J., Kim, J., Park, S. A., et al. (2021). Prevascularized Tracheal Scaffolds Using the Platysma Flap for Enhanced Tracheal Regeneration. *The Laryngoscope* 131, 1732–1740. doi:10.1002/lary.29178

Li, D., Cheng, P., Jiang, H., Cao, T., Wang, J., Gao, Y., et al. (2018). Vascularization Converts the Lineage Fate of Bone Mesenchymal Stem Cells to Endothelial Cells in Tissue-Engineered Bone Grafts by Modulating FGF2-RhoA/ROCK Signaling. *Cell Death Dis* 9, 959. doi:10.1038/s41419-018-0999-6

Li, S., Zhang, H.-G., Li, D.-D., Wu, J.-P., Sun, C.-Y., and Hu, Q.-X. (2017). Characterization of Engineered Scaffolds with Spatial Prevascularized Networks for Bulk Tissue Regeneration. *ACS Biomater. Sci. Eng.* 3, 2493–2501. doi:10.1021/acsbiomaterials.7b00355

Li, Z., Hu, S., Ghosh, Z., Han, Z., and Wu, J. C.Development (2011). Functional Characterization and Expression Profiling of Human Induced Pluripotent Stem Cell- and Embryonic Stem Cell-Derived Endothelial Cells. *Stem Cell Dev.* 20, 1701–1710. doi:10.1089/scd.2010.0426

Liang, X., Zhang, L., Wang, S., Han, Q., and Zhao, R. C. (2016). Exosomes Secreted by Mesenchymal Stem Cells Promote Endothelial Cell Angiogenesis by Transferring miR-125a. *J. Cel. Sci.* 129, 2182–2189. doi:10.1242/jcs.170373

Lindgren, A. G., Veldman, M. B., and Lin, S. (2015). ETV2 Expression Increases the Efficiency of Primitive Endothelial Cell Derivation from Human Embryonic Stem Cells. *Cell Regen* 4, 1–7. doi:10.1186/s13619-014-0014-3

Liu, H., Jiao, Y., Zhou, W., Bai, S., Feng, Z., Dong, Y., et al. (2018a). Endothelial Progenitor Cells Improve the Therapeutic Effect of Mesenchymal Stem Cell Sheets on Irradiated Bone Defect Repair in a Rat Model. *J. Transl Med.* 16, 137. doi:10.1186/s12967-018-1517-4

Liu, J., Zheng, H., Dai, X., Poh, P. S., Machens, H.-G., Schilling, A. F. J. F. I. B., et al. (2020). Transparent PDMS Bioreactors for the Fabrication and Analysis of Multi-Layer Pre-vascularized Hydrogels under Continuous Perfusion. *Front. Bioeng. Biotechnol.* 8, 568934. doi:10.3389/fbioe.2020.568934

Liu, X., Chen, W., Zhang, C., Thein-Han, W., Hu, K., Reynolds, M. A., et al. (2017). Co-seeding Human Endothelial Cells with Human-Induced Pluripotent Stem Cell-Derived Mesenchymal Stem Cells on Calcium Phosphate Scaffold Enhances Osteogenesis and Vascularization in Rats. *Tissue Eng. Part A* 23, 546–555. doi:10.1089/ten.tea.2016.0485

Liu, X., Jakus, A. E., Kural, M., Qian, H., Engler, A., Ghaedi, M., et al. (2018b). Vascularization of Natural and Synthetic Bone Scaffolds. *Cel Transpl.* 27, 1269–1280. doi:10.1177/0963689718782452

Lloyd-Griffith, C., Mcfadden, T. M., Duffy, G. P., Unger, R. E., Kirkpatrick, C. J., and O'Brien, F. J. (2015). The Pre-vascularisation of a Collagen-Chondroitin Sulphate Scaffold Using Human Amniotic Fluid-Derived Stem Cells to Enhance and Stabilise Endothelial Cell-Mediated Vessel Formation. *Acta Biomater.* 26, 263–273. doi:10.1016/j.actbio.2015.08.030

Loibl, M., Binder, A., Herrmann, M., Duttenhoefer, F., Richards, R. G., Nerlich, M., et al. (2014). Direct Cell-Cell Contact between Mesenchymal Stem Cells and Endothelial Progenitor Cells Induces a Pericyte-like Phenotype *In Vitro*. *Biomed. Research International* 2014, 395781. doi:10.1155/2014/395781

Lutton, C., Young, Y. W., Williams, R., Meedeniya, A. C. B., Mackay-Sim, A., and Goss, B. (2012). Combined VEGF and PDGF Treatment Reduces Secondary Degeneration after Spinal Cord Injury. *J. neurotrauma* 29, 957–970. doi:10.1089/neu.2010.1423

Lynch, M. D., and Watt, F. M. (2018). Fibroblast Heterogeneity: Implications for Human Disease. *J. Clin. Invest.* 128, 26–35. doi:10.1172/jci93555

Ma, J., Both, S. K., Ji, W., Yang, F., Prins, H.-J., Helder, M. N., et al. (2014a). Adipose Tissue-Derived Mesenchymal Stem Cells as Monocultures or Cocultures with Human Umbilical Vein Endothelial Cells: Performance *In Vitro* and in Rat Cranial Defects. *J. Biomed. Mater. Res.* 102, 1026–1036. doi:10.1002/jbm.a.34775

Ma, J., Yang, F., Both, S. K., Prins, H.-J., Helder, M. N., Pan, J., et al. (2014b). *In Vitro* and *In Vivo* Angiogenic Capacity of BM-MSCs/HUVECs and AT-MSCs/HUVECs Cocultures. *Biofabrication* 6, 015005. doi:10.1088/1758-5082/6/1/015005

Maacha, S., Sidahmed, H., Jacob, S., Gentilcore, G., Calzone, R., Grivel, J.-C., et al. (2020). Paracrine Mechanisms of Mesenchymal Stromal Cells in Angiogenesis. *Stem Cell Int.* 2020, 4356359. doi:10.1155/2020/4356359

Manikowski, D., Andrée, B., Samper, E., Saint-Marc, C., Olmer, R., Vogt, P., et al. (2018). Human Adipose Tissue-Derived Stromal Cells in Combination with Exogenous Stimuli Facilitate Three-Dimensional Network Formation of Human Endothelial Cells Derived from Various Sources. *Vasc. Pharmacol.* 106, 28–36. doi:10.1016/j.vph.2018.02.003

Masuda, S., Matsuura, K., Anazawa, M., Iwamiya, T., Shimizu, T., and Okano, T. (2015). Formation of Vascular Network Structures within Cardiac Cell Sheets from Mouse Embryonic Stem Cells. *Regenerative Ther.* 2, 6–16. doi:10.1016/j.reth.2015.10.002

Mcfadden, T. M., Duffy, G. P., Allen, A. B., Stevens, H. Y., Schwarzmaier, S. M., Plesnila, N., et al. (2013). The Delayed Addition of Human Mesenchymal Stem Cells to Pre-formed Endothelial Cell Networks Results in Functional Vascularization of a Collagen-Glycosaminoglycan Scaffold *In Vivo*. *Acta Biomater.* 9, 9303–9316. doi:10.1016/j.actbio.2013.08.014

Medina, R. J., O'neill, C. L., Humphreys, M. W., Gardiner, T. A., and Stitt, A. W. (2010). Outgrowth Endothelial Cells: Characterization and Their Potential for Reversing Ischemic Retinopathy. *Invest. Ophthalmol. Vis. Sci.* 51, 5906–5913. doi:10.1167/iovs.09-4951

Metz, R. P., Patterson, J. L., and Wilson, E. (2012). "Vascular Smooth Muscle Cells: Isolation, Culture, and Characterization," in *Cardiovascular Development* (Berlin, Germany: Springer), 169–176. doi:10.1007/978-1-61779-523-7_16

Michna, R., Gadde, M., Ozkan, A., Dewitt, M., and Rylander, M. (2018). Vascularized Microfluidic Platforms to Mimic the Tumor Microenvironment. *Biotechnol. Bioeng.* 115, 2793–2806. doi:10.1002/bit.26778

Miller, J. S., Stevens, K. R., Yang, M. T., Baker, B. M., Nguyen, D.-H. T., Cohen, D. M., et al. (2012). Rapid Casting of Patterned Vascular Networks for Perfusable Engineered Three-Dimensional Tissues. *Nat. Mater* 11, 768–774. doi:10.1038/nmat3357

Miyazaki, H., Tsunoi, Y., Akagi, T., Sato, S., Akashi, M., and Saitoh, D. (2019). A Novel Strategy to Engineer Pre-vascularized 3-dimensional Skin Substitutes to Achieve Efficient, Functional Engraftment. *Sci. Rep.* 9, 7797. doi:10.1038/s41598-019-44113-6

Modaresifar, K., Hadjizadeh, A., and Niknejad, H. (2018). Design and Fabrication of GelMA/chitosan Nanoparticles Composite Hydrogel for Angiogenic Growth Factor Delivery. *Artif. Cell Nanomed Biotechnol* 46, 1799–1808. doi:10.1080/21691401.2017.1392970

Moghadasi, S., Elveny, M., Rahman, H. S., Suksatan, W., Jalil, A. T., Abdelbasset, W. K., et al. (2021). A Paradigm Shift in Cell-free Approach: the Emerging Role of MSCs-Derived Exosomes in Regenerative Medicine. *J. translational Med.* 19, 1–21. doi:10.1186/s12967-021-02980-6

Montesano, R., Pepper, M. S., and Orci, L. (1993). Paracrine Induction of Angiogenesis *In Vitro* by Swiss 3T3 Fibroblasts. *J. Cel. Sci.* 105, 1013–1024. doi:10.1242/jcs.105.4.1013

Montezano, A. C., Lopes, R. A. M., Neves, K. B., Rios, F., and Touyz, R. M. (2017). "Isolation and Culture of Vascular Smooth Muscle Cells from Small and Large Vessels," in *Hypertension* (Berlin, Germany: Springer), 349–354. doi:10.1007/978-1-4939-6625-7_27

Mukai, N., Akahori, T., Komaki, M., Li, Q., Kanayasu-Toyoda, T., Ishii-Watabe, A., et al. (2008). A Comparison of the Tube Forming Potentials of Early and Late Endothelial Progenitor Cells. *Exp. Cel. Res.* 314, 430–440. doi:10.1016/j.yexcr.2007.11.016

Müller, A. M., Hermanns, M. I., Skrzynski, C., Nesslinger, M., Müller, K.-M., and Kirkpatrick, C. J. (2002). Expression of the Endothelial Markers PECAM-1, vWf, and CD34 *In Vivo* and *In Vitro*. *Exp. Mol. Pathol.* 72, 221–229. doi:10.1006/exmp.2002.2424

Natividad-Diaz, S. L., Browne, S., Jha, A. K., Ma, Z., Hossainy, S., Kurokawa, Y. K., et al. (2019). A Combined hiPSC-Derived Endothelial Cell and *In Vitro* Microfluidic Platform for Assessing Biomaterial-Based Angiogenesis. *Biomaterials* 194, 73–83. doi:10.1016/j.biomaterials.2018.11.032

Navone, S., Pascucci, L., Dossena, M., Ferri, A., Invernici, G., Acerbi, F., et al. (2014). Decellularized Silk Fibroin Scaffold Primed with Adipose Mesenchymal Stromal Cells Improves Wound Healing in Diabetic Mice. *Stem Cel Res. Ther.* 5, 7. doi:10.1186/scrt396

Ng, K., and Hutmacher, D. (2006). Reduced Contraction of Skin Equivalent Engineered Using Cell Sheets Cultured in 3D Matrices. *Biomaterials* 27, 4591–4598. doi:10.1016/j.biomaterials.2006.04.020

Nguyen, B. N. B., Moriarty, R. A., Kamalitdinov, T., Etheridge, J. M., and Fisher, J. P. (2017). C Ollagen Hydrogel Scaffold Promotes Mesenchymal Stem Cell and Endothelial Cell Coculture for Bone Tissue Engineering. *J. Biomed. Mater. Res.* 105, 1123–1131. doi:10.1002/jbm.a.36008

Niknejad, H., Paeini-Vayghan, G., Tehrani, F. A., Khayat-Khoei, M., and Peirovi, H. (2013). Side Dependent Effects of the Human Amnion on Angiogenesis. *Placenta* 34, 340–345. doi:10.1016/j.placenta.2013.02.001

Nilforoushzadeh, M. A., Mollapour Sisakht, M., Amirkhani, M. A., Seifalian, A. M., Banafshe, H. R., Verdi, J., et al. (2019). Engineered Skin Graft with Stromal Vascular Fraction Cells Encapsulated in Fibrin-collagen Hydrogel: A Clinical Study for Diabetic Wound Healing. *J. Tissue Eng. Regenerative Med.* 14, 424. doi:10.1002/term.3003

Nulty, J., Freeman, F. E., Browe, D. C., Burdis, R., Ahern, D. P., Pitacco, P., et al. (2021). 3D Bioprinting of Prevascularised Implants for the Repair of Critically-Sized Bone Defects. *Acta Biomater.* 126, 154–169. doi:10.1016/j.actbio.2021.03.003

Oki, N., Abe, T., Kunimatsu, R., Sumi, K., Awada, T., Tsuka, Y., et al. (2018). The Role of Vascular Endothelial Growth Factor and Mesenchymal Stem Cells during Angiogenesis. *Biomed. Res.* 29, 3079–3084. doi:10.4066/biomedicalresearch.29-18-887

Ong, C. S., Fukunishi, T., Zhang, H., Huang, C. Y., Nashed, A., Blazeski, A., et al. (2017). Biomaterial-free Three-Dimensional Bioprinting of Cardiac Tissue Using Human Induced Pluripotent Stem Cell Derived Cardiomyocytes. *Sci. Rep.* 7, 4566. doi:10.1038/s41598-017-05018-4

Orlidge, A., and D'amore, P. A. (1987). Inhibition of Capillary Endothelial Cell Growth by Pericytes and Smooth Muscle Cells. *J. Cel. Biol.* 105, 1455–1462. doi:10.1083/jcb.105.3.1455

Orlova, V. V., Drabsch, Y., Freund, C., Petrus-Reurer, S., Van Den Hil, F. E., Muenthaisong, S., et al. (2014). Functionality of Endothelial Cells and Pericytes from Human Pluripotent Stem Cells Demonstrated in Cultured Vascular Plexus and Zebrafish Xenografts. *Arterioscler Thromb. Vasc. Biol.* 34, 177–186. doi:10.1161/atvbaha.113.302598

Oswald, J., Boxberger, S., Jørgensen, B., Feldmann, S., Ehninger, G., Bornhäuser, M., et al. (2004). Mesenchymal Stem Cells Can Be Differentiated into Endothelial Cells *In Vitro*. *Stem Cells* 22, 377–384. doi:10.1634/stemcells.22-3-377

Owens, G. K., and Wise, G. (1997). Regulation of Differentiation/maturation in Vascular Smooth Muscle Cells by Hormones and Growth Factors. *Agents Actions. Supplements* 48, 3–24. doi:10.1007/978-3-0348-7352-9_1

Pang, Y., and Thomas, P. (2018). Progesterone Induces Relaxation of Human Umbilical Cord Vascular Smooth Muscle Cells through mPRα (PAQR7). *Mol. Cell Endocrinol.* 474, 20–34. doi:10.1016/j.mce.2018.02.003

Patel, Z. S., Young, S., Tabata, Y., Jansen, J. A., Wong, M. E. K., and Mikos, A. G. (2008). Dual Delivery of an Angiogenic and an Osteogenic Growth Factor for Bone Regeneration in a Critical Size Defect Model. *Bone* 43, 931–940. doi:10.1016/j.bone.2008.06.019

Pence, J. C., Clancy, K. B. H., and Harley, B. A. C. (2015). The Induction of Pro-angiogenic Processes within a Collagen Scaffold via Exogenous Estradiol and Endometrial Epithelial Cells. *Biotechnol. Bioeng.* 112, 2185–2194. doi:10.1002/bit.25622

Peng, J., Chen, L., Peng, K., Chen, X., Wu, J., He, Z., et al. (2019). Bone Marrow Mesenchymal Stem Cells and Endothelial Progenitor Cells Co-culture Enhances Large Segment Bone Defect Repair. *J Biomed. Nanotechnol* 15, 742–755. doi:10.1166/jbn.2019.2735

Perry, L., Merdler, U., Elishaev, M., and Levenberg, S. (2019). Enhanced Host Neovascularization of Prevascularized Engineered Muscle Following Transplantation into Immunocompetent versus Immunocompromised Mice. *Cells* 8, 1472. doi:10.3390/cells8121472

Peters, E. B., Christoforou, N., Leong, K. W., Truskey, G. A., and West, J. L. (2016). Poly(Ethylene Glycol) Hydrogel Scaffolds Containing Cell-Adhesive and Protease-Sensitive Peptides Support Microvessel Formation by Endothelial Progenitor Cells. *Cel. Mol. Bioeng.* 9, 38–54. doi:10.1007/s12195-015-0423-6

Peters, E. B. (2018). Endothelial Progenitor Cells for the Vascularization of Engineered Tissues. *Tissue Eng. Part B: Rev.* 24, 1–24. doi:10.1089/ten.teb.2017.0127

Phelps, E. A., Templeman, K. L., Thulé, P. M., and García, A. J. (2015). Engineered VEGF-Releasing PEG-MAL Hydrogel for Pancreatic Islet Vascularization. *Drug Deliv. Transl. Res.* 5, 125–136. doi:10.1007/s13346-013-0142-2

Pirlo, R. K., Wu, P., Liu, J., and Ringeisen, B. (2012). PLGA/hydrogel Biopapers as a Stackable Substrate for Printing HUVEC Networks via BioLP. *Biotechnol. Bioeng.* 109, 262–273. doi:10.1002/bit.23295

Pradhan, S., Keller, K. A., Sperduto, J. L., and Slater, J. H. (2017). Fundamentals of Laser-Based Hydrogel Degradation and Applications in Cell and Tissue Engineering. *Adv. Healthc. Mater.* 6, 1700681. doi:10.1002/adhm.201700681

Qian, Z., Sharma, D., Jia, W., Radke, D., Kamp, T., and Zhao, F. (2019). Engineering Stem Cell Cardiac Patch with Microvascular Features Representative of Native Myocardium. *Theranostics* 9, 2143–2157. doi:10.7150/thno.29552

Rambøl, M. H., Han, E., and Niklason, L. E. (2020). Microvessel Network Formation and Interactions with Pancreatic Islets in Three-Dimensional Chip Cultures. *Tissue Eng. Part A* 26, 556–568.

Rao, R. R., Peterson, A. W., Ceccarelli, J., Putnam, A. J., and Stegemann, J. P. (2012). Matrix Composition Regulates Three-Dimensional Network Formation by Endothelial Cells and Mesenchymal Stem Cells in Collagen/fibrin Materials. *Angiogenesis* 15, 253–264. doi:10.1007/s10456-012-9257-1

Redenski, I., Guo, S., Machour, M., Szklanny, A., Landau, S., Kaplan, B., et al. (2021). Engineered Vascularized Flaps, Composed of Polymeric Soft Tissue and Live Bone, Repair Complex Tibial Defects. *Adv. Funct. Mater.* 31, 2008687. doi:10.1002/adfm.202008687

Rezaie, J., Heidarzadeh, M., Hassanpour, M., Amini, H., Shokrollahi, E., Ahmadi, M., et al. (2019). "The Angiogenic Paracrine Potential of Mesenchymal Stem Cells," in *Update on Mesenchymal Induced Pluripotent Stem Cells*. Editor K. Al-Anazi (London, UK: Intechopen), 101–123. doi:10.5772/intechopen.84433

Rosca, A. M., Mitroi, D. N., Cismasiu, V., Badea, R., Necula-Petrareanu, G., Preda, M. B., et al. (2018). Collagen Regulates the Ability of Endothelial Progenitor Cells to Protect Hypoxic Myocardium through a Mechanism Involving miR-377/VE-PTP axis. *J. Cel Mol Med* 22, 4700–4708. doi:10.1111/jcmm.13712

Roux, B. M., Akar, B., Zhou, W., Stojkova, K., Barrera, B., Brankov, J., et al. (2018). Preformed Vascular Networks Survive and Enhance Vascularization in Critical Sized Cranial Defects. *Tissue Eng. Part A* 24, 1603–1615. doi:10.1089/ten.tea.2017.0493

Roux, B. M., Vaicik, M. K., Shrestha, B., Montelongo, S., Stojkova, K., Yang, F., et al. (2021). Induced Pluripotent Stem Cell-Derived Endothelial Networks Accelerate Vascularization but Not Bone Regeneration. *Tissue Eng. Part A* 27, 940–961. doi:10.1089/ten.tea.2020.0200

Samee, M., Kasugai, S., Kondo, H., Ohya, K., Shimokawa, H., and Kuroda, S. (2008). Bone Morphogenetic Protein-2 (BMP-2) and Vascular Endothelial Growth Factor (VEGF) Transfection to Human Periosteal Cells Enhances Osteoblast Differentiation and Bone Formation. *J. Pharmacol. Sci.* 108, 18–31. doi:10.1254/jphs.08036fp

Sasagawa, T., Shimizu, T., Yamato, M., and Okano, T. (2014). Expression Profiles of Angiogenesis-Related Proteins in Prevascular Three-Dimensional Tissues Using Cell-Sheet Engineering. *Biomaterials* 35, 206–213. doi:10.1016/j.biomaterials.2013.09.104

Sasaki, K., Akagi, T., Asaoka, T., Eguchi, H., Fukuda, Y., Iwagami, Y., et al. (2017). Construction of Three-Dimensional Vascularized Functional Human Liver Tissue Using a Layer-By-Layer Cell Coating Technique. *Biomaterials* 133, 263–274. doi:10.1016/j.biomaterials.2017.02.034

Sen, S., Mcdonald, S. P., Coates, P. T. H., and Bonder, C. S. (2011). Endothelial Progenitor Cells: Novel Biomarker and Promising Cell Therapy for Cardiovascular Disease. *Clin. Sci.* 120, 263–283. doi:10.1042/cs20100429

Shimazu, Y., Zhang, B., Yue, Z., Wallace, G. G., and Fukuda, J. (2019). Engineering of Perfusable Double-Layered Vascular Structures Using Contraction of Spheroid-Embedded Hydrogel and Electrochemical Cell Detachment. *J. Biosci. Bioeng.* 127, 114–120. doi:10.1016/j.jbiosc.2018.07.006

Shor, E., Merdler, U., Brosh, I., Shoham, S., and Levenberg, S. (2018). Induced Neuro-Vascular Interactions Robustly Enhance Functional Attributes of Engineered Neural Implants. *Biomaterials* 180, 1–11. doi:10.1016/j.biomaterials.2018.07.001

Shudo, Y., Goldstone, A. B., Cohen, J. E., Patel, J. B., Hopkins, M. S., Steele, A. N., et al. (2017). Layered Smooth Muscle Cell-Endothelial Progenitor Cell Sheets Derived from the Bone Marrow Augment Postinfarction Ventricular Function. *J. Thorac. Cardiovasc. Surg.* 154, 955–963. doi:10.1016/j.jtcvs.2017.04.081

Silva, A. S., Santos, L. F., Mendes, M. C., and Mano, J. F. (2020). Multi-layer Pre-vascularized Magnetic Cell Sheets for Bone Regeneration. *Biomaterials* 231, 119664. doi:10.1016/j.biomaterials.2019.119664

Sims, D. E. (1986). The Pericyte-A Review. *Tissue and Cell* 18, 153–174. doi:10.1016/0040-8166(86)90026-1

Skrzypek, K., Nibbelink, M. G., Karbaat, L. P., Karperien, M., Van Apeldoorn, A., and Stamatialis, D. (2018). An Important Step towards a Prevascularized Islet Macroencapsulation Device-Effect of Micropatterned Membranes on Development of Endothelial Cell Network. *J. Mater. Sci. Mater. Med.* 29, 91. doi:10.1007/s10856-018-6102-0

Song, S. Y., Kim, H., Yoo, J., Kwon, S. P., Park, B. W., Kim, J.-J., et al. (2020). Prevascularized, Multiple-Layered Cell Sheets of Direct Cardiac Reprogrammed Cells for Cardiac Repair. *Biomater. Sci.* 8, 4508–4520. doi:10.1039/d0bm00701c

Sorrell, J. M., Baber, M. A., and Caplan, A. I. (2007). A Self-Assembled Fibroblast-Endothelial Cell Co-culture System that Supports *In Vitro* Vasculogenesis by Both Human Umbilical Vein Endothelial Cells and Human Dermal Microvascular Endothelial Cells. *Cells Tissues Organs* 186, 157–168. doi:10.1159/000106670

Sorrell, J. M., Baber, M. A., and Caplan, A. I. (2009). Influence of Adult Mesenchymal Stem Cells onIn VitroVascular Formation. *Tissue Eng. Part A* 15, 1751–1761. doi:10.1089/ten.tea.2008.0254

Sousa, C. F. V., Saraiva, C. A., Correia, T. R., Pesqueira, T., Patrício, S. G., Rial-Hermida, M. I., et al. (2021). Bioinstructive Layer-By-Layer-Coated Customizable 3D Printed Perfusable Microchannels Embedded in Photocrosslinkable Hydrogels for Vascular Tissue Engineering. *Biomolecules* 11, 863. doi:10.3390/biom11060863

Später, T., Ampofo, E., Menger, M. D., and Laschke, M. W. (2020). Combining Vascularization Strategies in Tissue Engineering: The Faster Road to Success? *Front. Bioeng. Biotechnol.* 8, 592095. doi:10.3389/fbioe.2020.592095

Später, T., Frueh, F. S., Nickels, R. M., Menger, M. D., and Laschke, M. W. (2018). Prevascularization of Collagen-Glycosaminoglycan Scaffolds: Stromal Vascular Fraction versus Adipose Tissue-Derived Microvascular Fragments. *J. Biol. Eng.* 12, 24. doi:10.1186/s13036-018-0118-3

Stahl, A., Wenger, A., Weber, H., Stark, G. B., Augustin, H. G., and Finkenzeller, G. (2004). Bi-directional Cell Contact-dependent Regulation of Gene Expression between Endothelial Cells and Osteoblasts in a Three-Dimensional Spheroidal Coculture Model. *Biochem. biophysical Res. Commun.* 322, 684–692. doi:10.1016/j.bbrc.2004.07.175

Sukmawati, D., and Tanaka, R. (2015). Introduction to Next Generation of Endothelial Progenitor Cell Therapy: a Promise in Vascular Medicine. *Am. J. Transl Res.* 7, 411–421.

Sun, R., Huang, J., and Sun, B. (2020). Mobilization of Endothelial Progenitor Cells in Sepsis. *Inflamm. Res.* 69, 1–9. doi:10.1007/s00011-019-01299-9

Suresh, V., and West, J. L. (2020). 3D Culture Facilitates VEGF-Stimulated Endothelial Differentiation of Adipose-Derived Stem Cells. *Ann. Biomed. Eng.* 48, 1034–1044. doi:10.1007/s10439-019-02297-y

Swerlick, R. A., Lee, K. H., Wick, T. M., and Lawley, T. J. (1992). Human Dermal Microvascular Endothelial but Not Human Umbilical Vein Endothelial Cells Express CD36 *In Vivo* and *In Vitro*. *J. Immunol.* 148, 78–83.

Takeuchi, K., Nakazawa, M., and Ebina, Y. (2011). Effects of Trehalose on VEGF-Stimulated Angiogenesis and Myofibroblast Proliferation: Implications for Glaucoma Filtration Surgery. *Invest. Ophthalmol. Vis. Sci.* 52, 6987–6993. doi:10.1167/iovs.11-7478

Tocchio, A., Tamplenizza, M., Martello, F., Gerges, I., Rossi, E., Argentiere, S., et al. (2015). Versatile Fabrication of Vascularizable Scaffolds for Large Tissue Engineering in Bioreactor. *Biomaterials* 45, 124–131. doi:10.1016/j.biomaterials.2014.12.031

Umemoto, T., Yamato, M., Nishida, K., and Okano, T. (2013). Regenerative Medicine of Cornea by Cell Sheet Engineering Using Temperature-Responsive Culture Surfaces. *Chin. Sci. Bull.* 58, 4349–4356. doi:10.1007/s11434-013-5742-1

Valarmathi, M. T., Fuseler, J. W., Davis, J. M., and Price, R. L. (2017). A Novel Human Tissue-Engineered 3-D Functional Vascularized Cardiac Muscle Construct. *Front. Cel Dev. Biol.* 5, 2. doi:10.3389/fcell.2017.00002

Valarmathi, M. T., Fuseler, J. W., Potts, J. D., Davis, J. M., and Price, R. L. (2018). Functional Tissue Engineering: a Prevascularized Cardiac Muscle Construct for Validating Human Mesenchymal Stem Cells Engraftment Potential *In Vitro*. *Tissue Eng. Part A* 24, 157–185. doi:10.1089/ten.tea.2016.0539

Vidal, L., Brennan, M. Á., Krissian, S., De Lima, J., Hoornaert, A., Rosset, P., et al. (2020). *In Situ* production of Pre-vascularized Synthetic Bone Grafts for Regenerating Critical-Sized Defects in Rabbits. *Acta Biomater.* 114, 384–394. doi:10.1016/j.actbio.2020.07.030

Viswanathan, S., Shi, Y., Galipeau, J., Krampera, M., Leblanc, K., Martin, I., et al. (2019). Mesenchymal Stem versus Stromal Cells: International Society for Cell & Gene Therapy (ISCT) Mesenchymal Stromal Cell Committee Position Statement on Nomenclature. *Cytotherapy* 21, 1019–1024. doi:10.1016/j.jcyt.2019.08.002

Wang, B., Lv, X., Li, Z., Zhang, M., Yao, J., Sheng, N., et al. (2020a). Urethra-inspired Biomimetic Scaffold: a Therapeutic Strategy to Promote Angiogenesis for Urethral Regeneration in a Rabbit Model. *Acta Biomater.* 102, 247–258. doi:10.1016/j.actbio.2019.11.026

Wang, C., Li, Y., Yang, M., Zou, Y., Liu, H., Liang, Z., et al. (2018). Efficient Differentiation of Bone Marrow Mesenchymal Stem Cells into Endothelial Cells *In Vitro*. *Eur. J. Vasc. Endovascular Surg.* 55, 257–265. doi:10.1016/j.ejvs.2017.10.012

Wang, K., Lin, R. Z., Hong, X., Ng, A. H., Lee, C. N., Neumeyer, J., et al. (2020b). Robust Differentiation of Human Pluripotent Stem Cells into Endothelial Cells via Temporal Modulation of ETV2 with Modified mRNA. *Sci. Adv.* 6, eaba7606. doi:10.1126/sciadv.aba7606

Waters, J. P., Kluger, M. S., Graham, M., Chang, W. G., Bradley, J. R., and Pober, J. S. (2013). *In Vitro* self-assembly of Human Pericyte-Supported Endothelial Microvessels in Three-Dimensional Coculture: a Simple Model for Interrogating Endothelial-Pericyte Interactions. *J. Vasc. Res.* 50, 324–331. doi:10.1159/000353303

Weigand, A., Horch, R. E., Boos, A. M., Beier, J. P., and Arkudas, A. (2018). The Arteriovenous Loop: Engineering of Axially Vascularized Tissue. *Eur. Surg. Res.* 59, 286–299. doi:10.1159/000492417

Weyers, J. J., Gunaje, J. J., Van Biber, B., Martinson, A., Reinecke, H., Mahoney, W. M., et al. (2020). Sonic Hedgehog Upregulation Does Not Enhance the Survival and Engraftment of Stem Cell-Derived Cardiomyocytes in Infarcted Hearts. *PloS one* 15, e0227780. doi:10.1371/journal.pone.0227780

Wonil, H., Kim, J.-H., Singh, N., Park, D. J., Lee, E. B., Lee, H., et al. (2018). "3D Cell-Printing of Prevascularized Stem Cell Patch for Liver Cirrhosis Treatment," in 2018 annual meeting of Korean Society for Stem Cell Research (KSSCR), Seoul, South Korea: Korean Stem Cell Society, 170–170. Available at: http://oasis.postech.ac.kr/handle/2014.oak/95112 [absrtact].

Wu, K. H., Zhou, B., Lu, S. H., Feng, B., Yang, S. G., Du, W. T., et al. (2007). *In Vitro* and *In Vivo* Differentiation of Human Umbilical Cord Derived Stem Cells into Endothelial Cells. *J. Cel. Biochem.* 100, 608–616. doi:10.1002/jcb.21078

Wu, X., Wang, Q., Kang, N., Wu, J., Gu, C., Bi, J., et al. (2017). The Effects of Different Vascular Carrier Patterns on the Angiogenesis and Osteogenesis of BMSC-TCP-Based Tissue-Engineered Bone in Beagle Dogs. *J. Tissue Eng. Regen. Med.* 11, 542–552. doi:10.1002/term.2076

Xing, Z., Zhao, C., Liu, H., and Fan, Y. (2020). Endothelial Progenitor Cell-Derived Extracellular Vesicles: A Novel Candidate for Regenerative Medicine and Disease Treatment. *Adv. Healthc. Mater.* 9, 2000255. doi:10.1002/adhm.202000255

Xu, L., Zhou, J., Liu, J., Liu, Y., Wang, L., Jiang, R., et al. (2017). Different Angiogenic Potentials of Mesenchymal Stem Cells Derived from Umbilical Artery, Umbilical Vein, and Wharton's Jelly. *Stem Cell Int.* 2017, 3175748. doi:10.1155/2017/3175748

Xu, M., Li, J., Liu, X., Long, S., Shen, Y., Li, Q., et al. (2019). Fabrication of Vascularized and Scaffold-free Bone Tissue Using Endothelial and Osteogenic Cells Differentiated from Bone Marrow Derived Mesenchymal Stem Cells. *Tissue and Cell* 61, 21–29. doi:10.1016/j.tice.2019.08.003

Xueyong, L., Shaozong, C., Wangzhou, L., Yuejun, L., Xiaoxing, L., Jing, L., et al. (2008). Differentiation of the Pericyte in Wound Healing: The Precursor, the Process, and the Role of the Vascular Endothelial Cell. *Wound Repair Regen.* 16, 346–355. doi:10.1111/j.1524-475x.2008.00374.x

Yamato, M., and Okano, T. (2004). Cell Sheet Engineering. *Mater. Today* 7, 42–47. doi:10.1016/s1369-7021(04)00234-2

Yang, Y. P., Gadomski, B. C., Bruyas, A., Easley, J., Labus, K. M., Nelson, B., et al. (2021). Investigation of a Prevascularized Bone Graft for Large Defects in the Ovine Tibia. *Tissue Eng. Part A* [Epub ahead of print]. doi:10.1089/ten.tea.2020.0347

Yazdanpanah, G., Paeini-Vayghan, G., Asadi, S., and Niknejad, H. (2015). The Effects of Cryopreservation on Angiogenesis Modulation Activity of Human Amniotic Membrane. *Cryobiology* 71, 413–418. doi:10.1016/j.cryobiol.2015.09.008

Yoon, Y., Voloudakis, G., Doran, N., Zhang, E., Dimovasili, C., Chen, L., et al. (2020). PS1 FAD Mutants Decrease ephrinB2-Regulated Angiogenic Functions, Ischemia-Induced Brain Neovascularization and Neuronal Survival. *Mol. Psychiatry* 26, 1996–2012. doi:10.1038/s41380-020-0812-7

Yu, Y., Chen, J., Chen, R., Cao, L., Tang, W., Lin, D., et al. (2015). Enhancement of VEGF-Mediated Angiogenesis by 2-N,6-O-Sulfated Chitosan-Coated Hierarchical PLGA Scaffolds. *ACS Appl. Mater. Inter.* 7, 9982–9990. doi:10.1021/acsami.5b02324

Zhang, C., Hu, K., Liu, X., Reynolds, M. A., Bao, C., Wang, P., et al. (2017a). Novel hiPSC-Based Tri-culture for Pre-vascularization of Calcium Phosphate Scaffold to Enhance Bone and Vessel Formation. *Mater. Sci. Eng. C* 79, 296–304. doi:10.1016/j.msec.2017.05.035

Zhang, J., Schwartz, M. P., Hou, Z., Bai, Y., Ardalani, H., Swanson, S., et al. (2017c). A Genome-wide Analysis of Human Pluripotent Stem Cell-Derived Endothelial Cells in 2D or 3D Culture. *Stem Cel. Rep.* 8, 907–918. doi:10.1016/j.stemcr.2017.02.014

Zhang, L., Qian, Z., Tahtinen, M., Qi, S., and Zhao, F. (2018). Prevascularization of Natural Nanofibrous Extracellular Matrix for Engineering Completely Biological Three-Dimensional Prevascularized Tissues for Diverse Applications. *J. Tissue Eng. Regen. Med.* 12, e1325–e1336. doi:10.1002/term.2512

Zhang, L., Xing, Q., Qian, Z., Tahtinen, M., Zhang, Z., Shearier, E., et al. (2016). Hypoxia Created Human Mesenchymal Stem Cell Sheet for Prevascularized 3D Tissue Construction. *Adv. Healthc. Mater.* 5, 342–352. doi:10.1002/adhm.201500744

Zhang, S., Zhou, M., Ye, Z., Zhou, Y., and Tan, W.-S. (2017b). Fabrication of Viable and Functional Pre-vascularized Modular Bone Tissues by Coculturing MSCs and HUVECs on Microcarriers in Spinner Flasks. *Biotechnol. J.* 12, 1700008. doi:10.1002/biot.201700008

Zhang, W., Wray, L. S., Rnjak-Kovacina, J., Xu, L., Zou, D., Wang, S., et al. (2015). Vascularization of Hollow Channel-Modified Porous Silk Scaffolds with Endothelial Cells for Tissue Regeneration. *Biomaterials* 56, 68–77. doi:10.1016/j.biomaterials.2015.03.053

Zhu, S., Wang, J., and Sun, Z. (2018). Observation of Co-culturing Cells on Porous Silk Fibroin Films. *Bioinspired, Biomimetic & Nanobiomaterials* 8, 109–114.

Zimoch, J., Padial, J. S., Klar, A. S., Vallmajo-Martin, Q., Meuli, M., Biedermann, T., et al. (2018). Polyisocyanopeptide Hydrogels: A Novel Thermo-Responsive Hydrogel Supporting Pre-vascularization and the Development of Organotypic Structures. *Acta Biomater.* 70, 129–139. doi:10.1016/j.actbio.2018.01.042

Conflict of Interest: The authors declare that the research was conducted in the absence of any commercial or financial relationships that could be construed as a potential conflict of interest.

Publisher's Note: All claims expressed in this article are solely those of the authors and do not necessarily represent those of their affiliated organizations, or those of the publisher, the editors and the reviewers. Any product that may be evaluated in this article, or claim that may be made by its manufacturer, is not guaranteed or endorsed by the publisher.

frontiers in Bioengineering and Biotechnology

ORIGINAL RESEARCH
published: 23 December 2021
doi: 10.3389/fbioe.2021.790489

Tumor-Derived Extracellular Vesicles Induce Abnormal Angiogenesis *via* TRPV4 Downregulation and Subsequent Activation of YAP and VEGFR2

Brianna Guarino[1†], *Venkatesh Katari*[1,2], *Ravi Adapala*[1,2], *Neha Bhavnani*[1], *Julie Dougherty*[3,4], *Mahmood Khan*[3,4], *Sailaja Paruchuri*[2] *and Charles Thodeti*[1,2*]

[1]*Department of Integrative Medical Sciences, Northeast Ohio Medical University, Rootstown, OH, United States,* [2]*Department of Physiology and Pharmacology, University of Toledo, Toledo, OH, United States,* [3]*Dorothy M. Davis Heart and Lung Research Institute, The Ohio State University Wexner Medical Center, Columbus, OH, United States,* [4]*Department of Emergency Medicine, The Ohio State University, Columbus, OH, United States*

Tumor angiogenesis is initiated and maintained by the tumor microenvironment through secretion of autocrine and paracrine factors, including extracellular vesicles (EVs). Although tumor-derived EVs (t-EVs) have been implicated in tumor angiogenesis, growth and metastasis, most studies on t-EVs are focused on proangiogenic miRNAs and growth factors. We have recently demonstrated that conditioned media from human lung tumor cells (A549) downregulate TRPV4 channels and transform normal endothelial cells to a tumor endothelial cell-like phenotype and induce abnormal angiogenesis *in vitro, via* t-EVs. However, the underlying molecular mechanism of t-EVs on endothelial cell phenotypic transition and abnormal angiogenesis *in vivo* remains unknown. Here, we demonstrate that t-EVs downregulate TRPV4 expression post-translationally and induce abnormal angiogenesis by activating Rho/Rho kinase/YAP/VEGFR2 pathways. Further, we demonstrate that t-EVs induce abnormal vessel formation in subcutaneously implanted Matrigel plugs *in vivo* (independent of tumors), which are characterized by increased VEGFR2 expression and reduced pericyte coverage. Taken together, our findings demonstrate that t-EVs induce abnormal angiogenesis *via* TRPV4 downregulation-mediated activation of Rho/Rho kinase/YAP/VEGFR2 pathways and suggest t-EVs and TRPV4 as novel targets for vascular normalization and cancer therapy.

Keywords: endothelial cells, extracellular vesicles, transient receptor potential vanilloid 4, tumor angiogenesis, vascular endothelial growth factor receptor 2

OPEN ACCESS

Edited by:
Akiko Mammoto,
Medical College of Wisconsin, United States

Reviewed by:
Roopali Roy,
Boston Children's Hospital, United States
Ting-Yuan Tu,
National Cheng Kung University, Taiwan
Qing Miao,
New York University, United States

****Correspondence:***
Charles Thodeti
Charles.Thodeti@Utoledo.edu

†Present address:
Brianna Guarino,
Department of Biology and Medicine, Brown University, Providence, RI, United States

Specialty section:
This article was submitted to Tissue Engineering and Regenerative Medicine, a section of the journal Frontiers in Bioengineering and Biotechnology

Received: *07 October 2021*
Accepted: *03 December 2021*
Published: *23 December 2021*

Citation:
Guarino B, Katari V, Adapala R, Bhavnani N, Dougherty J, Khan M, Paruchuri S and Thodeti C (2021) Tumor-Derived Extracellular Vesicles Induce Abnormal Angiogenesis via TRPV4 Downregulation and Subsequent Activation of YAP and VEGFR2. Front. Bioeng. Biotechnol. 9:790489. doi: 10.3389/fbioe.2021.790489

INTRODUCTION

A key step in the formation of solid tumors is the growth of new vessels from pre-existing ones, a process known as tumor angiogenesis. The crosstalk of tumor cells and varying cell types within the tumor microenvironment (TME) is a crucial part of the tumor angiogenic process. However, this crosstalk eventually leads to the abnormal characteristics observed in the tumor vasculature (Lee et al., 2015). Tumor vessels exhibit decreased pericyte coverage and breakdown of basement membranes, leading to hyperpermeability, disorganization, and vessel enlargement (Baluk et al.,

2005; Nagy et al., 2006). Importantly, these vascular abnormalities decrease the efficacy of chemotherapies due to poor drug perfusion into the tumors (Saleem and Price, 2008; Dewhirst and Secomb, 2017). Traditional anti-angiogenic therapies target VEGF and show promise as cancer-treating agents, however, due to acquired drug resistance, favorable effects are limited to short-term treatment (Miller et al., 2007; Ratner et al., 2012). Therefore, there is an urgent need for drug targets that aim to "normalize" rather than impede the tumor vasculature.

Crosstalk between cells of the TME is accomplished *via* several autocrine, paracrine, and juxtacrine signaling mechanisms (Ge et al., 2019). Recently, it has become evident that extracellular vesicles (EVs) play key role in both the autocrine and paracrine signaling cascades involved in cancer progression and metastasis (Gangoda et al., 2015; Asare-Werehene et al., 2020). EVs are small nanovesicles (20–5,000 nm) consisting of exosomes, microvesicles, and apoptotic bodies, which contain cargo such as nucleic acids, miRNAs, proteins, and lipids (Doyle and Wang, 2019; Veziroglu and Mias, 2020). Once secreted, recipient cells internalize EVs via endocytosis, thus completing the trafficking of cargo (Joshi et al., 2020). In fact, it is well known that the cargo found in/on EVs is involved in the process of tumor angiogenesis. Tumor-derived EVs (t-EVs) have been shown to express heparin-bound VEGF on their surface, which induces endothelial cell migration and tube formation (Ko et al., 2019). Additionally, Skog et al. discovered angiogenic proteins TIMP-2, IL-6, IL-8, TIMP-1, VEGF, and angiogenin in glioblastoma-derived EVs (Skog et al., 2008). Angiogenic promoting microRNA, miR-181b-5p, has been identified in EVs secreted from esophageal squamous cell carcinomas, which can be received by endothelial cells to stimulate angiogenesis *via* PTEN and PHLPP2 targeting (Wang et al., 2020). Despite their known angiogenic effects, the role of t-EVs on endothelial cell transformation is not well understood.

The calcium permeable mechanosensitive ion channel, transient receptor potential vanilloid 4 (TRPV4), has many implications in cancer progression. For instance, it has been shown that knockdown of TRPV4 in breast cancer cells decreases blebbing, a process by which the cellular membrane detaches from the cortex due to pressure, which has implications in metastasis (Lee et al., 2016). Additionally, antagonism of TRPV4 channels in hepatocellular carcinoma (HCC) leads to decreased ERK phosphorylation/activation, a key pathway involved in cell proliferation (Fang et al., 2018). Notably, we have shown that TRPV4 is downregulated in tumor endothelial cells and that pharmacological activation of these channels normalizes the tumor vasculature and improves drug delivery (Adapala et al., 2016). Further, we have shown that the downregulation of TRPV4 increases basal Rho activity, endothelial cell proliferation via ERK phosphorylation, and VEGFR2 and YAP signaling (Thoppil et al., 2015; Thoppil et al., 2016; Kanugula et al., 2019). However, the angiogenic implications of TRPV4 modulation *via* t- EVs remains unknown. To elucidate this, previously, we found that tumor cell conditioned media (TCM) causes normal human endothelial cells (hNEC) to transform into a human tumor endothelial cell-like phenotype (hTEC) *via* TRPV4 downregulation, leading to abnormal tube formation *in vitro*. We also demonstrated that t-EVs isolated from TCM induces the abnormal tube formation seen in hTEC (Guarino et al., 2019). In the present study, we investigated if t-EVs downregulate endothelial TRPV4 channels and modulate various signaling pathways involved in angiogenesis. Further, we examined if t-EVs can induce abnormal angiogenesis *in vivo*, in wild-type (WT) mice, independent of tumors. Our findings suggest that t-EVs modulate the endothelial cell phenotype, TRPV4 channels, and downstream signaling mechanisms, which induces abnormal angiogenesis both *in vitro* and *in vivo*.

METHODS

Cell culture: Human microvascular endothelial cells (HMEC-1) were purchased from ATCC (Manassas, VA, United States) and were cultured as previously described (Guarino et al., 2019). Briefly, HMEC-1 were cultured in MCDB-131 media, supplemented with 10% FBS, 1% penicillin-streptomycin, 1% L-glutamine, 1% hydrocortisone, and 10 ng/ml human EGF.

Extracellular vesicle isolation and characterization: Adenocarcinomic human alveolar basal epithelial cells (A549) were purchased from ATCC and cultured in normal DMEM high glucose media supplemented with 10% fetal bovine serum (FBS) and 1% penicillin-streptomycin. Once the cells had reached ~80% confluence, complete media was replaced with serum-free media for 24 h, collected, and spun down to remove any cellular debris. Media was passed through a 0.22 μm syringe filter and stored at −80°C for future use. Extracellular vesicles were isolated and characterized as previously described (Guarino et al., 2019; Dougherty et al., 2020). In brief, TCM was concentrated 5X with 100 kD MWCO centrifugal filters, 1/5 volume of ExoQuick-TC reagent (SBI, Mountain View, CA, United States) was added to TCM, which was then incubated overnight at 4°C, followed by centrifugation at 1,500 x g for 30 min at 4°C. Centrifugation was performed a second time to remove residual supernatant. EVs were re-suspended in sterile PBS and stored at −80°C. For characterization, diluted EVs (PBS) were added to Malvern Nanosight NS300 and analyzed using Nanoparticle Tracking Analysis (NTA) software v3.3 (Malvern, United Kingdom) in triplicate runs. For total EV protein estimation, EVs were lysed in 1x RIPA buffer [150 mM NaCl, 50 mM Tris HCl pH 8.0, 5 mM EDTA, 10% v/v IGEPAL CA-630, 5% w/v sodium deoxycholate, 1% w/v sodium dodecyl sulfate, 1x comlplete protease inhibitor cocktail (Roche)] on ice for at least 10 min. EVs were appropriately diluted with PBS and protein estimation utilized the Protein Assay Dye Reagent Concentrate (BioRad), with absorbance measured on a spectrophotometer at 595nm, and interpolation to a BSA standard curve. EVs were tested in technical triplicate.

Calcium imaging: HMEC-1 cells were cultured as described above on MatTek glass bottom dishes (MatTek, Ashland, MA, United States). After 24 h, complete media was replaced with a combination of complete media and serum free media (25:75) and t-EVs were added to cells at a concentration of 100 μg/ml. After 48 h, cells were loaded with Fluo-4/AM (4 μM) for 25 min and were washed in previously described calcium media (Adapala et al., 2011; Adapala et al., 2016). Live cell imaging was done on an Olympus FluoView 300 microscope (Olympus, Shinjuku, Tokyo, Japan) after stimulation with GSK1016790A (100 nM), the TRPV4 agonist.

2D angiogenesis assays (in vitro): Growth factor reduced Matrigel® (BD biosciences, San Jose, CA, United States) was plated on a 48-well plate and placed at 37°C for 30 min (Adapala et al., 2016; Thoppil et al., 2016; Guarino et al., 2019). HMEC-1 were cultured and treated with 100 μg/ml of t-EVs for 48 h prior to angiogenesis assays, as described above. The Rho kinase inhibitor, Y27632, was added to cells (10 μM) just before plating on Matrigel. Images were taken at 24 h after plating the cells on Matrigel and tube length was quantified using ImageJ Software.

Immunocytochemistry: Cells were cultured in 6-well plates on glass coverslips and fixed with 4% paraformaldehyde (PFA) for 20 min. Cells were then washed 3x in—PBS, permeabilized for 15 min with 0.25% TritonX-100, blocked for 30 min in FBS-containing media, and incubated with VEGFR2 primary antibody (1:200; Cell Signaling Technology, Danvers, MA, United States) or YAP primary antibody (1:100; Santa Cruz Biotechnology, Dallas, TX, United States) for 1 h at room temperature. Following incubation, cells were again washed 3x in PBS, followed by incubation with appropriate Alexa Fluor (488 and 594) conjugated antibody (1:500; Thermo Fisher Scientific, Waltham, MA, United States). Cells were washed 3x in PBS and mounted with DAPI containing mounting media (Vector Laboratories, Burlingame, CA, United States) on glass slides. Images were obtaining using TCS SP5 laser scanning confocal microscope with MP at 63x (Leica Microsystems, Germany) and processed using ImageJ (NIH, Bethesda, Maryland, United States) software.

Western Blot: Cells were lysed in RIPA buffer containing 1X protease and phosphatase inhibitor cocktail (Millipore Sigma and Roche, Basel, Switzerland). Samples were prepared with 4X Laemmli sample buffer (Bio-Rad, Hercules, CA, United States) supplemented with β-mercaptoethanol. Lysates were loaded into 7.5% Mini-PROTEAN® TGX™ precast polyacrylamide gels (Bio-Rad, Hercules, CA, United States) for electrophoresis. Gels were transferred onto a PVDF membrane, which was briefly activated in methanol, and was blocked with 5% milk powder in tris-buffered saline with 0.1% Tween-20 (TBST). Membranes were incubated in primary antibodies (TRPV4, 1:300) (Alamone Labs, Jeru-salem, Israel; pVEGFR2 (1:1,000), VEGFR2 (1: 1,000), and GAPDH, (1:1,000) Cell Signaling Technology, Danvers, MA, United States) overnight at 4°C. The next day, membranes were washed in 1X TBST 3x for 15 min and incubated with secondary antibody, goat anti rabbit (1: 5,000) conjugated with horseradish peroxidase (Cell Signaling Technology, Danvers, MA, United States). Signals were detected with Luminata Crescendo (EMD Millipore, Burlington, MA, United States) and developed with a FluorChem M Simple Imager (Protein Simple, San Jose, CA, United States). Quantification of proteins was performed using ImageJ software (NIH, Bethesda, Maryland, United States).

In vivo Matrigel plug assays: All experiments were performed according to the approved protocol by the Institutional Animal Care and Use Committee (IACUC) at Northeast Ohio Medical University. t-EVs were isolated and characterized as described above. Phenol red free Matrigel was mixed with 0.25 μg/ml bFGF, 0.2 ng/ml mouse VEGF, and 0.58 μl/ml heparin (diluted in saline). 50μg/plug of EVs were added to Matrigel mixture and were mixed with an ice-cold pipette. C57BL/6 mice were anesthetized with isoflurane and were injected subcutaneously with 500 μl of the pre-mixed Matrigel solution in each flank region (2 injections per mouse). After 14 days post-injection, mice were euthanized with Fatal-Plus and plugs were harvested for histological analysis.

Immunohistochemistry: Matrigel plugs were harvested from mice 14 days post-injection and were immediately frozen in OCT for cryo-sectioning. Samples were sectioned (10 μm) using a cryo-stat and were permeabilized in ice-cold acetone. Next, slides were washed in 1X TBS 3x for 5 min each and then blocked with 5% normal donkey serum or 5% goat serum. After blocking the following primary antibodies were added: CD31 (1:50; Invitrogen, Waltham, MA, United States), NG2 (1:100; EMD Millipore, Burlington, MA, United States), VEGFR2 (1:200; Cell Signaling Technologies, Danvers, MA, United States). Slides were incubated in a humidified chamber overnight at 4°C, washed 3x in 1X TBS, and incubated with appropriate AlexaFluor (488 and 594) secondary antibodies (1:500). After washing 3x in 1X TBST, slides were mounted with DAPI containing mounting medium (Vector Laboratories, Burlingame CA, United States). Images were acquired using an IX81 Olympus microscope with a Fluoview FV1000 or confocal laser scanning system and fluorescence intensities were quantified using ImageJ (NIH, Bethesda, Maryland, United States) software.

RT-Quantitative PCR (qPCR): RNA was isolated from endothelial cells with the RNeasy Mini Kit (Qiagen, Hilden, Germany) and was quantified using Take3™ Micro-Volume Plate on the Epoch™ Microplate Spectrophotometer (BioTek Instruments, Inc., Winooski, VT, United States). cDNA synthesis was performed using the RevertAid First Strand cDNA Synthesis Kit (Thermo Fisher Scientific, Waltham, MA, United States). qPCR was done on the Fast-Real-Time PCR system using SYBR green master mix (Thermo Fisher Scientific, Waltham, MA, United States). The following real-time primer sets were purchased from Integrated DNA Technologies (Coralville, IA, United States): β-actin (forward-5′-ACGTTGCTATCCAGGCTGTG-3′, reverse-5′-GAGGGCATACCCCTCGTAGA-3′) TRPV4 (forward- 5′-TCACTCTCACCGCCTACTACCA-3': reverse- 5′-CCCAGT GAAGAGCGTAATGACC-3′). mRNA expression was normalized to housekeeping gene, β-actin, and ΔΔCt values were expressed as a fold change relative to untreated ECs.

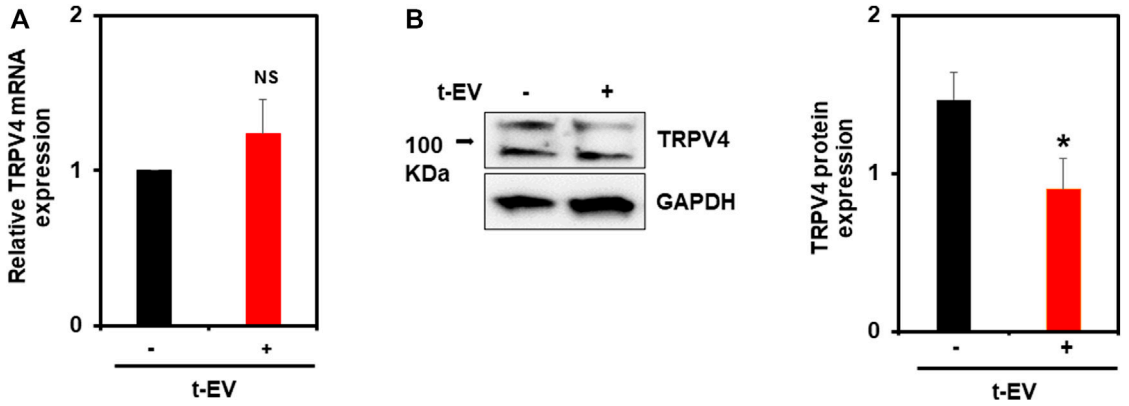

FIGURE 1 | t-EVs cause post-translational downregulation of endothelial TRPV4 channels. **(A)** qPCR analysis of TRPV4 mRNA expression from t-EV treated (+) or untreated (–) ECs. Note, no significant difference of TRPV4 mRNA between treated and untreated ECs (NS). TRPV4 mRNA expression was normalized to housekeeping gene, β-actin. **(B)** Representative western blots depicting decreased TRPV4 protein expression in t-EV treated ECs compared to untreated cells. Quantitative analysis demonstrating significantly decreased TRPV4 protein expression in t-EV treated ECs ($^*p \leq 0.05$; $n = 7$). Protein expression was normalized to GAPDH. The results shown are a mean ± SEM from three independent experiments.

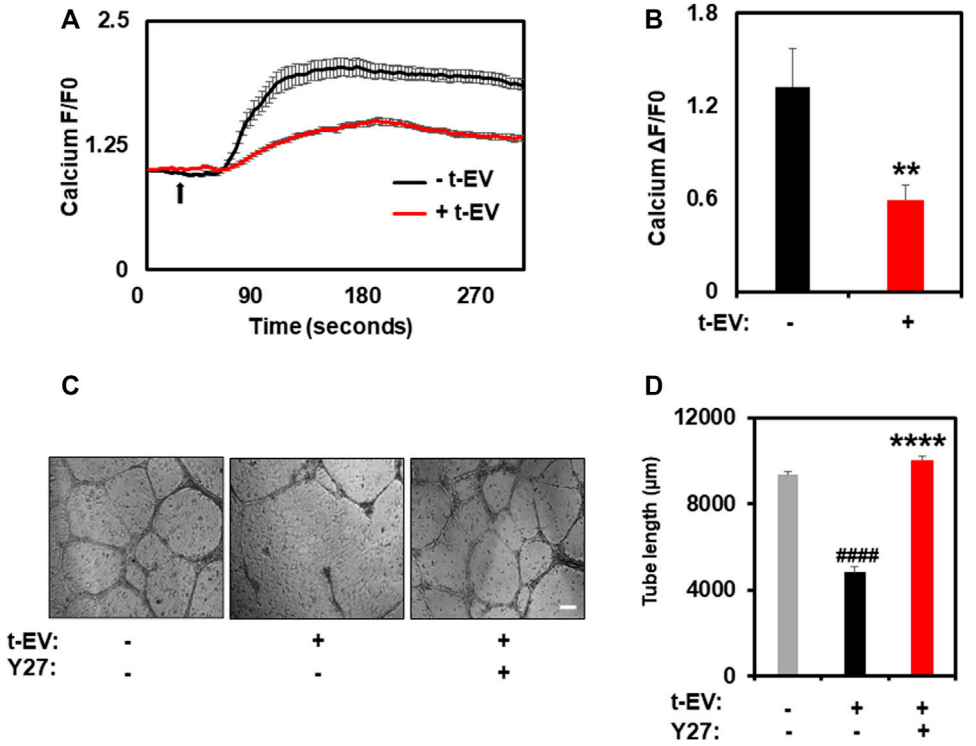

FIGURE 2 | t-EV treatment decreases functional activity of TRPV4 channels and inhibition of Rho kinase normalized t-EV induced abnormal angiogenesis. **(A)** Average traces showing calcium influx in response to the TRPV4 agonist, GSK1016790A (100 nM), in Fluo-4 loaded ECs treated with (+t-EV) or without (–t-EV) t-EVs. The arrow denotes time of stimulation with TRPV4 agonist. **(B)** Quantitative analysis of calcium influx showing a significant reduction ($^{****}p \leq 0.01$) in TRPV4-mediated calcium influx in + t-EV ECs compared to– t-EV ECs. (F/F0 = ratio of normalized fluorescent intensity relative to time 0). **(C)** Phase contrast micrographs (4x) of tube formation by ECs exposed to t-EVs with or without the Rho kinase inhibitor, Y-27632 (Y27) plated on 2D Matrigels. Scale bar = 200 μm. **(D)** Quantitative analysis of tube length demonstrating significantly increased tube length ($^{****}p \leq 0.0001$ indicates statistical significance relative to control cells; $\#\#\#\#p \leq 0.0001$ indicates statistical significance relative to t-EV-treated ECs without Y27; no statistical significance was observed between control ECs and t-EV/Y27 ECs) in + t-EV cells treated with the Rho kinase inhibitor, Y27, indicating vascular normalization. The results shown are a mean ± SEM from three independent experiments.

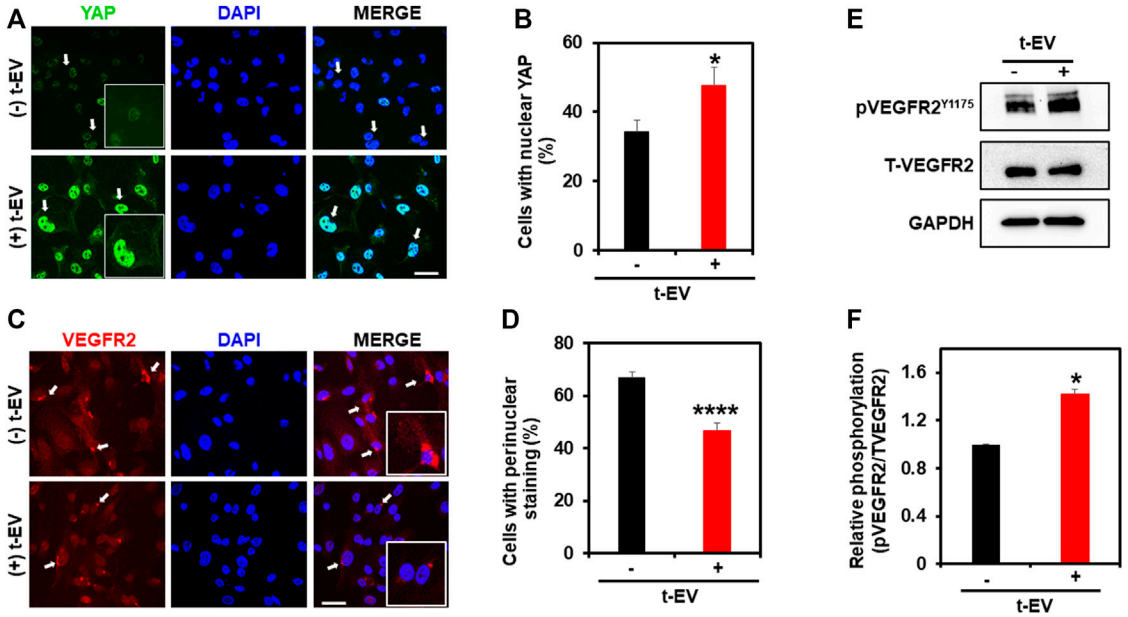

FIGURE 3 | t-EV treatment activates YAP nuclear translocation and reduces perinuclear VEGFR2 in ECs. **(A)** Representative confocal immunofluorescence images (63x) showing YAP (green) localization in t-EV-treated and untreated ECs. Cell nuclei were stained with DAPI (blue). Scale bar = 25 μm. Note, strong nuclear YAP localization (arrows) in t-EV-treated ECs (arrows; inset: zoomed image). **(B)** Quantitative analysis of the percent of cells with YAP nuclear staining, with or without t-EV treatment (n = 180–240 cells/condition). Note, the significantly increased (*$p \leq 0.05$) percent of ECs with YAP nuclear localization in + t-EV cells compared to – t-EVs. The results shown are a mean ± SEM from three independent experiments. **(C)** Representative confocal immunofluorescence images (63x) showing VEGFR2 (red) localization in t-EV treated and untreated ECs. Cell nuclei were stained with DAPI (blue). Scale bar = 25 μm. Note, strong perinuclear VEGFR2 localization (arrows; inset: zoomed image) in untreated ECs, which is diminished after t-EV exposure. **(D)** Quantitative analysis of the percent of cells with perinuclear VEGFR2 in the presence or absence of t-EVs. Note, the significantly decreased (****$p \leq 0.0001$) percent of ECs with perinuclear VEGFR2 in + t-EV compared to – t-EVs. The results shown are a mean ± SEM from three independent experiments. **(E)** Representative immunoblots showing the phosphorylation of VEGFR2 at Y1175 in the presence or absence of t-EVs in human microvascular endothelial cells **(Top panel)**. Total VEGFR2 and GAPDH are served as controls. **(F)** Quantitative analysis of immunoblots showing T-EV treatment enhanced the VEGFR2 phosphorylation compared to controls. The results shown are a mean ± SEM from two independent experiments.

Statistical analysis: All data was analyzed with independent sample t-test using SPSS V. 24 software. The significance was set at *$p \leq 0.05$; **$p \leq 0.01$; ***$p \leq 0.001$; ****$p \leq 0.0001$. All values were expressed as means ± SEM.

RESULTS

Tumor-Derived EVs (t-EVs) Downregulate Endothelial TRPV4 Channels Post-translationally

We previously showed that tumor cell conditioned media (TCM) causes abnormal tube formation *in vitro* (via downregulation of TRPV4), and that the exosome inhibitor, GW4869, attenuates this effect (Guarino et al., 2019). Here, we assessed the expression of endothelial TRPV4 channels after exposure to purified t-EVs (**Figures 1A,B**). We found no significant differences in TRPV4 mRNA expression between t-EV-treated and control ECs (**Figure 1A**). However, western blot analysis revealed significantly decreased TRPV4 protein expression in t-EV-treated ECs compared to control ECs (**Figure 1B**, $p \leq 0.05$). These results indicate that t-EVs induce TRPV4 downregulation post-translationally.

t-EVs Modulate Rho/Rho Kinase/YAP/VEGFR2 Signaling *via* Downregulation of TRPV4 Channels

To unequivocally confirm that t-EVs downregulate functional expression of TRPV4, we next performed calcium imaging to assess the activity of TRPV4 in ECs. Indeed, calcium imaging revealed significantly decreased calcium influx in ECs exposed to t-EVs in the presence of the TRPV4 agonist, GSK1 (**Figures 2A,B**; $p \leq 0.01$), compared to untreated ECs. We have previously shown that the downregulation of TRPV4 causes abnormal tube formation via increased Rho/Rho kinase activity (Thoppil et al., 2016). Therefore, we asked whether t-EV-dependent downregulation of TRPV4 modulates angiogenesis via Rho/Rho kinase signaling. Here, we confirm that t-EVs cause abnormal tube formation in ECs (**Figures 2C,D**; middle panel) as evidenced by collapse of tubular net-work compared to control EC. However, when t-EV-exposed ECs are treated with the Rho kinase inhibitor, Y27632, tube formation is normalized (**Figures 2C,D**, right panel; $p \leq 0.0001$). Next, we investigated the effects of t-EVs on YAP and VEGFR2 signaling. Yes-associated protein (YAP) is an important transcriptional coactivator that has been shown to localize to the nucleus of ECs during angiogenesis (He et al., 2018) and is known to be regulated by Rho/Rho kinase

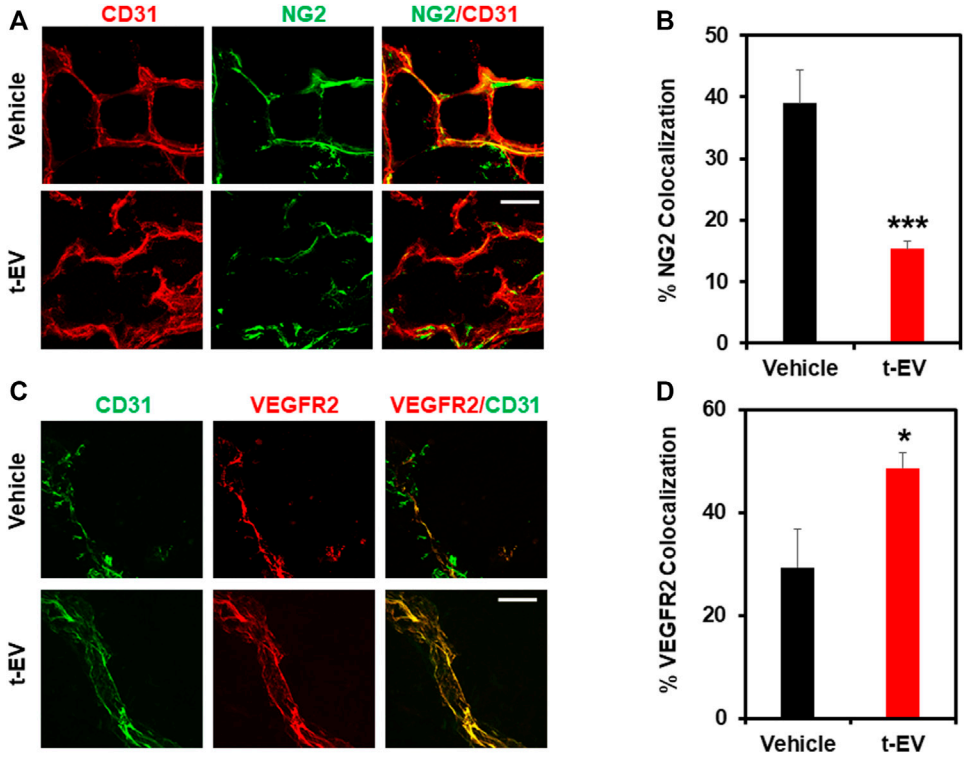

FIGURE 4 | t-EVs cause abnormal angiogenesis *in vivo* as evidenced by decreased pericyte coverage and increased VEGFR2 expression. **(A)** Representative immunofluorescence images (60x) of Matrigel sections stained with endothelial marker CD31 (red) and pericyte marker NG2 (green). Note, the reduced pericyte coverage and disorganized appearance of t-EV treated vessels. Scale bar = 100 μm. **(B)** Quantitative analysis revealing significantly decreased NG2/CD31 colocalization in t-EV Matrigel plugs (n = 7) (***$p \leq 0.001$) compared with vehicle alone (n = 4). **(C)** Representative immunofluorescence images (60X) taken from Matrigel plugs stained with endothelial marker CD31 (green) and VEGFR2 (red). Scale bar = 100 μm. **(D)** Quantitative analysis demonstrating significantly increased VEGFR2/CD31 colocalization (*$p \leq 0.05$) in t-EV treated Matrigel plugs (n = 7) compared to the vehicle (n = 4).

(Dupont et al., 2011; Yu et al., 2012; Ohgushi et al., 2015). Therefore, we asked if exposure to t-EVs mediates YAP nuclear localization. Immunostaining revealed significantly increased YAP nuclear localization in t-EV-treated ECs compared to untreated ECs (**Figures 3A,B**; $p \leq 0.05$; arrows and inset). Next, we found that VEGFR2 is mostly localized to perinuclear regions in un-treated ECs, which showed significant reduction in t-EV treated cells (**Figures 3C,D**; $p \leq 0.0001$; arrows and inset), consistent with our previous findings (Guarino et al., 2019; Kanugula et al., 2019). To independently confirm VEGFR2 activation, we have measured VEGFR2 phosphorylation at Y1175 in ECs treated or untreated with t-EVs. We found that t-EVs increased VEGFR2 phosphorylation suggesting the activation of VEGFR2 (**Figures 3E,F**; $p \leq 0.05$). Taken together, these data indicate that t-EVs downregulate the functional activity of TRPV4, and subsequently modulate Rho/Rho kinase/YAP/VEGFR2 pathways.

t-EVs Induce Abnormal Angiogenesis Independent of Solid Tumors

Based on our *in vitro* results, we investigated the effects of t-EVs on vessel growth *in vivo*, independent of tumors. To accomplish this, we injected Matrigel plugs with or without t-EVs (vehicle) into 8-week-old C57BL/6 WT mice. After 14 days, Matrigel plugs were removed and analyzed for vessel structure/integrity via immunohistochemistry for EC marker CD31, VEGFR2, and pericyte marker NG2 (**Figures 4A–D**; $p \leq 0.05$). We found vessels with distinct colocalization of NG2/CD31 in vehicle-treated Matrigel plugs, however, NG2/CD31 colocalization was reduced significantly in t-EV treated Matrigel plugs (**Figures 4A,B**; $p \leq 0.001$), indicative of decreased pericyte coverage. Next, we found significantly increased VEGFR2/CD31 colocalization in t-EV treated plugs compared to the vehicle (**Figures 4C,D**; $p \leq 0.05$), indicating that t-EVs compromise vessel integrity by causing increased expression of VEGFR2 and decreased pericyte coverage in otherwise healthy vessels.

DISCUSSION

In the current study, we demonstrate that tumor derived-EVs downregulate endothelial TRPV4 channels post-translationally and induce abnormal angiogenesis via Rho/Rho kinase/YAP/VEGFR2 pathway. Further, we demonstrate that independent of tumors, t-EVs stimulate a tumor angiogenesis-like phenotype in Matrigel plugs *in vivo*, which is evidenced by increased VEGFR2 positive vessels with reduced pericyte coverage.

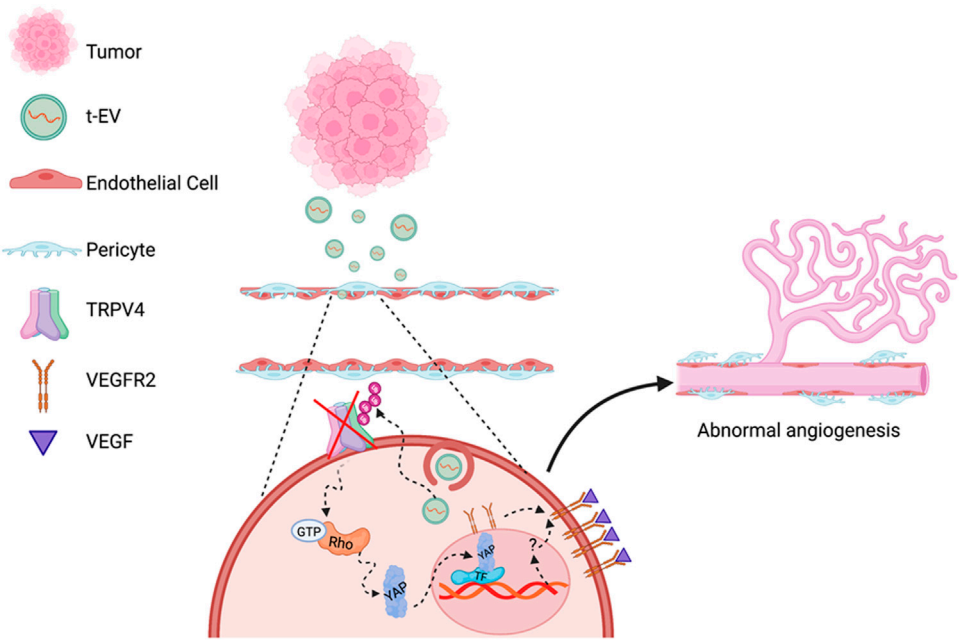

FIGURE 5 | Schematic of proposed molecular mechanisms of TRPV4 downregulation mediated abnormal angiogenesis. EVs secreted by tumors (t-EVs) released into the tumor microenvironment act on endothelial cells, leading to the downregulation of TRPV4 channels may be via ubiquitination. TRPV4 down-regulation, subsequently, induces Rho/Rho kinase mediated YAP nuclear translocation leading to VEGFR2 translocation from the perinuclear region to the plasma membrane (Kanugula et al., 2019). YAP commonly binds to transcription factors (TF) that initiate gene expression involved in cellular growth and proliferation (Huh et al., 2019), however, the mechanism by which YAP activates VEGFR2 translocation is unknown. VEGFR2 activation by VEGF, further induces EC proliferation, migration, and eventually, abnormal angiogenesis (Figure created with Biorender.com).

The vasculature of solid tumors is hyperpermeable and tortuous, which makes drug delivery difficult (Ma and Waxman, 2008; Stylianopoulos and Jain, 2013). Although vascular normalization improves the abnormal characteristics of tumor vessels and makes drug delivery more efficient (Mpekris et al., 2020; Moradi Kashkooli et al., 2021), these modalities are still dependent on classical anti-VEGF therapies. We have previously shown that the expression of mechanosensitive ion channel, TRPV4, is downregulated in tumor endothelial cells and activation of TRPV4 normalizes the tumor vasculature and improves chemotherapy (Adapala et al., 2016). However, the mechanisms by which tumors or the tumor microenvironment downregulate TRPV4 channels and influences angiogenesis *in vivo*, are not known. Here, we investigated the effects of t-EVs on endothelial TRPV4 channels and modulation of downstream signaling pathways, as well as angiogenesis *in vitro* and *in vivo*.

We have previously demonstrated that conditioned media (TCM) from human lung cancer cells transformed normal human endothelial cells into a tumor endothelial cell-like (TEC) phenotype via downregulation of TRPV4 channels (Guarino et al., 2019). Further, pre-treatment with exosome inhibitor GW4869 inhibited the TEC-like phenotype induced by TCM, indicating the role of t-EVs in this process. Indeed, treatment with purified t-EVs induced abnormal tube formation *in vitro*. Consistent with our previous findings that TCM downregulates TRPV4 expression and activity, purified t-EVs induced TRPV4 downregulation in ECs. Importantly, TRPV4 expression is reduced at the protein level but not at the mRNA level suggesting that t-EVs modulate TRPV4 expression, post-translationally. Calcium imaging experiments further confirmed the functional downregulation of TRPV4.

We have previously shown that downregulation or deletion of TRPV4 increases basal Rho/Rho kinase activity and induces abnormal angiogenesis (Thoppil et al., 2016). Indeed, we found that treatment with t-EVs induced abnormal tube formation, which was normalized by Rho kinase inhibitor, Y27632. YAP, a key transcriptional co-activator of the Hippo signaling pathway, is known to translocate to the nucleus in endothelial cells during angiogenesis (Hooglugt et al., 2021). Further, YAP was shown be activated by actin polymerization induced by Rho/Rho kinase (Dupont et al., 2011; Yu et al., 2012; Ohgushi et al., 2015). Importantly, VEGF has also been shown to stimulate nuclear translocation of YAP/TAZ and YAP/TAZ regulates VEGFR2 cellular localization/trafficking (Wang et al., 2017). The present study revealed significantly increased nuclear localization of YAP in ECs that were exposed to t-EVs. Moreover, we observed a reduction in perinuclear VEGFR2 after exposure to t-EVs, which is indicative of its plasma translocation and activation (Manickam et al., 2011). To delineate the molecular mechanism by which t-EVs downregulate endothelial TRPV4 channels, we checked TRPV4 expression at both the mRNA and protein level. Interestingly, there was no significant difference in TRPV4 mRNA expression, however, TRPV4 protein expression

was significantly downregulated. Since TRPV4 channels have been shown to undergo internalization via ubiquitination (Wegierski et al., 2006; Shukla et al., 2010), it is possible that t-EVs contain cargo that tag TRPV4 for ubiquitination, however, further studies are needed to determine the exact mechanisms by which t-EVs downregulate TRPV4 protein expression.

In the current study, we translated our *in vitro* findings to *in vivo* models of angiogenesis. When Matrigel plugs combined with t-EVs were implanted into WT mice, we found decreased pericyte coverage and increased VEGFR2 colocalization with the endothelium, which is reminiscent of pathological angiogenesis (Bergers and Song, 2005). The data presented in this study show, for the first time, that t-EVs downregulate the functional expression of TRPV4 and promote dysfunctional vascular growth independent of solid tumor formation. Moreover, we show that this is accomplished via Rho/Rho kinase/YAP/VEGFR2 signaling mechanisms preceding abnormal angiogenesis (**Figure 5**). Pathological angiogenesis is a hallmark of many diseases, including cancers, retinopathies, and rheumatoid arthritis (Aldebasi et al., 2013; Fallah et al., 2019). Traditional anti-angiogenic drugs targeting VEGF signaling pathways are often used to combat the abnormal angiogenesis observed in disease states by employing various mechanisms of action, including monoclonal anti-bodies, inhibition of tyrosine phosphorylation, decoy VEGF receptors, or ribosomal targeting (Cardones and Banez, 2006). However, these therapies have shown limited success, particularly in cancer (Miller et al., 2007; Ratner et al., 2012). Therefore, it is becoming increasingly important to explore other drug targets of tumor angiogenesis. Thus, our results indicate that both TRPV4 and t-EVs could prove to be novel targets for cancer therapies.

DATA AVAILABILITY STATEMENT

The raw data supporting the conclusion of this article will be made available by the authors, without undue reservation.

ETHICS STATEMENT

The animal study was reviewed and approved by the Institutional Animal Care and Use Committee (IACUC) at Northeast Ohio Medical University.

AUTHOR CONTRIBUTIONS

BG, VK, RA, NB, and JD performed research, analyzed the data, and edited the manuscript. MK and SP edited the manuscript. CT designed, interpreted, and analyzed data as well as wrote the manuscript.

FUNDING

This work was supported by National Institutes of Health (R15CA202847, R01HL119705, and R01HL148585; CKT and R01AI144115; SP and R01HL136232 to MK).

REFERENCES

Adapala, R. K., Talasila, P. K., Bratz, I. N., Zhang, D. X., Suzuki, M., Meszaros, J. G., et al. (2011). PKCα Mediates Acetylcholine-Induced Activation of TRPV4-dependent Calcium Influx in Endothelial Cells. *Am. J. Physiology-Heart Circulatory Physiol.* 301 (3), H757–H765. doi:10.1152/ajpheart.00142.2011

Adapala, R. K., Thoppil, R. J., Ghosh, K., Cappelli, H. C., Dudley, A. C., Paruchuri, S., et al. (2016). Activation of Mechanosensitive Ion Channel TRPV4 Normalizes Tumor Vasculature and Improves Cancer Therapy. *Oncogene* 35 (3), 314–322. doi:10.1038/onc.2015.83

Aldebasi, Y. H., Rahmani, A. H., Khan, A. A., and Aly, S. M. (2013). The Effect of Vascular Endothelial Growth Factor in the Progression of Bladder Cancer and Diabetic Retinopathy. *Int. J. Clin. Exp. Med.* 6 (4), 239–251.

Asare-Werehene, M., Nakka, K., Reunov, A., Chiu, C.-T., Lee, W.-T., Abedini, M. R., et al. (2020). The Exosome-Mediated Autocrine and Paracrine Actions of Plasma Gelsolin in Ovarian Cancer Chemoresistance. *Oncogene* 39 (7), 1600–1616. doi:10.1038/s41388-019-1087-9

Baluk, P., Hashizume, H., and McDonald, D. M. (2005). Cellular Abnormalities of Blood Vessels as Targets in Cancer. *Curr. Opin. Genet. Dev.* 15 (1), 102–111. doi:10.1016/j.gde.2004.12.005

Bergers, G., and Song, S. (2005). The Role of Pericytes in Blood-Vessel Formation and Maintenance. *Neuro Oncol.* 7 (4), 452–464. doi:10.1215/S1152851705000232

Cardones, A., and Banez, L. (2006). VEGF Inhibitors in Cancer Therapy. *Cpd* 12 (3), 387–394. doi:10.2174/138161206775201910

Dewhirst, M. W., and Secomb, T. W. (2017). Transport of Drugs from Blood Vessels to Tumour Tissue. *Nat. Rev. Cancer* 17 (12), 738–750. doi:10.1038/nrc.2017.93

Dougherty, J. A., Patel, N., Kumar, N., Rao, S. G., Angelos, M. G., Singh, H., et al. (2020). Human Cardiac Progenitor Cells Enhance Exosome Release and Promote Angiogenesis under Physoxia. *Front. Cel Dev. Biol.* 8. 130. doi:10.3389/fcell.2020.00130

Doyle, L., and Wang, M. (2019). Overview of Extracellular Vesicles, Their Origin, Composition, Purpose, and Methods for Exosome Isolation and Analysis. *Cells* 8 (7), 727. doi:10.3390/cells8070727

Dupont, S., Morsut, L., Aragona, M., Enzo, E., Giulitti, S., Cordenonsi, M., et al. (2011). Role of YAP/TAZ in Mechanotransduction. *Nature* 474 (7350), 179–183. doi:10.1038/nature10137

Fallah, A., Sadeghinia, A., Kahroba, H., Samadi, A., Heidari, H. R., Bradaran, B., et al. (2019). Therapeutic Targeting of Angiogenesis Molecular Pathways in Angiogenesis-dependent Diseases. *Biomed. Pharmacother.* 110, 775–785. doi:10.1016/j.biopha.2018.12.022

Fang, Y., Liu, G., Xie, C., Qian, K., Lei, X., Liu, Q., et al. (2018). Pharmacological Inhibition of TRPV4 Channel Suppresses Malignant Biological Behavior of Hepatocellular Carcinoma via Modulation of ERK Signaling Pathway. *Biomed. Pharmacother.* 101, 910–919. doi:10.1016/j.biopha.2018.03.014

Gangoda, L., Boukouris, S., Liem, M., Kalra, H., and Mathivanan, S. (2015). Extracellular Vesicles Including Exosomes Are Mediators of Signal Transduction: Are They Protective or Pathogenic? *Proteomics* 15 (2-3), 260–271. doi:10.1002/pmic.201400234

Ge, Y., Westphalen, C. B., Ma, W. W., Vega, K. J., and Weygant, N. (2019). Implications for Tumor Microenvironment and Epithelial Crosstalk in the Management of Gastrointestinal Cancers. *J. Oncol.* 2019, 1–11. doi:10.1155/2019/4835318

Guarino, B. D., Adapala, R. K., Kanugula, A. K., Lenkey, N. M., Dougherty, J. A., Paruchuri, S., et al. (2019). Extracellular Vesicles from Pathological Microenvironment Induce Endothelial Cell Transformation and Abnormal

Angiogenesis via Modulation of TRPV4 Channels. *Front. Cel Dev. Biol.* 7, 344. doi:10.3389/fcell.2019.00344

He, J., Bao, Q., Zhang, Y., Liu, M., Lv, H., Liu, Y., et al. (2018). Yes-Associated Protein Promotes Angiogenesis via Signal Transducer and Activator of Transcription 3 in Endothelial Cells. *Circ. Res.* 122 (4), 591–605. doi:10.1161/CIRCRESAHA.117.311950

Hooglugt, A., van der Stoel, M. M., Boon, R. A., and Huveneers, S. (2021). Endothelial YAP/TAZ Signaling in Angiogenesis and Tumor Vasculature. *Front. Oncol.* 10, 612802. doi:10.3389/fonc.2020.612802

Huh, H. D., Kim, D. H., Jeong, H. S., and Park, H. W. (2019). Regulation of TEAD Transcription Factors in Cancer Biology. *Cell* 8 (6). doi:10.3390/cells8060600

Joshi, B. S., de Beer, M. A., Giepmans, B. N. G., and Zuhorn, I. S. (2020). Endocytosis of Extracellular Vesicles and Release of Their Cargo from Endosomes. *ACS Nano* 14 (4), 4444–4455. doi:10.1021/acsnano.9b10033

Kanugula, A. K., Adapala, R. K., Midha, P., Cappelli, H. C., Meszaros, J. G., Paruchuri, S., et al. (2019). Novel Noncanonical Regulation of Soluble VEGF/VEGFR2 Signaling by Mechanosensitive Ion Channel TRPV4. *FASEB j.* 33 (1), 195–203. doi:10.1096/fj.201800509R

Ko, S. Y., Lee, W., Kenny, H. A., Dang, L. H., Ellis, L. M., Jonasch, E., et al. (2019). Cancer-derived Small Extracellular Vesicles Promote Angiogenesis by Heparin-Bound, Bevacizumab-Insensitive VEGF, Independent of Vesicle Uptake. *Commun. Biol.* 2, 386. doi:10.1038/s42003-019-0609-x

Lee, S. H., Jeong, D., Han, Y.-S., and Baek, M. J. (2015). Pivotal Role of Vascular Endothelial Growth Factor Pathway in Tumor Angiogenesis. *Ann. Surg. Treat. Res.* 89 (1), 1–8. doi:10.4174/astr.2015.89.1.1

Lee, W. H., Choong, L. Y., Mon, N. N., Lu, S., Lin, Q., Pang, B., et al. (2016). TRPV4 Regulates Breast Cancer Cell Extravasation, Stiffness and Actin Cortex. *Sci. Rep.* 6. 27903. doi:10.1038/srep27903

Ma, J., and Waxman, D. J. (2008). Combination of Antiangiogenesis with Chemotherapy for More Effective Cancer Treatment. *Mol. Cancer Ther.* 7 (12), 3670–3684. doi:10.1158/1535-7163.MCT-08-0715

Manickam, V., Tiwari, A., Jung, J.-J., Bhattacharya, R., Goel, A., Mukhopadhyay, D., et al. (2011). Regulation of Vascular Endothelial Growth Factor Receptor 2 Trafficking and Angiogenesis by Golgi Localized T-SNARE Syntaxin 6. *Blood* 117 (4), 1425–1435. doi:10.1182/blood-2010-06-291690

Miller, K., Wang, M., Gralow, J., Dickler, M., Cobleigh, M., Perez, E. A., et al. (2007). Paclitaxel Plus Bevacizumab versus Paclitaxel Alone for Metastatic Breast Cancer. *N. Engl. J. Med.* 357 (26), 2666–2676. doi:10.1056/NEJMoa072113

Moradi Kashkooli, F., Soltani, M., Momeni, M. M., and Rahmim, A. (2021). Enhanced Drug Delivery to Solid Tumors via Drug-Loaded Nanocarriers: An Image-Based Computational Framework. *Front. Oncol.* 11, 655781. doi:10.3389/fonc.2021.655781

Mpekris, F., Voutouri, C., Baish, J. W., Duda, D. G., Munn, L. L., Stylianopoulos, T., et al. (2020). Combining Microenvironment Normalization Strategies to Improve Cancer Immunotherapy. *Proc. Natl. Acad. Sci. USA* 117 (7), 3728–3737. doi:10.1073/pnas.1919764117

Nagy, J. A., Feng, D., Vasile, E., Wong, W. H., Shih, S.-C., Dvorak, A. M., et al. (2006). Permeability Properties of Tumor Surrogate Blood Vessels Induced by VEGF-A. *Lab. Invest.* 86 (8), 767–780. doi:10.1038/labinvest.3700436

Ohgushi, M., Minaguchi, M., and Sasai, Y. (2015). Rho-Signaling-Directed YAP/TAZ Activity Underlies the Long-Term Survival and Expansion of Human Embryonic Stem Cells. *Cell Stem Cell* 17 (4), 448–461. doi:10.1016/j.stem.2015.07.009

Ratner, E. S., Keane, F. K., Lindner, R., Tassi, R. A., Paranjape, T., Glasgow, M., et al. (2012). A KRAS Variant Is a Biomarker of Poor Outcome, Platinum Chemotherapy Resistance and a Potential Target for Therapy in Ovarian Cancer. *Oncogene* 31 (42), 4559–4566. doi:10.1038/onc.2011.539

Saleem, A., and Price, P. M. (2008). Early Tumor Drug Pharmacokinetics Is Influenced by Tumor Perfusion but Not Plasma Drug Exposure. *Clin. Cancer Res.* 14 (24), 8184–8190. doi:10.1158/1078-0432.CCR-08-1324

Shukla, A. K., Kim, J., Ahn, S., Xiao, K., Shenoy, S. K., Liedtke, W., et al. (2010). Arresting a Transient Receptor Potential (TRP) Channel. *J. Biol. Chem.* 285 (39), 30115–30125. doi:10.1074/jbc.M110.141549

Skog, J., Würdinger, T., van Rijn, S., Meijer, D. H., Gainche, L., Curry, W. T., et al. (2008). Glioblastoma Microvesicles Transport RNA and Proteins that Promote Tumour Growth and Provide Diagnostic Biomarkers. *Nat. Cel Biol* 10 (12), 1470–1476. doi:10.1038/ncb1800

Stylianopoulos, T., and Jain, R. K. (2013). Combining Two Strategies to Improve Perfusion and Drug Delivery in Solid Tumors. *Proc. Natl. Acad. Sci.* 110 (46), 18632–18637. doi:10.1073/pnas.1318415110

Thoppil, R. J., Adapala, R. K., Cappelli, H. C., Kondeti, V., Dudley, A. C., Gary Meszaros, J., et al. (2015). TRPV4 Channel Activation Selectively Inhibits Tumor Endothelial Cell Proliferation. *Sci. Rep.* 5, 14257. doi:10.1038/srep14257

Thoppil, R. J., Cappelli, H. C., Adapala, R. K., Kanugula, A. K., Paruchuri, S., and Thodeti, C. K. (2016). TRPV4 Channels Regulate Tumor Angiogenesis via Modulation of Rho/Rho Kinase Pathway. *Oncotarget* 7 (18), 25849–25861. doi:10.18632/oncotarget.8405

Veziroglu, E. M., and Mias, G. I. (2020). Characterizing Extracellular Vesicles and Their Diverse RNA Contents. *Front. Genet.* 11, 700. doi:10.3389/fgene.2020.00700

Wang, X., Freire Valls, A., Schermann, G., Shen, Y., Moya, I. M., Castro, L., et al. (2017). YAP/TAZ Orchestrate VEGF Signaling during Developmental Angiogenesis. *Dev. Cel.* 42 (5), 462–478. doi:10.1016/j.devcel.2017.08.002

Wang, Y., Lu, J., Chen, L., Bian, H., Hu, J., Li, D., et al. (2020). Tumor-Derived EV-Encapsulated miR-181b-5p Induces Angiogenesis to Foster Tumorigenesis and Metastasis of ESCC. *Mol. Ther. - Nucleic Acids* 20, 421–437. doi:10.1016/j.omtn.2020.03.002

Wegierski, T., Hill, K., Schaefer, M., and Walz, G. (2006). The HECT Ubiquitin Ligase AIP4 Regulates the Cell Surface Expression of Select TRP Channels. *EMBO J.* 25 (24), 5659–5669. doi:10.1038/sj.emboj.7601429

Yu, F.-X., Zhao, B., Panupinthu, N., Jewell, J. L., Lian, I., Wang, L. H., et al. (2012). Regulation of the Hippo-YAP Pathway by G-Protein-Coupled Receptor Signaling. *Cell* 150 (4), 780–791. doi:10.1016/j.cell.2012.06.037

Conflict of Interest: The authors declare that the research was conducted in the absence of any commercial or financial relationships that could be construed as a potential conflict of interest.

Publisher's Note: All claims expressed in this article are solely those of the authors and do not necessarily represent those of their affiliated organizations, or those of the publisher, the editors and the reviewers. Any product that may be evaluated in this article, or claim that may be made by its manufacturer, is not guaranteed or endorsed by the publisher.

frontiers in Bioengineering and Biotechnology

ORIGINAL RESEARCH
published: 08 February 2022
doi: 10.3389/fbioe.2022.764237

Vasculogenic Potency of Bone Marrow- and Adipose Tissue-Derived Mesenchymal Stem/Stromal Cells Results in Differing Vascular Network Phenotypes in a Microfluidic Chip

Anastasiia Mykuliak[1,2†], Alma Yrjänäinen[1,2*†], Antti-Juhana Mäki[3], Arjen Gebraad[1,2], Ella Lampela[1,2], Minna Kääriäinen[4], Toni-Karri Pakarinen[5], Pasi Kallio[3], Susanna Miettinen[1,2‡] and Hanna Vuorenpää[1,2‡]*

[1]Adult Stem Cell Group, Faculty of Medicine and Health Technology, Tampere University, Tampere, Finland, [2]Research, Development and Innovation Centre, Tampere University Hospital, Tampere, Finland, [3]Micro- and Nanosystems Research Group, Faculty of Medicine and Health Technology, Tampere University, Tampere, Finland, [4]Department of Plastic and Reconstructive Surgery, Tampere University Hospital, Tampere, Finland, [5]Coxa Hospital for Joint Replacement, Tampere, Finland

The vasculature is an essential, physiological element in virtually all human tissues. Formation of perfusable vasculature is therefore crucial for reliable tissue modeling. Three-dimensional vascular networks can be formed through the co-culture of endothelial cells (ECs) with stromal cells embedded in hydrogel. Mesenchymal stem/stromal cells (MSCs) derived from bone marrow (BMSCs) and adipose tissue (ASCs) are an attractive choice as stromal cells due to their natural perivascular localization and ability to support formation of mature and stable microvessels *in vitro*. So far, BMSCs and ASCs have been compared as vasculature-supporting cells in static cultures. In this study, BMSCs and ASCs were co-cultured with endothelial cells in a fibrin hydrogel in a perfusable microfluidic chip. We demonstrated that using MSCs of different origin resulted in vascular networks with distinct phenotypes. Both types of MSCs supported formation of mature and interconnected microvascular networks-on-a-chip. However, BMSCs induced formation of fully perfusable microvasculature with larger vessel area and length whereas ASCs resulted in partially perfusable microvascular networks. Immunostainings revealed that BMSCs outperformed ASCs in pericytic characteristics. Moreover, co-culture with BMSCs resulted in significantly higher expression levels of endothelial and pericyte-specific genes, as well as genes involved in vasculature maturation. Overall, our study provides valuable knowledge on the properties of MSCs as vasculature-supporting cells and highlights the importance of choosing the application-specific stromal cell source for vascularized organotypic models.

Keywords: *in vitro* vascularization, mesenchymal stem cells, endothelial cells, organ-on-a-chip, pericytes, microfluidic chip

OPEN ACCESS

Edited by:
Jonathan W. Song, The Ohio State University, United States

Reviewed by:
Yuji Nashimoto, Tohoku University, Japan
Terhi Heino, University of Turku, Finland

***Correspondence:**
Anastasiia Mykuliak
anastasiia.mykuliak@tuni.fi
Alma Yrjänäinen
alma.yrjanainen@tuni.fi

†These authors have contributed equally to this work and share first authorship

‡These authors have contributed equally to this work and share last authorship

Specialty section:
This article was submitted to Tissue Engineering and Regenerative Medicine, a section of the journal Frontiers in Bioengineering and Biotechnology

Received: *25 August 2021*
Accepted: *11 January 2022*
Published: *08 February 2022*

Citation:
Mykuliak A, Yrjänäinen A, Mäki A-J, Gebraad A, Lampela E, Kääriäinen M, Pakarinen T-K, Kallio P, Miettinen S and Vuorenpää H (2022) Vasculogenic Potency of Bone Marrow- and Adipose Tissue-Derived Mesenchymal Stem/Stromal Cells Results in Differing Vascular Network Phenotypes in a Microfluidic Chip. Front. Bioeng. Biotechnol. 10:764237. doi: 10.3389/fbioe.2022.764237

INTRODUCTION

Microvascular networks are fundamental elements of almost every human tissue. The vascular system is responsible for the delivery of oxygen and nutrients and removal of waste products. The vasculature maintains tissue homeostasis and regeneration by providing angiocrine signaling and regulating the transport of bioactive compounds and cells. In addition, vasculature plays an important role in many pathological conditions ranging from inflammation to cancer (Augustin and Koh 2017). Thus, tissue vascularization is an essential element in establishing relevant microenvironments for *in vitro* tissue modeling. Despite great improvements in artificial vascularization achieved in recent years, generating mature and functional vascular structures *in vitro* remains one of the major challenges. Current approaches for *in vitro* vascularization mimic the process of *in vivo* vasculogenesis and angiogenesis by exploiting the intrinsic ability of ECs to self-organize into vessel-like structures and to create new vessels from pre-existing ones (Chen et al., 2013; Jeon et al., 2014; Jusoh et al., 2015; Guo et al., 2019; Li et al., 2019). While these approaches have proven successful for particular applications, most of them suffer from the lack of supportive mural cells that are fundamental elements of physiological vasculature (Sweeney and Foldes 2018). The aforementioned approaches often fail to reproduce the structure of the vessels thus leading to formation of immature vascular networks and require the use of multiple angiogenic growth factors to promote the neovessel formation and maintain stability of the vasculature (Whisler et al., 2014).

Direct co-culture of ECs with supporting stromal cells appears to be the most effective approach to recapitulate *in vivo* vascularization resulting in microvascular networks with physiologically relevant structure and functionality (Jeon et al., 2014; Li et al., 2017; Campisi et al., 2018; Paek et al., 2019). The stromal cells take on the role of perivascular cells that form the mural coat, provide the essential angiogenic growth factors, and stabilize the developing endothelial tubes (Stratman and Davis 2012; Sweeney and Foldes 2018). Human fibroblasts have been widely investigated as vasculature supporting cells (Li et al., 2017; Paek et al., 2019), however, adult mesenchymal stem cells (MSCs) have proven to induce formation of more mature (Grainger et al., 2013), stable (Rambøl et al., 2020), and less permeable microvessels (Grainger and Putnam 2011). Indeed, MSCs, such as well characterized and easily accessible bone marrow-derived mesenchymal stem/stromal cells (BMSCs) and adipose tissue-derived mesenchymal stem/stromal cells (ASCs), could serve as a promising vasculogenesis supporting cell source due to their natural perivascular localization (Lin et al., 2010).

Initially derived from the mesenchyme, BMSCs and ASCs share similar characteristics of cell surface expression patterns, differentiation potentials and expression of genes related to cell self-renewal (Dominici et al., 2006). In terms of pericytic properties, various studies have shown that MSC tissue source affects microvascular network development, maturation, and functionality (Verseijden et al., 2009; Grainger and Putnam 2011; Grainger et al., 2013; Pill et al., 2015; Pill et al., 2018). For instance, ASCs and BMSCs promote angiogenesis via distinct cytokine and protease expression mechanisms (Kachgal and Putnam 2011). Moreover, ASCs have been reported to support the formation of denser vascular network with significantly higher expression of vascular endothelial growth factor (VEGF) in ASC-EC co-culture compared to BMSC-EC co-culture (Pill et al., 2018). However, these studies were performed using static cultures. The present study is the first to compare the vasculogenic potency of BMSCs and ASCs in dynamic conditions.

The combination of three-dimensional (3D) culture with a microfluidic device has been utilized for the generation of human microvascular networks (Smith and Gerecht 2014) and state-of-the-art organ-on-a-chip models (Wu et al., 2020). The use of a microfluidic chip platform allows for precise and spatiotemporal control of culturing conditions as well as incorporating a fluid flow thus ensuring nutrients and oxygen supply, waste removal, and providing physiological mechanical stimuli (Zhang et al., 2021).

In the present study, we investigated the potential of BMSCs and ASCs to support vasculogenesis in a 3D microfluidic chip platform. We compared the capacity of BMSCs and ASCs to induce the formation of mature and robust microvascular networks by ECs and their function as perivascular cells. We particularly studied effect of MSCs on vessel characteristics such as vasculature area, average vessel diameter, vessel length, and vasculature perfusability. We assessed MSC distribution in terms of pericyte area and pericyte coverage by immunohistochemical staining and quantitative analysis. Furthermore, we evaluated the expression of main vasculogenesis related genes. We found that different types of MSCs support the formation of microvascular networks with distinct phenotypes and quality. While both MSCs induced the formation of lumenized and interconnected networks by ECs, BMSCs promoted the formation of more mature microvascular networks-on-a-chip than ASCs, leading to a higher degree of perfusability. The pericyte area and vasculature coverage by pericytes were significantly greater in EC-BMSC co-cultures compared to EC-ASC co-cultures. The gene expression analysis revealed significant differences in the expression of endothelial-specific and pericyte-specific genes, as well as genes involved in vasculature maturation. The results suggest that BMSCs have stronger vasculogenic potential in 3D microfluidic chip platform compared to ASCs. Our study provides valuable knowledge on the properties of MSCs as vasculature supporting cells that could be utilized in bioengineering and *in vitro* modeling applications to facilitate tissue vascularization.

MATERIALS AND METHODS

Cell Isolation and Culture

Human BMSCs (herein denoted as BMSC 1–3) were isolated from bone marrow samples obtained from three donors (**Supplementary Table S1**) undergoing orthopedic surgery at the Tampere University Hospital Department of Orthopedics and Traumatology. Bone marrow samples were obtained with the donor's written informed consent and processed under ethical

approval of the Ethics Committee of the Expert Responsibility area of Tampere University Hospital, Tampere, Finland (R15174). The cells were isolated as described previously (Wang et al., 2019). The BMSCs were cultured in α-modified minimum essential medium (α-MEM; Gibco) supplemented with 5% human serum (HS; BioWest or Serana), 100 U/ml penicillin, 100 µg/ml streptomycin (Pen/Strep; Lonza), and 5 ng/ml basic fibroblast growth factor (bFGF; Miltenyi Biotec) and used between passages 3 and 6.

Human ASCs (herein denoted as ASC 1–3) were isolated from subcutaneous abdominal tissue samples obtained from three donors (**Supplementary Table S1**). Tissue samples were obtained at the Tampere University Hospital Department of Plastic Surgery with the donor's written informed consent and processed under ethical approval of the Ethics Committee of the Expert Responsibility area of Tampere University Hospital (R15161). The cells were isolated as described previously (Kyllönen et al., 2013). The ASCs were cultured in α-MEM supplemented with 5% HS (BioWest, PAA or Serana), 100 U/ml penicillin, and 100 µg/ml streptomycin and used between passages 3 and 5. The mesenchymal origin of BMSCs and ASCs was confirmed by surface marker expression analysis with flow cytometry (**Supplementary Table S2**) and assessment of adipogenic and osteogenic differentiation potential (**Supplementary Figure S1**).

Pooled human umbilical vein endothelial cells (HUVECs) expressing green fluorescent protein (GFP) were commercially obtained from Cellworks. GFP-HUVECs were cultured in Endothelial Cell Growth Medium-2 Bullet Kit (EGM-2; Lonza) consisting of Endothelial Cell Growth Basal Medium (EBM-2) and Endothelial Cell Growth Medium-2 Supplements. Instead of the fetal bovine serum supplied with the Kit, 2% HS (BioWest) was used. The cells were used between passages 3 and 6.

Microvascular Network Formation

Microvascular networks were formed inside microfluidic chips (DAX-1; Aim Biotech), consisting of a gel channel (1.3 mm wide and 250 µm high) flanked by two medium channels. Microvascular networks were formed through self-assembly of GFP-HUVECs and MSCs in fibrin hydrogel according to Jeon et al. (2014) with modifications. Briefly, GFP-HUVECs were combined with either BMSCs or ASCs at 5:1 cell ratio (final cell density 6 million cells/ml) and spun down. The cell pellet was then resuspended in 2 IU/ml human thrombin (Sigma-Aldrich, St. Louis, MI, United States) in EBM-2 and combined at 1:1 volume ratio with 5 mg/ml human fibrinogen (Sigma-Aldrich, St. Louis, MI, United States) in Dulbecco's Phosphate Buffered Saline (DPBS; Lonza). The resulting mixture (10 µl) was quickly injected into the gel channel of the microfluidic chip and allowed to polymerize in a humidified chamber for 15–20 min at room temperature (RT). Microvascular networks were cultured in EGM-2 with 2% HS (BioWest). To enhance vascular network formation, interstitial flow was used throughout the culture period (Kim et al., 2016; Abe et al., 2019). The interstitial flow was generated by adding 90 µl of culture medium into both reservoirs of one medium channel and 50 µl of medium into both reservoirs of the other medium channel. This procedure was repeated daily when changing medium and the flow direction was kept constant. In order to prevent tracer leakage from the medium channel into the hydrogel matrix and improve microvascular network perfusability, GFP-HUVECs were seeded into the medium channels of microfluidic devices used for bead flow assay and immunostainings at day 3 or 4 according to Campisi et al. (2018). To take into account the donor variability, cells derived from three different donors for each MSCs type (BMSCs and ASCs) were tested. GFP-HUVECs cultured without any supporting cells (hereafter referred to as "EC alone") were prepared and cultured at a final cell density of 5 million cells/ml in the same manner and served as a control for evaluating microvasculature parameters and vasculature perfusability.

Immunofluorescent Staining

The immunostaining protocol was adapted from Honkamäki et al. (2021) and performed on 2–4 technical replicates for each cell donor. After 6 days of culture microvascular networks were washed with DPBS and fixed with 4% paraformaldehyde (Sigma-Aldrich) in DPBS for 30 min at RT following by three washes with DPBS. The samples were then permeabilized with 0.1% Triton X-100 (Sigma-Aldrich, St. Louis, MI, United States) for 10 min and non-specific binding was blocked with blocking buffer [10% normal donkey serum (NDS; Millipore), 1% bovine serum albumin (BSA; Sigma-Aldrich, St. Louis, MI, United States), 0.1% Triton X-100 in DPBS] for 2 h at RT. We used primary antibodies against vascular endothelial cadherin (VE-cadherin; BD Pharmingen, 555,661; 1:200) to identify the presence of endothelial adherens junctions, collagen type IV (Sigma-Aldrich, C1926-.2ML; 1:150) as a marker of the basement membrane, and alpha-smooth muscle actin (α-SMA; Abcam, ab7817; 1:300) and PDGFR-beta (PDGFR-β; Abcam, ab32570; 1:100) as perivascular cell markers. Primary antibodies were diluted in PBS with 1% NDS, 1% BSA, 0.1% Triton X-100 and applied for 3 days at 4°C. The samples were then washed for at least 6 times with 1% BSA in DPBS over a period of 2 days in total. Alexa Fluor 568 conjugated secondary antibodies (Thermo Fisher, A11031 and A10042) diluted 1:400 in DPBS with 1% BSA were applied overnight at 4°C. The samples were washed 5 times over a period of 2 days, stained with 0.67 µg/ml DAPI for 2 h at RT followed by three washes in DPBS. The chips were imaged using a Zeiss LSM 800 laser scanning confocal microscope with high-sensitivity two-channel spectral PMT detector and LSM 780 laser scanning confocal microscope with a Quasar spectral GaAsP detector (all from Carl Zeiss) and processed with Fiji software (Schindelin et al., 2012) and Adobe Photoshop 2020. Negative controls for immunocytochemical stainings are shown in **Supplementary Figure S7**.

Microvascular Network Perfusion

To assess perfusability of the microvascular networks, 2 µm yellow-green fluorescent microbeads (FluoSpheres Carboxylate-Modified Microspheres, 2% solids, Thermo Fisher) were introduced as a fluorescent tracer into microfluidic devices containing living cells at day 7 of culture

and time-sequential images were captured. Briefly, medium was aspirated from all reservoirs, 25 µl of sterile water was added into the reservoirs of one channel and 50 µl was added into the reservoirs of the other channel followed by 50 µl of fluorescent microbeads diluted 1:2,000 in sterile water. Sterile water was used instead of DPBS to avoid the formation of microbead aggregates. The generated hydrostatic pressure between the two medium channels resulted in luminal flow through the microvascular network. The time-sequential images were acquired every 10 s during 3 min using EVOS FL cell imaging system (Thermo Fisher, Nungambakkam, TamilNadu). Animated GIF images were then generated using Fiji software.

Quantification of Microvascular Network Parameters

Microvascular networks morphology was analyzed using Fiji software. The GFP signal from the endothelial cells was used to quantify vascular area percentage, vascular network length, and average vessel diameter. The samples were fixed at day 6 and confocal z-stacked images were captured with 5 µm step (45 slices) using a Zeiss LSM 800 confocal microscope. Three regions of interest (ROIs; 798,63*798,63 μm^2) per chip were selected from the co-culture area excluding the hydrogel-restricting microposts and solely including microvascular networks. Quantitative image analysis was not performed blinded. Images were processed as described previously (Jeon et al., 2014; Campisi et al., 2018; Haase et al., 2019) with minor modifications. Briefly, the maximum intensity projections were generated, brightness and contrast were adjusted by the "window/level" tool (35/70), noise was filtered by applying "Gaussian blur" filter (sigma 3), and images were converted to a binary format by applying the "triangle" threshold method. Artefacts were removed using the "erode" and "remove outliers" (radius 5 pixels for bright and 10 pixels for dark) functions. All values were calculated per ROI. The vasculature area percentage and the total vasculature area were computed using "measure" function. The 2D "skeletonize" function was applied to calculate the total network length. Finally, the average diameter was computed by dividing the total vasculature area by the total network length. Three chips per donor cell line and 3 ROIs per device were used for quantified analysis and statistical testing.

Quantification of Mesenchymal Stem Cell Transition Toward Perivascular Cells

Perivascular distribution of MSCs was analyzed using Fiji software and quantified through the α-SMA signal in terms of pericyte area percentage and pericyte coverage. Immunofluorescent stained chips that had been fixed after 6 days of culture, were imaged completely with the Zeiss LSM 780 confocal microscope using Z stacks with 5 µm steps (41 slices). Maximum intensity projections were prepared and five ROIs (750*750 μm^2) per chip were selected. Quantitative image analysis was not performed blinded. The pericyte area percentage was quantified from the *α*-SMA channel as described above for vascular parameters with minor adjustments. The pericyte coverage was quantified as the overlapping area of α-SMA and GFP signals (Erickson et al., 2020). For that, an "AND" operation of Fiji image calculator was performed on *α*-SMA and GFP channels of the same ROIs pre-processed separately. The vasculature coverage by pericytes was calculated by dividing the computed values by the total vasculature area within each ROI. Three chips per donor cell line and 5 ROIs per device were analyzed.

Characterization of the Gravity-Driven Flow in the Microfluidic Chip

To characterize the gravity-driven flow generated daily, interstitial flow across the hydrogel area was measured in EC-BMSC and EC-ASC cocultures using fluorescence imaging. The flow measurements of EC-BMSCs and EC-ASCs were performed at days 0, 2, 4 and 7 using initial volumes of gravity-driven flow mimicking the flow condition. Measurements were performed at +37°C. First, medium was aspired from all reservoirs, 50 µl of 1xDPBS was added into two of the medium reservoirs (**Figure 1A**) followed by the addition of 90 µl of 100 µg/ml 70 kDa Rhodamine B isothiocyanate–Dextran (R9379, Sigma) in 1xDPBS to the two other reservoirs located opposite sides of the hydrogel area (**Figure 1A**). This generated a time-dependent hydrostatic pressure inside the chip resulting in a gravity-driven interstitial flow across the hydrogel area. To quantify the interstitial flow, sequential images of the fluorescent flow front across the hydrogel area were acquired by using a wide-field fluorescence microscope (Olympus IX 51) with sCMOS camera (Orca Flash4.0LT, Hamamatsu) using 5 seconds measurement intervals (**Figure 1B**). Each chip was manually placed on the microscope so that the center of the culture area was imaged. All measurements were performed as independent biological replicates N = 2 for each flow condition per coculture of one BMSC/ASC donor cell line.

Image analysis was performed using MATLAB (Version R2018b, The MathWorks, Inc., Natick, MA, United States) and scripts made in-house. First, stack images (.vsi) were read using BioFormats toolbox, greyscale images were binarized using 0.5 threshold value, and average locations of the flow front were tracked from the binarized images (**Figure 1B**). Based on differences in flow front locations between two consecutive indexes, known pixel size (0.615 µm), and known time interval between these two image indexes, an average flow velocity was calculated at each time point (**Figure 1C**, **Supplementary Figure S6**). An average flow rate at each time point was then calculated by multiplying the average velocities and the cross section of the hydrogel area (10,8 mm × 250 µm) (**Figure 7**). It should be noted that the accuracy of the developed analysis decreases within lower flow velocity, as smaller flow front movement between two consecutive image indexes is measured. This results in oscillation of the measured flow rate on day 4 (in **Figure 7C**), in which the flow rate was measured remarkably low (below 0.5 µl/min).

In the gravity-driven system, when assuming zero capillary forces, pressure difference $\Delta p(t)$ between inlet and outlet reservoirs is based on time-dependent hydraulic pressure $p_{hyd}(t)$. As described earlier, fluorescent dextran solution was used as a tracer for determining the spatial change of

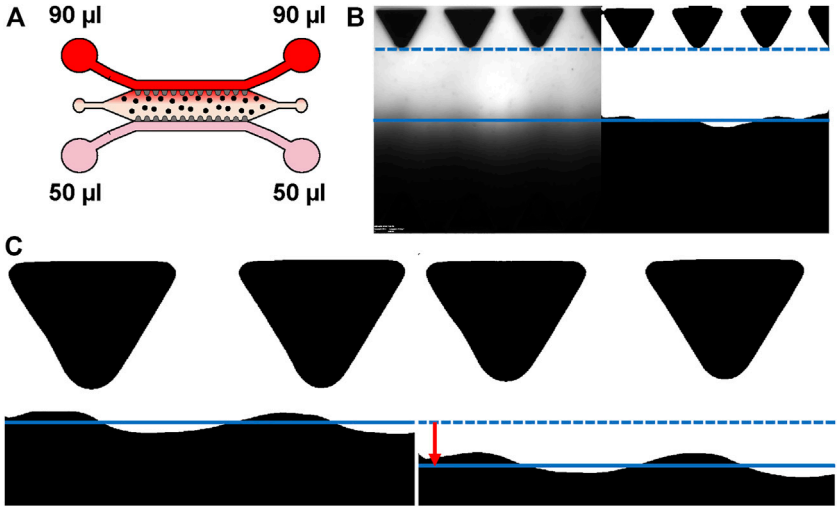

FIGURE 1 | Characterizing interstitial flow within the used microfluidic chip. **(A)** Schematic representation of the experimental set-up for flow measurements. Gravity-driven flow [(90 µl + 90 µl)+(50 µl + 50 µl)] across the hydrogel area was generated by applying 50 µl of 1xDPBS to the medium reservoirs (pink) and 90 µl of 70 kDa Rhodamine B isothiocyanate–Dextran in 1xDPBS for the opposing medium reservoirs (red). Spatial change of the fluorescent wave front was imaged sequentially. Cells are depicted as dots. **(B)** Example of original and binarized image used for estimating maximal flow rate. **(C)** Example of the tracked waveforms of two consecutive images. Solid and dashed lines demonstrate the averaged waveform locations presenting the difference (red arrow) between averaged waveform locations between these two image indexes. The average change is then used to estimate current flow rate. Donor cell lines BMSC 1 and ASC 3 were used for the flow characterization co-cultures.

the flow front preventing the possibility to record fluorescent intensity differences after the complete saturation of the hydrogel area. However, the constantly decreasing time-dependent gravity-driven flow rate thus flow duration can be estimated using following equations (Mäki et al., 2015). First, hydraulic pressure $p_{hyd}(t)$ is based on the liquid plug height difference $\Delta h(t)$ between inlet and outlet reservoirs and can be calculated by

$$\Delta p(t) = p_{hyd}(t) = \rho g \Delta h(t)$$

where ρ density of liquid and g is gravitational acceleration.

Hydraulic resistance of the system, R_{hyd}, was approximated based on measured initial flow rate from [(90 µl + 90 µl)+(50 µl + 50 µl)] volume condition and estimated initial hydraulic pressure $p_{hyd}(0)$ using following equation. Here, it is assumed that R_{hyd} is constant during the experiment.

$$\Delta p(t) = R_{hyd} Q(t) \Rightarrow R_{hyd} = \Delta p(0) / Q(0)$$

Then, the time-dependent flow rate $Q(t)$ can be estimated using equation

$$Q(t) = \frac{p_{hyd}(t)}{R_{hyd}} = \frac{\rho g \Delta h(t)}{R_{hyd}}$$
$$= \frac{\rho g \Delta h(t)}{\rho g \Delta h(0)} Q(0) = \frac{\Delta h(t)}{\Delta h(0)} Q(0)$$

In gravity-driven flow, $\Delta h(t)$ is continuously decreasing as liquid flows from the inlet reservoirs to the outlet reservoirs, thus reducing the hydraulic pressure and the flow rate. With known reservoir dimensions (a cylinder shape with a diameter of 5 mm), the plug height difference between inlet and outlet reservoirs at different time points can be calculated. This equation was solved using Simulink (The MathWorks). In theory, gravity-driven flow would continue infinitely long time as the flow rate is constantly decreasing, but in practice, flow will be stopped due to small friction losses. To account this issue, a minimum flow rate threshold was set to 0.02 µl/min thus ending the simulation when the flow rate dropped below this threshold value. The simulation end-point time was then used as an estimation of total flow rate duration.

Shear stress τ induced by the interstitial flow velocity v can be estimated using equation (Yang et al., 2021)

$$\tau \approx \frac{\mu v}{\sqrt{K_p}}$$

in which $K_p = 6.67 \times 10^{-12}$ m^2 is the permeability of the hydrogel material (Bachmann et al., 2018) and μ is the dynamic viscosity of the flow medium. Here, medium was assumed to have water-like properties at 37°C, thus $\mu = 0.6913 \times 10^{-3}$ Pa s was used.

RNA Extraction and Quantitative Real-Time PCR

At day 6 of culture, the medium was aspirated from all the media ports and chips were stored frozen at −80°C prior RNA extraction. The total RNA of EC-BMSC and EC-ASC co-cultures were extracted using TRIzol reagent (Invitrogen). Fibrin matrices containing cells were flushed out from the chips with TRIzol reagent and three chips were pooled for each BMSC/ASC donor cell line to collect higher

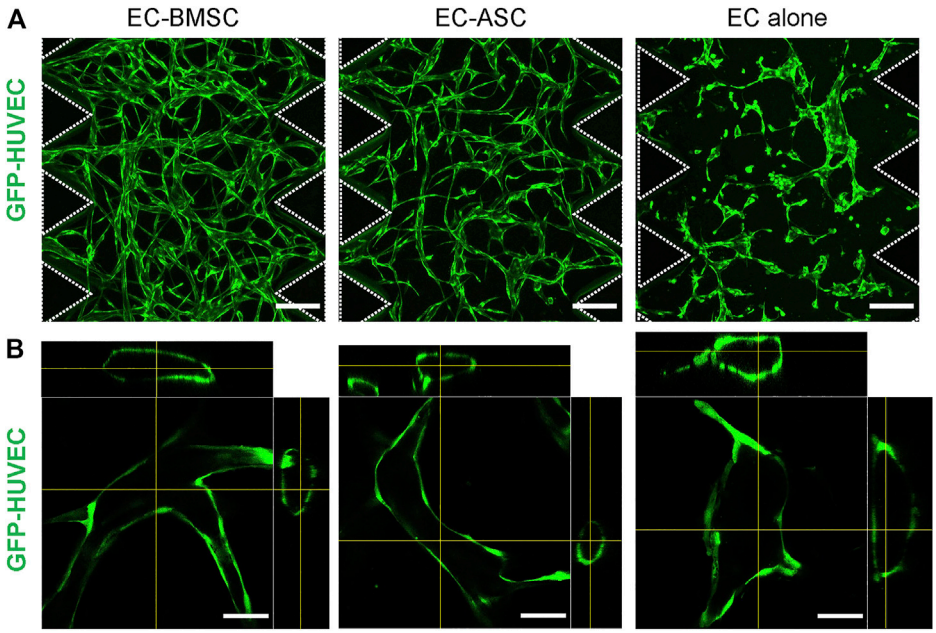

FIGURE 2 | Morphology of the microvascular networks formed by EC-BMSC and EC-ASC co-cultures and ECs cultured alone. Microvascular networks were formed *via* vasculogenesis process by GFP-HUVECs cultured alone or in combination with supporting stromal cells—BMSCs or ASCs, for 6 days. **(A)** Confocal micrographs representing the overall architecture of microvascular networks established by EC-BMSC and EC-ASC co-cultures (5 million ECs/ml and 1 million MSCs/ml) and ECs alone (5 million cells/ml). Scale bars, 200 μm. Both EC-BMSC and EC-ASC co-cultures formed interconnected microvascular networks spanning the entire hydrogel over the course of 6 days. ECs cultured alone formed multicellular aggregates but failed to develop interconnected networks. **(B)** Hollow lumens could be observed in the cross-section images in all three conditions. Scale bars, 50 μm. Dash line depicts microposts that separate hydrogel from media channels. Donor cell lines BMSC 1 and ASC 2 were used for generation of data presented in the figure.

amount of RNA. The samples were processed according to manufacturer's instructions and RNA concentration was measured with a spectrophotometer (Nanodrop 2000; Thermo Fisher). Complementary DNA was synthesized using the High Capacity cDNA Reverse Transcription Kit (Applied Biosystems) and quantitative real time reverse transcription polymerase chain reaction (qRT-PCR) was performed with QuantStudio 12K Flex Real-Time PCR System (Applied Biosystems) using approximately 20 ng cDNA per reaction, TaqMan Fast Advanced Master Mix (Thermo Fisher) and Custom TaqMan Array Plates (Applied Biosystems) according to manufacturers' instructions. TaqMan assay probes for genes of interest are listed in **Supplementary Table S3**. All measurements were performed using technical triplicates. 18S ribosomal RNA (18S), glyceraldehyde 3-phosphate dehydrogenase (*GAPDH*) and platelet and endothelial cell adhesion molecule 1 (*PECAM1*) were used as reference genes for normalizing qRT-PCR data. Gene expression analysis was performed for each EC-MSC co-cultures of three donor cell lines for both BMSCs and ASCs. Relative quantification of gene expression was performed using the $2^{-\Delta\Delta Ct}$ method (Livak and Schmittgen, 2001). Gene expression levels are shown relative to the average expression in EC-ASC co-cultures. Statistical analysis was performed on the mean ΔΔCt values from each donor cell line.

Heatmaps were generated from the mean ΔCt values for each donor cell line using the gplot package in R (Warnes et al., 2015). Hierarchical clustering and dendrograms were computed based on Euclidean distances.

Statistics

All data are represented as mean ± SD. Statistical analysis was performed using GraphPad Prism 9.0.0 (GraphPad Software, www.graphpad.com). Unpaired student's T-tests were used for significance testing between BMSCs and ASCs. p values were corrected to control the false discovery rate using the two-stage step-up method of Benjamini, Krieger and Yekutielio (Benjamini et al., 2006). The differences were considered statistically significant for $p < 0.05$ and represented as follows: * denotes $p < 0.05$, ** − $p < 0.01$, *** − $p < 0.001$, n. s − non-significant.

Data Availability Statement

The data sets generated and analyzed for the current study are available from the corresponding author on reasonable request.

RESULTS

Both BMSCs and ASCs Facilitate the Formation of Mature Interconnected Microvascular Networks-On-A-Chip

We examined two types of human primary MSCs—BMSCs and ASCs, for their ability to support microvascular network formation and maturation in fibrin matrix and act as perivascular cells when co-cultured with ECs in a

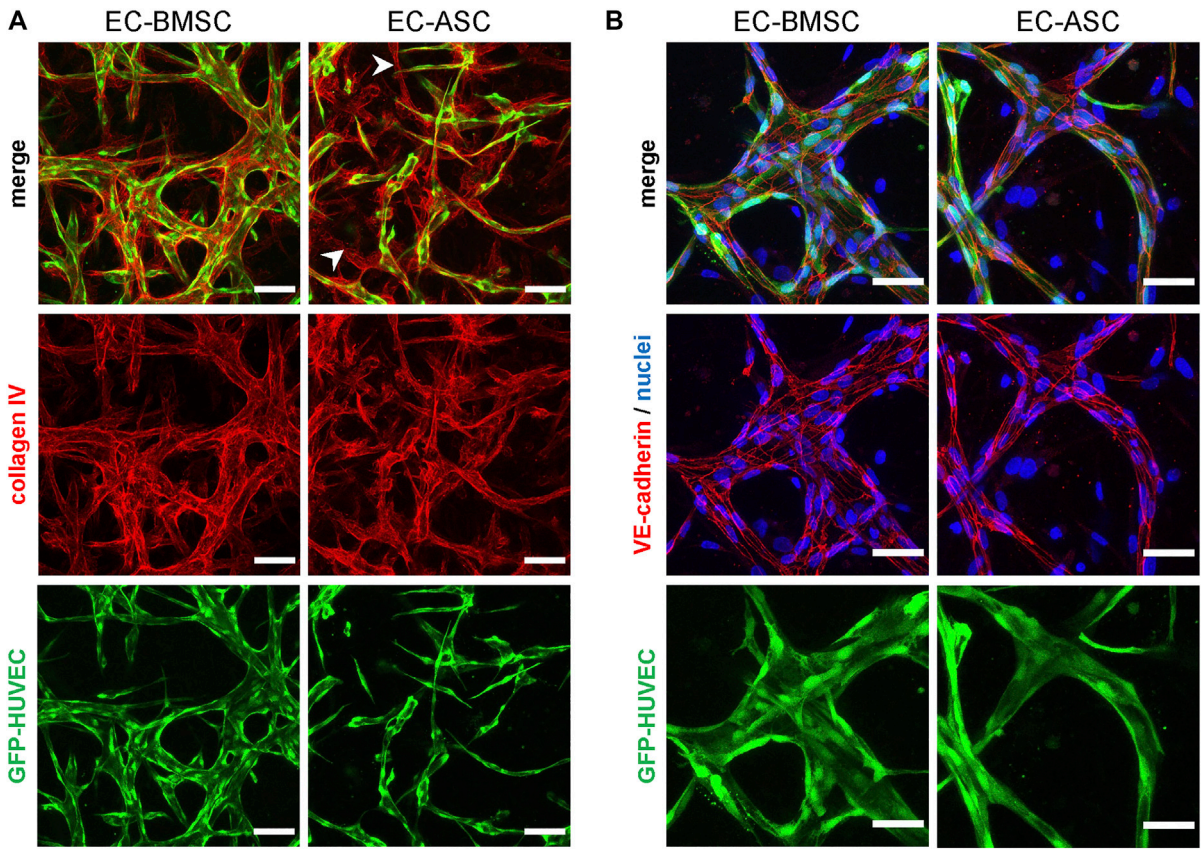

FIGURE 3 | Immunocytochemistry analysis of basement membrane deposition and endothelial cell-cell junction formation in MSCs supported microvascular networks. **(A)** The EC networks (green) are surrounded by collagen IV (red), one of the major components of basement membrane, in both EC-BMSC and EC-ASC co-cultures (5 million ECs/ml and 1 million MSCs/ml). Empty basement membrane sleaves found in EC-ASC co-culture are marked by arrowheads. Scale bars, 100 μm. **(B)** Continuous and intact intercellular connections (red) are present along the border of ECs (green) in both conditions, as shown by immunostaining for adherens junction protein VE-cadherin. Nuclei (blue) are stained with DAPI. Scale bars, 50 μm. Donor cell lines BMSC 2 and ASC 1 were used for generation of data presented in **(A)**. Donor cell lines BMSC 3 and ASC 2 were used for generation of data presented in **(B)**.

microfluidic chip environment. First, we examined morphological characteristics including 3D structure, lumen-containing vessel formation, basement membrane deposition, EC-EC cell junctions of the microvascular networks formed by EC-BMSC and EC-ASC co-cultures. By day 6 both EC-BMSC and EC ASC co-cultures gradually developed into lumenized interconnected vascular networks with randomly aligned morphology spanning the entire hydrogel (**Figure 2A**). However, the microvascular networks formed by EC-BMSC co-cultures were more organized, interconnected, and denser compared to EC-ASC co-cultures. Daily observations of the microvascular network formation revealed minor vasculature degradation in the middle part of the chip in EC-ASC co-cultures starting from day 5 (**Supplementary Figure S2**).

Importantly, cross-sectional images of the vessel segments confirmed the presence of hollow lumens in both EC-BMSC and EC-ASC co-cultures as well as in EC alone (**Figure 2B**). In contrast to MSCs supported co-cultures, ECs cultured alone formed multicellular aggregates of different sizes which eventually developed into primitive structures containing lumens but failed to form interconnected microvascular networks. Notably, unlike in EC-BMSC and EC-ASC co-cultures, not all ECs were engaged in vasculature formation when ECs were cultured alone.

We studied vascular maturation further by immunofluorescence staining for collagen type IV, a predominant vascular basement membrane component (LeBleu et al., 2007), and for VE-cadherin, a specific marker for endothelial cell-cell adherens junctions (Giannotta et al., 2013). Collagen type IV was deposited in the perivascular area surrounding the vessels in both EC-BMSC and EC-ASC co-cultures (**Figure 3A**). In EC-ASC co-cultures, however, collagen type IV staining was weaker and less prominent (**Supplementary Figure S3**). Moreover, here we detected regions of collagen type IV-positive basement membrane surrounding an empty lumen without ECs. VE-cadherin was strongly expressed at the intercellular contacts along the EC border in both EC-BMSC and EC-ASC co-cultures (**Figure 3B**) demonstrating formation of adherens junctions between ECs. No differences were observed between EC BMSC and EC-ASC co-cultures with VE-cadherin staining intensity.

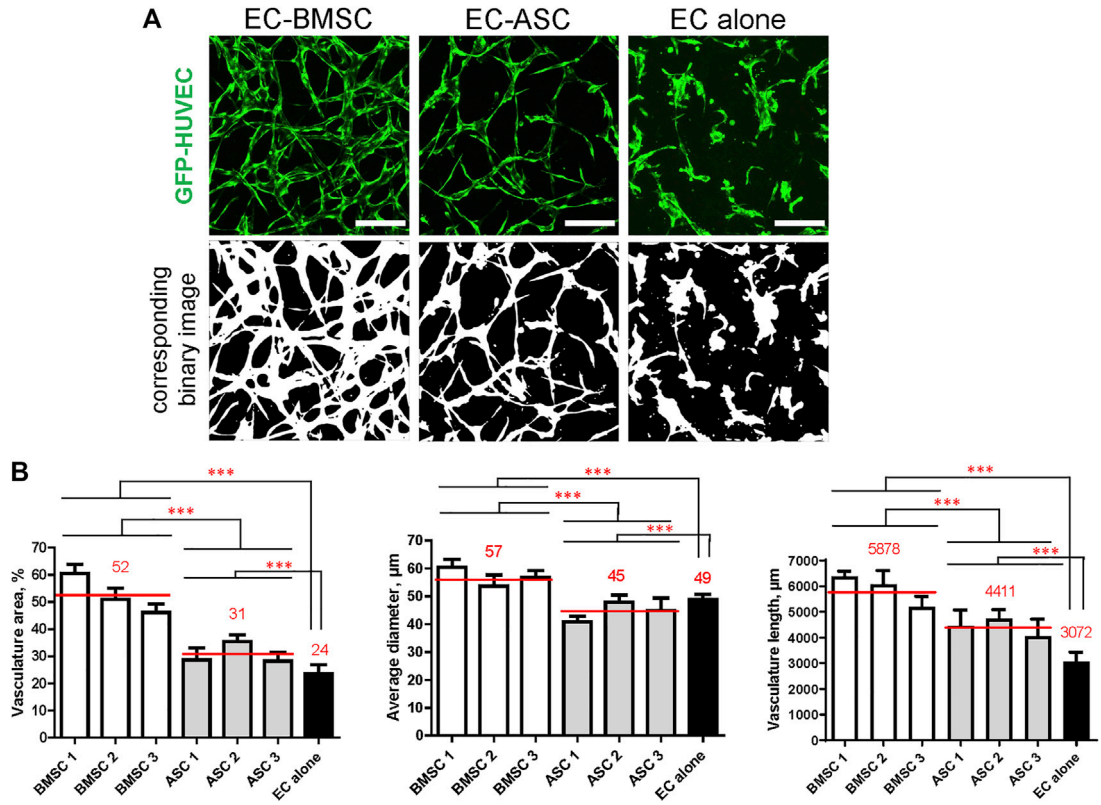

FIGURE 4 | MSCs of different origin induce microvascular network formation in ECs with significantly different vasculature area, vessel diameter, and vasculature length. The presence of MSCs greatly improves microvasculature parameters compared to ECs cultured alone. **(A)** Representative images of microvascular networks derived from EC-BMSC and EC-ASC co-cultures and EC alone at day 6 and corresponding binary images. Scale bars, 200 µm. **(B)** Morphological parameters (vasculature area, average vessel diameter, and vasculature length) of MSCs supported microvascular networks are shown individually for BMSCs and ASCs derived from different donors. Data are presented as means of 9 ROIs (3 devices, 3 ROIs per device). Comparison between BMSCs and ASCs as well as comparison of BMSCs and ASCs to EC alone was performed on mean values from EC-BMSC and EC-ASC co-cultures (3 donors, 3 devices per donor, 3 ROIs per device). ***—$p <$ 0.001 with Unpaired student's *t*-test. *p* values were corrected to control the false discovery rate. Donor cell lines BMSC 2 and ASC 1 were used for generation of data presented in **(A)**.

EC-BMSC Co-Cultures Form Consistently Perfusable Microvascular Networks Compared to EC-ASC Co-Cultures

Next, we examined perfusability of the microvascular networks formed by EC-BMSC and EC-ASC co-cultures, and ECs alone. The perfusability was assessed using 2 µm fluorescent microbeads after 7 days of culture. Microbeads were loaded into one of the medium channels and hydrostatic pressure drop was created between two medium channels so that the luminal flow across the microvascular network allows microbeads to travel through the established microvasculature. Only vessels that developed open lumens toward the media channels at the hydrogel-medium interface were able to carry beads through the network. To facilitate formation of microvasculature with open lumens, the ECs were also seeded into both medium channels of the microfluidic devices at day 3 or 4 and allowed to adhere to the hydrogel-medium interface and connect to the vascular network. With visual observation, we detected a great improvement in perfusability of the microvascular networks (data not shown). All three EC BMSC co-cultures resulted in formation of perfusable microvascular networks with multiple entry points upstream of the luminal flow and several exit points downstream of the luminal flow (**Supplementary Video S1**). In contrast, microvascular networks resulting from EC-ASC co-cultures demonstrated poor perfusability regardless of ASC line. Two ASC lines induced formation of partially perfusable microvessels (in only one chip out of 3 tested) with a couple entry points and only one exit point for microbeads (**Supplementary Video S2**). As expected, EC alone did not form perfusable microvascular networks as shown by bead flow assay (**Supplementary Video S3**).

Quantification of Microvascular Networks Parameters Reveals Significant Differences in EC-BMSC Co-Cultures Compared to EC-ASC Co-Cultures

Quantifying microvascular network parameters revealed a significantly larger vasculature area, wider vessels, and greater total vasculature length in EC-BMSC co-cultures compared to EC-ASC co-cultures

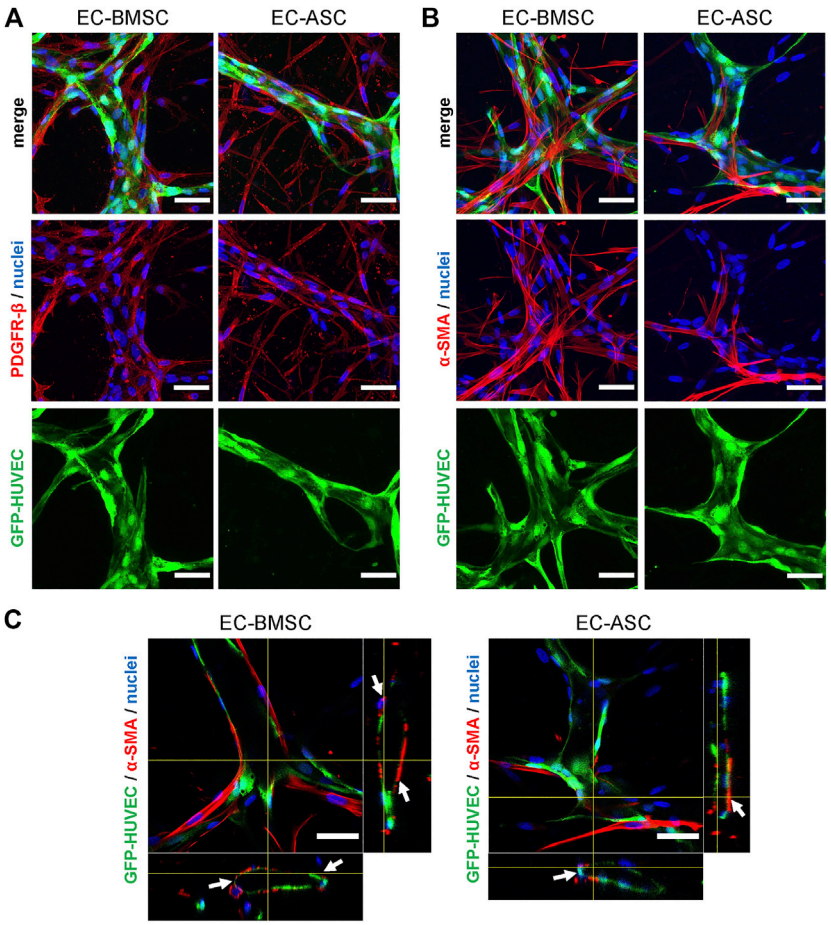

FIGURE 5 | Mesenchymal stem cell transition towards perivascular cells. **(A,B)** BMSCs as well as ASCs have pericytic characteristics marked by positive expression of PDGFR-β **(A)** and α-SMA **(B)**. The immunostaining revealed that majority of MSCs are stained for PDGFR-β in both co-cultures. BMSCs are more organized and localize closely to the microvessels whereas ASCs have random appearance scattered throughout the hydrogel. In contrast to PDGFR-β staining, considerably less MSCs were stained for a-SMA in EC-ASC co-culture compared to EC-BMSC co-culture. Scale bars, 50 μm. **(C)** α-SMA positive MSCs (red) localize in close proximity and wrap around the vascular structures (green) in both EC-BMSC and EC-ASC co-cultures. White arrowheads indicate interaction of pericytes (red) with ECs (green). Scale bars, 50 μm. Nuclei (blue) are stained with DAPI. Donor cell lines BMSC 3 and ASC 1 were used for generation of data presented in **(A)**. Donor cell lines BMSC 1 and ASC 2 were used for generation of data presented in **(B, C)**.

(**Figure 4**). Microvessels occupied 52% (46–60%) of area in EC-BMSC co-cultures and 31% (28–35%) of area in EC-ASC co-cultures, while those occupied 24% of area in EC alone. As expected, MSCs supported microvascular networks covered larger area than ECs alone. EC-BMSC co-cultures formed microvascular networks with an average vessel diameter of 57 μm (54–60 μm) and a total vasculature length of 5,877 μm (5,288–6,373 μm). The average vessel diameter in EC-ASC co-cultures was 45 μm (41–48 μm) and the total vessel length 4,411 μm (4,048–4,731 μm). The average vessel diameter in EC monocultures was 49 μm and the total vessel length 3,072 μm.

BMSCs Have More Potential to Function as Perivascular Cells and Interact With the Vascular Network than ASCs

To investigate the spatial distribution of BMSCs and ASCs as perivascular cells, the EC-BMSC and EC-ASC co-cultures were stained for known perivascular cell markers (Armulik et al., 2011; Holm et al., 2018; Sweeney and Foldes, 2018) PDGFR-β and α-SMA after 6 days of culture. Immunofluorescence staining showed that both BMSCs and ASCs express PDGRF-β and α-SMA when co-cultured with ECs (**Figures 5A,B**). Nearly all BMSCs and ASCs stained positively for perivascular cell marker PDGFR-β. Interestingly, BMSCs were found in close proximity to the vessel structures while ASCs were more frequently localized in areas distant from the vessels. On the contrary, immunostaining for α-SMA differed notably between EC-BMSC and EC-ASC co-cultures. A large fraction of BMSCs stained positively for α-SMA, whereas only few ASCs expressed α-SMA. The α -SMA positive MSCs had elongated morphology similar to *in vivo* and were wrapped around the microvessels or localized closely to the ECs in both EC-BMSC and EC-ASC co-cultures (**Figures 5B,C**).

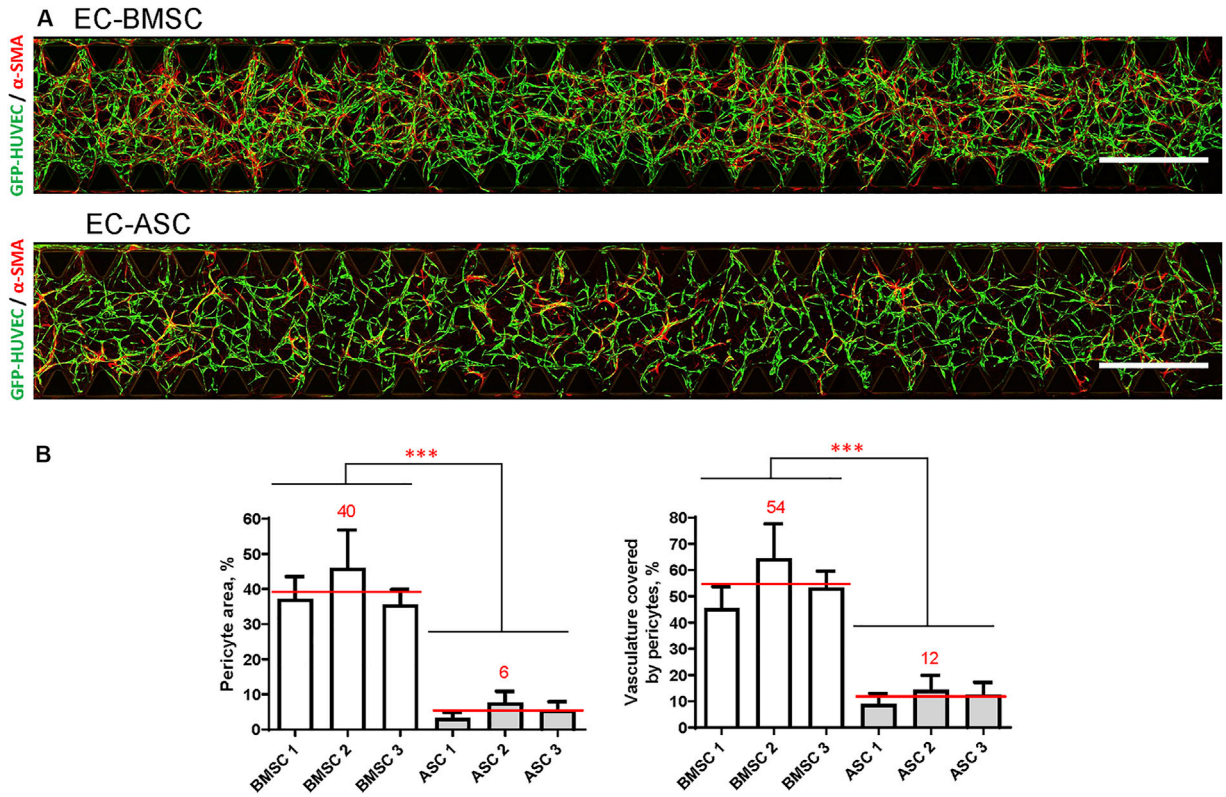

FIGURE 6 | BMSCs have greater pericytic capacity when co-cultured with ECs in a microfluidic chip compared to ASCs based on significantly higher pericyte area and pericytes coverage. **(A)** Whole chip scans showing alignment of perivascular MSCs (red, marked by α-SMA staining) with vasculature (green) in EC-BMSC and EC-ASC co-cultures at day 6. Images are maximum intensity projections of confocal stacks 200 μm height. Scale bars, 1 mm. **(B)** Quantifications of pericyte area and pericyte coverage (vasculature covered by pericytes) are shown individually for BMSCs and ASCs derived from different donors. Data are presented as means of 15 ROIs (3 devices, five ROIs per device); error bars, SD; *** denotes $p < 0.001$ with Unpaired student's *t*-test. Comparison between BMSCs and ASCs was performed on mean values from EC-BMSC and EC-ASC co-cultures (3 donors, 3 devices per donor, 5 ROIs per device). Donor cell lines BMSC 1 and ASC 2 were used for generation of data presented in **(A)**.

We further quantified MSCs transition toward perivascular cells using the α-SMA signal in terms of pericyte area percentage and pericyte coverage (**Figures 6A,B**). Quantification revealed that α-SMA positive BMSCs occupied an area (40%; 36–46%) that was more than 7-fold larger than the area occupied by α-SMA positive ASCs (6%; 3–8%) indicating stronger potential of BMSCs to function as perivascular cells compared to ASCs. We found that in EC-BMSC co-cultures, 54% (45–64%) of the vascular network was covered by α-SMA positive perivascular cells whereas in EC-ASC co-cultures – 12% (9–14%), suggesting that BMSCs have more potential to interact with and stabilize microvascular networks.

Flow Characterization Demonstrated the Presence of the Gravity-Driven Flow Across the Hydrogel Area

To demonstrate the presence of gravity-driven interstitial flow, we estimated the average flow rates by measuring spatial change of the wave front and computed the flow duration within the microfluidic chip using the gravity-driven model, both presented in Section *Characterization of the Gravity-Driven Flow in the Microfluidic Chip* (**Figure 7**). We verified the presence of gravity-driven flow across the hydrogel area within the microfluidic chip. At day 0, approximated initial flow rates Q (0) were 3.1 μl/min in EC-BMSC culture and 3.2 μl/min in EC-ASC culture (**Figure 7A**). Based on this, the estimated flow durations, where $Q(t) > 0.02$ μl/min, were approximately 1 h in both co-cultures (**Figure 8**). At day 2, measured Q (0) were approximately 1,1 μl/min and 0.55 μl/min (**Figure 7B**), prolonging the estimated flow durations from 1 h to two and 4 h for EC- BMSC and EC-ASC, respectively (**Figure 8**). At day 4, Q (0) were 0,35 μl/min and 0,25 μl/min (**Figure 7C**), resulting in >5 h and >6 h of estimated total flow duration for EC- BMSC and EC-ASC cultures, respectively (**Figure 8**). Flow characterization measurement for day 7 demonstrated unequal fluorescence wave front as we observed luminal flow *via* the formed vascular network (**Supplementary Figure S6**). The measured maximum interstitial flow velocity was $v \approx 0.024$ mm/s, resulting in maximal shear stress $\tau \sim 0.0065$ Pa, which falls within the physiological shear stress range (Yang et al., 2021).

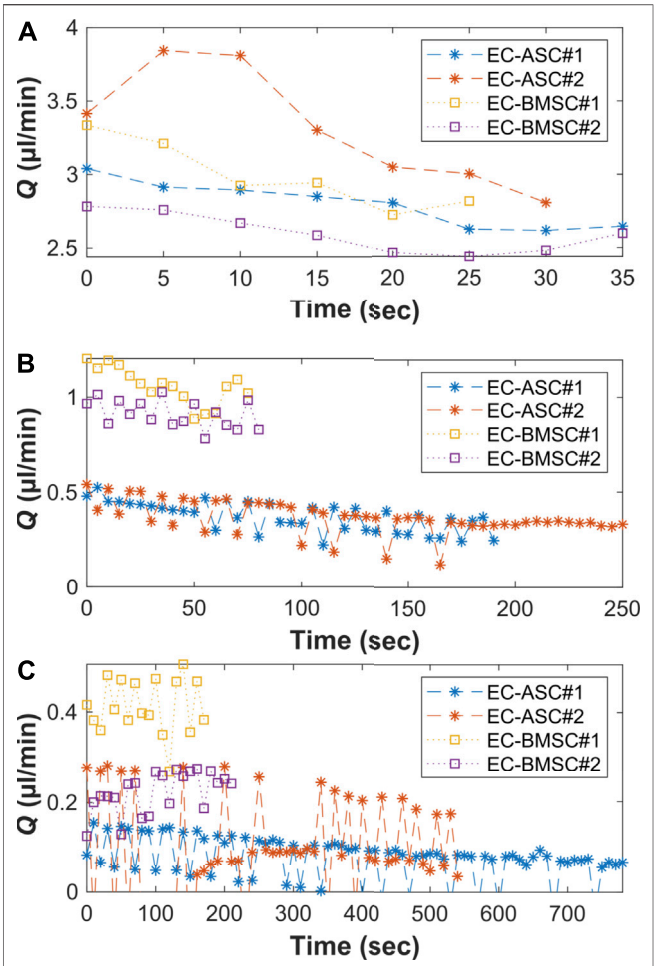

FIGURE 7 | Measured average flow rates (Q) [(90 µl + 90 µl)+(50 µl + 50 µl)] on two independent biological replicates (N = 2) on **(A)** day 0, **(B)** day 2, and **(C)** day 4 for both EC-ASC (*) and EC-BMSC (□) co-cultures. **(C)** At day 4, there is minimal flow front movement between two consecutive image indexes due to decreased flow rate. This results in reduced accuracy of the used analysis method that is seen as oscillation of the measured flow rate values. Donor cell lines BMSC 1 and ASC 3 were used for the flow characterization co-cultures.

Gene Expression Analysis Reveals Differences in Pericyte-Specific and Maturation Related Gene Expression Between EC-BMSC and EC-ASC Co-Cultures

To investigate differences in gene expression between EC-BMSC and EC-ASC co-cultures, we performed qRT-PCR analysis for both co-cultures considering pericyte-specific (*ACTA2*, *PDFGRB*, *CSPG4*) and endothelial-specific (*PECAM1*, *CDH5*, *VWF*) genes, basement membrane protein (*COL4A1*), angiogenic growth factors (*VEGFA*, *FGF2*), and other genes involved in vasculature morphogenesis and stability (*KDR*, *FLT1*, *ANGPT1*, *ANGPT2*) (**Figure 9**, **Supplementary Figure S4**). The mRNA expression of *ACTA2*, *PDFGRB*, *CSPG4*, *PECAM1*, *COL4A1*, *VEGFA*, *FGF2*, and *ANGPT1* in both co-cultures were measured relative to 18S and *GAPDH*. To assess changes in the number of ECs between EC-BMSC and EC-ASC co-cultures, we measured the mRNA expression of *PECAM1* relative to 18S and *GAPDH*. Expression of endothelial cell specific-genes *VWF*, *CDH5*, *KDR*, *FLT1* and *ANGPT2* were measured relative to *PECAM1* (**Supplementary Table S3**, **Supplementary Figure S4**) in both co-cultures. The qRT-PCR analysis revealed a significantly higher expression of pericyte marker genes *ACTA2* and *CSPG4* (9.5-fold and 4.5-fold, respectively), also known as α-SMA and NG2, in EC-BMSC co-cultures compared to EC-ASC co-cultures (**Supplementary Figure S4A**). The changes in the expression of *PDGFRB* were not significant between EC-BMSC and EC-ASC co-cultures. Furthermore, expression levels of *COL4A1*, encoding for the major basement membrane protein, were 4-times higher in EC-BMSC co-cultures compared to EC-ASC co-cultures (**Supplementary Figure S4C**). The qRT-PCR results confirmed our observations from the immunofluorescence stainings for *α*-SMA, PDGFR-*β*, and collagen type IV.

The expression of *PECAM1*, an endothelial marker gene, was markedly higher (3.3-fold change) in EC-BMSC co-cultures (**Supplementary Figure S4B**). Minor differences were found in the expression of other EC-specific (*CDH5* and *VWF*) genes (**Supplementary Figure S4B**). The expression of *CDH5* encoding VE-cadherin was 1.3-fold higher in EC-BMSC co-cultures than in EC-ASC co-cultures. The expression of main angiogenic growth factor genes, *VEGFA* and *FGF2*, did not differ between the co-cultures (**Supplementary Figure S4D**). In addition, changes in gene expression of VEGFA receptors were either not significant (*KDR*) or slightly decreased in EC-BMSC co-cultures (*FLT1*, 0.8-fold change) (**Supplementary Figure S4E**). Considering expression of *ANGPT1* and *ANGPT2* genes, main regulators of vessel stabilization and destabilization, we found no difference in *ANGPT2* expression between EC-BMSC and EC-ASC co-cultures (**Supplementary Figure S4E**). Interestingly, the *ANGPT1* expression was consistently more than 2.4-times increased in EC-BMSC co-cultures. However, due to donor variation in EC-ASC co-cultures (0.5-2-fold change), the changes were not significant.

Hierarchical gene clustering showed that microvascular networks supported by BMSCs and ASCs had distinct gene expression patterns (**Supplementary Figure S5**). Even though expression of genes normalized by *PECAM1* (*ANGPT1*, *CDH5*, *KDR*, *FLT1* and *VWF*) was similar in EC-BMSC and EC-ASC co-cultures, BMSCs and ASCs still formed their own clusters.

DISCUSSION

Perivascular cells are essential for proper maturation and stabilization of the forming vascular networks (Bergers and Song, 2005; Sweeney and Foldes, 2018). Previous studies investigating 3D vasculature formation have emphasized that network phenotype and maturation strongly depend on the used perivascular cell type (Grainger and Putnam, 2011; Jeon et al., 2014; Kniebs et al., 2020; Rambøl et al., 2020; Margolis et al., 2021). While various cell types have been reported to support

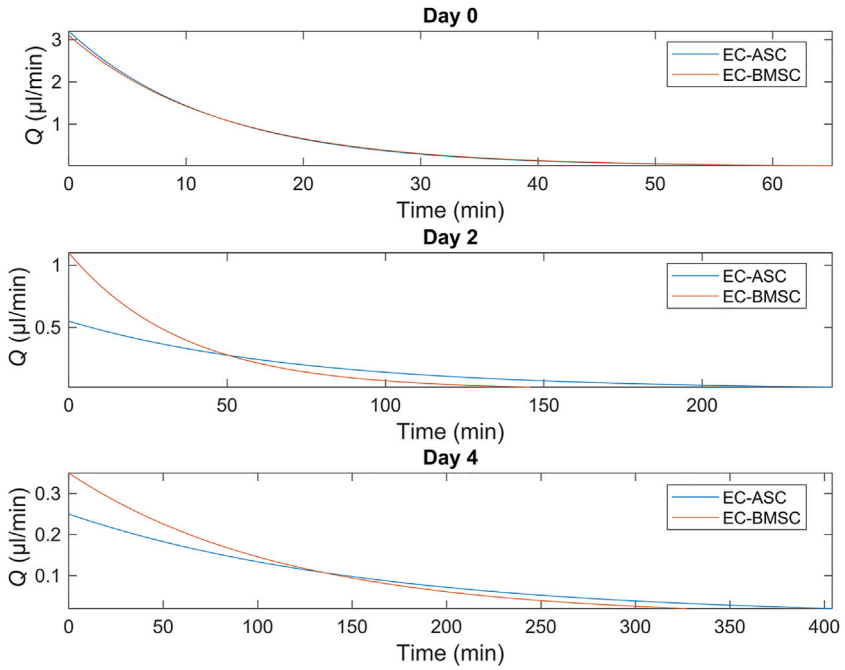

FIGURE 8 | Simulated flow profiles for EC-ASC (blue) and EC-BMSC (red) co-cultures at days 0, 2 and 4 show a general decrease in flow rates and increase in total flow duration from day 0–4. Donor cell lines BMSC 1 and ASC 3 were used for the flow characterization co-cultures.

vasculature formation in microfluidic devices (Kim et al., 2013; Li et al., 2017; Campisi et al., 2018; Zeinali et al., 2018; Rambøl et al., 2020), differences in experimental set-up complicate the direct comparison of the results obtained with different vasculature-supporting cells. Only few studies reported systematic comparisons done for BMSCs and ASCs (Pill et al., 2018; Kniebs et al., 2020). To our knowledge, this is the first study that has compared the vasculogenic capacities of BMSCs and ASCs in a microfluidic device. Here, we used a commercially available microfluidic chip platform for co-culture of ECs with MSCs in fibrin matrices with application of interstitial flow through the hydrogel.

Our results suggest that BMSCs have stronger vasculogenic capacity and promote formation of larger and more robust vascular networks than ASCs when co-cultured with ECs in a perfusable microfluidic chip. The use of BMSCs resulted in robust and well-interconnected microvascular networks, whereas co-culture with ASCs resulted in less-interconnected vessels that occupied smaller area compared to EC-BMSC co-cultures. Though it remains unclear whether the production of basement membrane protein collagen IV in BMSCs (Sillat et al., 2012) and ASCs (Patrikoski et al., 2017) is indeed intrinsically different or whether it is due to EC-co-culture conditions, we observed more robust vasculature formed by EC-BMSC co-cultures as well as stronger basement membrane deposition compared to EC-ASC co-cultures unlike previously reported by others (Pill et al., 2018). The observed differences in vasculature phenotypes of EC-BMSC and EC-ASC co-cultures could be explained by different experimental settings used in Pill et al. (2018) study including different EC:MSC ratio, cell concentration, and, importantly, static conditions.

To explain the differences in performance between co-cultures, we investigated the expression of pericyte markers α-SMA and PDGFR-β demonstrating the distribution and alignment of MSCs with ECs (Gerhardt and Betsholtz, 2003; Sweeney and Foldes, 2018). α-SMA and PDGFR-β are known to be intrinsically expressed in both BMSCs and ASCs (Talele et al., 2015; Milan et al., 2021; Sivaraj et al., 2021). Based on the α-SMA and PDGFR-β immunostaining we could identify perivascular MSCs in our co-cultures (Parthiban et al., 2020). Our results revealed substantial differences in immunostaining for pericyte marker α-SMA between MSCs of different origin. While in both EC-BMSC and EC-ASC co-cultures α-SMA-positive pericytes aligned with ECs and were wrapped around the vessels, further quantitative analysis revealed markedly higher pericyte area and vasculature coverage by pericytes in EC-BMSC co-cultures. Interestingly, no similar pattern was observed with pericyte marker PDGFR-β. PDGFR-β-positive BMSCs localized closely to the ECs. PDGFR-β-positive ASCs on the other hand, were scattered around the culture area and only a small portion of ASCs aligned in close proximity to the vessels. The results suggest that BMSCs migrate more closely towards developing vascular networks, and are therefore better positioned to act as functional pericytes when compared to ASCs.

Interstitial fluid flow was applied by generating a hydrostatic pressure across the hydrogel. According to our flow characterization, we verified the presence of interstitial flow in all measured timepoints day 0, day 2, day 4 and day 7. We

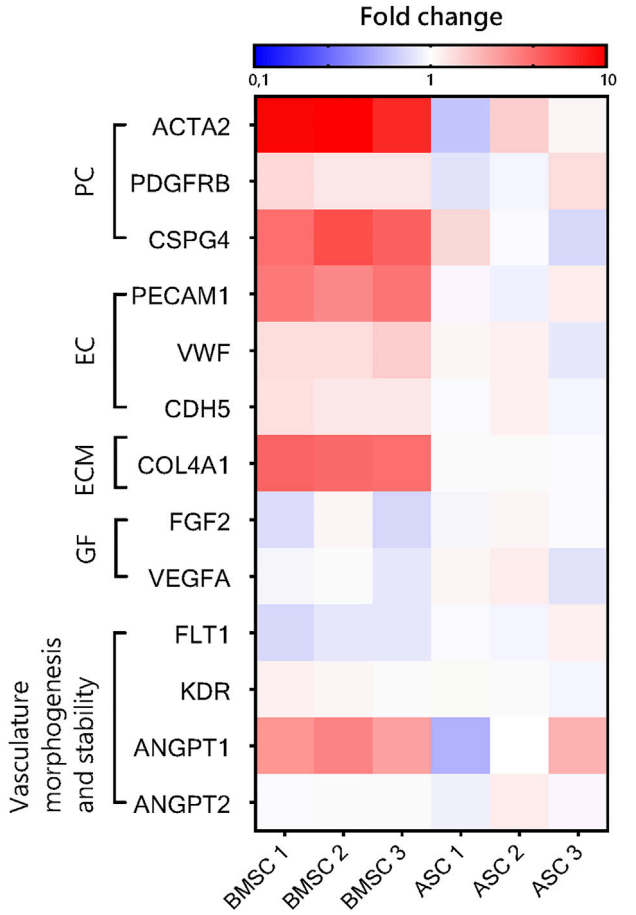

FIGURE 9 | Quantitative RT-PCR analysis of gene expression in ASC- and BMSC-supported microvascular networks. Heatmap shows relative mRNA expression of pericyte-specific (PC) and endothelial-specific (EC) genes, ECM protein (ECM), angiogenic growth factors (GF), and other genes involved in vasculature morphogenesis and stability in EC-ASC and EC-BMSC co-cultures after 6 days of culture. Gene expression fold change of EC-BMSC and EC-ASC cocultures was computed relative to the average expression in EC-ASC co-cultures. The reference genes were 18S and GAPDH (for PECAM1, VEGFA, PDGFRB, CSPG2, ACTA2, ANGPT1, FGF2) and PECAM1 (for VWF, CDH5, KDR, FLT1, ANGPT2).

observed decreased maximal flow rates in day 2 and day 4 compared to day 0 in both co-cultures. The results suggest that the changes in cellular distribution and increased cell number within the fibrin matrix decrease the maximal flow rate during culture. Maximal flow rate was further decreased at day 4 which might result from ECs seeded at day 2 which form a restricting monolayer in between the media channel and the hydrogel area. We demonstrated that the existence of interstitial flow actively replenishes fresh medium for ECs and MSCs compared to static flow condition. In terms of *in vivo*-relevancy, the measured maximum interstitial flow provides physiological, interstitial shear stress of 0.0065 Pa which is in line with the previously reported range (Kim et al., 2014; Yang et al., 2021). Hence, applying interstitial flow across the hydrogel with appropriate mechanical stress enhances the physiological relevancy of our *in vitro* vascular models (Kim et al., 2016; Haase and Kamm, 2017).

To describe the general flow characteristics in our study, we verified the formation of perfusable vessels after day 4, which led into a transition of the interstitial flow into luminal flow due to conjoining perfusable vessels across the hydrogel area. According to our bead flow assay at day 7, we verified the vessel capability to carry out particles in both co-cultures. This result is in line with immunocytochemical stainings showing the structural maturation at day 6. Still, we observed a considerable difference in vasculature perfusability between the two MSC types. BMSCs supported the formation of perfusable microvascular networks in all tested devices whereas EC-ASC co-cultures resulted in partially perfusable vasculature in only 2 out of 9 tested devices. This result is important, because perfusion capability is a key property of 3D vascularized *in vitro* models (Kim et al., 2013). Overall, our results highlight that in addition to immunocytochemical analyses of vessel maturation, functional measuring e.g. network perfusability is essential to assess the quality and functionality of the engineered vascular networks.

We found substantial differences in gene expression between EC-BMSC and EC-ASC co-cultures in genes related to pericytic and angiogenic activity supporting consistently our structural analysis. Relatively high expression levels of *ACTA2* and *CSPG4* indicate strong pericytic characteristics of BMSCs in accordance with abundant α-SMA staining shown in this study. Consistent with our immunohistochemical analysis and previous findings (Pill et al., 2018), *PDGFRB* expression was similar between co-cultures. We measured 4-fold higher expression of *COL4A1* in EC-BMSC, verifying our observations from immunohistochemistry that BMSCs more strongly support formation of the basement membrane. However, it remains unclear whether the COL4A1 expression is intrinsically different in BMSCs and ASCs or whether it is due to co-culture with ECs. We did not find differences in the expression of main angiogenic growth factor genes *VEGFA* and *FGF2*, neither in the main vasculature destabilizing gene *ANGPT2* between co-cultures which is in accordance with previous findings (Pill et al., 2018). However, we observed a trend in consistently higher expression levels of *ANGPT1* in EC-BMSC co-culture, a gene responsible for vessel maturation and stability. The results support our observations of more mature and stable microvascular networks in EC-BMSC co-cultures.

We found that endothelial cell marker gene *PECAM1* was over three times more expressed in EC-BMSC co-cultures than in EC-ASC co-cultures at the end of the 6-days culture period. This might indicate that ECs proliferate more and survive better in EC-BMSC than EC-ASC co-cultures. However, a previous study comparing vasculature-supporting properties of BMSCs and ASCs in a bulk hydrogel did not find significant changes in the number of ECs during 21-days culture period or between the co-cultures (Pill et al., 2018).

One possible explanation for the observed differences in vascular morphogenesis between EC-BMSC and EC-ASC co-cultures could be tissue-specific characteristics of MSCs as

vasculature supporting cells. Although BMSCs and ASCs share similar characteristics concerning cell morphology and surface marker expression (Bourin et al., 2013), significant biological differences have been shown for different types of MSCs, such as MSCs from bone marrow, skin dermis, and adipose tissue (Woo et al., 2016). Moreover, recent donor-matched comparison of BMSCs and ASCs revealed differences in proliferation and differentiation potential (Mohamed-Ahmed et al., 2018). It is important to remember that on macroscopic level, bone marrow and adipose tissue are remarkably different tissues. Thus, BMSCs and ASCs may differ concerning their vasculature supporting characteristics as well. Indeed, endothelial-to-pericyte ratio and vasculature coverage by pericytes vary considerably between different tissues ranging between 1:1 and 10:1 and 70 and 10% respectively (Armulik et al., 2011). For example, pericyte coverage in the bone marrow was measured to be 51 ± 20% (Zetterberg et al., 2007). Even though we measured significantly different pericyte coverage between EC-BMSC and EC-ASC co-cultures, both values fall within the range documented *in vivo*. Pericyte coverage correlates positively with endothelial barrier properties and endothelial cell turnover indicating the role of pericytes in regulating vessel permeability and stabilizing vascular networks (Armulik et al., 2011). Indeed, in our study we demonstrated higher pericyte coverage as well as higher expression of pericyte specific and maturation related genes in EC-BMSC co-cultures. Still, previous studies using other stromal cells demonstrate that altering the ratio of ECs to ASCs cell concentration, or hydrogel stiffness may be used to tailor vessel characteristics towards more robust, mature and perfusable microvasculature in EC-ASC co-cultures (Whisler et al., 2014; Tiruvannamalai Annamalai et al., 2016).

To summarize, we used a commercially available microfluidic device for generating interconnected, 3D vascular networks supported by either BMSCs or ASCs to systematically investigate the effect of chosen MSCs type on vascular network phenotype, functionality, and gene expression with commonly used HUVECs. We demonstrated that BMSCs have stronger pericytic ability and support mature vascular network formation under dynamic culture conditions. Our study demonstrates how vascular network phenotype depends on MSCs tissue source, resulting in differing gene expressions, vasculature morphology and characteristics, and ultimately, vascular network functionality. Therefore, we suggest considering these varying characteristics when developing advanced vascularized organ-on-a-chip platforms.

DATA AVAILABILITY STATEMENT

The original contributions presented in the study are included in the article/**Supplementary Materials**, further inquiries can be directed to the corresponding authors.

AUTHOR CONTRIBUTIONS

AM and AY: conceptualization, investigation, methodology, formal analysis, visualization, writing—original draft, writing—review and editing. A-JM: designing, implementing, and summarizing flow analysis, writing—original draft related to flow analysis, writing—review and editing. AG: writing—review and editing, formal analysis. MK and T-KP: resources (providing adipose tissue and bone marrow samples). EL: methodology, formal analysis, visualization. PK: supervision, funding acquisition. SM: conceptualization, validation, writing—review and editing, project administration, supervision, funding acquisition. HV: conceptualization, validation, writing—review and editing, project administration, supervision.

FUNDING

The financial support of Academy of Finland, Centre of Excellence in Body-on-a-Chip research grant numbers are 312413, 326588, 336666 and 336785, Business Finland, Competitive State Research Financing of the Expert Responsibility area of Tampere University Hospital, Tampere University Doctoral School and Finnish National Agency for Education are gratefully acknowledged.

ACKNOWLEDGMENTS

Tampere University Research Centre of Science Mimicking Life, Tampere Imaging Facility (TIF), and Cell Tech Laboratories of Tampere University are gratefully acknowledged. The authors thank Ms. Anna-Maija Honkala and Sari Kalliokoski for their excellent technical assistance.

SUPPLEMENTARY MATERIAL

The Supplementary Material for this article can be found online at: https://www.frontiersin.org/articles/10.3389/fbioe.2022.764237/full#supplementary-material

REFERENCES

Abe, Y., Watanabe, M., Chung, S., Kamm, R. D., Tanishita, K., and Sudo, R. (2019). Balance of Interstitial Flow Magnitude and Vascular Endothelial Growth Factor Concentration Modulates Three-Dimensional Microvascular Network Formation. *APL Bioeng.* 3 (3), 036102. doi:10.1063/1.5094735

Armulik, A., Genové, G., and Betsholtz, C. (2011). Pericytes: Developmental, Physiological, and Pathological Perspectives, Problems, and Promises. *Develop. Cel* 21 (2), 193–215. doi:10.1016/j.devcel.2011.07.001

Augustin, H. G., and Koh, G. Y. (2017). Organotypic Vasculature: From Descriptive Heterogeneity to Functional Pathophysiology. *Science* 357 (6353), eaal2379. doi:10.1126/science.aal2379

Bachmann, B., Spitz, S., Rothbauer, M., Jordan, C., Purtscher, M., Zirath, H., et al. (2018). Engineering of Three-Dimensional Pre-vascular Networks within

Fibrin Hydrogel Constructs by Microfluidic Control over Reciprocal Cell Signaling. *Biomicrofluidics* 12 (4), 042216. doi:10.1063/1.5027054

Benjamini, Y., Krieger, A. M., and Yekutieli, D. (2006). Adaptive Linear Step-Up Procedures that Control the False Discovery Rate. *Biometrika* 93 (3), 491–507. doi:10.1093/biomet/93.3.491

Bergers, G., and Song, S. (2005). The Role of Pericytes in Blood-Vessel Formation and Maintenance. *Neuro Oncol.* 7 (4), 452–464. doi:10.1215/S1152851705000232

Bourin, P., Bunnell, B. A., Casteilla, L., Dominici, M., Katz, A. J., March, K. L., et al. (2013). Stromal Cells from the Adipose Tissue-Derived Stromal Vascular Fraction and Culture Expanded Adipose Tissue-Derived Stromal/stem Cells: a Joint Statement of the International Federation for Adipose Therapeutics and Science (IFATS) and the International Society for Cellular Therapy (ISCT). *Cytotherapy* 15 (6), 641–648. doi:10.1016/j.jcyt.2013.02.006

Campisi, M., Shin, Y., Osaki, T., Hajal, C., Chiono, V., and Kamm, R. D. (2018). 3D Self-Organized Microvascular Model of the Human Blood-Brain Barrier with Endothelial Cells, Pericytes and Astrocytes. *Biomaterials* 180, 117–129. doi:10.1016/j.biomaterials.2018.07.014

Chen, M. B., Whisler, J. A., JeonJeon, J. S., and Kamm, R. D. (2013). Mechanisms of Tumor Cell Extravasation in an *In Vitro* Microvascular Network Platform. *Integr. Biol.* 5 (10), 1262–1271. doi:10.1039/c3ib40149a

Dominici, M., Le Blanc, K., Mueller, I., Slaper-Cortenbach, I., Marini, F. C., Krause, D. S., et al. (2006). Minimal Criteria for Defining Multipotent Mesenchymal Stromal Cells. The International Society for Cellular Therapy Position Statement. *Cytotherapy* 8 (4), 315–317. doi:10.1080/14653240600855905

Erickson, S., Ihara, H., Hanada, S., Nishiyama, K., Miura, T., and Yokokawa, R. (2020). "An On-Chip Vascular Network to Investigate Pericyte Migration and Intercellular Signaling," in *IEEE 33rd International Conference on Micro Electro Mechanical Systems (MEMS)* (Vancouver, Canada: IEEE). doi:10.1109/MEMS46641.2020.9056369

Gerhardt, H., and Betsholtz, C. (2003). Endothelial-Pericyte Interactions in Angiogenesis. *Cel Tissue Res.* 314, 15–23. doi:10.1007/s00441-003-0745-x

Giannotta, M., Trani, M., and Dejana, E. (2013). VE-cadherin and Endothelial Adherens Junctions: Active Guardians of Vascular Integrity. *Develop. Cel* 26 (5), 441–454. doi:10.1016/j.devcel.2013.08.020

Grainger, S. J., Carrion, B., Ceccarelli, J., and Putnam, A. J. (2013). Stromal Cell Identity Influences the *In Vivo* Functionality of Engineered Capillary Networks Formed by Co-delivery of Endothelial Cells and Stromal Cells. *Tissue Eng. A* 19 (9–10), 1209–1222. doi:10.1089/ten.TEA.2012.0281

Grainger, S. J., and Putnam, A. J. (2011). Assessing the Permeability of Engineered Capillary Networks in a 3D Culture. *PLoS ONE* 6 (7), e22086. doi:10.1371/journal.pone.0022086

Guo, Z., Yang, C. T., Maritz, M. F., Wu, H., Wilson, P., Warkiani, M. E., et al. (2019). Validation of a Vasculogenesis Microfluidic Model for Radiobiological Studies of the Human Microvasculature. *Adv. Mater. Technol.* 4 (4), 1800726. doi:10.1002/admt.201800726

Haase, K., Gillrie, M. R., Hajal, C., and Kamm, R. D. (2019). Pericytes Contribute to Dysfunction in a Human 3D Model of Placental Microvasculature through VEGF-Ang-Tie2 Signaling. *Adv. Sci.* 6, 1900878. doi:10.1002/advs.201900878

Haase, K., and Kamm, R. D. (2017). Advances in On-Chip Vascularization. *Regenerative Med.* 12 (3), 285–302. doi:10.2217/rme-2016-0152

Holm, A., Heumann, T., and Augustin, H. G. (2018). Microvascular Mural Cell Organotypic Heterogeneity and Functional Plasticity. *Trends Cel Biol.* 28 (4), 302–316. doi:10.1016/j.tcb.2017.12.002

Honkamäki, L., Joki, T., Grigoryev, N. A., Levon, K., Ylä-Outinen, L., and Narkilahti, S. (2021). Novel Method to Produce a Layered 3D Scaffold for Human Pluripotent Stem Cell-Derived Neuronal Cells. *J. Neurosci. Methods* 350, 109043. doi:10.1016/j.jneumeth.2020.109043

Hyväri, L., Ojansivu, M., Juntunen, M., Kartasalo, K., Miettinen, S., and Vanhatupa, S. (2018). Focal Adhesion Kinase and ROCK Signaling Are Switch-like Regulators of Human Adipose Stem Cell Differentiation towards Osteogenic and Adipogenic Lineages. *Stem Cell Int.* 2018, 1–13. doi:10.1155/2018/2190657

Hyväri, L., Vanhatupa, S., Halonen, H. T., Kääriäinen, M., and Miettinen, S. (2020). Myocardin-Related Transcription Factor A (MRTF-A) Regulates the Balance between Adipogenesis and Osteogenesis of Human Adipose Stem Cells. *Stem Cell Int.* 2020, 1–17. doi:10.1155/2020/8853541

Jeon, J. S., Bersini, S., Whisler, J. A., Chen, M. B., Dubini, G., Charest, J. L., et al. (2014). Generation of 3D Functional Microvascular Networks with Human Mesenchymal Stem Cells in Microfluidic Systems. *Integr. Biol.* 6 (5), 555–563. doi:10.1039/b000000x/NIH10.1039/c3ib40267c

Jusoh, N., Oh, S., Kim, S., Kim, J., and Jeon, N. L. (2015). Microfluidic Vascularized Bone Tissue Model with Hydroxyapatite-Incorporated Extracellular Matrix. *Lab. Chip* 15 (20), 3984–3988. doi:10.1039/C5LC00698H

Kachgal, S., and Putnam, A. J. (2011). Mesenchymal Stem Cells from Adipose and Bone Marrow Promote Angiogenesis via Distinct Cytokine and Protease Expression Mechanisms. *Angiogenesis* 14 (1), 47–59. doi:10.1007/s10456-010-9194-9

Kim, K. M., Choi, Y. J., Hwang, J.-H., Kim, A. R., Cho, H. J., Hwang, E. S., et al. (2014). Shear Stress Induced by an Interstitial Level of Slow Flow Increases the Osteogenic Differentiation of Mesenchymal Stem Cells through TAZ Activation. *PLOS ONE* 9 (3), e92427. doi:10.1371/JOURNAL.PONE.0092427

Kim, S., Chung, M., Ahn, J., Lee, S., and Jeon, N. L. (2016). Interstitial Flow Regulates the Angiogenic Response and Phenotype of Endothelial Cells in a 3D Culture Model. *Lab. Chip* 16, 4189–4199. doi:10.1039/c6lc00910g

Kim, S., Lee, H., Chung, M., and Jeon, N. L. (2013). Engineering of Functional, Perfusable 3D Microvascular Networks on a Chip. *Lab. Chip* 13 (8), 1489–1500. doi:10.1039/c3lc41320a

Kniebs, C., Kreimendahl, F., Köpf, M., Fischer, H., Jockenhoevel, S., and Thiebes, A. L. (2020). Influence of Different Cell Types and Sources on Pre-vascularisation in Fibrin and Agarose-Collagen Gels. *Organogenesis* 16 (1), 14–26. doi:10.1080/15476278.2019.1697597

Kyllönen, L., Haimi, S., Mannerström, B., Huhtala, H., Rajala, K. M., Skottman, H., et al. (2013). Effects of Different Serum Conditions on Osteogenic Differentiation of Human Adipose Stem Cells *In Vitro*. *Stem Cel Res. Ther.* 4, 17. doi:10.1186/scrt165

LeBleu, V. S., MacDonald, B., and Kalluri, R. (2007). Structure and Function of Basement Membranes. *Exp. Biol. Med. (Maywood)* 232 (9), 1121–1129. doi:10.3181/0703-MR-72

Li, Y., Hu, C., Wang, P., Liu, Y., Wang, L., Pi, Q., et al. (2019). Indoor Nanoscale Particulate Matter-Induced Coagulation Abnormality Based on a Human 3D Microvascular Model on a Microfluidic Chip. *J. Nanobiotechnol.* 17 (1), 20. doi:10.1186/s12951-019-0458-2

Li, Y., Pi, Q.-M. Pi., Wang, P.-C., LiuHan, L.-J., Han, Z.-G., Shao, Y., et al. (2017). Lie Ju LiuFunctional Human 3D Microvascular Networks on a Chip to Study the Procoagulant Effects of Ambient Fine Particulate Matter. *RSC Adv.* 7, 56108–56116. doi:10.1039/c7ra11357a

Lin, C. S., Xin, Z. C., Deng, C. H., Ning, H., Lin, G., and Lue, T. F. (2010). Defining Adipose Tissue-Derived Stem Cells in Tissue and in Culture. *Histol. Histopathol.* 25 (6), 807–815. doi:10.14670/HH-25.807

Livak, K. J., and Schmittgen, T. D. (2001). Analysis of Relative Gene Expression Data Using Real-Time Quantitative PCR and the 2−ΔΔCT Method. *Methods* 25 (4), 402–408. doi:10.1006/meth.2001.1262

Mäki, A. J., Hemmilä, S., Hirvonen, J., Girish, N. N., Kreutzer, J., Hyttinen, J., et al. (2015). Modeling and Experimental Characterization of Pressure Drop in Gravity-Driven Microfluidic Systems. *J. Fluids Eng.* 137 (2), 21105–21106. doi:10.1115/1.4028501/374648

Margolis, E. A., Cleveland, D. S., Kong, Y. P., Beamish, J. A., Wang, W. Y., Baker, B. M., et al. (2021). Stromal Cell Identity Modulates Vascular Morphogenesis in a Microvasculature-On-A-Chip Platform. *Lab. Chip* 21, 1150–1163. doi:10.1039/d0lc01092h

Milan, G., Conci, S., Sanna, M., Favaretto, F., Bettini, S., and Vettor, R. (2021). ASCs and Their Role in Obesity and Metabolic Diseases. *Trends Endocrinol. Metab.* 32 (12), 994–1006. doi:10.1016/J.TEM.2021.09.001

Mohamed-Ahmed, S., Fristad, I., Lie, S. A., Suliman, S., Mustafa, K., Vindenes, H., et al. (2018). Adipose-Derived and Bone Marrow Mesenchymal Stem Cells: A Donor-Matched Comparison. *Stem Cel Res. Ther.* 9 (1), 168. doi:10.1186/s13287-018-0914-1

Paek, J., ParkPark, S. E., Lu, Q., Park, K.-T., Cho, M., OhOh, J. M., et al. (2019). Microphysiological Engineering of Self-Assembled and Perfusable Microvascular Beds for the Production of Vascularized Three-Dimensional Human Microtissues. *ACS Nano* 13 (7), 7627–7643. doi:10.1021/acsnano.9b00686

Parthiban, S. P., He, W., Monteiro, N., Athirasala, A., França, C. M., and Bertassoni, L. E. (2020). Engineering Pericyte-Supported Microvascular

Capillaries in Cell-Laden Hydrogels Using Stem Cells from the Bone Marrow, Dental Pulp and Dental Apical Papilla. *Sci. Rep.* 10 (1), 21579. doi:10.1038/s41598-020-78176-7

Patrikoski, M., Juntunen, M., Boucher, S., Campbell, A., Vemuri, M. C., Mannerström, B., et al. (2013). Development of Fully Defined Xeno-free Culture System for the Preparation and Propagation of Cell Therapy-Compliant Human Adipose Stem Cells. *Stem Cel Res Ther* 4 (2), 27. doi:10.1186/scrt175

Patrikoski, M., Lee, M. H. C., Mäkinen, L. A., Ang, X. M., Mannerström, B., Raghunath, M., et al. (2017). Effects of Macromolecular Crowding on Human Adipose Stem Cell Culture in Fetal Bovine Serum, Human Serum, and Defined Xeno-Free/Serum-free Conditions. *Stem Cell Int.* 2017, 1–14. doi:10.1155/2017/6909163

Pill, K., Hofmann, S., Redl, H., and Holnthoner, W. (2015). Vascularization Mediated by Mesenchymal Stem Cells from Bone Marrow and Adipose Tissue: A Comparison. *Cel Regen.* 4 (1), 4:8. doi:10.1186/s13619-015-0025-8

Pill, K., Melke, J., Mühleder, S., Pultar, M., Rohringer, S., Priglinger, E., et al. (2018). Microvascular Networks from Endothelial Cells and Mesenchymal Stromal Cells from Adipose Tissue and Bone Marrow: A Comparison. *Front. Bioeng. Biotechnol.* 6, 156. doi:10.3389/fbioe.2018.00156

Rambøl, M. H., Han, E., and Niklason, L. E. (2020). Microvessel Network Formation and Interactions with Pancreatic Islets in Three-Dimensional Chip Cultures. *Tissue Eng. Part A* 26 (9–10), 556–568. doi:10.1089/ten.tea.2019.0186

Schindelin, J., Arganda-Carreras, I., Frise, E., Kaynig, V., Longair, M., Pietzsch, T., et al. (2012). Fiji: An Open-Source Platform for Biological-Image Analysis. *Nat. Methods* 9 (7), 676–682. doi:10.1038/nmeth.2019

Sillat, T., Saat, R., Pöllänen, R., Hukkanen, M., Takagi, M., and KonttinenKonttinen, Y. T. (2012). Basement Membrane Collagen Type IV Expression by Human Mesenchymal Stem Cells during Adipogenic Differentiation. *J. Cel. Mol. Med* 16 (7), 1485–1495. doi:10.1111/j.1582-4934.2011.01442.x

Sivaraj, K. K., Jeong, H.-W., Dharmalingam, B., Zeuschner, D., Adams, S., Potente, M., et al. (2021). Regional Specialization and Fate Specification of Bone Stromal Cells in Skeletal Development. *Cel Rep.* 36 (2), 109352. doi:10.1016/J.CELREP.2021.109352

Smith, Q., and Gerecht, S. (2014). Going with the Flow: Microfluidic Platforms in Vascular Tissue Engineering. *Curr. Opin. Chem. Eng.* 3, 42–50. doi:10.1016/j.coche.2013.11.001

Stratman, A. N., and Davis, G. E. (2012). Endothelial Cell-Pericyte Interactions Stimulate Basement Membrane Matrix Assembly: Influence on Vascular Tube Remodeling, Maturation, and Stabilization. *Microsc. Microanal.* 18 (1), 68–80. doi:10.1017/S1431927611012402

Sweeney, M., and Foldes, G. (2018). It Takes Two: Endothelial-Perivascular Cell Cross-Talk in Vascular Development and Disease. *Front. Cardiovasc. Med.* 5, 154. doi:10.3389/fcvm.2018.00154

Talele, N. P., Fradette, J., Davies, J. E., Kapus, A., and Hinz, B. (2015). Expression of α-Smooth Muscle Actin Determines the Fate of Mesenchymal Stromal Cells. *Stem Cel Rep.* 4, 1016–1030. doi:10.1016/j.stemcr.2015.05.004

Tiruvannamalai Annamalai, R., Rioja, A. Y., Putnam, A. J., and Stegemann, J. P. (2016). Vascular Network Formation by Human Microvascular Endothelial Cells in Modular Fibrin Microtissues. *ACS Biomater. Sci. Eng.* 2 (11), 1914–1925. doi:10.1021/acsbiomaterials.6b00274

Verseijden, F., Posthumus-van Sluijs, S. J., Pavljasevic, P., Hofer, S. O. P., van OschOsch, G. J. V. M., and Farrell, E. (2010). Adult Human Bone Marrow- and Adipose Tissue-Derived Stromal Cells Support the Formation of Prevascular-like Structures from Endothelial Cells *In Vitro*. *Tissue Eng. Part A* 16 (1), 101–114. doi:10.1089/ten.tea.2009.0106

Wang, X., Molino, B. Z., Pitkänen, S., Ojansivu, M., Xu, C., Hannula, M., et al. (2019). 3D Scaffolds of Polycaprolactone/Copper-Doped Bioactive Glass: Architecture Engineering with Additive Manufacturing and Cellular Assessments in a Coculture of Bone Marrow Stem Cells and Endothelial Cells. *ACS Biomater. Sci. Eng.* 5, 4496–4510. doi:10.1021/acsbiomaterials.9b00105

Warnes, G. R., Bolker, B., Bonebakker, L., Gentleman, R., Liaw, W. H. A., Lumley, T., et al. (2015). "Gplots: Various R Programming Tools for Plotting Data. R Package Version 2.17. 0. 2015

Whisler, J. A., Chen, M. B., and Kamm, R. D. (2014). Control of Perfusable Microvascular Network Morphology Using a Multiculture Microfluidic System. *Tissue Eng. C: Methods* 20 (7), 543–552. doi:10.1089/ten.TEC.2013.0370

Woo, D.-H., Hwang, H. S., and Shim, J. H. (2016). Comparison of Adult Stem Cells Derived from Multiple Stem Cell Niches. *Biotechnol. Lett.* 38 (5), 751–759. doi:10.1007/s10529-016-2050-2

Wu, Q., Liu, J., Wang, X., Feng, L., Wu, J., Zhu, X., et al. (2020). Organ-on-a-Chip: Recent Breakthroughs and Future Prospects. *Biomed. Eng. Online* 19, 9. doi:10.1186/s12938-020-0752-0

Yang, F., Carmona, A., Stojkova, K., Garcia Huitron, E. I., Goddi, A., Bhushan, A., et al. (2021). A 3D Human Adipose Tissue Model within a Microfluidic Device. *Lab Chip* 21 (2), 435–446. doi:10.1186/s12938-020-0752-0

Zeinali, S., Bichsel, C. A., Hobi, N., Funke, M., Marti, T. M., Schmid, R. A., et al. (2018). Human Microvasculature-On-A Chip: Anti-neovasculogenic Effect of Nintedanib *In Vitro*. *Angiogenesis* 21 (4), 861–871. doi:10.1007/s10456-018-9631-8

Zetterberg, E., Vannucchi, A. M., Migliaccio, A. R., Vainchenker, W., Tulliez, M., Dickie, R., et al. (2007). Pericyte Coverage of Abnormal Blood Vessels in Myelofibrotic Bone Marrows. *Haematologica* 92 (5), 597–604. doi:10.3324/haematol.11013

Zhang, S., Wan, Z., and Kamm, R. D. (2021). Vascularized Organoids on a Chip: Strategies for Engineering Organoids with Functional Vasculature. *Lab. Chip* 21 (3), 473–488. doi:10.1039/d0lc01186j

Conflict of Interest: The authors declare that the research was conducted in the absence of any commercial or financial relationships that could be construed as a potential conflict of interest.

Publisher's Note: All claims expressed in this article are solely those of the authors and do not necessarily represent those of their affiliated organizations, or those of the publisher, the editors and the reviewers. Any product that may be evaluated in this article, or claim that may be made by its manufacturer, is not guaranteed or endorsed by the publisher.

frontiers in Bioengineering and Biotechnology

ORIGINAL RESEARCH
published: 18 February 2022
doi: 10.3389/fbioe.2022.823642

Hydrostatic Pressure Controls Angiogenesis Through Endothelial YAP1 During Lung Regeneration

*Tadanori Mammoto[1,2], Tendai Hunyenyiwa[1,3], Priscilla Kyi[1,3], Kathryn Hendee[1], Kienna Matus[1], Sridhar Rao[1,3,4], Sang H. Lee[2], Diana M. Tabima[5], Naomi C. Chesler[5,6] and Akiko Mammoto[1,3]**

[1]Department of Pediatrics, Medical College of Wisconsin, Milwaukee, WI, United States, [2]Department of Pharmacology and Toxicology, Medical College of Wisconsin, Milwaukee, WI, United States, [3]Department of Cell Biology, Neurobiology and Anatomy, Medical College of Wisconsin, Milwaukee, WI, United States, [4]Blood Research Institute, Versiti, Milwaukee, WI, United States, [5]Biomedical Engineering, University of Wisconsin-Madison, Madison, WI, United States, [6]Edwards Lifesciences Foundation Cardiovascular Innovation and Research Center and Biomedical Engineering, University of California, Irvine, Irvine, CA, United States

OPEN ACCESS

Edited by:
Wolfgang Holnthoner,
AUVA Research Centre, Ludwig Boltzmann Institute for Experimental and Clinical Traumatology, Austria

Reviewed by:
George M Rodgers,
The University of Utah, United States
Kewal Asosingh,
Cleveland Clinic, United States
William Wang,
Cornell University, United States

***Correspondence:**
Akiko Mammoto
amammoto@mcw.edu

Specialty section:
This article was submitted to Tissue Engineering and Regenerative Medicine, a section of the journal Frontiers in Bioengineering and Biotechnology

Received: 27 November 2021
Accepted: 31 January 2022
Published: 18 February 2022

Citation:
Mammoto T, Hunyenyiwa T, Kyi P, Hendee K, Matus K, Rao S, Lee SH, Tabima DM, Chesler NC and Mammoto A (2022) Hydrostatic Pressure Controls Angiogenesis Through Endothelial YAP1 During Lung Regeneration. Front. Bioeng. Biotechnol. 10:823642. doi: 10.3389/fbioe.2022.823642

Pulmonary artery (PA) pressure increases during lung growth after unilateral pneumonectomy (PNX). Mechanosensitive transcriptional co-activator, yes-associated protein (YAP1), in endothelial cells (ECs) is necessary for angiogenesis during post-PNX lung growth. We investigate whether increases in PA pressure following PNX control-angiogenesis through YAP1. When hydrostatic pressure is applied to human pulmonary arterial ECs (HPAECs), the expression of YAP1, transcription factor TEAD1, and angiogenic factor receptor Tie2 increases, while these effects are inhibited when HPAECs are treated with YAP1 siRNA or YAP1S94A mutant that fails to bind to TEAD1. Hydrostatic pressure also stimulates DNA synthesis, cell migration, and EC sprouting in HPAECs, while YAP1 knockdown or YAP1S94A mutant inhibits the effects. Gene enrichment analysis reveals that the levels of genes involved in extracellular matrix (ECM), cell adhesion, regeneration, or angiogenesis are altered in post-PNX mouse lung ECs, which interact with YAP1. Exosomes are known to promote tissue regeneration. Proteomics analysis reveals that exosomes isolated from conditioned media of post-PNX mouse lung ECs contain the higher levels of ECM and cell-adhesion proteins compared to those from sham-operated mouse lung ECs. Recruitment of host lung ECs and blood vessel formation are stimulated in the fibrin gel containing exosomes isolated from post-PNX mouse lung ECs or pressurized ECs, while YAP1 knockdown inhibits the effects. These results suggest that increases in PA pressure stimulate angiogenesis through YAP1 during regenerative lung growth.

Keywords: angiogenesis, pressure, lung, Yap1, TEAD, Tie2

INTRODUCTION

Compensatory lung growth is induced in the remaining lung tissues after unilateral PNX in humans and other species (e.g., mice, dogs) (Hsia et al., 2001; Sakurai et al., 2007; Ding et al., 2011; Butler et al., 2012; Thane et al., 2014; Mammoto et al., 2016a; Liu et al., 2016; Mammoto T. et al., 2019; Hendee et al., 2021); the remaining alveolar units undergo epithelial and EC proliferation to

compensate for the initial loss. The mechanical environment is dramatically changed after PNX (Hsia et al., 2001; Dane et al., 2013; Filipovic et al., 2013; Thane et al., 2014; Dane et al., 2016; Liu et al., 2016). For example, increases in parenchymal strain due to the expansion of the remaining lobes contribute to post-PNX lung alveolar cell growth (Hsia et al., 2001; Dane et al., 2013; Filipovic et al., 2013; Liu et al., 2016). Increases in PA pressure due to redirection of the entire cardiac output through remaining lung lobes also play important roles in post-PNX lung growth (Dane et al., 2013; Dane et al., 2016).

Angiogenesis -growth of new capillaries-constitutes an essential part of the regenerative program (Sakurai et al., 2007; Ding et al., 2011; Mammoto et al., 2016a; Mammoto T. et al., 2019; Mammoto and Mammoto, 2019; Hendee et al., 2021). Inhibition of angiogenesis impairs compensatory lung growth after PNX in adult mice (Sakurai et al., 2007; Ding et al., 2011; Mammoto et al., 2016a; Mammoto T. et al., 2019; Hendee et al., 2021). Mechanical factors such as ECM stiffness, shear stress, and stretching forces control angiogenesis and vascular function (Mammoto et al., 2009; Thodeti et al., 2009; Mammoto A. et al., 2013; Mammoto T. et al., 2013; Mammoto and Mammoto, 2019). Hippo signaling transducer, YAP1, acts as a transcriptional co-activator and controls organ size, development, and regeneration (e.g., liver, heart, intestine, muscle, lung) (Barry et al., 2013; Piccolo et al., 2013; Lin and Pu, 2014; Mahoney et al., 2014; Yimlamai et al., 2014; Yu et al., 2015; Liu et al., 2016; Mammoto T. et al., 2019). In the lung, YAP1 activation in alveolar epithelial stem cells and ECs promotes post-PNX lung growth (Liu et al., 2016; Mammoto T. et al., 2019), while deregulation of YAP1 contributes to chronic obstructive pulmonary disease (Makita et al., 2008) and pulmonary fibrosis (Liu et al., 2015; Panciera et al., 2017). YAP1 stimulates angiogenesis in the retina and other organs (Choi et al., 2015; Nakajima et al., 2017; Mammoto A. et al., 2018; Boopathy and Hong, 2019). YAP1 is a mechanosensitive gene and its activity is controlled by mechanical stimuli (e.g., cell shape and size (Dupont et al., 2011; Panciera et al., 2017), cell density (Ota and Sasaki, 2008; Choi et al., 2015), rigidity and topology of ECM (Dupont et al., 2011; Bertero et al., 2016), shear stress (Dupont et al., 2011; Wang et al., 2016; Nakajima et al., 2017; Panciera et al., 2017), mechanical tension (Liu et al., 2016)). In our previous study, we demonstrated that YAP1 in ECs is necessary for angiogenesis during post-PNX lung growth (Mammoto T. et al., 2019). Given that 1) mechanical environment changes after PNX, which drives post-PNX lung growth (Hsia et al., 2001; Dane et al., 2013; Filipovic et al., 2013; Liu et al., 2016), 2) YAP1 senses various mechanical stimuli (Ota and Sasaki, 2008; Dupont et al., 2011; Choi et al., 2015; Bertero et al., 2016; Liu et al., 2016; Wang et al., 2016; Nakajima et al., 2017; Panciera et al., 2017), and 3) mechanical forces control angiogenesis (Mammoto et al., 2009; Thodeti et al., 2009; Mammoto A. et al., 2013; Mammoto T. et al., 2013; Mammoto and Mammoto, 2019), in this study we have investigated whether post-PNX changes in the mechanical forces control angiogenesis through endothelial YAP1. It has been reported that increased mechanical stretch after PNX induces post-PNX lung growth through epithelial YAP1 signaling (Liu et al., 2016). However, the effects of PA pressure altering during post-PNX lung growth on angiogenesis have not been explored. Here we examined whether increases in PA pressure after PNX stimulate angiogenesis through YAP1.

Exosomes are one of the types of extracellular vesicles produced by almost all cell types, including ECs (Thery et al., 2002; Pant et al., 2012; Kourembanas, 2015; Davidson et al., 2018). Exosomes contain numerous proteins, lipids, and various types of nucleic acids (DNA, mRNA, miRNA, noncoding RNA) (Thery et al., 2002; Kourembanas, 2015). Exosomes are released from cells to serve as a messenger of signals for cell-cell communications as well as to remove unused or harmful RNA and proteins, maintaining tissue homeostasis and function in normal physiology and in diseases (e.g., aging (Xie et al., 2018), cancer (Jakhar and Crasta, 2019), atherosclerosis (Chang et al., 2019), pulmonary hypertension (Lee et al., 2012; Klinger et al., 2020; Mohan et al., 2020; Sindi et al., 2020; Otsuki et al., 2021)) (Thery et al., 2002; Thery et al., 2009; Pant et al., 2012; Kourembanas, 2015; Jakhar and Crasta, 2019; Otsuki et al., 2021). Exosomes promote angiogenesis and stimulate cardiac regeneration (Ibrahim et al., 2014; Shanmuganathan et al., 2018) and recovery from ischemia (Sahoo et al., 2011; Bang et al., 2014; Shanmuganathan et al., 2018). It has been reported that human mesenchymal stem cell (MSC)-derived exosomes ameliorate various lung diseases in animal models (e.g., pulmonary hypertension, bronchopulmonary dysplasia (BPD), airway inflammation, pulmonary fibrosis) (Lee et al., 2012; Cruz et al., 2015; Willis et al., 2018; Genschmer et al., 2019; Mansouri et al., 2019; Dinh et al., 2020; Klinger et al., 2020; Mohan et al., 2020; Sindi et al., 2020). However, the role of exosomes from ECs in lung regeneration has not been studied before.

Here we demonstrate that increases in PA pressure after PNX stimulate angiogenesis through endothelial YAP1 signaling. Exosomes isolated from post-PNX mouse lung ECs or pressured ECs stimulate angiogenesis in the mouse lungs. Modulation of mechanical environment or endothelial YAP1 signaling could improve the strategy for regenerative lung growth.

MATERIALS AND METHODS

Materials

Anti-CD31 and -GM130 antibodies were from BD Biosciences (Franklin Lakes, NJ). Anti-YAP1- and -flotillin-1 antibodies were from Cell Signaling (Danvers, MA). Anti-β-actin antibody was from Sigma (St. Louis, MO). Anti-Tie2 monoclonal antibody was from Upstate (Lake Placid, NY). Anti-YAP1 and -CD63 antibodies were from Santa Cruz Biotechnology (Dallas, TX). Anti-ki67 antibody was from eBioscience (San Diego, CA). Anti-SPB and -ERG antibodies were from Abcam (Waltham, MA). Human pulmonary arterial endothelial cells (HPAECs, Lonza) were cultured in EBM2 medium containing 5% FBS and growth factors (VEGF, bFGF and PDGF).

Gene Knockdown and Overexpression

Gene knockdown was performed using the RNA interference technique. siRNA for human YAP1 (5′-GACAUCUUCUGG UCAGAGA-3′ and 5′- UCUCUGACCAGAAGAUGUC-3′) was purchased from Sigma Genosys (St. Louis, MO) (Mammoto A. et al., 2018; Mammoto T. et al., 2019). HPAECs were transfected using siLentFect (BioRad, Hercules, CA) (Mammoto et al., 2009; Mammoto T. et al., 2019). As a control, siRNA duplex with an irrelevant sequence (QIAGEN, Germantown, MD) was used. The retroviral pQCXIH-myc-YAP (human) construct was a gift from Kunliang Guan. The lentiviral pLX304-YAP1(S94A) (human) construct was a gift from William Hahn. Generation of viral vectors was accomplished as reported (Mammoto et al., 2009; Mammoto et al., 2016a; Mammoto T. et al., 2019). HPAECs were incubated with viral stocks in the presence of 5 μg/ml polybrene (Sigma) and 90–100% infection was achieved 3 days later (Mammoto et al., 2009; Mammoto et al., 2016a; Mammoto T. et al., 2019).

Molecular Biological and Biochemical Methods

Quantitative reverse transcription (qRT)-PCR was performed with the iScript reverse transcription and iTaq SYBR Green qPCR kit (BioRad) using the BioRad real time PCR system. β2 microglobulin controlled for overall cDNA content. The primers for human YAP1, TEAD1, Tie2, and β2 microglobulin were previously described (Mammoto et al., 2009; Mammoto A. et al., 2018; Mammoto T. et al., 2019). The primers for human CYR61 forward; CATTCCTCTGTGTCCCCAAGAA and reverse; TACTATCCTCGTCACAGACCCA, human ANKRD1 forward; TGATTATGTATGGCGCGGATCT and reverse; GCG AGAGGTCTTGTAGGAGTTC, and human KLF2 forward; GCCCUACCACUGCAACUGGUU and reverse; CCAGUU GCAGUGGUAGGGCUU.

In vitro Pressure Experiment

To analyze the effects of hydrostatic pressure, HPAECs were pressurized in a pressure chamber that fits into a cell culture incubator (Prystopiuk et al., 2018) (Strex Cell, SanDiego, CA). Cells were exposed to graded pressures ranging from 0 to 50 mmHg (6.6 kPa). Since human PA pressure is 15–20 mmHg and PA pressure increases by 1.8–2.0 times in an *in vivo* mouse PNX model, we pressurized HPAECs with the range of 0–40 mmHg (0, 15, 30, 40 mmHg). As a control, cells were cultured in a standard incubator.

DNA synthesis of HPAECs pressurized (0, 40 mmHg) for 16 h was analyzed using an EdU assay. EdU-positive cells were analyzed using a Nikon A1 confocal imaging system (Mammoto A. et al., 2018; Mammoto T. et al., 2018; Mammoto T. et al., 2019). EC migration was measured using a modified transwell migration assay. Since we focus on YAP1-Tie2 signaling in this study, we used a Tie2 ligand angiopoietin1 (Ang1) as a chemoattractant in the migration assay. The cells that migrated towards Ang1 (10 ng/ml) in 0.5% serum EBM-2 through the membrane were stained with Giemsa, counted and averaged in three or more independent experiments.

In vitro fibrin gel angiogenesis assay was performed as previously described (Mammoto et al., 2016a; Mammoto et al., 2016b; Mammoto T. et al., 2019). Briefly, 1×10^5 HPAECs were incubated with 3,000 Cytodex 3 microcarrier beads (GE Healthcare Life Sciences, Pittsburgh, PA) in 1 ml 5% FBS/EGM2 in a glass tube for 4 h with gentle agitation. The beads coated with the cells were transferred to 25 cm^2 tissue culture flask and incubated with YAP1 siRNA or virus treatment. As a control, cells were treated with control siRNA with irrelevant sequence or control virus (full length YAP1). After 16 h incubation, 250 beads coated with HPAECs were suspended in 500 μl of 2.5 mg/ml fibrinogen solution (Sigma) and mixed with 500 μl of thrombin solution (0.5 U) in a 24-well plate. After fibrin gels were solidified, 1 ml of 1% FBS/EGM2 containing 2×10^4 human lung fibroblasts was seeded on top of each fibrin gel in a 24-well plate. Ang1 (20 ng/ml total protein) was added to the medium at day 1 and the medium was changed every other day. After incubation of beads in the fibrin gels for 5 days, the area of the sprout from the beads was quantified using ImageJ software.

Mouse Lung Endothelial Cells Isolation and Culture

Mouse lung ECs were isolated using anti-CD31 conjugated magnetic beads (Mammoto T. et al., 2018; Mammoto T. et al., 2019; Mammoto et al., 2020). We cut mouse lung tissue into small pieces using small scissors and treated the tissue with 5 ml collagenase A (1 mg/ml) for 30 min at 37°C. The tissue suspension was filtered through a 40 μm cell strainer (Falcon) to remove the undigested tissue clumps and separate single cells. Cells were centrifuged (180 g, 5 min) at room temperature (RT) and the pellet was resuspended into 0.5 ml RBC Lysis Buffer (Sigma, 1 min, RT). The lysis reaction was stopped by adding 10 ml 10% FBS/DMEM, being centrifuged (180 g, 5 min, RT), and the pellet was resuspended into 0.5 ml 4% FBS/PBS with APC anti-mouse CD31 (Biolegend, 1/100), incubated (20 min, on ice) and washed three times with 4% FBS/PBS. Cells were centrifuged (180 g, 5 min, RT) and resuspended into 0.1 ml 4% FBS/PBS with anti-APC conjugated microbeads (Miltenyl Biotec, Somerville, MA), incubated (10 min, on ice) and washed three times with 4% FBS/PBS. The cells were then resuspended in 0.5 ml 4% FBS/PBS and CD31-positive ECs were magnetically separated using MACS column (Miltenyl Biotec) according to the manufacturer's instruction. To increase the purity of the magnetically separated fraction, the eluted fraction was enriched over a second new MACS column. Isolated ECs were cultured on tissue culture dishes under 5% FBS/EGM2 for the subsequent experiments.

Unilateral Pneumonectomy

The *in vivo* animal study was carried out in strict accordance with the recommendations in the Guide for the Care and Use of Laboratory Animals of the National Institutes of Health. The protocol was reviewed and approved by the Animal Care and Use Committee of Medical College of Wisconsin. Unilateral PNX was performed as described (Mammoto et al., 2016a; Mammoto T. et al., 2019; Hendee et al., 2021). Briefly, mice (CD1, C57BL6J,

8–12 week old, approximately 25 g, both male and female mice were used except for RNAseq samples where only male mice were used) were anesthetized with Ketamine (100 mg/kg)/Xylazine (10 mg/kg, intraperitoneal injection), intubated and mechanically ventilated using a rodent ventilator (MiniVent, Harvard Apparatus, Holliston, MA). After ensuring adequate anesthesia, thoracotomy was performed and the left lung was lifted through the incision and a 5–0 silk suture was passed around the hilum and tied. The hilum was then transected distal to the tie. The remaining portions of the hilum and tie were returned to the thoracic cavity. Sham-operated mice underwent thoracotomy without PNX. Meloxicam (5 mg/kg, subcutaneous injection, 3 days) was used as a postoperative analgesic. The proximal PA pressure was measured by PA cannulation under thoracotomy (Mammoto T. et al., 2018). DNA synthesis and proliferation of ECs ($CD31^+$, VE-$Cadherin^+$, $CD45^-$) and epithelial cells ($EpCAM^+$) in the mouse lungs were analyzed by measuring the number of bromodeoxyuridine $(BrdU)^+$ cells using FACS (BD Biosciences BrdU flow kit) (Mammoto A. et al., 2019) and ki67 staining. Since there is not a significant difference between male and female in the effects of PNX on lung weight and PA pressure (not shown), we pooled the data from male and female in this study.

RNA Sequencing and Analysis

ECs were isolated from mouse lungs 7 days after PNX and sham-operated C57BL6J mouse lungs (8 week old, n = 2 per group, each *n* was pooled from 2 male mice. Jackson Laboratory, stock # 664) as described above and isolated ECs were validated by FACS for EC markers ($CD31^+$, VE-$Cadherin^+$, $CD45^-$). We used only male mice for RNAseq analysis to avoid hormonal effects. RNA was extracted using RNeasy mini kit (QIAGEN). Total RNA samples were submitted to the Institute for Systems Biology Molecular and Cell Core (Seattle, WA) for RNA sequencing. Library preparation was employed using the Illumina TruSeq Stranded mRNA kit. Sequencing was performed using the Illumina NextSeq500. Paired end sequencing was performed on a high output 150 cycle kit v2.5. The RNA sequencing reads were aligned to the mm10 reference genome. Differential gene expression analysis and Fragments Per Kilobase Million (FPKM) calculation were performed by Basepair Tech (www.basepairtech.com) using the DEseq2 pipeline (**Supplementary Table S3**). 831 upregulated and 180 downregulated significantly differentially expressed genes were defined as having a log2 fold change > 1 or < -1 and a p-adjusted value <0.01 with the FDR cutoff of 0.01 calculated by the Benjamini–Hochberg adjustment. Biological Processes Gene ontology (BP GO) analysis of significant targets was done via The Database for Annotation, Visualization and Integrated Discovery (DAVID) v 6.8 using the Functional Annotation Chart tool. Three different GO Terms charts were generated. The first examined all 1,011 significantly differentially expressed genes and produced 345 BP GO Term categories (**Supplementary Table S4**). For the second, a focus on mechanosensitive-related genes led to 522 significantly differentially expressed genes—460 upregulated and 62 downregulated—being detected as appearing on a master list comprised of Gene Card and BP GO Term categories relating to extracellular matrix (ECM), cell-cell junctions, the Hippo pathway, and cellular responses to mechanical forces including shear stress, tension, pressure, and stiffness/elasticity. 416 BP GO categories were returned from the resulting DAVID analysis (**Supplementary Table S5**). Network generation was performed on the 522 mechanosensitive significantly differentially expressed genes with Ingenuity Pathway Analysis (IPA) software (QIAGEN). The network was constructed by starting with the shortest interactions identified between the mechanosensitive genes and Yap1, then determining the shortest connections between those connected to Yap1 and all others, and finally adding the shortest connections between all genes connected to Yap1 and only the remaining unconnected genes. Many genes were trimmed if they connected to less than 4 other genes. The resulting network was comprised of 233 genes -220 upregulated and 13 downregulated-that underwent BP GO analysis in DAVID to generate the third BP GO Term table with 371 categories. The BP GO Terms in this third table were color-coded into groups relating to: development, regeneration, and angiogenesis; ECM and cell adhesion; cell growth, proliferation, and migration; cell cycle, repair, metabolism, senescence, and apoptosis; cellular signaling and protein processing; and inflammatory and immune responses (**Supplementary Table S6**, **Figure 2B**). These groups were also used to color the network genes accordingly. Heatmaps of the top 20 upregulated and 13 downregulated network genes as well as the 46 network genes comprising the top 25 BP GO Term categories were generated by Basepair (**Supplementary Figure S3**). RNAseq results are available in NCBI Geo (GSE154110).

Exosome Isolation and Purification

ECs isolated from C57BL6J mouse lungs were plated at 1×10^6 cells per 6 cm tissue culture dish with EGM2 medium containing 5% exosome depleted FBS (Thermo Fisher Scientific) and pre-filtered (0.2 μm) conditioned media was collected after 24 h. Exosomes were isolated from conditioned media and mouse serum using Total Exosome Isolation Reagent from Cell Culture Media and serum (Thermo Fisher Scientific, Waltham, MA), respectively, according to the manufacturer's protocol (Gartz et al., 2018; Doyle and Wang, 2019; Gartz et al., 2020). The exosome pellet was resuspended in 25 μl of filtered (0.2 μm) PBS. Isolated exosomes were confirmed with exosome marker proteins (CD63, flotillin-1) using immunoblotting (IB).

For transmission electron microscopy (TEM) to analyze the ultrastructure of the exosome, resuspended exosomes were adsorbed onto freshly ionized, 400 mesh formvar/carbon grids, washed once with distilled water, and negatively stained with 2% aqueous Uranyl acetate. Exosome preparations were viewed in a Hitachi H600 transmission electron microscope and images were recorded with a Hamamatsu CCD camera using AMT image capture software.

Size and concentration distributions of exosomes were determined using nanoparticle tracking analysis (NTA; NanoSight LM10 system, Malvern instruments, Malvern, United Kingdom) (Gartz et al., 2018).

Proteomics Analysis

Proteomics analysis of exosomes was performed by the Northwestern University Proteomics Core Facility. Isolated exosomes were briefly tip sonicated (~10 s) to break the exosome membrane and purified proteins by acetone/TCA precipitation. Then, the proteins were reduced, alkylated, and digested with trypsin according to the optimized protocol. Digested peptides were desalted on C18 columns then subjected to mass spectrometry analysis. Data was searched against a Mus musculus database. Proteomics data analysis on two control (sham) and three PNX (7 days after PNX) mouse exosome replicates was performed using Scaffold 5.1.0 software. 228 proteins were identified in at least one of both the control and PNX sample replicates. A cutoff threshold of greater than or equal to eight Total Spectrum Counts in at least one overall replicate was used to further narrow the list to 152 proteins of interest (**Supplementary Table S2**). The differentially expressed genes associated with the 152 proteins underwent BPGO analysis via the Functional Annotation Chart feature of the DAVID v6.8 software (**Figure 5D**).

Fibrin Gel Implantation on the Mouse Lung *in vivo*

Fibrin gel was fabricated as described (Mammoto et al., 2016b; Mammoto T. et al., 2018; Mammoto T. et al., 2019). Briefly, we added thrombin (2.5 U/ml) and isolated exosomes (4 μg) to the fibrinogen solution (12.5 mg/ml), mixed well, and incubated drops of the mixture (total 30 μl) at 37°C for 30 min until they solidified (Mammoto et al., 2016b; Mammoto T. et al., 2018; Mammoto T. et al., 2019). For gel implantation on the mouse lungs (Mammoto et al., 2016b; Mammoto T. et al., 2018; Mammoto T. et al., 2019), C57BL6J mice were mechanically ventilated and thoracotomy was performed in the fifth left intercostal space. After thoracotomy, a small area of the left visceral pleura (0.5 mm^2) was scraped using forceps and the fabricated fibrin gel was implanted on the mouse lung surface using a fibrin glue. We implanted the gel on the mouse lungs for 7 days. To examine the effects of pressure and YAP1, we isolated ECs from *Yap1*$^{fl/fl}$-*Cdh5*(*PAC*)-*Cre*^{ERT2} or *Yap1*$^{fl/fl}$ mouse lungs after tamoxifen induction (Mammoto T. et al., 2019), exposed ECs to pressure (40 mmHg), collected exosomes, mixed exosomes into the fibrin gel, and implanted the gel to the mouse lungs (Mammoto et al., 2016b; Mammoto T. et al., 2018; Mammoto T. et al., 2019). *Yap1*$^{fl/fl}$ mice were obtained from Dr. Fernando Camargo (Harvard Medical School) (Schlegelmilch et al., 2011) and crossed with *Cdh5(PAC)-Cre*^{ERT2} mice (obtained from Dr. Ralf Adams, Max Planck Institute) (Wang et al., 2010), an inducible cre deleter under the control of VE-cadherin promoter, to create VEcadherin-specific Yap1 conditional knockout (*Yap1*$^{fl/fl}$-*Cdh5*(*PAC*)-*Cre*^{ERT2}) mice, in which cre recombination is induced in ECs by administration of tamoxifen (125 μg/mouse, 5 days) (Mammoto T. et al., 2019). Angiogenesis is evaluated by density of blood vessels that are stained positive for EC marker (CD31) from five different areas of the gel (Mammoto et al., 2016b; Mammoto T. et al., 2018; Mammoto T. et al., 2019). To evaluate the connection of newly formed blood vessels in the gel to host vasculature, rhodamine-labeled concanavalinA (conA) (Vector Laboratories, Burlingame, CA) was intravenously injected to the host mouse (Mammoto et al., 2009). Barrier function of newly formed blood vessels in the gel was examined by measuring leakage of low MW rhodamine-labeled dextran (MW 4000, Sigma) intravenously injected to the host mouse (Mammoto A. et al., 2013). To analyze the lumen formation of the newly formed blood vessels in the gel, a z-stack of optical sections was taken using a confocal microscopy. Intravascular red blood cells carried in the gel implanted on the mouse lung were analyzed in the hematoxylin and eosin (H and E) stained histological sections (Mammoto T. et al., 2019). To track the exosomes in the gel, exosomes were labeled with ExoGlow-Protein EV labeling kit (System Biosciences, Palo Alto, CA) according to the manufacturer's instruction and mixed in the gel. Fluorescent images were taken on a Nikon A1 confocal imaging system and morphometric analysis was performed using ImageJ software as we reported (Mammoto et al., 2012; Mammoto et al., 2016a; Mammoto et al., 2016b; Mammoto A. et al., 2018; Mammoto T. et al., 2018; Mammoto T. et al., 2019).

Statistical Analysis

All phenotypic analysis was performed by masked observers unaware of the identity of experimental groups. Error bars (SEM) and *p* values were determined from the results of three or more independent experiments. Student's t-test was used for statistical significance for two groups. For more than two groups, one-way ANOVA with a post-hoc analysis using the Bonferroni test was conducted.

RESULTS

Pulmonary Artery Pressure Increases After Pneumonectomy

Consistent with others' report using dogs (Dane et al., 2013; Dane et al., 2016), when we measured the proximal PA pressure by PA cannulation under thoracotomy in mice (Mammoto T. et al., 2018), right PA pressure increased by 1.8-fold following left PNX (**Figure 1A**), in which lung size (not shown) (Mammoto et al., 2016a) and the ratio of the weight of right lobes to mouse body weight (BW) increased by 1.3-fold (**Figure 1B**) (Mammoto et al., 2016a; Mammoto T. et al., 2019). The levels of BrdU-positive $CD31^+$ VE-$cadherin^+$ $CD45^-$ ECs and $EpCAM^+$ epithelial cells measured by FACS were also 16.6- and 2.3- times higher in the post-PNX lungs compared to those in the sham-operated mice (**Figures 1C,D**). We also conducted immunohistochemical analysis of $ki67^+$ ERG^+ ECs and $ki67^+SPB^+$ alveolar epithelial type 2 (AT2) cells, which differentiate into AT1 cells and contribute to neoalveolarization (Liu et al., 2016; Lechner et al., 2017; Kobayashi et al., 2020), at the proximal and

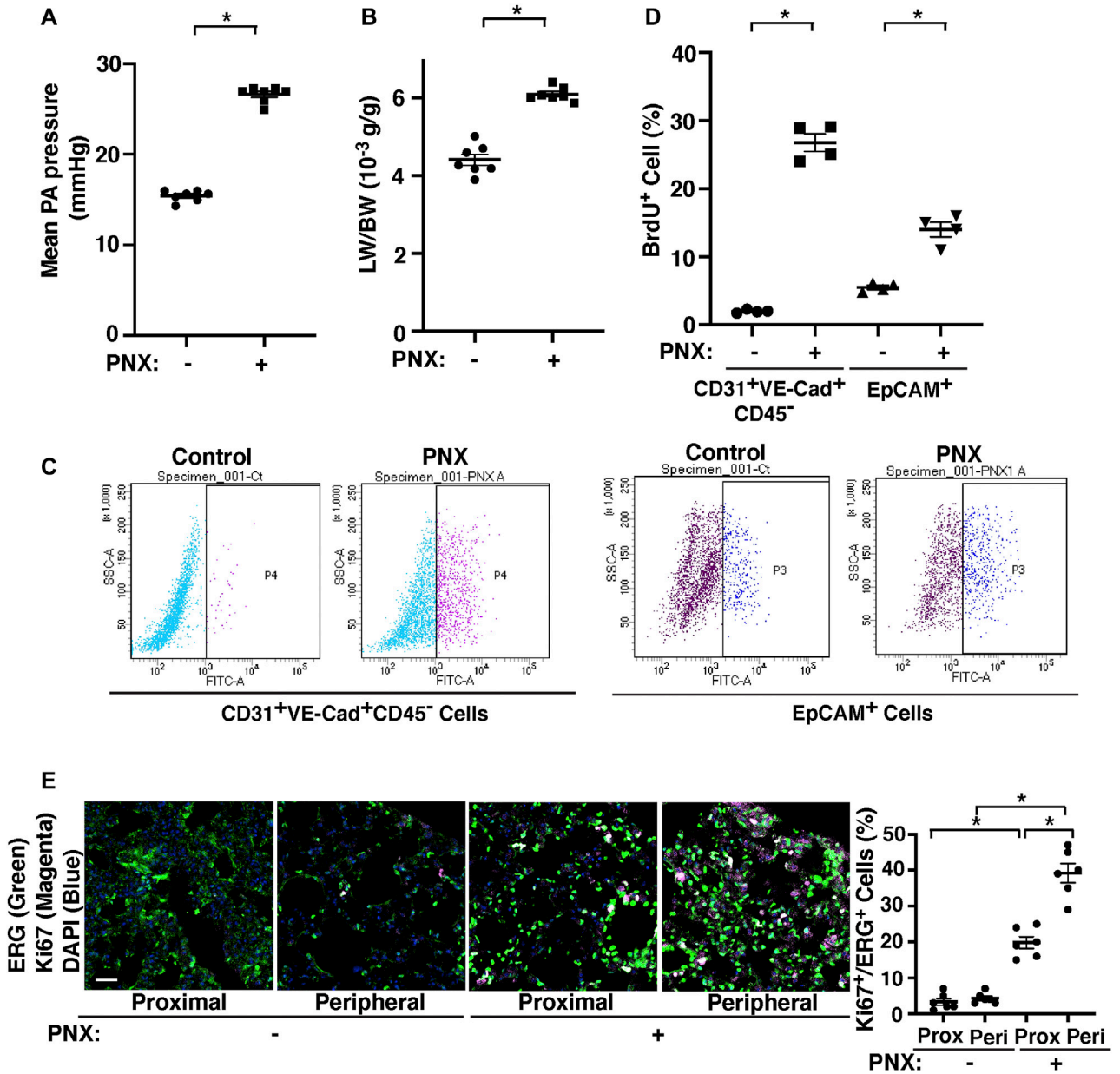

FIGURE 1 | PA pressure increases after left PNX. **(A)** Graph showing the mean PA pressure 7 days after PNX in CD1 mice (n = 7, mean ± s.e.m., *$p < 0.05$). **(B)** Graph showing the ratio of the weight of right lung lobes (LW) to mouse BW 7 days after left PNX in CD1 mice (n = 7, mean ± s.e.m., *$p < 0.05$). **(C)** Representative FACS plots showing BrdU-positive CD31$^+$VE-cadherin$^+$CD45$^-$ cells (fraction P4) and EpCAM$^+$ cells (fraction P3) 7 days after left PNX in CD1 mice. **(D)** Graph showing BrdU-positive CD31$^+$VE-cadherin$^+$CD45$^-$ cells and EpCAM$^+$ cells analyzed using FACS 7 days after left PNX in CD1 mice (n = 4, mean ± s.e.m., *$p < 0.05$). **(E)** Immunofluorescence (IF) micrographs showing staining of ki67 (magenta), ERG (green) and DAPI (blue) in the proximal or peripheral region of post-PNX or sham-operated mouse lungs. Scale bar, 50 μm. Graph showing the percentage of ki67-positive ERG$^+$ cells in the post-PNX or sham-operated mouse lungs (n = 6, mean ± s.e.m., *$p < 0.05$).

peripheral regions of the lungs and examined where ECs and epithelial cells proliferate in the lungs after PNX. The number of ki67$^+$ proliferative ECs and AT2 cells were significantly higher in the post-PNX mouse lungs (**Figure 1E**, **Supplementary Figure S1A,B**). Regarding the region of proliferation, ki67$^+$ proliferative ECs and AT2 cells significantly increased in the peripheral region of the lungs compared to proximal region after PNX (**Figure 1E**, **Supplementary Figure S1A,B**).

To identify critical changes in the mechanobiology-related gene expression after PNX, we conducted unbiased RNA

A

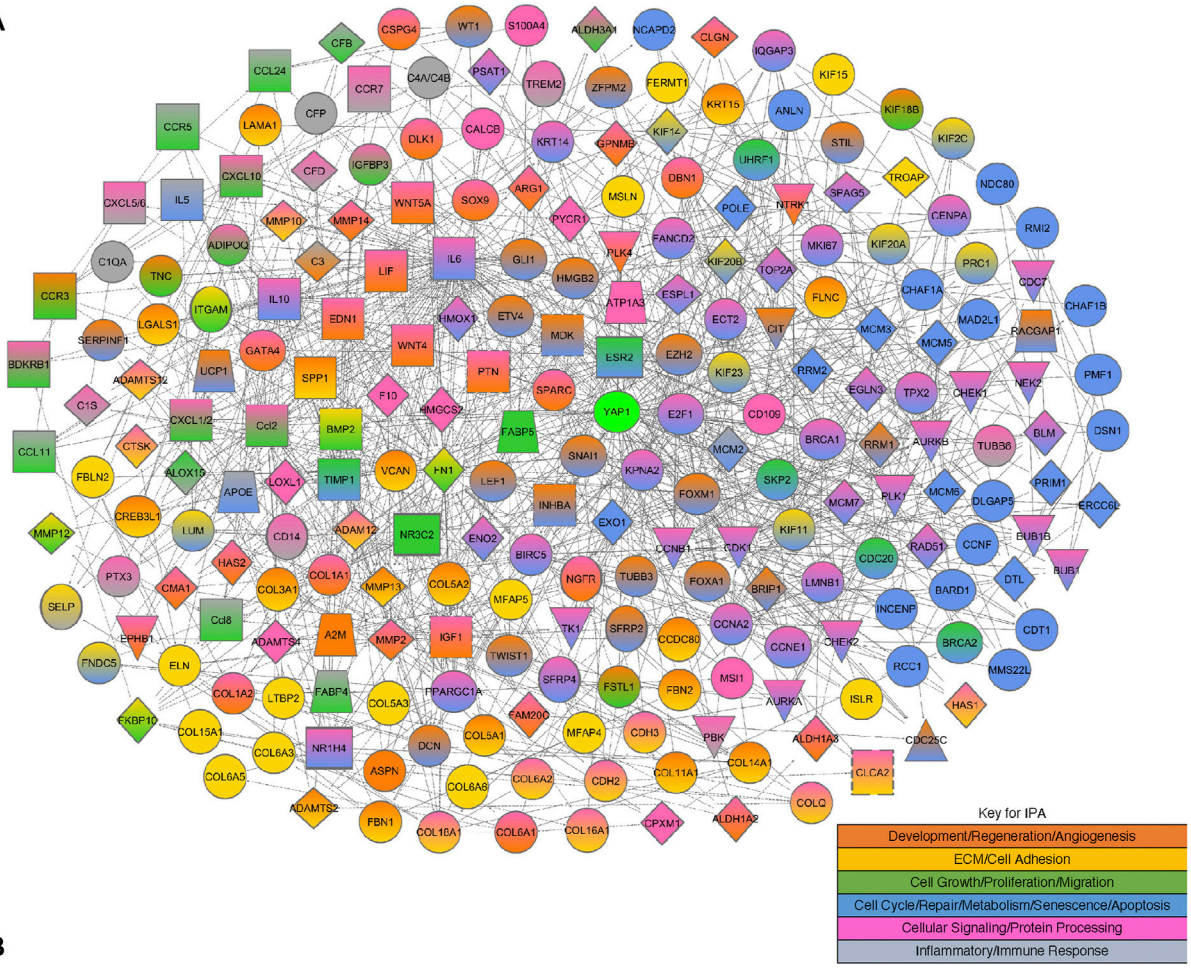

B

Biological Processes GO Terms	PValue	Fold Enrichment	Genes
actomyosin contractile ring assembly	0.025278564	78.27705628	RACGAP1, KIF23
mitotic recombination-dependent replication fork processing	0.025278564	78.27705628	RAD51, BRCA2
negative regulation of endodermal cell differentiation	0.025278564	78.27705628	COL5A1, COL5A2
sequestering of TGFbeta in extracellular matrix	0.025278564	78.27705628	FBN2, FBN1
regulation of mitotic centrosome separation	0.000950421	58.70779221	CHEK1, NEK2, KIF11
adaptive thermogenesis	0.037678228	52.18470418	UCP1, PPARGC1A
deoxyribonucleotide biosynthetic process	0.037678228	52.18470418	RRM1, RRM2
development of primary male sexual characteristics	0.037678228	52.18470418	SFRP2, WNT5A
embryonic heart tube anterior/posterior pattern specification	0.037678228	52.18470418	BMP2, GATA4
extracellular polysaccharide biosynthetic process	0.037678228	52.18470418	HAS1, HAS2
negative regulation of female gonad development	0.037678228	52.18470418	WT1, ZFPM2
negative regulation of hair follicle development	0.037678228	52.18470418	NGFR, INHBA
odontoblast differentiation	0.037678228	52.18470418	LEF1, FAM20C
prostate gland stromal morphogenesis	0.037678228	52.18470418	FOXA1, IGF1
regulation of endothelial tube morphogenesis	0.037678228	52.18470418	CXCL10, ADAMTS12
renal vesicle induction	0.037678228	52.18470418	SOX9, WNT4
retinal rod cell differentiation	0.037678228	52.18470418	SOX9, PTN
spindle checkpoint	0.037678228	52.18470418	BIRC5, AURKB
tendon development	0.037678228	52.18470418	COL5A1, COL11A1
regulation of attachment of spindle microtubules to kinetochore	6.84663E-05	44.72974644	RACGAP1, SPAG5, NEK2, ECT2
collagen biosynthetic process	0.002336371	39.13852814	COL1A1, COL5A1, ARG1
intramembranous ossification	0.002336371	39.13852814	COL1A1, CTSK, MMP2
mitotic spindle midzone assembly	0.002336371	39.13852814	RACGAP1, KIF23, AURKB
cellular response to xenobiotic stimulus	0.049920831	39.13852814	MCM7, E2F1
epithelial cell maturation involved in prostate gland development	0.049920831	39.13852814	FOXA1, ESR2

FIGURE 2 | Gene expression profiles and networks in ECs isolated from post-PNX mouse lungs. **(A)** IPA network analysis of three rounds of interactions between the 233 mechanosensitive significantly differentially expressed genes and Yap1. Orange: Development, regeneration, and angiogenesis. Gold: ECM and cell adhesion. Dark green: Cell growth, proliferation, and migration. Blue: Cell cycle, repair, metabolism, senescence, and apoptosis. Pink: Cellular signaling and protein processing. Grey: Inflammatory and immune responses. **(B)** Top 25 BP GO Terms table derived from the 233 significantly differentially expressed mechanosensitive genes appearing in the IPA network. The color-coding corresponds to the network color key.

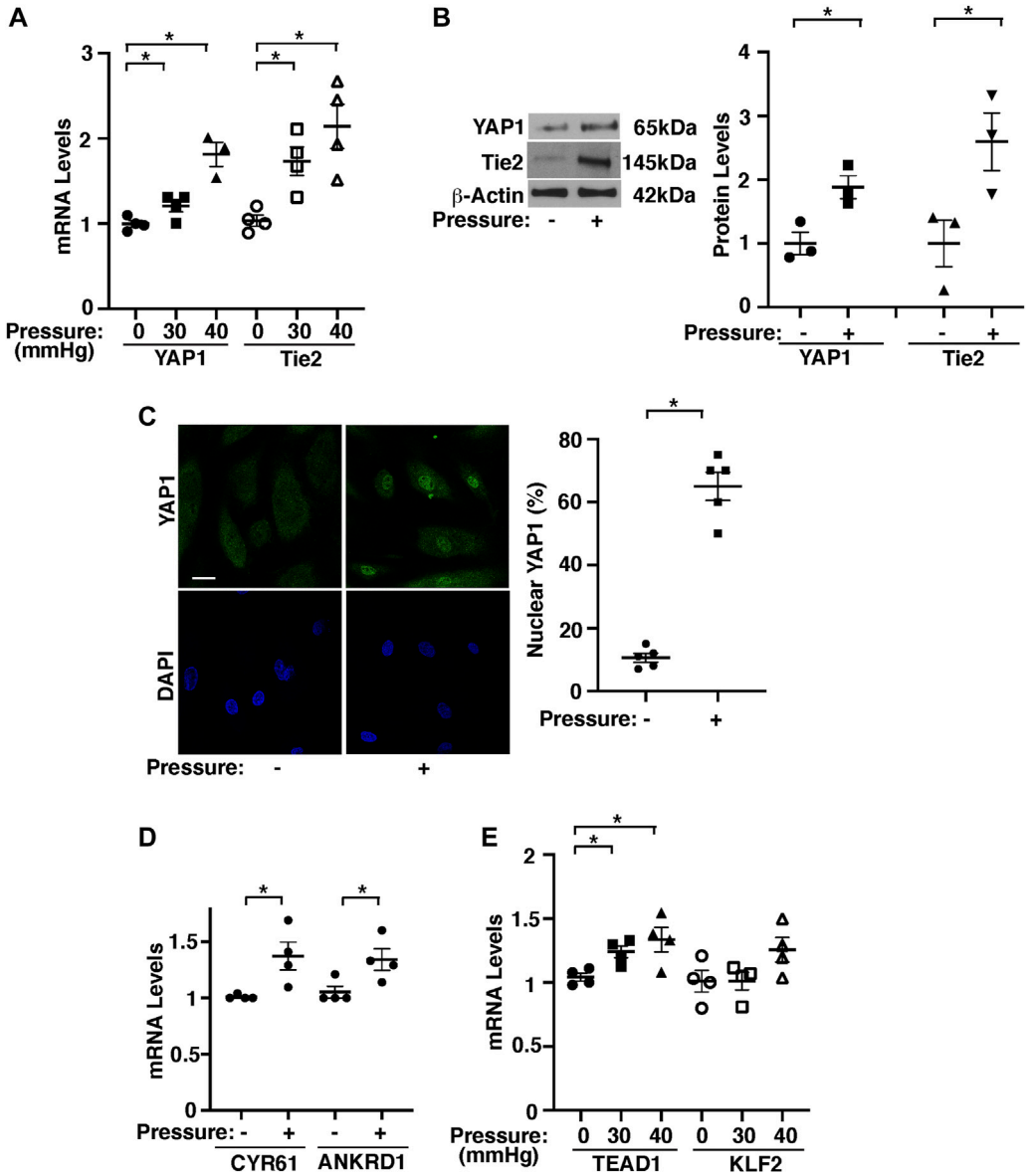

FIGURE 3 | Hydrostatic pressure controls YAP1-TEAD1 signaling in HPAECs. **(A)** Graph showing YAP1 and Tie2 mRNA levels in HPAECs exposed to pressure (30, 40 mmHg, n = 3-4, mean ± s.e.m., *$p < 0.05$). **(B)** Representative immunoblots showing YAP1, Tie2, and β-actin protein levels in HPAECs exposed to hydrostatic pressure (*left*, 40 mmHg). Graph showing the quantification of immunoblots (*right*, n = 3, mean ± s.e.m., *$p < 0.05$). **(C)** IF micrographs showing nuclear localization of YAP1 in pressurized HPAECs (*left*, 40 mmHg). Scale bar, 10 μm. Graph showing nuclear localization of YAP1 (*right*, 40 mmHg, n = 5, mean ± s.e.m., *$p < 0.05$). **(D)** Graph showing the mRNA levels of CYR61 and ANKRD1 in HPAECs exposed to pressure (40 mmHg, n = 4, mean ± s.e.m., *$p < 0.05$). **(E)** Graph showing TEAD1 and KLF2 mRNA levels in HPAECs exposed to pressure (30, 40 mmHg, n = 4, mean ± s.e.m., *$p < 0.05$).

sequencing analysis. RNAseq analysis revealed that a total of 17,328 genes were determined to alter between ECs isolated from the post-PNX mouse lungs (7 days) and those from control sham-operated mouse lungs. Differential gene expression analysis revealed that 831 upregulated and 180 downregulated significantly differentially expressed genes met the criteria of a log2 fold change >1 or < -1 and p-adjusted value <0.01 (**Supplementary Table S3**, **Supplementary Figure S2**) and generated 345 BP GO Terms categories (**Supplementary Table S4**). Of these genes, 522 significantly differentially expressed genes (460 upregulated and 62 downregulated) were identified as mechanosensitive genes appeared on a master list comprised of Gene Card and BP GO Term categories relating to ECM, cell-cell junctions, the Hippo pathway, and cellular responses to mechanical forces including shear stress, tension, pressure, and stiffness/elasticity; these mechanosensitive genes appeared in 416 BP GO categories (**Supplementary Table S5**). IPA network analysis demonstrated that among these 522 mechanosensitive significantly differentially expressed genes, 233 genes (220 upregulated, 13 downregulated;

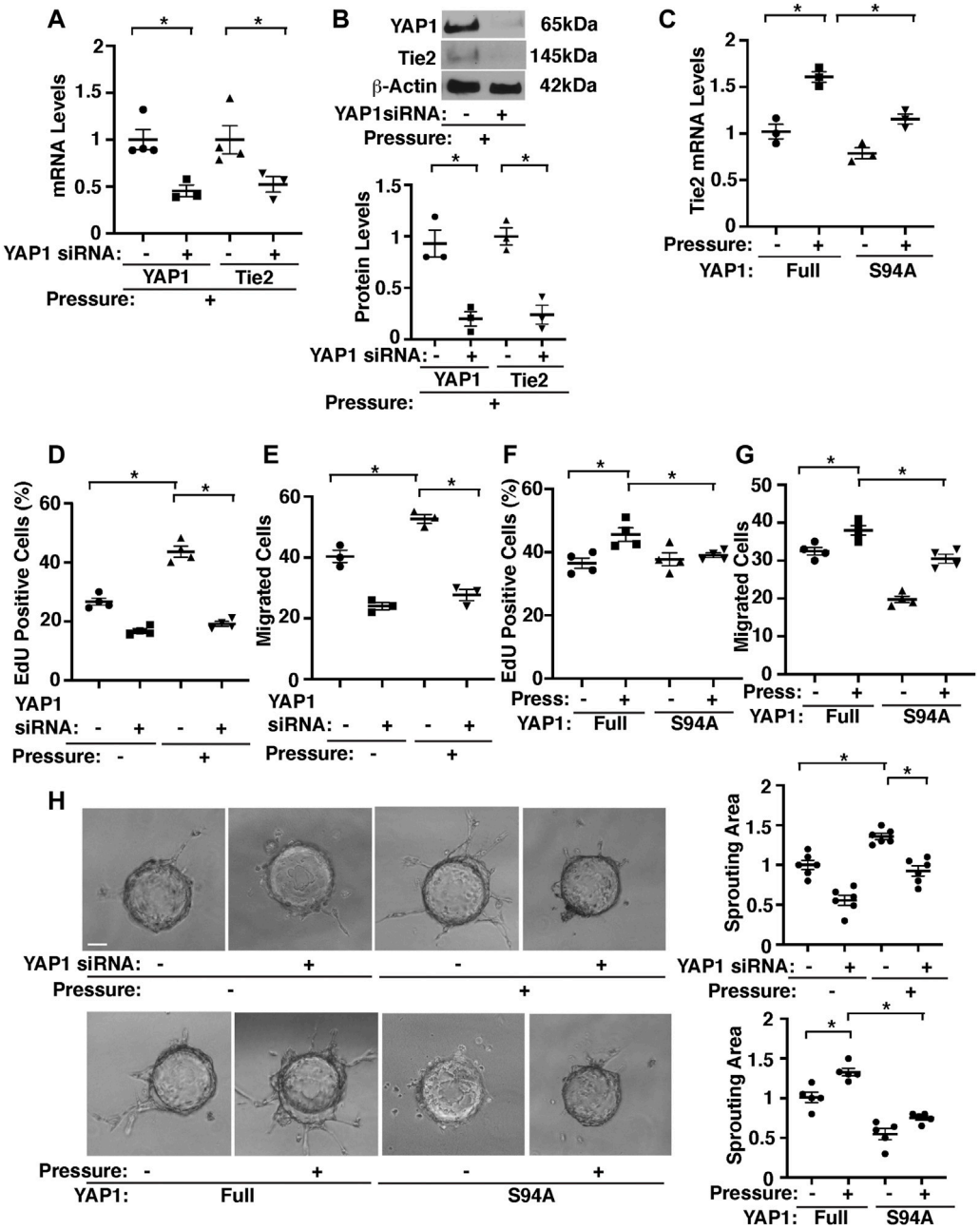

FIGURE 4 | Hydrostatic pressure controls angiogenic activity through YAP1-TEAD1 signaling in HPAECs. **(A)** Graph showing the mRNA levels of YAP1 and Tie2 in HPAECs treated with YAP1 siRNA or control siRNA and exposed to pressure (40 mmHg, n = 3-4, mean ± s.e.m., $*p < 0.05$). **(B)** Representative immunoblots showing YAP1, Tie2, and β-actin protein levels in HPAECs treated with YAP1 siRNA or control siRNA with irrelevant sequences and exposed to hydrostatic pressure (*top*, 40 mmHg). Graph showing the quantification of immunoblots (*bottom*, n = 3, mean ± s.e.m., $*p < 0.05$). **(C)** Graph showing the mRNA levels of Tie2 in HPAECs treated with YAP1 full length (Full) or YAP1S94A mutant construct and exposed to pressure (40 mmHg, n = 3, mean ± s.e.m., $*p < 0.05$). **(D)** Graph showing the percentage of EdU-positive HPAECs treated with YAP1 siRNA or control siRNA and exposed to pressure (40 mmHg, n = 4, mean ± s.e.m., $*p < 0.05$). **(E)** Graph showing the migration of HPAECs treated with YAP1 siRNA or control siRNA and exposed to pressure (40 mmHg, n = 3, mean ± s.e.m., $*p < 0.05$). **F)** Graph showing the percentage of EdU-positive HPAECs treated with YAP1 Full or YAP1S94A mutant construct and exposed to pressure (40 mmHg, n = 4, mean ± s.e.m., $*p < 0.05$). **(G)** Graph showing the migration of HPAECs treated with YAP1 Full or YAP1S94A mutant construct and exposed to pressure (40 mmHg, n = 4, mean ± s.e.m., $*p < 0.05$). **(H)** Phase contrast images showing EC sprouting from each bead in HPAECs treated with Ang1 or in combination with YAP1 siRNA, lentivirus (YAP1 Full or YAP1S94A mutant construct), or control siRNA with irrelevant sequences and exposed to pressure (40 mmHg). Scale bar, 20 μm. Graphs showing changes in sprout area in HPAECs treated with Ang1 or in combination with YAP1 siRNA, lentivirus (YAP1 Full or YAP1S94A mutant construct), or control siRNA and exposed to pressure (40 mmHg) (n = 5-6, mean ± s.e.m., $*p < 0.05$).

heatmaps of top 20 upregulated and 13 downregulated genes in **Supplementary Figure S3A**), which produced 371 BP Go Term categories color-coded into groups encompassing development, regeneration, and angiogenesis; ECM/cell adhesion; cell growth, proliferation, and migration; cell cycle, repair, metabolism, senescence, and apoptosis; cellular signaling and protein processing; and inflammatory and immune responses (**Supplementary Table S6**, the top 25 of BP GO Terms in **Figure 2B**, the heatmap of the genes in top 25 of BP GO Terms in **Supplementary Figure S3B**), interact closely with Yap1 (**Figure 2A**).

Pressurization of Endothelial Cells Stimulates YAP1 and Tie2 Expression and Angiogenic Activity *in vitro*

To study the effects of pressurization of ECs on angiogenesis, we exposed HPAECs to elevated hydrostatic pressure (30–40 mmHg) using a pressure chamber for 16 h. Since human PA pressure is 15–20 mmHg and PA pressure increases by 1.8–2.0 times in an *in vivo* mouse PNX model, we pressurized HPAECs with the range of 0–40 mmHg. There was no significant difference in the expression of YAP1 and Tie2 in ECs exposed to 15 mmHg compared to that in nonpressurized ECs (**Supplementary Figure S1C**), and therefore we used the nonpressurized condition as a control. The mRNA and protein levels of YAP1 and Tie2 were 1.8- and 2.1- times and 1.8- and 2.4-times higher, respectively, in HPAECs under pressure (40 mmHg) compared to those in the nonpressurized condition (**Figure 3A,B**). Similar trends were observed in HPAECs under 30 mmHg pressure (**Figure 3A**). YAP1 was also localized in the nucleus 5.6- times more in pressurized HPAECs when analyzed using immunocytochemistry (40 mmHg, **Figure 3C**). The mRNA expression of YAP1 target genes, CYR61 and ANKRD1 was also 1.4- and 1.3-times higher, respectively, in pressurized HPAECs (**Figure 3D**). Pressurization also significantly increased the levels of TEAD1, which binds to YAP1 and controls Tie2 expression (Mammoto A. et al., 2018; Mammoto T. et al., 2019) (**Figure 3E**).

Knockdown of YAP1 using siRNA transfection decreased Tie2 mRNA and protein expression by 49 and 82%, respectively in HPAECs under pressure (40 mmHg) compared to those treated with control siRNA that does not inhibit YAP1 expression (**Figures 4A,B**). Consistently, YAP1S94A mutant construct, which inhibits YAP1 and TEAD1 interaction (Mammoto A. et al., 2018), inhibited the Tie2 expression in HPAECs under pressure (40 mmHg, **Figure 4C**), suggesting that YAP1-TEAD1 interaction is necessary for Tie2 expression in HPAECs under pressure.

Pressurization of HPAECs treated with control siRNA (40 mmHg, 16 h) also significantly stimulated DNA synthesis and migration analyzed by an EdU assay and a transwell migration assay, respectively; EdU-positive ECs and EC migration towards a Tie2 ligand, Ang1 increased by 1.7- times and 1.3-times, respectively, while siRNA-based knockdown of YAP1 inhibited the effects (**Figures 4D,E**). YAP1S94A mutant construct also inhibited the DNA synthesis and migration under pressure (**Figures 4F,G**).

To examine whether pressurization of HPAECs controls blood vessel formation through YAP1 signaling *in vitro*, we performed a three-dimensional (3D) EC sprouting assay, in which microbeads coated with HPAECs were cultured in the fibrin gel for 5 days and sprouting from the beads was quantified (Mammoto et al., 2016a; Mammoto et al., 2016b; Mammoto T. et al., 2019). Consistent with DNA synthesis and migration, pressurization of HPAECs treated with control siRNA (40 mmHg, 16 h) stimulated EC sprouting; sprouting area increased by 1.3-times, while siRNA-based knockdown of YAP1 inhibited the effects (**Figure 4H**). YAP1S94A mutant construct also inhibited EC sprouting under pressure (**Figure 4H**). These results suggest that YAP1-TEAD1 signaling mediates the effects of EC pressurization on angiogenic activity.

Exosomes From Pressurized Endothelial Cells Stimulate Angiogenesis in the Fibrin Gel Implanted on the Mouse Lungs

Exosomes promote angiogenesis and stimulate tissue regeneration (Ibrahim et al., 2014; Shanmuganathan et al., 2018). When exosomes were isolated from pre-filtered (0.2 μm) conditioned media of ECs (1×10^6 cells) isolated from post-PNX or sham-operated C57BL6J mouse lungs using total exosome isolation reagent (Gartz et al., 2018; Doyle and Wang, 2019; Gartz et al., 2020), the isolated exosome population was positive for established exosome markers (CD63, Flotillin-1) and negative for the cellular marker GM130 when analyzed using IB (**Figure 5A**). Nanoparticle tracking analysis (NTA) revealed that isolated EC exosomes were heterogenous in diameter with 90–180 nm (**Figure 5B**). Transmission electron microscopy (TEM) exhibited the round vesicular looking morphology with approximately 80–120 nm in size (**Figure 5C**) (Hung and Leonard, 2015; Ludwig et al., 2017; Gartz et al., 2018; Lee et al., 2018; Zhang et al., 2018).

Proteomics analysis of exosomes isolated from conditioned media of two sham-operated vs three post-PNX (7 days) mouse lung EC replicates identified 228 proteins present in at least one of both the control and PNX sample replicates. A cutoff threshold of greater than or equal to eight Total Spectrum Counts in at least one overall replicate further narrowed the list to 152 proteins of interest (**Supplementary Table S2**). Consistent with RNAseq results, the top 25 Biological Processes GO Term categories derived from the differentially expressed genes associated with the 152 proteins ranged from extracellular matrix organization, cell adhesion, actin cytoskeleton remodeling to protein localization, stabilization, and folding among other functions (**Figure 5D**).

To examine the effects of exosomes isolated from post-PNX mouse lung ECs on blood vessel formation, we implanted the fibrin gel containing exosomes on the mouse lungs. First, we tracked exosomes in the gel and examined how exosomes are incorporated into the fibrin gel. When we labeled exosome cargos, mixed labeled exosomes into the gel, and implanted on

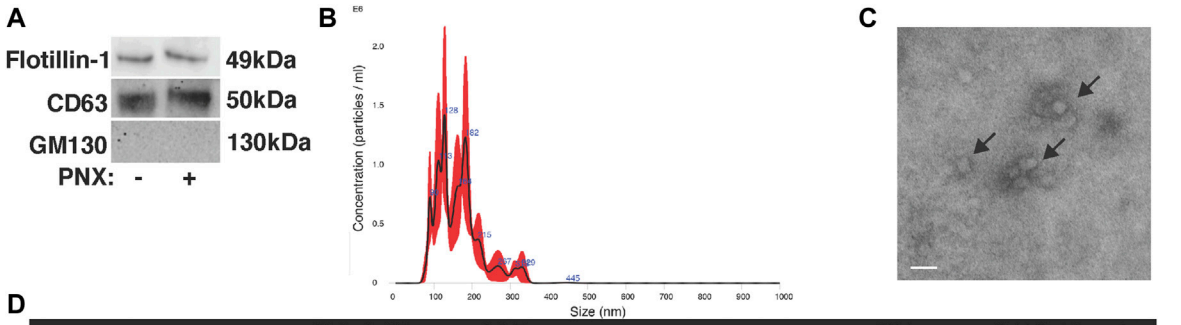

D

Biological Processes GO Terms	PValue	Fold Enrichment
extracellular matrix organization	2.26482E-14	17.14746325
cell adhesion	8.73225E-12	6.045806631
protein folding	9.27732E-08	10.49947213
positive regulation of protein localization to Cajal body	2.86176E-07	76.3597973
positive regulation of establishment of protein localization to telomere	5.11859E-07	67.87537538
extracellular matrix disassembly	7.81319E-07	33.32063882
positive regulation of telomerase RNA localization to Cajal body	5.33824E-06	40.72522523
positive regulation of cell migration	6.37198E-06	6.62035681
protein stabilization	9.90155E-06	8.590477196
actin filament capping	1.17419E-05	33.93768769
endodermal cell differentiation	6.36181E-05	22.62512513
positive regulation of gene expression	0.000103992	3.980661112
negative regulation of substrate adhesion-dependent cell spreading	0.000109751	40.72522523
positive regulation of telomere maintenance via telomerase	0.000126304	19.08994932
regulation of cell shape	0.000141878	7.031693564
angiogenesis	0.000149951	5.111952957
toxin transport	0.000180459	17.45366795
glycolytic process	0.000201741	16.96884384
binding of sperm to zona pellucida	0.000201741	16.96884384
platelet aggregation	0.000249639	16.0757468
Arp2/3 complex-mediated actin nucleation	0.000272775	30.54391892
establishment of endothelial barrier	0.000272775	30.54391892
microtubule-based process	0.000336081	14.89947264
positive regulation of cell-substrate adhesion	0.000369127	14.54472329
positive regulation of protein localization to early endosome	0.000389671	91.63175676

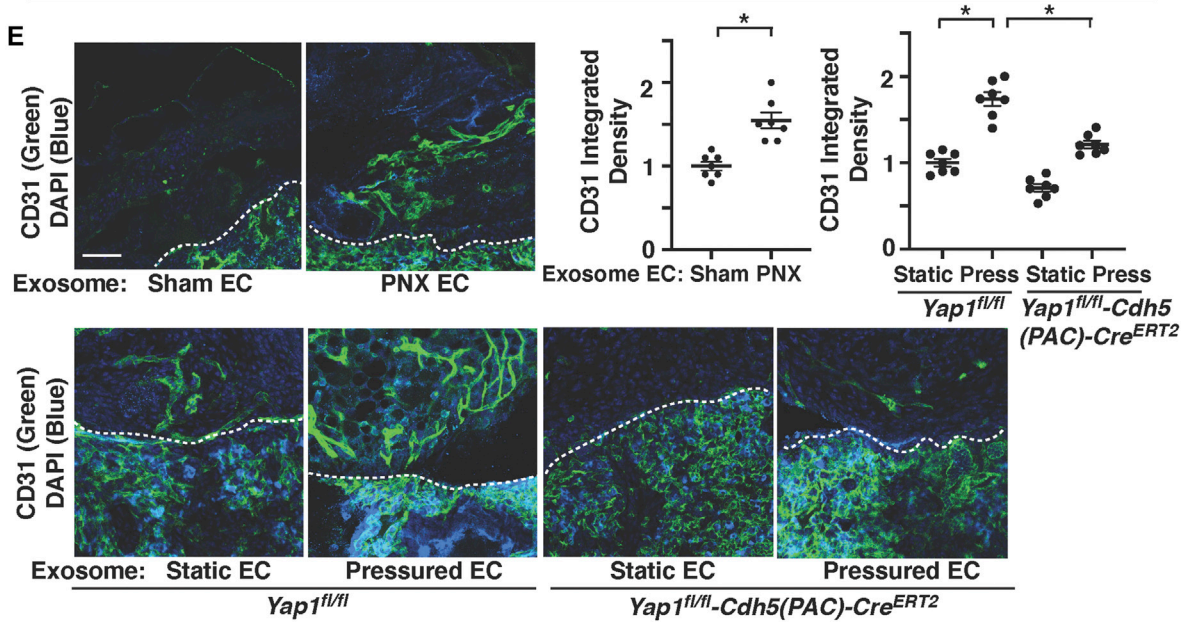

FIGURE 5 | Post-PNX mouse lung EC exosomes stimulate vascular formation in the gel implanted on the mouse lungs. **(A)** IB analysis of Flotillin-1, CD63, and GM130 in exosomes collected from conditioned media of ECs isolated from post-PNX mouse lungs or sham-operated mouse lungs. **(B)** Size distribution and particle concentration of isolated exosomes analyzed using NTA. **(C)** TEM image of exosome morphology. Scale bar: 150 nm. Arrows indicate exosomes. **(D)** Top 25 Biological Processes GO Term categories by *p*-value derived from the 152 differentially expressed genes identified in PNX vs sham-operated mouse EC exosome proteomics analysis. **(E)** Vascular formation in the implanted fibrin gel supplemented with exosomes isolated from conditioned media of post-PNX or sham-operated mouse lung ECs (*top*). Vascular formation in the implanted fibrin gel supplemented with exosomes isolated from conditioned media of unpressured or pressured *Yap1*$^{fl/fl}$-*Cdh5*(*PAC*)-*Cre*^{ERT2} or *Yap1*$^{fl/fl}$ mouse lung ECs (*bottom*). Scale bar: 50 μm. Dashed lines indicate the interface between implanted fibrin gel and host lung. Graphs showing quantification of vessel density (n = 7, mean ± s.e.m., $^{*}p < 0.05$).

the mouse lungs, the labeled exosomes were in the gel just after implantation (day 0). Exosomes remained in the gel 3 days after implantation, in which most of the exosomes attached to the surface of the recruited cells and/or were internalized into the cells. The number of exosomes in the gel decreased 7 days after implantation (**Supplementary Figure S4A**). Recruitment of host mouse ECs and vascular formation were significantly stimulated in the gel containing exosomes isolated from conditioned media of post-PNX (7 days) mouse lung ECs compared to that supplemented with exosomes from sham-operated mouse lung ECs (**Figure 5E**). To examine the effects of pressure and YAP1, we isolated ECs from *Yap1*$^{fl/fl}$-*Cdh5*(*PAC*)-*Cre*^{ERT2} or *Yap1*$^{fl/fl}$ mouse lungs after tamoxifen induction (Mammoto T. et al., 2019), exposed ECs to pressure (40 mmHg), collected exosomes, mixed exosomes into the fibrin gel, and implanted the gel on the mouse lungs (Mammoto et al., 2016b; Mammoto A. et al., 2018; Mammoto T. et al., 2019). Exosomes isolated from conditioned media of pressurized *Yap1*$^{fl/fl}$ mouse lung ECs promoted recruitment of host mouse ECs and vascular formation in the gel compared to those supplemented with exosomes from unpressurized ECs (**Figure 5E**). Exosomes from *Yap1*$^{fl/fl}$-*Cdh5*(*PAC*)-*Cre*^{ERT2} mouse lung ECs inhibited the effects (**Figure 5E**), suggesting that endothelial YAP1 is necessary for isolated exosomes to induce vascular formation in the gel. It is important to note that the newly formed blood vessels in the gel containing exosomes from pressurized ECs 1) connected to host vasculature; intravenous injection of rhodamine labeled concanavalinA (conA) to the host mouse labeled the newly formed blood vessels in the gel containing exosomes from pressured ECs (**Supplementary Figure S4B**), 2) had lumens; 3D reconstruction and z-stack of confocal microscopy images reveal that there are lumen structures in the newly formed vasculatures (**Supplementary Figure S4C**), 3) had sufficient barrier function; low MW rhodamine labeled dextran (MW 4000) intravenously injected to the mouse did not leak out of newly formed blood vessels in the gel (**Supplementary Figure S4D**), and 4) carried red blood cells; H&E-stained image shows that red blood cells were carried in the gel containing exosomes implanted on the mouse lungs (**Supplementary Figure S4E**), suggesting that EC-derived exosomes induce functional vascular formation in the gel.

DISCUSSION

In this report, we demonstrate that hydrostatic pressure, which significantly increases after unilateral PNX, stimulates angiogenic activities through endothelial YAP1 signaling. We also found that exosomes isolated from conditioned media of post-PNX lung ECs or pressurized ECs stimulate blood vessel formation in the fibrin gel implanted on the mouse lungs (**Supplementary Figure S5**). Gene enrichment analysis confirms that mechanosensitive genes altered in post-PNX mouse lung ECs interact with YAP1. Modulation of either the mechanical environment or endothelial YAP1 signaling can pave the way for the development of more efficient strategies for lung regeneration.

Our RNAseq and proteomics results demonstrate that the levels of the genes related to ECM, cell adhesion, organ development and regeneration are significantly altered after PNX (**Figure 2B**, **Figure 5D**, **Supplementary Table S6**). YAP1 is a mechanosensitive gene and mediates post-PNX lung growth (Mammoto T. et al., 2019). In fact, the genes listed in the BP GO terms of mechanosensitive cellular responses interact with YAP1 (**Figure 2A**). Other Hippo molecules such as AMOT, which mediates shear-induced YAP1 activation in a zebrafish model (Nakajima et al., 2017), WW domain containing transcription regulator 1 (WWTR1, TAZ) and LATS, the activity of which is controlled by actin cytoskeleton (Zhao et al., 2010; Piccolo et al., 2013; Panciera et al., 2017), mammalian STE20-like (MST) 1/2, Merlin and Expanded, which are responsible for membrane and actin cytoskeleton association, are known to act upstream of the Hippo pathway (Hamaratoglu et al., 2006) and may also mediate the mechanical force-dependent lung growth after PNX. It has been reported that YAP1 activity is controlled by Wnt signaling and vice versa (Azzolin et al., 2014) and that Wnt co-receptor, LDL receptor related protein5 (LRP5) controls Tie2 expression in ECs and modulates lung development and regeneration (Mammoto et al., 2012; Mammoto T. et al., 2013; Mammoto et al., 2016a). Given that ECM-stiffness controls postnatal lung development through LRP5-Tie2 signaling (Mammoto T. et al., 2013), changes in the mechanical forces after PNX may control YAP1 activity through LRP5 as well. YAP1 also regulates expression of another mechanosensitive transcription factor, Twist1 (Farge, 2003; Zhang et al., 2014), which also controls post-PNX lung growth (Hendee et al., 2021) and may be involved in the mechanism. In fact, Twist1 interacts with YAP1 in the network derived from significantly differentially expressed genes after PNX (**Figure 2A**).

While endothelial YAP1 mediates post-PNX lung growth and PA-pressure-induced EC proliferation and migration, YAP1 is not significantly differentially expressed in post-PNX lung ECs in our bulk RNAseq data. This may be because; 1) YAP1 is phosphorylated at multiple sites, which controls nuclear translocation of YAP1 and its co-transcriptional activity (Szulzewsky et al., 2021). For example, YAP1S127 phosphorylation sequesters YAP1 to the cytoplasm and suppresses YAP1 gene transcriptional activity (Ota and Sasaki, 2008; Piccolo et al., 2014). In fact, there was significant increase in YAP1 nuclear expression co-stained with ERG in the post-PNX mouse lungs, suggesting that YAP1 activity is significantly increased in ECs after PNX (**Supplementary Figure S1D**). This is consistent with the *in vitro* results using cells under pressure (**Figure 3C**). In addition, 2) it has been reported that there is a vast heterogeneity of EC populations in the lung (Gillich et al., 2020). 3) The levels of mechanical forces altered following PNX may also be different at different portions of the lungs; while PA pressure is significantly increased after PNX, the increase will be less at the capillary level and negligible in the veins. On the contrary, changes in other mechanical forces such as stretching forces following PNX are more prominent at the peripheral region of the lungs, where ECs and AT2 cells are proliferating more compared to proximal region (**Figure 1E**, **Supplementary Figure S1A,B**). In our immunohistochemical analysis, there were

YAP1-negative ERG-positive ECs in the post-PNX lungs, especially in the proximal region (**Supplementary Figure S1D**). This spatial and EC subpopulation-dependent difference in YAP1 expression and the post-translational modification may explain why Yap1 is not detected as a significantly differentially expressed gene in our RNAseq results, while it mediates pressure-dependent angiogenic factor expression and EC behaviors *in vitro*. Different EC subpopulations (e.g., PA, capillary, vein) in the lungs may sense different types of mechanical forces in a spatiotemporal manner during post-PNX lung growth. These spatial differences in the different types of mechanical forces altered after PNX may differentially alter YAP1 expression depending on EC subpopulations and regions of the lungs, which cannot be accurately profiled by bulk RNAseq. Future investigation using single cell RNAseq or bulk RNAseq with specific EC subpopulations enriching for pulmonary artery EC markers (Gja5+ Bmx+) (Manning et al., 2021) would further elucidate the mechanism of pressure-induced angiogenesis during post-PNX lung growth.

Increases in flow change shear stress in the lung after PNX. However, although hydrostatic pressure increased TEAD1 and Tie2 expression, it did not change the levels of a major shear stress-induced transcription factor, KLF2 (**Figure 3E**). The distinct signaling pathways may mediate the mechanism in a cooperative way. Spatiotemporal controls of multiple gene expression lead to the fine vascular and alveolar morphogenesis during lung regeneration. It remains unknown whether TEAD1 directly regulates Tie2 transcription and how the mechanical environment altered after PNX controls the mechanism. Given that Tie2 promoter contains M-CAT-like TEAD1 binding motif, TEAD1 may directly control Tie2 transcription. Further investigation including ChIPseq will uncover the transcriptional mechanism.

Increases of PA pressure after PNX may only be transient and restored at the later stage; however, these transient changes in PA pressure may trigger the mechanosensitive gene expression and activity. Pressure-independent effects, such as indirect paracrine effects, neurohormonal effects or changes in oxygen concentration may change YAP1 activity and also be involved in the mechanism. It has been demonstrated that various types of EC progenitor cells are involved in lung development and regeneration (Ren et al., 2019; Gillich et al., 2020; Niethamer et al., 2020). The response to pressure may be different among the EC populations and the portions of the lungs where specific EC progenitors are localized, as well as during the time course of post-PNX lung growth. Further study using EC lineage tracing will be necessary to elucidate the entire mechanism.

We focus on the effects of PA pressure on endothelial YAP1 expression/activity and angiogenic activities. Other lung cells (e.g., epithelial cells, smooth muscle cells, immune cells) (Stevens et al., 2008) may interact with ECs and contribute to post-PNX lung growth. In fact, both $CD31^+$ VE-Cad^+ $CD45^-$ ECs and $EpCAM^+$ epithelial cells proliferate after PNX (**Figures 1C,D**) and YAP1 expresses in alveolar epithelial cells and contributes to lung regeneration (Liu et al., 2016). These other cells may also sense changes in mechanical environment after PNX and secrete angiogenic and other chemical factors, and indirectly control vascular formation after PNX in a spatiotemporal manner. It has been reported that after PNX, 1) AT2 cells, one of the major alveolar epithelial progenitor cells, proliferate (5–7 days after PNX) when analyzed using a BrdU incorporation assay (Liu et al., 2016), which is consistent with the IHC analysis of ki67 staining (**Supplementary Figure S1A,B**); 2) these AT2 cells differentiate into AT1 cells that are specialized for gas exchange when analyzed using a lineage trancing assay (3–4 weeks after PNX) (Liu et al., 2016; Lechner et al., 2017; Kobayashi et al., 2020); and 3) alveolar number increases in the post PNX mouse lungs (Liu et al., 2016; Mammoto T. et al., 2019; Hendee et al., 2021). These results suggest that neoalveolarization takes place in the post-PNX mouse lungs. Further investigation of the effects of PA pressure on post-PNX alveolar formation would delineate the mechanism of post-PNX regenerative lung growth.

We demonstrate that exosomes collected from post-PNX mouse lung ECs or pressured ECs stimulate vascular formation in the gel implanted on the mouse lungs (**Figure 5E**). It has been reported that exosomes are also in the mouse circulation (Cavallari et al., 2020; Chen et al., 2021). Consistently, when we collected exosomes from sham vs post-PNX mouse serum and examined the effects on angiogenic activity, the post-PNX mouse serum-derived exosomes stimulated EC sprouting *in vitro* (**Supplementary Figure S4F**). Thus, serum-derived exosomes may also contribute to angiogenesis in the post-PNX mouse lungs. Blood vessels induced by EC-derived exosomes seem to be physiological and functional because blood vessels stimulated by pressured EC-derived exosomes have organized lumen structures and sufficient barrier functions with carrying red blood cells in the implanted gel (**Supplementary Figure S4B,C,D,E**). Thus, exosomes may have potential to be a better strategy for lung regeneration or repair from injury, in which angiogenesis and mechanical forces are involved. Although we focus on the effects of exosomes on angiogenesis in this study, exosomes may also target other cells (e.g., epithelial cells, immune cells, fibroblasts) in the mouse lungs to control post-PNX lung growth. Our proteomics analysis of exosomes reveals that ECM or actin cytoskeleton remodeling proteins are altered after PNX, which may remodel the fibrin gel structures or mechanics, and control blood vessel formation in the gel. Further analysis of exosomes isolated from different time points, different portions of the lungs, or specific EC populations and their effects not only on ECs but also on other types of cells will elucidate the mechanism.

It is known that exosomes have different fates in the cell; exosomes secreted into the extracellular spaces 1) interact with the surface receptors of recipient cells, 2) fuse with the plasma membrane to release their contents into cytosol, or 3) are internalized into the recipient cells. Internalized exosomes are sorted into late endosomes and the exosome contents are released into the nucleus, endoplasmic reticulum or cytosol. Exosomes are also degraded in the lysosomes or exocytosed again to the extracellular space through the recycling endosomes (Gurung et al., 2021). These exosome fates are determined depending on the contents of exosomes and are different among cell populations/conditions, which will change the number/concentration of exosomes in the gel over time. Thus, even if we mixed the gel with the same protein amount of exosomes, the concentration would be differentially changed, which leads to the

changes in vascular morphogenesis in the gel. Further time course investigation of exosome fates, trafficking, and components in different cell types recruited into the gel would uncover the mechanism.

In summary, we have demonstrated that changes in the mechanical environment after PNX such as increased PA pressure control endothelial YAP1 expression and angiogenic activities. Modulation of mechanical environment or endothelial YAP1 signaling may improve the strategies for lung regeneration.

DATA AVAILABILITY STATEMENT

The datasets presented in this study can be found in online repositories. The names of the repository/repositories and accession number(s) can be found in NCBI GEO GSE154110.

ETHICS STATEMENT

The animal study was reviewed and approved by Medical College of Wisconsin.

AUTHOR CONTRIBUTIONS

Conceived and designed the experiments: TM and AM. Performed the experiments: TM, TH, PK, KH, KM, and AM. Analyzed the data: TM, TH, PK, KH, SR, SL, DT, NC, and AM. Contributed reagents/materials/analysis tools: TM, TH, PK, KH, SR, and AM. Wrote the paper: TM, KH, AM.

FUNDING

This work was supported by funds from NIH R21AG054830 (to AM, to TM), R01HL139638 (to AM, to TM), R21AG062893 (to AM, to TM), R01HL142578 (to AM, TM), R21HL129047 (to NC), R01CA204231 (to SR), and AHA 18TPA34170129 (to AM).

ACKNOWLEDGMENTS

Proteomics analysis was performed by the Northwestern Proteomics Core Facility, supported by NCI CCSG P30 CA060553 awarded to the Robert H Lurie Comprehensive Cancer Center, instrumentation award (S10OD025194) from NIH Office of Director, and the National Resource for Translational and Developmental Proteomics supported by P41 GM108569.

SUPPLEMENTARY MATERIAL

The Supplementary Material for this article can be found online at: https://www.frontiersin.org/articles/10.3389/fbioe.2022.823642/full#supplementary-material

Supplementary Figure 1 | Cellular proliferation and YAP1 expression in the post-PNX mouse lungs. **(A)** IF micrographs showing staining of ki67 (magenta), SPB (green) and DAPI (blue) in the proximal or peripheral region of post-PNX or sham-operated mouse lungs. Scale bar, 50 μm. **(B)** Graph showing the percentage of ki67-positive SPB+ cells in the post-PNX or sham-operated mouse lungs (n = 6, mean ± s.e.m., $^*p < 0.05$). **(C)** Graph showing YAP1 and Tie2 mRNA levels in HPAECs exposed to pressure (15 mmHg, n = 4, mean ± s.e.m.). **(D)** IF micrographs showing staining of YAP1 (magenta), ERG (green) and DAPI (blue) in the proximal or peripheral region of post-PNX or sham-operated mouse lungs (top). Scale bar, 50 μm. Graph showing the percentage of YAP1-positive ERG+ cells in the post-PNX or sham-operated mouse lungs (n = 6, mean ± s.e.m., $^*p < 0.05$).

Supplementary Figure 2 | Top 50 genes significantly differentially expressed in post-PNX mouse lung ECs. The list of top 50 genes significantly differentially expressed in ECs isolated from the post-PNX mouse lungs (7 days) compared to those from control sham-operated mouse lungs analyzed by RNAseq. RNAseq results are filtered for genes with a >2-fold change and an adjusted p-value <0.01.

Supplementary Figure 3 | Gene expression heatmaps of ECs isolated from post-PNX mouse lungs. **(A)** Heatmaps of the top 20 upregulated and 13 downregulated genes of the 233 significantly differentially expressed mechanosensitive-related genes comprising the IPA network. **(B)** Heatmap of the 46 IPA network genes comprising the top 25 BP GO Term categories listed in Fig. 2B. Genes are color-coded as IPA network. Orange: Development, regeneration, and angiogenesis. Gold: ECM and cell adhesion. Blue: Cell cycle, repair, metabolism, senescence, and apoptosis. Pink: Cellular signaling and protein processing.

Supplementary Figure 4 | Pressurized EC exosomes stimulate vascular formation in the gel implanted on the mouse lungs. **(A)** IF micrographs showing the implanted gel containing green fluorescence-labeled exosomes from pressured ECs 0, 3 and 7 days after implantation. Scale bar: 50 μm. **(B)** IF micrograph showing $CD31^+$ blood vessels (green) labeled with intravenously injected rhodamine-labeled conA (magenta) in the gel containing exosomes from pressured ECs. Scale bar: 50 μm. Dashed line indicates the interface between implanted fibrin gel and host lung. **(C)** 3D reconstructed IF image of vascular formation in the implanted fibrin gel supplemented with exosomes from pressured ECs (top). Z-stack image of vascular lumen formation in the implanted fibrin gel supplemented with exosomes from pressured ECs (bottom). Scale bar: 20 μm. **(D)** IF micrograph showing $CD31^+$ blood vessels (green) and intravenously injected low MW rhodamine-labeled dextran leakage (magenta) in the gel containing exosomes from pressured ECs. Scale bar: 50 μm. Dashed line indicates the interface between implanted fibrin gel and host lung. **(E)** H&E-stained micrographs showing the gel containing exosomes from pressured ECs implanted on the mouse lung that contains red blood cells. Scale bar: 100 μm. Dashed line indicates the interface between implanted fibrin gel and host lung. Arrows in the higher magnification image (right) indicate red blood cells. **(F)** Phase contrast images showing EC sprouting from bead covered with HPAECs treated with exosomes from post-PNX or sham-operated mouse serum. Scale bar, 20 μm. Graph showing changes in sprout area in HPAECs treated with exosomes from post-PNX or sham-operated mouse serum (n = 6, mean ± s.e.m., $^*p < 0.05$).

Supplementary Figure 5 | Schematic illustration of the effects of post-PNX increases in PA pressure on angiogenesis in the lungs. PA pressure increases after PNX. Hydrostatic pressure upregulates the expression of YAP1 and Tie2, and induces EC DNA synthesis, migration, and sprouting *in vitro*. Exosomes from post-PNX mouse lung ECs or pressurized ECs stimulate angiogenesis through YAP1 signaling.

REFERENCES

Azzolin, L., Panciera, T., Soligo, S., Enzo, E., Bicciato, S., Dupont, S., et al. (2014). YAP/TAZ Incorporation in the β-Catenin Destruction Complex Orchestrates the Wnt Response. *Cell* 158 (1), 157–170. doi:10.1016/j.cell.2014.06.013

Bang, C., Batkai, S., Dangwal, S., Gupta, S. K., Foinquinos, A., Holzmann, A., et al. (2014). Cardiac Fibroblast-Derived microRNA Passenger Strand-Enriched Exosomes Mediate Cardiomyocyte Hypertrophy. *J. Clin. Invest.* 124 (5), 2136–2146. doi:10.1172/jci70577

Barry, E. R., Morikawa, T., Butler, B. L., Shrestha, K., de la Rosa, R., Yan, K. S., et al. (2013). Restriction of Intestinal Stem Cell Expansion and the Regenerative Response by YAP. *Nature* 493 (7430), 106–110. doi:10.1038/nature11693

Bertero, T., Oldham, W. M., Cottrill, K. A., Pisano, S., Vanderpool, R. R., Yu, Q., et al. (2016). Vascular Stiffness Mechanoactivates YAP/TAZ-dependent Glutaminolysis to Drive Pulmonary Hypertension. *J. Clin. Invest.* 126 (9), 3313–3335. doi:10.1172/jci86387

Boopathy, G. T. K., and Hong, W. (2019). Role of Hippo Pathway-YAP/TAZ Signaling in Angiogenesis. *Front. Cel Dev. Biol.* 7, 49. doi:10.3389/fcell.2019.00049

Butler, J. P., Loring, S. H., Patz, S., Tsuda, A., Yablonskiy, D. A., and Mentzer, S. J. (2012). Evidence for Adult Lung Growth in Humans. *N. Engl. J. Med.* 367 (3), 244–247. doi:10.1056/nejmoa1203983

Cavallari, C., Figliolini, F., Tapparo, M., Cedrino, M., Trevisan, A., Positello, L., et al. (2020). miR-130a and Tgfβ Content in Extracellular Vesicles Derived from the Serum of Subjects at High Cardiovascular Risk Predicts Their *In-Vivo* Angiogenic Potential. *Sci. Rep.* 10 (1), 706. doi:10.1038/s41598-019-55783-7

Chang, Y.-J., Li, Y.-S., Wu, C.-C., Wang, K.-C., Huang, T.-C., Chen, Z., et al. (2019). Extracellular MicroRNA-92a Mediates Endothelial Cell-Macrophage Communication. *Atvb* 39 (12), 2492–2504. doi:10.1161/atvbaha.119.312707

Chen, L., Qin, L., Chen, C., Hu, Q., Wang, J., and Shen, J. (2021). Serum Exosomes Accelerate Diabetic Wound Healing by Promoting Angiogenesis and ECM Formation. *Cell Biol Int* 45 (9), 1976–1985. doi:10.1002/cbin.11627

Choi, H.-J., Zhang, H., Park, H., Choi, K.-S., Lee, H.-W., Agrawal, V., et al. (2015). Yes-associated Protein Regulates Endothelial Cell Contact-Mediated Expression of Angiopoietin-2. *Nat. Commun.* 6, 6943. doi:10.1038/ncomms7943

Cruz, F. F., Borg, Z. D., Goodwin, M., Sokocevic, D., Wagner, D. E., Coffey, A., et al. (2015). Systemic Administration of Human Bone Marrow-Derived Mesenchymal Stromal Cell Extracellular Vesicles Ameliorates Aspergillus Hyphal Extract-Induced Allergic Airway Inflammation in Immunocompetent Mice. *Stem Cell Transl Med* 4 (11), 1302–1316. doi:10.5966/sctm.2014-0280

Dane, D. M., Yilmaz, C., Estrera, A. S., and Hsia, C. C. W. (20131985). Separating *In Vivo* Mechanical Stimuli for Postpneumonectomy Compensation: Physiological Assessment. *J. Appl. Physiol.* 114 (1), 99–106. doi:10.1152/japplphysiol.01213.2012

Dane, D. M., Yilmaz, C., Gyawali, D., Iyer, R., Ravikumar, P., Estrera, A. S., et al. (20161985). Perfusion-related Stimuli for Compensatory Lung Growth Following Pneumonectomy. *J. Appl. Physiol.* 121 (1), 312–323. doi:10.1152/japplphysiol.00297.2016

Davidson, S. M., Riquelme, J. A., Zheng, Y., Vicencio, J. M., Lavandero, S., and Yellon, D. M. (2018). Endothelial Cells Release Cardioprotective Exosomes that May Contribute to Ischaemic Preconditioning. *Sci. Rep.* 8 (1), 15885. doi:10.1038/s41598-018-34357-z

Ding, B.-S., Nolan, D. J., Guo, P., Babazadeh, A. O., Cao, Z., Rosenwaks, Z., et al. (2011). Endothelial-derived Angiocrine Signals Induce and Sustain Regenerative Lung Alveolarization. *Cell* 147 (3), 539–553. doi:10.1016/j.cell.2011.10.003

Dinh, P.-U. C., Paudel, D., Brochu, H., Popowski, K. D., Gracieux, M. C., Cores, J., et al. (2020). Inhalation of Lung Spheroid Cell Secretome and Exosomes Promotes Lung Repair in Pulmonary Fibrosis. *Nat. Commun.* 11 (1), 1064. doi:10.1038/s41467-020-14344-7

Doyle, L., and Wang, M. (2019). Overview of Extracellular Vesicles, Their Origin, Composition, Purpose, and Methods for Exosome Isolation and Analysis. *Cells* 8 (7), 727. doi:10.3390/cells8070727

Dupont, S., Morsut, L., Aragona, M., Enzo, E., Giulitti, S., Cordenonsi, M., et al. (2011). Role of YAP/TAZ in Mechanotransduction. *Nature* 474 (7350), 179–183. doi:10.1038/nature10137

Farge, E. (2003). Mechanical Induction of Twist in the Drosophila Foregut/stomodeal Primordium. *Curr. Biol.* 13 (16), 1365–1377. doi:10.1016/s0960-9822(03)00576-1

Filipovic, N., Gibney, B. C., Kojic, M., Nikolic, D., Isailovic, V., Ysasi, A., et al. (20131985). Mapping Cyclic Stretch in the Postpneumonectomy Murine Lung. *J. Appl. Physiol.* 115 (9), 1370–1378. doi:10.1152/japplphysiol.00635.2013

Gartz, M., Darlington, A., Afzal, M. Z., and Strande, J. L. (2018). Exosomes Exert Cardioprotection in Dystrophin-Deficient Cardiomyocytes via ERK1/2-P38/MAPK Signaling. *Sci. Rep.* 8 (1), 16519. doi:10.1038/s41598-018-34879-6

Gartz, M., Lin, C.-W., Sussman, M. A., Lawlor, M. W., and Strande, J. L. (2020). Duchenne Muscular Dystrophy (DMD) Cardiomyocyte-Secreted Exosomes Promote the Pathogenesis of DMD-Associated Cardiomyopathy. *Dis. Model. Mech.* 13 (11) 045559 doi:10.1242/dmm.045559

Genschmer, K. R., Russell, D. W., Lal, C., Szul, T., Bratcher, P. E., Noerager, B. D., et al. (2019). Activated PMN Exosomes: Pathogenic Entities Causing Matrix Destruction and Disease in the Lung. *Cell* 176 (1-2), 113–126. e115. doi:10.1016/j.cell.2018.12.002

Gillich, A., Zhang, F., Farmer, C. G., Travaglini, K. J., Tan, S. Y., Gu, M., et al. (2020). Capillary Cell-type Specialization in the Alveolus. *Nature* 586 (7831), 785–789. doi:10.1038/s41586-020-2822-7

Gurung, S., Perocheau, D., Touramanidou, L., and Baruteau, J. (2021). The Exosome Journey: from Biogenesis to Uptake and Intracellular Signalling. *Cell Commun Signal* 19 (1), 47. doi:10.1186/s12964-021-00730-1

Hamaratoglu, F., Willecke, M., Kango-Singh, M., Nolo, R., Hyun, E., Tao, C., et al. (2006). The Tumour-Suppressor Genes NF2/Merlin and Expanded Act through Hippo Signalling to Regulate Cell Proliferation and Apoptosis. *Nat. Cel Biol* 8 (1), 27–36. doi:10.1038/ncb1339

Hendee, K., Hunyenyiwa, T., Matus, K., Toledo, M., Mammoto, A., and Mammoto, T. (2021). Twist1 Signaling in Age-dependent Decline in Angiogenesis and Lung Regeneration. *Aging* 13, 7781–7799. doi:10.18632/aging.202875

Hsia, C. C. W., Wu, E. Y., Wagner, E., and Weibel, E. R. (2001). Preventing Mediastinal Shift after Pneumonectomy Impairs Regenerative Alveolar Tissue Growth. *Am. J. Physiology-Lung Cell Mol. Physiol.* 281 (5), L1279–L1287. doi:10.1152/ajplung.2001.281.5.l1279

Hung, M. E., and Leonard, J. N. (2015). Stabilization of Exosome-Targeting Peptides via Engineered Glycosylation. *J. Biol. Chem.* 290 (13), 8166–8172. doi:10.1074/jbc.m114.621383

Ibrahim, A. G.-E., Cheng, K., and Marbán, E. (2014). Exosomes as Critical Agents of Cardiac Regeneration Triggered by Cell Therapy. *Stem Cel Rep.* 2 (5), 606–619. doi:10.1016/j.stemcr.2014.04.006

Jakhar, R., and Crasta, K. (2019). Exosomes as Emerging Pro-tumorigenic Mediators of the Senescence-Associated Secretory Phenotype. *Ijms* 20 (10), 2547. doi:10.3390/ijms20102547

Klinger, J. R., Pereira, M., Del Tatto, M., Brodsky, A. S., Wu, K. Q., Dooner, M. S., et al. (2020). Mesenchymal Stem Cell Extracellular Vesicles Reverse Sugen/Hypoxia Pulmonary Hypertension in Rats. *Am. J. Respir. Cel Mol Biol* 62 (5), 577–587. doi:10.1165/rcmb.2019-0154oc

Kobayashi, Y., Tata, A., Konkimalla, A., Katsura, H., Lee, R. F., Ou, J., et al. (2020). Persistence of a Regeneration-Associated, Transitional Alveolar Epithelial Cell State in Pulmonary Fibrosis. *Nat. Cel Biol* 22 (8), 934–946. doi:10.1038/s41556-020-0542-8

Kourembanas, S. (2015). Exosomes: Vehicles of Intercellular Signaling, Biomarkers, and Vectors of Cell Therapy. *Annu. Rev. Physiol.* 77, 13–27. doi:10.1146/annurev-physiol-021014-071641

Lechner, A. J., Driver, I. H., Lee, J., Conroy, C. M., Nagle, A., Locksley, R. M., et al. (2017). Recruited Monocytes and Type 2 Immunity Promote Lung Regeneration Following Pneumonectomy. *Cell Stem Cell* 21 (1), 120–134. e127. doi:10.1016/j.stem.2017.03.024

Lee, C., Mitsialis, S. A., Aslam, M., Vitali, S. H., Vergadi, E., Konstantinou, G., et al. (2012). Exosomes Mediate the Cytoprotective Action of Mesenchymal Stromal Cells on Hypoxia-Induced Pulmonary Hypertension. *Circulation* 126 (22), 2601–2611. doi:10.1161/circulationaha.112.114173

Lee, S. H., Shin, S. M., Zhong, P., Kim, H.-T., Kim, D.-I., Kim, J. M., et al. (2018). Reciprocal Control of Excitatory Synapse Numbers by Wnt and Wnt Inhibitor PRR7 Secreted on Exosomes. *Nat. Commun.* 9 (1), 3434. doi:10.1038/s41467-018-05858-2

Lin, Z., and Pu, W. T. (2014). Harnessing Hippo in the Heart: Hippo/Yap Signaling and Applications to Heart Regeneration and Rejuvenation. *Stem Cel Res.* 13 (3 Pt B), 571–581. doi:10.1016/j.scr.2014.04.010

Liu, F., Lagares, D., Choi, K. M., Stopfer, L., Marinković, A., Vrbanac, V., et al. (2015). Mechanosignaling through YAP and TAZ Drives Fibroblast Activation and Fibrosis. *Am. J. Physiology-Lung Cell Mol. Physiol.* 308 (4), L344–L357. doi:10.1152/ajplung.00300.2014

Liu, Z., Wu, H., Jiang, K., Wang, Y., Zhang, W., Chu, Q., et al. (2016). MAPK-mediated YAP Activation Controls Mechanical-Tension-Induced Pulmonary Alveolar Regeneration. *Cel Rep.* 16 (7), 1810–1819. doi:10.1016/j.celrep.2016.07.020

Ludwig, S., Floros, T., Theodoraki, M.-N., Hong, C.-S., Jackson, E. K., Lang, S., et al. (2017). Suppression of Lymphocyte Functions by Plasma Exosomes Correlates

with Disease Activity in Patients with Head and Neck Cancer. *Clin. Cancer Res.* 23 (16), 4843–4854. doi:10.1158/1078-0432.ccr-16-2819

Mahoney, J. E., Mori, M., Szymaniak, A. D., Varelas, X., and Cardoso, W. V. (2014). The Hippo Pathway Effector Yap Controls Patterning and Differentiation of Airway Epithelial Progenitors. *Develop. Cel* 30 (2), 137–150. doi:10.1016/j.devcel.2014.06.003

Makita, R., Uchijima, Y., Nishiyama, K., Amano, T., Chen, Q., Takeuchi, T., et al. (2008). Multiple Renal Cysts, Urinary Concentration Defects, and Pulmonary Emphysematous Changes in Mice Lacking TAZ. *Am. J. Physiology-Renal Physiol.* 294 (3), F542–F553. doi:10.1152/ajprenal.00201.2007

Mammoto, A., Connor, K. M., Mammoto, T., Yung, C. W., Huh, D., Aderman, C. M., et al. (2009). A Mechanosensitive Transcriptional Mechanism that Controls Angiogenesis. *Nature* 457 (7233), 1103–1108. doi:10.1038/nature07765

Mammoto, A., Hendee, K., Muyleart, M., and Mammoto, T. (2020). Endothelial Twist1-PDGFB Signaling Mediates Hypoxia-Induced Proliferation and Migration of αSMA-positive Cells. *Sci. Rep.* 10. doi:10.1038/s41598-020-64298-5

Mammoto, A., Mammoto, T., Kanapathipillai, M., Wing Yung, C., Jiang, E., Jiang, A., et al. (2013). Control of Lung Vascular Permeability and Endotoxin-Induced Pulmonary Oedema by Changes in Extracellular Matrix Mechanics. *Nat. Commun.* 4, 1759. doi:10.1038/ncomms2774

Mammoto, A., and Mammoto, T. (2019). Vascular Niche in Lung Alveolar Development, Homeostasis, and Regeneration. *Front. Bioeng. Biotechnol.* 7, 318. doi:10.3389/fbioe.2019.00318

Mammoto, A., Muyleart, M., Kadlec, A., Gutterman, D., and Mammoto, T. (2018). YAP1-TEAD1 Signaling Controls Angiogenesis and Mitochondrial Biogenesis through PGC1α. *Microvasc. Res.* 119, 73–83. doi:10.1016/j.mvr.2018.04.003

Mammoto, A., Muyleart, M., and Mammoto, T. (2019). LRP5 in Age-Related Changes in Vascular and Alveolar Morphogenesis in the Lung. *Aging* 11 (1), 89–103. doi:10.18632/aging.101722

Mammoto, T., Chen, J., Jiang, E., Jiang, A., Smith, L. E., Ingber, D. E., et al. (2012). LRP5 Regulates Development of Lung Microvessels and Alveoli through the Angiopoietin-Tie2 Pathway. *PLoS ONE* 7 (7), e41596. doi:10.1371/journal.pone.0041596

Mammoto, T., Chen, Z., Jiang, A., Jiang, E., Ingber, D. E., and Mammoto, A. (2016a). Acceleration of Lung Regeneration by Platelet-Rich Plasma Extract through the Low-Density Lipoprotein Receptor-Related Protein 5-Tie2 Pathway. *Am. J. Respir. Cel Mol Biol* 54, 103–113. doi:10.1165/rcmb.2015-0045oc

Mammoto, T., Jiang, A., Jiang, E., and Mammoto, A. (2016b). Role of Twist1 Phosphorylation in Angiogenesis and Pulmonary Fibrosis. *Am. J. Respir. Cel Mol Biol* 55, 633–644. doi:10.1165/rcmb.2016-0012oc

Mammoto, T., Jiang, E., Jiang, A., and Mammoto, A. (2013). Extracellular Matrix Structure and Tissue Stiffness Control Postnatal Lung Development through the Lipoprotein Receptor-Related Protein 5/Tie2 Signaling System. *Am. J. Respir. Cel Mol Biol* 49, 1009–1018. doi:10.1165/rcmb.2013-0147oc

Mammoto, T., Muyleart, M., Konduri, G. G., and Mammoto, A. (2018). Twist1 in Hypoxia-Induced Pulmonary Hypertension through Transforming Growth Factor-β-Smad Signaling. *Am. J. Respir. Cel Mol Biol* 58 (2), 194–207. doi:10.1165/rcmb.2016-0323oc

Mammoto, T., Muyleart, M., and Mammoto, A. (2019). Endothelial YAP1 in Regenerative Lung Growth through the Angiopoietin-Tie2 Pathway. *Am. J. Respir. Cel Mol Biol* 60, 117–127. doi:10.1165/rcmb.2018-0105oc

Manning, E. P., Ramachandra, A. B., Schupp, J. C., Cavinato, C., Raredon, M. S. B., Bärnthaler, T., et al. (2021). Mechanisms of Hypoxia-Induced Pulmonary Arterial Stiffening in Mice Revealed by a Functional Genetics Assay of Structural, Functional, and Transcriptomic Data. *Front. Physiol.* 12, 726253. doi:10.3389/fphys.2021.726253

Mansouri, N., Willis, G. R., Fernandez-Gonzalez, A., Reis, M., Nassiri, S., Mitsialis, S. A., et al. (2019). Mesenchymal Stromal Cell Exosomes Prevent and Revert Experimental Pulmonary Fibrosis through Modulation of Monocyte Phenotypes. *JCI Insight* 4 (21). doi:10.1172/jci.insight.128060

Mohan, A., Agarwal, S., Clauss, M., Britt, N. S., and Dhillon, N. K. (2020). Extracellular Vesicles: Novel Communicators in Lung Diseases. *Respir. Res.* 21 (1), 175. doi:10.1186/s12931-020-01423-y

Nakajima, H., Yamamoto, K., Agarwala, S., Terai, K., Fukui, H., Fukuhara, S., et al. (2017). Flow-Dependent Endothelial YAP Regulation Contributes to Vessel Maintenance. *Develop. Cel* 40 (6), 523–536. e526. doi:10.1016/j.devcel.2017.02.019

Niethamer, T. K., Stabler, C. T., Leach, J. P., Zepp, J. A., Morley, M. P., Babu, A., et al. (2020). Defining the Role of Pulmonary Endothelial Cell Heterogeneity in the Response to Acute Lung Injury. *Elife* 9. doi:10.7554/eLife.53072

Ota, M., and Sasaki, H. (2008). Mammalian Tead Proteins Regulate Cell Proliferation and Contact Inhibition as Transcriptional Mediators of Hippo Signaling. *Development* 135 (24), 4059–4069. doi:10.1242/dev.027151

Otsuki, S., Saito, T., Taylor, S., Li, D., Moonen, J.-R., Marciano, D. P., et al. (2021). Monocyte Released HERV-K dUTPase Engages TLR4 and MCAM Causing Endothelial Mesenchymal Transition. *JCI Insight* 6(15).doi:10.1172/jci.insight.146416

Panciera, T., Azzolin, L., Cordenonsi, M., and Piccolo, S. (2017). Mechanobiology of YAP and TAZ in Physiology and Disease. *Nat. Rev. Mol. Cel Biol* 18, 758–770. doi:10.1038/nrm.2017.87

Pant, S., Hilton, H., and Burczynski, M. E. (2012). The Multifaceted Exosome: Biogenesis, Role in normal and Aberrant Cellular Function, and Frontiers for Pharmacological and Biomarker Opportunities. *Biochem. Pharmacol.* 83 (11), 1484–1494. doi:10.1016/j.bcp.2011.12.037

Piccolo, S., Cordenonsi, M., and Dupont, S. (2013). Molecular Pathways: YAP and TAZ Take center Stage in Organ Growth and Tumorigenesis. *Clin. Cancer Res.* 19 (18), 4925–4930. doi:10.1158/1078-0432.ccr-12-3172

Piccolo, S., Dupont, S., and Cordenonsi, M. (2014). The Biology of YAP/TAZ: Hippo Signaling and beyond. *Physiol. Rev.* 94 (4), 1287–1312. doi:10.1152/physrev.00005.2014

Prystopiuk, V., Fels, B., Simon, C. S., Liashkovich, I., Pasrednik, D., Kronlage, C., et al. (2018). A Two-phase Response of Endothelial Cells to Hydrostatic Pressure. *J. Cel Sci* 131 (12), 206920. doi:10.1242/jcs.206920

Ren, X., Ustiyan, V., Guo, M., Wang, G., Bolte, C., Zhang, Y., et al. (2019). Postnatal Alveologenesis Depends on FOXF1 Signaling in C-Kit+ Endothelial Progenitor Cells. *Am. J. Respir. Crit. Care Med.* 200 (9), 1164–1176. doi:10.1164/rccm.201812-2312oc

Sahoo, S., Klychko, E., Thorne, T., Misener, S., Schultz, K. M., Millay, M., et al. (2011). Exosomes from Human CD34 + Stem Cells Mediate Their Proangiogenic Paracrine Activity. *Circ. Res.* 109 (7), 724–728. doi:10.1161/circresaha.111.253286

Sakurai, M. K., Lee, S., Arsenault, D. A., Nose, V., Wilson, J. M., Heymach, J. V., et al. (2007). Vascular Endothelial Growth Factor Accelerates Compensatory Lung Growth after Unilateral Pneumonectomy. *Am. J. Physiology-Lung Cell Mol. Physiol.* 292 (3), L742–L747. doi:10.1152/ajplung.00064.2006

Schlegelmilch, K., Mohseni, M., Kirak, O., Pruszak, J., Rodriguez, J. R., Zhou, D., et al. (2011). Yap1 Acts Downstream of α-Catenin to Control Epidermal Proliferation. *Cell* 144 (5), 782–795. doi:10.1016/j.cell.2011.02.031

Shanmuganathan, M., Vughs, J., Noseda, M., and Emanueli, C. (2018). Exosomes: Basic Biology and Technological Advancements Suggesting Their Potential as Ischemic Heart Disease Therapeutics. *Front. Physiol.* 9, 1159. doi:10.3389/fphys.2018.01159

Sindi, H. A., Russomanno, G., Satta, S., Abdul-Salam, V. B., Jo, K. B., Qazi-Chaudhry, B., et al. (2020). Therapeutic Potential of KLF2-Induced Exosomal microRNAs in Pulmonary Hypertension. *Nat. Commun.* 11 (1), 1185. doi:10.1038/s41467-020-14966-x

Stevens, T., Phan, S., Frid, M. G., Alvarez, D., Herzog, E., and Stenmark, K. R. (2008). Lung Vascular Cell Heterogeneity: Endothelium, Smooth Muscle, and Fibroblasts. *Proc. Am. Thorac. Soc.* 5 (7), 783–791. doi:10.1513/pats.200803-027hr

Szulzewsky, F., Holland, E. C., and Vasioukhin, V. (2021). YAP1 and its Fusion Proteins in Cancer Initiation, Progression and Therapeutic Resistance. *Develop. Biol.* 475, 205–221. doi:10.1016/j.ydbio.2020.12.018

Thane, K., Ingenito, E. P., and Hoffman, A. M. (2014). Lung Regeneration and Translational Implications of the Postpneumonectomy Model. *Translational Res.* 163 (4), 363–376. doi:10.1016/j.trsl.2013.11.010

Théry, C., Ostrowski, M., and Segura, E. (2009). Membrane Vesicles as Conveyors of Immune Responses. *Nat. Rev. Immunol.* 9 (8), 581–593. doi:10.1038/nri2567

Théry, C., Zitvogel, L., and Amigorena, S. (2002). Exosomes: Composition, Biogenesis and Function. *Nat. Rev. Immunol.* 2 (8), 569–579. doi:10.1038/nri855

Thodeti, C. K., Matthews, B., Ravi, A., Mammoto, A., Ghosh, K., Bracha, A. L., et al. (2009). TRPV4 Channels Mediate Cyclic Strain-Induced Endothelial Cell Reorientation through Integrin-To-Integrin Signaling. *Circ. Res.* 104 (9), 1123–1130. doi:10.1161/circresaha.108.192930

Wang, K.-C., Yeh, Y.-T., Nguyen, P., Limqueco, E., Lopez, J., Thorossian, S., et al. (2016). Flow-dependent YAP/TAZ Activities Regulate Endothelial Phenotypes

and Atherosclerosis. *Proc. Natl. Acad. Sci. USA* 113 (41), 11525–11530. doi:10.1073/pnas.1613121113

Wang, Y., Nakayama, M., Pitulescu, M. E., Schmidt, T. S., Bochenek, M. L., Sakakibara, A., et al. (2010). Ephrin-B2 Controls VEGF-Induced Angiogenesis and Lymphangiogenesis. *Nature* 465 (7297), 483–486. doi:10.1038/nature09002

Willis, G. R., Fernandez-Gonzalez, A., Anastas, J., Vitali, S. H., Liu, X., Ericsson, M., et al. (2018). Mesenchymal Stromal Cell Exosomes Ameliorate Experimental Bronchopulmonary Dysplasia and Restore Lung Function through Macrophage Immunomodulation. *Am. J. Respir. Crit. Care Med.* 197 (1), 104–116. doi:10.1164/rccm.201705-0925oc

Xie, Y., Gao, Y., Zhang, L., Chen, Y., Ge, W., and Tang, P. (2018). Involvement of Serum-Derived Exosomes of Elderly Patients with Bone Loss in Failure of Bone Remodeling via Alteration of Exosomal Bone-Related Proteins. *Aging Cell* 17 (3), e12758. doi:10.1111/acel.12758

Yimlamai, D., Christodoulou, C., Galli, G. G., Yanger, K., Pepe-Mooney, B., Gurung, B., et al. (2014). Hippo Pathway Activity Influences Liver Cell Fate. *Cell* 157 (6), 1324–1338. doi:10.1016/j.cell.2014.03.060

Yu, F.-X., Zhao, B., and Guan, K.-L. (2015). Hippo Pathway in Organ Size Control, Tissue Homeostasis, and Cancer. *Cell* 163 (4), 811–828. doi:10.1016/j.cell.2015.10.044

Zhang, D., Lee, H., Wang, X., Rai, A., Groot, M., and Jin, Y. (2018). Exosome-Mediated Small RNA Delivery: A Novel Therapeutic Approach for Inflammatory Lung Responses. *Mol. Ther.* 26 (9), 2119–2130. doi:10.1016/j.ymthe.2018.06.007

Zhang, H., von Gise, A., Liu, Q., Hu, T., Tian, X., He, L., et al. (2014). Yap1 Is Required for Endothelial to Mesenchymal Transition of the Atrioventricular Cushion. *J. Biol. Chem.* 289 (27), 18681–18692. doi:10.1074/jbc.m114.554584

Zhao, B., Li, L., and Guan, K.-L. (2010). Hippo Signaling at a Glance. *J. Cel Sci* 123 (Pt 23), 4001–4006. doi:10.1242/jcs.069070

Conflict of Interest: The authors declare that the research was conducted in the absence of any commercial or financial relationships that could be construed as a potential conflict of interest.

Publisher's Note: All claims expressed in this article are solely those of the authors and do not necessarily represent those of their affiliated organizations, or those of the publisher, the editors, and the reviewers. Any product that may be evaluated in this article, or claim that may be made by its manufacturer, is not guaranteed or endorsed by the publisher.

frontiers in Bioengineering and Biotechnology

ORIGINAL RESEARCH
published: 08 March 2022
doi: 10.3389/fbioe.2022.794037

Hyaluronic Acid Facilitates Angiogenesis of Endothelial Colony Forming Cell Combining With Mesenchymal Stem Cell *via* CD44/MicroRNA-139-5p Pathway

Yufang Luo[1], Fang Liang[1], Xinxing Wan[1], Shengping Liu[1], Lanfang Fu[2], Jiake Mo[3], Xubiao Meng[,2] and Zhaohui Mo[*,1]*

[1]Department of Endocrinology, Third Xiangya Hospital of Central South University and Diabetic Foot Research Center of Central South University, Changsha, China, [2]Department of Endocrinology, Haikou People's Hospital and Haikou Affiliated Hospital of Central South University Xiangya School of Medicine, Haikou, China, [3]School of Medicine, Hunan Normal University, Changsha, China

OPEN ACCESS

Edited by:
Tadanori Mammoto,
Medical College of Wisconsin,
United States

Reviewed by:
Elisa Boscolo,
University of Cincinnati, United States
Lan Huang,
Boston Children's Hospital and
Harvard Medical School, United States

***Correspondence:**
Xubiao Meng
32170485@qq.com
Zhaohui Mo
easd04mzh@126.com

Specialty section:
This article was submitted to Tissue Engineering and Regenerative Medicine, a section of the journal Frontiers in Bioengineering and Biotechnology

Received: 13 October 2021
Accepted: 19 January 2022
Published: 08 March 2022

Citation:
Luo Y, Liang F, Wan X, Liu S, Fu L, Mo J, Meng X and Mo Z (2022) Hyaluronic Acid Facilitates Angiogenesis of Endothelial Colony Forming Cell Combining With Mesenchymal Stem Cell via CD44/MicroRNA-139-5p Pathway. Front. Bioeng. Biotechnol. 10:794037. doi: 10.3389/fbioe.2022.794037

Stem cells and progenitor cells have been identified as potential new therapeutic options for severe limb ischemia to induce angiogenesis, and hyaluronic acid (HA) is commonly applied as a biomaterial in tissue engineering. However, the efficiency of HA combined with human umbilical cord blood-derived endothelial colony forming cells (ECFCs) and human umbilical-derived mesenchymal stem cells (MSCs) on angiogenesis is unclear. In the present study, we showed that HA promoted angiogenesis induced by MSCs-ECFCs in Matrigel plugs and promoted blood perfusion of murine ischemic muscles. Laser confocal microscopy revealed that human-derived cells grew into the host vasculature and formed connections, as shown by mouse-specific $CD31^+$/human-specific $CD31^+$ double staining. *In vitro* assays revealed that HA supported cell proliferation and migration, enhanced CD44 expression and reduced microRNA (miR)-139-5p expression. Further analysis revealed that miR-139-5p expression was negatively regulated by CD44 in ECFCs. Flow cytometry assays showed that HA increased CD31 positive cells proportion in MSC-ECFC and could be reversed by miR-139-5p mimics transfection. Moreover, the improvement of MSC-ECFC proliferation and migration induced by HA could be blocked by upregulation of miR-139-5p expression. In conclusion, HA facilitates angiogenesis of MSCs-ECFCs, and this positive effect be associated with activation of the CD44/miR-139-5p pathway, providing a promising strategy for improving severe limb ischemia.

Keywords: hyaluronic acid, endothelial colony-forming cells, mesenchymal stem cells, angiogenesis, CD44, miR-139-5p

INTRODUCTION

Peripheral arterial disease (PAD) is a progressive disorder characterized by stenosis and/or occlusion of large and medium-sized arteries, most of which occur in the lower extremities. It is estimated that more than 200 million patients suffer from PAD worldwide (Shu and Santulli, 2018). Patients with PAD suffer an increased risk of coronary and cerebrovascular mortality and morbidity (Criqui and Aboyans, 2015), especially those with diabetes (Fadini et al., 2020). PAD progresses to a more severe

disease stage without appropriate treatment: critical limb ischemia (CLI). The 5-year survival rate of CLI is less than 50% (Gao et al., 2019). Traditional treatment strategies are aimed at restoring perfusion of the ischemic limb and involve surgical bypass or endovascular interventions. But as 40% of patients miss the chance for surgical revascularization and intervention (Das, 2009), improving therapeutic measures for PAD is necessary.

It has been suggested that quickly restoring blood flow is essential to save organs, and cell therapy may be a promising strategy for PAD (Creager et al., 2012; Frangogiannis, 2018). Endothelial colony forming cells (ECFCs), also termed late outgrowth endothelial precursor cells (EPCs), display high clonogenic potential and can originate *de novo* blood vessels *in vivo*. ECFC transplantation has been shown to improve various ischemic disorders, including PAD, and these cells are considered a promising tissue-engineered material (Faris et al., 2020). Further evidence revealed that the regenerative efficacy of ECFCs was enhanced when they were transplanted in combination with mesenchymal stem cells (MSCs), a kind of pluripotent stem cell that can differentiate into perivascular mural cells (Lin et al., 2014; Rossi et al., 2017). In addition to directly participating in vascular construction, MSCs can secrete growth factors, anti-inflammatory factors and cytokines and therefore improve the efficiency and safety of ECFC transplantation (Kang et al., 2017; Souidi et al., 2017). However, the application of cell therapy is challenged by limited engraftment of cells after transplantation; factors such as exposure of the cells to ischemia and inflammation, mechanical washout of cells from the vasculature and leaking of the cell suspension from the targeted injection site contribute to poor cell retention (Robey et al., 2008).

To improve the hostile microenvironment for resident stem cells, we have tried to optimize the administration method of cells. The application of extracellular matrix has attracted attention due to its biodegradable and biocompatible properties. Of note, hyaluronic acid (HA) is one of the most abundant components of the extracellular matrix. Composed of repeating polymeric glucuronic acid and N-acetyl-glucosamine disaccharides, HA is abundantly expressed in several tissues. Currently, HA is commonly applied as a biomaterial in tissue engineering (Bonafè et al., 2014; López-Ruiz et al., 2019). HA-based hydrogel-embedded EPCs promoted angiogenesis in ischemic limbs (Ratliff et al., 2010) and in ischemic myocardium (Gaffey et al., 2015; Gaffey et al., 2019) compared with EPC administration alone. However, the underlying mechanism is unclear. Recently, our team reported that HA combined with ECFCs-MSCs accelerated healing of refractory diabetic foot ulcers (Zhao et al., 2020). However, the efficiency of HA-MSC-ECFC combined therapy on angiogenesis in ischemic disorders is unclear.

As an important ligand of several membrane receptors activating intracellular signaling cascades, HA and its interactions with the transmembrane receptor CD44 play an essential role by modulating cellular growth, development, adhesion, and migration (Gupta et al., 2019). High CD44 expression on ECFCs is a trophic factor in neovasculature (Sakimoto et al., 2017). As one of the major cell surface HA receptors, CD44 has been proven to be tightly correlated with the development of multiple malignances by regulating microRNAs (miRs) (Bourguignon et al., 2010; Bourguignon et al., 2012a; Bourguignon et al., 2012b). In ischemic kidneys, CD44-targeted HA combined with adipose-derived MSCs decreased the expression of miR-21, miR-17-5p and miR-10a, miRs involved in the inhibition of inflammation and apoptosis during renal ischemia (Awadalla et al., 2021). Recently, miR-139-5p was reported to play a vital role in regulating ECFC function (Luo et al., 2020). To date, no evidence exists on the role of CD44/miR-139-5p pathway in tissue regeneration and angiogenesis. We wonder whether HA promotes MSC-ECFC angiogenesis through CD44/miR-139-5p signaling.

Here, we show that HA facilitates angiogenesis of ECFCs combined with MSCs and reveal the underlying mechanism by which the CD44/miR-139-5p pathway participate in this process.

MATERIALS AND METHODS

Cell Isolation and Characterization

The study was approved by the Third Xiangya Hospital Review Board. ECFCs were isolated from human umbilical cord blood samples as described previously (Luo et al., 2020). Briefly, human umbilical cord blood samples (40 ml) were collected in heparinized solution. The mononuclear cell fraction was isolated by density gradient fractionation, resuspended in complete EGM-2 medium (Lonza, Rockland, ME, United States), and then plated to 6-well tissue culture plates (5×10^7 cells/well) precoated with type 1 rat tail collagen (BD Biosciences, Bedford, MA, United States). The medium was changed daily for a week and then every other day until the first passage. Isolated ECFCs were cultured to passages four to seven for cellular assays.

MSCs were isolated from human umbilical cord as described preciously (Yue et al., 2020). Briefly, collected umbilical cords were rinsed in sterile saline, and digested at 37°C for 4 h in Dulbecco's modified Eagle's medium (DMEM; Gibco, United States) containing 0.1% collagenase I (Sigma-Aldrich Co., United States) after cutting into 2–3 mm sections. The resulting cell suspension was filtered, centrifuged and then cultured in complete low-glucose DMEM medium (FBS; Gibco). Nonadherent cells were removed 2 days after seeding. The medium was changed every other day until the first passage. Isolated MSCs were cultured to passages three to six for cellular assays.

In Vivo Matrigel Plug Assays

All animal studies were approved by the Institutional Animal Care Committee of Central South University. Matrigel (500 μL) containing PBS, HA, ECFCs, HA-ECFCs, MSCs, HA-MSCs, ECFCs-MSCs or HA-ECFCs-MSCs was injected subcutaneously into the abdomen of nude mice ($n = 3$). The total cell number were 5×10^6 cells/gel and the ratio of MSC to ECFC was 3:2. The Matrigel was removed 12 days after transplantation and prepared for paraffin sections (**Figure 2A**).

Post-preparation, the blood vessels were stained with human specific CD31 antibody and examined by microscope (Olympus, Lake Success, NY, United States).

Hindlimb Ischemia Model and Limb Perfusion Ratio Assessment

A severe model of murine hindlimb ischemia was performed as previously described (Luo et al., 2020). After anesthetizing with 1% pentobarbital intraperitoneal injection, the entire right superficial femoral artery and vein (from just below the deep femoral arteries to the popliteal artery and vein) were ligated with 8–0 silk sutures, cut and excised with an electrical coagulator. The overlying skin was closed with 5–0 silk sutures. After surgery, 40 mice were selected and randomly divided into four groups. Mice in group A received intramuscular injection of PBS, group B received intramuscular injection of HA, group C received intramuscular injection of 5×10^6 MSCs-ECFCs (3:2), and mice in group D were injected with mixture of HA and 5×10^6 MSCs-ECFCs (3:2). Ischemic muscles were collected 14 days after transplantation and then prepared for paraffin sections.

A real-time microcirculation imaging analysis was performed using a PeriCam Perfusion Speckle Imager (PSI) based on the laser speckle contrast analysis technology (Perimed Inc., Kings Park, NY, United States). It was used to evaluate the limb perfusion ratio [ischemic limb (right)/normal limb (left)] at days 0, 7, and 14 after ischemia. Ambulatory impairment was scored using the criteria described previously (Zhang et al., 2018). Skin temperature was measured using a digital thermometer.

Histological Assessment and Detection of Vascular Density

After antigen retrieval and endogenous peroxidase blockade, the dewaxed paraffin section of tissue was incubated overnight with anti-CD31 mouse monoclonal antibody (1:100, Servicebio, Wuhan, China) or anti-CD31 human polyclonal antibody (1:200, Servicebio, Wuhan, China) at 4°C, respectively. The slide was washed and incubated with goat anti-mouse secondary antibody (1:300, Servicebio, Wuhan, China) or goat anti-rabbit secondary antibody (1:400, Servicebio, Wuhan, China) at room temperature for 2 h. The slide was then subjected to blockage with biotin and avidin (ABC) solution, color development with 3,3′-diaminobenzidine (DAB) solution, dehydration, and sealing. Under normal optical microscope, three high-power fields (400X) were randomly selected for each slice to count vascular density, and three high-power fields (200X) were randomly selected for each slice to count CD31-stained positive area (brown) and vessel size. CD31-stained positive area represented of proportion of cells stained by CD31 antibody, and vascular size measured the area of vascular, which surrounded by $CD31^+$ cells. $CD31^+$ staining was quantified by ImageJ. Double staining of human specific $CD31^+$ and mouse specific $CD31^+$ cells were detected and photographed under laser confocal microscopy high-power fields (400x). Morphological changes of muscle tissue were observed by hematoxylin staining under normal optical microscope.

Cell Proliferation

CCK-8 assays were performed for evaluation of cell proliferation. Briefly, cells were seeded in 96-well plates at a density of 5×10^3 cells/well (co-cultured MSCs-ECFCs at ratio of 3:2) and incubated at 37°C for 24 h. Equal volume of 0.5 mg/ml or 1.0 mg/ml HA dilution, or PBS was added in the medium subsequently. Then 10 μL of CCK-8 solution (Sangon Biotech, Shanghai, China) was added to each well of the plate. After incubation for 2 h, the absorbance at 450 nm was measured.

In Vitro Scratch Assays

Cell migration was evaluated with an *in vitro* scratch assay as previously described (Yue et al., 2020). MSCs, ECFCs and MSCs-ECFCs (at ratio of 3:2) were seeded in six-well plates at a density of 2×10^5 cells/well. The cells were cultured at 37°C for approximately 24 h until full confluence, and a straight-line scratch was made with a 10-μL pipette tip. And then fresh serum-free medium was added. The cells were photographed immediately, 6, 12, 18 and 24 h after scratch. The migration of cells to the scratch bed was quantified using ImageJ software.

Cell Transfection

miR-139-5p mimic (miR10000250), miR-139-5p inhibitor (miR20000250), NC mimic, NC inhibitor and CD44 siRNA were synthesized by RiboBio (Guangzhou, China), and CD44 plasmids were purchased from Vigene (Jinan, China). The final concentration of miR-139-5p mimic, miR-139-5p inhibitor, NC mimic, NC inhibitor and CD44 siRNA in the transfection system was 100 nM and the concentration of CD44 plasmid in the transfection system was 1ug/ml. Cells were transfected with Lipofectamine 3000 (Invitrogen, Carlsbad, CA, United States) when the confluence was approximately 70–80%. Cell lysate for qPCR assays was collected 48 h after transfection, and for Western blot assays 72 h after transfection, respectively.

Western Blot Assay

Western blot was performed as previously reported (Luo et al., 2020). Primary antibodies include CD44 (Abcam, Cambridge, United States), VEGF (Cell Signaling Technology, Danvers, MA, United States), PDGF-B (Abcam, Cambridge, United States), Tubulin (Proteintech, Wuhan, China) and GAPDH (Proteintech, Wuhan, China). The immunoblotted proteins were visualized using an ECL Western blotting luminal reagent (Advansta, United States) and quantified using a universal Hood II chemiluminescence detection system (Bio-Rad, United States).

Real-Time Reverse Transcription Polymerase Chain Reaction (qPCR)

The total RNA was isolated with TRIzol reagent (Life technology) and reverse transcription performed using stem-loop RT primer for miRNA with Superior III RT Supermix (Innogene biotech, Beijing, China). PCR was performed with the SYBR Green I Fast qPCR Mix (Tsingke, Beijing, China). The experiments were performed as per the protocols. Real-time PCR was performed using the Roche LightCycler480 II. The expression was quantified

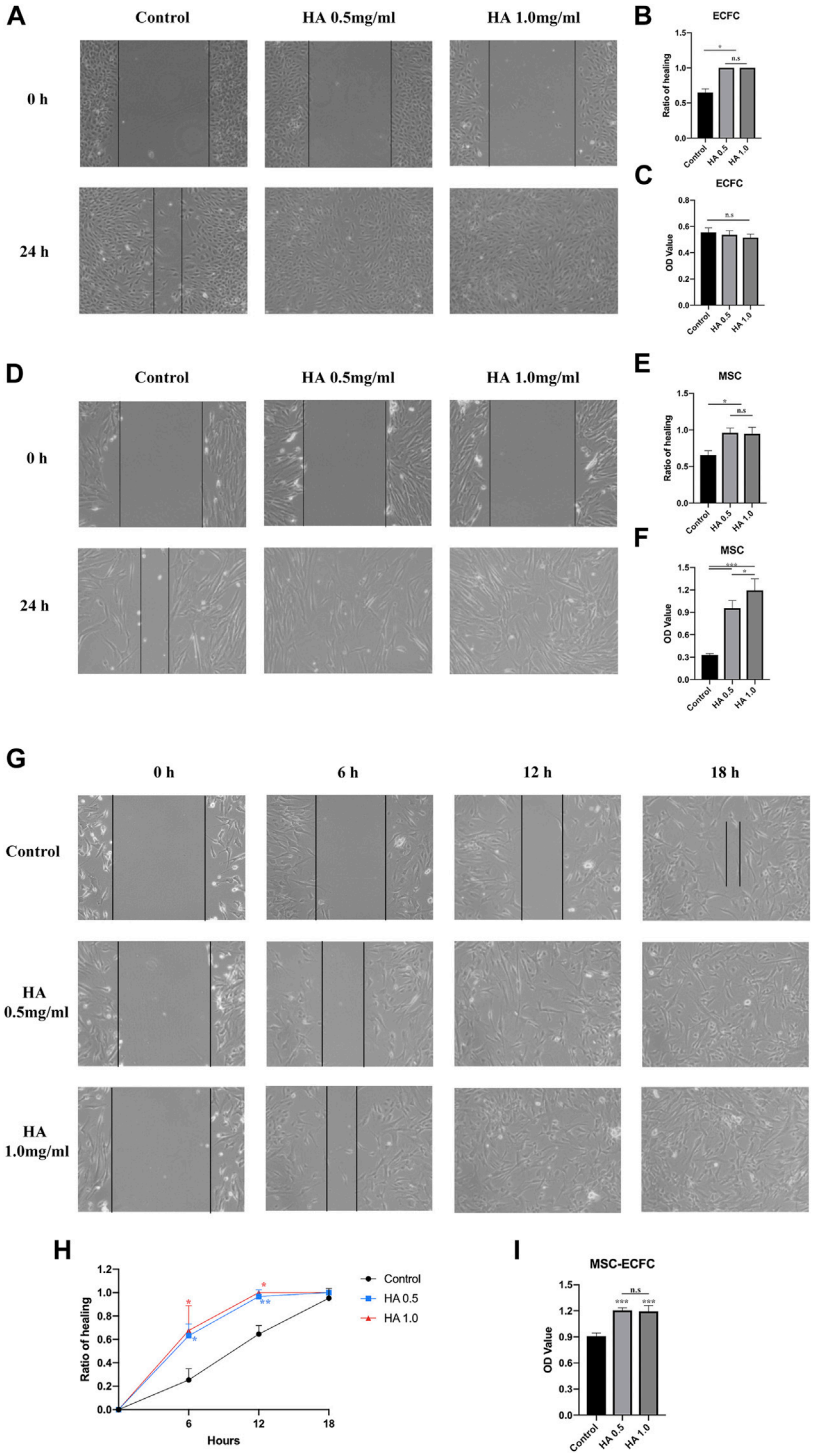

FIGURE 1 | Effect of HA dilutions on cell viability and migration. Following 24 h of exposure to HA, wound healing assays were performed to assess the migration of ECFCs **(A,B)**, MSCs **(D,E)** and MSCs-ECFCs **(G,H)**. CCK-8 assays were performed to assess the proliferation of ECFCs **(C)**, MSCs **(F)**, and MSCs-ECFCs **(I)**. (n = 3 independent experiments. Error bars: mean ± SD. $^{*}p < 0.05$, $^{**}p < 0.01$, $^{***}p < 0.001$).

relative to the housekeeping gene (glyceraldehyde-3-phosphate dehydrogenase) for mRNA and U6 for miRNA.

Flow Cytometry

MSCs and ECFCs at passages three to five were harvested and plated into 6-well plates (2 × 105/well, at ratio of MSCs: ECFCs = 3:2) with EGM-2 medium. For the transfection group, miR-139-5p mimics or NC mimics was transfected 24 h after cell seeded and cells were cultured in the subsequent 48 h. HA was added 24 h before the flow cytometry assays. Cells were digested with 0.25% trypsin-EDTA (Gibco, United States) and 1×10^6 cells were re-suspended in 100 μL PBS, followed by incubating with 5 μL fluorescein isothiocyanate (FITC)-conjugated anti-human CD31 antibodies (eBioscience, United States) on ice in the dark for 30 min. Cytometric analysis was performed using a flow cytometer (BD FACSAria II3, United States) and the results were analyzed using FlowJo (Tree Star Inc.; Ashland, OR, United States).

Statistical Analysis

Data are expressed as mean ± SD. Two groups were compared by the unpaired Student's *t*-test and multiple groups were analyzed by 1-way analysis of variance. When the condition of homogeneity of variance is satisfied, Tukey test was used for pairwise comparison between groups. When the variance is uneven and the pairwise comparison between all groups is concerned, the Game-Howell test was used (SPSS 23.0, NY, United States). $p < 0.05$ was considered significant.

RESULTS

HA Enhanced the Proliferation and Migration of MSCs and ECFCs

To investigate the effect of HA on MSCs and ECFCs, we initially analyzed the effect of 0.5 mg/ml or 1.0 mg/ml HA on proliferation and migration. Wound scratch assays showed that MSCs or ECFCs treated with HA dilution displayed significantly accelerated migration and achieved confluence within 24 h, while no differences in migration are observed between two HA concentrations (**Figures 1A,B,D,E**). CCK8 assays showed that HA promoted the proliferation of MSCs (concentration-dependent), but not that of ECFCs (**Figures 1C,F**).

Then, we tested the effect of HA dilution on cocultured MSCs-ECFCs. Wound scratch assays showed that HA accelerated the cell migration rate; thus, the HA-treated MSC-ECFC mixed cells achieved confluence within 18 h (**Figures 1G,H**). These results indicated that MSC-ECFC coculture improved migration compared with MSCs or ECFCs cultured alone, and HA exposure further accelerated the migration rate of MSCs-ECFCs. CCK-8 assays (**Figure 1I**) showed that HA dilution significantly promoted the proliferation of MSCs-ECFCs. No significant difference in mixed cells migration and proliferation are observed between two HA concentrations. Therefore, we used 0.5 mg/ml concentration for subsequent experiments.

HA Promoted MSC-ECFC Induced Angiogenesis

To test the *in vivo* angiogenesis of HA combined with stem cells, we performed *in vivo* Matrigel plug assays (**Figure 2A**). Results showed that implants of HA alone were devoid of vessels, indicating that vehicle alone was unable to form vasculature. Implants of MSC alone could generated vascular, however, there were no significant increased compared with control groups. While ECFC plugs contained a certain number of vascular, MSC-ECFC (3:2) cotransplantation significantly increased vessel numbers compared with MSC or ECFC plugs as previous study demonstrated (Melero-Martin et al., 2008). Moreover, we noticed that HA promoted angiogenesis of MSC, ECFC and MSC-ECFC, respectively. Implants of HA-MSC-ECFC were thoroughly reddish in color, indicating abundant blood flow perfusion. H&E staining showed numerous vessels containing erythrocytes in implants containing MSCs-ECFCs. Moreover, vessels with large diameters appeared in the HA-MSC-ECFC plugs. HA cotransplantation with MSCs-ECFCs resulted in additive effects on the vessel density, vessel size and CD31-positive areas (**Figures 2B–F**). These results demonstrated that *in vivo* angiogenesis induced by MSC-ECFC dual cells is stronger than mono-cell, and HA coadministration further increased the MSC-ECFC-induced vascular network.

HA Promoted Angiogenesis of MSCs-ECFCs and Blood Flow Restoration of Ischemic Hindlimb in Mice

Next, we established mouse hindlimb ischemia models to verify that HA could improve the neovascularization of MSCs-ECFCs *in vivo*. Ischemia was induced in the right hindlimb (**Figure 3A**). Subsequent perfusion speckle imaging (PSI) verified that the blood flow in the ischemic right hindlimb was lower than that in the control left hindlimb after surgery (**Figure 3B**). PBS, HA, MSCs-ECFCs or HA-MSCs-ECFCs were injected into the ischemic sites intramuscularly 1 day after surgery. PSI showed that HA injection did not enhance blood flow compared with PBS injection throughout the observation period. Although both MSC-ECFC and HA-MSC-ECFC treatment enhanced blood flow recovery in response to HLI, the HA-MSC-ECFC group displayed a quicker recovery rate than the MSC-ECFC group 7 days after surgery (**Figures 3B,H**). Consistently, the mice treated with HA-MSCs-ECFCs showed rapid recovery of the ambulatory impairment index and skin temperature (**Figures 3F,G**).

Neovascularization in ischemic muscles was evaluated by immunofluorescence staining of CD31-positive capillaries. Increased numbers of host vessels in the ischemic muscles of the MSC-ECFC group were observed compared with those in the vehicle group. As expected, the density of host vessels was further increased by HA coadministration (**Figures 3C,I**). Besides, we noticed that MSC-ECFC injection did not significantly improved human-derived vessels density compared with control groups while HA-MSC-ECFC coadministration did (**Figures 3D,J**),

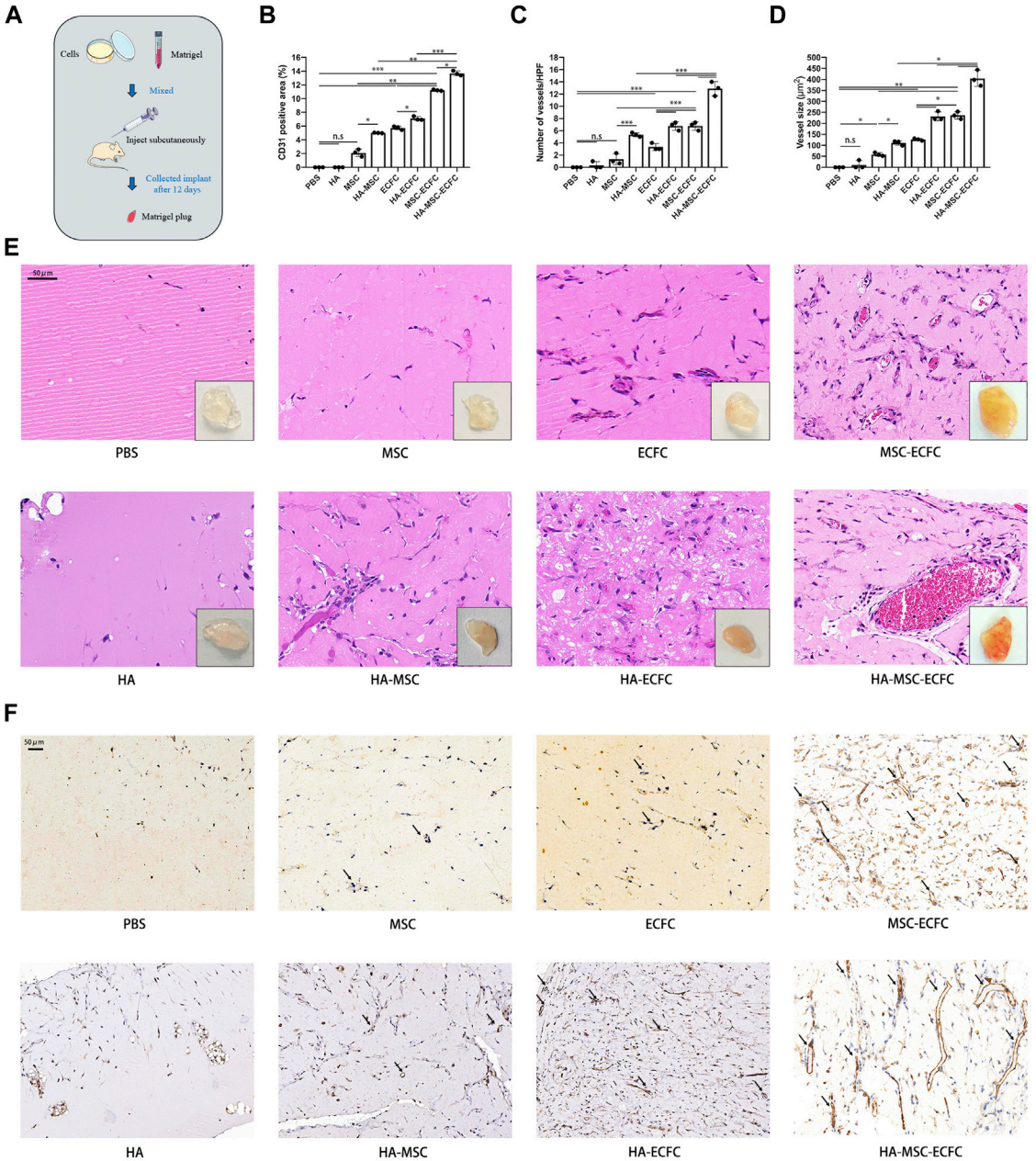

FIGURE 2 | HA promotes MSC-ECFC-induced angiogenesis of Matrigel plugs *in vivo*. **(A)**. The procedure for Matrigel plug *in vivo* assays. **(B–D)**. Quantitation of vessel number from the H&E-stained paraffin sections and quantitation of the human-specific CD31-positive percentage and vessel size. **(E, F)** Representative images of macroscope view of explanted Matrigel plugs, H&E staining (magnification ×400) and immunobiological human CD31 staining (magnification ×200) of explanted Matrigel plugs. (n = 3 independent experiments. Scale bar represents 50 μm. Error bars: mean ± SD. $^{*}p < 0.05$, $^{**}p < 0.01$, $^{***}p < 0.001$).

which indicated that HA improved human-derived cells retention. Mouse-specific $CD31^{+}$/human-specific $CD31^{+}$ double staining verified that human-derived cells grew into the host vasculature and formed connections in muscles injected with HA-MSCs-ECFCs (**Figure 3E**). The increased numbers of $CD31^{+}$ vessels provide a histological basis for the increased blood flow and tissue viability in the ischemic limb. These results clearly indicated that HA-MSCs-ECFCs contributed to highly effective functional blood vessel formation, leading to improved therapeutic angiogenesis for the treatment of critical limb ischemia.

HA-MSC-ECFC Administration was Associated With CD44/miR-139-5p Signaling in Ischemic Tissue

Previous studies revealed that CD44 could mediate HA-induced inhibition of miR-139-5p in ovarian cancer cells

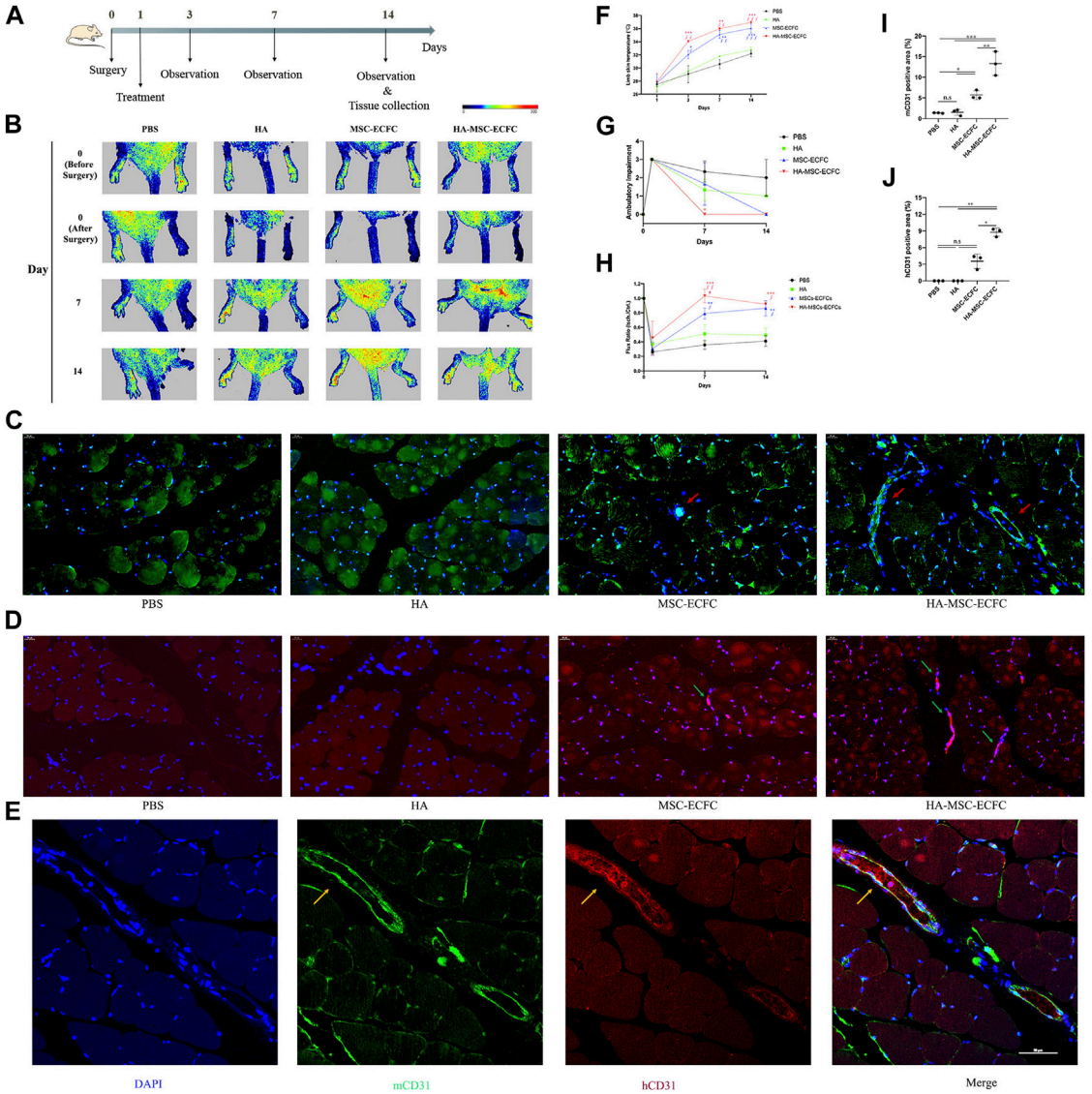

FIGURE 3 | HA improves MSC-ECFC-induced blood flow recovery of HLI in mice. **(A)**. The process of generating mouse models of hindlimb ischemia. **(B)**. Improvements in blood flow recovery were evaluated using PSI analysis in the ischemic limbs of 8-week-old mice injected with PBS, HA, MSCs-ECFCs or HA-MSCs-ECFCs before surgery and 0-, 7- and 14-days post-surgery. **(C,D)**. Representative fluorescent images of mouse-specific CD31$^+$ tissue **(C)** and human-specific CD31$^+$ tissue **(D)** at 14 days after surgery (magnification ×400, arrows indicate vessels) and quantitation of the CD31-positive percentage **(I,J)**, respectively (n = 3 independent experiments. Error bars: mean ± SD. *p < 0.5, **p < 0.1, ***p < 0.001). **(E)**. Representative confocal images of mouse-specific CD31$^+$/human-specific CD31$^+$ double-stained muscles derived from ischemic tissue injected with HA-MSCs-ECFCs (magnification ×400, yellow arrow indicates human-derived endothelial cells). **(F)**. Time course of the skin temperature in the ischemic limbs of the mice. **(G)**. Ambulatory impairment was scored at each time point: plantar/toe flexion to resist gentle tail traction; 1: plantar but not toe flexion; 2: no plantar or toe flexion; and 3: no use of foot. **(H)**. Blood perfusion is presented as the ratio of blood flow in the ischemic limb divided by that in the normal hindlimb. (n = 3 independent experiments. Scale bar represents 50 μm. Error bars: mean ± SD. *p < 0.5, **p < 0.1, ***p < 0.001 vs. the control group, ϕp < 0.5, ϕϕp < 0.01, ϕϕϕp < 0.001 vs. the HA group, #p < 0.5 vs. the MSC-ECFC group).

(Zhao et al., 2014). Recently, we reported that miR-139-5p mediates the impaired function of diabetic ECFCs(Luo et al., 2020). Thus, HA may enhance angiogenesis of MSCs-ECFCs through the CD44/miR-139-5p pathway. Next, we explore the mechanism of HA enhancing angiogenesis of MSCs-ECFCs in the ischemic limb. We assessed the expression levels of CD44, miR-139-5p and the downstream angiogenesis-related molecules VEGF and PDGF in ischemic muscles. MSC-ECFC administration significantly decreased the level of miR-139-5p (**Figure 4A**) while improving the levels of CD44, VEGF and PDGF (**Figure 4B**) in ischemic muscles compared with control, and HA coadministration further enhanced this effect. These results indicated that HA enhances angiogenesis of MSCs-ECFCs, probably by activating CD44 and repressing the miR-139-5p pathway.

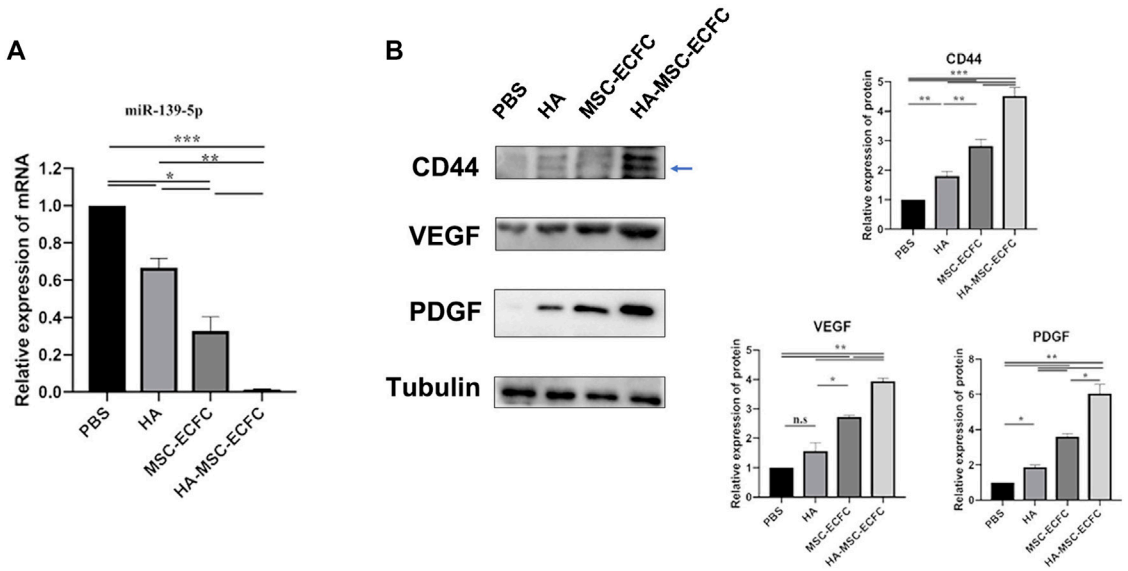

FIGURE 4 | CD44 and miR-139-5p expression in ischemic tissue. **(A)**. Relative miR-139-5p expression and **(B)** relative CD44, VEGF and PDGF protein expression in the gastrocnemius muscle of the ischemic lower extremity (n = 3 independent experiments. Error bars: mean ± SD. $^*p < 0.5$, $^*p < 0.01$, $^*p < 0.001$).

Downregulation of miR-139-5p Expression was Induced by HA by Activating CD44 and was Involved in HA Promotion of Angiogenesis

To clarify the effect of HA on the expression of miR-139-5p in MSCs and ECFCs, we tested the expression of CD44 and miR-139-5p with or without HA dilution in MSCs, ECFCs and cocultured MSCs-ECFCs, respectively. As shown in **Figure 5**, the expression of CD44 was increased in different type of cells after exposure to HA (**Figures 5A–D**). The level of miR-139-5p was significantly decreased in the ECFCs and MSCs-ECFCs treated with HA, while no change of miR-139-5p expression in MSCs alone was observed (**Figure 5E**). Then, we transfected CD44 plasmids to overexpress CD44 (**Supplementary Figures S1A,B**) in ECFCs and found that miR-139-5p expression was significantly repressed (**Figure 5F**). Knockdown of CD44 expression through transfection with small interfering RNAs (siRNAs) in ECFCs (**Supplementary Figure S1C**) effectively enhanced miR-139-5p expression and abrogated the HA-mediated downregulation of miR-139-5p expression (**Figure 5G**). These results indicated that CD44 is a negative regulator of miR-139-5p and that HA could decrease miR-139-5p expression through CD44 in ECFCs. Since HA did not regulate miR-139-5p expression in MSCs, we wondered whether it would make affect in the co-culture system. We sorted $CD31^+$ and $CD31^-$cells in MSC-ECFC co-culture mixed cells using flow cytometry, respectively. Results showed that the proportion of $CD31^+$ cells was significantly higher in the HA-treated group (**Figure 5H**). Moreover, the significantly decreased miR-139-5p expression in the $CD31^+$ group (**Figure 5I**) explained the reduced overall expression of miR-139-5p in the HA-MSC-ECFC group.

To determine whether miR-139-5p is involved in HA-mediated promotion of MSCs-ECFCs function, we transfected MSCs-ECFCs with miR-139-5p inhibitors and transfected HA-MSCs-ECFCs with miR-139-5p mimics, respectively (**Supplementary Figures S1D,E**). Results showed that upregulation of miR-139-5p expression dampened the HA-improved MSC-ECFC proliferation and migration; in contrast, downregulation of miR-139-5p expression significantly improved MSC-ECFC proliferation and migration (**Figures 6A–C**). Furthermore, we found that the proportion of $CD31^+$ cells was significantly reduced in HA-MSC-ECFC transfected with miR-139-5p mimics (**Figures 6D,E**), which indicated that HA regulate ECFCs viability in the HA-MSC-ECFC co-culture system through miR-139-5p. In conclusion, these results suggested that HA promotes angiogenesis of MSCs-ECFCs at least partly through the CD44/miR-139-5p pathway.

DISCUSSION

Therapeutic angiogenesis is an emerging approach to reconstruct the damaged vascular network by promoting local angiogenesis and stimulating *de novo* blood vessel formation. Among these approaches, cell therapy is a promising strategy. ECFCs are a subset of EPCs that arise from circulation. In particular, human cord blood-derived ECFCs have a high proliferative capacity and potently form stable and functioning blood vessels *in vivo* (Jokubaitis et al., 2008). We and others have proposed that ECFC significantly rescues blood perfusion at 14 days post-injection by vascular incorporation (Schwarz et al., 2012; Luo et al., 2020). Some studies have revealed that combining MSCs at a certain ratio with ECFCs enables the formation of lasting microvascular networks that anastomose with the host

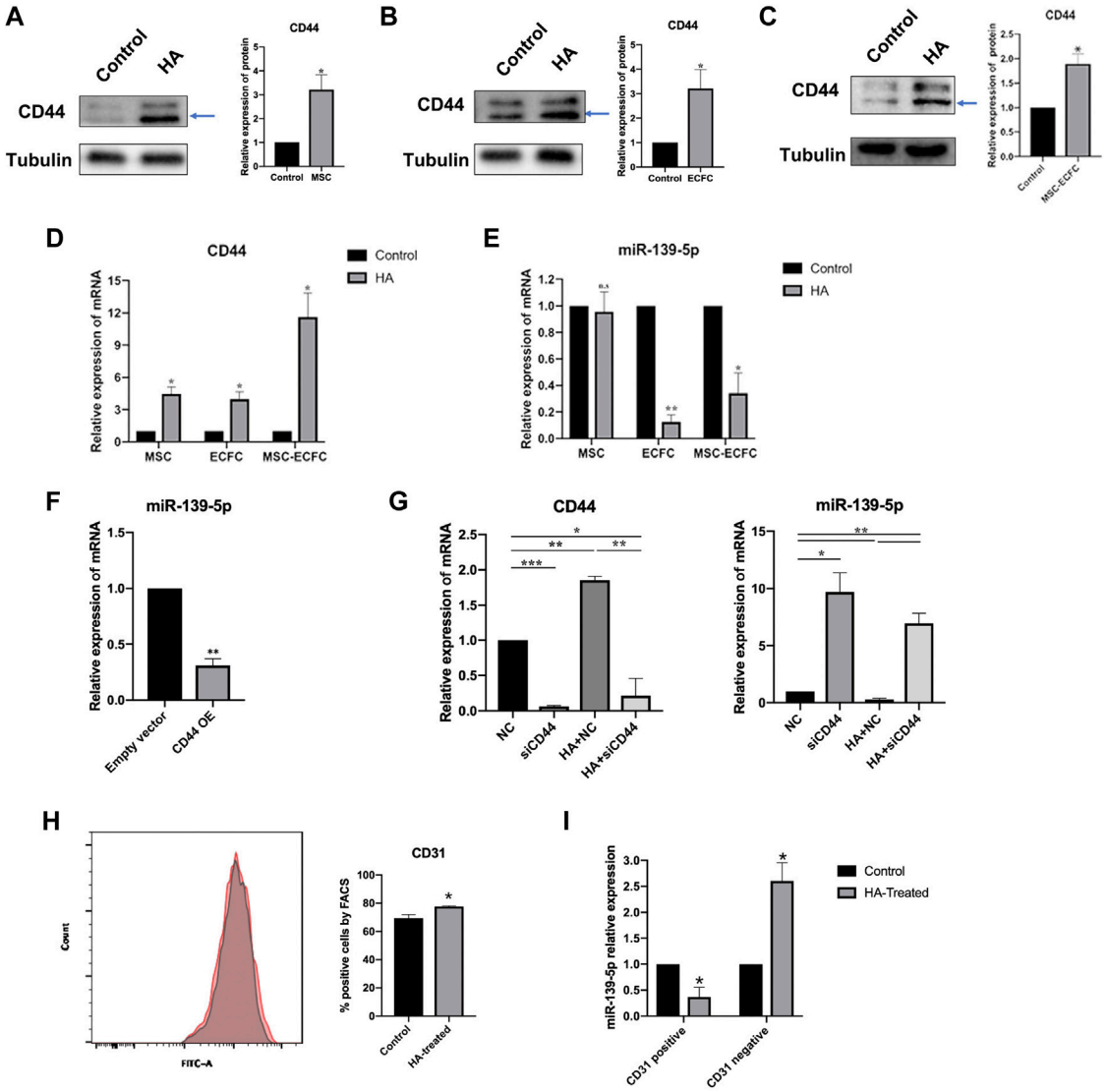

FIGURE 5 | HA inhibits miR-139-5p expression by activating CD44. **(A–C)**. Western blot assays and qPCR assays **(D,E)** were performed to test CD44 and miR-139-5p expression after HA treatment in MSCs, ECFCs and MSCs-ECFCs, respectively. **(F)**. Relative miR-139-5p expression in ECFCs transfected with CD44 overexpression plasmid. **(G)**. qPCR assays were performed to test the CD44 and miR-139-5p mRNA expression in ECFCs transfected with CD44 siRNA, with or without administration of HA, respectively. **(H)**. Flow cytometry of CD31 sorted from MSC-ECFC co-cultured system, with (red) or without (grey) administration of HA, and quantification of flow cytometry. **(I)**. Relative miR-139-5p expression in the sorted $CD31^+$ cells and $CD31^-$cells, respectively. ($n = 3$ independent experiments. Error bars: mean ± SD. $^*p < 0.05$, $^{**}p < 0.01$, $^{***}p < 0.001$).

vasculature following transplantation *in vivo* (Melero-Martin et al., 2008) and improves blood flow in ischemic limbs compared with ECFC or MSC administration alone (Creager et al., 2012; Kang et al., 2017). Generally, the interaction between endothelial cells and mural cells (pericytes and vascular smooth muscle) is essential for vascular development and maintenance. ECFCs can differentiate into endothelial cells in ischemic tissues (Critser and Yoder, 2010; O'Neill et al., 2018), while MSCs can differentiate into perivascular cells, which envelop endothelial cells in the vascular structure (Melero-Martin et al., 2008). In addition, MSCs secrete a plethora of proangiogenic factors, such as VEGF-A and FGF2, to induce the proliferation, migration, and tube formation of ECFCs, thereby rescuing local blood perfusion (Lin et al., 2012). Other mechanisms of MSC-synergized ECFCs in angiogenesis include modulated ECFC angiogenic activity *via* direct contact by priming ECFCs toward a mesenchymal phenotype, which enhances adhesive and tubulogenic properties (Shafiee et al., 2017), potentiates ECFC retention by recruiting host myeloid cells (Kang et al., 2017) and reduces intragraft immune cell infiltration and endothelial HLA-DR expression, thus lowering the risk of ECFC rejection (Souidi et al., 2017). A previous study suggested that mixing MSCs-

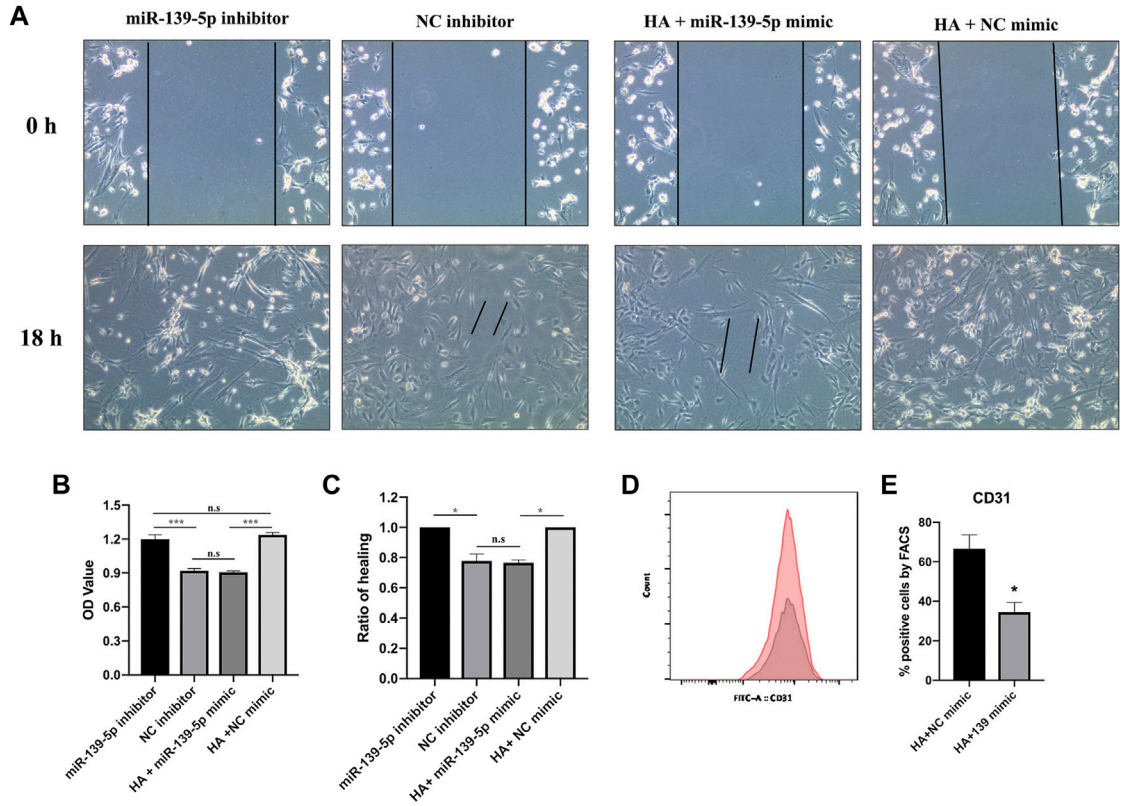

FIGURE 6 | HA promotes MSCs-ECFCs proliferation and migration through miR-139-5p. **(A,C)**. Wound healing assays were performed to assess the migration of MSCs-ECFCs transfected with miR-139-5p mimics and HA-MSCs-ECFCs transfected with miR-139-5p inhibitors, respectively. **(B)**. CCK8 assays were performed to assess the proliferation. **(D)**. Flow cytometry of CD31 sorted from HA-MSC-ECFC transfected with NC mimics (red) or miR-139-5p mimics (grey). **(E)**. Quantification of flow cytometry. (n = 3 independent experiments, Error bars: mean ± SD. $^{*}p < 0.05$, $^{**}p < 0.01$, $^{***}p < 0.001$).

EPCs at a ratio of 60:40 increased vessel density. The present study demonstrated that MSC-ECFC (3:2) cotransplantation formed more vascular networks in Matrigel plugs than MSC or ECFC transplantation alone.

Concomitant administration of MSCs and ECFCs was safe and had synergistic effects on angiogenesis and tissue regeneration (Shah and Kang, 2018), but the unsatisfactory treatment efficiency due to low engraftment and survival after transplantation was a concern (Karp and Leng Teo, 2009; Moubarik et al., 2011). To improve this situation, researchers have assessed new compounds as injectable and biological vehicles for delivery (Heo et al., 2014; Goto et al., 2016; Ullah et al., 2019). The injection of biomaterials combined with stem cells represents a promising solution to treat ischemic disorders (Prestwich et al., 2012). HA is an extracellular matrix component with good biocompatibility, biodegradability, and nonimmunogenicity and exerts antioxidative, anti-inflammatory, and analgesic effects *in vivo*. As a physiological component, it is not expected to produce adverse reactions after administration in clinical trials (Bowman et al., 2018). Therefore, HA is currently applied in arthritis therapy, medical cosmetology and tissue engineering (Gupta et al., 2019; López-Ruiz et al., 2019). Zullo et al. recently showed that HA-based hydrogen-coembedded EPCs and MSCs alleviated inflammation and improved cell viability *in vivo* (Zullo et al., 2015). Our previous work revealed that HA, MSCs and ECFCs could safely synergize to accelerate the healing of refractory diabetic foot ulcers (Zhao et al., 2020). These results indicated that HA-MSC-ECFC treatment may be a promising strategy for clinical use. Here, we used Matrigel plug assays to test *in vivo* angiogenesis. Clearly, HA enhanced angiogenesis of MSCs, ECFCs and MSCs-ECFCs, as more capillaries and vasculature with large diameters were observed in the HA-MSC-ECFC plugs. Moreover, HA-MSC-ECFC administration in mouse ischemic muscle accelerated blood perfusion and promoted neovascularization in tissues. These results suggested that HA-MSC-ECFC combined therapy may be a promising strategy for ischemic diseases.

Consistent with other research (Liu et al., 2016; Corradetti et al., 2017; Wang et al., 2020), the present work demonstrated that HA promotes MSC proliferation and migration. To the best of our knowledge, no data concerning the influence of HA on ECFCs have been reported. Our study showed that HA promoted the migration of ECFCs without damaging proliferation. Moreover, we found that HA significantly improved the migration and proliferation of cocultured MSCs-ECFCs. To choose the appropriate concentration, we tested 0.5 mg/ml and 1 mg/ml concentration of HA dilution. Both concentration of HA

induced a positive effect on cell migration and proliferation. Co-cultured MSCs-ECFCs displayed no significance in proliferation and between two HA concentration groups. Therefore, we used the concentration of 0.5 mg/ml HA in the subsequent study. Mechanistically, HA regulates cell proliferation and migration by targeting specific receptors such as CD44 (Tavianatou et al., 2019; Skandalis et al., 2019). HA was shown to improve MSC survival, proliferation and migration by targeting CD44 (Corradetti et al., 2017). Previous work proved that ECFCs with high CD44 expression were more effective at facilitating regeneration of retinal vasculature than those with lower CD44 expression in an oxygen-induced retinopathy model (Sakimoto et al., 2017). The present study showed that HA promoted CD44 expression in MSCs, ECFCs and cocultured MSCs-ECFCs, respectively, which indicated that HA may improve MSC-ECFC function by targeting CD44.

Interestingly, HA-CD44 interactions regulate tumor progression by activating miRNAs(Bourguignon, 2019). Several studies have demonstrated that CD44 could inhibit miR-139-5p expression in tumor cells (Bao et al., 2011; Zhao et al., 2014). miR-139-5p regulated the biological process of cells by targeting a variety of target genes, such as c-Jun (AP-1), IGF-1R, Notch, CXCR4, etc. Growth factors such as VEGF, PDGF and c-jun are regulated by miR-139-5p in endothelial cells (Zhang et al., 2021). Here, we found that the levels of CD44, VEGF and PDGF were increased, while miR-139-5p expression was decreased in ischemic muscles treated with HA-MSCs-ECFCs compared with that in the MSC-ECFC group. *In vitro* assays revealed that miR-139-5p expression was downregulated in ECFCs and cocultured MSCs-ECFCs treated with HA dilution. miR-139-5p expression negatively regulated by CD44 in ECFCs showed by the gain- or loss-function experiments. Precious study revealed that conditional medium derived from MSC increased CD31 expression in EPC(Fauza et al., 2018). In the present study, flow cytometry assays showed that CD31 positive cells rose to 60% in MSC-ECFC group, verified that coculture with MSCs improved ECFC viability. Although HA did not improve ECFCs proliferation when monoculture, CD31 positive cells further increase (77.6%) in HA-MSC-ECFC coculture group demonstrated that HA significantly enhanced ECFCs viability in MSC-ECFC co-culture system. These results suggest that all three ingredients were important and indispensable in the HA-MSC-ECFC system. Besides, we found that enhanced proportion $CD31^+$ cell in HA-MSC-ECFC co-cultured system could be reversed by upregulation of miR-139-5p. We considered that HA improved ECFCs viability through miR-139-5p in the HA-MSC-ECFC co-culture system. Generally, MSC could directional differentiated into endothelial cells in the medium supplemented with cytokines (Wang et al., 2018; Zhang et al., 2020) and miRs participate in the process (Arderiu et al., 2019). Decreased miR-139-5p expression in CD31 positive cells induced by HA may regulate target genes expression such as increased expression of VEGF and PDGF, which may further induced endothelial differentiation and proliferation. However, whether the increased CD31 positive proportion may partly due to the MSC endothelial differentiation or downregulation of miR-139-5p reflects differentiation of MSCs leaves us an intriguing question and need further research. On the other hand, we noticed that miR-139-5p expression was increased in CD31 negative cells in the HA-MSC-ECFC coculture system, which could inhibits MSCs proliferation (our unpublish data) and also may be associated with decreased MSC proportion in coculture system. Moreover, we found that upregulation of miR-139-5p expression could dampen HA-improved MSCs-ECFCs proliferation and migration, while downregulation of miR-139-5p expression improved MSCs-ECFCs proliferation and migration. These results indicated that HA promoted MSC-ECFC angiogenesis through the CD44/miR-139-5p pathway.

In summary, the present study demonstrates that HA facilitates angiogenesis of MSCs-ECFCs, revealing new mechanistic insights into the CD44/miR-139-5p signaling pathways involved, and provides novel and practical treatment approaches for vascular diseases.

DATA AVAILABILITY STATEMENT

The raw data supporting the conclusion of this article will be made available by the authors, without undue reservation.

ETHICS STATEMENT

The animal study was reviewed and approved by the Institutional Animal Care Committee of Central South University.

AUTHOR CONTRIBUTIONS

Study concepts were prepared by ZM. The study was designed by ZM, YL, and XM. Data acquisition was performed by YL, XW, and LF. Quality control of data and algorithms was done by FL and SL, Data analysis and interpretation were done by YL and ZM. Statistical analysis was done by YL and JM. The manuscript was prepared and edited by YL and ZM. All the authors approved the final version of the manuscript.

FUNDING

This work was supported by the National Natural Science Foundation of China (No. 81970724), the Provincial Natural Science Foundation of China (No. 2019JJ40454) and the Provincial Natural Science Foundation of China (No. 2018JJ3804).

SUPPLEMENTARY MATERIAL

The Supplementary Material for this article can be found online at: https://www.frontiersin.org/articles/10.3389/fbioe.2022.794037/full#supplementary-material

REFERENCES

Arderiu, G., Peña, E., Aledo, R., Juan-Babot, O., Crespo, J., Vilahur, G., et al. (2019). MicroRNA-145 Regulates the Differentiation of Adipose Stem Cells toward Microvascular Endothelial Cells and Promotes Angiogenesis. *Circ. Res.* 125 (No. 1), 74–89. doi:10.1161/CIRCRESAHA.118.314290

Awadalla, A., Hussein, A. M., Ali, M., Barakat, N., Hamam, E. T., Magar, R. W., et al. (2021). Possible Mechanisms for the Renoprotective Action of Adipose-Derived Mesenchymal Stem Cells with CD44-Targeted Hyaluronic Acid against Renal Ischemia. *Life Sci.* 272, 119221.

Bao, W., Fu, H. J., Xie, Q. S., Wang, L., Zhang, R., Guo, Z. Y., et al. (2011). HER2 Interacts with CD44 to Up-Regulate CXCR4 via Epigenetic Silencing of microRNA-139 in Gastric Cancer Cells. *Gastroenterology* 141 (No. 6), 2076–e6. doi:10.1053/j.gastro.2011.08.050

Bonafè, F., Govoni, M., Giordano, E., Caldarera, C. M., Guarnieri, C., and Muscari, C. (2014). Hyaluronan and Cardiac Regeneration. *J. Biomed. Sci.* 21 (No. 100), 100. doi:10.1186/s12929-014-0100-4

Bourguignon, L. Y., Earle, C., Wong, G., Spevak, C. C., and Krueger, K. (2012). Stem Cell Marker (Nanog) and Stat-3 Signaling Promote MicroRNA-21 Expression and Chemoresistance in hyaluronan/CD44-Activated Head and Neck Squamous Cell Carcinoma Cells. *Oncogene* 31 (No. 2), 149–160. doi:10.1038/onc.2011.222

Bourguignon, L. Y., Wong, G., Earle, C., and Chen, L. (2012). Hyaluronan-CD44v3 Interaction with Oct4-Sox2-Nanog Promotes miR-302 Expression Leading to Self-Renewal, Clonal Formation, and Cisplatin Resistance in Cancer Stem Cells from Head and Neck Squamous Cell Carcinoma. *J. Biol. Chem.* 287 (No. 39), 32800–32824. doi:10.1074/jbc.M111.308528

Bourguignon, L. Y., Wong, G., Earle, C., Krueger, K., and Spevak, C. C. (2010). Hyaluronan-CD44 Interaction Promotes C-Src-Mediated Twist Signaling, microRNA-10b Expression, and RhoA/RhoC Up-Regulation, Leading to Rho-Kinase-Associated Cytoskeleton Activation and Breast Tumor Cell Invasion. *J. Biol. Chem.* 285 (No. 47), 36721–36735. doi:10.1074/jbc.M110.162305

Bourguignon, L. Y. W. (2019). Matrix Hyaluronan-CD44 Interaction Activates MicroRNA and LncRNA Signaling Associated with Chemoresistance, Invasion, and Tumor Progression. *Front. Oncol.* 9 (No. 492), 492. doi:10.3389/fonc.2019.00492

Bowman, S., Awad, M. E., Hamrick, M. W., Hunter, M., and Fulzele, S. (2018). Recent Advances in Hyaluronic Acid Based Therapy for Osteoarthritis. *Clin. Transl Med.* 76 (No. 1), 6. doi:10.1186/s40169-017-0180-3

Corradetti, B., Taraballi, F., Martinez, J. O., Minardi, S., Basu, N., Bauza, G., et al. (2017). Hyaluronic Acid Coatings as a Simple and Efficient Approach to Improve MSC Homing toward the Site of Inflammation. *Sci. Rep.* 7 (No. 1), 7991. doi:10.1038/s41598-017-08687-3

Creager, M. A., Kaufman, J. A., and Conte, M. S. (2012). Clinical Practice. Acute Limb Ischemia. *N. Engl. J. Med.* 366 (No. 23), 2198–2206. doi:10.1056/NEJMcp1006054

Criqui, M. H., and Aboyans, V. (2015). *"Epidemiology Peripheral Artery Disease" Circ. Res.* 116 (No. 9), 1509–1526. doi:10.1161/circresaha.116.303849

Critser, P. J., and Yoder, M. C. (2010). Endothelial colony-forming Cell Role in Neoangiogenesis and Tissue Repair. *Curr. Opin. Organ. Transpl.* 15 (No. 1), 68–72. doi:10.1097/MOT.0b013e32833454b5

Das, A. K. (2009). Stem Cell Therapy for Critical Limb Ischaemia - a Review. *Indian J. Surg.* 71 (No. 4), 177–181. doi:10.1007/s12262-009-0059-7

Fadini, G. P., Spinetti, G., Santopaolo, M., and Madeddu, P. (2020). Impaired Regeneration Contributes to Poor Outcomes in Diabetic Peripheral Artery Disease. *Arterioscler. Thromb. Vasc. Biol.* 40 (No. 1), 34–44. doi:10.1161/ATVBAHA.119.312863

Faris, P., Negri, S., Perna, A., Rosti, V., Guerra, G., and Moccia, F. (2020). Therapeutic Potential of Endothelial Colony-Forming Cells in Ischemic Disease: Strategies to Improve Their Regenerative Efficacy. *Int. J. Mol. Sci.* 21 (No. 19). doi:10.3390/ijms21197406

Fauza, D., Lagonda, C. A., Tjahjadi, F. B., and Kusnadi, Y. (2018)., 20. Supplement, S36–S37. doi:10.1016/j.jcyt.2018.02.09092 - Mesenchymal Stem Cells-Derived Vascular Endothelial Growth Factor Improves Characteristics of Endothelial Progenitor Cells. *Cytotherapy,* No. 5.

Frangogiannis, N. G. (2018). Cell Therapy for Peripheral Artery Disease. *Curr. Opin. Pharmacol.* 39 (No. 27), 27–34. doi:10.1016/j.coph.2018.01.005

Gaffey, A. C., Chen, M. H., Trubelja, A., Venkataraman, C. M., Chen, C. W., Chung, J. J., et al. (2019). Delivery of Progenitor Cells with Injectable Shear-Thinning Hydrogel Maintains Geometry and Normalizes Strain to Stabilize Cardiac Function after Ischemia. *J. Thorac. Cardiovasc. Surg.* 157 (No. 4), 1479–1490. doi:10.1016/j.jtcvs.2018.07.117

Gaffey, A. C., Chen, M. H., Venkataraman, C. M., Trubelja, A., Rodell, C. B., Dinh, P. V., et al. (2015). Injectable Shear-Thinning Hydrogels Used to Deliver Endothelial Progenitor Cells, Enhance Cell Engraftment, and Improve Ischemic Myocardium. *J. Thorac. Cardiovasc. Surg.* 150 (No. 5), 1268–1276. doi:10.1016/j.jtcvs.2015.07.035

Gao, W., Chen, D., Liu, G., and Ran, X. (2019). Autologous Stem Cell Therapy for Peripheral Arterial Disease: a Systematic Review and Meta-Analysis of Randomized Controlled Trials. *Stem Cel. Res. Ther.* 10140 (No. 1), 140. doi:10.1186/s13287-019-1254-5

Goto, K., Takemura, G., Takahashi, T., Okada, H., Kanamori, H., Kawamura, I., et al. (2016). Intravenous Administration of Endothelial Colony-Forming Cells Overexpressing Integrin β1 Augments Angiogenesis in Ischemic Legs. *Stem Cell Transl. Med.* 5 (No. 2), 218–226. doi:10.5966/sctm.2015-0096

Gupta, R. C., Lall, R., Srivastava, A., and Sinha, A. (2019). Hyaluronic Acid: Molecular Mechanisms and Therapeutic Trajectory. *Front. Vet. Sci.* 6 (No. 192), 192. doi:10.3389/fvets.2019.00192

Heo, S. C., Kwon, Y. W., Jang, I. H., Jeong, G. O., Yoon, J. W., Kim, C. D., et al. (2014). WKYMVm-induced Activation of Formyl Peptide Receptor 2 Stimulates Ischemic Neovasculogenesis by Promoting Homing of Endothelial colony-forming Cells. *Stem Cells* 32 (No. 3), 779–790. doi:10.1002/stem.1578

Jokubaitis, V. J., Sinka, L., Driessen, R., Whitty, G., Haylock, D. N., Bertoncello, I., et al. (2008). Angiotensin-converting Enzyme (CD143) marks Hematopoietic Stem Cells in Human Embryonic, Fetal, and Adult Hematopoietic Tissues. *Blood* 111 (No. 8), 4055–4063. doi:10.1182/blood-2007-05-091710

Kang, K. T., Lin, R. Z., Kuppermann, D., Melero-Martin, J. M., and Bischoff, J. (2017). Endothelial colony Forming Cells and Mesenchymal Progenitor Cells Form Blood Vessels and Increase Blood Flow in Ischemic Muscle. *Sci. Rep.* 7770 (No. 1), 770. doi:10.1038/s41598-017-00809-1

Karp, J. M., and Leng Teo, G. S. (2009). Mesenchymal Stem Cell Homing: the Devil Is in the Details. *Cell Stem Cell* 4 (No. 3), 206–216. doi:10.1016/j.stem.2009.02.001

Lin, R. Z., Moreno-Luna, R., Li, D., Jaminet, S. C., Greene, A. K., and Melero-Martin, J. M. (2014). Human Endothelial colony-forming Cells Serve as Trophic Mediators for Mesenchymal Stem Cell Engraftment via Paracrine Signaling. *Proc. Natl. Acad. Sci. U S A.* 111 (No. 28), 10137–10142. doi:10.1073/pnas.1405388111

Lin, R. Z., Moreno-Luna, R., Zhou, B., Pu, W. T., and Melero-Martin, J. M. (2012). Equal Modulation of Endothelial Cell Function by Four Distinct Tissue-specific Mesenchymal Stem Cells. *Angiogenesis* 15 (No. 3), 443–455. doi:10.1007/s10456-012-9272-2

Liu, R. M., Sun, R. G., Zhang, L. T., Zhang, Q. F., Chen, D. X., Zhong, J. J., et al. (2016). Hyaluronic Acid Enhances Proliferation of Human Amniotic Mesenchymal Stem Cells through Activation of Wnt/β-Catenin Signaling Pathway. *Exp. Cel. Res.* 345 (No. 2), 218–229. doi:10.1016/j.yexcr.2016.05.019

López-Ruiz, E., Jiménez, G., Álvarez de Cienfuegos, L., Antic, C., Sabata, R., Marchal, J. A., et al. (2019). Advances of Hyaluronic Acid in Stem Cell Therapy and Tissue Engineering, Including Current Clinical Trials. *Eur. Cel. Mater.* 37 (No. 186)–213.

Luo, Y. F., Wan, X. X., Zhao, L. L., Guo, Z., Shen, R. T., Zeng, P. Y., et al. (2020)., 12. Albany NY), 1186–1211. doi:10.18632/aging.202257MicroRNA-139-5p Upregulation Is Associated with Diabetic Endothelial Cell Dysfunction by Targeting C-Jun. *Aging (Albany NY),* No. 1.

Melero-Martin, J. M., De Obaldia, M. E., Kang, S. Y., Khan, Z. A., Yuan, L., Oettgen, P., et al. (2008). Engineering Robust and Functional Vascular Networks *In Vivo* with Human Adult and Cord Blood-Derived Progenitor Cells. *Circ. Res.* 103 (No. 2), 194–202. doi:10.1161/CIRCRESAHA.108.178590

Moubarik, C., Guillet, B., Youssef, B., Codaccioni, J. L., Piercecchi, M. D., Sabatier, F., et al. (2011). Transplanted Late Outgrowth Endothelial Progenitor Cells as Cell Therapy Product for Stroke. *Stem Cel. Rev. Rep.* 7 (No. 1), 208–220. doi:10.1007/s12015-010-9157-y

O'Neill, C. L., McLoughlin, K. J., Chambers, S. E. J., Guduric-Fuchs, J., Stitt, A. W., and Medina, R. J. (2018). The Vasoreparative Potential of Endothelial Colony Forming Cells: A Journey through Pre-clinical Studies. *Front. Med. (Lausanne)* 5 (No. 273), 273. doi:10.3389/fmed.2018.00273

Prestwich, G. D., Erickson, I. E., Zarembinski, T. I., West, M., and Tew, W. P. (2012). The Translational Imperative: Making Cell Therapy Simple and Effective. *Acta Biomater.* 8 (No. 12), 4200–4207. doi:10.1016/j.actbio.2012.06.043

Ratliff, B. B., Ghaly, T., Brudnicki, P., Yasuda, K., Rajdev, M., Bank, M., et al. (2010). Endothelial Progenitors Encapsulated in Bioartificial Niches Are Insulated from Systemic Cytotoxicity and Are Angiogenesis Competent. *Am. J. Physiol. Ren. Physiol* 299 (No. 1), F178–F186. doi:10.1152/ajprenal.00102.2010

Robey, T. E., Saiget, M. K., Reinecke, H., and Murry, C. E. (2008). Systems Approaches to Preventing Transplanted Cell Death in Cardiac Repair. *J. Mol. Cel. Cardiol.* 45 (No. 4), 567–581. doi:10.1016/j.yjmcc.2008.03.009

Rossi, E., Smadja, D., Goyard, C., Cras, A., Dizier, B., Bacha, N., et al. (2017). Co-injection of Mesenchymal Stem Cells with Endothelial Progenitor Cells Accelerates Muscle Recovery in Hind Limb Ischemia through an Endoglin-dependent Mechanism. *Thromb. Haemost.* 117 (No. 10), 1908–1918. doi:10.1160/TH17-01-0007

Sakimoto, S., Marchetti, V., Aguilar, E., Lee, K., Usui, Y., Murinello, S., et al. (2017). CD44 Expression in Endothelial colony-forming Cells Regulates Neurovascular Trophic Effect. *JCI Insight* 2 (No. 2), e89906. doi:10.1172/jci.insight.89906

Schwarz, T. M., Leicht, S. F., Radic, T., Rodriguez-Arabaolaza, I., Hermann, P. C., Berger, F., et al. (2012). Vascular Incorporation of Endothelial colony-forming Cells Is Essential for Functional Recovery of Murine Ischemic Tissue Following Cell Therapy. *Arterioscler. Thromb. Vasc. Biol.* 32 (No. 2), e13–21. doi:10.1161/ATVBAHA.111.239822

Shafiee, A., Patel, J., Wong, H. Y., Donovan, P., Hutmacher, D. W., Fisk, N. M., et al. (2017). Priming of Endothelial colony-forming Cells in a Mesenchymal Niche Improves Engraftment and Vasculogenic Potential by Initiating Mesenchymal Transition Orchestrated by NOTCH Signaling. *Faseb j* 31 (No. 2), 610–624. doi:10.1096/fj.201600937

Shah, S., and Kang, K. T. (2018). Two-Cell Spheroid Angiogenesis Assay System Using Both Endothelial Colony Forming Cells and Mesenchymal Stem Cells. *Biomol. Ther. (Seoul)* 26 (No. 5), 474–480. doi:10.4062/biomolther.2018.134

Shu, J., and Santulli, G. (2018). Update on Peripheral Artery Disease: Epidemiology and Evidence-Based Facts. *Atherosclerosis* 275 (No. 379), 379–381. doi:10.1016/j.atherosclerosis.2018.05.033

Skandalis, S. S., Karalis, T. T., Chatzopoulos, A., and Karamanos, N. K. (2019). Hyaluronan-CD44 axis Orchestrates Cancer Stem Cell Functions. *Cell Signal* 63, 109377. doi:10.1016/j.cellsig.2019.109377

Souidi, N., Stolk, M., Rudeck, J., Strunk, D., Schallmoser, K., Volk, H. D., et al. (2017). Stromal Cells Act as Guardians for Endothelial Progenitors by Reducing Their Immunogenicity after Co-transplantation. *Stem Cells* 35 (No. 5), 1233–1245. doi:10.1002/stem.2573

Tavianatou, A. G., Caon, I., Franchi, M., Piperigkou, Z., Galesso, D., and Karamanos, N. K. (2019). Hyaluronan: Molecular Size-dependent Signaling and Biological Functions in Inflammation and Cancer. *Febs j* 286 (No. 15), 2883–2908. doi:10.1111/febs.14777

Ullah, M., Liu, D. D., and Thakor, A. S. (2019). Mesenchymal Stromal Cell Homing: Mechanisms and Strategies for Improvement. *iScience* 15 (No. 421), 421–438. doi:10.1016/j.isci.2019.05.004

Wang, A. T., Zhang, Q. F., Wang, N. X., Yu, C. Y., Liu, R. M., Luo, Y., et al. (2020). Cocktail of Hyaluronic Acid and Human Amniotic Mesenchymal Cells Effectively Repairs Cartilage Injuries in Sodium Iodoacetate-Induced Osteoarthritis Rats. *Front. Bioeng. Biotechnol.* 8 (No. 87), 87. doi:10.3389/fbioe.2020.00087

Wang, C., Li, Y., Yang, M., Zou, Y., Liu, H., Liang, Z., et al. (2018). Efficient Differentiation of Bone Marrow Mesenchymal Stem Cells into Endothelial Cells *In Vitro*. *Eur. J. Vasc. Endovasc. Surg.* 55 (No. 2), 257–265. doi:10.1016/j.ejvs.2017.10.012

Yue, C., Guo, Z., Luo, Y., Yuan, J., Wan, X., and Mo, Z. (2020). c-Jun Overexpression Accelerates Wound Healing in Diabetic Rats by Human Umbilical Cord-Derived Mesenchymal Stem Cells. *Stem Cell Int.* 2020, 7430968. doi:10.1155/2020/7430968

Zhang, J., Li, Y., Li, H., Zhu, B., Wang, L., Guo, B., et al. (2018). GDF11 Improves Angiogenic Function of EPCs in Diabetic Limb Ischemia. *Diabetes* 67 (No. 10), 2084–2095. doi:10.2337/db17-1583

Zhang, S., Zhang, W., Li, Y., Ren, L., Deng, H., Yin, X., et al. (2020). Human Umbilical Cord Mesenchymal Stem Cell Differentiation into Odontoblast-like Cells and Endothelial Cells: A Potential Cell Source for Dental Pulp Tissue Engineering. *Front. Physiol.* 11 (No. 593), 593. doi:10.3389/fphys.2020.00593

Zhang, Z., Song, C., Wang, T., Sun, L., Qin, L., and Ju, J. (2021). miR-139-5p Promotes Neovascularization in Diabetic Retinopathy by Regulating the Phosphatase and Tensin Homolog. *Arch. Pharm. Res.* 44 (No. 2), 205–218. doi:10.1007/s12272-021-01308-8

Zhao, G., Zhou, X., Fang, T., Hou, Y., and Hu, Y. (2014). Hyaluronic Acid Promotes the Expression of Progesterone Receptor Membrane Component 1 via Epigenetic Silencing of miR-139-5p in Human and Rat Granulosa Cells. *Biol. Reprod.* 91116 (No. 5), 116. doi:10.1095/biolreprod.114.120295

Zhao, L., Guo, Z., Chen, K., Yang, W., Wan, X., Zeng, P., et al. (2020). Combined Transplantation of Mesenchymal Stem Cells and Endothelial Colony-Forming Cells Accelerates Refractory Diabetic Foot Ulcer Healing. *Stem Cell Int.* 2020, 8863649. doi:10.1155/2020/8863649

Zullo, J. A., Nadel, E. P., Rabadi, M. M., Baskind, M. J., Rajdev, M. A., Demaree, C. M., et al. (2015). The Secretome of Hydrogel-Coembedded Endothelial Progenitor Cells and Mesenchymal Stem Cells Instructs Macrophage Polarization in Endotoxemia. *Stem Cell Transl. Med.* 4 (No. 7), 852–861. doi:10.5966/sctm.2014-0111

Conflict of Interest: The authors declare that the research was conducted in the absence of any commercial or financial relationships that could be construed as a potential conflict of interest.

Publisher's Note: All claims expressed in this article are solely those of the authors and do not necessarily represent those of their affiliated organizations, or those of the publisher, the editors and the reviewers. Any product that may be evaluated in this article, or claim that may be made by its manufacturer, is not guaranteed or endorsed by the publisher.

frontiers | Frontiers in Bioengineering and Biotechnology

ORIGINAL RESEARCH
published: 13 June 2022
doi: 10.3389/fbioe.2022.860138

Enhanced Microvasculature Formation and Patterning in iPSC–Derived Kidney Organoids Cultured in Physiological Hypoxia

Anika Schumacher[1], *Nadia Roumans*[1], *Timo Rademakers*[1], *Virginie Joris*[1], *Maria José Eischen-Loges*[1,2], *Martijn van Griensven*[1] *and Vanessa L.S. LaPointe*[1]*

[1]Department of Cell Biology–Inspired Tissue Engineering, MERLN Institute for Technology-Inspired Regenerative Medicine, Maastricht University, Maastricht, Netherlands, [2]Department of Instructive Biomaterials Engineering, MERLN Institute for Technology-Inspired Regenerative Medicine, Maastricht University, Maastricht, Netherlands

OPEN ACCESS

Edited by:
Akiko Mammoto, Medical College of Wisconsin, United States

Reviewed by:
Ryuji Morizane, Massachusetts General Hospital and Harvard Medical School, United States
Martin Johannes Hoogduijn, Erasmus University Rotterdam, Netherlands

***Correspondence:**
Vanessa L.S. LaPointe
v.lapointe@maastrichtuniversity.nl

Specialty section:
This article was submitted to Tissue Engineering and Regenerative Medicine, a section of the journal Frontiers in Bioengineering and Biotechnology

Received: *22 January 2022*
Accepted: *05 May 2022*
Published: *13 June 2022*

Citation:
Schumacher A, Roumans N, Rademakers T, Joris V, Eischen-Loges MJ, van Griensven M and LaPointe VLS (2022) Enhanced Microvasculature Formation and Patterning in iPSC–Derived Kidney Organoids Cultured in Physiological Hypoxia. Front. Bioeng. Biotechnol. 10:860138. doi: 10.3389/fbioe.2022.860138

Stem cell–derived kidney organoids have been shown to self-organize from induced pluripotent stem cells into most important renal structures. However, the structures remain immature in culture and contain endothelial networks with low connectivity and limited organoid invasion. Furthermore, the nephrons lose their phenotype after approximately 25 days. To become applicable for future transplantation, further maturation *in vitro* is essential. Since kidneys *in vivo* develop in hypoxia, we studied the modulation of oxygen availability in culture. We hypothesized that introducing long-term culture at physiological hypoxia, rather than the normally applied non-physiological, hyperoxic 21% O_2, could initiate angiogenesis, lead to enhanced growth factor expression and improve the endothelial patterning. We therefore cultured the kidney organoids at 7% O_2 instead of 21% O_2 for up to 25 days and evaluated nephrogenesis, growth factor expression such as VEGF-A and vascularization. Whole mount imaging revealed a homogenous morphology of the endothelial network with enhanced sprouting and interconnectivity when the kidney organoids were cultured in hypoxia. Three-dimensional vessel quantification confirmed that the hypoxic culture led to an increased average vessel length, likely due to the observed upregulation of VEGFA-189 and VEGFA-121, and downregulation of the antiangiogenic protein VEGF-A165b measured in hypoxia. This research indicates the importance of optimization of oxygen availability in organoid systems and the potential of hypoxic culture conditions in improving the vascularization of organoids.

Keywords: kidney organoid, hypoxia, VEGF-A, endothelial cells, vascularization, induced pluripoten stem cells, nephrogenesis, angiogenesis

INTRODUCTION

Organoid models have become an irreplaceable alternative to two-dimensional cell culture because of their greater cellular and architectural complexity, which is alike native tissue. Induced pluripotent stem cells can be differentiated into kidney organoids that develop nephrons resembling capillary loop–stage nephrons. (Takasato et al., 2016) The large variety of renal cell types they possess, similar to the developing kidney (Schumacher et al., 2021), makes them promising models for regenerative medicine, drug testing and developmental biology (Gupta et al., 2021). However, these organoids

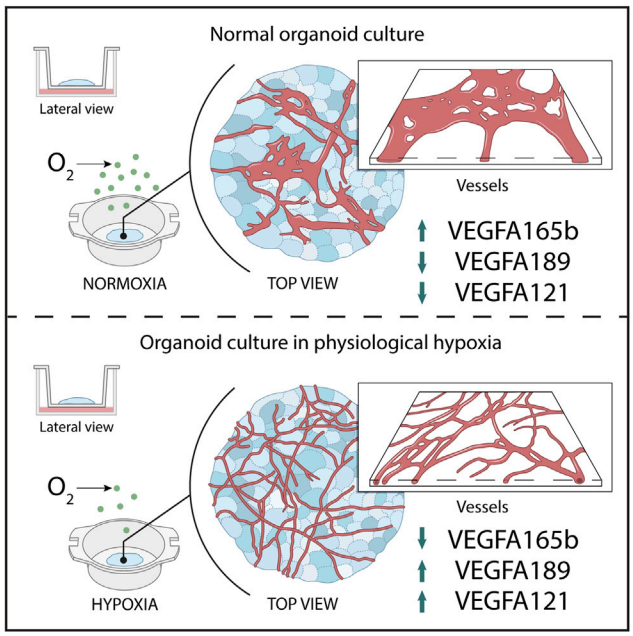

GRAPHICAL ABSTRACT |

have several drawbacks—such as the limited culture duration, loss of nephrogenic potential, immaturity and lack of vasculature (Nishinakamura, 2019; Takasato and Wymeersch, 2020) —perhaps due the lack of an *in vivo*–like culture environment, which is increasingly being investigated. (Rossi et al., 2018) Moreover, kidney organoids are one of the largest organoid models, growing up to 1.5 mm in thickness. (Takasato et al., 2016) This draws attention to one aspect of a physiological environment, which is the oxygenation of the tissue.

Cell culture in hypoxia, defined as a state where cells no longer have sufficient oxygen available to use oxidative phosphorylation to generate ATP (Nishinakamura, 2019; Takasato and Wymeersch, 2020), has been performed for more than a decade, for example to maintain stem cells (Ma et al., 2009). Hypoxia is also known to act as a morphogen in cell communication of various cell lineages and for certain cell types to partially determine cellular differentiation. (Wörsdörfer and Ergün, 2021) If not optimized to the model system, hypoxia is known to have detrimental effects in cell and tissue culture. Nevertheless, to date, there is little knowledge on the effects of hypoxia in organoid cultures. Briefly, hypoxic culture (5% O_2) of intestinal organoids was considered detrimental due to a reduced number of crypts. (Okkelman et al., 2017) In contrast, microwell-cultured kidney organoids cultured for 24 h in hypoxia (1 and 3% O_2) showed enhanced functionality measured by secretion of erythropoietin (EPO). (Ding et al., 2020) These results argue that oxygen levels critically affect maturation of organoids, in a model-sensitive manner.

Kidney organoids are cultured, like explanted kidneys (Grobstein, 1956), at an air–liquid interface and therefore are directly exposed to incubator air (21% O_2), commonly defined as normoxia. However, it has been previously well described that 21% O_2 is non-physiological. (Place et al., 2017) For this reason, and the fact that the physiological environment of the developing kidney is hypoxic, we do consider 21% O_2 to be hyperoxic and non-physiological. This is particularly the case for endothelial cells, which largely reside on the organoids' surface. Hyperoxia is known to negatively impact kidney development *in vivo,* such as significantly reducing the size of the nephrogenic zone and glomeruli. (Buchholz et al., 2016) *In vitro*, the detrimental effects of hyperoxic cell and tissue culture are also well established (Li et al., 2004; Jagannathan et al., 2016), such as the formation of reactive oxygen species in endothelial cells (Brueckl et al., 2006). By contrast, there is significant evidence that hypoxia enhances the proliferation of endothelial cells as well as stem cell differentiation towards an endothelial lineage. (Han et al., 2010; Prado-Lopez et al., 2010; Salomon et al., 2013; Bekhite et al., 2014; Yuan et al., 2015; Shang et al., 2019; Podkalicka et al., 2020) Murine metanephric explants showed enhanced endothelial cell proliferation when cultured in hypoxia (3% O_2). (Tufro-McReddie et al., 1997; Loughna et al., 1998) Furthermore, the mammalian uterus is hypoxic and fetal organs develop in hypoxic environments. (Fischer and Bavister, 1993; Lee et al., 2001) Therefore, modulating the oxygen concentrations could be a step towards *in vivo*–like kidney organoid culture with improved vascularization.

In developing kidneys in the hypoxic mammalian uterus (Fischer and Bavister, 1993; Fajersztajn and Veras, 2017), nephrogenesis starts in the avascular nephrogenic zone. (Hemker et al., 2016; Gerosa et al., 2017) Later in the capillary loop stage of nephrogenesis, mainly angiogenesis and to a lesser

extent vascularization start to take place. (Nishinakamura, 2019) Only when blood vessels enter the kidney and new vessels are formed, oxygen levels increase to finally reach 4–9.5 kPa (30–71 mmHg) in the adult human cortex and 2 kPa (15 mmHg) in the adult human medulla. (Keeley and Mann, 2019) Due to the invasive nature of the measurements, the oxygen tensions in developing human cortex and medulla have not been determined. Recapitulating this *in vivo* hypoxic environment in the kidney organoid culture could enable the transcription of genes essential in kidney organogenesis. Below 5% O_2, binding of prolyl hydroxylases to cytoplasmic hypoxia-inducible factor alpha (HIFα) is inhibited, leading to reduced or inhibited proteosomal degradation. Consequently, HIFα rapidly accumulates, translocates into the nucleus and its dimerization with HIFβ is initiated. (Hemker et al., 2016) Dimer binding to hypoxia responsive element (HRE) promoters leads to the transcription of a variety of genes. While this process occurs in all tissue types, it is known that various HIF-regulated genes are implicated in angiogenesis and vascularization in kidney organogenesis. In kidney development, nuclear HIF translocation occurs in metanephric mesenchyme and subsequently in podocytes, leading to VEGF-A transcription, which attracts endothelial cells to vascularize the nephrons. (Tufró, 2000; Bernhardt et al., 2006).

Developmentally, kidney organoids, normally cultured at non-physiological hyperoxic 21% O_2 (≈160 mmHg), are comparable to kidneys in the first to early second trimester. (Takasato et al., 2015) Since, however, the oxygen concentrations in the developing human kidney are unknown, we hypothesized whether a culture at 7% O_2 (≈53 mmHg), comparable to the adult human cortex, would lead to intra-organoid oxygen concentrations more closely resembling developing non-vascularized kidneys *in vivo,* and initiate angiogenesis in the organoids. After up to 25 days of culture, we analyzed nephrogenesis, the expression of angiogenic markers (particularly VEGF) and endothelialisation to determine whether hypoxic cultures of the organoids improved these characteristics compared to cultures at 21% O_2. We found that long-term hypoxic culture enhances endothelial patterning and sprouting and consequently could enhance kidney organoid cultures towards a more *in vivo*–like model.

MATERIALS AND METHODS

Induced Pluripotent Stem Cell Differentiation and Kidney Organoid Culture

Induced pluripotent stem cells (iPSCs) were differentiated and the organoids were cultured according to the previously published protocol by van den Berg, Ritsma (van den Berg et al., 2018) (**Figure 1A**). Briefly, the iPSC line LUMC0072iCTRL01 (male fibroblasts reprogrammed using RNA Simplicon reprogramming kit, Millipore) obtained from the hiPSC core facility at the Leiden University Medical Center, were passaged biweekly and maintained in 3 ml of Essential 8 Medium (Thermo Fisher Scientific) supplemented with 1% penicillin–streptomycin in 6-well plates coated with truncated recombinant human vitronectin (Thermo Fisher Scientific). The iPSC line was previously assessed for pluripotency and normal karyotype. (Geuens et al., 2021) For differentiation, 80,000 cells per well were seeded into a six well plate and differentiated according to the published protocol in organoid culture medium composed of STEMdiff APEL2 medium (STEMCELL Technologies), supplemented with 1% antibiotic-antimycotic and 1% protein-free hybridoma medium II (PFHM 2) (Thermo Fisher Scientific) and the respective growth factors and small molecules (8 μM GSK-3 inhibitor CHIR99021 (R&D Systems), 200 ng/ml FGF9 (fibroblast growth factor 9; R&D Systems), and 1 μg/ml heparin (Sigma-Aldrich)). After 7 days of differentiation, the cells were aggregated by centrifugation and spotted on transwell tissue culture plates with 0.4 μm pore polyester membrane inserts (Corning) and cultured at an air–liquid interface. For an additional 5 days, denoted as day 7 + 5, the organoids were cultured in organoid medium containing the growth factors and small molecules. From day 7 + 5 onwards, the organoids were cultured in organoid culture medium either in a hypoxia incubator (37°C, 5% CO_2, 7% O_2) or in normoxia (37°C, 5% CO_2, 21% O_2). The medium was refreshed every 2 days. At day 7 + 18 and day 7 + 25, the organoids were assessed.

Darkfield Imaging

The organoids were fixed at day 7 + 18 and day 7 + 25 in 2% (v/v) paraformaldehyde (20 min, 4°C) and were subsequently embedded in 10% gelatin in PBS (phosphate-buffered saline) in a cryomold. Once hardened, the gel was pealed out of the mold and placed on a darkfield imaging stage with circular illumination (Nikon). Images were acquired using a 1 × air objective on a Nikon SMX25 automated stereomicroscope with a customized Nikon darkfield illumination holder.

Cryopreservation and Cryosectioning

After fixing the organoids at day 7 + 18 or day 7 + 25 in 2% (v/v) paraformaldehyde (20 min, 4°C), the organoids were cryoprotected. The organoids were immersed in 15% (w/v) sucrose in 0.1 M phosphate buffer containing 0.1 M dibasic sodium phosphate and 0.01 M monobasic sodium phosphate in MilliQ water (24 h, 4°C, rotating), and subsequently in 30% (w/v) sucrose in 0.1 M phosphate buffer (48 h, 4°C, rotating). After cryoprotection, the organoids were embedded in freezing medium (15% (w/v) sucrose and 7.5% (w/v) gelatin in 1 M phosphate buffer) and hardened on ice. Freezing was performed in an isopentane bath in liquid nitrogen and the blocks were stored at −30°C until cryosectioning at −18°C into 12 μm–thick sections. The sections were stored at −80°C until use.

Oxygen Measurement

The oxygen concentration within the organoids was measured using an optical oxygen microsensor (PM-PSt7, Presens in Regensburg, Germany). The probe was calibrated according to the manufacturer's instructions. Briefly, the pressure settings were set to the elevation of the lab (997 kPa) and the probe was calibrated in an oxygen-depleted solution (water containing 70 mM sodium sulfite and 500 mM cobalt nitrate) followed by an oxygen-enriched solution (water connected to a room air valve).

All solutions were equilibrated to room temperature before calibration and room temperature (20°C) was put as standard in the software. At day 7 + 18 and day 7 + 25, organoids in both normoxia and hypoxia were measured using the calibrated sensor. The sensor was fixed to a micromanipulator and was inserted into the bottom of the organoid, approximately 1 mm in depth, close to the insert membrane of the transwell. The incubator was kept closed to ensure a stable gas concentration and measurements were continued until the signal reached a steady state (taking approximately 30–90 min).

Hypoxia Imaging

Hypoxia was measured in living organoids using the Image-iT Green Hypoxia Reagent (Thermo Fisher Scientific), which produces a green fluorescent signal below 5% O_2. The organoid was fully immersed in 5 µM ImageIT Green reagent dissolved in organoid culture medium for 4 h in normoxia. Subsequently, the staining solution was replaced with fresh medium and the organoids were moved to the incubator set to either the 7% O_2 or the 21% O_2 for 6 h, after which they were fixed for cryosectioning or imaged live. For live imaging, the organoids were imaged using a 10× air objective on an automated Nikon Eclipse Ti-E equipped with a spinning disk with a 70 µm pore size, a Lumencor Spectra X light source and Photometrics Prime 95B sCMOS camera. For cryosectioning, the method in Section 2.3 was applied. The sections were imaged with the same microscope using a 20× air objective and a 40× oil objective. All images were processed using Fiji (Schindelin et al., 2012), in which the rolling ball function was applied in the case of poor signal to noise ratio.

Immunofluorescence

The cryosections were warmed to RT (room temperature) and subsequently incubated in pre-warmed PBS (15 min, 37°C), to remove the sucrose and gelatin. Next, the cryosections were blocked with PBS containing 0.2% (v/v) Tween, 10% (w/v) BSA (bovine serum albumin) and 0.1 M glycine (20 min, RT) and incubated in primary antibodies (**Supplementary Table S1**) diluted in the dilution buffer of PBS containing 0.2% (v/v) Tween, 1% (w/v) BSA and 0.1 M glycine (overnight, 4°C). After washing in PBS containing 0.2% (v/v) Tween, the slides were incubated with appropriate secondary antibodies (**Supplementary Table S1**) diluted in the dilution buffer (1 h, RT). Finally, the slides were washed and mounted with Prolong Gold (Thermo Fisher Scientific). After curing for 2 days, imaging was performed on the automated Nikon Eclipse Ti-E microscope using a 20× air and a 40× oil objective. All images were processed using Fiji (Schindelin et al., 2012), in which the rolling ball function was applied in the case of poor signal to noise ratio.

Luminex Assay

The VEGF-A concentration in the culture medium was analyzed using a VEGF-A Human ProcartaPlex Simplex Kit (Cat. no. EPX01A-10277-901, Invitrogen), specific for the detection of VEGF-A165. The medium was collected on days 7 + 7, 7 + 12, 7 + 17, 7 + 21, and 7 + 24 and centrifuged (10 min, 4°C, 239 x g). The supernatant was immediately stored at −80°C. The assay was performed according to the manufacturer's instructions. In brief, samples were diluted 1:50 in universal assay buffer and 50 µL was added to the wells containing the antibody-coupled beads, along with the standards provided with the assay (30 min, RT, shaking). After an overnight incubation (4°C) and a final incubation (30 min, RT, shaking), detection antibody–biotin reporters were added to each well (30 min, RT, shaking). Next, fluorescent conjugate streptavidin–phycoerythrin was added (30 min, RT, shaking). After a final washing step, the beads were resuspended in 120 µL reading buffer. Fluorescence intensities were measured using a Luminex100 instrument (Bio-Rad) which was calibrated before each use. Data acquisition was done with the Bio-Plex Manager 6.0 software. The data were normalized to the standard curve dilutions delivered with the kit according to manufacturer's instructions.

Western Blot

After snap freezing in liquid nitrogen, the organoids were resuspended in 70 µL RIPA (radioimmunoprecipitation assay) lysis buffer (Sigma-Aldrich) supplemented with phosphatase inhibitor tablets PhosSTOP (Sigma-Aldrich) and protease inhibitor cOmplete ULTRA Tablets (Sigma-Aldrich). The protein concentrations were determined using a Pierce BCA Protein Assay Kit (Thermo Fisher Scientific) according to the manufacturer's protocol. Per well, 15 µg of protein was loaded. The migration was performed in migration buffer (Tris [tris(hydroxymethyl) aminomethane]-EDTA (ethylenediaminetetraacetic acid), SDS (sodium dodecyl sulfate), glycine, Bio-Rad) at 120 V. Subsequently, the proteins were transferred onto a nitrocellulose membrane at 350 mA for 90 min in a transfer buffer (Tris-base, glycine, SDS, 20% methanol). After the transfer, the membranes were blocked in blocking buffer [TBS (Tris-buffered saline), 0.1% Tween (v/v), 5% BSA (w/v)] (1 h, RT, shaking). Next, the membranes were incubated with primary antibodies (Table 1) (overnight, 4°C, shaking) in TBS-Tween, 5% BSA (w/v). The membranes were washed in TBS-Tween and incubated with the peroxidase-conjugated secondary antibody (Bio-Rad, Table 1) for 1 h at RT. The membranes were incubated with Clarity Western ECL substrate (Bio-Rad) and were developed using a ChemiDoc (Bio-Rad). The protein bands were quantified by densitometry using ImageJ, normalized to GAPDH. (Schneider et al., 2012).

RNA Isolation and qPCR

Organoids stored in TRIzol at −80°C were thawed and pipetted vigorously to homogenize the samples. Then, 500 µL was transferred to a Phasemaker tube (Thermo Fisher Scientific) after which, 100 µL of chloroform were added, shaken thoroughly and incubated for 5 min at RT. The mixture was centrifuged at 12,000 × g (15 min, 4°C). The aqueous phase was carefully transferred to a new microcentrifuge tube containing 250 µL isopropanol and 1 µL glycogen. After an additional centrifugation step (15 min, 4°C, 12,000 × g) the pellet was washed twice with 200 mM NaOAc in 75% ethanol. The supernatant was discarded, and the pellet was dried at 55°C, resuspended in 25 µL nuclease-free water. CDNA was synthesized using the iScript cDNA synthesis kit (Bio-Rad) and 500 ng/µL of RNA was loaded per sample. Quantitative

PCR was carried out with iQ SYBR Green Supermix (Bio-Rad), 5 ng cDNA per reaction, on a CFX96TM Real-Time system (Bio-Rad). Primer sequences (**Supplementary Table S2**) were verified using total human kidney RNA (Takara Bio). *PSMB4* was determined as the most stable housekeeping gene using the method described by Xie, Xiao (Xie et al., 2012), and *GAPDH* was used as a second housekeeping gene to ensure valid results. The data were normalized to *PSMB4* and plotted relative to the expression of the control samples day 7+18 normoxia. Each data point represents one organoid of three distinct iPSC differentiations. The statistics were performed on the log (fold change) and plotted onto the fold change graphs.

Whole Mount Immunofluorescence, Tissue Clearing and Automated Imaging

Whole organoids were fixed in 2% paraformaldehyde (20 min, 4°C) and blocked in PBS containing 10% goat serum, 0.1 M glycine and 0.5% Triton X-100 (overnight, 4°C, shaking). They were incubated in primary antibodies (**Supplementary Table S1**) diluted in PBS containing 10% goat serum, 0.1 M glycine and 0.06% Triton X-100 (3 days, 4°C, shaking). After two washes in 0.3% Triton X-100 in PBS (2 h, RT, shaking), the organoids were incubated with the appropriate secondary antibodies (**Supplementary Table S1**) diluted in PBS containing 1% goat serum, 0.1 M glycine and 0.06% Triton X-100 (3 days, 4°C, shaking). After two washes (2 h, RT, shaking), the organoids were cleared using the method of Klingberg, Hasenberg (Klingberg et al., 2017). Briefly, the organoids were dehydrated in a series of 30–100% molecular biology–grade ethanol and submerged in ethyl cinnamate (overnight, RT followed by 1 h, 37°C). Imaging was done immediately after on an automated Nikon Eclipse Ti-E with the 70 µm spinning disk in place. Imaging was automated using a Nikon JOBS tool. Briefly, a 10× air objective was used for automated detection of the organoid, while a 20× air objective with an extra-long working distance was used to image at higher resolution with a z increment size of 5 µm.

Automated Image Processing and Vessel Quantification

Immunofluorescence of VEGF-A on cryo-sections was quantified using FIJI. The FIJI default threshold was applied on the DAPI channel and the Renyi Entropy threshold on the VEGF-A channel. Next, the area of both thresholded signals was measured and the area of VEGF-A was normalized to the area of DAPI signal to correct for different sizes of sections. The results are presented as percent area.

Whole mount images were processed within a processing and quantification JOB specifically made for these samples, integrated in the NIS-Elements AR (Advance Research) (Nikon) software. In summary, background was removed using the clarify AI tool prior to the segmentation of the CD31 signal. The CD31 signal was thresholded by intensity and segmented by measuring the longest medial axis in 3D. Falsely segmented pixels, due to intense background signal, were excluded by circularity and minimal size if needed. The volume of the segmented signal was measured in 3D for the full organoid. The volume of the total organoid was measured by segmenting the organoid based on the strong background. The percentage of vascularization was determined by calculating the CD31+ cell volume as a fraction of the total organoid volume. Furthermore, the segmented CD31 signal was skeletonized to measure the cumulative and average length of all fragments in 3D. Stepwise details on the used JOB can be found in **Supplementary Figure S1**.

Statistical Analysis

All statistical analyses were performed using GraphPad Prism 9. For all immunofluorescence protein analyses, three organoids (n = 3) each arising from one of three independent organoid cultures (N = 3) were assessed. One organoid (n = 1) arising from one of three (N = 3) independent organoid cultures was quantified in 3D. For the gene expression analysis and Luminex assay, three organoids (n = 3) each arising from one of two independent organoid cultures (N = 3) were analyzed. Two organoids (n = 2), each arising from one of three independent organoid cultures (N = 3) were assessed for the darkfield measurement and oxygen measurement. Individual samples were excluded only for technical failures. For each figure, the exact N and n are reported in the figure caption. A two-way ANOVA was performed for each experiment to assess the contribution of both row (time point) and column (oxygen concentration) factors. All p-values can be found in the Results section. Statistical significance was only concluded for p-values below 0.05.

RESULTS

Macro-Morphology and Oxygen Concentrations in Normoxic and Hypoxic Organoid Culture

To replicate the *in vivo* hypoxic environment, we cultured kidney organoids in 7% O_2 and compared them to their counterparts cultured in 21% O_2 (**Graphic Abstract**). Brightfield analysis revealed no differences in macro morphology, density or size until day 7 + 25 (**Graphic Abstract**, **Supplementary Figure S2**). Darkfield imaging was performed to assess the shape and thickness of the organoids (**Graphic Abstract**). No statistically significant differences in thickness were found comparing organoids cultured in normoxia and hypoxia (p = 0.839; **Graphic Abstract**).

To quantify the oxygen concentration, we inserted an optical microsensor into the bottom of the organoid (close to the filter). In normoxia, the lowest oxygen concentration we measured was 7.53 ± 1.47% on day 7 + 18, which significantly decreased to 2.15 ± 0.66% by day 7 + 25 (p < 0.0001). This value at day 7 + 25 was not significantly different from the oxygen concentration measured in the organoids cultured in hypoxia on day 7 + 18 (1.28 ± 0.76%; p = 0.439) or day 7 + 25 (1.00 ± 0.21%; p = 0.211) (**Graphic Abstract**).

To investigate whether the organoids had a hypoxic core, we imaged living organoids and cryosections at the center of the

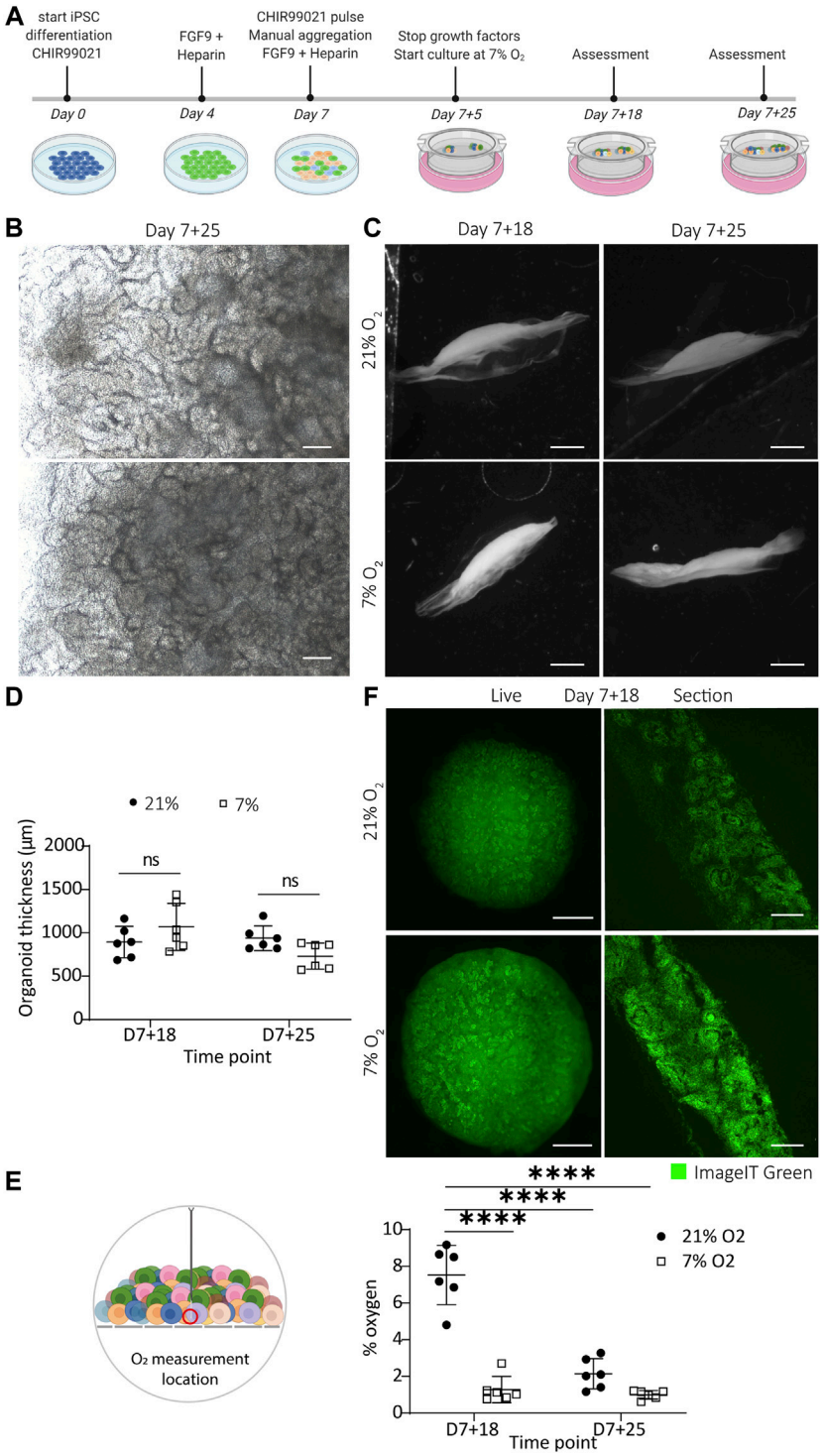

FIGURE 1 | Kidney organoids cultured in uterine-like hypoxic environment structurally form like their normoxic counterparts without the appearance of a hypoxic core. **(A)**. Schematic representation of the iPSC differentiation and organoid culture. Human iPSCs are differentiated for 7 days, after which aggregates are spotted on the air–liquid interface and cultured as organoids for up to 25 additional days (termed day 7 + 25). **(B)**. Brightfield images display comparable morphologies of the organoids cultured in 7 and 21% O_2 at the culture endpoint day 7 + 25. Scale bar: 200 µm. **(C)**. Darkfield images show that the macro-anatomy of the organoids is comparable in both oxygen concentrations. Scale bar: 2 mm. **(D)**. Quantification of the organoid thickness from the darkfield images shows no difference between 21% O_2 and 7% O_2. ($n = 2$, $N = 3$). **(E)**. Oxygen measurement in the bottom part of the organoids towards the transwell filter shows that organoids in 7% oxygen have a comparable oxygen concentration to their normoxic counterparts at day 7 + 25, which is significantly lower compared to the normoxic condition at day 7 + 18. ($n = 2$, $N = 3$; **** = $p \leq 0.0001$) **(F)**. Organoids (left column) and cryosections of their central core (right column) stained on day 7 + 18 with the hypoxia dye ImageIT Green that produces a fluorescent signal below 5% O_2. The organoids display no hypoxic core but the dye stains all nephrons. Scale bar "live": 1 mm, scale bar "section": 100 µm.

organoids with a hypoxia dye (ImageIT Green) (**Graphic Abstract**). The cryosections, cut through the center of the organoids, revealed a higher intensity (meaning lower O_2) in hypoxia. We saw the dye localized largely to nephron structures and less to the surrounding stroma. We did not see evidence of a hypoxic core in the center of any organoids.

Next, we explored if culture in hypoxia would affect the differentiation and organization of various cell types in the kidney organoids. To assess this, we stained vertically cut cryosections throughout the whole organoids for well-established markers to label the major cell types found in kidney organoids. We found no differences in either the presence of the cell types or their organization into proximal tubules (LTL), distal tubules (ECAD), loop of Henle (SLC12A1) or glomeruli (NPHS1-positive podocytes) (**Figures 2A,B**).

Nephrons Express Varied Levels of Nuclear HIF1α and a Constant Nuclear Expression of HIF2α

Nuclear HIF translocation during kidney development is crucial for nephrogenesis and angiogenesis. We investigated which cells showed responsiveness to hypoxia in terms of nuclear translocation of HIF1α and HIF2α. For this, we performed immunofluorescence staining of HIF1α and HIF2α on vertically cut cryosections throughout the whole kidney organoids at days 7 + 18 and 7 + 25 (**Figure 3**). Qualitative analysis showed that HIF1α was differentially expressed in hypoxia and normoxia (**Figure 3A**). At day 7 + 25, particularly the podocytes had more nuclear translocation in both normoxia and hypoxia compared to other cell types. Furthermore, in normoxia, podocytes at the bottom of the organoid, towards the medium interface, expressed nuclear HIF1α, while in hypoxia this was seen in podocytes throughout the whole organoid. In all conditions and time points, interstitial cells and most tubules did not express nuclear HIF1α. HIF2α was expressed in the nuclei of all cells of the kidney organoids at days 7 + 18 and 7 + 25 (**Figure 3B**). Particularly the interstitial cells had heterogeneous expression. We did not detect differences between organoids cultured in normoxia or hypoxia in terms of HIF2α nuclear translocation.

VEGF-A Protein Expression in Proximal Tubules

VEGF-A is a major angiogenic factor primarily produced in distal tubules, collecting duct and podocytes. (Freeburg et al., 2003) It is regulated by hypoxia by the binding of nuclear, dimerized HIFs to the HRE promotor. We performed immunofluorescence on vertically cut cryosections throughout whole organoids to determine if there was a difference in expression between normoxia- and hypoxia-cultured organoids (**Figure 4A**), and which cell types expressed VEGF-A (**Figure 4B**). We found expression on the apical side of some tubular structures, mainly in normoxia and to a lesser extent in hypoxia (**Figures 4A,B**). VEGF-A was significantly less expressed in hypoxia compared to normoxia at both time points (p = 0.02 at d7+18, p = 0.013 at d7+25), but there was no difference between the two time points (p = 0.362 in normoxia, p = 0.461 in hypoxia) (**Figure 4D**). The VEGF-A+ tubules in both normoxia and hypoxia co-expressed both SLC12A1 marking the loop of Henle (thick ascending limb) and LTL marking proximal tubules (**Figure 4B**). We validated this co-

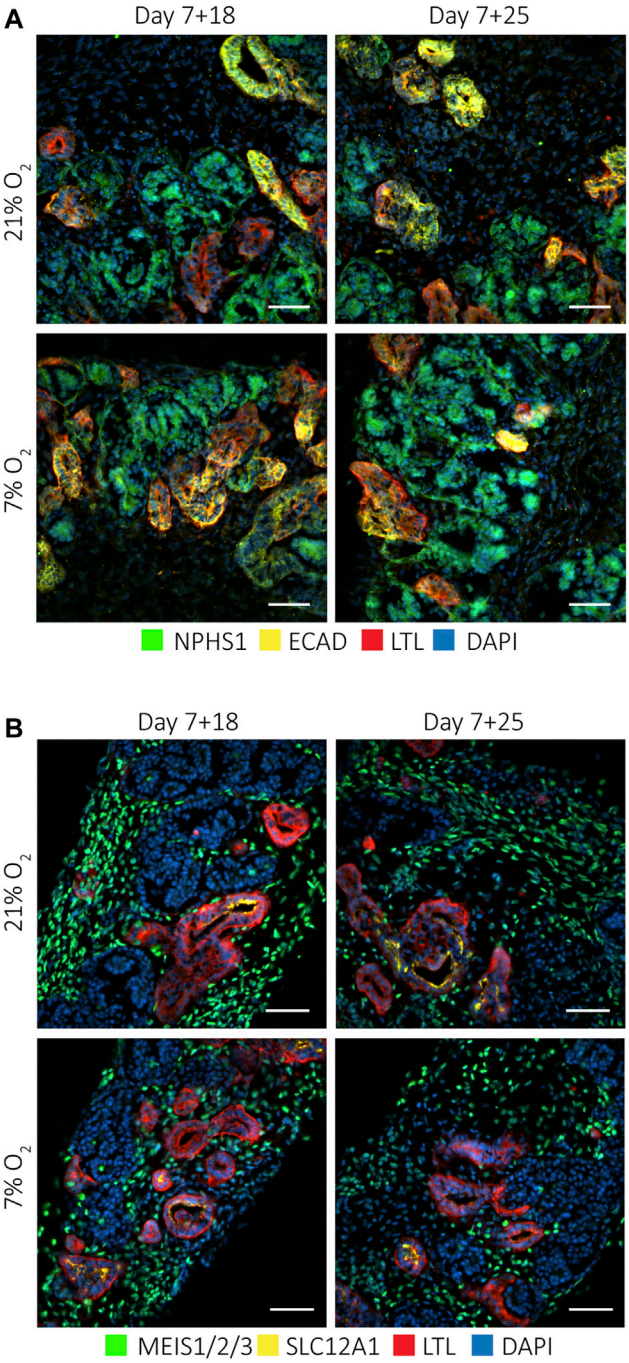

FIGURE 2 | Kidney organoids cultured at 7 and 21% O_2 develop the same cell types. Immunofluorescence staining for **(A)**. podocytes (NPHS1; green), proximal tubules (LTL; red) and distal tubules (ECAD; yellow) and nuclei (DAPI; blue), and **(B)**. interstitial cells (MEIS1/2/3; green), loop of Henle (SLC12A1; yellow) and proximal tubules (LTL; red), showed these different cell types in all conditions. (n = 3, N = 3). Scale bars: 50 μm.

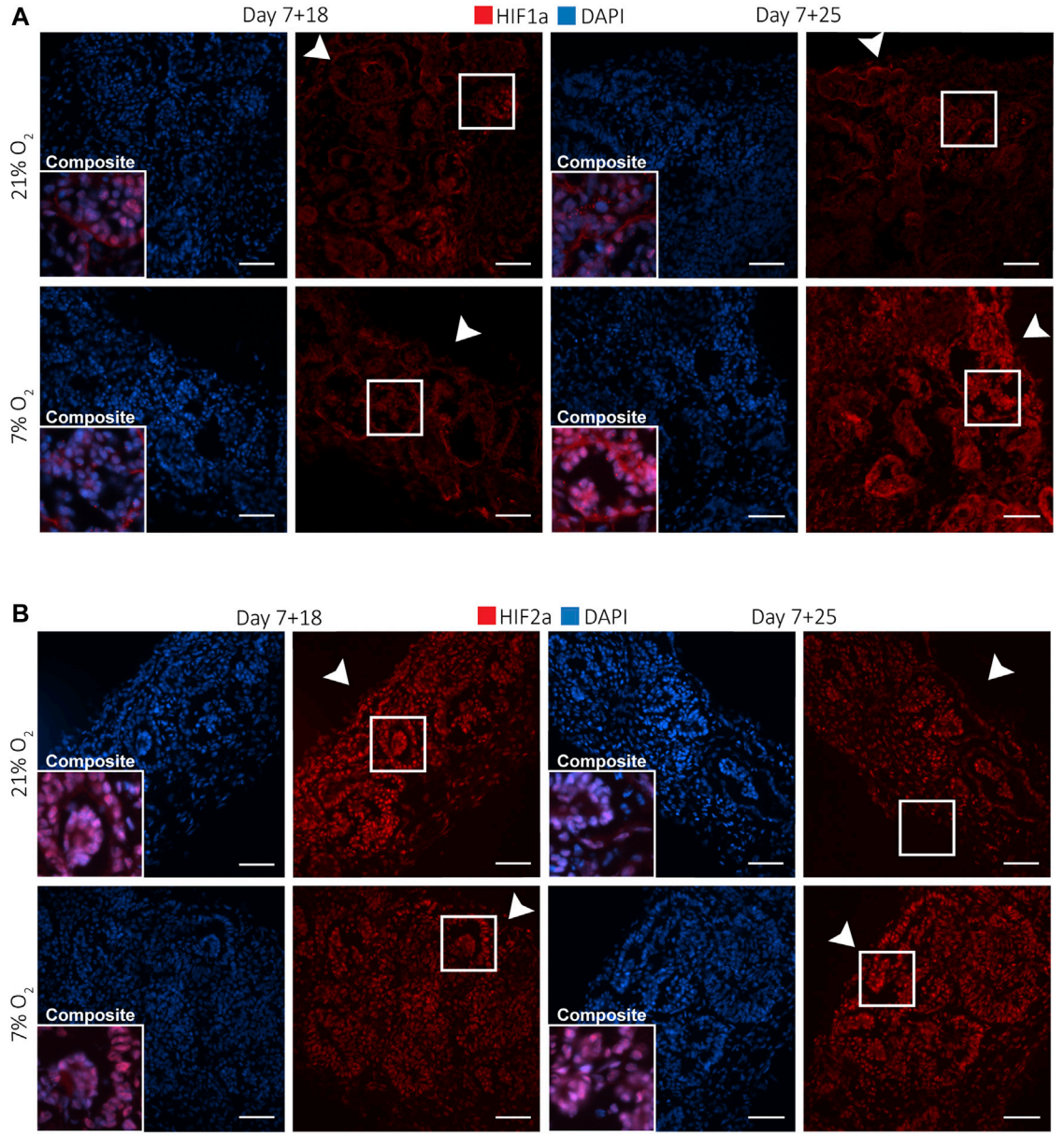

FIGURE 3 | Kidney organoids cultured in both 7 and 21% O_2 show differential nuclear translocation of HIF1a and HIF2a. **(A)**. Immunofluorescence staining for HIF1a (red) and DAPI (blue) shows increased nuclear translocation in podocytes (composite), particularly in 7% O_2 at day 7 + 25. Scale bar: 50 µm. **(B)**. HIF2a (red) and DAPI (blue) immunofluorescence staining shows nuclear translocation in most cells within the organoid irrespective of the oxygen concentration or time point. ($n = 3$, $N = 3$). Scale bar: 50 µm. Arrowheads indicate the (air-exposed) surface of the organoids.

expression of SLC12A1, LTL and VEGF-A on adult kidney sections and in scRNA sequencing datasets of organoids (**Supplementary Figure S3**). Glomerular expression of VEGF-A in the normoxia and hypoxia organoids rarely found. We hypothesized that the lower VEGF-A expression in the proximal tubules in hypoxia could be due to a switch to a more soluble VEGF-A isoform or that the time point of secretion would be different. Therefore, soluble VEGF-A was measured using a Luminex assay validated for the VEGF-A165 isoform in the culture medium on days 7 + 7, 7 + 12, 7 + 17, 7 + 21, 7 + 24 (**Figure 4C**). There was an increase over time from day 7 + 7 until 7 + 17 for organoids in both hypoxia and normoxia. After day 7 + 17, the soluble VEGF-A decreased until day 7 + 21. There was no significant difference between organoids in normoxia or hypoxia ($p = 0.544$). The protein expression of the antiangiogenic isoform VEGF-A165b normalized to GAPDH expression was determined by Western blot (**Figure 4E**, **Supplementary Figure S4**). VEGF-A165b was significantly upregulated in normoxia from day 7 + 18 to day 7 + 25 ($p = 0.003$), while there was a significant reduction in hypoxia compared to normoxia at day 7 + 25 ($p = 0.001$).

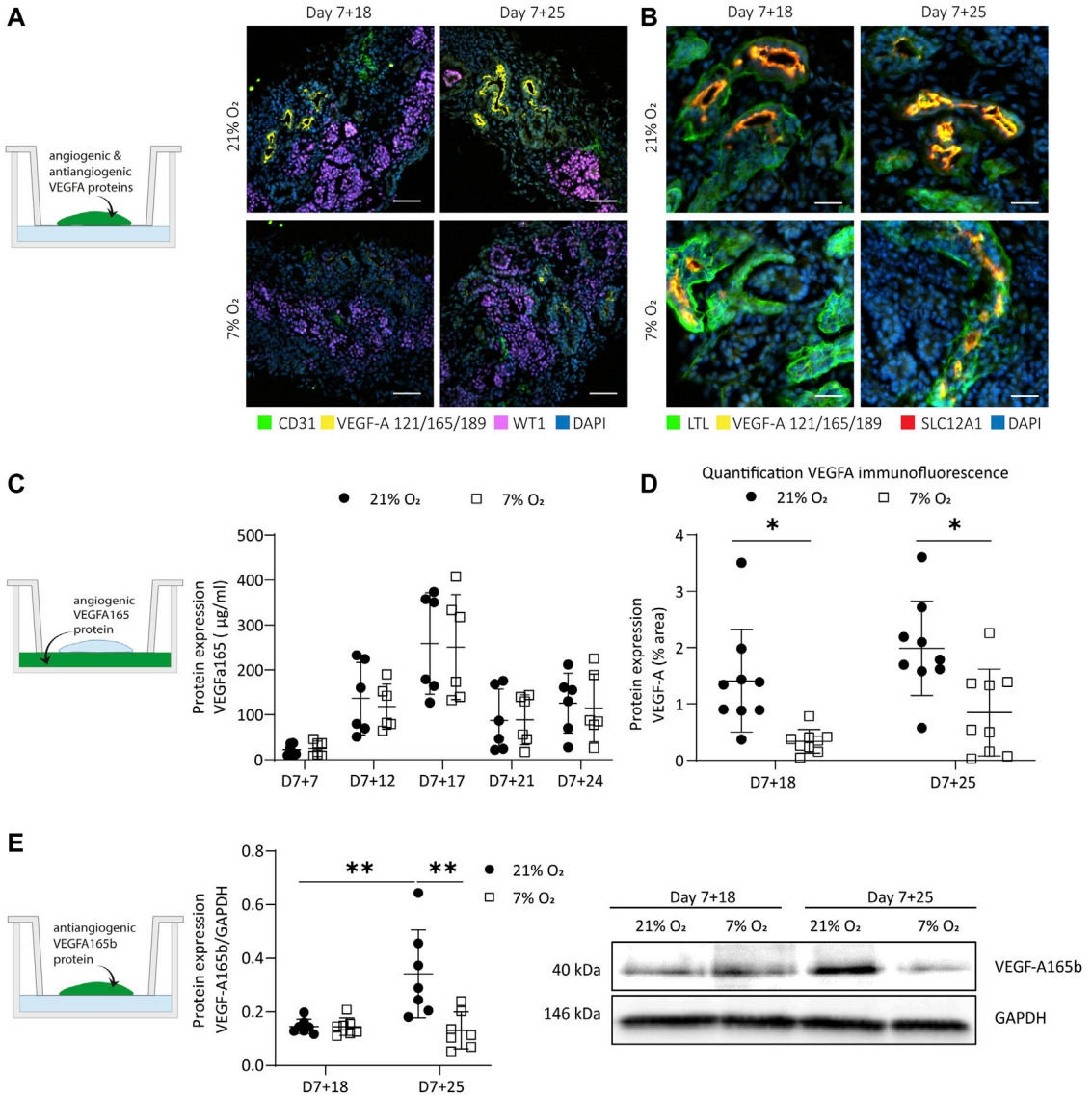

FIGURE 4 | Expression of hypoxia-responsive VEGF-A in organoids cultured in 21 and 7% O_2. **(A)**. Immunofluorescence for VEGF-A (121, 165, 189 isoforms; yellow), endothelial cells (CD31; green), podocytes (WT1; magenta) and nuclei (DAPI; blue) displays a reduction of VEGF-A in 7% O_2 compared to 21% O_2 at both day 7 + 18 and day 7 + 25. (n = 3, N = 3). Scale bar: 50 µm. **(B)**. Immunofluorescence shows localization of VEGF-A to the apical side of proximal tubules co-positive for loop of Henle marker (SLC12A1; red). (n = 3, N = 3). Scale bar: 25 µm. **(C)**. VEGF-A165 protein expression measured in the culture medium was differentially expressed over time, but not significantly different in hypoxia compared to normoxia. (n = 3, N = 2). **(D)**. Quantification of immunofluorescence images confirm that VEGF-A was significantly lower expressed in hypoxia compared to normoxia. (n = 3, N = 3) **(E)**. The anti-angiogenic VEGF-A165b isoform was significantly upregulated over time in normoxia and significantly downregulated in hypoxia compared to normoxia at day 7 + 25. (n = 2, N = 3). *= $p \leq 0.02$, ** = $p < 0.003$.

Differential Expression of Angiogenesis-Regulating Genes in Hypoxic Culture

VEGF-A is known to exist in various splice variants with distinct biological functions. *VEGF-A165* is the most prominent variant, followed by *189* and *121* in the adult human kidney. (Vempati et al., 2014) We investigated *VEGF-A* variant expression in the organoids by quantitative polymerase chain reaction (qPCR). VEGF-A189 was significantly higher in hypoxia cultures than in normoxia, with a 1.8 fold-change (FC) at day 7+18 ($p = 0.001$) and 1.9 fold-change at day 7+25 ($p = 0.032$) relative to the control samples expression (day 7+18 normoxia) (**Figure 5A**). VEGF-A165 was significantly upregulated at day 7+18 relative to the control samples (FC = 2.06; $p = 0.0014$), but there was no significant difference between organoids in normoxia or hypoxia at day 7+25 (**Figure 5B**). VEGF-A121 was significantly upregulated in hypoxia compared to normoxia at both day 7+18 (FC: 1.49; $p = 0.0004$) and day 7+25 (FC: 1.617; $p = 0.002$) (**Figure 5C**). The ANOVA main effect analysis showed that time did have a limited effect on the

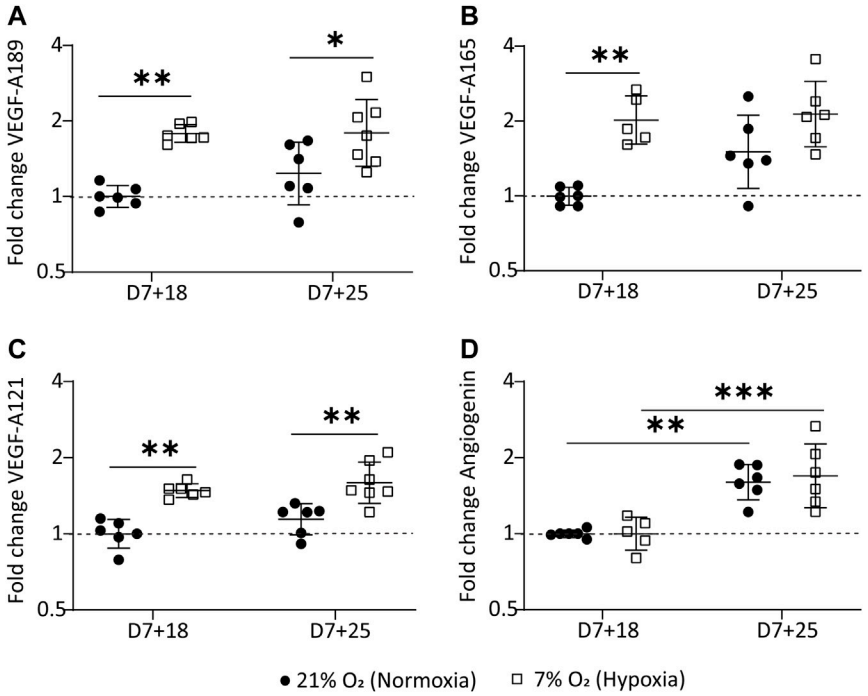

FIGURE 5 | Hypoxic organoid culture differentially regulates VEGF-A variants. **(A)**. VEGF-189 is significantly upregulated at both time points in the hypoxic culture. **(B)**. VEGF-A165 is significantly upregulated at day 7+18 in the hypoxic culture and **(C)**. VEGF-121 is significantly upregulated at both time points in the hypoxic culture. **(D)**. Angiogenin mRNA is significantly upregulated over time in both the normoxic and hypoxic culture. The data is plotted relative to day 7+18 normoxia (n=3, N=3 with excluded technical failures). *= $p \leq 0.03$, ** = $p \leq 0.002$, *** = $p \leq 0.0004$.

observed differences in VEGF-A variant expression (VEGF-A189: $p = 0.243$; VEGF-A121: $p = 0.085$; VEGF-A165: $p = 0.047$) and could largely be attributed to the hypoxic culture (VEGF-A189: $p < 0.0001$; VEGF-A121: $p < 0.0001$; VEGF-A165: $p = 0.0001$).

We also determined mRNA expression of *ANG*, the gene encoding angiogenin, another hypoxia-regulated angiogenic factor, in our kidney organoid culture. *ANG* mRNA was significantly upregulated over time ($p < 0.0001$) but with no differences between hypoxia and normoxia cultures (**Figure 5D**).

Hypoxia-Induced Angiogenesis: Homogenous Micro-vessel Formation and Sprouting

Hypoxia is well known to enhance angiogenesis in both development and pathologies. (Otrock et al., 2007) In both, endothelial cells undergo sprouting to form new blood vessels. In the normoxia culture, endothelial cells largely reside on the surface of the organoids and are therefore directly exposed to the non-physiological oxygen concentrations (**Supplementary Figure S5**). We investigated the effect of hypoxia on the endothelial patterning by whole mount immunostaining with the endothelial marker CD31. Whole mount imaging and quantification in 3D revealed enhanced micro-vessel formation with more homogenous morphology, enhanced branching and sprouting in organoids cultured in hypoxia compared to normoxia (**Figures 6A,C**). We observed a reduced intensity of CD31 (not quantified) in hypoxia and normoxia at day 7 + 25 (**Figure 6B**). However, the endothelial phenotype was maintained, as confirmed by co-expression of CD31 and VE-cadherin in both normoxia- and hypoxia-cultured organoids at day 7 + 25 (**Supplementary Figure S6**). We set up an automatic 3D segmentation and quantification pipeline and found that hypoxia induced a significant increase in the fraction of endothelial cells of the total organoid volume (40.3 ± 12.50%) compared to normoxia (14.3 ± 2.60%) ($p = 0.019$; **Figure 6E**) at day 7 + 18 that was not observed at day 7 + 25 ($p = 0.318$). Interestingly, the average vessel length was significantly higher in hypoxia compared to normoxia at day 7 + 25 (hypoxia: 170 ± 26 μm; normoxia: 97 ± 11 μm; $p = 0.014$) (**Figure 6D**). There was no significant difference at D7+18 ($p = 0.068$). Three-dimensional segmentation additionally revealed that the endothelial network in organoids cultured in normoxia largely resided in a two-dimensional plane (parallel to the transwell), while in hypoxia culture, the network was mainly interconnected in three dimensions (Supplementary video 1 and 2).

DISCUSSION

Our aim was to investigate if a lower oxygen concentration applied to the kidney organoid culture that mimics the *in vivo* hypoxic environment during nephrogenesis could improve

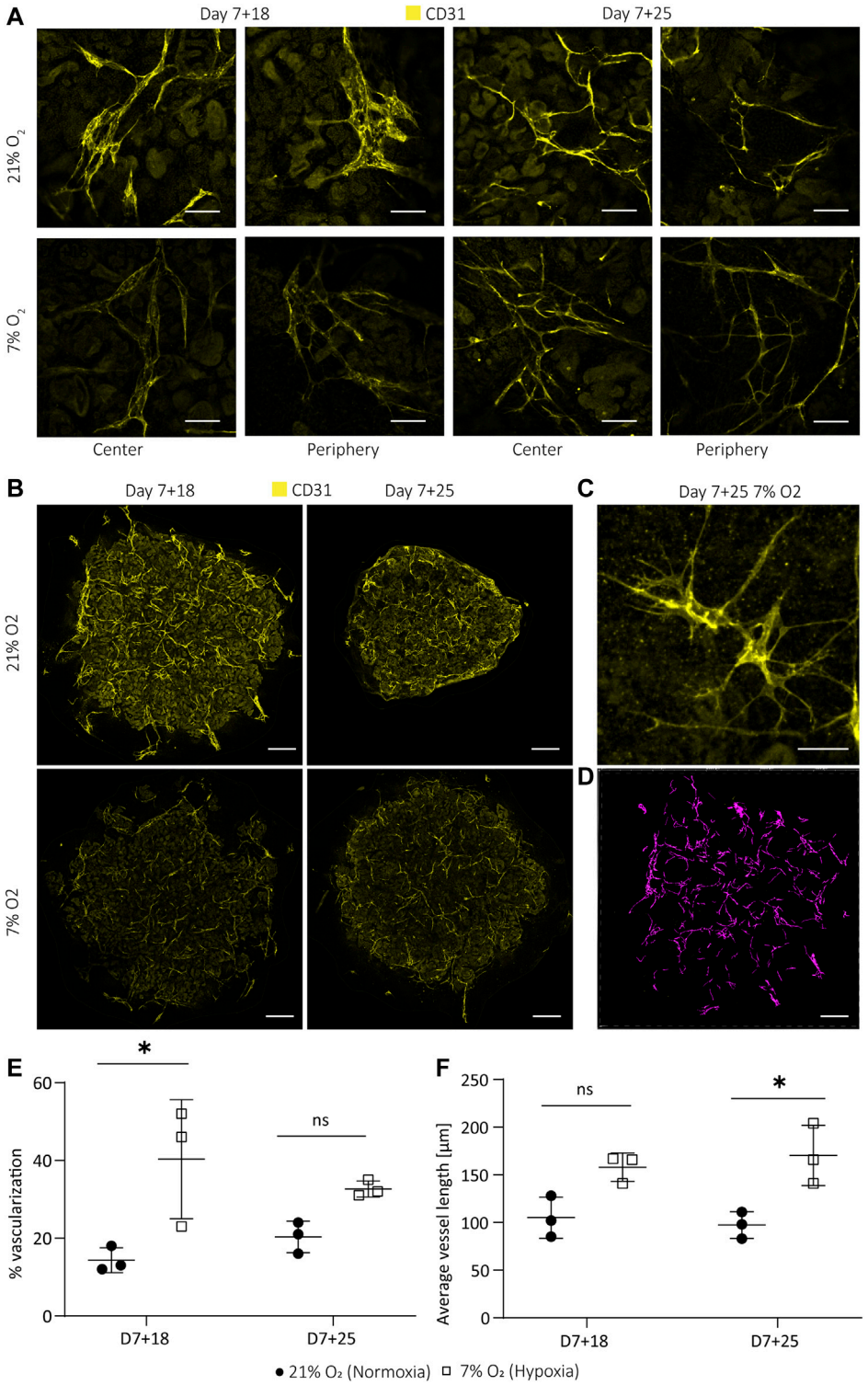

FIGURE 6 | Hypoxic organoid culture promotes interconnected microvasculature formation and sprouting. **(A)**. The endothelial network (CD31; yellow) has a more homogeneous morphology and enhanced interconnectivity and branching in organoids cultured in 7% O_2. **(B)**. Z-intensity projected images of whole mount imaged organoids show less intense CD31 staining, likely due to smaller vessel size. **(C)**. Hypoxia-induced sprouting of endothelial vessels at day 7 + 25. **(D)**. Example of 3D segmentation of endothelial network of a day 7 + 18 normoxia organoid. Scale bars: 50 µm **(A,C)**; 600 µm **(B,D)**. Quantification in 3D reveals **(E)**. an increase in the volume fraction of endothelial cells at day 7 + 18 in hypoxia and **(F)**. an increased average vessel length in hypoxia compared to normoxia at D7+25. ($n = 1$, $N = 3$). * = $p \leq 0.019$.

angiogenesis and organoid vascularization. The mRNA expression of endothelial markers (*CD31*, *KDR*) in the normoxic culture was downregulated over time (**Supplementary Figure S7**), indicating the need for stimuli to activate angiogenesis. We opted for a long-term hypoxic culture (20 days), because long-term hypoxia (hours to days, depending on the model) enhances the expression of angiogenic cytokines and growth factors such as PDGF and VEGF in comparison to acute hypoxia that is known to activate the release of inflammatory factors. (Michiels et al., 2000; Haddad and Harb, 2005) VEGF-A in particular is known to be crucial for endothelial cell differentiation, proliferation and migration (Abhinand et al., 2016), as well as glomerular capillary formation, podocyte survival and slit diaphragm integrity in autocrine podocyte signaling. (Guan et al., 2006) We therefore included VEGF-A mRNA and protein expression in our investigations.

Kidney organoids developed similarly in normoxic and hypoxic conditions. The hypoxic culture did not impair nephron specification and organization, nor organoid size (**Figures 1B,C**, **Figures 2A,B**), indicating that hypoxia did not interfere with normal organoid development. Our measurements of oxygen concentration on the bottom of the organoid culture plate (1.0 ± 0.21% in hypoxia on day 7 + 25) were lower compared to the poorly vascularized medullas in adults (1.9% O_2 at atmospheric pressure derived from the measured 15 mmHg). (Keeley and Mann, 2019) We therefore expected our hypoxic culture to more closely resemble avascular, hypoxic kidneys during early development, although *in vivo* data are still lacking. (Freeburg and Abrahamson, 2003) This similarity indicates that growing organoids at 7% O_2 could mimic the *in vivo* hypoxic environment and help study organoid maturation in a more physiological model.

In addition to oxygen levels, we found a similar transcriptional program activated in the kidney organoids as in the developing human kidney. Specifically, severe hypoxia and consequently HIF stabilization was found to be essential in nephrogenesis (41), with HIF-1α expressed in cortical and medullary collecting duct, nephrogenic zone and glomerular cells. (Bernhardt et al., 2006) While the collecting duct lineage does not exist in the organoids, podocytes deeper within the organoid, showed nuclear HIF-1α expression at day 7 + 18 in normoxia (**Figure 3A**). According to our measurements, these podocytes would reside in regions close to 7.53 ± 1.47% O_2. Likely, only podocytes experiencing less than 5% O_2 showed nuclear translocation of HIF-1α. (Hemker et al., 2016) Indeed, even peripheral podocytes of the hypoxia-cultured organoids, where the oxygen concentration was 1.0 ± 0.21% at the bottom of the organoids, showed nuclear HIF-1α translocation (**Figure 3A**). While certainly not all podocytes responded by nuclear HIF-1α translocation, the hypoxic culture clearly induces nuclear HIF-1α in podocytes throughout the organoids.

Comparable to HIF-1α, nuclear HIF-2α is important to *in vivo* kidney development, where it is known to be expressed only in interstitial cells and podocytes (13), as shown in week 14 fetal kidneys (33), as well as in developing tubules in newborns (41). In our kidney organoids, HIF-2α expression was not limited to interstitial cells and podocytes, but was expressed in all cell types examined in both hypoxia and normoxia (**Figure 3B**). There were clear differences in intensity of nuclear HIF-2α in interstitial cells within the organoids in normoxia and hypoxia, while the nephrons equally expressed nuclear HIF-2α. The reason for this observed difference is unclear. Clarification is also needed for why all interstitial cells, even in the most oxygenated condition (day 7 + 18 normoxia), do express nuclear HIF-2α. There is a need for further investigation, since recent findings in mice suggest that chronic HIF-2α expression in stromal progenitors impairs kidney development, in particular nephron formation, tubular maturation, and the differentiation of FOXD1+ stromal cells into smooth muscle, renin, and mesangial cells. (Gerl et al., 2017) This was found to be regulated by the inhibition of PhD2 and PhD3. (Kobayashi et al., 2017) The fact that the organoids do not mature further and mesangial cells and renin cells are thought to be absent in this kidney organoid model (Yousef Yengej et al., 2020), could indicate impaired *in vitro* differentiation of FOXD1+ progenitor cells. Therefore, future research could investigate the role of HIF-2α nuclear translocation in this context.

In vivo, pericytes derived from FOXD1+ progenitors are known to show HIF-2α nuclear translocation that induces EPO production. However, in our organoids, HIF-2α nuclear translocation did not induce EPO mRNA transcription in either normoxia or hypoxia (**Supplementary Figure S8**). The fact that EPO was not transcribed in the organoids in normoxia and hypoxia could potentially be due to a fibrotic stromal population found in the organoids (Li et al., 2004; Jagannathan et al., 2016) and subsequent hyper-methylation of the EPO 5' and HRE, inhibiting HIF2/HIFβ dimer binding, as found in adult fibrotic kidneys (Shih et al., 2018). Future research could clarify mechanistically, if nuclear HIF-2α is actually leading to target gene transcriptions or if this is inhibited, consequently being one reason for limited organoid maturation. (Gerl et al., 2017)

As with HIF-2α expression, we found differences in the expression of VEGF-A in our kidney organoids compared to fetal human developing kidneys. Comparing the normoxic and hypoxic organoid culture, a decrease in VEGF-A protein expression could be seen. VEGF-A, being one of the most important angiogenic factors, is known for its function in nephrogenesis to induce blood vessel formation in glomeruli through branching angiogenesis and consequently to induce maturation of glomerular cells. (Kim et al., 2002) In fetal human developing kidneys, VEGF-A is expressed in the epithelial cells in the s-shaped body and collecting duct. (Tufró, 2000) Later in nephrogenesis, VEGF-A uptake by convoluted tubules has been observed. (Bevan et al., 2008) In the organoids, VEGF-A was localized on the apical side of LTL+ proximal tubules, co-expressing the LoH marker SLC12A1. We rarely detected expression in podocytes, which is needed to initiate the formation of glomerular capillaries. (Eremina and Quaggin, 2004) Consequently, glomeruli containing endothelial cells is a rare event in the organoids. The amount of VEGF-A expression differed between differentiations. However, VEGF-A was reliably less expressed in hypoxia. The location of VEGF-A at the

apical side of SCL12A1+ tubules remained the same in hypoxia (**Figure 4** A–B, D). We hypothesized that there could be differences in the VEGF-A isoform and transcript variant expression, which could remain hidden by targeting three isoforms with the same antibody as performed in **Figures 4A,B**. *In vivo*, podocytes are the main source of VEGF-A and synthesize three VEGF-A isoforms (VEGF-A-121, VEGF-A-165, VEGF-A-189) by alternative mRNA splicing. (Guan et al., 2006)

VEGF-A variants were differentially expressed in the organoids in hypoxia (**Figures 5A–C**), consistent with previous studies. (Farina et al., 2020) *VEGF-A189* was significantly upregulated in organoids cultured in hypoxia, which is associated with microvessel formation (Li et al., 2004; Jagannathan et al., 2016) and enhanced migration of endothelial cells (Dahan et al., 2021). Being positively charged in some domains, encoded for by exons 6a, 6b and 7, VEGF-A189 binds negatively charged extracellular matrix and heparan sulphate proteoglycans on cell surfaces, remaining spatially localized and becomes biologically active upon mobilization by heparinase. (Cébe Suarez et al., 2006; Roodink et al., 2006) This allows the attraction of vessels into hypoxic tissue. Enhanced cell migration is also confirmed in a variety of cell lines cultured at 0.5% O_2 and modified to overexpress VEGF-A189. (Salton et al., 2014). In contrast to VEGF-189, VEGF-A121 lacks both exon 6 and 7 and is therefore a readily diffusible, active isoform. Hypoxia-induced pro-angiogenic VEGF-A gene alternative splicing is also known for the VEGF-A121 and VEGF-A165 variants (Farina et al., 2020). Their upregulation in the hypoxic culture could indicate an overall higher availability of the three isoforms throughout the organoid. While we could not prove the localization of these isoforms in the organoids due to unavailability of isoform-specific antibodies, we did find an improved patterning of the endothelial network in hypoxia compared to normoxia. Microvessels were homogenously sprouting (**Figures 6A–C**) with larger vessel length (**Figure 6F**) and larger connectivity in 3D (Supplementary video 1 and 2) in hypoxia. In normoxia, there was comparatively less connectivity, hetereogenous vessel morphologies and planar growth.

The VEGF-A165b isoform was downregulated in hypoxia compared to normoxia (**Figure 4E**). VEGF-A165b is a low efficacy agonist, binding VEGFR2 with a stronger affinity and thereby reducing binding of VEGF-A165, resulting in strongly decreased signal transduction via the VEGFR2 receptor. (Peach et al., 2018; Mamer et al., 2020) VEGF-A165b is upregulated in quiescent vessels and in adult kidneys (Li et al., 2004; Jagannathan et al., 2016), inhibiting endothelial cell migration (Li et al., 2004; Jagannathan et al., 2016), and is downregulated in nephrogenesis during capillary loop formation (Bevan et al., 2008; Stolz and Sims-Lucas, 2015). Downregulation of the VEGF-A165b isoform in hypoxia at day 7 + 25 could indicate increased binding of VEGF-A165 to the VEGFR2 receptor, enhanced signal transduction and consequently the initiation of angiogenesis. Earlier research confirms the phosphorylation of SRSF1 splice factor by hypoxia targeting the exon 8a proximal splice site, leading to the expression of angiogenic VEGF-A isoforms. (Farina et al., 2020) While the increased vessel sprouting observed in the hypoxia-cultured organoids is an indication of angiogenesis (Tahergorabi and Khazaei, 2012) (**Figures 6A–C**), more research is needed to prove causality with the downregulated VEGF-A165b isoform. Furthermore, to our knowledge, alternative splicing of VEGF-A in non-pathological developmental angiogenesis is insufficiently studied and would be highly valuable in the context of organoid vascularization and maturation. Finally, *in vivo* glomerular maturation is VEGF-A dose dependent, however, it is only hypothesized that the antiangiogenic isoforms have a dose dependent effect in glomerulogenesis as well. (Bevan et al., 2008).

The results of our study show that modulation of the oxygen concentrations in kidney organoid culture can improve the patterning of endothelial cells and therefore is potentially a relevant factor to integrate in regular organoid culture. Sprouting and interconnected vessels in hypoxia indicated the activation of angiogenesis, which is important for further nephron maturation. Future research is, however, needed to confirm the mechanism by which this enhanced patterning of the endothelial network takes place and to elucidate the roles of the different VEGF-A isoforms. This understanding will help to further enhance the endothelial network in kidney organoids and can potentially be applied to other systems as well. An important challenge in this context will be to understand the batch variations in VEGFA expression and number of endothelial cells in the organoids. Furthermore, we hypothesize that a culture in a hypoxic chamber could be a more controlled environment to study the effects of a hypoxic culture on organoid development. This setup would allow medium changes at the desired hypoxia instead of at ambient oxygen concentrations and would consequently avoid repeated reoxygenation of the organoids. Future research could investigate the effects of hypoxia on nephrons beyond structural development and cell type specific marker expression, such as mitochondrial functionality and cell type specific changes in metabolism. Ideal would be a comparison of the transcriptome of fetal human kidneys with organoids in different oxygen concentrations. Finally, it remains to be determined how VEGF-A expression by podocytes can be increased to allow vascularization and maturation of glomeruli.

CONCLUSION

In conclusion, kidney organoid culture in physiological hypoxia induced the formation of a homogenous and interconnected endothelial network, while maintaining renal cell types and their spatial organization. We found that VEGF-A189, VEGF-A165 and VEGF-A121 mRNA is upregulated in hypoxia. At day 7+25 VEGF-A165 is no longer upregulated. Protein expression analysis of the antiangiogenic VEGF-A165b isoform confirmed significant downregulation in hypoxia at day 7+25, being a

potential reason for the enhanced endothelial sprouting. While further vessel maturation, i.e., tube formation and glomerular vascularization, are still unresolved, we believe that culture in physiological hypoxia is an important driving force for organoid vascularization and is translatable to other organoid models in a model-specific manner.

DATA AVAILABILITY STATEMENT

All data generated for this article, including high resolution **Supplementary Videos**, was made publicly available for download from https://doi.org/10.34894/KMRJPD.

AUTHOR CONTRIBUTIONS

AS conceived the idea, designed the experiments, analyzed the experimental data and wrote the manuscript. AS and NR performed most experiments. TR developed the automated imaging and image analysis pipeline. VJ contributed to experimental ideas. VJ and ME provided some experimental data. MvG and VL supervised the research and revised the manuscript. VL funded the research. All authors contributed to the final paper and agreed to the published version.

ACKNOWLEDGMENTS

The authors wish to thank the Physiology department at the Maastricht University for the opportunity to use their hypoxia incubator and Hang Nguyen for reviewing this manuscript. Furthermore, the authors would like to thank Carlos Julio Peniche Silva and Daniel Carvalho from the MERLN Institute for initial support with the oxygen measurements, Sven Hildebrand from Cognitive Neuroscience at Maastricht University for vivid discussions on tissue clearing and Jasmin Dehnen for the support with designing variant-specific primer pairs. **Figure 1A** was created with BioRender.com.

SUPPLEMENTARY MATERIAL

The Supplementary Material for this article can be found online at: https://www.frontiersin.org/articles/10.3389/fbioe.2022.860138/full#supplementary-material

REFERENCES

Abhinand, C. S., Raju, R., Soumya, S. J., Arya, P. S., and Sudhakaran, P. R. (2016). VEGF-A/VEGFR2 Signaling Network in Endothelial Cells Relevant to Angiogenesis. *J. Cell Commun. Signal.* 10 (4), 347–354. doi:10.1007/s12079-016-0352-8

Bekhite, M. M., Finkensieper, A., Rebhan, J., Huse, S., Schultze-Mosgau, S., Figulla, H.-R., et al. (2014). Hypoxia, Leptin, and Vascular Endothelial Growth Factor Stimulate Vascular Endothelial Cell Differentiation of Human Adipose Tissue-Derived Stem Cells. *Stem Cells Dev.* 23 (4), 333–351. doi:10.1089/scd.2013.0268

Bernhardt, W. M., Schmitt, R., Rosenberger, C., Münchenhagen, P. M., Gröne, H.-J., Frei, U., et al. (2006). Expression of Hypoxia-Inducible Transcription Factors in Developing Human and Rat Kidneys. *Kidney Int.* 69 (1), 114–122. doi:10.1038/sj.ki.5000062

Bevan, H. S., van den Akker, N. M. S., Qiu, Y., Polman, J. A. E., Foster, R. R., Yem, J., et al. (2008). The Alternatively Spliced Anti-Angiogenic Family of VEGF Isoforms VEGFxxxb in Human Kidney Development. *Nephron Physiol.* 110 (4), p57–p67. doi:10.1159/000177614

Brueckl, C., Kaestle, S., Kerem, A., Habazettl, H., Krombach, F., Kuppe, H., et al. (2006). Hyperoxia-Induced Reactive Oxygen Species Formation in Pulmonary Capillary Endothelial CellsIn Situ. *Am. J. Respir. Cell Mol. Biol.* 34 (4), 453–463. doi:10.1165/rcmb.2005-0223oc

Buchholz, B., Schley, G., and Eckardt, K.-U. (2016). The Impact of Hypoxia on Nephrogenesis. *Curr. Opin. Nephrol. Hypertens.* 25 (3), 180–186. doi:10.1097/mnh.0000000000000211

Cébe Suarez, S., Pieren, M., Cariolato, L., Arn, S., Hoffmann, U., Bogucki, A., et al. (2006). A VEGF-A Splice Variant Defective for Heparan Sulfate and Neuropilin-1 Binding Shows Attenuated Signaling Through VEGFR-2. *Cell. Mol. Life Sci.* 63 (17), 2067–2077. doi:10.1007/s00018-006-6254-9

Dahan, S., Sharma, A., Cohen, K., Baker, M., Taqatqa, N., Bentata, M., et al. (2021). VEGFA's Distal Enhancer Regulates its Alternative Splicing in CML. *Nar Cancer* 3 (3), zcab029. doi:10.1093/narcan/zcab029

Ding, B., Sun, G., Liu, S., Peng, E., Wan, M., Chen, L., et al. (2020). Three-Dimensional Renal Organoids from Whole Kidney Cells: Generation, Optimization, and Potential Application in Nephrotoxicology *In Vitro*. *Cell Transpl.* 29, 963689719897066. doi:10.1177/0963689719897066

Eremina, V., and Quaggin, S. E. (2004). The Role of VEGF-A in Glomerular Development and Function. *Curr. Opin. Nephrol. Hypertens.* 13 (1), 9–15. doi:10.1097/00041552-200401000-00002

Fajersztajn, L., and Veras, M. M. (2017). Hypoxia: From Placental Development to Fetal Programming. *Birth Defects Res.* 109 (17), 1377–1385. doi:10.1002/bdr2.1142

Farina, A. R., Cappabianca, L., Sebastiano, M., Zelli, V., Guadagni, S., and Mackay, A. R. (2020). Hypoxia-Induced Alternative Splicing: The 11th Hallmark of Cancer. *J. Exp. Clin. Cancer Res.* 39 (1), 110. doi:10.1186/s13046-020-01616-9

Fischer, B., and Bavister, B. D. (1993). Oxygen Tension in the Oviduct and Uterus of Rhesus Monkeys, Hamsters and Rabbits. *Reproduction* 99 (2), 673–679. doi:10.1530/jrf.0.0990673

Freeburg, P. B., and Abrahamson, D. R. (2003). Hypoxia-inducible Factors and Kidney Vascular Development. *J. Am. Soc. Nephrol.* 14 (11), 2723–2730. doi:10.1097/01.asn.0000092794.37534.01

Freeburg, P. B., Robert, B., St. John, P. L., and Abrahamson, D. R. (2003). Podocyte Expression of Hypoxia-Inducible Factor (HIF)-1 and HIF-2 During Glomerular Development. *J. Am. Soc. Nephrol.* 14 (4), 927–938. doi:10.1097/01.asn.0000059308.82322.4f

Gerl, K., Steppan, D., Fuchs, M., Wagner, C., Willam, C., Kurtz, A., et al. (2017). Activation of Hypoxia Signaling in Stromal Progenitors Impairs Kidney Development. *Am. J. Pathology* 187 (7), 1496–1511. doi:10.1016/j.ajpath.2017.03.014

Gerosa, C., Fanni, D., Faa, A., Van Eyken, P., Ravarino, A., Fanos, V., et al. (2017). Low Vascularization of the Nephrogenic Zone of the Fetal Kidney Suggests a Major Role for Hypoxia in Human Nephrogenesis. *Int. Urol. Nephrol.* 49 (9), 1621–1625. doi:10.1007/s11255-017-1630-y

Geuens, T., Ruiter, F. A. A., Schumacher, A., Morgan, F. L. C., Rademakers, T., Wiersma, L. E., et al. (2021). Thiol-ene Cross-Linked Alginate Hydrogel Encapsulation Modulates the Extracellular Matrix of Kidney Organoids by Reducing Abnormal Type 1a1 Collagen Deposition. *Biomaterials* 275, 120976. doi:10.1016/j.biomaterials.2021.120976

Grobstein, C. (1956). Trans-Filter Induction of Tubules in Mouse Metanephrogenic Mesenchyme. *Exp. Cell Res.* 10 (2), 424–440. doi:10.1016/0014-4827(56)90016-7

Guan, F., Villegas, G., Teichman, J., Mundel, P., and Tufro, A. (2006). Autocrine VEGF-A System in Podocytes Regulates Podocin and its Interaction with

CD2AP. *Am. J. Physiology-Renal Physiology* 291 (2), F422–F428. doi:10.1152/ajprenal.00448.2005

Gupta, N., Dilmen, E., and Morizane, R. (2021). 3D Kidney Organoids for Bench-To-Bedside Translation. *J. Mol. Med.* 99 (4), 477–487. doi:10.1007/s00109-020-01983-y

Haddad, J. J., and Harb, H. L. (2005). Cytokines and the Regulation of Hypoxia-Inducible Factor (HIF)-1α. *Int. Immunopharmacol.* 5 (3), 461–483. doi:10.1016/j.intimp.2004.11.009

Han, Y., Kuang, S.-Z., Gomer, A., and Ramirez-Bergeron, D. L. (2010). Hypoxia Influences the Vascular Expansion and Differentiation of Embryonic Stem Cell Cultures Through the Temporal Expression of Vascular Endothelial Growth Factor Receptors in an ARNT-Dependent Manner. *Stem Cells* 28 (4), 799–809. doi:10.1002/stem.316

Hemker, S. L., Sims-Lucas, S., and Ho, J. (2016). Role of Hypoxia During Nephrogenesis. *Pediatr. Nephrol.* 31 (10), 1571–1577. doi:10.1007/s00467-016-3333-5

Jagannathan, L., Cuddapah, S., and Costa, M. (2016). Oxidative Stress Under Ambient and Physiological Oxygen Tension in Tissue Culture. *Curr. Pharmacol. Rep.* 2 (2), 64–72. doi:10.1007/s40495-016-0050-5

Keeley, T. P., and Mann, G. E. (2019). Defining Physiological Normoxia for Improved Translation of Cell Physiology to Animal Models and Humans. *Physiol. Rev.* 99 (1), 161–234. doi:10.1152/physrev.00041.2017

Kim, B.-S., Chen, J., Weinstein, T., Noiri, E., and Goligorsky, M. S. (2002). VEGF Expression in Hypoxia and Hyperglycemia: Reciprocal Effect on Branching Angiogenesis in Epithelial-Endothelial Co-Cultures. *J. Am. Soc. Nephrol.* 13 (8), 2027–2036. doi:10.1097/01.asn.0000024436.00520.d8

Klingberg, A., Hasenberg, A., Ludwig-Portugall, I., Medyukhina, A., Männ, L., Brenzel, A., et al. (2017). Fully Automated Evaluation of Total Glomerular Number and Capillary Tuft Size in Nephritic Kidneys Using Lightsheet Microscopy. *J. Am. Soc. Nephrol.* 28 (2), 452–459. doi:10.1681/asn.2016020232

Kobayashi, H., Liu, J., Urrutia, A. A., Burmakin, M., Ishii, K., Rajan, M., et al. (2017). Hypoxia-Inducible Factor Prolyl-4-Hydroxylation in FOXD1 Lineage Cells Is Essential for Normal Kidney Development. *Kidney Int.* 92 (6), 1370–1383. doi:10.1016/j.kint.2017.06.015

Lee, Y. M., Jeong, C.-H., Koo, S.-Y., Son, M. J., Song, H. S., Bae, S.-K., et al. (2001). Determination of Hypoxic Region by Hypoxia Marker in Developing Mouse Embryos *in Vivo*: A Possible Signal for Vessel Development. *Dev. Dyn.* 220 (2), 175–186. doi:10.1002/1097-0177(20010201)220:2<175::aid-dvdy1101>3.0.co;2-f

Li, J., Gao, X., Qian, M., and Eaton, J. W. (2004). Mitochondrial Metabolism Underlies Hyperoxic Cell Damage. *Free Radic. Biol. Med.* 36 (11), 1460–1470. doi:10.1016/j.freeradbiomed.2004.03.005

Loughna, S., Yuan, H.-T., and Woolf, A. S. (1998). Effects of Oxygen on Vascular Patterning in *Tie1/Lac* ZMetanephric Kidneys in Vitro. *Biochem. Biophysical Res. Commun.* 247 (2), 361–366. doi:10.1006/bbrc.1998.8768

Ma, T., Grayson, W. L., Fröhlich, M., and Vunjak-Novakovic, G. (2009). Hypoxia and Stem Cell-Based Engineering of Mesenchymal Tissues. *Biotechnol. Prog.* 25 (1), 32–42. doi:10.1002/btpr.128

Mamer, S. B., Wittenkeller, A., and Imoukhuede, P. I. (2020). VEGF-A Splice Variants Bind VEGFRs with Differential Affinities. *Sci. Rep.* 10 (1), 14413. doi:10.1038/s41598-020-71484-y

Michiels, C., Arnould, T., and Remacle, J. (2000). Endothelial Cell Responses to Hypoxia: Initiation of a Cascade of Cellular Interactions. *Biochimica Biophysica Acta (BBA) - Mol. Cell Res.* 1497 (1), 1–10. doi:10.1016/s0167-4889(00)00041-0

Nishinakamura, R. (2019). Human Kidney Organoids: Progress and Remaining Challenges. *Nat. Rev. Nephrol.* 15 (10), 613–624. doi:10.1038/s41581-019-0176-x

Okkelman, I. A., Foley, T., Papkovsky, D. B., and Dmitriev, R. I. (2017). Live Cell Imaging of Mouse Intestinal Organoids Reveals Heterogeneity in Their Oxygenation. *Biomaterials* 146, 86–96. doi:10.1016/j.biomaterials.2017.08.043

Otrock, Z., Mahfouz, R., Makarem, J., and Shamseddine, A. (2007). Understanding the Biology of Angiogenesis: Review of the Most Important Molecular Mechanisms. *Blood Cells, Mol. Dis.* 39 (2), 212–220. doi:10.1016/j.bcmd.2007.04.001

Peach, C., Mignone, V., Arruda, M., Alcobia, D., Hill, S., Kilpatrick, L., et al. (2018). Molecular Pharmacology of VEGF-A Isoforms: Binding and Signalling at VEGFR2. *Ijms* 19 (4), 1264. doi:10.3390/ijms19041264

Place, T. L., Domann, F. E., and Case, A. J. (2017). Limitations of Oxygen Delivery to Cells in Culture: An Underappreciated Problem in Basic and Translational Research. *Free Radic. Biol. Med.* 113, 311–322. doi:10.1016/j.freeradbiomed.2017.10.003

Podkalicka, P., Stępniewski, J., Mucha, O., Kachamakova-Trojanowska, N., Dulak, J., and Łoboda, A. (2020). Hypoxia as a Driving Force of Pluripotent Stem Cell Reprogramming and Differentiation to Endothelial Cells. *Biomolecules* 10 (12). doi:10.3390/biom10121614

Prado-Lopez, S., Conesa, A., Armiñán, A., Martínez-Losa, M., Escobedo-Lucea, C., Gandia, C., et al. (2010). Hypoxia Promotes Efficient Differentiation of Human Embryonic Stem Cells to Functional Endothelium. *Stem Cells* 28 (3), 407–418. doi:10.1002/stem.295

Roodink, I., van der Laak, J., Kusters, B., Wesseling, P., Verrijp, K., de Waal, R., et al. (2006). Development of the Tumor Vascular Bed in Response to Hypoxia-Induced VEGF-A Differs from that in Tumors with Constitutive VEGF-A Expression. *Int. J. Cancer* 119 (9), 2054–2062. doi:10.1002/ijc.22072

Rossi, G., Manfrin, A., and Lutolf, M. P. (2018). Progress and Potential in Organoid Research. *Nat. Rev. Genet.* 19 (11), 671–687. doi:10.1038/s41576-018-0051-9

Salomon, C., Ryan, J., Sobrevia, L., Kobayashi, M., Ashman, K., Mitchell, M., et al. (2013). Exosomal Signaling During Hypoxia Mediates Microvascular Endothelial Cell Migration and Vasculogenesis. *PLoS One* 8 (7), e68451. doi:10.1371/journal.pone.0068451

Salton, M., Voss, T. C., and Misteli, T. (2014). Identification by High-Throughput Imaging of the Histone Methyltransferase EHMT2 as an Epigenetic Regulator of VEGFA Alternative Splicing. *Nucleic Acids Res.* 42 (22), 13662–13673. doi:10.1093/nar/gku1226

Schindelin, J., Arganda-Carreras, I., Frise, E., Kaynig, V., Longair, M., Pietzsch, T., et al. (2012). Fiji: An Open-Source Platform for Biological-Image Analysis. *Nat. Methods* 9 (7), 676–682. doi:10.1038/nmeth.2019

Schneider, C. A., Rasband, W. S., and Eliceiri, K. W. (2012). NIH Image to ImageJ: 25 Years of Image Analysis. *Nat. Methods* 9 (7), 671–675. doi:10.1038/nmeth.2089

Schumacher, A., Rookmaaker, M. B., Joles, J. A., Kramann, R., Nguyen, T. Q., van Griensven, M., et al. (2021). Defining the Variety of Cell Types in Developing and Adult Human Kidneys by Single-Cell RNA Sequencing. *NPJ Regen. Med.* 6 (1), 45. doi:10.1038/s41536-021-00156-w

Shang, T., Li, S., Zhang, Y., Lu, L., Cui, L., and Guo, F. F. (2019). Hypoxia Promotes Differentiation of Adipose-Derived Stem Cells into Endothelial Cells Through Demethylation of EphrinB2. *Stem Cell Res. Ther.* 10 (1), 133. doi:10.1186/s13287-019-1233-x

Shih, H.-M., Wu, C.-J., and Lin, S.-L. (2018). Physiology and Pathophysiology of Renal Erythropoietin-Producing Cells. *J. Formos. Med. Assoc.* 117 (11), 955–963. doi:10.1016/j.jfma.2018.03.017

Stolz, D. B., and Sims-Lucas, S. (2015). Unwrapping the Origins and Roles of the Renal Endothelium. *Pediatr. Nephrol.* 30 (6), 865–872. doi:10.1007/s00467-014-2798-3

Tahergorabi, Z., and Khazaei, M. (2012). A Review on Angiogenesis and its Assays. *Iran. J. Basic Med. Sci.* 15 (6), 1110–1126.

Takasato, M., Er, P. X., Chiu, H. S., and Little, M. H. (2016). Generation of Kidney Organoids from Human Pluripotent Stem Cells. *Nat. Protoc.* 11 (9), 1681–1692. doi:10.1038/nprot.2016.098

Takasato, M., Er, P. X., Chiu, H. S., Maier, B., Baillie, G. J., Ferguson, C., et al. (2015). Kidney Organoids from Human iPS Cells Contain Multiple Lineages and Model Human Nephrogenesis. *Nature* 526 (7574), 564–568. doi:10.1038/nature15695

Takasato, M., and Wymeersch, F. J. (2020). Challenges to Future Regenerative Applications Using Kidney Organoids. *Curr. Opin. Biomed. Eng.* 13, 144–151. doi:10.1016/j.cobme.2020.03.003

Tufró, A. (2000). VEGF Spatially Directs Angiogenesis During Metanephric Development *in Vitro*. *Dev. Biol.* 227 (2), 558–566. doi:10.1006/dbio.2000.9845

Tufro-McReddie, A., Norwood, V. F., Aylor, K. W., Botkin, S. J., Carey, R. M., and Gomez, R. A. (1997). Oxygen Regulates Vascular Endothelial Growth Factor-Mediated Vasculogenesis and Tubulogenesis. *Dev. Biol.* 183 (2), 139–149. doi:10.1006/dbio.1997.8513

van den Berg, C. W., Ritsma, L., Avramut, M. C., Wiersma, L. E., van den Berg, B. M., Leuning, D. G., et al. (2018). Renal Subcapsular Transplantation of PSC-Derived Kidney Organoids Induces Neo-Vasculogenesis and Significant Glomerular and Tubular Maturation *In Vivo*. *Stem Cell Rep.* 10 (3), 751–765. doi:10.1016/j.stemcr.2018.01.041

Vempati, P., Popel, A. S., and Mac Gabhann, F. (2014). Extracellular Regulation of VEGF: Isoforms, Proteolysis, and Vascular Patterning. *Cytokine & growth factor Rev.* 25 (1), 1–19. doi:10.1016/j.cytogfr.2013.11.002

Wörsdörfer, P., and Ergün, S. (2021). The Impact of Oxygen Availability and Multilineage Communication on Organoid Maturation. *Antioxid. Redox Signal* 35 (3), 217–233. doi:10.1089/ars.2020.8195

Xie, F., Xiao, P., Chen, D., Xu, L., and Zhang, B. (2012). miRDeepFinder: A miRNA Analysis Tool for Deep Sequencing of Plant Small RNAs. *Plant Mol. Biol.* 80, 75–84. doi:10.1007/s11103-012-9885-2

Yousef Yengej, F. A., Jansen, J., Rookmaaker, M. B., Verhaar, M. C., and Clevers, H. (2020). Kidney Organoids and Tubuloids. *Cells* 9 (6), 1326. doi:10.3390/cells9061326

Yuan, C., Wang, P., Zhu, L., Dissanayaka, W. L., Green, D. W., Tong, E. H., et al. (2015). Coculture of Stem Cells from Apical Papilla and Human Umbilical Vein Endothelial Cell Under Hypoxia Increases the Formation of Three-Dimensional Vessel-Like Structures *in Vitro*. *Tissue Eng. Part A* 21 (5-6), 1163–1172. doi:10.1089/ten.TEA.2014.0058

Conflict of Interest: The authors declare that the research was conducted in the absence of any commercial or financial relationships that could be construed as a potential conflict of interest.

Publisher's Note: All claims expressed in this article are solely those of the authors and do not necessarily represent those of their affiliated organizations, or those of the publisher, the editors and the reviewers. Any product that may be evaluated in this article, or claim that may be made by its manufacturer, is not guaranteed or endorsed by the publisher.

frontiers | Frontiers in Bioengineering and Biotechnology

ORIGINAL RESEARCH
published: 13 June 2022
doi: 10.3389/fbioe.2022.888492

3D-Cultured Vascular-Like Networks Enable Validation of Vascular Disruption Properties of Drugs *In Vitro*

Prabhusrinivas Yavvari[1], *Anna Laporte*[2], *Laura Elomaa*[1], *Fabian Schraufstetter*[1], *Inga Pacharzina*[1], *Aline Dominique Daberkow*[1], *Anke Hoppensack*[1] *and Marie Weinhart*[1,2]*

[1]*Institute of Chemistry and Biochemistry, Freie Universität Berlin, Berlin, Germany,* [2]*Institute of Physical Chemistry and Electrochemistry, Leibniz Universität Hannover, Hannover, Germany*

Vascular-disrupting agents are an interesting class of anticancer compounds because of their combined mode of action in preventing new blood vessel formation and disruption of already existing vasculature in the immediate microenvironment of solid tumors. The validation of vascular disruption properties of these drugs *in vitro* is rarely addressed due to the lack of proper *in vitro* angiogenesis models comprising mature and long-lived vascular-like networks. We herein report an indirect coculture model of human umbilical vein endothelial cells (HUVECs) and human dermal fibroblasts (HDFs) to form three-dimensional profuse vascular-like networks. HUVECs embedded and sandwiched in the collagen scaffold were cocultured with HDFs located outside the scaffold. The indirect coculture approach with the vascular endothelial growth factor (VEGF) producing HDFs triggered the formation of progressively maturing lumenized vascular-like networks of endothelial cells within less than 7 days, which have proven to be viably maintained in culture beyond day 21. Molecular weight-dependent Texas red-dextran permeability studies indicated high vascular barrier function of the generated networks. Their longevity allowed us to study the dose-dependent response upon treatment with the three known antiangiogenic and/or vascular disrupting agents brivanib, combretastatin A4 phosphate (CA4P), and 6´-sialylgalactose (SG) *via* semi-quantitative brightfield and qualitative confocal laser scanning microscopic (CLSM) image analysis. Compared to the reported data on *in vivo* efficacy of these drugs in terms of antiangiogenic and vascular disrupting effects, we observed similar trends with our 3D model, which are not reflected in conventional *in vitro* angiogenesis assays. High-vascular disruption under continuous treatment of the matured vascular-like network was observed at concentrations ≥3.5 ng·ml^{-1} for CA4P and ≥300 nM for brivanib. In contrast, SG failed to induce any significant vascular disruption *in vitro*. This advanced model of a 3D vascular-like network allows for testing single and combinational antiangiogenic and vascular disrupting effects with optimized dosing and may thus bridge the gap between the *in vitro* and *in vivo* experiments in validating hits from high-throughput screening. Moreover, the physiological 3D environment mimicking *in vitro* assay is not only highly relevant to *in vivo* studies linked to cancer but also to the field of tissue regeneration.

Keywords: vascular disruption, antiangiogenesis, sandwich assay, lumen, *in vitro* drug testing

OPEN ACCESS

Edited by:
Tadanori Mammoto, Medical College of Wisconsin, United States

Reviewed by:
Yunqing (Kevin) Kang, Florida Atlantic University, United States
Bingmei M. Fu, City College of New York (CUNY), United States

***Correspondence:**
Marie Weinhart
marie.weinhart@fu-berlin.de
marie.weinhart@pci.uni-hannover.de

Specialty section:
This article was submitted to Tissue Engineering and Regenerative Medicine, a section of the journal Frontiers in Bioengineering and Biotechnology

Received: *02 March 2022*
Accepted: *13 April 2022*
Published: *13 June 2022*

Citation:
Yavvari P, Laporte A, Elomaa L, Schraufstetter F, Pacharzina I, Daberkow AD, Hoppensack A and Weinhart M (2022) 3D-Cultured Vascular-Like Networks Enable Validation of Vascular Disruption Properties of Drugs In Vitro. Front. Bioeng. Biotechnol. 10:888492. doi: 10.3389/fbioe.2022.888492

INTRODUCTION

Angiogenesis is the process of new capillary formation out of an existing vasculature by endothelial cells (ECs) in living tissues (Adams and Alitalo, 2007). It is mainly triggered by growth factors that facilitate differentiation and restructuring of polarized endothelial cells in a timed cascade of signaling events to produce a vascular network made of hollow and lumenized capillaries (Carmeliet, 2005). Using these networks, oxygen as well as nutrient transport and supply of the surrounding tissue is ensured. Therefore, solid tumors often exploit angiogenesis from the healthy periphery to cope with their high growth rate-related, excessive supply demands (Bergers and Benjamin, 2003; De Palma et al., 2017). Specially the treatment of late-stage invasive tumors benefits from targeted disruption and degeneration of already established vascular tumor networks compared to conventional antiangiogenic treatment. Classical antiangiogenic compounds target angiogenic signaling pathways such as the vascular endothelial growth factor (VEGF) pathway by either blocking the secreted VEGF or its receptors on the cell surface. Often antiangiogenic, small molecule drugs also alter the existing vasculature and thus exhibit multiple modes of action. Brivanib and its prodrug brivanib alaninate belong to the group of classical antiangiogenic drugs with multiple targets. As an investigational phase III drug, brivanib exhibits antiangiogenic effects *in vitro* and *in vivo* (Siu et al., 2013). Predominantly, tyrosine kinases are inhibited by brivanib blocking VEGF and fibroblast growth factor (FGF) family receptors with IC_{50} values in the nanomolar range (Huynh et al., 2008; Chou and Finn, 2012). In contrast, small-molecule vascular disrupting agents (VDAs) discriminate mature and healthy networks from tumorous capillary networks *via* distinct differences in EC proliferation and permeability (Smolarczyk et al., 2021). Flavonoids such as 5,6-dimethyl-9-oxo-9H-xanthene-4-acetic acid (DMXAA) as potent cytokine inducers or tubulin-binding agents such as combretastatin A4 with its water-soluble prodrug combretastatin A4 disodium phosphate (CA4P) are prominent representatives of VDAs (Hinnen and Eskens, 2007; Porcù et al., 2014). Both drug types increase the permeability of the tumor vasculature resulting in blood leakage, uncontrolled blood coagulation, rapid shutdown of the tumor core from blood supply, and subsequent tumor tissue necrosis (Nagaiah and Remick, 2010; Drzyzga et al., 2021; LINCS, 2022; PubChem, 2022). In clinical trials, a variety of carcinomas have indeed been effectively treated with such antiangiogenic drugs and/or VDAs. However, cancerous cells in the carcinoma rim often survive the VDA treatment and quickly repopulate the tumor. Therefore, simultaneous application of vascular-targeting agents with conventional cytotoxic anticancer therapeutics or sequential combination with radiotherapy to curb tumor proliferation is encountered a promising strategy in the treatment of solid tumors (Siemann and Horsman, 2009; Drzyzga et al., 2021). Current challenges of VDAs in single and combination therapies are adverse effects such as cardiovascular toxicity observed in preclinical and clinical studies, which manifests as cardiac ischemia, hypertension, or atrial fibrillation and requires the establishment of meticulous clinical management protocols (Gill et al., 2019).

When addressing pharmacokinetics, drug metabolism and therapeutic drug effects, *in vivo* animal studies are currently irreplaceable. Yet, advanced *in vitro* models that closely mimic the native vascular network are powerful tools according to the 3R (replace, reduce, and refine) principles with the potential to reduce the number of animal experiments (Langhans, 2018; Weinhart et al., 2019). This is particularly the case, as more reliable estimates of the therapeutic window for subsequent *in vivo* experimentation can be deduced from 3D vs. 2D assays through more refined information on dose-dependent drug efficacies and their respective cytotoxicity profiles. Furthermore, *in vitro* assays generally bear the potential for cost-efficient adaption into a scalable assay platform to screen antiangiogenic compounds in combination with other drugs (Siller et al., 2020; Van Duinen et al., 2020). To our knowledge, there has been no *in vitro* 3D model described to simultaneously validate the antiangiogenic as well as vascular disrupting properties of drugs. In contrast, a myriad of *in vitro* models exists for studying *de novo* angiogenesis processes and to screen antiangiogenic drug properties (Simons et al., 2015). A common method, known as tube formation assay, utilizes the self-assembly potential of ECs grown on the surface of basement membrane extract coatings (DeCicco-Skinner et al., 2014). The formation of chord- or tube-like structures localized in one plane is observed after 2 h with a maximum between 4 and 6 h. These structures resemble vascular networks of early-stage angiogenesis that are short-lived from 24 h to a maximum of 7 days (Kubota et al., 1988) and often lack a proper capillary-like lumen particularly when cultured on laminin-rich matrices (Senger and Davis, 2011). The limited longevity and consequently the inability of such models to mature to complex vascular structures mimicking the (patho)physiology *in vivo* prevents their use for studying long-term drug effects, for example, under repeated dosing or vascular disruption (Brassard-Jollive et al., 2020).

Profuse vascular 3D networks *in vitro* are established when culturing ECs in extracellular matrix mimicking gels such as collagen (Koh et al., 2008), fibrin (Nakatsu and Hughes, 2008), or synthetic hydrogels (Liu et al., 2021) with additional proangiogenic supplements such as phorbol 12-myristate 13-acetate, sphingosine-1-phosphate, and/or angiogenic growth factors such as VEGF. Furthermore, the importance of organo-typic coculture conditions for successful *in vitro* prevascularization has been emphasized (Shafiee et al., 2021). Coculturing ECs with other cells such as mesenchymal stem cells (Uwamori et al., 2017) or human adipose stem cells (hASCs) (Kang et al., 2018; Manikowski et al., 2018; Andrée et al., 2019) within a gel scaffold resulted in the generation of a 3D vascular network that was stable up to day 14.

Though these strategies have demonstrated the importance of the coculture conditions for generating a long-term stable

vascular network *in vitro*, they still hold some bottlenecks toward their application for drug screening studies. A) Coculturing ECs with cells of higher metabolic and proliferative rates can cause competition for nutrition and space, thereby interfering with vascular network formation and the balance of matrix degradation and restructuring; B) owing to the presence of a mixed population of cells along with ECs, identifying the individual response of ECs or their morphological changes during vascularization in response to the other cocultured cells is challenging or requires permanent staining (Hetheridge et al., 2011); C) there is still lack of evidence whether the presence of other cells in the vicinity of ECs would have any effect on the structural integrity of the vascular networks formed (Andrée et al., 2019).

Herein, we report the development of an indirect coculture model of human umbilical vein endothelial cells (HUVECs) and human dermal fibroblasts (HDFs), to generate long-lasting, profuse vascular-like networks, while simultaneously overcoming the aforementioned current limitations. Detailed brightfield and confocal microscopy experiments supported by ELISA assays were performed to study the formation and maturation of the vascular-like structures. We present the expedience of our advanced 3D model by studying drug efficacies toward antiangiogenesis and/or vascular disruption with higher accuracy than the still popular tube forming assay.

MATERIALS AND METHODS

Materials

HUVECs and the VascuLife® VEGF Endothelial Medium Complete Kit including basal medium as well as growth factors and supplements (Lifefactors®: rh FGF-b [5 ng/ml], ascorbic acid [50 µg/ml], hydrocortisone [1 µg/ml], FBS, L-glutamine [10 mM], rh IGF-1 [15 ng/ml], rh EGF [5 ng/ml], rh VEGF [5 ng/ml], and heparin [0.75 U/ml]) were obtained from CellSystems® (Troisdorf, Germany). Rat collagen type I was supplied from R&D Systems (Minneapolis, United States) under the trade name Cultrex® 3D Culture Matrix. Hoechst 33342, calcein-AM, fluorescein diacetate (FDA), dextran, Texas Red™ (10 and 70 kDa), and the human VEGF/ELISA kit were purchased from Thermo Fisher Scientific (Waltham, MA, United States), propidium iodide (PI), Accutase® (400–600 units/ml), and Dulbecco's phosphate buffered saline without $CaCl_2$ und $MgCl_2$ (DPBS) were from Sigma-Aldrich (St. Louis, MO, United States). Albumin fraction V, sodium hydroxide, and Triton X-100 were from Carl Roth (Karlsruhe, Germany) and fetal bovine serum (FBS) from PAN Biowest (Nuaillé, France). High glucose (4.5 g/L) and low glucose (1 g/L) Dulbecco's modified Eagle's medium (HG-DMEM and LG-DMEM; 1 mM pyruvate), penicillin/streptomycin, and trypsin 0.5% (10×, W/ EDTA) were ordered from Life Technologies, Gibco (Darmstadt, Germany) and CELLSTAR® 12-well suspension culture plates as well as T-75 cell culture flasks were obtained from Greiner Bio-One (Kremsmünster, Austria) and Costar® Transwell® 12 mm inserts with a 0.4 µm polyethylene terephthalate (PET) membrane from Corning (New York, NY, United States). The human FGF basic ELISA kit (FGF2) was purchased from Abcam (Cambridge, United Kingdom), monoclonal mouse anti-human CD31 antibody from Agilent Technologies (Santa Clara, CA, United States), Alexa Fluor® 488 goat anti-mouse IgG1 antibody from Thermo Fisher Scientific (Waltham, MA, United States), combretastatin A4 phosphate disodium salt from TCI chemicals (Tokyo, Japan), brivanib from Biomol (Hamburg, Germany), and 6'-sialylgalactose sodium salt from Carbosynth (Berkshire, United Kingdom).

Ethics Statement

HDF isolation from juvenile foreskin subsequent to circumcision (age between 5 and 18 months) and their usage for the studies was following the approval of the Ethics Committee at Charité Universitätsmedizin Berlin, Germany EA1/081/13, after obtaining written informed consent from their parents.

Cell Culture

HUVECs obtained from Cellsystems® in passage 3 (p3) were thawed and cultured at 5,000 cells·cm^{-2} in 10 ml Vasculife® Lifefactors® VEGF medium in a T-75 cell culture flask at 37°C in a humidified atmosphere with 5% CO_2. For further cultivation and expansion, cells were seeded at 5,000 cells·cm^{-2} per flask (T-75) after enzymatic detachment with Accutase (0.6 ml, 400–600 units·ml^{-1}). Medium exchange was performed every 3 days. For the indirect coculture assay HUVECs in p4-6 were used.

HDFs originating from human foreskin samples were isolated by using a collagenase and dispase protocol as reported previously (Stöbener et al., 2017). Donors were of different ages between 5 and 18 months. Primary fibroblasts were then cultured from p4-7 using HG-DMEM supplemented with 10% FBS at 37°C in a humidified atmosphere with 5% CO_2. Detachment was performed with 0.05% trypsin. Fibroblasts in p4-8 were used for experiments.

Indirect Coculture Assay

Fibroblasts were seeded at a density of 12×10^3 cells·cm^{-2} in a 12-well culture plate (~3.8 cm^2 surface area) in 1.5 ml LG-DMEM (10% FBS) and cultured for 24 h. Tissue culture treated 12 mm Transwell® inserts with a 0.4 µm pore size were used for the culture of HUVECs inside a collagen gel. Prior to the addition of the gel the inserts were incubated with 1× DPBS for 3 min to wet the surface of the PET membrane. Afterward, a total of 160 µl of collagen solution (type 1 collagen of rat tail origin, 2.5 mg·ml^{-1}, details on the preparation can be found in the supporting information (SI)) were added to the inserts (1.1 cm^2 surface area) in two iterative steps of 100 and 60 µl, respectively, with a 30 min incubation time in between to avoid meniscus formation within the bottom gel layer. Subsequently, the inserts were incubated for 45 min to ensure complete solidification of the gel. HUVECs were then seeded on top of the collagen gel in 500 µl of Vasculife® Lifefactors® VEGF medium at a density of 60×10^3 cells·cm^{-2} and were left to

adhere overnight. On the following day, the HUVEC culture medium was gently aspirated, and a second layer of collagen solution (160 µl, 2.5 mg·ml^{-1}) was added onto the cells. After 45 min of incubation, the Transwell® inserts were transferred into the wells of the 12-well plate containing a monolayer of fibroblasts with 1.5 ml LG-DMEM (10% FBS). Vasculife® Lifefactors® VEGF medium (500 µl) with a reduced FBS content of 0.5% was added into the Transwell®, and this timepoint is referred to as "day 0". Media exchange with the respective media in both compartments was conducted every 2–3 days. The samples were imaged using a Zeiss Axiovert 200 brightfield microscope equipped with a Zeiss Axiovert camera and a heated stage at regular intervals. For the control condition of HUVEC culture without fibroblasts, the inserts were immersed in 1.5 ml of LG-DMEM in the wells of the 12-well plate only. For studying the VEGF and/or bFGF dependence of vascular network formation, 500 µl of Vasculife® Lifefactors® Medium void of VEGF and/or bFGF (0.5% (v/v) FBS) were used for culture of HUVECs.

Quantification of Vascular Endothelial Growth Factor and Fibroblast Growth Factor by ELISA

Respective culture supernatants from HDFs and HUVECs were collected before media exchange on day 2, 7, 9, and 14 and were stored at −80°C until further analysis. For ELISA using VEGF Human ELISA Kit (detection limit: 15.6–1,500 pg·ml^{-1}, Invitrogen) and Human FGF basic ELISA Kit (FGF2, detection limit: 15.6–1,000 pg·ml^{-1}, Abcam), the medium samples were diluted, if required, using the dilution buffer provided by the respective kit (maximum of 1:50) to ensure the concentration of the growth factors to be within the optimal detection range. The assay was performed according to the manufacturer's protocol.

Quantification of Vascular-Like Networks

The images obtained from brightfield microscopy of HUVECs were imported to *Image J*, and the number of each type of branching points was manually identified using the cell counter tool. Due to the vast z-extension on the networks, all our attempts to use automated image analysis failed. Two fields of view per technical replicate were evaluated, and the average was calculated for $n = 3–4$. Representative examples of different types of branching points are included in the supplementary material (**Supplementary Figure S1**). Normalization to achieve the distribution of each type of branching point was carried out using **Eq. 1** (where X is the number of branches originating from a branching point, which can be 3, 4, 5, 6, or 7).

$$\text{Distribution of branching points} = \frac{\text{number of branching points of type X}}{\text{total number of branching points}} \cdot 100 \quad (1)$$

The profuseness of the vascular-like networks was determined using the method described by Gondi et al. (2004): The total number of branches was calculated as the sum of branches weighted by the number of branches arising from each branching node, shown by **Eq. 2** ($x_{\#}$ indicates branching point type with # representing the number of branches).

$$\text{Total number of branches} = 3 \cdot x_3 + 4 \cdot x_4 + 5 \cdot x_5 + 6 \cdot x_6 + 7 \cdot x_7 \quad (2)$$

Immunofluorescence Staining

Adapted from the literature (Auler et al., 2017), cells in collagen were fixed with 4% PFA for 2 h before staining. Afterward, the samples were blocked using 5% w/v bovine serum albumin in DPBS for 3 h and subsequently stained with a monoclonal mouse anti-human CD31 primary antibody (1:50) overnight at 4 °C. Following thorough washing with DPBS containing 0.05wt% Tween for 7 h, the primary antibody was detected by incubation with Alexa Fluor® 488 goat anti-mouse IgG1 as a secondary antibody (1:400) overnight. After another washing step using DPBS containing 0.05wt% Tween for 7 h and counterstaining with Hoechst 33342 (1:400), the samples were immersed in mounting medium on custom-made PET slides and imaged *via* confocal laser scanning microscopy (CLSM) using a Zeiss LSM800 confocal microscope.

Live–Dead Assay and Imaging

To evaluate the viability of cells, a co-staining using FDA (0.46 µM) as a stain for living and PI (16 µM) as a stain for dead cells was conducted. Staining solution (200 µl) (1× DPBS) was added directly onto the collagen scaffolds containing HUVECs and incubated for 8 min at room temperature. Additional Hoechst solution was added to the samples (10 µg·ml^{-1}) to counterstain the nuclei wherever required. Subsequently, the solution was removed and the collagen gels were washed thrice with 1x DPBS. The samples were then placed on PET slides for imaging *via* CLSM using a Zeiss LSM 800 confocal microscope. Fifty microliter of 1× DPBS were added onto the collagen gels to prevent drying of the gels during imaging.

Calcein-AM and Texas Red-Dextran Staining

Collagen gels with HUVEC networks from indirect coculture after day 21 were treated with 1 mg·ml^{-1} of 10 or 70 kDa Texas red-dextran (TD, dissolved in Vasculife® Lifefactors® medium supplemented with 0.5% FBS) for 24 h and subsequently washed twice with PBS. The samples were then incubated with calcein-AM (10 µM in Vasculife® Lifefactors® medium supplemented with 0.5% FBS) for 2–5 min. Afterward, the samples were washed with PBS, transferred onto PET slides, covered with mounting medium, and imaged *via* CLSM (Zeiss LSM 800 confocal microscope).

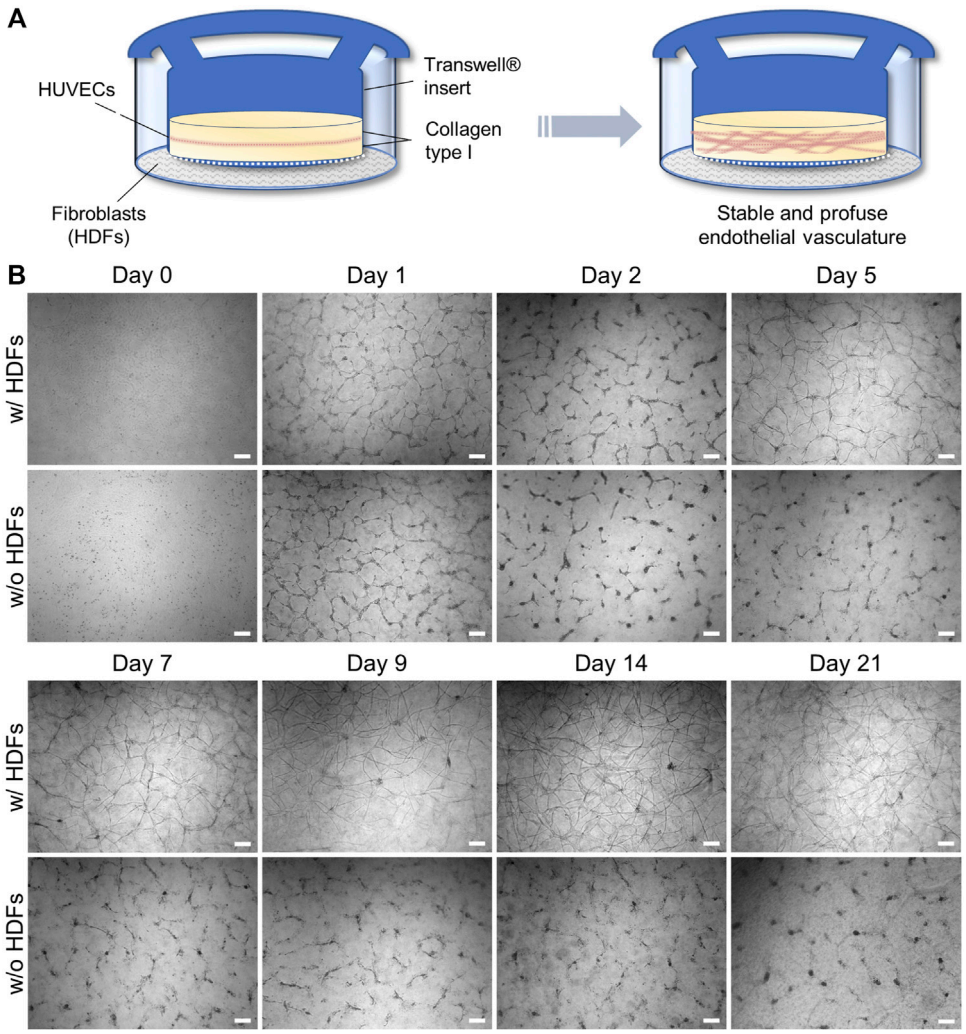

FIGURE 1 | (A) Schematic setup of an indirect coculture angiogenesis assay of HUVECs with HDFs to induce 3D vascular-like network formation; **(B)** Representative, time-dependent brightfield microscopy images of the forming HUVEC network cultured with and without fibroblasts. Note that slight meniscus formation at the insert wall during collagen gelation results in a darker contrast at the outer regions of the insert during brightfield imaging (scale bar 200 µm, $n = 3$).

Drug Treatment of the Vascular-Like Networks

The indirect coculture models were prepared and directly incubated inside the Transwell® compartment with different concentrations of investigational drug or prodrug molecules (brivanib (LINCS, 2022)), combretastatin A4 phosphate (CA4P (PubChem, 2022)), or a drug under development (6'-silaylgalactose (SG) (Chung et al., 2019)) in 500 µl Vasculife® Lifefactors® medium (0.5% (v/v) FBS) void of VEGF, either starting from day 0 or day 7 of culture. The drug solutions were replaced on every alternate day with the media exchange. As controls, equal volumes of PBS were added to the HUVECs and for brivanib an additional DMSO vehicle control was conducted. For drug treatment starting from day 7, the fibroblasts in the bottom compartment were replaced 1 day before the commencement of drug treatment. Models were observed for up to 14 days starting from the first administration of the respective drug.

Statistical Evaluation

Statistical significance of all data was calculated with the software *GraphPad Prism 9.0* (San Diego, CA). The respective number of individual experiments *n* is stated in the figure caption. Error bars indicate standard deviations (SD) in the graphs unless otherwise stated.

RESULTS AND DISCUSSION

Indirect Coculture for Long-Term Stable Vascular-Like Networks

We redesigned an established 3D angiogenesis assay (Montesano et al., 1983) comprising confluent HUVECs sandwiched between layers of rat tail collagen type I to generate a powerful assay setup for long-term drug testing and validation *in vitro*. Transferring the conventional sandwich assay into an insert-culture format

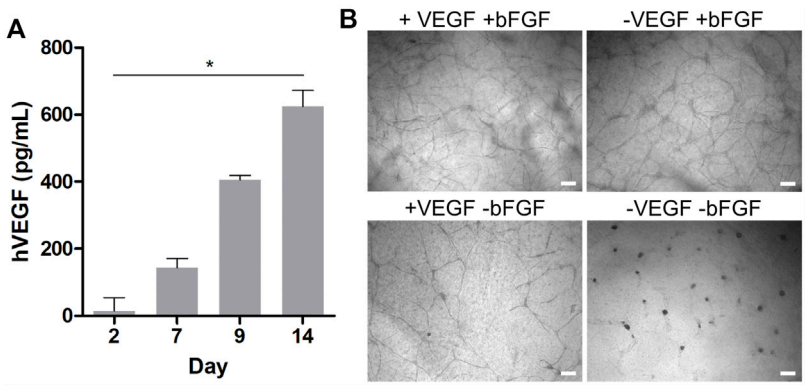

FIGURE 2 | (A) Time-dependent quantification of the hVEGF concentration in HDF culture medium *via* ELISA during indirect coculture of HUVECs and HDFs. Data presented as mean ± SD ($n = 4$, $^*p < 0.05$ as determined by Friedman ANOVA); **(B)** brightfield microscopy images of HUVECs grown in indirect coculture on day 14, with and without VEGF and/or bFGF supplementation in the HUVEC medium (scale bar 200 µm, $n = 3$).

according to **Figure 1A** enables the indirect coculture of HUVECs sandwiched in between two gel layers in the insert with confluent HDFs cultured on the outer well compartment. The key to produce a long-lived vascular-like network *in vitro* in our assay configuration is the indirect coculture with HDFs, which allows potential crosstalk with HUVECs through the membrane of the insert (**Figure 1B**).

It thus combines the advantages of cell–cell signaling as observed in direct coculture (Montesano et al., 1993; Uwamori et al., 2017; Kang et al., 2018; Manikowski et al., 2018) with the spatial separation of cell types in insert cultures to prevent cellular overgrowth of one cell type. The latter was observed in our initial attempts of a direct coculture of HUVECs and HDFs in a collagen gel (data not shown). During indirect coculture both HUVECs and HDFs were grown in their respective culture media, that is, LG-DMEM supplemented with 10% FBS in the HDF compartment. In the HUVEC compartment VascuLife® VEGF endothelial medium, which is supplemented with recombinant VEGF and basic FGF (bFGF) as important proangiogenic growth factors but with reduced serum concentration (0.5% v/v FBS), was used in order to encourage cellular self-organization over proliferation. The chosen collagen concentration of 2.5 $mg{\cdot}ml^{-1}$ did not require further stiffness or supplement adjustment of the gel by, for example, blending with agarose or Matrigel™ as reported by Ichanti et al. (2020) to enable efficient EC migration and vascular network formation.

In the absence of HDFs (**Figure 1B**), the HUVEC capillary structures in this sandwich assay build up through progressive reorganization of the monolayer within 2 days as described in the literature (Montesano et al., 1983; Nakatsu and Hughes, 2008). However, it starts to regress and disintegrate after day 2 when the culture time is extended. Interestingly, in the presence of fibroblasts, the same trend is initially observed, but latest on day 5–7 a full recovery of the vascular-like structures can be detected *via* brightfield microscopy (**Figure 1B**). These recovered structures appear even more defined than the initial ones on day 1. They form multicellular nodes that give rise to new vascular-like branches or extensions and can viably be maintained beyond day 21. The majority of the vascular network-like structures were developed by day 14, after which the density of the tubular network remained nearly constant, opening the possibility for extended drug testing of, for example, antiangiogenic or vascular disrupting agents under multiple dosing.

The beneficial effect of primary, non-tumor-derived fibroblasts in this setup can be attributed to their potential to produce a myriad of proangiogenic growth factors including members of the VEGF family and bFGF, which synergize in the formation and development of lumenized vascular networks *in vitro* (Newman et al., 2011). To this end, the human VEGF and bFGF content in the HDF and HUVEC compartments was quantified *via* an enzyme-linked immunosorbent assay (ELISA) in a time-dependent manner. Interestingly, no quantifiable amounts of VEGF or bFGF could be detected in the supernatants of the HUVEC compartment at any time starting on day 2, both in the presence or absence of HDFs. However, under indirect coculture, corresponding measurements with supernatants collected from the outer HDF compartment indeed revealed a significant increase of VEGF from 14 to 600 $pg{\cdot}ml^{-1}$ from day 2 to 14 (**Figure 2A**). In contrast, no quantifiable amounts of VEGF were found in HDF supernatants from cultures without HUVECs in the insert (data not shown), suggesting that the VEGF production depends mainly on the crosstalk between HDFs and HUVECs in indirect coculture. Our efforts to quantify bFGF by ELISA in the indirect coculture setup in the presence and absence of HUVECs yielded no quantifiable amounts in the supernatants of the fibroblast compartments, although we were able to detect the exogenous bFGF supplement in fresh HUVEC medium (data not shown).

It is well known that unbound growth factors such as VEGF or bFGF are unstable under cell culture conditions with half-lives from 1 to 8 h in the presence of cells (Vempati et al., 2014). At the same time, HUVECs and fibroblasts produce and secrete matrix components such as fibronectin or proteoglycans, which accumulate in the collagen gel and strongly bind and adsorb growth factors. Our results suggest that within 48 h VEGF and

bFGF supplemented in the HUVEC culture medium are degraded, consumed, or bound to matrix components in the collagen gel (Griffith et al., 2005). Thus, they might become undetectable in supernatants *via* ELISA. Accordingly, the measurable HDF-derived VEGF concentration in the outer compartment of the assay might reflect only a fractional amount of the VEGF within the gel.

In addition to the effect of HDFs in coculture, we also investigated the effect of the exogenous growth factor supplements in the HUVEC medium on tubular network formation under indirect coculture conditions with HDFs. Therefore, qualitative network assessment was performed in comparison with structures obtained with VEGF and/or bFGF-deficient HUVEC medium in the coculture setup with HDFs. Representative brightfield images on day 14 of the experiments in the presence of HDFs are shown in **Figure 2B**. While no notable alterations in the formation of HUVEC networks were observed in the presence and absence of VEGF supplement, a clear drop in the network density was observed in bFGF-deficient medium. In the absence of both VEGF and bFGF supplements in the HUVEC medium no network was observable. Because bFGF as a strong proangiogenic inducer is not produced in quantifiable amounts by HDFs in the coculture assay, its supplementation ($5\ ng{\cdot}ml^{-1}$) in the HUVEC medium is essential to arrive at a high network density in this assay. In contrast, supplementation of the HUVEC medium with VEGF ($5\ ng{\cdot}ml^{-1}$) in the presence of HDFs and bFGF supplement is not necessarily required to efficiently generate networks. Notably, the HDF secreted VEGF level quantified in the outer compartment of the indirect coculture assay was eight-fold lower than the exogenous VEGF supplement in the HUVEC medium, but might be much higher within the gel as discussed previously. Nevertheless, the presence of exogenous VEGF does not substitute for HDFs in this assay because no long-lived vascular network formed in the absence of fibroblasts (**Figure 1B**). Similar observations were made by Newman et al. (2011) with angiogenesis experiments under coculture conditions in fibrin gels. They concluded from their study that a cocktail of proangiogenic factors other than VFGF and bFGF secreted by HDFs is the major trigger of an angiogenic phenotype in endothelial cells, which is consistent with our findings. In the absence of HDFs, exogenous VEGF and bFGF supplementation in HUVEC medium at day 2 appears to be insufficient to further support maturation and stabilization of the generated chord-like structures, leading to their regression and disappearance over time (**Figure 1B**). However, in the presence of HDFs, the increasingly released HDF-derived VEGF presumably in synergy with other growth factors appears to induce a proangiogenic recovery and further maturation of the tubular network observable latest on day 5–7 in indirect coculture (**Figure 1B**). Thus, the general VEGF level ($5\ ng{\cdot}ml^{-1}$) in the supplemented HUVEC cell culture medium alone could only initiate the migration and chord-like assembly of HUVECs observed on day 1–2 (with or without coculture) (**Figure 1B**) but not the subsequent maturation into a 3D vascular-like network. The latter requires the presence of presumably multiple growth factors secreted by fibroblasts.

Potential diffusion-based VEGF gradients from the media compartments toward the initial 2D cell seeding plane within the gel, rationalize the presence of profuse 3D vascular-like networks with a vertical expansion of up to a maximum of 600 μm (**Supplementary Figure S2**). The profuse nature of the formed 3D vascular-like networks within the gels does not allow automated image analysis, particularly with brightfield images. Therefore, the number of branching points and the number of branches arising from each node (degree of branching) as a function of time was quantitatively accessed from representative images by manual counting (Gondi et al., 2004). In line with visual inspection, the quantitative analysis of the brightfield microscopy images regarding the number of branching points confirms a strong expansion of the vascular-like HUVEC networks from day 2 to 21 (**Figure 3A**). Analyzing the distribution of the total number of branches arising from each branching point gave more cues on the maturation of the vascular-like networks. In general, we observe mostly nodes with three to five branches between day 5 and 21, while nodes with six branches or more occur less frequent (**Figure 3B**). The distribution of branching points stays almost constant over the whole assay period. However, latest from day 7 onward it was not possible to get all formed structures in focus during brightfield imaging indicating that the forming vascular-like networks start to grow vertically out of the seeding plane toward the surrounding (**Figure 1B**). As a result, a highly mature, complex network is observed on day 21 of the culture after CD31 staining (**Supplementary Figure S2B**, **Figure 3C**). In addition to straightforward visualization, the CD31-positive network indicates maintenance of the endothelial cell identity during network formation. Furthermore, the presence of CD31 is an essential prerequisite for endothelial cell junctional integrity and thus barrier function (Privratsky and Newman, 2014) similar to vascular endothelial (VE)-cadherin (Gavard, 2014), which was also detectable along the formed vascular-like structures *via* immunohistochemistry (**Supplementary Figure S3**). From confocal microscopy, the network z-dimensions were determined to be ranging from 100 to 300 μm on average with local extrema up to 600 μm (**Figure 3D**).

Although brightfield microscopy indicated the disintegration of the initially formed vascular-like structures in the absence of HDFs, HUVEC viability was not affected over the time course of the experiment. Confocal microscopy from live–dead staining of the samples, both in the presence and absence of fibroblasts, indicated hardly any PI-positive, dead HUVECs over the time course of the experiment (**Figure 4**). This is in general agreement with findings of direct coculture angiogenesis assays of endothelial cells with mural cells (Evensen et al., 2009). In the absence of HDFs, HUVECs tended to simply proliferate in the initial cell seeding plane after disintegration of the transient chord-like structures on day 2.

In summary, conditions favoring angiogenesis will promote HUVECs to generate capillary networks, whereas confluent cell layers are formed when angiogenesis is discouraged, for example, by a lack of important growth factors. This is in line with the results from previously published literature on direct cocultures of HUVECs with HDFs (Costa-Almeida et al., 2015) or hASCs

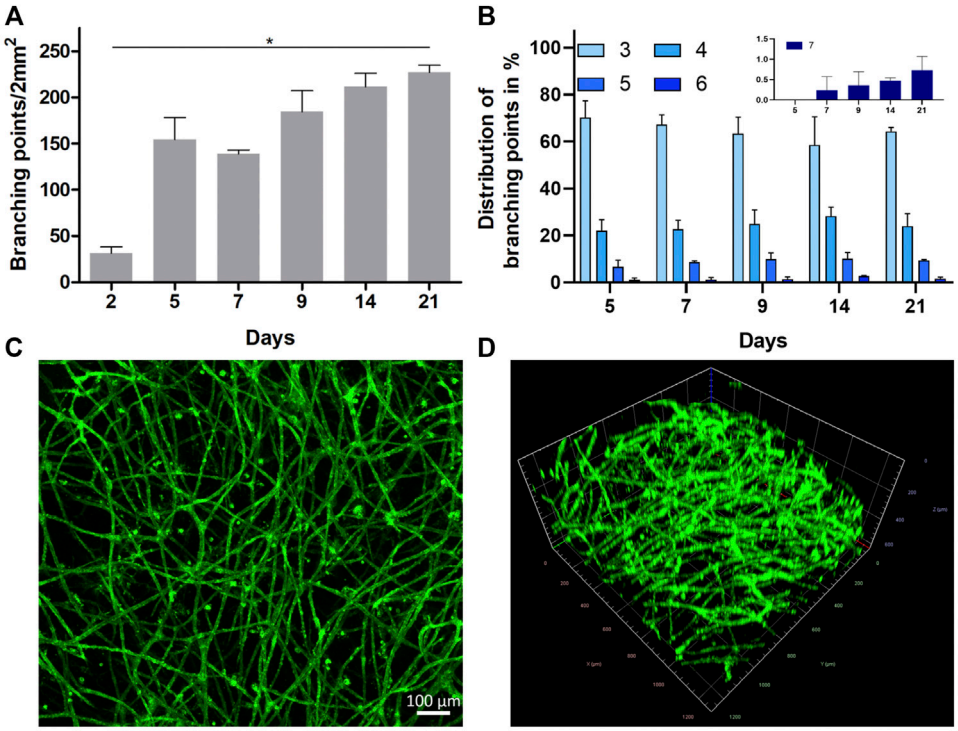

FIGURE 3 | (A) Profuseness of the vascular-like network represented as time-dependent total number of branching points per 2 mm^2 (mean ± SD, $n = 3$, $^*p < 0.05$ as determined by Kruskal–Wallis ANOVA with Dunn's multiple comparison *post-hoc* test). **(B)** Time-dependent percentage distribution of different branching points in the vascular network (inset shows the zoomed in data of seven branching points for all the groups (mean ± SD, $n = 4$)). **(C,D)** Representative CLSM images (tile stitched) showing the structure of the 3D HUVEC vascular-like network in collagen on day 21 as **(C)** orthogonal projection (scale bar 100 µm, $n = 4$) and **(D)** 3D projection imaged over a z-range of 600 µm after live cell staining with CD31 (1.2 mm^2).

(Manikowski et al., 2018). However, in our indirect coculture, the induction of capillary-tube formation can be purely assigned to soluble factors from HDFs or molecular crosstalk between HUVECs and the cocultured HDFs, while in direct coculture additional HUVEC-supporting cell–cell contacts or the reorganization of the matrix hydrogels by supporting cells cannot be excluded as mechanistic driving force for tube formation.

Anastomosing and Lumenized Vascular-Like Networks

The presence of an active and healthy vascular network *in vivo* is accompanied by anastomosis of newly forming vascular sprouts (Chen et al., 2010; Diaz-Santana et al., 2015) with simultaneous lumen formation (Lammert and Axnick, 2012; Charpentier and Conlon, 2014) improving vascular connectivity and nutrient supply. The indirect coculture strategy and the transparency of the collagen gel matrix allowed us to follow all structural changes of HUVECs during angiogenesis and vascular-like network formation by simple brightfield imaging. The day-wise imaging of the samples at the same positions indicated multiple instances of anastomosis, forming new branching points upon longer experimental time periods (**Figure 5A**).

Confocal laser scanning microscopy (CLSM) of FDA or calcein-AM stained vascular-like networks indicated the presence of hollow lumenized structures. While the thicker strands exhibited a lumen with a diameter of up to 70 µm (**Figure 5B**), the thinner vascular structures exhibited a circumferentially uniform lumen of around 10–30 µm (**Figure 5C**). The lumenized vascular-like networks observed in our studies were in close resemblance to those reported for fibroblast coculture assays by Kim et al. (2013) on a microfluidic chip or by Newman et al. (2011) on beads in a fibrin gel. In conclusion, our current 3D coculture model allows us to form dynamic vascular-like networks that keep growing throughout the experimental time of 21 days with simultaneous lumen formation.

Early Growing and Mature Vasculature-Like Structures Exhibit Differential Vascular Barrier Function

The intercellular adhesive points, known as adherens and tight junctions, between the ECs forming the vascular networks dictate their stability. In addition to influencing the differentiation of the ECs during vascular maturation, mural cells (Kurzen et al., 2002; Alimperti et al., 2017) and endogenously produced proteins and growth factors, such as VEGF (Bates, 2010), also assist in the

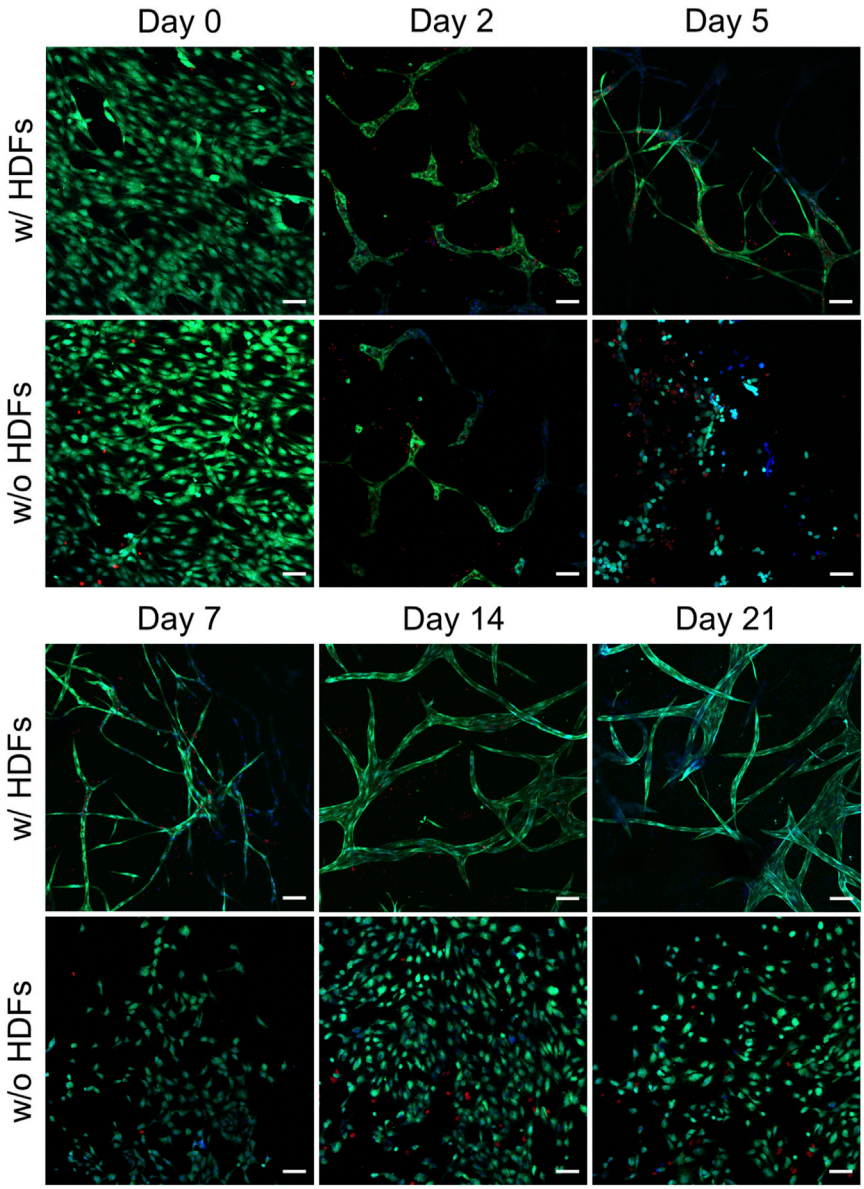

FIGURE 4 | Representative CLSM images from the live–dead assay of HUVECs in collagen gels when cultured with and without fibroblasts (scale bar 100 μm). All images were recorded in a single-confocal plane (day 0, 2, 5, and 7) or within a short z-range of 20 μm (for day 14 and 21). All the images display the merging of Hoechst (blue), FDA (green), and PI (red) channels (n = 2).

development and stabilization of stronger intercellular EC contacts increasing the vascular barrier (Jain, 2003). This generally results in lower vascular permeability for endo- and exogenous compounds in blood extravasating the vessel or entering the blood stream from tissue (Heinolainen et al., 2017). To access the structural integrity and the permeability of the vascular-like structures, we employed TD of different molecular weights and detected their uptake into the luminal space after 24 h static TD exposure in the gel (**Figure 6**). The low-molecular weight dextran (10 kDa) generally permeates endothelial capillaries in both directions *in vitro* and *in vivo*, although the exact mechanism is not known (Egawa et al., 2013; Andrée et al., 2019). In contrast, the 70 kDa TD typically only penetrates EC vascular walls with impaired cell–cell junction integrity and thus lowered vascular barrier function (Alimperti et al., 2017) while it does not penetrate vascular walls reflecting physiological barrier function.

CLSM analysis of the vascular-like 3D-structures exposed to TD for 24 h on day 21 indicated that thin capillaries (3–30 μm diameter) display a higher permeability to 10 kDa TD compared to thicker structures (40–70 μm diameter), while both are impermeable to 70 kDa TD (**Figure 6**). Thus, we attribute features of immature newly forming or early vascular strands to the thinner vascular structures while the thicker diameter

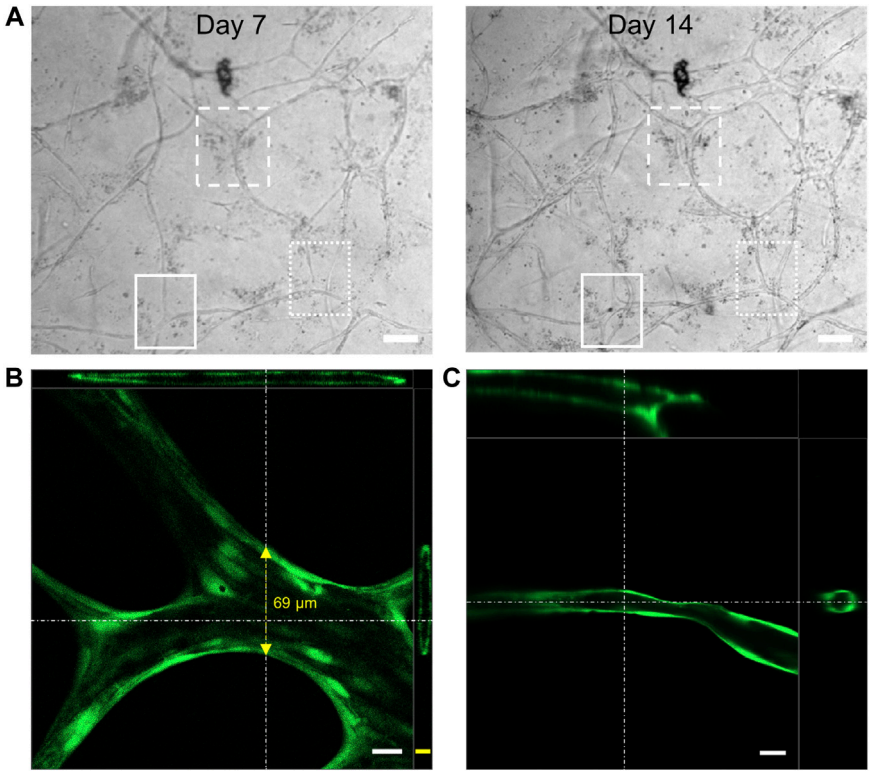

FIGURE 5 | (A) Representative brightfield microscopy images of the HUVEC vascular-like network showing anastomosis (highlighted areas) of the cellular extensions giving rise to new junctions (scale bar 100 µm); 3D cross section image generated from confocal microscopy of **(B)** FDA or **(C)** calcein-AM (both green) treated HUVEC network, showing a hollow lumen structure on day 21 (scale bar 20 µm (white), 10 µm (yellow), top-XZ plane projection, right most-YZ plane projection, $n = 4$).

strands reflect more mature vasculature characteristics. Compared to the direct cocultures of green-fluorescent protein (GFP)-expressing HUVECs and hASCs (Andrée et al., 2019), the amount of internalized 10 kDa TD observed in our study is low and was most prominent only at a few sites of early vascular-like structures. Control experiments with GFP-HUVECs under our indirect coculture conditions indicate a lower barrier function of GFP-HUVECs than non-transfected HUVECs based on the amount of accumulated TD inside the lumen (**Supplementary Figure S4**). Hence, it appears that the indirect coculture of HDFs and HUVECs results in more stable and less permeable vascular-like networks. In addition to adherens (**Supplementary Figure S3**) and tight junction formation, in general the luminally located endothelial glycocalyx contributes significantly to the barrier function of the capillary wall and will as such be addressed in future studies.

Blocking the Vascular Endothelial Growth Factor Signaling in Human Umbilical Vein Endothelial Cells Prevents Vascular Network Formation

Since the vascular network formation in our setup is highly dependent on HDF-produced proteins and growth factors such as VEGF, we evaluated the HUVEC network formation under indirect coculture conditions in the presence of a VEGF receptor 2 signaling inhibitor in the HUVEC medium compartment. Therefore, brivanib as effective VFGF and bFGF receptor inhibitor was used as the model drug (Chou and Finn, 2012). Although the route of drug exposure in our model does not exactly mimic the intravenous route of administration, the observed effects may mimic the consequences after intratumoral and intraperitoneal injections or drug extravasation from leaky blood vessels at the tumor site. In all these scenarios, the drug acts directly on the outer surface of the vascular networks.

Continuous treatment of the indirect coculture with brivanib starting on day 0 was accomplished through bolus administration (300 and 900 nM) to the HUVEC medium in the upper compartment, which was repeated every other day simultaneous to the medium exchange. A concentration-dependent efficacy toward the inhibition of angiogenesis was observed by a marked reduction in continuous vascular-like networks resulting in total suppression on day 14 with 900 nM brivanib (**Figure 7**). In addition, the indirect coculture model was treated with an equivalent amount of DMSO as the vehicle control for the respective brivanib doses with subsequent live–dead staining of the cultures. No regression of angiogenesis or dead cells were observed in either of the vehicle controls (**Supplementary Figure S5A**). Interestingly, we also have

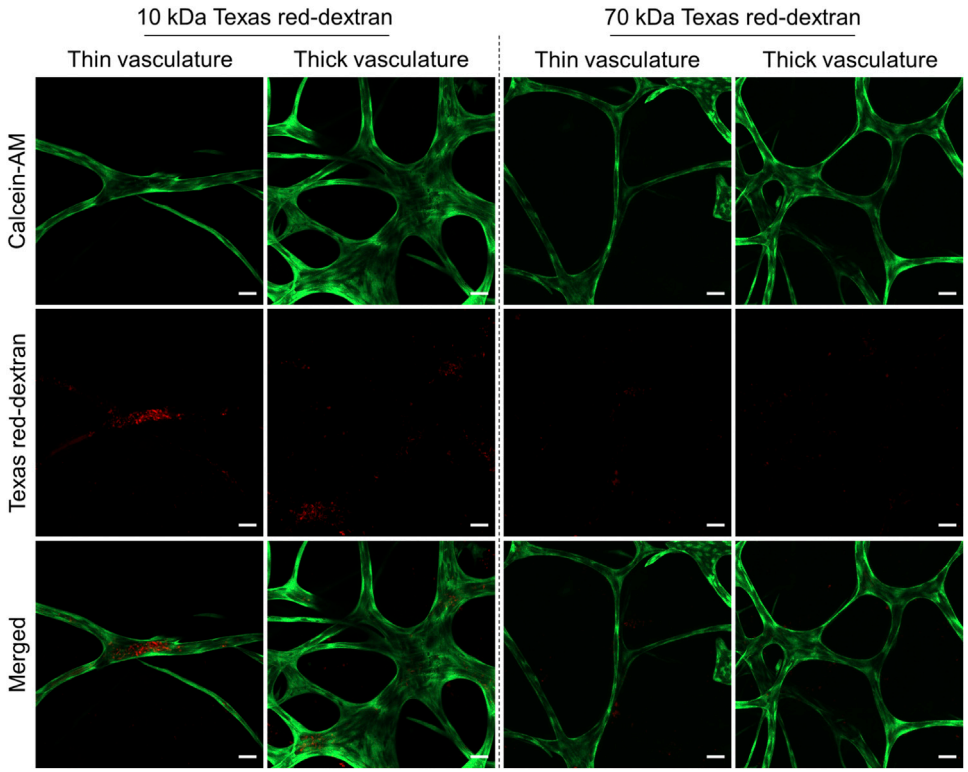

FIGURE 6 | Representative CLSM images showing the permeability of thin and thick branches of the vascular-like networks toward Texas red-dextran (TD, red) of molecular weights of 10 and 70 kDa. HUVECs were stained using calcein-AM (green). All the staining experiments were performed after 21 days of culture (n = 4, scale bar 50 μm).

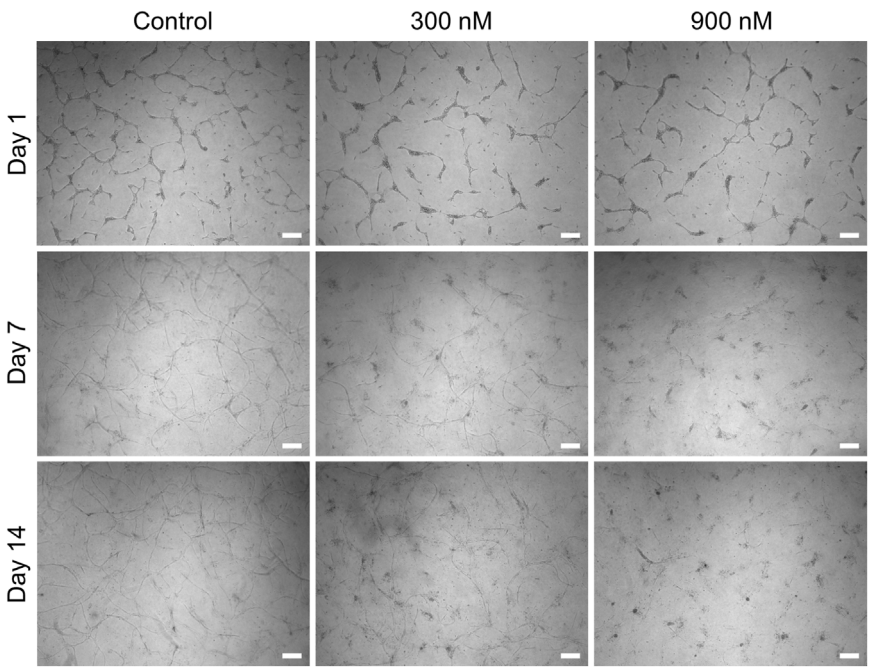

FIGURE 7 | Representative brightfield images showing the concentration-dependent effect of brivanib (0, 300, and 900 nM) on HUVEC network formation in the indirect coculture model (scale bar 200 μm, n = 3).

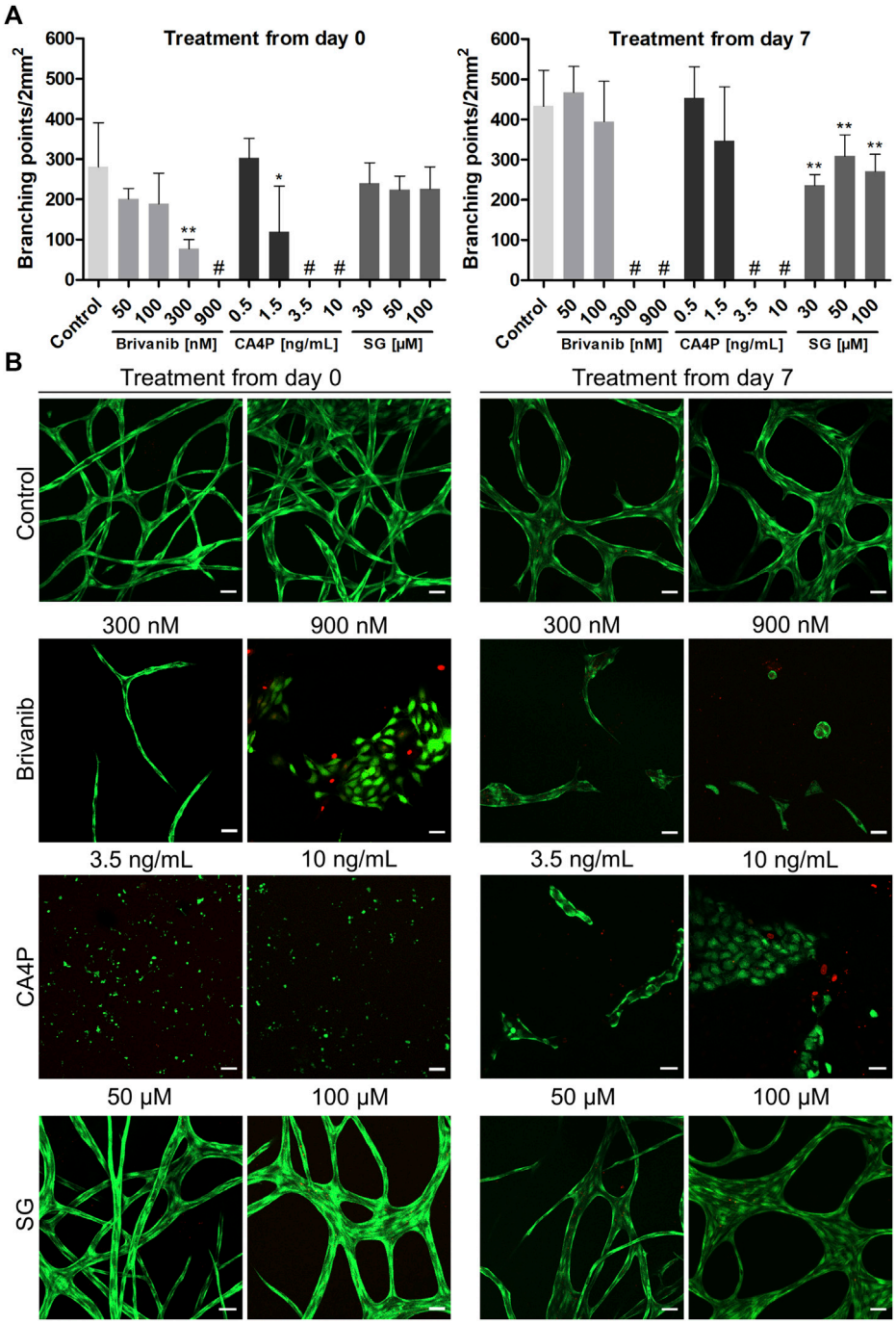

FIGURE 8 | Influence of concentration-dependent drug treatment with brivanib, CA4P, and SG toward angiogenesis (treatment from day 0 onward) and vascular network disruption (treatment starting from day 7) for 14 days, respectively, in indirect coculture of HUVECs and HDFs. **(A)** Quantitative analysis of the respective vascular networks' number of branching points per area at the end point of the drug treatment (# indicates lack of any quantifiable continuous vascular networks) (mean ± SD, $n = 5$, $^{*}p < 0.05$, and $^{**}p < 0.01$ value is significantly different from control as tested by a non-parametric Mann–Whitney U-Test); **(B)** Representative CLSM images of live–dead stained samples [FDA (green), PI (red)] after concentration-dependent treatment with brivanib, CA4P, or SG, respectively, compared to controls without treatment on day 14 and 21 (scale bar 50 µm, $n = 5$).

found that withdrawal of brivanib treatment in the indirect coculture setting on day 14 allowed the HUVECs to proliferate and recover the vascular-like networks within the following 14 days (**Supplementary Figure S5B**), clearly indicating the reversible effect of brivanib on capillary formation in this assay setup by targeting the VEGF/VEGF receptor 2 axis. This reversibility of the vascular-like network generation reflected by our model makes it a valuable tool, especially when accessing optimized timepoints for repeated drug

dosing. Motivated by the response of this advanced model toward drug treatment and the differential permeability of the early and mature vascular-like networks, we further investigated the effect of other known vascular targeting drugs such as VDAs.

Validation of Vascular Disruption Properties of Drugs on Vascular-Like Networks From the 3D Culture Model

In addition to brivanib, we chose combretastatin A4 phosphate (CA4P), an investigational drug belonging to the group of tubulin-binding VDAs (West and Price, 2004), and 6'-silaylgalactose (SG), a recent experimental molecule targeting the VEGF receptor 2 on endothelial cells (Chung et al., 2019), to further challenge and validate our model. CA4P induces microtubule destabilization by ß-tubulin binding in endothelial cells which in turn reduces the stability of vascular networks. Simultaneous impairment of the functional engagement of the endothelial cell-specific junctional molecule VE-cadherin hinders stabile neovessel formation, resulting in both antiangiogenic and vascular disrupting effects *in vivo* (Vincent et al., 2005). The antiangiogenic property of the synthetic disaccharide SG was reported *in vivo* while its vascular disrupting properties have not been studied yet (Chung et al., 2019). Thus, we tested for the antiangiogenic effect of the drugs by starting the treatment on day 0 of the indirect coculture as described for brivanib above. Additionally, the evaluation of their vascular disrupting properties on already established vascular-like structures was accomplished by starting the drug treatment on day 7 of the coculture experiment, which was continued until day 21. In both cases, the drugs were administered as bolus to the HUVEC compartment simultaneous to the media exchange which was repeated every other day for 14 days. The combined quantitative analysis of the number of network branching points per area in brightfield images from concentration-dependent brivanib, CA4P and SG treatments starting on day 0 and day 7 are graphically illustrated in **Figure 8A**. Rational drug concentrations were deduced from *in vitro* data on the tube formation assays with endothelial cells on Matrigel^{TM} reported in literature which locate in the medium nM to low µM-range for brivanib (Li et al., 2020), the low nM-range for CA4P (Vincent et al., 2005) and the low µM-range for SG (Chung et al., 2019). Based on the metabolic activity of viable HUVECs and HDFs in the presence and absence of the drugs, their concentration-dependent cytocompatibility was accessed with an MTS proliferation assay (**Supplementary Figure S6**). Therefore, cells were seeded on TCPS at seeding densities resembling the ones in the indirect coculture setup. Cell viabilities of drug treated HDFs and HUVECs were not significantly different from controls at all tested concentrations. Only with CA4P a slightly reduced metabolic activity of HUVECs was observed at the highest dose of 3.5 and 10 ng·ml^{-1} (**Supplementary Figure S6A**).

At the end of 14-day drug treatments, all samples were imaged *via* CLSM after a live–dead staining to qualitatively access the network structure and cell viability (**Figure 8B**). The concentration-dependent antiangiogenic efficacy of brivanib indicated in brightfield and CLSM images is in general agreement and is markedly visible by a significantly reduced network integrity at concentrations ≥300 nM brivanib, while full inhibition of angiogenesis is observed at 900 nM brivanib. Brightfield images at lower concentrations of 100 and 50 nM brivanib (**Supplementary Figure S7**) show a slightly reduced network density at 100 nM compared to 50 nM brivanib treatment and control. Furthermore, brivanib was also able to induce significant vascular disruption of existing vasculature starting at concentrations between 100 and 300 nM during a 14-day treatment. At 900 nM complete disruption was observed (**Figure 8**; **Supplementary Figure S8**).

Similarly, CA4P turned out to be very effective in preventing angiogenesis as well as inducing vascular disruption in a 14-day treatment at concentrations ≥3.5 ng·ml^{-1} (**Figure 8**; **Supplementary Figures S9, S10**). Closer evaluation of different z-layers in the live–dead stained samples revealed a toxic effect of the drug on HUVECs at the high concentration of 10 ng·ml^{-1} (**Supplementary Figure S11**), which was more pronounced when treatment started on day 0 of the indirect coculture. This could be an effect of prolonged exposure to the drug and was similarly observed in other *in vitro* studies showing that CA4P is cytotoxic for proliferating but not for quiescent HUVECs (Dark et al., 1997). For brivanib-treated cells, evaluation of different z-planes revealed a lower cell number for 900 nM starting from day 0 and already for 300 nM starting from day 7 (**Supplementary Figure S11**). This effect was also observed in *in vitro* studies showing the VEGF- and bFGF-stimulated HUVEC proliferation to be reduced in the presence of brivanib (Bhide et al., 2006). In addition, a distinct morphological change with reduced cell surface of the HUVECs was observed after treatment (**Supplementary Figure S11**), most prominent with CA4P, but also for brivanib treatment with 900 nM starting from day 7, which is for CA4P well described in literature and concomitantly observed with cytoskeleton alterations finally leading to cell apoptosis (Galbraith et al., 2001; Kim et al., 2012).

In the case of SG treatment brightfield microscopy and CLSM images indicated a clearly less pronounced antiangiogenic and/or vascular disrupting effect if compared to the other two tested drugs (**Figure 8**; **Supplementary Figures S12, S13**). For treatment starting from day 7, a significantly reduced number of branching points was visible for all tested concentrations if compared to controls but the effect was nowhere near a complete vascular disruption (**Figure 8**). At 100 µM concentration, additionally, a minor impact on the network morphology was observable for treatments starting on day 0 and 7 with thicker junctions (**Supplementary Figures S12, S13**). Moreover, with all concentrations of SG tested, no cytotoxicity for the vascular-like network was observed (**Figure 8B**), which is in line with HUVEC proliferation assays reported in the literature (Chung et al., 2019) or MTS data shown in **Supplementary Figure S6**.

For direct comparison with the effective drug concentrations identified in our indirect coculture assay, we additionally performed a conventional 24h-tube forming Matrigel^{TM} assay with bolus administration of the drugs along with HUVEC medium (**Supplementary Figure S14**) similar to previous reports (Vincent et al., 2005; Chung et al., 2019; Li et al.,

2020). We found brivanib and CA4P to completely inhibit angiogenesis at concentrations as low as 50 nM and 0.3 ng·ml^{-1}, respectively, and largely inhibited angiogenesis at 10 μM SG (**Supplementary Figure S14**). Thus, the inhibitory concentrations obtained from this tube formation assay are clearly overestimating the efficacy of the drugs compared to our long-term 3D assay in indirect coculture, even when considering the slightly higher cell numbers used in the indirect coculture compared to the tube formation assay. The pure 3D collagen type I matrix acts as an additional extracellular barrier to the drug and resembles the interstitial matrix of tumors in terms of permeability for small molecules (Ramanujan et al., 2002).

Expectedly, CA4P showed the strongest antiangiogenic and vascular disruption effect of all three tested drugs with efficacies already in the low nanomolar range, followed by brivanib while SG displayed only a minor effect. Neither prevention of angiogenesis nor effective vascular disruption was observed in the 3D environment of our advanced model at the highest tested SG concentration of 100 μM. This is in general agreement with the relatively high SG concentration (30 μM) required to inhibit VEGF-induced VEGF receptor 2 phosphorylation in HUVECs (Chung et al., 2019). Although reported as effective antiangiogenic agent in various mouse models (Chung et al., 2019), including a model of pathologic angiogenesis in the mouse retina, its potential as a single-antitumor drug is debatable as SG, based on our experiments, does not benefit from a strong combined antiangiogenic and vascular disruption effect *in vitro*.

Throughout the drug treatment experiment, the confluent HDF monolayer in the lower compartment of the assay was retained without any obvious cytotoxic effects of the drug as detected by brightfield microscopy and MTS viability assays (**Supplementary Figures S15, S16**). This reinstates the advantage of the indirect coculture enabling to study the behavior of HUVECs toward drug treatment selectively and independent of neighboring cocultured mural cells. Since both HUVECs and HDFs generally transit to a quiescent state once the vascular structures or the confluent monolayer have formed, they are less prone to cytotoxic effects of the drugs, particularly with CA4P (Dark et al., 1997). Therefore, the option to screen drug effects on an already established vascular-like network of quiescent endothelial cells combines with reduced susceptibility of the network for cytotoxic drug effects in this advanced assay.

CONCLUSION

In summary, we have established an indirect coculture setup to generate long-lasting, profuse HUVEC-based vascular-like networks in type I rat collagen gels that feature permeability characteristics of mature as well as early vasculature with tubular branches capable to anastomose *in vitro*. The HDF-produced soluble proangiogenic and network stabilizing factors such as VEGF in this system enabled the continuous growth and maturation of lumenized vascular-like networks throughout the whole experimentation period up to day 21 and beyond. Unlike conventional *in vitro* angiogenesis assays that are typically short-lived, the unique combination of long lasting, profuse networks offered by our 3D model allows us to directly image morphological changes in the HUVEC-only network, offering advantages in analyzing drug efficacy with prolonged drug administration up to 14 days. Importantly, the model enables the study of both antiangiogenic and vascular disrupting drug efficacies. The drug effects are selectively acting on ECs without interference of surrounding mural cells, which can otherwise compete for nutrients or space. These truly 3D vascular-like networks expanding up to 600 μm in z-direction attenuated the antiangiogenic drug effects of the model drugs brivanib, CA4P, and SG compared to conventional tube forming assays. The closer resemblance of *in vivo* conditions by the 3D features including the extracellular matrix barrier, the unique possibility to study the antiangiogenic and disrupting drug effects on both early and mature vascular-like structures as well as their longevity highlight the superiority of this advanced model over current state-of-the-art *in vitro* angiogenesis models. In an upcoming study the perfusion of such tubular structures will be addressed. With the established model, particularly information on repeated, prolonged drug administration effects become accessible. Therefore, we envision this advanced model as a predictive tool when validating hits from prescreenings of vascular targeting therapeutics *via* conventional, fast angiogenesis assays, thus bridging the gap between *in vitro* and *in vivo* studies.

DATA AVAILABILITY STATEMENT

The datasets presented in this article will be made available by the first author upon reasonable request. Requests to access the datasets should be directed to PV, prabhusrinivas.y@gmail.com.

ETHICS STATEMENT

The studies involving human cells and tissue were reviewed and approved by Ethics Committee at Charité Universitätsmedizin Berlin, Germany EA1/081/13. Written informed consent to use the material for research purposes was provided by the participants' legal guardian/next of kin.

AUTHOR CONTRIBUTIONS

PY, FS, AH, IP, LE, and AD performed the experiments and data analysis. MW, PY, AH, and AL designed the study and MW, AL, PY, and LE wrote the manuscript.

FUNDING

We would like to acknowledge financial support from the Federal Ministry of Education and Research Germany (BMBF) through Grant FKZ:13N13523 and the assistance of the Core Facility BioSupraMol supported by the German Research Foundation

(DFG). We acknowledge support by the Open Access Publication Initiative of Freie Universität Berlin.

ACKNOWLEDGMENTS

FS and MW kindly thank Dr. S. Hemmati-Sadeghi for technical support during the establishment of the assay. MW and AL are thankful for technical assistance in image acquisition from M. Lindner. MW is grateful for the continuous supporting cooperation with the Institute of Pharmacy (Prof. Dr. M. Schäfer-Korting, Prof. Dr. S. Hedtrich, Prof. Dr. B. Kleuser) of Freie Universität Berlin.

SUPPLEMENTARY MATERIAL

The Supplementary Material for this article can be found online at: https://www.frontiersin.org/articles/10.3389/fbioe.2022.888492/full#supplementary-material

REFERENCES

Adams, R. H., and Alitalo, K. (2007). Molecular Regulation of Angiogenesis and Lymphangiogenesis. *Nat. Rev. Mol. Cell Biol.* 8 (6), 464–478. doi:10.1038/nrm2183

Alimperti, S., Mirabella, T., Bajaj, V., Polacheck, W., Pirone, D. M., Duffield, J., et al. (2017). Three-Dimensional Biomimetic Vascular Model Reveals a RhoA, Rac1, and N-Cadherin Balance in Mural Cell-Endothelial Cell-Regulated Barrier Function. *Proc. Natl. Acad. Sci. U.S.A.* 114 (33), 8758–8763. doi:10.1073/pnas.1618333114

Andrée, B., Ichanti, H., Kalies, S., Heisterkamp, A., Strauß, S., Vogt, P. M., et al. (2019). Formation of Three-Dimensional Tubular Endothelial Cell Networks Under Defined Serum-Free Cell Culture Conditions in Human Collagen Hydrogels. *Sci. Rep.* 9 (1), 5437. doi:10.1038/s41598-019-41985-6

Auler, M., Pitzler, L., Pöschl, E., Zhou, Z., and Brachvogel, B. (2017). Mimicking Angiogenesis *In Vitro*: Three-Dimensional Co-Culture of Vascular Endothelial Cells and Perivascular Cells in Collagen Type I Gels. *Bio-Protocol* 7 (8), e2247. doi:10.21769/BioProtoc.2247

Bates, D. O. (2010). Vascular Endothelial Growth Factors and Vascular Permeability. *Cardiovasc. Res.* 87 (2), 262–271. doi:10.1093/cvr/cvq105

Bergers, G., and Benjamin, L. E. (2003). Tumorigenesis and the Angiogenic Switch. *Nat. Rev. Cancer* 3 (6), 401–410. doi:10.1038/nrc1093

Bhide, R. S., Cai, Z.-W., Zhang, Y.-Z., Qian, L., Wei, D., Barbosa, S., et al. (2006). Discovery and Preclinical Studies of (R)-1-(4-(4-Fluoro-2-Methyl-1H-Indol-5-yloxy)-5- Methylpyrrolo[2,1-f][1,2,4]Triazin-6-yloxy)Propan-2-ol (BMS-540215), an *In Vivo* Active Potent VEGFR-2 Inhibitor. *J. Med. Chem.* 49 (7), 2143–2146. doi:10.1021/jm051106d

Brassard-Jollive, N., Monnot, C., Muller, L., and Germain, S. (2020). *In Vitro* 3D Systems to Model Tumor Angiogenesis and Interactions with Stromal Cells. *Front. Cell Dev. Biol.* 8, 594903. doi:10.3389/fcell.2020.594903

Carmeliet, P. (2005). Angiogenesis in Life, Disease and Medicine. *Nature* 438 (7070), 932–936. doi:10.1038/nature04478

Charpentier, M. S., and Conlon, F. L. (2014). Cellular and Molecular Mechanisms Underlying Blood Vessel Lumen Formation. *BioEssays* 36 (3), 251–259. doi:10.1002/bies.201300133

Chen, X., Aledia, A. S., Popson, S. A., Him, L., Hughes, C. C. W., and George, S. C. (2010). Rapid Anastomosis of Endothelial Progenitor Cell-Derived Vessels with Host Vasculature is Promoted by a High Density of Cotransplanted Fibroblasts. *Tissue Eng. Part A* 16 (2), 585–594. doi:10.1089/ten.tea.2009.0491

Chou, T., and Finn, R. S. (2012). Brivanib: A Review of Development. *Future Oncol.* 8 (9), 1083–1090. doi:10.2217/fon.12.104

Chung, T.-W., Kim, E.-Y., Choi, H.-J., Han, C. W., Jang, S. B., Kim, K.-J., et al. (2019). 6′-Sialylgalactose Inhibits Vascular Endothelial Growth Factor Receptor 2-Mediated Angiogenesis. *Exp. Mol. Med.* 51 (10), 1–13. doi:10.1038/s12276-019-0311-6

Costa-Almeida, R., Gomez-Lazaro, M., Ramalho, C., Granja, P. L., Soares, R., and Guerreiro, S. G. (2015). Fibroblast-Endothelial Partners for Vascularization Strategies in Tissue Engineering. *Tissue Eng. Part A* 21 (5–6), 1055–1065. doi:10.1089/ten.TEA.2014.0443

Dark, G. G., Hill, S. A., Prise, V. E., Tozer, G. M., Pettit, G. R., and Chaplin, D. J. (1997). Combretastatin A-4, an Agent that Displays Potent and Selective Toxicity Toward Tumor Vasculature. *Cancer Res.* 57 (10), 1829–1834.

De Palma, M., Biziato, D., and Petrova, T. V. (2017). Microenvironmental Regulation of Tumour Angiogenesis. *Nat. Rev. Cancer* 17 (8), 457–474. doi:10.1038/nrc.2017.51

DeCicco-Skinner, K. L., Henry, G. H., Cataisson, C., Tabib, T., Gwilliam, J. C., Watson, N. J., et al. (2014). Endothelial Cell Tube Formation Assay for the *In Vitro* Study of Angiogenesis. *JoVE* 91, e51312. doi:10.3791/51312

Diaz-Santana, A., Shan, M., and Stroock, A. D. (2015). Endothelial Cell Dynamics During Anastomosisin Vitro. *Integr. Biol.* 7 (4), 454–466. doi:10.1039/c5ib00052a

Drzyzga, A., Cichoń, T., Czapla, J., Jarosz-Biej, M., Pilny, E., Matuszczak, S., et al. (2021). The Proper Administration Sequence of Radiotherapy and Anti-Vascular Agent-DMXAA Is Essential to Inhibit the Growth of Melanoma Tumors. *Cancers* 13 (16), 3924. doi:10.3390/cancers13163924

Egawa, G., Nakamizo, S., Natsuaki, Y., Doi, H., Miyachi, Y., and Kabashima, K. (2013). Intravital Analysis of Vascular Permeability in Mice Using Two-Photon Microscopy. *Sci. Rep.* 3 (1), 1932. doi:10.1038/srep01932

Evensen, L., Micklem, D. R., Blois, A., Berge, S. V., Aarsæther, N., Littlewood-Evans, A., et al. (2009). Mural Cell Associated VEGF Is Required for Organotypic Vessel Formation. *PLOS One* 4 (6), e5798. doi:10.1371/journal.pone.0005798

Galbraith, S. M., Chaplin, D. J., Lee, F., Stratford, M. R., Locke, R. J., Vojnovic, B., et al. (2001). Effects of Combretastatin A4 Phosphate on Endothelial Cell Morphology *In Vitro* and Relationship to Tumour Vascular Targeting Activity *In Vivo*. *Anticancer Res.* 21 (1a), 93–102.

Gavard, J. (2014). Endothelial Permeability and VE-Cadherin. *Cell. Adhesion Migr.* 8 (2), 158–164. doi:10.4161/cam.29026

Gill, J. H., Rockley, K. L., De Santis, C., and Mohamed, A. K. (2019). Vascular Disrupting Agents in Cancer Treatment: Cardiovascular Toxicity and Implications for Co-Administration with Other Cancer Chemotherapeutics. *Pharmacol. Ther.* 202, 18–31. doi:10.1016/j.pharmthera.2019.06.001

Gondi, C. S., Lakka, S. S., Dinh, D. H., Olivero, W. C., Gujrati, M., and Rao, J. S. (2004). Downregulation of uPA, uPAR and MMP-9 Using Small, Interfering, Hairpin RNA (siRNA) Inhibits Glioma Cell Invasion, Angiogenesis and Tumor Growth. *Neuron Glia Biol.* 1 (2), 165–176. doi:10.1017/s1740925x04000237

Griffith, C. K., Miller, C., Sainson, R. C., Calvert, J. W., Jeon, N. L., Hughes, C. C., et al. (2005). Diffusion Limits of an *In Vitro* Thick Prevascularized Tissue. *Tissue Eng.* 11 (1-2), 257–266. doi:10.1089/ten.2005.11.257

Heinolainen, K., Karaman, S., D'Amico, G., Tammela, T., Sormunen, R., Eklund, L., et al. (2017). VEGFR3 Modulates Vascular Permeability by Controlling VEGF/VEGFR2 Signaling. *Circ. Res.* 120 (9), 1414–1425. doi:10.1161/circresaha.116.310477

Hetheridge, C., Mavria, G., and Mellor, H. (2011). Uses of the *In Vitro* Endothelial-Fibroblast Organotypic Co-Culture Assay in Angiogenesis Research. *Biochem. Soc. Trans.* 39 (6), 1597–1600. doi:10.1042/bst20110738

Hinnen, P., and Eskens, F. A. L. M. (2007). Vascular Disrupting Agents in Clinical Development. *Br. J. Cancer* 96 (8), 1159–1165. doi:10.1038/sj.bjc.6603694

Huynh, H., Ngo, V. C., Fargnoli, J., Ayers, M., Soo, K. C., Koong, H. N., et al. (2008). Brivanib Alaninate, a Dual Inhibitor of Vascular Endothelial Growth Factor Receptor and Fibroblast Growth Factor Receptor Tyrosine Kinases, Induces Growth Inhibition in Mouse Models of Human Hepatocellular Carcinoma. *Clin. Cancer Res.* 14 (19), 6146–6153. doi:10.1158/1078-0432.ccr-08-0509

Ichanti, H., Sladic, S., Kalies, S., Haverich, A., Andrée, B., and Hilfiker, A. (2020). Characterization of Tissue Engineered Endothelial Cell Networks in Composite Collagen-Agarose Hydrogels. *Gels* 6 (3), 27. doi:10.3390/gels6030027

Jain, R. K. (2003). Molecular Regulation of Vessel Maturation. *Nat. Med.* 9 (6), 685–693. doi:10.1038/nm0603-685

Kang, B., Shin, J., Park, H. J., Rhyou, C., Kang, D., Lee, S. J., et al. (2018). High-Resolution Acoustophoretic 3D Cell Patterning to Construct Functional Collateral Cylindroids for Ischemia Therapy. *Nat. Commun.* 9 (1), 5402–5413. doi:10.1038/s41467-018-07823-5

Kim, S., Lee, H., Chung, M., and Jeon, N. L. (2013). Engineering of Functional, Perfusable 3D Microvascular Networks on a Chip. *Lab. Chip* 13 (8), 1489–1500. doi:10.1039/c3lc41320a

Kim, S., Peshkin, L., and Mitchison, T. J. (2012). Vascular Disrupting Agent Drug Classes Differ in Effects on the Cytoskeleton. *PLoS One* 7 (7), e40177. doi:10.1371/journal.pone.0040177

Koh, W., Stratman, A. N., Sacharidou, A., and Davis, G. E. (2008). Chapter 5 *In Vitro* Three Dimensional Collagen Matrix Models of Endothelial Lumen Formation During Vasculogenesis and Angiogenesis. *Meth. Enzymol.* 443, 83–101. doi:10.1016/s0076-6879(08)02005-3

Kubota, Y., Kleinman, H. K., Martin, G. R., and Lawley, T. J. (1988). Role of Laminin and Basement Membrane in the Morphological Differentiation of Human Endothelial Cells into Capillary-Like Structures. *J. Cell Biol.* 107 (4), 1589–1598. doi:10.1083/jcb.107.4.1589

Kurzen, H., Manns, S., Dandekar, G., Schmidt, T., Prätzel, S., and Kräling, B. M. (2002). Tightening of Endothelial Cell Contacts: A Physiologic Response to Cocultures with Smooth-Muscle-Like 10T1/2 Cells. *J. Investigative Dermatol.* 119 (1), 143–153. doi:10.1046/j.1523-1747.2002.01792.x

Lammert, E., and Axnick, J. (2012). Vascular Lumen Formation. *Cold Spring Harb. Perspect. Med.* 2 (4), a006619. doi:10.1101/cshperspect.a006619

Langhans, S. A. (2018). Three-Dimensional *In Vitro* Cell Culture Models in Drug Discovery and Drug Repositioning. *Front. Pharmacol.* 9, 6. doi:10.3389/fphar.2018.00006

Li, L., Zhu, M., Wu, W., Qin, B., Gu, J., Tu, Y., et al. (2020). Brivanib, a Multitargeted Small-Molecule Tyrosine Kinase Inhibitor, Suppresses Laser-Induced CNV in a Mouse Model of Neovascular AMD. *J. Cell. Physiol.* 235 (2), 1259–1273. doi:10.1002/jcp.29041

LINCS (2022). Brivanib. Available at: https://lincs.hms.harvard.edu/db/sm/10177-101/?sort=classmin (Accessed 01 08, 2022).

Liu, J., Long, H., Zeuschner, D., Räder, A. F., Polacheck, W. J., Kessler, H., et al. (2021). Synthetic Extracellular Matrices with Tailored Adhesiveness and Degradability Support Lumen Formation during Angiogenic Sprouting. *Nat. Commun.* 12 (1), 1–12. doi:10.1038/s41467-021-23644-5

Manikowski, D., Andrée, B., Samper, E., Saint-Marc, C., Olmer, R., Vogt, P., et al. (2018). Human Adipose Tissue-Derived Stromal Cells in Combination with Exogenous Stimuli Facilitate Three-Dimensional Network Formation of Human Endothelial Cells Derived from Various Sources. *Vasc. Pharmacol.* 106, 28–36. doi:10.1016/j.vph.2018.02.003

Montesano, R., Pepper, M. S., and Orci, L. (1993). Paracrine Induction of Angiogenesis *In Vitro* by Swiss 3T3 Fibroblasts. *J. Cell. Sci.* 105 (Pt 4), 1013–1024. doi:10.1242/jcs.105.4.1013

Montesano, R., Orci, L., and Vassalli, P. (1983). *In Vitro* Rapid Organization of Endothelial Cells into Capillary-Like Networks is Promoted by Collagen Matrices. *J. Cell. Biol.* 97 (5), 1648–1652. doi:10.1083/jcb.97.5.1648

Nagaiah, G., and Remick, S. C. (2010). Combretastatin A4 Phosphate: A Novel Vascular Disrupting Agent. *Future Oncol.* 6 (8), 1219–1228. doi:10.2217/fon.10.90

Nakatsu, M. N., and Hughes, C. C. W. (2008). Chapter 4 An Optimized Three-Dimensional *In Vitro* Model for the Analysis of Angiogenesis. *Meth. Enzymol.* 443, 65–82. doi:10.1016/s0076-6879(08)02004-1

Newman, A. C., Nakatsu, M. N., Chou, W., Gershon, P. D., and Hughes, C. C. W. (2011). The Requirement for Fibroblasts in Angiogenesis: Fibroblast-Derived Matrix Proteins are Essential for Endothelial Cell Lumen Formation. *MBoC* 22 (20), 3791–3800. doi:10.1091/mbc.e11-05-0393

Porcù, E., Bortolozzi, R., Basso, G., and Viola, G. (2014). Recent Advances in Vascular Disrupting Agents in Cancer Therapy. *Future Med. Chem.* 6 (13), 1485–1498. doi:10.4155/fmc.14.104

Privratsky, J. R., and Newman, P. J. (2014). PECAM-1: Regulator of Endothelial Junctional Integrity. *Cell. Tissue Res.* 355 (3), 607–619. doi:10.1007/s00441-013-1779-3

PubChem (2022). Combretastatin A4 Disodium Phosphate. Available at: https://pubchem.ncbi.nlm.nih.gov/compound/Fosbretabulin-disodium (Accessed 01 08, 2022).

Ramanujan, S., Pluen, A., McKee, T. D., Brown, E. B., Boucher, Y., and Jain, R. K. (2002). Diffusion and Convection in Collagen Gels: Implications for Transport in the Tumor Interstitium. *Biophysical J.* 83 (3), 1650–1660. doi:10.1016/S0006-3495(02)73933-7

Senger, D. R., and Davis, G. E. (2011). Angiogenesis. *Cold Spring Harb. Perspect. Biol.* 3 (8), a005090. doi:10.1101/cshperspect.a005090

Shafiee, S., Shariatzadeh, S., Zafari, A., Majd, A., and Niknejad, H. (2021). Recent Advances on Cell-Based Co-Culture Strategies for *In Vitro* Pre-Vascularization. *Front. Bioeng. Biotechnol.* 1155. doi:10.3389/fbioe.2021.745314

Siemann, D. W., and Horsman, M. R. (2009). Vascular Targeted Therapies in Oncology. *Cell. Tissue Res.* 335 (1), 241–248. doi:10.1007/s00441-008-0646-0

Siller, I. G., Epping, N.-M., Lavrentieva, A., Scheper, T., and Bahnemann, J. (2020). Customizable 3D-Printed (Co-)Cultivation Systems for *In Vitro* Study of Angiogenesis. *Materials* 13 (19), 4290. doi:10.3390/ma13194290

Simons, M., Alitalo, K., Annex, B. H., Augustin, H. G., Beam, C., Berk, B. C., et al. (2015). State-of-the-Art Methods for Evaluation of Angiogenesis and Tissue Vascularization: A Scientific Statement from the American Heart Association. *Circ. Res.* 116 (11), e99–132. doi:10.1161/RES.0000000000000054

Siu, L. L., Shapiro, J. D., Jonker, D. J., Karapetis, C. S., Zalcberg, J. R., Simes, J., et al. (2013). Phase III Randomized, Placebo-Controlled Study of Cetuximab Plus Brivanib Alaninate versus Cetuximab Plus Placebo in Patients with Metastatic, Chemotherapy-Refractory, Wild-Type K-RAS Colorectal Carcinoma: the NCIC Clinical Trials Group and AGITG CO.20 Trial. *J. Clin. Oncol.* 31 (19), 2477–2484. doi:10.1200/JCO.2012.46.0543

Smolarczyk, R., Czapla, J., Jarosz-Biej, M., Czerwinski, K., and Cichoń, T. (2021). Vascular Disrupting Agents in Cancer Therapy. *Eur. J. Pharmacol.* 891, 173692. doi:10.1016/j.ejphar.2020.173692

Stöbener, D. D., Uckert, M., Cuellar-Camacho, J. L., Hoppensack, A., and Weinhart, M. (2017). Ultrathin Poly(Glycidyl Ether) Coatings on Polystyrene for Temperature-Triggered Human Dermal Fibroblast Sheet Fabrication. *ACS Biomater. Sci. Eng.* 3 (9), 2155–2165. doi:10.1021/acsbiomaterials.7b00270

Uwamori, H., Higuchi, T., Arai, K., and Sudo, R. (2017). Integration of Neurogenesis and Angiogenesis Models for Constructing a Neurovascular Tissue. *Sci. Rep.* 7 (1), 17349. doi:10.1038/s41598-017-17411-0

Van Duinen, V., Stam, W., Mulder, E., Famili, F., Reijerkerk, A., Vulto, P., et al. (2020). Robust and Scalable Angiogenesis Assay of Perfused 3D Human iPSC-Derived Endothelium for Anti-Angiogenic Drug Screening. *Int. J. Mol. Sci.* 21 (13), 4804. doi:10.3390/ijms21134804

Vempati, P., Popel, A. S., and Mac Gabhann, F. (2014). Extracellular Regulation of VEGF: Isoforms, Proteolysis, and Vascular Patterning. *Cytokine Growth Factor Rev.* 25 (1), 1–19. doi:10.1016/j.cytogfr.2013.11.002

Vincent, L., Kermani, P., Young, L. M., Cheng, J., Zhang, F., Shido, K., et al. (2005). Combretastatin A4 Phosphate Induces Rapid Regression of Tumor Neovessels and Growth Through Interference with Vascular Endothelial-Cadherin Signaling. *J. Clin. Invest.* 115 (11), 2992–3006. doi:10.1172/jci24586

Weinhart, M., Hocke, A., Hippenstiel, S., Kurreck, J., and Hedtrich, S. (2019). 3D Organ Models-Revolution in Pharmacological Research? *Pharmacol. Res.* 139, 446–451. doi:10.1016/j.phrs.2018.11.002

West, C. M. L., and Price, P. (2004). Combretastatin A4 Phosphate. *Anti-Cancer Drugs* 15 (3), 179–187. doi:10.1097/00001813-200403000-00001

Conflict of Interest: The authors declare that the research was conducted in the absence of any commercial or financial relationships that could be construed as a potential conflict of interest.

Publisher's Note: All claims expressed in this article are solely those of the authors and do not necessarily represent those of their affiliated organizations, or those of the publisher, the editors, and the reviewers. Any product that may be evaluated in this article, or claim that may be made by its manufacturer, is not guaranteed or endorsed by the publisher.

frontiers | Frontiers in Bioengineering and Biotechnology

MINI REVIEW
published: 20 June 2022
doi: 10.3389/fbioe.2022.912073

A Challenge for Engineering Biomimetic Microvascular Models: How do we Incorporate the Physiology?

*Arinola O. Lampejo[1†], Nien-Wen Hu[1†], Daniela Lucas[1], Banks M. Lomel[1], Christian M. Nguyen[1], Carmen C. Dominguez[1], Bing Ren[2], Yong Huang[2] and Walter L. Murfee[1]**

[1]J. Crayton Pruitt Family Department of Biomedical Engineering, University of Florida, Gainesville, FL, United States, [2]Department of Mechanical and Aerospace Engineering, University of Florida, Gainesville, FL, United States

OPEN ACCESS

Edited by:
Jonathan W. Song,
The Ohio State University,
United States

Reviewed by:
William C. W. Chen,
University of South Dakota,
United States
Cheng-Hsien Liu,
National Tsing Hua University, Taiwan

***Correspondence:**
Walter L. Murfee
wmurfee@bme.ufl.edu

[†]These authors have contributed equally to this work and share first authorship

Specialty section:
This article was submitted to Tissue Engineering and Regenerative Medicine, a section of the journal Frontiers in Bioengineering and Biotechnology

Received: 03 April 2022
Accepted: 23 May 2022
Published: 20 June 2022

Citation:
Lampejo AO, Hu N-W, Lucas D, Lomel BM, Nguyen CM, Dominguez CC, Ren B, Huang Y and Murfee WL (2022) A Challenge for Engineering Biomimetic Microvascular Models: How do we Incorporate the Physiology? Front. Bioeng. Biotechnol. 10:912073. doi: 10.3389/fbioe.2022.912073

The gap between *in vitro* and *in vivo* assays has inspired biomimetic model development. Tissue engineered models that attempt to mimic the complexity of microvascular networks have emerged as tools for investigating cell-cell and cell-environment interactions that may be not easily viewed *in vivo*. A key challenge in model development, however, is determining how to recreate the multi-cell/system functional complexity of a real network environment that integrates endothelial cells, smooth muscle cells, vascular pericytes, lymphatics, nerves, fluid flow, extracellular matrix, and inflammatory cells. The objective of this mini-review is to overview the recent evolution of popular biomimetic modeling approaches for investigating microvascular dynamics. A specific focus will highlight the engineering design requirements needed to match physiological function and the potential for top-down tissue culture methods that maintain complexity. Overall, examples of physiological validation, basic science discoveries, and therapeutic evaluation studies will emphasize the value of tissue culture models and biomimetic model development approaches that fill the gap between *in vitro* and *in vivo* assays and guide how vascular biologists and physiologists might think about the microcirculation.

Keywords: angiogenesis, lymphangiogenesis, microcirculation, tissue engeneering, biomimetic

MOTIVATION

Almost every tissue in our bodies has blood and lymphatic vessels. Growth and remodeling of these vessels involves multiple cell types and can be associated with most diseases. Consequently, designing therapies to combat pathological conditions spanning tumor metastasis, diabetic retinopathy, islet transplantation, skin graft survival, and tissue ischemia necessitates understanding the cell dynamics involved in microvascular remodeling and how cells interact with each other in response to microenvironmental molecular cues. A challenge, however, is observing cells over the time course of these processes. The most common time-lapse *in vivo* approaches include multi-photon microscopy in the brain (Berthiaume et al., 2018; Bonney et al., 2021), dorsal window chamber preparations (Peirce et al., 2004), and the use of zebrafish (Gore et al., 2012; Venero Galanternik et al., 2017; Gore et al., 2018). The need for higher throughput and tunable methods has motivated an emerging area of research focused on biomimetic microvascular model development.

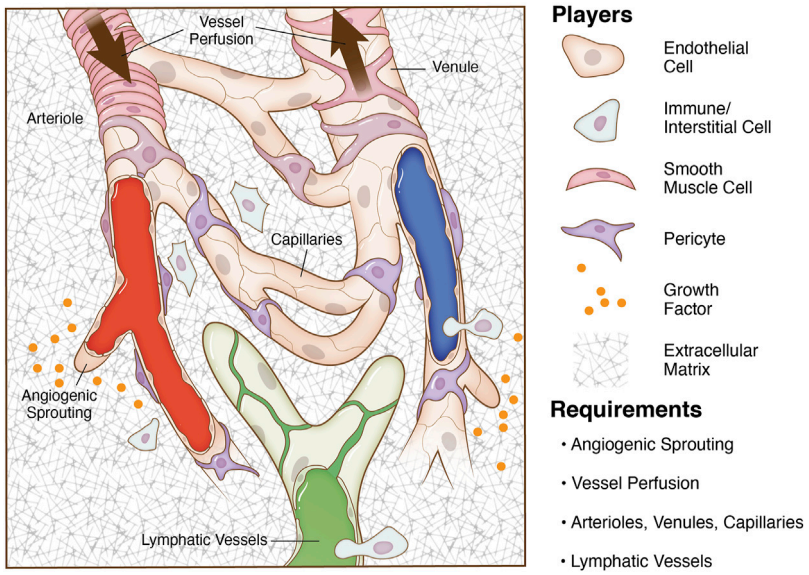

FIGURE 1 | Key microvascular players and model requirements. The microcirculation consists of blood vessels and initial lymphatic vessels. Mimicking the complexity of an intact microvascular network during angiogenesis and lymphangiogesis entails the incorporation of multiple cell types in system relevant patterns, chemical cues, vessel perfusion, and an appropriate matrix environment. A goal for tissue engineering and biomimetic microvascular model development is to recapitulate the multi-cell/system interactions and vessel functionality.

At the intersection of tissue engineering and physiology, biomimetic microvascular model development overlaps with lab-on-a-chip and organoid design with the end goal being to recapitulate the complexity of a real, microvascular network environment. Most common *in vitro* models can be characterized as bottom-up approaches that add one, two, or three cell types into a matrix environment (Kaunus et al., 2011). More technologically influenced approaches involve patterning cell and/or matrix through, for example, bioprinting or microfluidic based platforms (Song and Munn, 2011; Wang et al., 2016; Haase and Kamm, 2017; Campisi et al., 2018; Osaki et al., 2018; Henderson et al., 2021; Shirure et al., 2021; Ren et al., 2022). In recent years, these models have enabled reductionist experiments focused on isolating the effects of the individual components. A limitation of these systems is that they do not look like real microvascular networks and as a result engineers struggle to convince physiologists of their approach's relevance.

The objective of this mini-review is to overview the recent evolution of popular biomimetic modeling approaches for investigating microvascular dynamics and highlight the potential of the mesentery tissue culture model to fill the gap between *in vitro* and *in vivo* models. By emphasizing key players involved in microvascular remodeling, we identify key characteristics that can be considered model design requirements. We then provide examples of how our work in recent years has established the mesentery tissue culture model and its use for making scientific discoveries. Recognizing that every model has limitations and that a model is only as valuable as the scientific questions it is used to answer, our overview and examples frame the future potential for biomimetic models.

KEY PLAYERS IN MICROVASCULAR REMODELING

One of the main advantages that can help biomimetic models provide a more physiologically relevant environment in which to study new microvascular dynamics is the incorporation of multiple cell types. Endothelial cells, pericytes, smooth muscle cells, and macrophages all play key functional roles in a network microenvironment. Processes such as angiogenesis, vasculogenesis, and arteriogenesis, rely on the interplay between these different cell types. Thus, understanding the specific functions that endothelial cells, pericytes, smooth muscle cells, and macrophages have on their environment and on each other can help discover new phenomena that could be critical to more accurately modeling different disease pathologies. More importantly for the context of this article, incorporation of these players and characteristics can be viewed as design requirements for developing a biomimetic microvascular model (**Figure 1**).

Endothelial Cells

Endothelial cells are key regulators of multiple important vascular mechanisms. Endothelial cells control the uptake of various molecules and proteins into the circulatory system, sense and respond to changes in shear stress, modulate vessel dilation and constriction, and regulate inflammatory processes. One of the

most important functions that endothelial cells participate in is angiogenesis, characterized by the growth of new blood vessels from existing vessel networks. During angiogenesis, nearby endothelial cell adhesions are weakened, which allows for the formation of a capillary sprout from an existing vessel. Capillary sprouts are comprised of a migrating tip cells and proliferating stalk cells. Following paracrine signals released from supporting perivascular cells, capillary sprouts migrate from the vessel of origin into the extracellular matrix and can eventually form connections with other vessels or capillary sprouts. A more extensive review of endothelial cell functionality can be found here (Carmeliet, 2000; Gerhardt and Betsholtz, 2003; Peirce and Skalak, 2003; Kelly-Goss et al., 2014).

Pericytes

Another cell type that participates in remodeling and angiogenesis is the pericyte. Pericytes, which are characterized by markers such as smooth muscle actin, PDGFR-β, and neuron-glial antigen 2 (NG2), act as support cells along capillaries. Evidence suggests they play an important role in regulating vessel diameter, influencing vascular permeability, stabilizing vessels through direct and paracrine interactions, and promoting endothelial cell survival and proliferation. During angiogenesis, pericytes work with other mural cells to deposit components of the basement membrane such as laminin and collagen which support the growth of new capillary sprouts. Pericytes can also help guide and stimulate outgrowth of sprouts by secreting VEGF, bFGF, and other important growth factors. Additional references on the role of pericyte in angiogenesis are provided here (Murfee et al., 2006; Kelly-Goss et al., 2014; Stapor et al., 2014).

Smooth Muscle Cells

Smooth muscle cells are mural cells that reside along larger arterioles and venules. Smooth muscle cells regulate several vascular dynamics including maintenance of vessel function, constriction, and dilation. While mostly associated with vasoregulation (i.e., diameter control) and characterized by the expression of contractile proteins, smooth muscle cells can also play a critical role in the initiation of angiogenesis. For example, smooth muscle cells help start the process by detaching from blood vessels in response to Ang2 stimulation. This results in an increase in vascular permeability which triggers vasodilation and destabilization of endothelial adhesions. For more comprehensive discussion of the affect of smooth muscle cell on vascular dynamics see the references (Lilly, 2014; Motherwell et al., 2017).

Macrophages

Finally, macrophages are another cell type that warrant inclusion due to their presence in inflammatory environments. Macrophages can be sorted into two separate subgroups based on their role in inflammation. M1 macrophages are pro-inflammatory macrophages that can secrete cytotoxic agents while M2 macrophages more commonly secrete anti-inflammatory agents that stimulate angiogenesis. In addition to paracrine mechanisms, macrophage involvement in angiogenesis has also been suggested to include guiding capillary sprouting *via* local extracellular matrix degradation, facilitating pruning and maturation of vessel segments, and even transdifferentiating into endothelial cells (Corliss et al., 2016; Du Cheyne et al., 2020). Macrophages also play an important role in remodeling in disease settings, as shown by their roles as pro-angiogenic cells in the tumor microenvironment (Fu et al., 2020) as well as their upregulation of MMPs during pathological processes including tumor growth, HIV, and multiple sclerosis (Bar-Or et al., 2003; Webster and Crowe, 2006). The relative contribution of the various mechanisms during angiogenesis remains to be comprehensively evaluated and additional evidence for phenotypic overlaps with pericytes and observations of pericyte-like behavior continues to be uncovered, suggesting that our understanding of macrophage involvement in angiogenesis is incomplete. See these references for more detailed review of macrophages interacting with the microvasculature (Corliss et al., 2016; Du Cheyne et al., 2020).

While a model's necessary level of complexity and whether a model can satisfy the requirements for physiological relevance remain to be debated, it is important to emphasize that developing a microvascular model depends on the incorporation of specific cell types. Each cell type can be freshly isolated from tissues or obtained commercially. Critical decisions include consideration of cell origin (e.g., microvessels versus macrovessels or arterial versus venous) and phenotypic drift during culture. In order to mimic the microvasculature, multiple cells must be spatially assembled in relevant patterns. As an alternative bottom-up approach to build vessels, stem cell populations have been used as heterogeneous cell sources based on the premise that stem cells can undergo appropriate differentiation or even self-assemble into capillary networks (Kusuma et al., 2013; Zanotelli et al., 2016; Jones et al., 2021; Tracy et al., 2022). Regardless of the approach, the tissue engineering challenge of mimicking physiological relevance is highlighted by comparison to a real network (**Figure 1**).

Now consider the coordination between angiogenesis and lymphangiogenesis, the analogous growth of initial lymphatic vessels, the influence of local growth factor and matrix cues, the potential involvement of other cell populations, and the importance of local hemodynamics. Altogether multiple cell types and systems dance in concert to make up the architecture of a perfused microvascular network. For example, lymphatic and blood vessel coordination important for tissue homeostasis and the presence of lymphatic vessels has been shown to influence angiogenesis—an effect thought to be related to competitive binding of common growth factors (Sweat et al., 2012). Lymphatic vessels also are able to transdifferentiate into blood vessels (Azimi et al., 2020a). Other cell populations influencing capillary sprouting include fibroblasts, which can secrete growth factors and cytokines, and/or interstitial precursor cell populations, which can also secrete factors and differentiate into vascular cells. As for local hemodynamics, shear stress has been linked to angiogenesis as it is a regulator of endothelial cell behavior and phenotypes (Song and Munn 2011; dela Paz, et al., 2012; Galie, et al., 2014; Baeyens, et al., 2015; Driessen, et al., 2018; Peacock, et al., 2020).

Recognizing the importance of multi-cellular/system dynamics, critical questions remain regarding temporal relationships, cell plasticity, and cell-cell interactions. To complicate issues, answers to these questions depend on the environment and what milieu of players are present. From a vascular biologist's point of view, physiological relevance can be qualified by the multi-cellular/system complexity of a functional network.

OVERVIEW OF *IN VITRO* BIOMIMETIC MICROVASCULAR MODEL APPROACHES

In microvascular research, *in vitro* models provide a platform to study various growth and remodeling dynamics that may not be discernable *in vivo*. Common *in vitro* approaches used to study angiogenesis and lymphangiogenesis include three-dimensional (3D) cell culture models, bioprinting, and microfluidic devices.

Cell Culture Models

Basic cell culture systems incorporating endothelial cells, fibroblasts, or a combination of the two or more cell types cultured on basement membrane or Matrigel matrix have been used to study the formation of networks *via* anatamosing cords (Emonard et al., 1987; Vernon et al., 1992; Donovan et al., 2001). 3D cultures aimed at studying angiogenesis can usually also incorporate co-culture of different cell types but are distinguished from 2D systems by their incorporation of tunable gels or biomaterials that better mimic extra cellular matrix. 3D models have thus excelled in allowing researchers to study vacuolation, lumen formation, and integrin-dependent matrix remodeling during network formation, angiogenesis, and vasculogenesis (Bayless et al., 2000; Stratman et al., 2010; Krishnan et al., 2008; Darland and D'Amore, 2001; Stratman et al., 2009). Cutting-edge 3D models characteristically involve culturing endothelial cells and support cells to create networks of multi-cellular vessels. The ability to tune the matrix composition, include multiple cell types, and introduce interstitial flow allows for investigating vessel assembly and capillary network formation.

Bioprinting

Bioprinting represents an approach for controlling the spatial patterning of specific extracellular matrix proteins and/or cell types. More recently, the use of bioprinting technologies has emerged to create vessels within thick 3D matrix structures. In one example that highlights the state of the field, sacrificial inks have been printed in thick tissue constructs and then removed afterwards to create perfusable channels (Ren et al., 2022). Such perfusable channels are connected to a perfusion system, mimicking large vessels to supply nutrients and oxygen to and remove wastes from nearby tissues and secondary vascular structures.

Microfluidic Models

Two main microfluidic platforms dominate the literature. In one platform, perfused endothelial cell lined channels are separated by a matrix region (Song and Munn, 2011; Campisi et al., 2018). Endothelial cells are able to elongate and migrate into the matrix region and connect with vessels originating from the other side. Importantly the new network of endothelial cell segments becomes perfused. The seeding of cells, for example cancer cells, into the matrix region enables investigation of cell trafficking to the vessels. Physiological relevance is increased within this platform by tuning the material used for patterning the channels and the verification of vessel permeability (Qiu et al., 2018). Finally, an application for investigating lymphangiogenesis is made possible by seeding the channels with lymphatic endothelial cells (Osaki et al., 2018; Henderson et al., 2021). The second common microfluidic platform for mimicking the microcirculation is best described by a matrix region with an inlet and outlet channel (Wang et al., 2016; Shirure et al., 2021). Seeding the matrix region with endothelial cells and mural support cells resulted in the assembly of a perfusable capillary network with connections to both the inlet and outlet channels.

Each modeling strategy has advantages and disadvantages and depending on your scientific question or objective the required complexity could vary. 3D cell culture experiments have provided useful information on how different matrices and spatial cues affect vascular function (Lee et al., 2014; Knezevic et al., 2017; Robering et al., 2018), but often lack flow or feature limited interactions with other microvascular cell types. While microfluidic models are beneficial because of their ability to incorporate flow (Barkefors et al., 2009; Kim et al., 2016; Yamamoto et al., 2019), these models still face drawbacks such as a limited number of incorporated cell types and a lack of physiologically relevant microvascular network interactions. And with regards to bioprinting, assembly of vessels with multiple cell layers and small vessels with a diameter less than 50 μm remains challenging. All models have limitations, and the impact of the limitations depends on whether they impact the interpretations of results. Models with fewer players allow focusing on specific interactions, yet the questions remain—how complicated does a biomimetic model need to be and does a model with fewer players adequately mimic a real tissue? Regardless of the model, verification of physiological relevance is paramount.

FILLING THE GAP WITH THE MESENTERY CULTURE MODEL

Compared to the *in vitro* approaches, tissue culture models represent a top-down approach to recreating *in vivo* complexity by maintaining players *in situ*. Tissue culture models are not new; for example, using brain slice tissue explants has been a common tool for acute physiological studies (Stoppini et al., 1991). The aortic ring assay, in which slices of aorta are cultured in a 3D gel and multi-cellular sprouts grow radially outward over the time course of days, is probably the most common tissue culture model used to study angiogenesis (Nicosia and Ottinetti, 1990; Nicosia et al., 1994). Advantages include the maintenance of endothelial cell and pericyte dynamics while a weakness is the unknown relevance of investigating sprouting from a larger macro-vessel structure. An analogous tissue culture model is the lymphatic ring model,

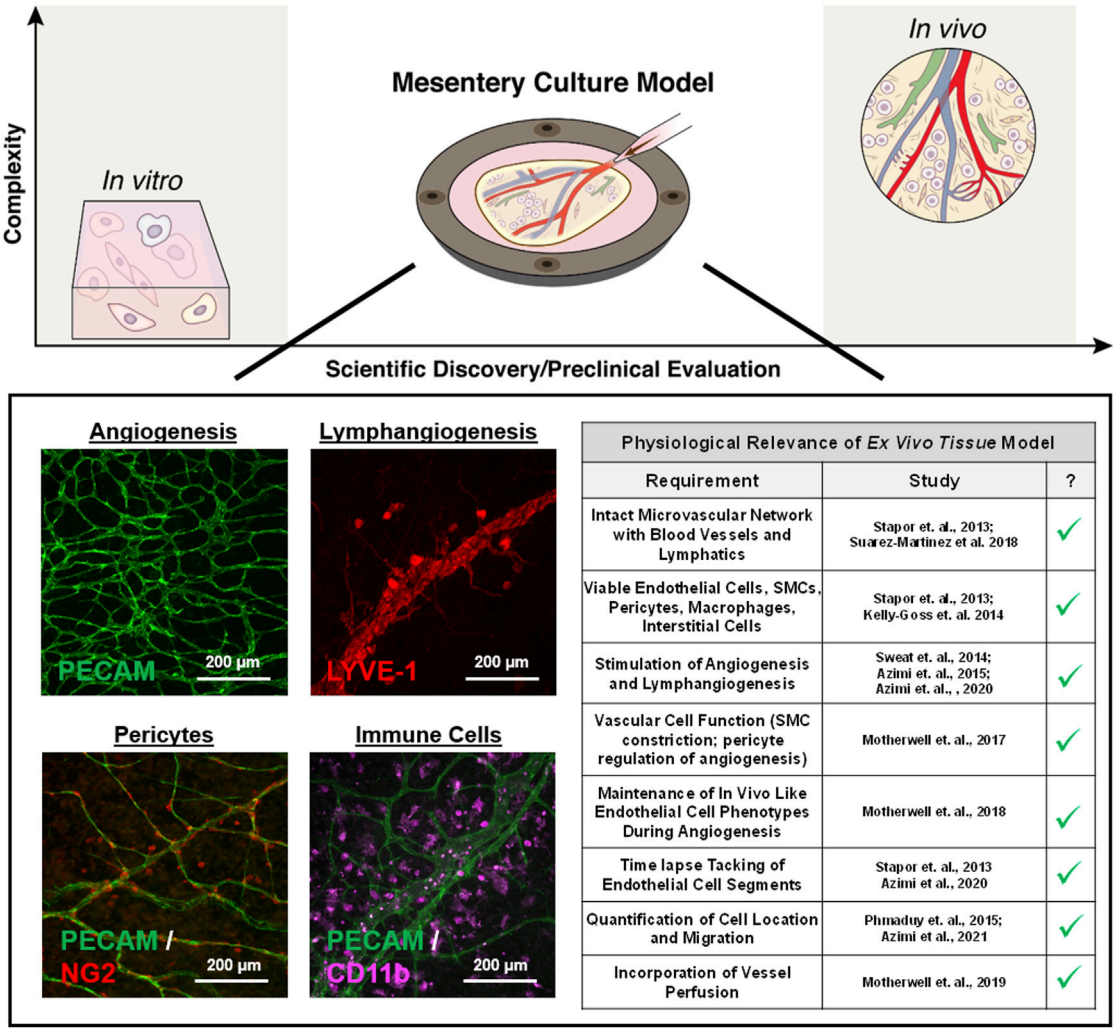

Physiological Relevance of *Ex Vivo Tissue* Model		
Requirement	Study	?
Intact Microvascular Network with Blood Vessels and Lymphatics	Stapor et. al., 2013; Suarez-Martinez et al. 2018	✓
Viable Endothelial Cells, SMCs, Pericytes, Macrophages, Interstitial Cells	Stapor et. al., 2013; Kelly-Goss et. al. 2014	✓
Stimulation of Angiogenesis and Lymphangiogenesis	Sweat et. al., 2014; Azimi et. al., 2015; Azimi et. al., , 2020	✓
Vascular Cell Function (SMC constriction; pericyte regulation of angiogenesis)	Motherwell et. al., 2017	✓
Maintenance of In Vivo Like Endothelial Cell Phenotypes During Angiogenesis	Motherwell et. al., 2018	✓
Time lapse Tacking of Endothelial Cell Segments	Stapor et. al., 2013 Azimi et al., 2020	✓
Quantification of Cell Location and Migration	Phmaduy et. al., 2015; Azimi et al., 2021	✓
Incorporation of Vessel Perfusion	Motherwell et. al., 2019	✓

FIGURE 2 | Filling the gap in biomimetic microvascular model development. The mesentery culture model aims to fill the gap between *in vitro* and *in vivo*. Recent work has demonstrated the utility of the approach for investigating angiogenesis and lymphangiogenesis at the same time. Multi-cellular complexity is highlighted by the presence of intact networks, endothelial cells, smooth muscle cells, pericytes, and immune cells. Cells display expected vessel-specific morphologies, and the model's physiological relevance is supported by maintained vasoreactivity, *in vivo* like cell phenotypes, and the incorporation of vessel perfusion.

which can be used to visualize lymphangiogenic sprouting dynamics (Bruyère et al., 2008; Iqbal et al., 2017; Katakia et al., 2020). Both ring models do not incorporate flow and cannot be used to study angiogenesis and lymphangiogenesis at the same time. Whether both models include microvascular networks is debatable. Conceivably for the aortic ring model, the new radial vessel segments could originate from the aortic endothelial cell layer or the adventitia's vasa vasorum. Also, the radial segments can connect to each other. Regardless, the resulting radial segments do not mimic the hierarchy of vessels associated with a microvascular network composed of arterioles, capillaries, and venules. An alternative approach is to use tissues with intact microvascular networks such as retina explants (Murakami et al., 2006). Because of the ease of harvesting and historical use for intravital studies, our laboratory has recently focused on using rat and murine mesenteric tissues and has developed a mesentery culture model (**Figure 2**). This culture model enables time-lapse investigation of cell—cell interactions at specific locations across blood and lymphatic microvascular networks.

Model Introduction

The mesentery culture model can be used with tissues from both rats and mice, although the use of mouse tissues requires pre-vascularization of the tissues before harvesting. Mesenteric windows, defined as the translucent connective tissues found between artery/vein pairs feeding the small intestine, are harvested starting from the ileum section. The model is simple and entails cutting tissues out and culturing them (Stapor et al., 2013; Azimi et al., 2017) post harvesting, in individual wells in a

6-well culture plate. During culture, minimum essential media can be supplemented with serum or specific growth factors to stimulate network growth. The mesentery tissue is attractive for the development of a biomimetic microvascular model that mimics the complexity of a real *in vivo* microenvironment. Mesentery tissue is 20–40 μm thick, making it ideal for culturing and imaging. The cell dynamics involved in angiogenesis in the mesentery reflect those in other tissues and it has been used for the evaluation of microvascular function. Rationales for using mesentery beyond its simple culture protocol include the tissue's historical use to gain foundational insights about lymphatic physiology, cell dynamics during angiogenesis, and microvascular function.

Physiological Verification

During culture, blood endothelial cells, pericytes, smooth muscle cells, interstitial immune cells, lymphatic endothelial cells, and even nerves can remain viable (Stapor et al., 2013; Sweat et al., 2014; Suarez-Martinez et al., 2018a; Hodges et al., 2020). The physiological relevance is further supported by the demonstration of the functional effects of pericytes on endothelial cell sprouting, smooth muscle cell contraction along arterioles, the maintenance of *in vivo* like endothelial cell phenotypes along with capillary sprouts during angiogenesis, and preferential vessel sprouting of capillaries and venules versus arterioles (**Figure 2**; Stapor et al., 2013; Motherwell et al., 2017; Motherwell et al., 2018; Azimi et al., 2020b). We have also demonstrated the ability to induce lymphangiogenesis (Sweat et al., 2014) and network perfusion which can introduce physiologically relevant flow velocities in capillaries during culture (Motherwell et al., 2019). Single-pass perfusion was accomplished using a peristaltic pump in series with the biochamber placed inside an incubator set to standard culture conditions. Flow passed through the vasculature and drained out of the venous side to be collected in a waste reservoir. A major difference highlighting the trade-offs between biomimetic approaches is that compared to microfluidic systems, which have controlled inlet and outlet ports (Song and Munn, 2011; Akbari et al., 2017; Hasse and Kamm, 2017; Shirure et al., 2021), the open loop system in the mesentery model allows control of fluid velocities, but not pressures—a difference that highlights the trade-offs between different biomimetic approaches.

Importantly, physiological verification of the mesentery culture model motivates future experiments. Published data supports tissue viability out to 7 days (Stapor et al., 2013) when cultured in serum free media and unpublished data suggests that tissues can remain viable out to 2 weeks. However, in serum free media smooth muscle and pericyte coverage become less consistent by 5–7 days (Stapor et al., 2013) and networks start to lose their hierarchical organization. Vessel perfusion has only been maintained out to 2 days and the impact of perfusion on hierarchical cell and vessel structure remains to be determined. Another important characteristic to evaluate is possible phenotypic drift at later time points. Motherwell et al. (2018), demonstrated that serum stimulated capillary sprouts after 3 days of culture display similar VEGF-R2, UNC-5b, and CD36 expression patterns compared to angiogenic sprouts *in vivo* and an earlier study confirmed that NG2-positive pericytes remain functional during angiogenesis in culture over the same time duration (Stapor et al., 2013). While these results support maintenance of phenotypes, additional studies focused on other cell types are needed.

Impact on Discovery

The mesentery tissue culture model's potential impact on scientific discovery is highlighted by the ability to view cell dynamics over the time course of network remodeling and to deliver unique comprehensive readouts including vessel permeability, endothelial cell junctional integrity, lymphatic/blood vessel malformations, cancer cell migration, and cancer cell invasion. Recently, we utilized double transgenic lineage mice to discover the ability of pericytes to detach from vessels (Payne et al., 2021) and migrate into the interstitial space during angiogenesis. We also have observed endothelial cells jumping off of one capillary sprout and connecting with another neighboring sprout (Suarez-Martiniez et al., 2018b). The observation of endothelial jumping resonates with the discovery of vascular island incorporation as a new type of endothelial cell dynamic during angiogenesis. Time-lapse imaging of disconnected endothelial segments confirmed their ability to connect with nearby networks during remodeling (Kelly-Goss et al., 2012; Kelly-Goss et al., 2013; Stapor et al., 2013). The value of our model is maybe best supported by the time-lapse visualization of vessel malformations associated with lymphatic-to-blood vessel transition—a discovery also made possible by the unique view of the model (Azimi et al., 2020a). Evidence for lymphatic-to-blood vessel transition in cultured tissues is supported by 1) real-time tracking of lymphatic segments, 2) observation of the formation of lymphatic-to-blood and blood-to-lymphatic vessel connections, and 3) loss of both LYVE-1 and podoplanin labeling along remodeling initial lymphatic vessels (Azimi et al., 2020b). The ability to watch where cells go and how cells interact with one another during microvascular remodeling will undoubtedly offer new insights by combining the approach using mouse and rat tissues with bioprinting and cell transfection technologies to enable tracking of endogenous and exogenous cell types.

Potential for Future Applications

The physiological relevance and ability to track cell populations uniquely position the mesentery tissue culture to make a big impact, especially through more applied studies focused on evaluating microvascular interactions with exogenous cells. For example, recent studies have demonstrated the feasibility of anti-angiogenic drug testing and adding various stem and cancer cell populations into the mesentery microenvironment (Azimi et al., 2015; Burks et al., 2016; Azimi et al., 2020a; Suarez-Martinez et al., 2021). These advances prime the utility of the model to investigate drug testing and the therapeutic effects of cell targeted therapeutic strategies during angiogenesis and lymphangiogenesis. In addition, the use of real tissues enables the evaluation of these dynamics within aging or disease settings (Hodges et al., 2018).

CONCLUSION AND CHALLENGES FOR THE FIELD

Mimicking *in vivo* complexity is a key challenge for biomimetic model development and highlights a disconnect between tissue engineers and physiologists or vascular biologists. Regardless of the approach (bottom-up or top-down), key characteristics will not be included. Such a reality provokes a more appropriate question: What is the value of a biomimetic model? Future discussion is warranted, yet an important note remains—any model is only as good as the question being asked. So moving forward, we suggest that a more appropriate question for connecting research perspectives should be related to the discoveries and applications made possible by innovative approaches versus traditional *in vivo* studies.

AUTHOR CONTRIBUTIONS

AL, N-WH, DL, BL, CN, CD, BR, YH, and WM contributed to the ideation, literature searches, and writing involved in the initial development of the article. The development process entailed multiple laboratory meetings, literature search reports, and discussions. N-WH, AL, and WM were responsible for assembling text drafts and incorporating final edits. BR and YH additionally contribute by providing feedback based on their biofabrication perspective.

FUNDING

This work was supported by the National Institute of Aging (Grant No. R01AG049821) and by the University of Florida Health Cancer Center Pilot Grant No. 00096885 CA-FY22-03.

ACKNOWLEDGMENTS

We would like to thank all current and past members of the Microvascular Dynamics Laboratory for their contribution and efforts to advance biomimetic model development for viewing angiogenesis and lymphangiogenesis in new ways.

REFERENCES

Akbari, E., Spychalski, G. B., and Song, J. W. (2017). Microfluidic Approaches to the Study of Angiogenesis and the Microcirculation. *Microcirculation* 24 (5). doi:10.1111/micc.1236310.1111/micc.12363

Azimi, M. S., Motherwell, J. M., Dutreil, M., Fishel, R. L., Nice, M., Hodges, N. A., et al. (2020a). A Novel Tissue Culture Model for Evaluating the Effect of Aging on Stem Cell Fate in Adult Microvascular Networks. *GeroScience* 42 (2), 515–526. doi:10.1007/s11357-020-00178-0

Azimi, M. S., Motherwell, J. M., Hodges, N. A., Rittenhouse, G. R., Majbour, D., Porvasnik, S. L., et al. (2020b). Lymphatic-to-blood Vessel Transition in Adult Microvascular Networks: A Discovery Made Possible by a Top-down Approach to Biomimetic Model Development. *Microcirculation* 27 (2), e12595. doi:10.1111/micc.12595

Azimi, M. S., Motherwell, J. M., and Murfee, W. L. (2017). An *Ex Vivo* Method for Time-Lapse Imaging of Cultured Rat Mesenteric Microvascular Networks. *JoVE* 9 (120), 55183. doi:10.3791/55183

Azimi, M. S., Myers, L., Lacey, M., Stewart, S. A., Shi, Q., Katakam, P. V., et al. (2015). An *Ex Vivo* Model for Anti-angiogenic Drug Testing on Intact Microvascular Networks. *PloS One* 10 (3), e0119227. doi:10.1371/journal.pone.0119227

Baeyens, N., Nicoli, S., Coon, B. G., Ross, T. D., Van den Dries, K., Han, J., et al. (2015). Vascular Remodeling Is Governed by a VEGFR3-dependent Fluid Shear Stress Set Point. *eLife* 4, e04645. doi:10.7554/eLife.04645

Bar-Or, A., Nuttall, R. K., Duddy, M., Alter, A., Kim, H. J., Ifergan, I., et al. (2003). Analyses of All Matrix Metalloproteinase Members in Leukocytes Emphasize Monocytes as Major Inflammatory Mediators in Multiple Sclerosis. *Brain* 126 (Pt 12), 2738–2749. doi:10.1093/brain/awg285

Barkefors, I., Thorslund, S., Nikolajeff, F., and Kreuger, J. (2009). A Fluidic Device to Study Directional Angiogenesis in Complex Tissue and Organ Culture Models. *Lab. Chip* 9 (4), 529–535. doi:10.1039/b814691h

Bayless, K. J., Salazar, R., and Davis, G. E. (2000). RGD-dependent Vacuolation and Lumen Formation Observed during Endothelial Cell Morphogenesis in Three-Dimensional Fibrin Matrices Involves the αvβ3 and α5β1 Integrins. *Am. J. pathology* 156 (5), 1673–1683. doi:10.1016/s0002-9440(10)65038-9

Berthiaume, A.-A., Grant, R. I., McDowell, K. P., Underly, R. G., Hartmann, D. A., Levy, M., et al. (2018). Dynamic Remodeling of Pericytes *In Vivo* Maintains Capillary Coverage in the Adult Mouse Brain. *Cell. Rep.* 22 (1), 8–16. doi:10.1016/j.celrep.2017.12.016

Bonney, S. K., Sullivan, L. T., Cherry, T. J., Daneman, R., and Shih, A. Y. (2021). Distinct Features of Brain Perivascular Fibroblasts and Mural Cells Revealed by *In Vivo* Two-Photon Imaging. *J. Cereb. Blood Flow. Metab.* 42, 966–978. doi:10.1177/0271678X211068528

Bruyère, F., Melen-Lamalle, L., Blacher, S., Roland, G., Thiry, M., Moons, L., et al. (2008). Modeling Lymphangiogenesis in a Three-Dimensional Culture System. *Nat. Methods* 5 (5), 431–437. doi:10.1038/nmeth.1205

Burks, H. E., Phamduy, T. B., Azimi, M. S., Saksena, J., Burow, M. E., Collins-Burow, B. M., et al. (2016). Laser Direct-Write onto Live Tissues: A Novel Model for Studying Cancer Cell Migration. *J. Cell. Physiol.* 231 (11), 2333–2338. doi:10.1002/jcp.25363

Campisi, M., Shin, Y., Osaki, T., Hajal, C., Chiono, V., and Kamm, R. D. (2018). 3D Self-Organized Microvascular Model of the Human Blood-Brain Barrier with Endothelial Cells, Pericytes and Astrocytes. *Biomaterials* 180, 117–129. doi:10.1016/j.biomaterials.2018.07.014

Carmeliet, P. (2000). Mechanisms of Angiogenesis and Arteriogenesis. *Nat. Med.* 6 (4), 389–395. doi:10.1038/74651

Corliss, B. A., Azimi, M. S., Munson, J. M., Peirce, S. M., and Murfee, W. L. (2016). Macrophages: An Inflammatory Link between Angiogenesis and Lymphangiogenesis. *Microcirculation* 23 (2), 95–121. doi:10.1111/micc.12259

Darland, D. C., and D'Amore, P. A. (2001). TGF Beta Is Required for the Formation of Capillary-like Structures in Three-Dimensional Cocultures of 10T1/2 and Endothelial Cells. *Angiogenesis* 4 (1), 11–20. doi:10.1023/a:1016611824696

dela Paz, N. G., Walshe, T. E., Leach, L. L., Saint-Geniez, M., and D'Amore, P. A. (2012). Role of Shear-Stress-Induced VEGF Expression in Endothelial Cell Survival. *J. Cell. Sci.* 125 (Pt 4), 831–843. doi:10.1242/jcs.084301

Donovan, D., Brown, N. J., Bishop, E. T., and Lewis, C. E. (2001). Comparison of Three *In Vitro* Human 'angiogenesis' Assays with Capillaries Formed *In Vivo*. *Angiogenesis* 4 (2), 113–121. doi:10.1023/a:1012218401036

Driessen, R. C. H., Stassen, O. M. J. A., Sjöqvist, M., Suarez Rodriguez, F., Grolleman, J., Bouten, C. V. C., et al. (2018). Shear Stress Induces Expression, Intracellular Reorganization and Enhanced Notch Activation Potential of Jagged1. *Integr. Biol.* 10 (11), 719–726. doi:10.1039/c8ib00036k

Du Cheyne, C., Tay, H., and De Spiegelaere, W. (2020). The Complex TIE Between Macrophages and Angiogenesis. *Anat. Histol. Embryol.* 49 (5), 585–585. doi:10.1111/ahe.12518

Emonard, H., Calle, A., Grimaud, J.-A., Peyrol, S., Castronovo, V., Noel, A., et al. (1987). Interactions between Fibroblasts and a Reconstituted Basement Membrane Matrix. *J. Investigative Dermatology* 89 (2), 156–163. doi:10.1111/1523-1747.ep12470552

Fu, L.-Q., Du, W.-L., Cai, M.-H., Yao, J.-Y., Zhao, Y.-Y., and Mou, X.-Z. (2020). The Roles of Tumor-Associated Macrophages in Tumor Angiogenesis and Metastasis. *Cell. Immunol.* 353, 104119. doi:10.1016/j.cellimm.2020.104119

Galanternik, M. V., Castranova, D., Gore, A. V., Blewett, N. H., Jung, H. M., Stratman, A. N., et al. (2017). A Novel Perivascular Cell Population in the Zebrafish Brain. *eLife* 6, e24369. doi:10.7554/eLife.24369

Galie, P. A., Nguyen, D.-H. T., Choi, C. K., Cohen, D. M., Janmey, P. A., and Chen, C. S. (2014). Fluid Shear Stress Threshold Regulates Angiogenic Sprouting. *Proc. Natl. Acad. Sci. U.S.A.* 111 (22), 7968–7973. doi:10.1073/pnas.1310842111

Gerhardt, H., and Betsholtz, C. (2003). Endothelial-Pericyte Interactions in Angiogenesis. *Cell Tissue Res.* 314 (1), 15–23. doi:10.1007/s00441-003-0745-x

Gore, A. V., Monzo, K., Cha, Y. R., Pan, W., and Weinstein, B. M. (2012). Vascular Development in the Zebrafish. *Cold Spring Harb. Perspect. Med.* 2 (5), a006684. doi:10.1101/cshperspect.a006684

Gore, A. V., Pillay, L. M., Venero Galanternik, M., and Weinstein, B. M. (2018). The Zebrafish: A Fintastic Model for Hematopoietic Development and Disease. *WIREs Dev. Biol.* 7 (3), e312. doi:10.1002/wdev.312

Haase, K., and Kamm, R. D. (2017). Advances in On-Chip Vascularization. *Regen. Med.* 12 (3), 285–302. doi:10.2217/rme-2016-0152

Henderson, A. R., Ilan, I. S., and Lee, E. (2021). A Bioengineered Lymphatic Vessel Model for Studying Lymphatic Endothelial Cell-cell Junction and Barrier Function. *Microcirculation* 28 (8), e12730. doi:10.1111/micc.12730

Hodges, N. A., Barr, R. W., and Murfee, W. L. (2020). The Maintenance of Adult Peripheral Adult Nerve and Microvascular Networks in the Rat Mesentery Culture Model. *J. Neurosci. Methods* 346, 108923. doi:10.1016/j.jneumeth.2020.108923

Hodges, N. A., Suarez-Martinez, A. D., and Murfee, W. L. (2018). Understanding Angiogenesis during Aging: Opportunities for Discoveries and New Models. *J. Appl. Physiology* 125 (6), 1843–1850. doi:10.1152/japplphysiol.00112.2018

Iqbal, F., Gratch, Y. S., Szaraz, P., and Librach, C. L. (2017). The Aortic Ring Co-culture Assay: A Convenient Tool to Assess the Angiogenic Potential of Mesenchymal Stromal Cells *In Vitro*. *JoVE* (127), 56083. doi:10.3791/56083

Jones, V. M., Suarez-Martinez, A. D., Hodges, N. A., Murfee, W. L., Llull, R., and Katz, A. J. (2021). A Clinical Perspective on Adipose-derived Cell Therapy for Enhancing Microvascular Health and Function: Implications and Applications for Reconstructive Surgery. *Microcirculation* 28 (3), e12672. doi:10.1111/micc.12672

Katakia, Y. T., Duddu, S., S., N., Kumar, P., Rahman, F., Kumaramanickavel, G., et al. (2020). *Ex Vivo* model for Studying Endothelial Tip Cells: Revisiting the Classical Aortic-Ring Assay. *Microvasc. Res.* 128, 103939. doi:10.1016/j.mvr.2019.103939

Kaunas, R., Kang, H., and Bayless, K. J. (2011). Synergistic Regulation of Angiogenic Sprouting by Biochemical Factors and Wall Shear Stress. *Cel. Mol. Bioeng.* 4 (4), 547–559. doi:10.1007/s12195-011-0208-5

Kelly-Goss, M. R., Sweat, R. S., Azimi, M. S., and Murfee, W. L. (2013). Vascular Islands during Microvascular Regression and Regrowth in Adult Networks. *Front. Physiol.* 4, 108. doi:10.3389/fphys.2013.00108

Kelly-Goss, M. R., Sweat, R. S., Stapor, P. C., Peirce, S. M., and Murfee, W. L. (2014). Targeting Pericytes for Angiogenic Therapies. *Microcirculation* 21 (4), 345–357. doi:10.1111/micc.12107

Kelly-Goss, M. R., Winterer, E. R., Stapor, P. C., Yang, M., Sweat, R. S., Stallcup, W. B., et al. (2012). Cell Proliferation along Vascular Islands during Microvascular Network Growth. *BMC Physiol.* 12, 7. doi:10.1186/1472-6793-12-7

Kim, S., Chung, M., and Jeon, N. L. (2016). Three-dimensional Biomimetic Model to Reconstitute Sprouting Lymphangiogenesis *In Vitro*. *Biomaterials* 78, 115–128. doi:10.1016/j.biomaterials.2015.11.019

Knezevic, L., Schaupper, M., Mühleder, S., Schimek, K., Hasenberg, T., Marx, U., et al. (2017). Engineering Blood and Lymphatic Microvascular Networks in Fibrin Matrices. *Front. Bioeng. Biotechnol.* 5, 25. doi:10.3389/fbioe.2017.00025

Krishnan, L., Underwood, C. J., Maas, S., Ellis, B. J., Kode, T. C., Hoying, J. B., et al. (2008). Effect of Mechanical Boundary Conditions on Orientation of Angiogenic Microvessels. *Cardiovasc. Res.* 78 (2), 324–332. doi:10.1093/cvr/cvn055

Kusuma, S., Shen, Y.-I., Hanjaya-Putra, D., Mali, P., Cheng, L., and Gerecht, S. (2013). Self-organized Vascular Networks from Human Pluripotent Stem Cells in a Synthetic Matrix. *Proc. Natl. Acad. Sci. U.S.A.* 110 (31), 12601–12606. doi:10.1073/pnas.1306562110

Lee, E., Lee, S. J., Koskimaki, J. E., Han, Z., Pandey, N. B., and Popel, A. S. (2014). Inhibition of Breast Cancer Growth and Metastasis by a Biomimetic Peptide. *Sci. Rep.* 4, 7139. doi:10.1038/srep07139

Lilly, B. (2014). We Have Contact: Endothelial Cell-Smooth Muscle Cell Interactions. *Physiology* 29 (4), 234–241. doi:10.1152/physiol.00047.2013

Motherwell, J. M., Anderson, C. R., and Murfee, W. L. (2018). Endothelial Cell Phenotypes Are Maintained during Angiogenesis in Cultured Microvascular Networks. *Sci. Rep.* 8 (1), 5887. doi:10.1038/s41598-018-24081-z

Motherwell, J. M., Azimi, M. S., Spicer, K., Alves, N. G., Hodges, N. A., Breslin, J. W., et al. (2017). Evaluation of Arteriolar Smooth Muscle Cell Function in an *Ex Vivo* Microvascular Network Model. *Sci. Rep.* 7 (1), 2195. doi:10.1038/s41598-017-02272-4

Motherwell, J. M., Rozenblum, M., Katakam, P. V. G., and Murfee, W. L. (2019). Bioreactor System to Perfuse Mesentery Microvascular Networks and Study Flow Effects during Angiogenesis. *Tissue Eng. Part C. Methods* 25 (8), 447–458. doi:10.1089/ten.TEC.2019.0119

Murakami, T., Suzuma, K., Takagi, H., Kita, M., Ohashi, H., Watanabe, D., et al. (2006). Time-lapse Imaging of Vitreoretinal Angiogenesis Originating from Both Quiescent and Mature Vessels in a Novel *Ex Vivo* System. *Investig. Ophthalmol. Vis. Sci.* 47 (12), 5529–5536. doi:10.1167/iovs.06-0373

Murfee, W. L., Rehorn, M. R., Peirce, S. M., and Skalak, T. C. (2006). Perivascular Cells along Venules Upregulate NG2 Expression during Microvascular Remodeling. *Microcirculation* 13 (3), 261–273. doi:10.1080/10739680600559153

Nicosia, R. F., Nicosia, S. V., and Smith, M. (1994). Vascular Endothelial Growth Factor, Platelet-Derived Growth Factor, and Insulin-like Growth Factor-1 Promote Rat Aortic Angiogenesis *In Vitro*. *Am. J. Pathol.* 145 (5), 1023–1029.

Nicosia, R. F., and Ottinetti, A. (1990). Growth of Microvessels in Serum-free Matrix Culture of Rat Aorta. A Quantitative Assay of Angiogenesis *In Vitro*. *Lab. Investig.* 63 (1), 115–122.

Osaki, T., Serrano, J. C., and Kamm, R. D. (2018). Cooperative Effects of Vascular Angiogenesis and Lymphangiogenesis. *Regen. Eng. Transl. Med.* 4 (3), 120–132. doi:10.1007/s40883-018-0054-2

Payne, L. B., Darden, J., Suarez-Martinez, A. D., Zhao, H., Hendricks, A., Hartland, C., et al. (2021). Pericyte Migration and Proliferation Are Tightly Synchronized to Endothelial Cell Sprouting Dynamics. *Integr. Biol. Quantitative Biosci. Nano Macro* 13 (2), 31–43. doi:10.1093/intbio/zyaa027

Peacock, H. M., Tabibian, A., Criem, N., Caolo, V., Hamard, L., Deryckere, A., et al. (2020). Impaired SMAD1/5 Mechanotransduction and Cx37 (Connexin37) Expression Enable Pathological Vessel Enlargement and Shunting. *Atvb* 40 (4), e87–e104. doi:10.1161/ATVBAHA.119.313122

Peirce, S. M., Price, R. J., and Skalak, T. C. (2004). Spatial and Temporal Control of Angiogenesis and Arterialization Using Focal Applications of VEGF164and Ang-1*. *Am. J. Physiology-Heart Circulatory Physiology* 286 (3), H918–H925. doi:10.1152/ajpheart.00833.2003

Peirce, S., and Skalak, T. (2003). Microvascular Remodeling: a Complex Continuum Spanning Angiogenesis to Arteriogenesis. *Microcirculation* 10 (1), 99–111. doi:10.1038/sj.mn.780017210.1080/713773592

Qiu, Y., Ahn, B., Sakurai, Y., Hansen, C. E., Tran, R., Mimche, P. N., et al. (2018). Microvasculature-on-a-chip for the Long-Term Study of Endothelial Barrier Dysfunction and Microvascular Obstruction in Disease. *Nat. Biomed. Eng.* 2, 453–463. doi:10.1038/s41551-018-0224-z

Ren, B., Song, K., Sanikommu, A. R., Chai, Y., Longmire, M. A., Chai, W., et al. (2022). Study of Sacrificial Ink-Assisted Embedded Printing for 3D Perfusable Channel Creation for Biomedical Applications. *Appl. Phys. Rev.* 9 (1), 011408. doi:10.1063/5.0068329

Robering, J. W., Weigand, A., Pfuhlmann, R., Horch, R. E., Beier, J. P., and Boos, A. M. (2018). Mesenchymal Stem Cells Promote Lymphangiogenic Properties of Lymphatic Endothelial Cells. *J. Cell. Mol. Medi* 22 (8), 3740–3750. doi:10.1111/jcmm.13590

Shirure, V. S., Hughes, C. C. W., and George, S. C. (2021). Engineering Vascularized Organoid-On-A-Chip Models. *Annu. Rev. Biomed. Eng.* 23, 141–167. doi:10.1146/annurev-bioeng-090120-094330

Song, J. W., and Munn, L. L. (2011). Fluid Forces Control Endothelial Sprouting. *Proc. Natl. Acad. Sci. U.S.A.* 108 (37), 15342–15347. doi:10.1073/pnas.1105316108

Stapor, P. C., Azimi, M. S., Ahsan, T., and Murfee, W. L. (2013). An Angiogenesis Model for Investigating Multicellular Interactions across Intact Microvascular Networks. *Am. J. Physiol. Heart Circ. Physiol.* 304 (2), H235–H245. doi:10.1152/ajpheart.00552.2012

Stapor, P. C., Sweat, R. S., Dashti, D. C., Betancourt, A. M., and Murfee, W. L. (2014). Pericyte Dynamics during Angiogenesis: New Insights from New Identities. *J. Vasc. Res.* 51 (3), 163–174. doi:10.1159/000362276

Stoppini, L., Buchs, P.-A., and Muller, D. (1991). A Simple Method for Organotypic Cultures of Nervous Tissue. *J. Neurosci. Methods* 37 (2), 173–182. doi:10.1016/0165-0270(91)90128-m

Stratman, A. N., Malotte, K. M., Mahan, R. D., Davis, M. J., and Davis, G. E. (2009). Pericyte Recruitment during Vasculogenic Tube Assembly Stimulates Endothelial Basement Membrane Matrix Formation. *Blood* 114 (24), 5091–5101. doi:10.1182/blood-2009-05-222364

Stratman, A. N., Schwindt, A. E., Malotte, K. M., and Davis, G. E. (2010). Endothelial-derived PDGF-BB and HB-EGF Coordinately Regulate Pericyte Recruitment during Vasculogenic Tube Assembly and Stabilization. *Blood* 116 (22), 4720–4730. doi:10.1182/blood-2010-05-286872

Suarez-Martinez, A. D., Bierschenk, S., Huang, K., Kaplan, D., Bayer, C. L., Meadows, S. M., et al. (2018a). A Novel *Ex Vivo* Mouse Mesometrium Culture Model for Investigating Angiogenesis in Microvascular Networks. *J. Vasc. Res.* 55 (3), 125–135. doi:10.1159/000489102

Suarez-Martinez, A. D., Peirce, S. M., Isakson, B. E., Nice, M., Wang, J., Lounsbury, K. M., et al. (2018b). Induction of Microvascular Network Growth in the Mouse Mesentery. *Microcirculation* 25 (8), e12502. doi:10.1111/micc.12502

Suarez-Martinez, A. D., Sole-Gras, M., Dykes, S. S., Wakefield, Z. R., Bauer, K., Majbour, D., et al. (2021). Bioprinting on Live Tissue for Investigating Cancer Cell Dynamics. *Tissue Eng. Part A* 27 (7-8), 438–453. doi:10.1089/ten.TEA.2020.0190

Sweat, R. S., Sloas, D. C., and Murfee, W. L. (2014). VEGF-C Induces Lymphangiogenesis and Angiogenesis in the Rat Mesentery Culture Model. *Microcirculation* 21 (6), 532–540. doi:10.1111/micc.12132

Sweat, R. S., Stapor, P. C., and Murfee, W. L. (2012). Relationships between Lymphangiogenesis and Angiogenesis during Inflammation in Rat Mesentery Microvascular Networks. *Lymphatic Res. Biol.* 10 (4), 198–207. doi:10.1089/lrb.2012.0014

Tracy, E. P., Stielberg, V., Rowe, G., Benson, D., Nunes, S. S., Hoying, J. B., et al. (2022). State of the Field: Cellular and Exosomal Therapeutic Approaches in Vascular Regeneration. *Am. J. Physiology-Heart Circulatory Physiology* 322 (4), H647–H680. doi:10.1152/ajpheart.00674.2021

Vernon, R. B., Angello, J. C., Iruela-Arispe, M. L., Lane, T. F., and Sage, E. H. (1992). Reorganization of Basement Membrane Matrices by Cellular Traction Promotes the Formation of Cellular Networks *In Vitro*. *Lab. Investig.* 66 (5), 536–547.

Wang, X., Phan, D. T. T., Sobrino, A., George, S. C., Hughes, C. C. W., and Lee, A. P. (2016). Engineering Anastomosis between Living Capillary Networks and Endothelial Cell-Lined Microfluidic Channels. *Lab. Chip* 16 (2), 282–290. doi:10.1039/c5lc01050k

Webster, N. L., and Crowe, S. M. (2006). Matrix Metalloproteinases, Their Production by Monocytes and Macrophages and Their Potential Role in HIV-Related Diseases. *J. Leukoc. Biol.* 80 (5), 1052–1066. doi:10.1189/jlb.0306152

Yamamoto, K., Tanimura, K., Watanabe, M., Sano, H., Uwamori, H., Mabuchi, Y., et al. (2019). Construction of Continuous Capillary Networks Stabilized by Pericyte-like Perivascular Cells. *Tissue Eng. Part APart A* 25 (5-6), 499–510. doi:10.1089/ten.TEA.2018.0186

Zanotelli, M. R., Ardalani, H., Zhang, J., Hou, Z., Nguyen, E. H., Swanson, S., et al. (2016). Stable Engineered Vascular Networks from Human Induced Pluripotent Stem Cell-Derived Endothelial Cells Cultured in Synthetic Hydrogels. *Acta biomater.* 35, 32–41. doi:10.1016/j.actbio.2016.03.001

Conflict of Interest: The authors declare that the research was conducted in the absence of any commercial or financial relationships that could be construed as a potential conflict of interest.

Publisher's Note: All claims expressed in this article are solely those of the authors and do not necessarily represent those of their affiliated organizations, or those of the publisher, the editors and the reviewers. Any product that may be evaluated in this article, or claim that may be made by its manufacturer, is not guaranteed or endorsed by the publisher.

frontiers | Frontiers in Bioengineering and Biotechnology

ORIGINAL RESEARCH
published: 14 July 2022
doi: 10.3389/fbioe.2022.952537

Non-Invasive Dynamic Reperfusion of Microvessels *In Vivo* Controlled by Optical Tweezers

Meng Shao[1], *Min-Cheng Zhong*[1]*, *Zixin Wang*[2], *Zeyu Ke*[2], *Zhensheng Zhong*[2] and *Jinhua Zhou*[2]*

[1]Anhui Province Key Laboratory of Measuring Theory and Precision Instrument, School of Instrument Science and Optoelectronics Engineering, Hefei University of Technology, Hefei, China, [2]School of Biomedical Engineering, Anhui Medical University, Hefei, China

Distributive shock is considered to be a condition of microvascular hypoperfusion, which can be fatal in severe cases. However, traditional therapeutic methods to restore the macro blood flow are difficult to accurately control the blood perfusion of microvessels, and the currently developed manipulation techniques are inevitably incompatible with biological systems. In our approach, infrared optical tweezers are used to dynamically control the microvascular reperfusion within subdermal capillaries in the pinna of mice. Furthermore, we estimate the effect of different optical trap positions on reperfusion at branch and investigate the effect of the laser power on reperfusion. The results demonstrate the ability of optical tweezers to control microvascular reperfusion. This strategy allows near-noninvasive reperfusion of the microvascular hypoperfusion *in vivo*. Hence, our work is expected to provide unprecedented insights into the treatment of distributive shock.

Keywords: optical tweezers, reperfusion, distributive shock, blood flow, *in vivo*

OPEN ACCESS

Edited by:
Jonathan W. Song,
The Ohio State University,
United States

Reviewed by:
Mingyang Xie,
Nanjing University of Aeronautics and Astronautics, China
Jochen Fick,
UPR2940 Institut Neel (NEEL), France

***Correspondence:**
Min-Cheng Zhong
zhongmch@hfut.edu.cn
Jinhua Zhou
zhoujinhua@ahmu.edu.cn

Specialty section:
This article was submitted to Biomechanics, a section of the journal Frontiers in Bioengineering and Biotechnology

Received: *25 May 2022*
Accepted: *22 June 2022*
Published: *14 July 2022*

Citation:
Shao M, Zhong M-C, Wang Z, Ke Z, Zhong Z and Zhou J (2022) Non-Invasive Dynamic Reperfusion of Microvessels In Vivo Controlled by Optical Tweezers. Front. Bioeng. Biotechnol. 10:952537. doi: 10.3389/fbioe.2022.952537

1 INTRODUCTION

Distributive shock is a condition defined by the presence of the microvascular hypoperfusion despite the normalization of systemic and regional blood flow (Vincent and De Backer, 2013). In this case, fatal results will be caused when the oxygen delivery does not meet the metabolic needs of the tissue in vital organs (Pan et al., 2020). In order to keep the blood flowing in the microvessel and thus improve the oxygen delivery, several treatments such as fluid resuscitation, vasoactive drugs, positive inotropic drugs, obstruction relief, and mechanical assistance are commonly used (Legrand et al., 2018; Boros and Bauer, 2021; Jha et al., 2021; Jiang et al., 2021; Motwani and Saunders, 2021; Scheeren et al., 2021). In fact, these treatments with implementing methods aim to recover the macrocirculation function. However, an ideal target for resuscitation in clinics could be to improve microcirculation more promptly and accurately to avoid further organ damage. As a result, controlling microvascular reperfusion is an important strategy in the treatment of distributive shock. Although the development of several techniques such as magnetic (Galanzha et al., 2009), acoustic (Lenshof et al., 2009; Galanzha et al., 2016), and electrical devices (Wachter et al., 2011; Han et al., 2014) have reported positive effects in controlling the microvessel *in vivo* (Wang et al., 2014; Weijts et al., 2018), most of them required implantation of exogenous materials. To control blood microflow with high precision and in a non-invasive way, a biocompatible and single-cell-level strategy is highly desirable (Abdullah and Perez-Soler, 2012; Herbert et al., 2012; Sugden et al., 2017).

In this context, optical tweezers (Ashkin et al., 1986; Neuman and Block, 2004) have been used to manipulate and investigate microscopic particles for many years, and the ability to study living cells

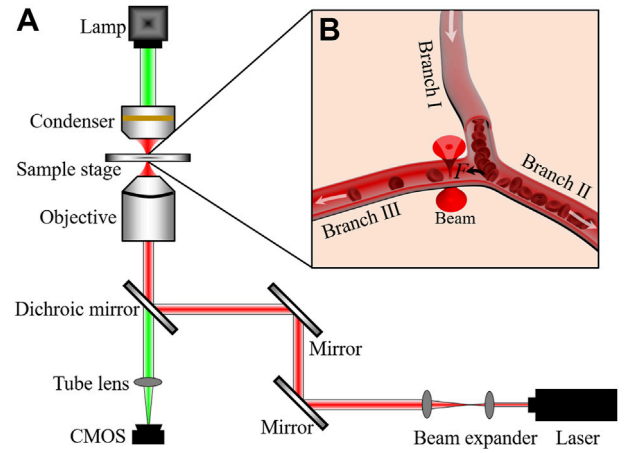

FIGURE 1 | (A) Optical tweezers setup. **(B)** Schematic illustration of blood flow controlled by optical trap. White arrows indicate the directions of blood flows. ***F*** is the optical trapping force.

at the single-cell level have been proven (Zhang and Liu, 2008; Zhao et al., 2020; Vasse et al., 2021). Significant progress has been made in the manipulation of biological cells rotation with optical tweezers for orientation-based cell surgery (Xie et al., 2015a; Xie et al., 2015b; Xie et al., 2018a). In addition, study on the deformation of red blood cells (RBCs) by optical tweezers has long been a topic of real-life significance (Henon et al., 1999; Avsievich et al., 2020). Particularly, there have been developments toward optical trapping RBCs *in vivo* recently (Zhong et al., 2013a; Zhong et al., 2013b; Johansen et al., 2016; Horner et al., 2017; Zhong et al., 2017; Liu et al., 2020; Gao et al., 2021). Such as trap and manipulate RBCs within subdermal capillaries in living mice (Zhong et al., 2013a; Zhong et al., 2013b; Zhong et al., 2017). In addition, a recent report illustrates that optical tweezers were employed to manipulate, arrange, and rotate RBCs in the capillaries of zebrafish (Liu et al., 2020). However, optical trapping *in vivo* is still more challenging and complex due to scattering and power loss through biological tissue. To date, the experiments of optical micromanipulation *in vivo* has been applied to RBCs, injected nanoparticles, and macrophages (Johansen et al., 2016). Therefore, using optical tweezers, microvascular reperfusion *in vivo* may be carried out in a non-contact and non-invasive way.

In this study, a method for controlling dynamic reperfusion of mouse auricle microvessel using optical tweezers is introduced for the first time. We investigated the reperfusion ability by changing the position of optical trap and laser power when the reperfusion of microvascular branch was guided. The experimental results show that the control of microvascular reperfusion by optical tweezers at about 200~550 mW of laser entering pupil is universal in the recovery of microvascular hypoperfusion. Moreover, a physical model was established to analyze reperfusion efficiency of the optical tweezers with the laser power. According to our analysis, as the laser power increases, the reperfusion efficiency increases at first and then decreases. The implementation of this technique is almost non-invasive in controlling dynamic reperfusion of microvessel *in vivo*, which has not yet been achieved by any other techniques, thereby gaining novel insights into the treatment involved in distributive shock.

2 MATERIALS AND METHODS

2.1 Optical Tweezer Setup

Our optical tweezers setup is based on an Olympus IX73 inverted microscope, as shown in **Figure 1A**. A 1064-nm laser (Amonics, Hong Kong, AFL-1064-37-R-CL, cw) was used as the trapping laser source. The laser beam was expanded to fulfill the pupil of objective (8 mm) with the beam expander. For better trapping and imaging of RBCs in the microvessel of the pinna of mice (Zhong et al., 2013a), a water immersion objective (LUMFLN, × 60, numerical aperture 1.20, Olympus, Japan) was also used here. A CMOS camera (MindVision, China, MV-SUA231GM-T, 20 frames per second) was used to connect to the computer for the real-time image acquisition and video recording of the intravital manipulation. The laser power was measured at the pupil of the objective.

2.2 Mice Preparation

Kunming mice (8-week-old, 30 ± 2 g) were used in the experiments. They were purchased from the Experimental Animal Center of Anhui Medical University. To ensure that the mice keeps alive and immobilized during the whole operation process, 10% chloral hydrate (7 μl·g^{-1}) was injected *via* the abdominal cavity to anesthetise them. The hair on the pinna of the mice was removed by cream and then glycerin was smeared on the pinna for avoid drying out the skin. During the experiments, the optical trap (red cone beam in **Figure 1B**) was located at a branch of the microvessel. When the optical trap applied an attractive force on an RBC passing the junction of microvessel, the cell will be guided to the Branch III and added the number of RBCs in Branch III, as schematized in **Figure 1B**. The study was approved by the Ethical Committee of the Hefei University of Technology.

3 RESULTS AND DISCUSSION

3.1 Optical Trap–Controlled Reperfusion of a Microvessel

The optical tweezers can only manipulate the RBCs in depth smaller than 100 μm. Here, we have demonstrated the insufficient microvascular perfusion in a branching microvessel, which was with ~40 μm depth beneath the surface of mice pinna skin, as in **Figure 2**. As shown in **Figure 2A** and **Supplementary Video S1**, the RBCs flowed from Branch I into Branch II and Branch III in a certain proportion, but there was not enough or even no blood flowing to Branch III. This phenomenon was very common in the pinna of anesthetized mice, which might due to the hypothermia of the anesthetized mice. The paths of all RBCs within 4 s were traced using ImageJ software. The tracking results were presented in **Figure 2D**, and only one RBC entered Branch III in 4 s. When the optical trap worked on the Branch III, the blood flow was

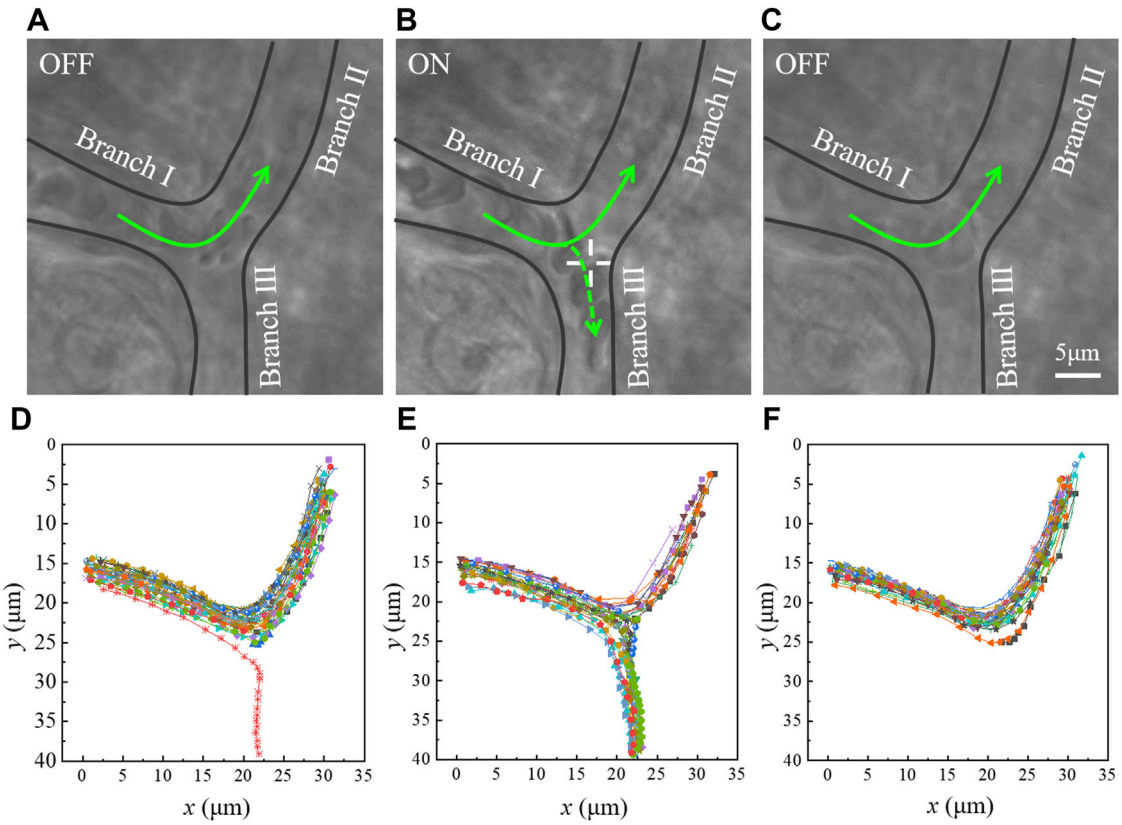

FIGURE 2 | Dynamic reperfusion of the microvascular blood flow by optical tweezers. The laser is **(A)** off (**Supplementary Video S1**), **(B)** on (**Supplementary Video S1**), and **(C)** off (**Supplementary Video S1**). '+' indicates the optical trap. **(D–F)** Path tracing of the RBCs. The points record the position coordinates of RBCs in each frame of the images, and each curve represents the flowing path of an RBC.

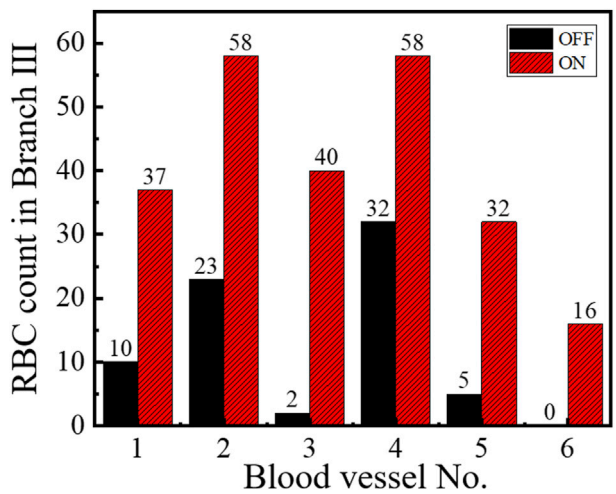

FIGURE 3 | RBCs count of reperfusion in six different branching microvessels within 10 s.

redistributed. One example was demonstrated in **Figure 2B** and **Supplementary Video S2**. The laser power was 221 mW. It can be observed that some RBCs were directed into Branch III, and the tracing of RBCs was shown in **Figure 2E**. As the optical trap was turned off again, the phenomenon of insufficient RBC perfusion in Branch III appeared again, as shown in **Figure 2C** (**Supplementary Video S3**) and **Figure 2F**. The experiment results showed that the optical trap can apply force on the RBCs flowing in the microvessels, which would change the blood distribution inside the microvascular branches.

3.2 Universal Applicability of Optical Trap–Controlled Reperfusion

To check the universal applicability of microvascular reperfusion by optical tweezers, we conducted a series of experiments. **Figure 3** shows the RBC counts of the six groups of branch vessels under the optimal condition of optical tweezers, respectively. The recording time for each group was 10 s, and the RBCs were counted at the microvascular Branch III. The red bar represented the optical trap was working, and the black bar represented the optical trap was not working. The experimental results in **Figure 3** showed that optical tweezers can increase the perfusion of RBCs in different microvessels. For the microvessels 1–5 with low blood flow perfused, the average rate of improvement was 588%. The maximum number of microvascular reperfusion cells could increase by 1900% for

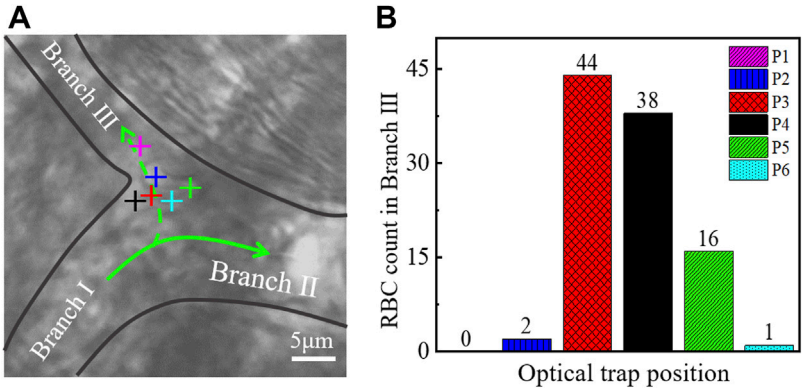

FIGURE 4 | (A) Optical trap was located in different positions in a microvessel. Different colors of '+' represent different positions of the optical trap. **(B)** Relationship between the position of the optical trap and the amount of redirection RBCs. The color of the histogram corresponds to the color of the optical trap in **(A)**. '+' indicates the optical trap.

the microvessel 3 controlled by optical tweezers. The analysis of experimental results showed that the optical tweezers could control their reperfusion for the low perfused microvessels. The efficiency of optical tweezers–controlled reperfusion was significant, especially in the case of severe microvascular hypoperfusion.

3.3 Effect of Optical Trap Position on Reperfusion Efficiency

In the reperfusion experiments at different positions, an effective redirection of RBCs was required. In microfluidic channels, the efficiencies of cell manipulation and sorting can be enhanced by moving the position of optical trap (Wang et al., 2011; Landenberger et al., 2012; Zhou et al., 2021). Here, the suitable position of the optical trap should be obtained for redirection of RBCs in the microvessels *in vivo*.

An experiment was conducted to determine the relationship between optical trap position and reperfusion efficiency as shown in **Figure 4A**. We selected six typical positions at the branch of vessels for optical trap working, as marked with '+' in **Figure 4A**. Then we recorded the blood flow with 30 s videos for each working location, and the erythrocytes in Branch III were counted. The results were indicated in **Figure 4B**, the microvascular reperfusion was obviously better when the optical trap position was located at P3 (red) and P4 (black). The reason behind such better performance of the microvascular reperfusion might be that the optical trap was redirecting the RBCs rather than trapping them. Fortunately, the optical trap can change the flowing direction of RBCs and then attracted the RBCs into the Branch III. Therefore, the optimal optical trap position for the reperfusion can be determined roughly. At P3 and P4 in **Figure 4A**, the redirected RBCs were trapped and flowed into the Branch III one by one.

When the optical trap was located at P3 (red), P4 (black), and P5 (green), some RBCs flowing to Branch II initially were within the action range of the optical trap. These RBCs can be attracted and flowed to the Branch III eventually. The optical trap has reperfusion ability. When the optical trap was located at P1 (purple) and P2 (blue) as in **Figure 4A**, the most of RBCs flowing to Branch II were not in the action range of optical trap, so the numbers of reperfusion RBCs were poor. When the optical trap was located at P6 (cyan) as in **Figure 4A**, the optical trap has no reperfusion capability because the optical trapping force cannot overcome the dragged force from the blood flow of Branch II, and the RBCs cannot redirect and flow to Branch III.

Since the geometry of each branch *in vivo* is different, it is difficult to determine a unified standard to apply to all branches when the relationship between the optical trap position and the reperfusion efficiency was investigated. The results shown in **Figure 4** suggest that the optical trap position is one of the important factors affecting the efficiency of optical tweezers to control microvascular reperfusion. Combined with experiments, however, the possible optimal location for reperfusion can still be given. We believe that the optimal trap location is more likely to be near the branch entrance. Microvascular reperfusion could be achieved when the optical trap location within the range of is ~2 μm near the branch entrance. In fact, this range is easily identified.

3.4 Effect of Laser Power on Reperfusion Efficiency

To investigate the effect of laser power on reperfusion, the optical trap position was fixed at the optimal location, as shown in **Figure 5A**, and the laser power was gradually increased for reperfusion experiment. In this experiment, the 30-s videos were recorded at each power. The reperfusion efficiency η is given as $\eta=(q_{III}/q_{I})\times100\%$, where q_{I} and q_{III} represented the RBC amounts flowed into Branch I and Branch III, respectively. **Figure 5B** showed the reperfusion efficiency with increasing laser power. The results showed that optical trap cannot control the reperfusion of RBCs when the power of laser entering pupil was less than 200 mW for this microvessel. When the laser power was about 200~550 mW, reperfusion efficiency decreased with increasing laser power. When the

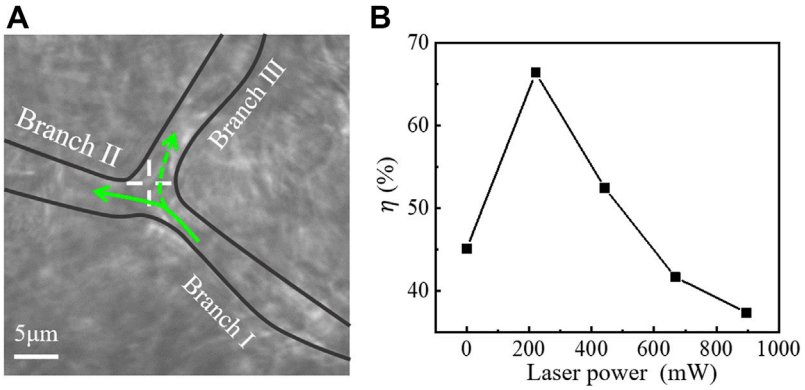

FIGURE 5 | (A) Optical tweezers control of blood flow in a branching microvessel. '+' indicates the optical trap. **(B)** Relationship between laser power and reperfusion efficiency (η).

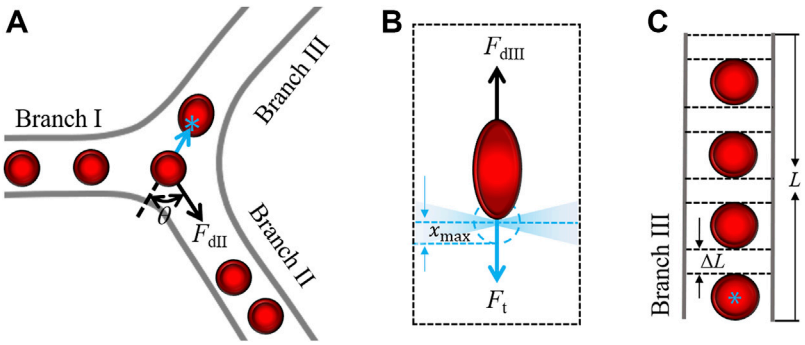

FIGURE 6 | Theoretical analysis model. **(A)** RBC is redirected and flows to Branch III under the action of optical trap. '*' indicates the optical trap. **(B)** Forces on the RBC being dragged by the blood flow. x_{max}, the maximum action range of trapping force; **(C)** RBCs in Branch III. F_t, optical trapping force; F_{dII} and F_{dIII} represents drag force from blood flow in Branch II and Branch III, respectively; and ΔL, increased length without RBC in the microvessel during the staying time t.

laser power was greater than 550 mW, the RBCs were trapped at the entrance of Branch III and decreased the blood flow of Branch III.

The experimental results reported in **Figure 5** indicate that an appropriate laser power was crucial in determining the ability of blood reperfusion. For *in vivo* trapping, the maximum tested power was almost up to 1000 mW, the heat-induced thermal damage should be discussed. During the reperfusion controlled by optical tweezers, there was no observable damage to microvessels or cells. And no burning spots were observed on the pinna of the mice for several weeks after the experiments. Studies have shown that under the same trapping conditions, Chinese hamster ovary cells exhibit an average temperature rise of nearly 1.15 ± 0.25 °C/100 mW (Liu et al., 1995). This thermal damage, which can be almost ignored, seems to be explained by the weaker absorption of organisms at 1064 nm wavelength relative to visible light (Liu et al., 1995; Liu et al., 1996; Neuman et al., 1999; Peterman et al., 2003). In addition, RBCs with high thermal conductivity can carry away some of the heat induced by the absorption through the fast blood flow, and this also prevents local thermal accumulation (Gao et al., 2021). In **Section 3.5**, we will analyze the relationship between reperfusion efficiency and the laser power.

3.5 Physical Model

The microvascular reperfusion efficiency is correlated with the optical trap force, which is proportional to the laser power. To explain reperfusion efficiency of the optical tweezers with the laser power, a physical model was established. The forces on an RBC passing junction is described in **Figure 6A**, the cell will flow into Branch II without the optical trap working. We assumed that blood flows are steady flows in all branches. The RBC experiences a drag force F_{dII} from blood flow of the Branch II. When the laser power was larger than a critical trapping power P_c, the optical trapping force F_t can overcome the component of drag force $F_{dII}\cos\theta$, and an RBC originally flowing from Branch I to Branch II can be redirected to Branch III, as in **Figure 6A**.

From the experimental videos (**Supplementary Video S4**), the redirected RBCs were stretched in the trap by the drag force F_{dIII} from the blood flow of Branch III. The forces on the trapped RBC are described in **Figure 6B**. When the RBC passes through the trap, the cell will be trapped at the position where the F_{dIII} and F_t

are balanced. The F_t acts on a part of the RBC actually. Here, the effective part of the RBC is described with stretch ratio (λ) as in **Figure 6B**. The stretch ratio λ is defined as the ratio of the length of an RBC stretched to its diameter. Before the RBC is stretched, initial stretch ratio is set as λ_0. With the increase of the optical trapping force, the stretching ratio of RBC increases. The optical trapping force is proportional to the stretch ratio of trapped object (Rohrbach, 2005). When the RBC is stretched to long enough, the F_t will be smaller than F_{dIII}, and the RBC will escape from the trap. The escaping RBC enters Branch III and increases the number of RBCs in Branch III. However, the RBC cannot be stretched to infinity, so there is a maximum stretching ratio (λ_{max}). When the F_t increases with increasing laser power to a certain value P_m, the RBC will be stretched to the maximum stretch ratio, the F_t (λ_{max}) can overcome the drag force F_{dIII}. The RBC will be trapped and clog the entrance of Branch III, the number of RBCs in Branch III will be smaller than that of before the optical trap working. The relation between the laser power P and the trapping force F_t is summed as follows:

$$\begin{cases} F_{trap} < F_{dII}\cos\theta, & P < P_c, \\ F_{dII}\cos\theta \le F_t(\lambda_0) \& F_t(\lambda_{max}) \le F_{dIII}, & P_c \le P \le P_m. \\ F_t(\lambda_{max}) > F_{dIII}, & P > P_m, \end{cases} \quad (1)$$

In **Equation 1**, we describe the different relationship between the optical trapping force and the blood flow drag force on RBC caused by the increase of laser power. The further analysis is the effect of optical trapping force on microvascular reperfusion efficiency with the increase of laser power. Here, the time t spent in the range of optical trap for each RBC was used to reflect the efficiency of reperfusion. The cell flowing to Branch II initially is trapped at the entrance of Branch III due to the action of optical trapping force. Then, the RBCs in the optical trap are stretched under the drag force of blood flow, and the relationship between the maximum stretch ratio λ_{max} and time t can be expressed as follows (Hochmuth et al., 1979; Lim et al., 2004):

$$\frac{(\lambda_0^2-1)(\lambda_{max}^2+1)}{(\lambda_0^2+1)(\lambda_{max}^2-1)} = exp\left(-\frac{t}{t_c}\right). \quad (2)$$

When the RBC is stretched to the maximum stretched length, it escapes from the optical trap. t_c is the characteristic time (Hochmuth et al., 1979; Lim et al., 2004). If the cell can escape from the optical trap, the cell receives the maximum optical trapping force when it is at x_{max} from the optical trap center. In fact, x_{max} may increase slightly as the laser power increases. In this case, the stretch ratio of cell is the maximum, as in **Figure 6B**. The maximum stretch ratio λ_{max} of an RBC can be estimated by (Evans, 1983; Parker and Winlove, 1999; Sleep et al., 1999)

$$\lambda_{max} = \frac{kx_{max}}{\sqrt[3]{125BrH^2}}, \quad (3)$$

where H and B represent Shear modulus and bending modulus of cell membrane, respectively, r is the initial radius of the RBC, and k represents the optical trap stiffness. Therefore, the time for cell staying in the optical trap t can be described as follows:

$$t = -t_c\, ln\left(\frac{(\lambda_0^2-1)(k^2x_{max}^2+25\sqrt[3]{B^2r^2H^4})}{(\lambda_0^2+1)(k^2x_{max}^2-25\sqrt[3]{B^2r^2H^4})}\right). \quad (4)$$

When the laser power increases, k and t increases, as shown in **Eqn. 4**. In other words, with the increase of laser power, the optical trapping force acting on RBC will be increased, thus increasing the residence time of RBC at the branch. For simplicity, we assume the RBCs flow into the Branch III one by one. The number of RBCs in the Branch III before optical trap working is represented as q_0, the number of reperfused RBCs is set as Δq when the optical trap can work at the laser power P_c, and the blood flow velocity v_f is assumed as a constant. For the Branch III with length L, the 'rescaled' diameter of RBC d can be obtained by $d = L/(q_0+\Delta q)$. When the laser power is larger than the P_c, the RBC stays in the optical trap within the time t, and there is an increasing RBC unfilled length ΔL during the time t, as in **Figure 6C**. The numbers of reperfusion RBCs can be expressed as follows:

$$\Delta q = \frac{L}{d+\Delta L} - q_0 = \frac{L}{d+v_f t} - q_0. \quad (5)$$

From **Eqn. 4**, the staying time t increases with increasing laser power and optical stiffness. Therefore, the number of reperfusion RBC Δq decreases with increasing laser power. When the laser power increases to larger than P_m, the cell cannot escape from the optical trap. The trapped RBCs will clog the entrance of Branch III, and stop the other flowing RBCs into Branch III. According to the above analysis, we can express the effect of optical trap on RBC reperfusion controlling as follows:

$$\Delta q \begin{cases} = 0, & P < P_c, \\ = \dfrac{L}{d+\Delta L} - q_0 = \dfrac{L}{d+v_f t} - q_0, & P_c \le P \le P_m, \\ < 0, & P > P_m. \end{cases} \quad (6)$$

According to the **Eqn. 6**, the results in **Figure 5B** can be explained qualitatively. When the laser power was less than 200 mW, the optical trapping force was smaller than the drag force of blood flow, the all RBCs were dragged into the Branch II, and the reperfusion of RBCs to Branch III cannot be controlled. When the laser power was 200~550 mW, the optical trapping force can guide the reperfusion of RBCs to Branch III. However, when the power was greater than 550 mW, RBCs were trapped in the optical trap at the entrance of Branch III, resulting in microvascular obstruction. The cells initially flowing to Branch III were also inhibited, which worsened the microvascular ischemia of Branch III.

Since the complexity of the environment *in vivo*, the blood pressure of different microvessels in pinna of mice may be slightly different. This leads to differences in the optimal laser power for controlling reperfusion. However, the reperfusion experiments by optical tweezers in this manuscript were all carried out at 200~550 mW of laser entering pupil. Only one data is shown in **Figure 4**, illustrating the effect of laser power on reperfusion,

but visualizations in **Figure 3** show the universal applicability of reperfusion.

In the experiment, the optical trapping force decreased with the increase of the depth of the reperfusion microvessels. This is the result of laser energy loss due to the strong scattering characteristic of biological tissue. With the depth of the optical trap inside the body increasing, the loss of laser energy will be increased. Moreover, the trap stiffness decreases with the increase of laser optical trap depth. The solution of these two problems requires increasing laser power, thus affecting the optimal laser power of reperfusion. Therefore, the optimal laser power for optimal reperfusion is within a range.

To improve the trap stiffness of the optical trap position, increasing laser power is an effective strategy. However, this may cause photodamage to blood vessels and RBCs. Therefore, methods to reduce light damage need to be used. Recently, some practical progress has been made toward decreasing photodamage in optical trapping systems. Azimuthally polarized beams achieve higher axial trapping efficiency and lower photodamage than linearly polarized Gaussian beams when used for optical trapping of individual RBCs (Yu et al., 2020). Moreover, many indirect-based cell manipulation strategies have been developed to significantly avoid photodamage to the target cell (Chowdhury et al., 2013a; Xie et al., 2018b; Stoev et al., 2021; Chen et al., 2022). Previous reports suggesting that the photodamage can be totally eliminated for pushing-based cell manipulation, as opposed to occurrence rates of 67 and 33% for direct trapping and tool attachment or gripping, respectively, (Chowdhury et al., 2013b; Banerjee et al., 2014). Therefore, reducing the contact between the laser and the target cell is an effective strategy to avoid photodamage in optical trap manipulation using near-infrared laser. We consider optical tweezers combined with these indirect-based manipulation methods could help achieving reperfusion of microvessels with deeper.

4 CONCLUSION

In conclusion, we have derived an efficient method of microvascular reperfusion *in vivo*, and it is the first time to reperfusion the microvascular hypoperfusion in the pinna of mice. The effect of the position of the optical trap center and the laser power on the reperfusion was studied experimentally for carrying out the experiment of reperfusion under suitable optical trap position and laser power. The results showed that microvascular reperfusion could be achieved by optical tweezers near the branch entrance of microvascular hypoperfusion with 200~550 mW of laser entering pupil. In addition, a series of experiments have demonstrated the universal applicability of microvascular reperfusion by optical tweezers.

As far as we know, the current treatment for distributive shock ensures blood perfusion of macrocirculation. Precise treatment of the microvascular hypoperfusion is difficult (Vincent and De Backer, 2013; Pan et al., 2020). The development of various techniques has provided new ideas for the treatment of the microvascular hypoperfusion (Galanzha et al., 2009; Lenshof et al., 2009; Galanzha et al., 2016). In this study, optical tweezers were used to control microvascular reperfusion at branch. Experimental results on the pinna of mice show that the method is effective in the treatment of the microvascular hypoperfusion. The implementation of this technique is almost non-invasive in controlling dynamic reperfusion of microvessels *in vivo*, which has not yet been achieved by any other techniques. However, the treatment of distributive shock with this technique still faces some challenges. One is that traditional Gaussian optical tweezers cannot form an effective optical trap in deep tissue due to the strong scattering characteristics of biological tissue, and the other is the lack of real-time and clear imaging methods in deep tissue. This is why we are working in mice pinna.

Moreover, experimental results indicate that optical trapping force should be maintained at the branch in order to treat microvascular hypoperfusion. The method we propose will be a pertinent treatment of hypoperfusion if the optical trapping force remains at the branch for a short time, allowing continuous reperfusion of microvessels. We will seriously discuss and pay attention to this issue in the following research.

As a basic study, however, optical tweezers can be used as a new method to control microvascular reperfusion *in vivo*, and this non-invasive and precise method of microvascular reperfusion is expected to provide new insights into the treatment of distributive shock.

DATA AVAILABILITY STATEMENT

The original contributions presented in the study are included in the article/**Supplementary Material**; further inquiries can be directed to the corresponding authors.

ETHICS STATEMENT

The animal study was reviewed and approved by the Ethical Committee of the Hefei University of Technology.

AUTHOR CONTRIBUTIONS

M-CZ, MS, and JZ conceived the idea. MS performed the experiment and analyzed the data. MS and M-CZ wrote and edited the manuscript. ZW and ZZ contributed to analyze the data and review the manuscript. ZK contributed to constructing the experimental setup. All the authors reviewed and revised the manuscript.

FUNDING

This work was supported by a grant from the National Natural Science Foundation of China (Grant No. 11874138), Research Fund of Anhui Institute of translational medicine (2021zhyx-

B16), and Natural Science Foundation of Anhui Province in China (1908085MA14), and the Key Research and Development Program of Anhui Province in China (2022a05020028).

ACKNOWLEDGMENTS

We are grateful to Professor Xiaoyan He (School of Life Sciences, Anhui Medical University) for giving Kunming mice kindly and Min Gao (The First Affiliated Hospital of Anhui Medical University) for her guidance in anesthetic treatment of mice.

SUPPLEMENTARY MATERIAL

The Supplementary Material for this article can be found online at: https://www.frontiersin.org/articles/10.3389/fbioe.2022.952537/full#supplementary-material

REFERENCES

Abdullah, S. E., and Perez-Soler, R. (2012). Mechanisms of Resistance to Vascular Endothelial Growth Factor Blockade. *Cancer* 118 (14), 3455–3467. doi:10.1002/cncr.26540

Ashkin, A., Dziedzic, J. M., Bjorkholm, J. E., and Chu, S. (1986). Observation of a Single-Beam Gradient Force Optical Trap for Dielectric Particles. *Opt. Lett.* 11 (5), 288–290. doi:10.1364/OL.11.000288

Avsievich, T., Tarakanchikova, Y., Zhu, R., Popov, A., Bykov, A., Skovorodkin, I., et al. (2020). Impact of Nanocapsules on Red Blood Cells Interplay Jointly Assessed by Optical Tweezers and Microscopy. *Micromachines* 11 (1), 19. doi:10.3390/mi11010019

Banerjee, A., Chowdhury, S., and Gupta, S. K. (2014). Optical Tweezers: Autonomous Robots for the Manipulation of Biological Cells. *IEEE Robot. Autom. Mag.* 21 (3), 81–88. doi:10.1109/MRA.2014.2332407

Boros, M., and Bauer, I. (2021). Editorial: Microcirculation Guided/Targeted Resuscitation. *Front. Med.* 8, 649828. doi:10.3389/fmed.2021.649828

Chen, Z., Li, J., and Zheng, Y. (2022). Heat-mediated Optical Manipulation. *Chem. Rev.* 122 (3), 3122–3179. doi:10.1021/acs.chemrev.1c00626

Chowdhury, S., Thakur, A., Svec, P., Wang, C., Losert, W., and Gupta, S. K. (2013a). Automated Manipulation of Biological Cells Using Gripper Formations Controlled by Optical Tweezers. *IEEE Trans. Autom. Sci. Eng.* 11 (2), 338–347. doi:10.1109/TASE.2013.2272512

Chowdhury, S., Thakur, A., Wang, C., Svec, P., Losert, W., and Gupta, S. K. (2013b). "Automated Indirect Manipulation of Irregular Shaped Cells with Optical Tweezers for Studying Collective Cell Migration," in 2013 IEEE International Conference on Robotics and Automation (ICRA) (Karlsruhe, Germany: IEEE), 2789–2794. doi:10.1109/ICRA.2013.6630962

Evans, E. A. (1983). Bending Elastic Modulus of Red Blood Cell Membrane Derived from Buckling Instability in Micropipet Aspiration Tests. *Biophysical J.* 43 (1), 27–30. doi:10.1016/S0006-3495(83)84319-7

Galanzha, E. I., Shashkov, E. V., Kelly, T., Kim, J.-W., Yang, L., and Zharov, V. P. (2009). *In Vivo* magnetic Enrichment and Multiplex Photoacoustic Detection of Circulating Tumour Cells. *Nat. Nanotech* 4 (12), 855–860. doi:10.1038/nnano.2009.333

Galanzha, E. I., Viegas, M. G., Malinsky, T. I., Melerzanov, A. V., Juratli, M. A., Sarimollaoglu, M., et al. (2016). *In Vivo* acoustic and Photoacoustic Focusing of Circulating Cells. *Sci. Rep.* 6, 21531. doi:10.1038/srep21531

Gao, Q., Wang, W., Li, X., Li, Y., Ferraro, P., Jiao, X., et al. (2021). Cell Nucleus as Endogenous Biological Micropump. *Biosens. Bioelectron.* 182, 113166. doi:10.1016/j.bios.2021.113166

Henon, S., Lenormand, G., Richert, A., and Gallet, F. (1999). A New Determination of the Shear Modulus of the Human Erythrocyte Membrane Using Optical Tweezers. *Biophysical J.* 76 (2), 1145–1151. doi:10.1016/S0006-3495(99)77279-6

Horner, F., Meissner, R., Polali, S., Pfeiffer, J., Betz, T., Denz, C., et al. (2017). Holographic Optical Tweezers-Based *In Vivo* Manipulations in Zebrafish Embryos. *J. Biophot.* 10 (11), 1492–1501. doi:10.1002/jbio.201600226

Han, C.-H., Song, H., Kang, Y.-G., Kim, B.-M., and Im, C.-H. (2014). Hemodynamic Responses in Rat Brain during Transcranial Direct Current Stimulation: a Functional Near-Infrared Spectroscopy Study. *Biomed. Opt. Express* 5 (6), 1812–1821. doi:10.1364/BOE.5.001812

Herbert, S. P., Cheung, J. Y. M., and Stainier, D. Y. R. (2012). Determination of Endothelial Stalk versus Tip Cell Potential during Angiogenesis by H2.0-like Homeobox-1. *Curr. Biol.* 22 (19), 1789–1794. doi:10.1016/j.cub.2012.07.037

Hochmuth, R. M., Worthy, P. R., and Evans, E. A. (1979). Red-cell Extensional Recovery and the Determination of Membrane Viscosity. *Biophys. J.* 26 (1), 101–114. doi:10.1016/S0006-3495(79)85238-8

Jha, A., Zilahi, G., and Rhodes, A. (2021). Vasoactive Therapy in Shock. *BJA Educ.* 21 (7), 270–277. doi:10.1016/j.bjae.2021.03.002

Jiang, S., Wu, M., Lu, X., Zhong, Y., Kang, X., Song, Y., et al. (2021). Is Restrictive Fluid Resuscitation Beneficial Not Only for Hemorrhagic Shock but Also for Septic Shock?: A Meta Analysis. *Med. Baltim.* 100 (12), e25143. doi:10.1097/MD.0000000000025143

Johansen, P. L., Fenaroli, F., Evensen, L., Griffiths, G., and Koster, G. (2016). Optical micromanipulation of nanoparticles and cells inside living zebrafish. *Nat. Commun.* 7, 10974. doi:10.1038/ncomms10974

Landenberger, B., Höfemann, H., Wadle, S., and Rohrbach, A. (2012). Microfluidic sorting of arbitrary cells with dynamic optical tweezers. *Lab Chip* 12 (17), 3177–3183. doi:10.1039/c2lc21099a

Legrand, M., Ait-Oufella, H., and Ince, C. (2018). Could resuscitation be based on microcirculation data? Yes. *Intensive Care Med.* 44 (6), 944–946. doi:10.1007/s00134-018-5121-0

Lenshof, A., Ahmad-Tajudin, A., Järås, K., Swärd-Nilsson, A.-M., Åberg, L., Marko-Varga, G., Malm, J., and Lilja (2009). Acoustic Whole Blood Plasmapheresis Chip for Prostate Specific Antigen Microarray Diagnostics. *Anal. Chem.* 81 (15), 6030–6037. doi:10.1021/ac9013572

Lim, C. T., Dao, M., Suresh, S., Sow, C. H., and Chew, K. T. (2004). Large Deformation of Living Cells Using Laser Traps. *Acta Mater.* 52 (7), 1837–1845. doi:10.1016/j.actamat.2003.12.028

Liu, X., Gao, Q., Zhang, Y., Li, Y., and Li, B. (2020). *In Vivo* optofluidic Switch for Controlling Blood Microflow. *Adv. Sci.* 7 (14), 2001414. doi:10.1002/advs.202001414

Liu, Y., Cheng, D. K., Sonek, G. J., Berns, M. W., Chapman, C. F., and Tromberg, B. J. (1995). Evidence for Localized Cell Heating Induced by Infrared Optical Tweezers. *Biophysical J.* 68 (5), 2137–2144. doi:10.1016/S0006-3495(95)80396-6

Liu, Y., Sonek, G. J., Berns, M. W., and Tromberg, B. J. (1996). Physiological Monitoring of Optically Trapped Cells: Assessing the Effects of Confinement by 1064-nm Laser Tweezers Using Microfluorometry. *Biophysical J.* 71 (4), 2158–2167. doi:10.1016/S0006-3495(96)79417-1

Motwani, S. K., and Saunders, H. (2021). Inotropes. *Anaesth. Intensive Care Med.* 22 (4), 243–248. doi:10.1016/j.mpaic.2021.02.011

Neuman, K. C., and Block, S. M. (2004). Optical Trapping. *Rev. Sci. Instrum.* 75 (9), 2787–2809. doi:10.1063/1.1785844

Neuman, K. C., Chadd, E. H., Liou, G. F., Bergman, K., and Block, S. M. (1999). Characterization of Photodamage to *Escherichia coli* in Optical Traps. *Biophysical J.* 77 (5), 2856–2863. doi:10.1016/S0006-3495(99)77117-1

Pan, P., Su, L., Liu, D., and Wang, X. (2020). Microcirculation-guided Protection Strategy in Hemodynamic Therapy. *Clin. Hemorheol. Microcirc.* 75 (2), 243–253. doi:10.3233/CH-190784

Parker, K. H., and Winlove, C. P. (1999). The Deformation of Spherical Vesicles with Permeable, Constant-Area Membranes: Application to the Red Blood Cell. *Biophysical J.* 77 (6), 3096–3107. doi:10.1016/S0006-3495(99)77140-7

Peterman, E. J. G., Gittes, F., and Schmidt, C. F. (2003). Laser-induced Heating in Optical Traps. *Biophysical J.* 84 (2), 1308–1316. doi:10.1016/S0006-3495(03)74946-7

Rohrbach, A. (2005). Stiffness of Optical Traps: Quantitative Agreement between Experiment and Electromagnetic Theory. *Phys. Rev. Lett.* 95 (16), 168102. doi:10.1103/PhysRevLett.95.168102

Scheeren, T. W. L., Bakker, J., Kaufmann, T., Annane, D., Asfar, P., Boerma, E. C., et al. (2021). Current Use of Inotropes in Circulatory Shock. *Ann. Intensive Care* 11 (1), 21. doi:10.1186/s13613-021-00806-8

Sleep, J., Wilson, D., Simmons, R., and Gratzer, W. (1999). Elasticity of the Red Cell Membrane and its Relation to Hemolytic Disorders: an Optical Tweezers Study. *Biophysical J.* 77 (6), 3085–3095. doi:10.1016/S0006-3495(99)77139-0

Stoev, I. D., Seelbinder, B., Erben, E., Maghelli, N., and Kreysing, M. (2021). Highly Sensitive Force Measurements in an Optically Generated, Harmonic Hydrodynamic Trap. *eLight* 1 (1), 7. doi:10.1186/s43593-021-00007-7

Sugden, W. W., Meissner, R., Aegerter-Wilmsen, T., Tsaryk, R., Leonard, E. V., Bussmann, J., et al. (2017). Endoglin Controls Blood Vessel Diameter through Endothelial Cell Shape Changes in Response to Haemodynamic Cues. *Nat. Cell Biol.* 19 (6), 653–665. doi:10.1038/ncb3528

Vasse, G. F., Buzón, P., Melgert, B. N., Roos, W. H., and Rijn, P. (2021). Single Cell Reactomics: Real-Time Single-Cell Activation Kinetics of Optically Trapped Macrophages. *Small Methods* 5 (4), 2000849. doi:10.1002/smtd.202000849

Vincent, J.-L., and De Backer, D. (2013). Circulatory Shock. *N. Engl. J. Med.* 369 (18), 1726–1734. doi:10.1056/NEJMra1208943

Wachter, D., Wrede, A., Schulz-Schaeffer, W., Taghizadeh-Waghefi, A., Nitsche, M. A., Kutschenko, A., et al. (2011). Transcranial Direct Current Stimulation Induces Polarity-specific Changes of Cortical Blood Perfusion in the Rat. *Exp. Neurol.* 227 (2), 322–327. doi:10.1016/j.expneurol.2010.12.005

Wang, C., Sun, X., Cheng, L., Yin, S., Yang, G., Li, Y., et al. (2014). Multifunctional Theranostic Red Blood Cells for Magnetic-Field-Enhanced *In Vivo* Combination Therapy of Cancer. *Adv. Mat.* 26 (28), 4794–4802. doi:10.1002/adma.201400158

Wang, X., Chen, S., Kong, M., Wang, Z., Costa, K. D., Li, R. A., et al. (2011). Enhanced Cell Sorting and Manipulation with Combined Optical Tweezer and Microfluidic Chip Technologies. *Lab. Chip* 11 (21), 3656–3662. doi:10.1039/c1lc20653b

Weijts, B., Gutierrez, E., Saikin, S. K., Ablooglu, A. J., Traver, D., Groisman, A., et al. (2018). Blood Flow-Induced Notch Activation and Endothelial Migration Enable Vascular Remodeling in Zebrafish Embryos. *Nat. Commun.* 9 (1), 1–11. doi:10.1038/s41467-018-07732-7

Xie, M., Mills, J. K., Li, X., Wang, Y., and Sun, D. (2015a). "Modelling and Control of Optical Manipulation for Cell Rotation," in 2015 IEEE International Conference on Robotics and Automation (ICRA) (Seattle, WA: IEEE), 956–961. doi:10.1109/ICRA.2015.7139292

Xie, M., Mills, J. K., Wang, Y., Mahmoodi, M., and Sun, D. (2015b). Automated Translational and Rotational Control of Biological Cells with a Robot-Aided Optical Tweezers Manipulation System. *IEEE Trans. Autom. Sci. Eng.* 13 (2), 543–551. doi:10.1109/TASE.2015.2411271

Xie, M., Shakoor, A., Shen, Y., Mills, J. K., and Sun, D. (2018a). Out-of-plane Rotation Control of Biological Cells with a Robot-Tweezers Manipulation System for Orientation-Based Cell Surgery. *IEEE Trans. Biomed. Eng.* 66 (1), 199–207. doi:10.1109/TBME.2018.2828136

Xie, M., Shakoor, A., and Wu, C. (2018b). Manipulation of Biological Cells Using a Robot-Aided Optical Tweezers System. *Micromachines* 9 (5), 245. doi:10.3390/mi9050245

Yu, P., Liu, Y., Zhao, Q., Wang, Z., Li, Y.-M., and Gong, L. (2020). Reducing Photodamage in Optical Trapping of Individual Cells in Living Zebrafish. *Appl. Phys. Express* 13 (3), 032008. doi:10.35848/1882-0786/ab7484

Zhang, H., and Liu, K.-K. (2008). Optical Tweezers for Single Cells. *J. R. Soc. Interface.* 5 (24), 671–690. doi:10.1098/rsif.2008.0052

Zhao, Q., Wang, H.-W., Yu, P.-P., Zhang, S.-H., Zhou, J.-H., Li, Y.-M., et al. (2020). Trapping and Manipulation of Single Cells in Crowded Environments. *Front. Bioeng. Biotechnol.* 8, 422. doi:10.3389/fbioe.2020.00422

Zhong, M.-C., Gong, L., Zhou, J.-H., Wang, Z.-Q., and Li, Y.-M. (2013a). Optical Trapping of Red Blood Cells in Living Animals with a Water Immersion Objective. *Opt. Lett.* 38 (23), 5134–5137. doi:10.1364/OL.38.005134

Zhong, M.-C., Wang, Z.-Q., and Li, Y.-M. (2017). Aberration Compensation for Optical Trapping of Cells within Living Mice. *Appl. Opt.* 56 (7), 1972–1976. doi:10.1364/AO.56.001972

Zhong, M.-C., Wei, X.-B., Zhou, J.-H., Wang, Z.-Q., and Li, Y.-M. (2013b). Trapping Red Blood Cells in Living Animals Using Optical Tweezers. *Nat. Commun.* 4 (1), 1–7. doi:10.1038/ncomms2786

Zhou, Q., Xia, T., Liao, W., Liu, Y., Lin, D., Yang, J., et al. (2021). Microparticle Sorting with a Virtual Optical Chip. *Rev. Sci. Instrum.* 92 (5), 053201. doi:10.1063/5.0047316

Conflict of Interest: The authors declare that the research was conducted in the absence of any commercial or financial relationships that could be construed as a potential conflict of interest.

frontiers | Frontiers in Bioengineering and Biotechnology

TYPE Review
PUBLISHED 29 August 2022
DOI 10.3389/fbioe.2022.962040

OPEN ACCESS

EDITED BY
Tadanori Mammoto,
Medical College of Wisconsin,
United States

REVIEWED BY
Enrico Gherlone,
Vita-Salute San Raffaele University, Italy
Yoshihiro Komatsu,
Univ of Texas Medical School at Houston, United States
Eric Van Otterloo,
The University of Iowa, United States

*CORRESPONDENCE
Abigail S. Tucker,
abigail.tucker@kcl.ac.uk

SPECIALTY SECTION
This article was submitted to Tissue Engineering and Regenerative Medicine, a section of the journal Frontiers in Bioengineering and Biotechnology

RECEIVED 05 June 2022
ACCEPTED 28 July 2022
PUBLISHED 29 August 2022

CITATION
Asrar H and Tucker AS (2022), Endothelial cells during craniofacial development: Populating and patterning the head.
Front. Bioeng. Biotechnol. 10:962040.
doi: 10.3389/fbioe.2022.962040

Endothelial cells during craniofacial development: Populating and patterning the head

Hiba Asrar and Abigail S. Tucker*

Centre for Craniofacial and Regenerative Biology, Faculty of Dentistry, Oral and Craniofacial Sciences, Guy's Hospital, Kings College London, London, United Kingdom

Major organs and tissues require close association with the vasculature during development and for later function. Blood vessels are essential for efficient gas exchange and for providing metabolic sustenance to individual cells, with endothelial cells forming the basic unit of this complex vascular framework. Recent research has revealed novel roles for endothelial cells in mediating tissue morphogenesis and differentiation during development, providing an instructive role to shape the tissues as they form. This highlights the importance of providing a vasculature when constructing tissues and organs for tissue engineering. Studies in various organ systems have identified important signalling pathways crucial for regulating the cross talk between endothelial cells and their environment. This review will focus on the origin and migration of craniofacial endothelial cells and how these cells influence the development of craniofacial tissues. For this we will look at research on the interaction with the cranial neural crest, and individual organs such as the salivary glands, teeth, and jaw. Additionally, we will investigate the methods used to understand and manipulate endothelial networks during the development of craniofacial tissues, highlighting recent advances in this area.

KEYWORDS

angiogenesis, vasculogenesis, cell signalling, vascular biology, tooth, gland, neural crest

Introduction

The vasculature acts as a major transport mechanism with blood as a constant flowing medium being distributed through vessels. It serves as a multipurpose delivery system providing essential nutrients and removing toxic metabolites (Rajendran et al., 2013). Blood vessels are part of a complex circulatory system responsible for development and maintenance of organ systems. Any dysregulation in the mechanisms underlying blood vessel regulation or abnormal blood vessel formation contributes to development of widespread pathologies including peripheral vascular diseases, metastatic conditions and bone diseases (Rajendran et al., 2013; Ramasamy et al., 2015).

Blood vessels formation is a highly organized sequential event comprised of two distinct mechanisms, vasculogenesis and angiogenesis, which occur throughout the body.

These tightly regulated processes commence during embryonic life and continue postnatally. During embryonic development vasculogenesis begins in tissues through the *in-situ* differentiation of endothelial precursors forming an immature vascular network that coalesce to form *de novo* tubes (Schmeisser and Strasser, 2002). Post-natal blood vessel formation generally occurs through angiogenesis, involving new vessels sprouting from pre-existing vessels (Moore, 2002). The entire vasculature is lined chiefly by endothelial cells. These cells carry out primary roles as cell barriers controlling movement of cells and substances in and out of blood vessels. Moreover, they control critical functions such as regulation of vascular tone, coagulation and homeostasis (Sandoo et al., 2010). A number of proteins, such as CD31 (also known as PECAM1) is present evenly over the cell surface and can be used as an endothelial cell marker. In embryonic tissues endothelial cells keep pace with growth and development, whereas in adult tissue they continue to allow renewal, remodelling and reconstruction. During early vascular development important molecular signals such as Bone morphogenetic protein-4 (BMP4) initiate endothelial cell differentiation from various multipotent mesenchymal cells while fibroblast growth factor (FGF) stimulates cells by inducing early endothelial markers (Dejana et al., 2017). Vascular endothelial growth factor (VEGF) expression controls blood vessel growth and remodelling, providing mitogenic and survival stimuli to endothelial cells, with FGF signalling in endothelial cells controlling the sensitivity of the response (Murakami and Simons, 2008). Endothelial cells acquire support from contractile cells called pericytes and smooth muscle cells (collectively referred to as mural cells) that attach to the abluminal surface of endothelial cells (Armulik et al., 2011). These mural cells/perivascular cells express common markers, such as neuron- glial-antigen (NG2), Cd146, α-SMA, and platelet derived growth factor- β (Bergers and Song, 2005).

The focus of this review is on the function of endothelial cells (ECs) in the craniofacial region and the molecular signatures that regulate endothelial cell migration in the cranium. We discuss perfusion independent roles of the vasculature in directing tissue morphogenesis/cell differentiation in different cranial structures. Moreover, we discuss technical advancements that aid in the investigation of the roles of endothelial cells.

Endothelial cell origin in the cranial region

The craniofacial region houses the sense organs, brain and masticatory organs, all of which are well supplied by the vasculature (Figure 1). The face is created from the fusion of the pharyngeal arches and nasal processes (lateral, medial and frontal) that form during early craniofacial development. Endothelial cells develop around the forming pharyngeal arch arteries in the centre of each pharyngeal arch and are derived from *Mesp1*-lineage positive mesoderm (Liang et al., 2014). In contrast, the surrounding pericytes and smooth muscle cells are derived from the neural crest (Etchevers et al., 2001). Previously, tracing of the embryonic vasculature suggested that the vasculature of the pharyngeal arches formed as an extension of the dorsal aorta, with the endothelial cells sprouting from the larger vessel (angiogenesis) (Hiruma et al., 2002). However, genetic labelling using *Tie2cre* has revealed that vessels in the arches arise *de novo* directly from the pharyngeal mesoderm (vasculogenesis), rather than as extensions of existing vessels (Li et al., 2012).

Two distinct sources of endothelial cells have been described to populate the pharyngeal arches (Wang et al., 2017). The exact source of embryonic tissue that gives rise to anterior arch endothelium in mice is still unclear, but in the more posterior pharyngeal arches (arch 3–6) the endothelial cells derive from the secondary heart field (SHF) (Wang et al., 2017). The SHF is a subset of the *Mesp1* progenitor population defined by the *Isl1* transcription factor (Verzi et al., 2005; Evans et al., 2010). Quantitative analysis revealed that 95% of the endothelial cell population in pharyngeal arch 3–6 was derived from the SHF. VEGFR2 expressing cells in the SHF delaminate and migrate into the pharyngeal mesenchyme to form a primitive vascular network (Wang et al., 2017). These small blood vessels undergo remodelling to create the pharyngeal arch arteries in arch 3–6th, which eventually give rise to the aortic arch arteries (Hutson and Kirby, 2007). Even after extensive vascular remodelling the aortic arch arteries retain the SHF derived endothelium (Wang et al., 2017).

Vasculogenesis of the pharyngeal arch arteries is regulated by retinoic acid signalling (Li et al., 2012). Compromised retinoic acid signalling caused defects in both the pharyngeal endoderm and arch arteries, with retinoic acid receptor activity required for proper coalescence of endothelial cells into nascent blood vessels in the pharyngeal mesoderm (Wendling et al., 2000). *Rara1/Rarb* mutants showed bilateral absence or hypoplasia of the 4/6th arch artery (Li et al., 2012). *Mesp1cre/Rara* conditional knock out embryos had no effect on terminal differentiation of endothelial cells but led to scattered endothelial cells that failed to aggregate to form nascent vessels, highlighting the need for retinoic acid signalling for effective vasculogenesis (Li et al., 2012).

In zebrafish, time lapse imaging using the transgenic *Etsrp: GFP* line, where GFP labels vascular endothelial and myeloid progenitors, identified two bilateral angioblast clusters called the rostral organizing centre and midbrain organizing centre, which gave rise to cranial vessels (Proulx et al., 2010). These organizing centres contained endothelial clusters that formed by vasculogenesis and eventually gave rise to cranial vessels through angiogenesis (Proulx et al., 2010). At the 14–15 somite stage angiogenic extensions from the rostral organizing centre developed and endothelial cells migrated posteriorly and laterally giving rise to most rostral cranial vessels (Proulx et al., 2010). In contrast, the midbrain organizing centre progenitors collectively migrated and formed midbrain/hindbrain cranial vessels.

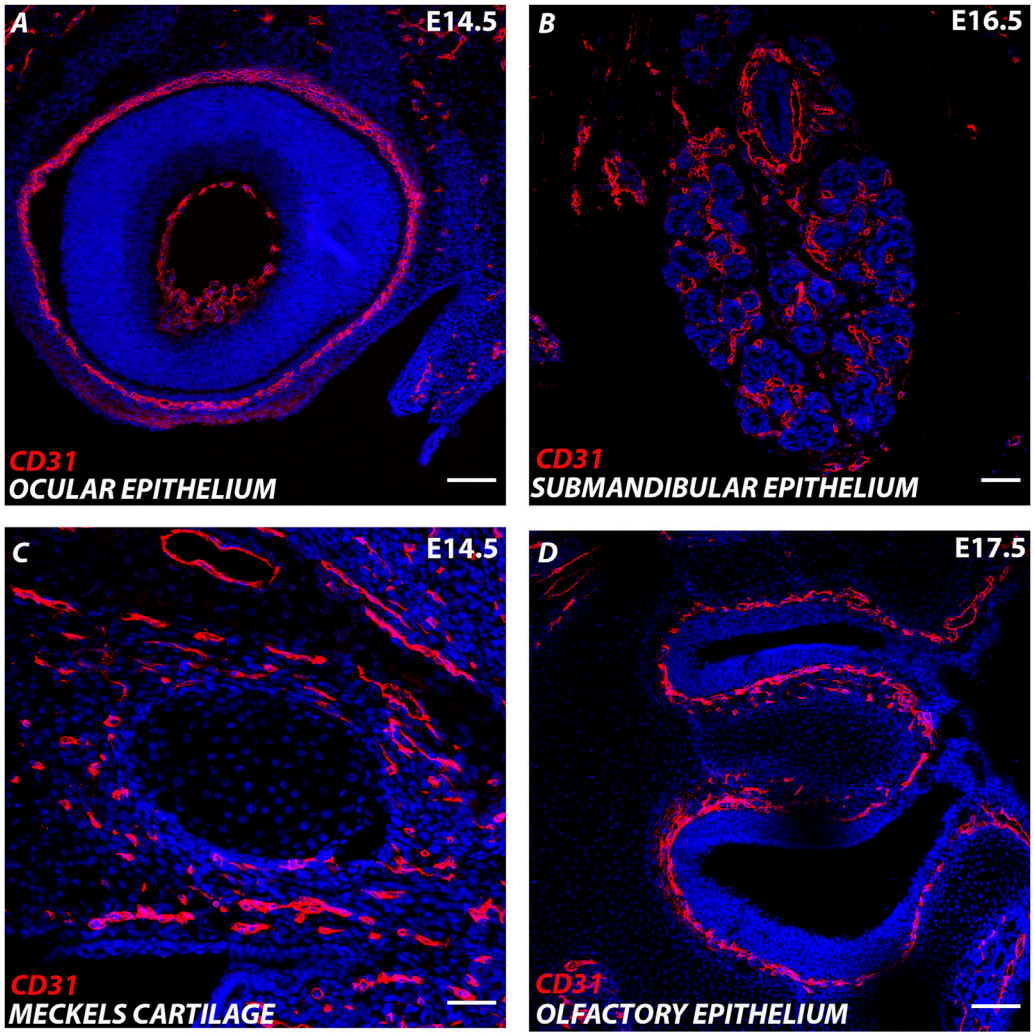

FIGURE 1
Endothelial cells in the developing cranial region. **(A–D)** Murine cranial tissue CD31 expression in red. Nuclei stained with DAPI in blue. **(A)** E (embryonic day) 14.5 Developing eye. **(B)** E16.5 Developing submandibular gland. **(C)** E14.5 Developing Meckel's cartilage (centre) surrounded by CD31 cells in the surrounding mesenchyme. **(D)** E17.5 Developing olfactory epithelium. Scale bar = 100 μm.

Etsrp is a Ets transcription factor that controls vascular and haematopoietic development and is homologous to *Etv2* in mammals. In *Etsrp* morphant zebrafish, the cranial vasculature was absent and scattered angioblasts were observed (Proulx et al., 2010). Interestingly, the endothelial progenitors appeared to change fate in the absence of *Etsrp*, forming skeletal muscle, suggesting a role for this transcription factor in determining endothelial fate (Chestnut et al., 2020).

Migrating with the cranial neural crest

The cranial vasculature shares common migration pathways with cranial neural crest cells (McKinney et al., 2016). Neural crest cells form important structures in the craniofacial region, which are intimately linked with the cranial vasculature. Alteration in neural crest cell migration can give rise to craniofacial syndromes, known as neurocristopathies (Trainor, 2010). Cranial neural crest cell and endothelial cells, despite having distinct origins, migrate towards a common region in close proximity (McKinney et al., 2016). The vasculature is regulated by a family of essential growth factors called Angiopoietins (Davis et al., 1996; Suri et al., 1996) that are also highly expressed in cranial neural crest cells, the otic vesicle and neural tube (McKinney et al., 2016). During migration, frequent collisions were recorded between endothelial and r6 neural crest cells that led to changes in endothelial cell behaviour and cell shape (McKinney et al.,

2016). Overexpression of *Angiopoietin 2* in neural crest cells perturbed endothelial cell migration and motility, with fewer, more unstable endothelial sprouts that underwent regression (McKinney et al., 2016). The interaction appears to go both ways, as highlighted in conditional *Flk1 (VEGFR2)* mutants. *VEGFR2* is indispensable for development of endothelial and haematopoietic lineages, with knockdown of this gene resulting in embryonic lethality during early embryogenesis due to disruption of the endothelial pool in the anterior region of the developing head (Eichmann et al., 1997; Shibuya, 2011). In the absence of cardio-cranial endothelial cells, the cranial neural crest cells were also deficient, with loss of neural crest markers in the second pharyngeal arch (Milgrom-Hoffman et al., 2014). Interestingly, loss of endothelial cells led to changes in the extra cellular matrix, which then impacted neural crest survival and migration and led to cell death of the cranial neural crest cells (Milgrom-Hoffman et al., 2014). This research, therefore, suggests an instructive role of the cranial vasculature in controlling neural crest decisions.

Analysis of *Ephrin* mutants, however, suggests that the cues that control the guidance of the cranial neural crest and vasculature are complex. In the *Ephrin B2* null mouse, both the cranial neural crest and the vasculature were defective, with an absent or significantly reduced second branchial arch (hyoid) and loss of the associated blood vessels (Adams et al., 2001). Endothelial cells were irregularly arranged and failed to form tubular network with numerous abnormal sprouts and branches invading somitic tissues (Adams et al., 2001). In contrast, loss of the cytoplasmic domain of *Ephrin B2* in a truncated mutant caused vascular and angiogenic defects in the head but did not disrupt cranial neural crest cell migration (Adams et al., 2001). These findings suggest the importance of full length *Ephrin B2* for remodelling and formation of cranial vasculature. However, a conditional knockin mouse, where *Ephrin B2* was rescued in the vasculature in *Ephrin B2* null mice, but not in the neural crest, led to normal neural crest migration. The defect in the neural crest in the mutant is, therefore, due to the defect in the vasculature (Lewis et al., 2015). These findings highlight the importance of endothelial-neural crest cell coordination during early stages of head morphogenesis.

Guiding endothelial cells in the head

Endothelial cells need to be guided to particular organs during development and form an integral part of their development. This involves key molecules that guide endothelial cells throughout the body by a combination of attraction and repulsion.

The VEGF signalling pathway has been shown to be an important vascular attractant in a range of different tissues (Shibuya, 2011). VEGFR2 is largely found in high calibre arteries whereas VEGFR3 expression is restricted to veins and capillaries (Rocha and Adams, 2009). In the developing head, the vasculature expresses *VEGFR2* (Shadad et al., 2019). VEGF expression has been followed using LacZ reporters throughout mouse embryogenesis, with high levels in the cranial region, particularly associated with the developing tooth, whisker follicles, pituitary, and choroid plexus at E14.5 (Miquerol et al., 1999). In the whisker follicle, VEGF was expressed in the condensing mesenchyme but not in the epithelium, while in the tooth, VEGF was expressed in the dental epithelium, not in the dental papilla but in the mesenchyme of the dental sac (Miquerol et al., 1999). Expression of *VEGF* in the tooth epithelium is maintained throughout development and is closely associated with the enamel knots, signalling centres that control tooth morphogenesis (Shadad et al., 2019). *VEGF* has additionally been shown to be expressed in the mesenchyme surrounding Meckel's cartilage (Wiszniak et al., 2015), a transient structure that forms the template for the lower jaw in vertebrates (Svandova et al., 2020). Craniofacial organs, therefore, have an organ specific expression pattern of VEGF, attracting the VEGFR2 positive vasculature to different regions of the cranial organs as they develop.

Sema3 family members compete with VEGF to bind to Nrp1 to inhibit VEGF induced angiogenesis (Parker et al., 2012). Several *in vitro* studies have explored the role of Sema3s in controlling endothelial cell migration (Gu and Giraudo, 2013). Chick forelimb studies reveal how Sema-3A coated beads disintegrate vascular network assembly whereas exogenous application of Sema-3A antibody led to local rescue of vasculature (Bates et al., 2003). During craniofacial development, semaphorin class 3 members such as *Sema3A Sema3B Sema3C* and *Sema3E* are expressed in developing brain stem, otic vesicle, eye (periocular mesenchyme), trigeminal ganglion and branchial arches (Chilton and Guthrie, 2003). In the first pharyngeal arch, *Sema 3C* was expressed mainly in the arch epithelium, while *Sema3D* was expressed in a patch in the arch mesenchyme (Chilton and Guthrie, 2003). Studies on murine embryonic development have reported expression of *Sema3G* in the retinal/brain endothelial cells and *Sema3A/Sema3C* in the submandibular gland (Chung et al., 2007; Tan et al., 2019; Chen et al., 2021). Similarly, zebrafish studies have reported expression domains of *Sema3G* in the midbrain, diencephalon, telencephalon and pharyngeal arches during early development. In the retina, *Sema3G* is expressed in endothelial cells and acts as a vascular remodelling factor. Conditional deletion of *Sema3G* in endothelial cells led to hyper-pruned vascular networks with leaky immature retinal vessels (Chen et al., 2021). Semas, may therefore, have a greater role in remodelling the vasculature, rather than in guiding migration as first envisioned. VEGF, thus, guide the endothelial cells into the head to reach specific organs at distinct timepoints, and then Semas act to remodel the vasculature.

Instructive role of endothelial cells in controlling morphogenesis/cell differentiation in craniofacial structures

As observed for the neural crest, the vasculature not only functions as a transport system bringing nutrients and oxygen and removing waste but can have an instructive role controlling cell migration and building organ architecture. These perfusion independent roles have been studied in the forming head in the context of the salivary glands, tooth, jaw cartilage and brain.

Endothelial cell control of salivary gland morphogenesis

During development, CD31+ve endothelial cells intimately surround developing salivary glands wrapping around the epithelial end buds from E12.5 onwards (Kwon et al., 2017). Notably, VEGFR2+ cells were detected inside clefts that define the boundary between terminal proacinar structures and secondary duct epithelium. Blocking VEGFR2 tyrosine kinase activity with inhibitors such as ZM323881 and SU5416 or with VEGFR2 siRNA, inhibited vascular development in culture and altered epithelial branching with fewer endbuds, wider excretory ducts and decreased total ductal area (Kwon et al., 2017). These findings suggest that the vasculature is essential for submandibular gland morphogenesis. Immuno-depletion of $CD31^{+}$ endothelial cells, using a novel *ex-vivo* SMG cell fractionation/reconstitution assay, led to loss of the vasculature and increased end bud size (Kwon et al., 2017) (Figure 2). Epithelial gland architecture was rescued by supplementation of the depleted gland cultures with endothelial cells, which supported end bud formation with thin secondary ducts and partially restored the vasculature (Kwon et al., 2017). Inhibition of VEGFR2 resulted in longer and wider K19 + developing ducts with expansion of K19+ ductal population and reduction of Kit+ cells relative to the control group. Interestingly, exogenous addition of endothelial cell-regulated mesenchymal factors such as IGFBP2 and IGFBP3 restored epithelial patterning (Kwon et al., 2017). These results highlight that endothelial cells can promote expansion of progenitor populations and suppress premature ductal differentiation during SMG development.

Angiocrine factors facilitating jaw and cartilage morphogenesis

During embryonic development, VEGF is strongly expressed in the neural crest derived mesenchyme surrounding Meckel's cartilage (Wiszniak et al., 2015). Genetic ablation of *VEGF* from cranial neural crest cells led to cranial hypoplasia, cleft palate, maxillary bone defects and an abnormal bow shaped mandible (Wiszniak et al., 2015). In these conditional mutants, neural crest cell specification and migration into the first pharyngeal arch was not altered excluding the possibility of VEGF directly influencing early NCC development (Wiszniak et al., 2015). *VEGF* deletion perturbed chondrogenesis and led to the formation of a dysmorphic Meckel's cartilage which failed to acquire its normal arrowhead morphology. Persistence of this abnormal phenotype between E14.5 to E17.5 confirmed defective growth of the cartilage linked to a defect in vascularisation of the first arch (Wiszniak et al., 2015). Downregulated CD31 expression confirmed reduction of micro-vessel density and loss of mandibular artery in mutant jaws. *In vitro* co-culture of arterial tissue with neural crest cell or chondrocytes confirmed that neural crest cell derived VEGF regulates blood vessels, which in turn secrete angiocrine factors to instruct chondrogenesis. A similar defect in the mandibular artery resulting in craniofacial defects was observed in the *Tie2creNrp1fl/fl* mouse, validating the instructive role of blood vessels during jaw morphogenesis (Wiszniak et al., 2015).

As an extension to this study, *invitro*/*ex-vivo* tissue explants were used to investigate specific vascular mitogens that might promote Meckel's cartilage proliferation to facilitate jaw extension. A murine chondrogenic cell line, ATDC5, was stimulated with aorta-conditioned media, which activated insulin receptor *Akt,ERK1/2* and *Stat3* (Marchant et al., 2020). RT-PCR revealed high expression of *IGF1*, minimal expression of *IGF2*, and no detectable levels of *Ins1* or *Ins2*, highlighting that IGF1 is the main angiocrine factor secreted from aortic rings (Marchant et al., 2020). In keeping with this, IGF1 was reduced in cranial neural crest specific conditional *VEGF* mutants, suggesting that the cranial blood vessels are a key source of IGF1 driving mandibular extension (Marchant et al., 2020). Genetic deletion of *IGF1* from endothelial cells resulted in a shortened Meckel's cartilage with reduced proliferative capacity while exogenous supplementation of IGF1 rescued the proliferation deficit in cultured mandibles. These findings point towards a crucial angiocrine function of IGF-1 during craniofacial cartilage development.

Angiogenic-odontogenic coupling during tooth development

VEGF is highly expressed in the developing tooth bud (Miquerol et al., 1999) and all endothelial cells in the surrounding vasculature show high immunoreactivity for *VEGFR2* (Shadad et al., 2019). Postnatally, endothelial cells at the periphery of the tooth express *VEGFR1* and *VEGFR2* concomitantly at high levels (Matsubara et al., 2022). These *Vegfr + ve* capillaries lacked smooth muscle coverage, expanded and perforated the basal layer of odontoblasts (dentin producing cells) before the onset of active

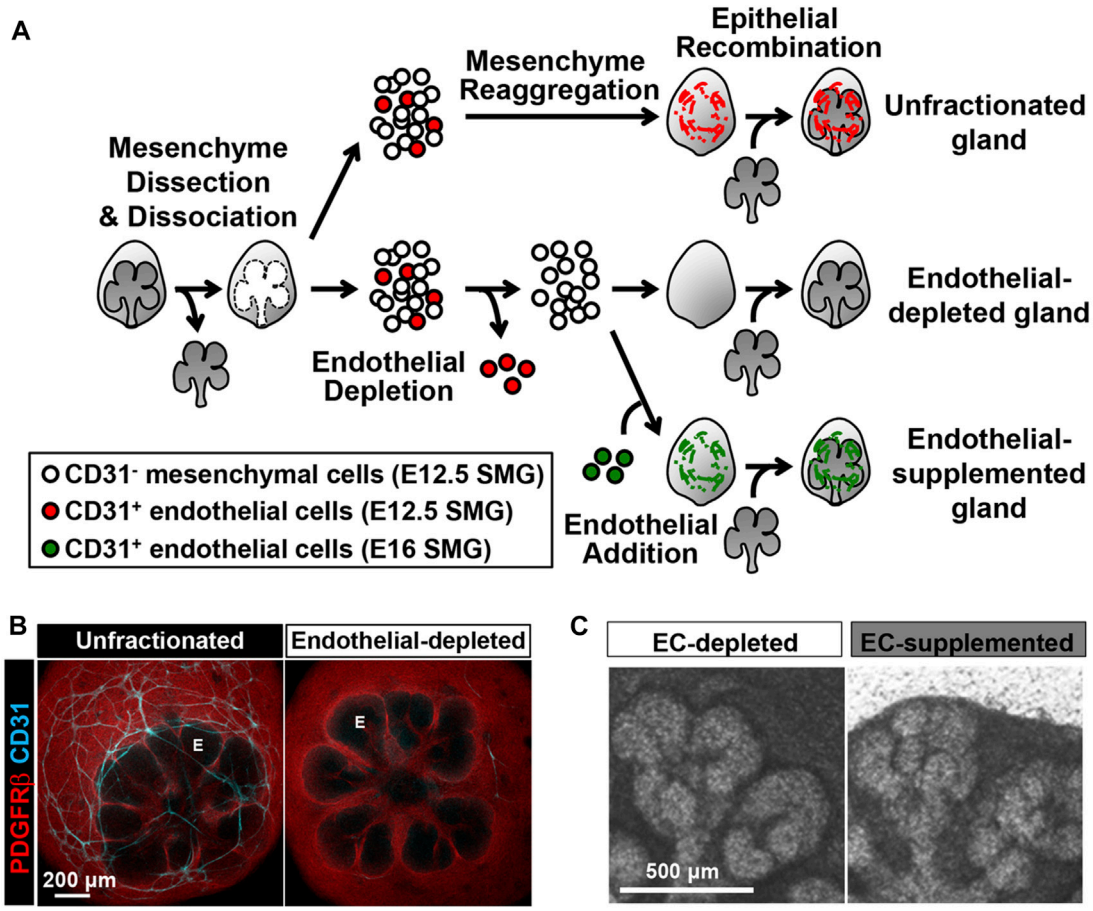

FIGURE 2
CD31 cell-dependent vasculature development promotes epithelial patterning in an SMG cell fractionation/reconstitution assay. **(A)** SMG cell fractionation/reconstitution assay schematic. Unfractionated SMG mesenchyme amenable to cell immunodepletion was generated by microdissection of the mesenchyme from the epithelium followed by enzymatic dissociation of the mesenchyme to single cells and re-aggregation of the isolated mesenchymal cell population. Re-aggregated mesenchyme was then reconstituted with an intact microdissected E13 epithelial rudiment. For endothelial cell depletion, $CD31^+$ endothelial cells were immunodepleted from fully dissociated mesenchyme cells using MACS with CD31 microbeads prior to re-aggregation of the dissociated mesenchyme and reconstitution with an intact epithelium. For endothelial cell supplementation, endothelial-depleted mesenchymal cells were mixed with MACSisolated endothelial cells collected from E16 glands, prior to re-aggregation of the mesenchyme and reconstitution with an intact epithelium. The reconstituted glands were cultured *ex vivo* for 48 h post-reconstitution **(B)** Confocal images (maximum projection images) consistently showed a change in the epithelial patterning (no marker, black) with a mesenchymal marker (PDGFRβ in red) defining the mesenchymal shape. $CD31^+$ vasculature (cyan) was present in unfractionated, but not in endothelial depleted mesenchyme. E, endbud. **(C)** Endothelial supplementation promoted epithelial branching. Taken with permission from Kwon et al., 2017.

dentinogenesis (Matsubara et al., 2022). Deletion of *VEGFR2* from endothelial cells postnatally led to loss of the vasculature by apoptosis, particularly near the odontoblast layer, and a knockon effect on the width of the odontoblasts and dentin delayed odontoblast maturation. Metabolomic analysis of *VEGFR2* null mice revealed a decrease in ATP/ADP and creatine phosphate levels, indicating a decline in the phosphate pathway, highlighting a potential systemic effect on the teeth. Interestingly, the peripheral endothelial cells were shown to express *TGFβ1, Ptn* and *Jag2*, all of which are known to promote odontoblast maturation, with addition of these factors leading to rescue of dentin markers in the conditional *VEGFR2* knockout in culture (Matsubara et al., 2022). These results highlight the importance of the vasculature in facilitating post-natal tooth development and maintaining dentin mineralization by the provision of multiple angiocrine factors.

Bidirectional neural/endothelial communication regulating oligodendrogenesis

TGFβ1 produced by endothelial cells has additionally been shown to impact development of oligodendrocyte progenitor

cells (OPCs) (Paredes et al., 2021). During embryogenesis, CNS vascularization coincides with neural progenitor cell proliferation and differentiation (Peguera et al., 2021). Notably, blood vessels develop intimately aligned to neural progenitors without migrating into neurogenic regions (Nie et al., 2010). *Angiopoeitin-1* (*Ang1*), produced by the CNS, was shown to signal through *Tie2* on endothelial cells, which in turn signalled back to the OPCs to regulate their specification (Paredes et al., 2021). *TGFβ1* expression in endothelial cells coincided with OPC specification (Hamaguchi et al., 2019). Endothelial cell derived TGFβ1 was shown to act downstream of *Ang1/Tie2* with reduced pSMAD3+Olig2+ progenitors in *Ang1 fl/fl*$^{Nestin:Cre}$ embryos, highlighting the endothelial-neural bidirectional cross talk necessary for coordinated development (Paredes et al., 2021). Notably, recombinant TGFβ1 was able to rescue neural specification in spinal cord explants from *Ang1fl/fl*$^{Nestin:Cre}$ and *Tie2 fl/fl*$^{Pdgfb:CreERT2}$ transgenic mice.

An understanding of the instructive role of the vasculature during development in multiple organs, highlights the importance of providing endothelial cells when constructing tissues and organs. It also highlights the issue with many explant culture techniques, where the vasculature is not maintained over time, resulting in loss of potentially key signals *in vitro*.

Technical advances to study the role of endothelial cells

In order to understand the instructive signals provided by cranial endothelial cells further, various hurdles need to be overcome. We need to be able to identify different subpopulations of endothelial cells to understand tissue specific roles. We need to be able to isolate tissue-specific endothelial cells to investigate the effects of depletion and augmentation *in vivo* and *in vitro*. We need to understand the cross talk between cranial organs and endothelial cells, and be able to track endothelial cells *in vivo* to understand dynamic tissue relationships. Luckily new culture techniques, new biomaterials, imaging techniques, sorting techniques, transcriptomics, and the use of transgenic animals, all make these areas a reality.

Identifying endothelial subpopulations

Endothelial cells can be identified by cell markers such as CD31, CD34, endo-mucin and ib4 (Goncharov et al., 2017). However, endothelial cells exhibit heterogeneity and express unique transcriptional signatures with different properties depending on their location (McCarron et al., 2019). The level of Notch activation, for example, can regulate their proliferation state (Chesnais et al., 2022). With this in mind it is important to understand tissue specific roles and contexts for endothelial cells. An excellent understanding of endothelial cell heterogeneity during different developmental timepoints and in different developing tissues can be achieved through single cell RNA sequencing. Using this method, a unique endothelial subtype was identified in the tooth specialised for dentinogenesis (Matsubara et al., 2022). Interestingly, in the cardiac field, developing endothelial cells initially segregated by lineage but later by tissue localisation, with adult endothelial cells being more homogeneous with respect to lineage and location (Phansalkar et al., 2021). Drastic changes in retinal endothelial gene expression were also observed during postnatal development, between P6 and P10 (Zarkada et al., 2021). These changes were attributed to EC maturation, arterial specification, proliferation and blood-retina barrier formation (Zarkada et al., 2021). scRNA-seq analysis identified two distinct cell clusters (D-Tip and S-Tip) guiding retinal vascularisation and expressing known tip cell markers such as *Mcam, Chst1, Nid2* and *Rhoc*. Several markers were identified to differentiate between both tip cell types, however D-Tip cells displayed higher ECM genes but lower TCA cycle and glycolysis scores as compared to S-Tip cells, indicating different ECM and metabolic need (Zarkada et al., 2021). Notably, D-Tip cells displayed higher TGFb signalling scores and genetic ablation of *TGFb receptor* using *Cdh5Cre* driver led to haemorrhagic malformations (Zarkada et al., 2021). These findings have helped in the identification of unique transcriptional signatures of D-Tip retinal endothelial cells that acquire blood retina barrier characteristics for proper retinal vascularization (Zarkada et al., 2021). Therefore, sc-RNA seq can help identify different endothelial clusters and their functions in various organs during development.

Sorting and recombining endothelial cells

Given the above heterogeneity of endothelial cells during development, it is important to be able to isolate organ-specific endothelial cells in order to investigate tissue patterning. Fluorescent activated cell sorting (FACS) offers flexibility and allows separation of multiple cell population, however, to isolate specific cells from large populations magnetic activated cell sorting (MACS) has been shown to be more advantageous (Liao et al., 2016). Kwon et al. (2017) utilized MACS and gland reconstitution techniques to investigate perfusion independent roles of endothelial cells during salivary gland morphogenesis (Figure 2). For isolation of CD31+ve endothelial cells, primary mesenchymal cells from glands at key stages were suspended with mouse CD31 microbeads for immunomagnetic separation (Kwon et al., 2017). This technique allowed stage and tissue specific endothelial cells to be isolated in order to investigate the impact of endothelial cells on gland architecture (Kwon et al., 2017).

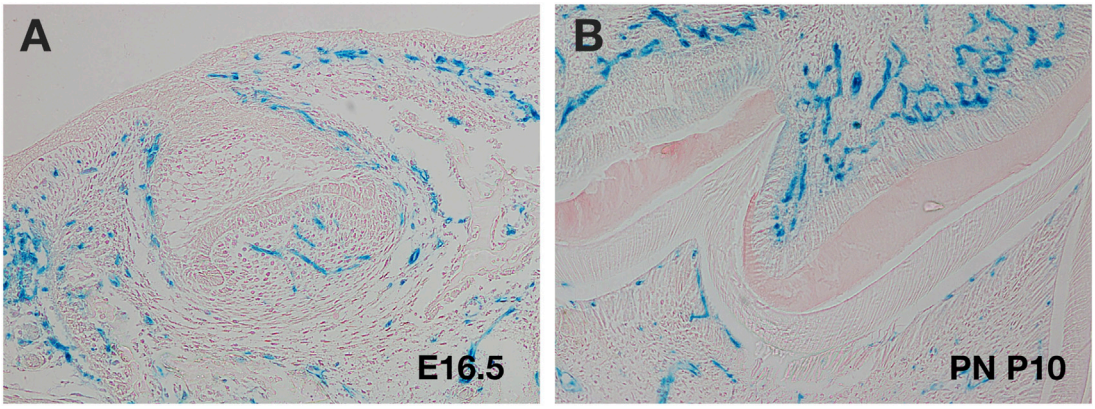

FIGURE 3
Use of *Mesp1cre* transgenics to follow cranial endothelial cells. **(A,B)** Murine molar tooth in *Mesp1creLacZ* mouse (blue cells). **(A)** E16.5 late cap stage showing migration of endothelial cells into the papilla. **(B)** Postnatal (PN) day 10 M tooth showing invasion of endothelial cells on both sides of the dental hard tissue.

Tissues can be deconstructed and reconstituted with and without endothelial cells, or with additional sources of endothelial cells added (Figure 2). Such reconstitution assays are an excellent experimental technique to study perfusion independent effect of endothelial cells and have been successfully carried out to understand the role of endothelial cells during salivary gland development (Kwon et al., 2017). Additionally, these reconstitution techniques can be adapted to combine endothelial cells from different tissues and different stages in order to understand how stage of differentiation and tissue specific signatures impact the vascular-tissue crosstalk (Figure 2).

In addition to reconstituted explants, organoids provide an excellent way to understanding cell behaviour and recapitulating development taking a reductionist approach. Organoids created from organ-specific cells can be cultured with and without endothelial cells to answer questions about morphogenesis and differentiation. This method has been used to study the impact of endothelial cells on mammary gland organoids, where the culture system allowed epithelial branching to recapitulate many aspects of mammary gland development (Wang et al., 2021).

Imaging cranial endothelial cells *in vivo* and in culture

Several transgenic mice have been utilised to label endothelial cell populations during different developmental stages (Payne et al., 2018). In the neural crest derived parts of the head (which include the facial region and front of the calvaria), the only mesodermal components are the muscles and endothelial cells (Yoshida et al., 2008). *Mesp1cre* reporter mice, which label the mesoderm, are therefore particularly useful to follow the development of the cranial vasculature. These mice have been used to study the contribution of endothelial cells to developing cranial tissue over time, with tooth germ explant cultures used to follow migration of endothelial cells into the dental papilla (Rothova et al., 2011) (Figure 3). Additionally, *Vegfr* reporter lines, have been used to follow the contribution of endothelial cells to different tissues, allowing high resolution of endothelial cells structure to visualise structures such as filopodia (Matsubara et al., 2022). Such labelling techniques, combined with the ability to image at high resolution with light sheet microscopy, means we can now trace endothelial cell movement, and follow the process of migration and remodelling *in situ* in 3 and 4D (Prahst et al., 2020).

Making vascular scaffolds to enhance development and repair

Several attempts have been made to tissue engineer vascular scaffolds to allow angiogenesis and vasculogenesis *in vitro* and *invitro* studies. Techniques such as lyophilization, electrospinning, decellularization and 3D bioprinting are frequently used in vascular tissue engineering. To incorporate beneficial properties of natural materials researchers have fabricated scaffolds with fibronectin, fibrin, elastin, Matrigel, collagen loaded with cells and reported vascular tissue formation (Cooper and Sefton, 2011; Yang et al., 2020). Collagen1/fibronectin gel implants seeded with endothelial cells have facilitated capillary formation and vascular network assembly in mice (Cooper and Sefton, 2011). Some cell types, such as adipose stromal cells have been shown to release signals to encourage angiogenesis (Rehman et al., 2004). However, in the presence of a nanostructured collagen-based scaffold the release of angiogenic factors, such as VEGF, was reduced in human

adipose-derived stem cells as they underwent differentiation (Borgese et al., 2020). There is therefore a need to create scaffolds that enhance not hamper angiogenesis.

To overcome degradation problems associated with natural polymers, several synthetic materials such as hydrogel based polymers, poly (acrylonitrile-co-methyl-acrylate (PAN-MA) polyglycolic acid (PGA), poly-L-lactic acid (PLLA), polyhydroxyalkanoates (PHA's) and poly ethylene glycol (PEG) have been used in scaffold fabrication for tissue vascularization (Wang et al., 2022).

Scaffolds that encourage angiogenesis have been investigated in the context of dental stem cells. Dental stem cells have been extensively researched due to their ease of accessibility and the availability of multiple sources in the oral cavity providing a promising source of cells for bone and dental regeneration (Cappare et al., 2020). Co-cultures of periodontal ligament stem cells and umbilical cord endothelial cells have been used to prevascularise scaffolds to promote osteogenic differentiation (Zhao et al., 2021). Such scaffolds can then be combined with other techniques to encourage osteogenesis, such as the use of low-level laser irradiation (Ballini et al., 2015). Prevascularisation can reduce the time-period when implanted scaffolds are avascular, and thereby reduce the time when cells are subject to hypoxic conditions. However, whether such prevascularised scaffolds using non-tissue specific endothelial cells can provide the correct instructive signals as highlighted above, is yet to be determined. Interestingly, dental pulp stem cells (DPSCs) can also be induced to differentiate into endothelial cells, by culture in gel moulds (Sasaki et al., 2020). These DPSC endothelial cells can then support pulp-like tissue regeneration (Katata et al., 2021). DPSCs are neural crest derived while endothelial cells are mesodermal, emphasising the plasticity of the neural crest in being able to form a wide variety of tissue types. These studies highlight the benefits and issues associated with tissue engineered vascular scaffolds, but overall, such scaffolds have great potential to lead to novel regenerative therapeutic solutions.

Conclusion

In this review, we have discussed the origin of cranial endothelial cells and highlighted key signalling molecules and other cell types that influence their migration into the craniofacial region. Once the endothelial cells have arrived, they not only provide a source of nutrients and waste removal, but actively contribute to the development of cranial organs by provision of angiocrine factors. In the head these signals have been identified so far as IGFs and Tgfbs. Tgfb1 has been shown to play a key instructive role in both the tooth and the brain, highlighting that some of these signals may not be tissue specific but have general functions in the control of differentiation. Instructions from the vasculature are also required for tissue engineering strategies to encourage repair and regeneration of cranial tissue. In keeping with this need, new tissue engineering strategies are being developed to encourage vascularisation of cranial tissue, either through host tissue recruitment or pre-vascularisation of engineered tissue (Li et al., 2022). For enhanced repair and to simulate regeneration, there is much to be learn from understanding the expanding role of endothelial cells in cranial development.

Author contributions

HA was responsible for writing the manuscript draft and creation of figures. AT helped shape the review and contributed to the final writing. Both authors contributed to the manuscript discussion.

Conflict of interest

The authors declare that the research was conducted in the absence of any commercial or financial relationships that could be construed as a potential conflict of interest.

Publisher's note

References

Adams, R. H., Diella, F., Hennig, S., Helmbacher, F., Deutsch, U., and Klein, R. (2001). The cytoplasmic domain of the ligand ephrinB2 is required for vascular morphogenesis but not cranial neural crest migration. *Cell* 104, 57–69. doi:10.1016/s0092-8674(01)00191-x

Armulik, A., Genové, G., and Betsholtz, C. (2011). Pericytes: Developmental, physiological, and pathological perspectives, problems, and promises. *Dev. Cell* 21, 193–215. doi:10.1016/j.devcel.2011.07.001

Ballini, A., Mastrangelo, F., Gastaldi, G., Tettamanti, L., Bukvic, N., Cantore, S., et al. (2015). Osteogenic differentiation and gene expression of dental pulp stem cells under low-level laser irradiation: A good promise for tissue engineering. *J. Biol. Regul. Homeost. Agents* 29, 813–822.

Bates, D., Taylor, G. I., Minichiello, J., Farlie, P., Cichowitz, A., Watson, N., et al. (2003). Neurovascular congruence results from a shared patterning mechanism that utilizes Semaphorin3A and Neuropilin-1. *Dev. Biol.* 255, 77–98. doi:10.1016/s0012-1606(02)00045-3

Bergers, G., and Song, S. (2005). The role of pericytes in blood-vessel formation and maintenance. *Neuro Oncol.* 7, 452–464. doi:10.1215/s1152851705000232

Borgese, M., Barone, L., Rossi, F., Raspanti, M., Papait, R., Valdatta, L., et al. (2020). Effect of nanostructured scaffold on human adipose-derived stem cells: Outcome of *in vitro* experiments. *Nanomater. (Basel)* 10, 822. doi:10.3390/nano10091822

Capparè, P., Tetè, G., Sberna, M. T., and Panina-Bordignon, P. (2020). The emerging role of stem cells in regenerative dentistry. *Curr. Gene Ther.* 20, 259–268. doi:10.2174/1566523220999200818115803

Chen, D. Y., Sun, N. H., Chen, X., Gong, J. J., Yuan, S. T., Hu, Z. Z., et al. (2021). Endothelium-derived semaphorin 3G attenuates ischemic retinopathy by coordinating β-catenin-dependent vascular remodeling. *J. Clin. Invest.* 131, 296. doi:10.1172/JCI135296

Chesnais, F., Hue, J., Roy, E., Branco, M., Stokes, R., Pellon, A., et al. (2022). High-content image analysis to study phenotypic heterogeneity in endothelial cell monolayers. *J. Cell Sci.* 135, 104. doi:10.1242/jcs.259104

Chestnut, B., Casie Chetty, S., Koenig, A. L., and Sumanas, S. (2020). Single-cell transcriptomic analysis identifies the conversion of zebrafish Etv2-deficient vascular progenitors into skeletal muscle. *Nat. Commun.* 11, 2796. doi:10.1038/s41467-020-16515-y

Chilton, J. K., and Guthrie, S. (2003). Cranial expression of class 3 secreted semaphorins and their neuropilin receptors. *Dev. Dyn.* 228, 726–733. doi:10.1002/dvdy.10396

Chung, L., Yang, T. L., Huang, H. R., Hsu, S. M., Cheng, H. J., and Huang, P. H. (2007). Semaphorin signaling facilitates cleft formation in the developing salivary gland. *Development* 134, 2935–2945. doi:10.1242/dev.005066

Cooper, T. P., and Sefton, M. V. (2011). Fibronectin coating of collagen modules increases *in vivo* HUVEC survival and vessel formation in SCID mice. *Acta Biomater.* 7, 1072–1083. doi:10.1016/j.actbio.2010.11.008

Davis, S., Aldrich, T. H., Jones, P. F., Acheson, A., Compton, D. L., Jain, V., et al. (1996). Isolation of angiopoietin-1, a ligand for the TIE2 receptor, by secretion-trap expression cloning. *Cell* 87, 1161–1169. doi:10.1016/s0092-8674(00)81812-7

Dejana, E., Hirschi, K. K., and Simons, M. (2017). The molecular basis of endothelial cell plasticity. *Nat. Commun.* 8, 14361. doi:10.1038/ncomms14361

Eichmann, A., Corbel, C., Nataf, V., Vaigot, P., Bréant, C., and Le Douarin, N. M. (1997). Ligand-dependent development of the endothelial and hemopoietic lineages from embryonic mesodermal cells expressing vascular endothelial growth factor receptor 2. *Proc. Natl. Acad. Sci. U.S.A.* 94, 5141–5146. doi:10.1073/pnas.94.10.5141

Etchevers, H. C., Vincent, C., Le Douarin, N. M., and Couly, G. F. (2001). The cephalic neural crest provides pericytes and smooth muscle cells to all blood vessels of the face and forebrain. *Development* 128, 1059–1068. doi:10.1242/dev.128.7.1059

Evans, S. M., Yelon, D., Conlon, F. L., and Kirby, M. L. (2010). Myocardial lineage development. *Circ. Res.* 107, 1428–1444. doi:10.1161/circresaha.110.227405

Goncharov, N. V., Nadeev, A. D., Jenkins, R. O., and Avdonin, P. V. (2017). Markers and biomarkers of endothelium: When something is rotten in the state. *Oxid. Med. Cell Longev.* 2017, 9759735. doi:10.1155/2017/9759735

Gu, C., and Giraudo, E. (2013). The role of semaphorins and their receptors in vascular development and cancer. *Exp. Cell Res.* 319, 1306–1316. doi:10.1016/j.yexcr.2013.02.003

Hamaguchi, M., Muramatsu, R., Fujimura, H., Mochizuki, H., Kataoka, H., and Yamashita, T. (2019). Circulating transforming growth factor-β1 facilitates remyelination in the adult central nervous system. *Elife* 8, 41869. doi:10.7554/eLife.41869

Hiruma, T., Nakajima, Y., and Nakamura, H. (2002). Development of pharyngeal arch arteries in early mouse embryo. *J. Anat.* 201, 15–29. doi:10.1046/j.1469-7580.2002.00071.x

Hutson, M. R., and Kirby, M. L. (2007). Model systems for the study of heart development and disease. *Seminars Cell & Dev. Biol.* 18, 101–110. doi:10.1016/j.semcdb.2006.12.004

Katata, C., Sasaki, J. I., Li, A., Abe, G. L., Nör, J. E., Hayashi, M., et al. (2021). Fabrication of vascularized DPSC constructs for efficient pulp regeneration. *J. Dent. Res.* 100, 1351–1358. doi:10.1177/00220345211007427

Kwon, H. R., Nelson, D. A., DeSantis, K. A., Morrissey, J. M., and Larsen, M. (2017). Endothelial cell regulation of salivary gland epithelial patterning. *Development* 144, 211–220. doi:10.1242/dev.142497

Lewis, A. E., Hwa, J., Wang, R., Soriano, P., and Bush, J. O. (2015). Neural crest defects in ephrin-B2 mutant mice are non-autonomous and originate from defects in the vasculature. *Dev. Biol.* 406, 186–195. doi:10.1016/j.ydbio.2015.08.021

Li, P., Pashmforoush, M., and Sucov, H. M. (2012). Mesodermal retinoic acid signaling regulates endothelial cell coalescence in caudal pharyngeal arch artery vasculogenesis. *Dev. Biol.* 361, 116–124. doi:10.1016/j.ydbio.2011.10.018

Li, Y., Fraser, D., Mereness, J., Van Hove, A., Basu, S., Newman, M., et al. (2022). Tissue engineered neurovascularization strategies for craniofacial tissue regeneration. *ACS Appl. Bio Mat.* 5, 20–39. doi:10.1021/acsabm.1c00979

Liang, D., Wang, X., Mittal, A., Dhiman, S., Hou, S. Y., Degenhardt, K., et al. (2014). Mesodermal expression of integrin α5β1 regulates neural crest development and cardiovascular morphogenesis. *Dev. Biol.* 395, 232–244. doi:10.1016/j.ydbio.2014.09.014

Liao, X., Makris, M., and Luo, X. M. (2016). Fluorescence-activated cell sorting for purification of plasmacytoid dendritic cells from the mouse bone marrow. *J. Vis. Exp.*, 54641. doi:10.3791/54641

Marchant, C., Anderson, P., Schwarz, Q., and Wiszniak, S. (2020). Vessel-derived angiocrine IGF1 promotes Meckel's cartilage proliferation to drive jaw growth during embryogenesis. *Development* 147, 190488. doi:10.1242/dev.190488

Matsubara, T., Iga, T., Sugiura, Y., Kusumoto, D., Sanosaka, T., Tai-Nagara, I., et al. (2022). Coupling of angiogenesis and odontogenesis orchestrates tooth mineralization in mice. *J. Exp. Med.* 219, 1789. doi:10.1084/jem.20211789

McCarron, J. G., Wilson, C., Heathcote, H. R., Zhang, X., Buckley, C., and Lee, M. D. (2019). Heterogeneity and emergent behaviour in the vascular endothelium. *Curr. Opin. Pharmacol.* 45, 23–32. doi:10.1016/j.coph.2019.03.008

McKinney, M. C., McLennan, R., and Kulesa, P. M. (2016). Angiopoietin 2 signaling plays a critical role in neural crest cell migration. *BMC Biol.* 14, 111. doi:10.1186/s12915-016-0323-9

Milgrom-Hoffman, M., Michailovici, I., Ferrara, N., Zelzer, E., and Tzahor, E. (2014). Endothelial cells regulate neural crest and second heart field morphogenesis. *Biol. Open* 3, 679–688. doi:10.1242/bio.20148078

Miquerol, L., Gertsenstein, M., Harpal, K., Rossant, J., and Nagy, A. (1999). Multiple developmental roles of VEGF suggested by a LacZ-tagged allele. *Dev. Biol.* 212, 307–322. doi:10.1006/dbio.1999.9355

Moore, M. A. (2002). Putting the neo into neoangiogenesis. *J. Clin. Invest.* 109, 313–315. doi:10.1172/jci0214940

Murakami, M., and Simons, M. (2008). Fibroblast growth factor regulation of neovascularization. *Curr. Opin. Hematol.* 15, 215–220. doi:10.1097/moh.0b013e3282f97d98

Nie, K., Molnár, Z., and Szele, F. G. (2010). Proliferation but not migration is associated with blood vessels during development of the rostral migratory stream. *Dev. Neurosci.* 32, 163–172. doi:10.1159/000301135

Paredes, I., Vieira, J. R., Shah, B., Ramunno, C. F., Dyckow, J., Adler, H., et al. (2021). Oligodendrocyte precursor cell specification is regulated by bidirectional neural progenitor-endothelial cell crosstalk. *Nat. Neurosci.* 24, 478–488. doi:10.1038/s41593-020-00788-z

Parker, M. W., Xu, P., Guo, H. F., and Vander Kooi, C. W. (2012). Mechanism of selective VEGF-A binding by neuropilin-1 reveals a basis for specific ligand inhibition. *PLoS One* 7, e49177. doi:10.1371/journal.pone.0049177

Payne, S., De Val, S., and Neal, A. (2018). Endothelial-specific cre mouse models. *Arterioscler. Thromb. Vasc. Biol.* 38, 2550–2561. doi:10.1161/atvbaha.118.309669

Peguera, B., Segarra, M., and Acker-Palmer, A. (2021). Neurovascular crosstalk coordinates the central nervous system development. *Curr. Opin. Neurobiol.* 69, 202–213. doi:10.1016/j.conb.2021.04.005

Phansalkar, R., Krieger, J., Zhao, M., Kolluru, S. S., Jones, R. C., Quake, S. R., et al. (2021). Coronary blood vessels from distinct origins converge to equivalent states during mouse and human development. *Elife* 10, 70246. doi:10.7554/eLife.70246

Prahst, C., Ashrafzadeh, P., Mead, T., Figueiredo, A., Chang, K., Richardson, D., et al. (2020). Mouse retinal cell behaviour in space and time using light sheet fluorescence microscopy. *Elife* 9, 49779. doi:10.7554/eLife.49779

Proulx, K., Lu, A., and Sumanas, S. (2010). Cranial vasculature in zebrafish forms by angioblast cluster-derived angiogenesis. *Dev. Biol.* 348, 34–46. doi:10.1016/j.ydbio.2010.08.036

Rajendran, P., Rengarajan, T., Thangavel, J., Nishigaki, Y., Sakthisekaran, D., Sethi, G., et al. (2013). The vascular endothelium and human diseases. *Int. J. Biol. Sci.* 9, 1057–1069. doi:10.7150/ijbs.7502

Ramasamy, S. K., Kusumbe, A. P., and Adams, R. H. (2015). Regulation of tissue morphogenesis by endothelial cell-derived signals. *Trends Cell Biol.* 25, 148–157. doi:10.1016/j.tcb.2014.11.007

Rehman, J., Traktuev, D., Li, J., Merfeld-Clauss, S., Temm-Grove, C. J., Bovenkerk, J. E., et al. (2004). Secretion of angiogenic and antiapoptotic factors by human adipose stromal cells. *Circulation* 109, 1292–1298. doi:10.1161/01.cir.0000121425.42966.f1

Rocha, S. F., and Adams, R. H. (2009). Molecular differentiation and specialization of vascular beds. *Angiogenesis* 12, 139–147. doi:10.1007/s10456-009-9132-x

Rothova, M., Feng, J., Sharpe, P. T., Peterkova, R., and Tucker, A. S. (2011). Contribution of mesoderm to the developing dental papilla. *Int. J. Dev. Biol.* 55, 59–64. doi:10.1387/ijdb.103083mr

Sandoo, A., Veldhuijzen van Zanten, J. J., Metsios, G. S., Carroll, D., and Kitas, G. D. (2010). The endothelium and its role in regulating vascular tone. *Open Cardiovasc Med. J.* 4, 302–312. doi:10.2174/1874192401004010302

Sasaki, J. I., Zhang, Z., Oh, M., Pobocik, A. M., Imazato, S., Shi, S., et al. (2020). VE-cadherin and anastomosis of blood vessels formed by dental stem cells. *J. Dent. Res.* 99, 437–445. doi:10.1177/0022034520902458

Schmeisser, A., and Strasser, R. H. (2002). Phenotypic overlap between hematopoietic cells with suggested angioblastic potential and vascular endothelial cells. *J. hematotherapy stem Cell Res.* 11, 69–79. doi:10.1089/152581602753448540

Shadad, O., Chaulagain, R., Luukko, K., and Kettunen, P. (2019). Establishment of tooth blood supply and innervation is developmentally regulated and takes place through differential patterning processes. *J. Anat.* 234, 465–479. doi:10.1111/joa.12950

Shibuya, M. (2011). Vascular endothelial growth factor (VEGF) and its receptor (VEGFR) signaling in angiogenesis: A crucial target for anti- and pro-angiogenic therapies. *Genes & Cancer* 2, 1097–1105. doi:10.1177/1947601911423031

Suri, C., Jones, P. F., Patan, S., Bartunkova, S., Maisonpierre, P. C., Davis, S., et al. (1996). Requisite role of angiopoietin-1, a ligand for the TIE2 receptor, during embryonic angiogenesis. *Cell* 87, 1171–1180. doi:10.1016/s0092-8674(00)81813-9

Svandova, E., Anthwal, N., Tucker, A. S., and Matalova, E. (2020). Diverse fate of an enigmatic structure: 200 Years of meckel's cartilage. *Front. Cell Dev. Biol.* 8, 821. doi:10.3389/fcell.2020.00821

Tan, C., Lu, N. N., Wang, C. K., Chen, D. Y., Sun, N. H., Lyu, H., et al. (2019). Endothelium-derived semaphorin 3G regulates hippocampal synaptic structure and plasticity via neuropilin-2/PlexinA4. *Neuron* 101, 920–937. doi:10.1016/j.neuron.2018.12.036

Trainor, P. A. (2010). Craniofacial birth defects: The role of neural crest cells in the etiology and pathogenesis of Treacher Collins syndrome and the potential for prevention. *Am. J. Med. Genet.* 152A, 2984–2994. doi:10.1002/ajmg.a.33454

Verzi, M. P., McCulley, D. J., De Val, S., Dodou, E., and Black, B. L. (2005). The right ventricle, outflow tract, and ventricular septum comprise a restricted expression domain within the secondary/anterior heart field. *Dev. Biol.* 287, 134–145. doi:10.1016/j.ydbio.2005.08.041

Wang, X., Chen, D., Chen, K., Jubran, A., Ramirez, A., and Astrof, S. (2017). Endothelium in the pharyngeal arches 3, 4 and 6 is derived from the second heart field. *Dev. Biol.* 421, 108–117. doi:10.1016/j.ydbio.2016.12.010

Wang, J., Song, W., Yang, R., Li, C., Wu, T., Dong, X. B., et al. (2021). Endothelial Wnts control mammary epithelial patterning via fibroblast signaling. *Cell Rep.* 34, 108897. doi:10.1016/j.celrep.2021.108897

Wang, Y., Kankala, R. K., Ou, C., Chen, A., and Yang, Z. (2022). Advances in hydrogel-based vascularized tissues for tissue repair and drug screening. *Bioact. Mater.* 9, 198–220. doi:10.1016/j.bioactmat.2021.07.005

Wendling, O., Dennefeld, C., Chambon, P., and Mark, M. (2000). Retinoid signaling is essential for patterning the endoderm of the third and fourth pharyngeal arches. *Development* 127, 1553–1562. doi:10.1242/dev.127.8.1553

Wiszniak, S., Mackenzie, F. E., Anderson, P., Kabbara, S., Ruhrberg, C., and Schwarz, Q. (2015). Neural crest cell-derived VEGF promotes embryonic jaw extension. *Proc. Natl. Acad. Sci. U.S.A.* 112, 6086–6091. doi:10.1073/pnas.1419368112

Yang, G., Mahadik, B., Choi, J. Y., and Fisher, J. P. (2020). Vascularization in tissue engineering: Fundamentals and state-of-art. *Prog. Biomed. Eng. (Bristol)* 2, 5637. doi:10.1088/2516-1091/ab5637

Yoshida, T., Vivatbutsiri, P., Morriss-Kay, G., Saga, Y., and Iseki, S. (2008). Cell lineage in mammalian craniofacial mesenchyme. *Mech. Dev.* 125, 797–808. doi:10.1016/j.mod.2008.06.007

Zarkada, G., Howard, J. P., Xiao, X., Park, H., Bizou, M., Leclerc, S., et al. (2021). Specialized endothelial tip cells guide neuroretina vascularization and blood-retina-barrier formation. *Dev. Cell* 56, 2237–2251. e2236. doi:10.1016/j.devcel.2021.06.021

Zhao, Z., Sun, Y., Qiao, Q., Zhang, L., Xie, X., Weir, M. D., et al. (2021). Human periodontal ligament stem cell and umbilical vein endothelial cell Co-culture to prevascularize scaffolds for angiogenic and osteogenic tissue engineering. *Int. J. Mol. Sci.* 22, 12363. doi:10.3390/ijms222212363

frontiers | Frontiers in Bioengineering and Biotechnology

TYPE Brief Research Report
PUBLISHED 01 September 2022
DOI 10.3389/fbioe.2022.888431

OPEN ACCESS

EDITED BY
Jose Manuel Garcia-Aznar,
University of Zaragoza, Spain

REVIEWED BY
Alejandra Gonzalez Loyola,
University of Lausanne, Switzerland
William J. Polacheck,
University of North Carolina at Chapel Hill, United States

*CORRESPONDENCE
Dinesh K. Ahirwar,
dineshahirwar@iitj.ac.in
Ramesh K. Ganju,
ramesh.ganju@osumc.edu
Jonathan W. Song,
song.1069@osu.edu

†These authors have contributed equally to this work

SPECIALTY SECTION
This article was submitted to Tissue Engineering and Regenerative Medicine, a section of the journal Frontiers in Bioengineering and Biotechnology

RECEIVED 02 March 2022
ACCEPTED 13 July 2022
PUBLISHED 01 September 2022

CITATION
Holter JC, Chang C-W, Avendano A, Garg AA, Verma AK, Charan M, Ahirwar DK, Ganju RK and Song JW (2022), Fibroblast-derived CXCL12 increases vascular permeability in a 3-D microfluidic model independent of extracellular matrix contractility.
Front. Bioeng. Biotechnol. 10:888431.
doi: 10.3389/fbioe.2022.888431

Fibroblast-derived CXCL12 increases vascular permeability in a 3-D microfluidic model independent of extracellular matrix contractility

Jacob C. Holter[1†], Chia-Wen Chang[2†], Alex Avendano[1†], Ayush A. Garg[3], Ajeet K. Verma[4,5], Manish Charan[4], Dinesh K. Ahirwar[4,6]*, Ramesh K. Ganju[4,5]* and Jonathan W. Song[3,5]*

[1]Department of Biomedical Engineering, The Ohio State University, Columbus, OH, United States, [2]Department of Chemical and Biomolecular Engineering, The Ohio State University, Columbus, OH, United States, [3]Department of Mechanical and Aerospace Engineering, The Ohio State University, Columbus, OH, United States, [4]Department of Pathology, College of Medicine, The Ohio State University, Columbus, OH, United States, [5]Comprehensive Cancer Center, The Ohio State University, Columbus, OH, United States, [6]Department of Bioscience and Bioengineering, Indian Institute of Technology, Jodhpur, RJ, India

Cancer-associated fibroblasts (CAFs) play an active role in remodeling the local tumor stroma to support tumor initiation, growth, invasion, metastasis, and therapeutic resistance. The CAF-secreted chemokine, CXCL12, has been directly implicated in the tumorigenic progression of carcinomas, including breast cancer. Using a 3-D *in vitro* microfluidic-based microtissue model, we demonstrate that stromal CXCL12 secreted by CAFs has a potent effect on increasing the vascular permeability of local blood microvessel analogues through paracrine signaling. Moreover, genetic deletion of fibroblast-specific CXCL12 significantly reduced vessel permeability compared to CXCL12 secreting CAFs within the recapitulated tumor microenvironment (TME). We suspected that fibroblast-mediated extracellular matrix (ECM) remodeling and contraction indirectly accounted for this change in vessel permeability. To this end, we investigated the autocrine effects of CXCL12 on fibroblast contractility and determined that antagonistic blocking of CXCL12 did not have a substantial effect on ECM contraction. Our findings indicate that fibroblast-secreted CXCL12 has a significant role in promoting a leakier endothelium hospitable to angiogenesis and tumor cell intravasation; however, autocrine CXCL12 is not the primary upstream trigger of CAF contractility.

KEYWORDS

microfluidics, tumor microenvironment, cancer-associated fibroblast, paracrine signaling, collagen hydrogel, microtissue analogue

Introduction

The emerging role of the tumor microenvironment (TME) on cancer development has become increasingly evident over the past two decades, highlighted within the hallmarks of cancer (Hanahan, 2022). Along with cancer cells, the host of nonmalignant cellular and noncellular components that arise during the course of tumorigenesis results in a local tumor niche, or TME (Valkenburg et al., 2018). These non-cancer-cell constituents of the tumor stroma include cancer-associated fibroblasts (CAFs), immune cells, endothelial cells (ECs), pericytes, and adipocytes, as well as extracellular matrix (ECM) components, among others (Valkenburg et al., 2018; Jin and Jin, 2020). Increasing evidence shows that a set of these cell types are co-opted by cancer cells and cancer stem cells (CSCs) contributing to tumor initiation, growth, invasion, metastasis, and therapeutic resistance (Jin and Jin, 2020). As a result, stromal cells are widely believed to contribute to the initiation of epithelial carcinomas and subsequent tumor progression (Wiseman and Werb, 2002; Orimo et al., 2005). Specific to breast cancer, clinical evidence and various neoplastic models have linked mammary stromal cells to tumorigenesis (Finak et al., 2008; Trimboli et al., 2009; Maller et al., 2021). Despite these discoveries implicating the tumor stroma in carcinogenesis, a robust understanding of the cell signaling pathways between various components of the TME remains to be seen. Therefore, elucidating the signaling that underpins stromal-epithelial crosstalk and communication amongst stromal cells is critical to progress the translation of TME-based anticancer therapies and address the broad clinical challenge of metastasis.

Fibroblasts are found in various carcinomas and are often the most abundant cell population of the tumor stroma (Hanahan and Weinberg, 2011; Kalluri, 2016). While normal fibroblasts have multiple physiological functions—from the connective tissue-producing role of secreting fibrous collagens to the recruitment of immune cells and regulation of inflammation—CAFs play an active role in reshaping the TME to support tumor cell survival and proliferation (Houthuijzen and Jonkers, 2018). In breast cancer, CAFs can originate from a variety of sources, including cancer stem cells (Nair et al., 2017) and reprogrammed native fibroblastic cells (Kojima et al., 2020); however, independent of their origin, CAFs are classified by their activated state resembling myofibroblasts during inflammation and wound healing (Shiga et al., 2015). The activated state of CAFs leads to the excessive deposition of various ECM proteins, e.g., type I collagen, thereby implicating CAFs in the creation of a desmoplastic stroma common in epithelial tumors, including breast cancer (Orimo et al., 2005). In addition to fibrosis and increased matrix stiffness (Mouw et al., 2014), CAFs have been demonstrated to induce cancer proliferation and enhance migration, invasion, and distant metastasis in breast cancer (Houthuijzen and Jonkers, 2018).

One of the more recent strategies to combat the effects of CAFs on tumorigenesis has been to target CAF-secreted growth factors (Park et al., 2014) and chemokines, e.g., stromal cell-derived factor 1 (SDF-1), also known as CXCL12 (Chen et al., 2019). The success of this approach relies heavily on a comprehensive understanding of the signaling network between CAFs and other cellular constituents of the TME. In 2005, Orimo et al. first showed that CAFs play a central role in promoting the proliferation of breast cancer cells through their ability to secrete CXCL12 (Orimo et al., 2005). CXCL12 acts directly on mammary carcinoma cells through the cognate receptor CXCR4 to stimulate tumor growth (Müller et al., 2001; Littlepage et al., 2005; Luker et al., 2012). Additionally, CAFs were able to induce angiogenesis through CXCL12-mediated recruitment of endothelial progenitor cells (EPCs) (Orimo et al., 2005). As an extension of this pioneering work, continued efforts have been made to characterize the regulatory role of fibroblast-derived CXCL12 within the TME and its mechanistic effect on metastasis (Ahirwar et al., 2018). Herein, we demonstrate in an *in vitro* microfluidic model that stromal CXCL12 secreted by CAFs enhances vascular permeability. These findings suggest that CXCL12 secreted by CAFs promotes metastasis through the expansion of a leaky tumor vasculature. Furthermore, we evaluate the autocrine role of CXCL12 on CAFs' ability to contract and remodel the ECM. These findings collectively bolster the understanding of fibroblast-derived CXCL12 to facilitate tumor angiogenesis and intravasation, ultimately leading to metastasis.

Materials and methods

Ethics statement

Usage of mice and experimentation with their harvested cells was approved by the Institutional Animal Care and Use Committee (IACUC) at the Ohio State University.

Cell culture

Mouse embryonic endothelial cells (MEECs) were a generous gift from Dr. Nam Y. Lee of the Ohio State University (OSU). MEECs were cultured in endothelial cell media with an endothelial cell supplement kit, including 5% fetal bovine serum (FBS), vascular endothelial growth factor (VEGF) and heparin (Cell Biologics). Endothelial cells were cultured in T-75 flasks in a humidified incubator at 37°C and 5% CO_2 with media exchange every 2 days. Cell passage numbers of 5–10 were used for the study. MEECs were harvested from flasks using 0.05%

Trypsin-EDTA (Invitrogen), centrifuged, and resuspended in cell media at a concentration of ~7×10^6 cells ml^{-1}. MEECs were then pipetted into both lateral microchannels of the device and allowed to adhere within the cell culture incubator overnight at 37°C to obtain an endothelial monolayer. Endothelial media was exchanged daily after seeding to promote healthy cell growth. For experimental conditions with conditioned media, cells were permitted to be cultured within the device for 1 day prior to the introduction of conditioned media to stabilize the microvessel analogues and ensure treatment arms did not influence initial cell attachment.

Normal mouse mammary gland fibroblasts (MMFs) were harvested from the mammary glands of either Cxcl12 floxed control ($Cxcl12^{f/f}$) mice to obtain $CXCL12^{f/f}$ fibroblasts (also denoted as "f/f" fibroblasts), or from fibroblast-specific conditional knockout ($Cxcl12^{\Delta/\Delta}$) mice to obtain $CXCL12^{\Delta/\Delta}$ fibroblasts (also denoted as "Δ/Δ" fibroblasts), as previously described (Ahirwar et al., 2018). Briefly, with respect to the knockout allele, the Cxcl12 gene was flanked by LoxP sites. To delete the LoxP-flanked Cxcl12 gene, we introduced Cre recombinase by breeding Cxcl12 transgenic mice with FSP-Cre expressing mice. The Cre recombinase expression in FSP-Cre mice is driven by fibroblast-specific protein (FSP) promoter. As FSP is specifically expressed by fibroblasts, the Cxcl12 gene in double transgenic mice (Cxcl12 f/f; FSP-Cre or $Cxcl12^{\Delta/\Delta}$) will specifically be deleted in the fibroblasts. Normal mammary glands harvested from 8-week-old FVB female mice were minced and digested with a cocktail of collagenase IV and hyaluronidase in the presence of hydrocortisone, insulin, and antibiotics penicillin and streptomycin in a 5% CO_2 incubator for 2 h at 37°C. Digested tissue was resuspended in a medium with 10% FBS, and supernatants were subjected four more times to gravity sedimentation for 12–15 min to obtain isolated MMFs.

To acquire cancer-associated fibroblasts (CAFs), the mouse mammary tumor virus (MMTV) promoter Polyoma middle T antigen (PyT) (Jackson laboratories) was intercrossed with either Cxcl12 floxed control ($Cxcl12^{f/f}$) mice to generate $Cxcl12^{f/f}$; PyT mice, or with fibroblast-specific conditional knockout ($Cxcl12^{\Delta/\Delta}$) mice to generate $Cxcl12^{\Delta/\Delta}$; PyT mice (Ahirwar et al., 2018). The tumor-bearing mammary glands of $Cxcl12^{f/f}$; PyT mice were used to harvest $CXCL12^{f/f}$; PyT cancer-associated fibroblasts (also denoted as "f/f; PyT" CAFs), while the tumor-bearing mammary glands of $Cxcl12^{\Delta/\Delta}$; PyT mice were used to harvest $CXCL12^{\Delta/\Delta}$; PyT cancer-associated fibroblasts (also denoted as "Δ/Δ; PyT" CAFs). The PyT tumors of 8-week-old FVB female mice were similarly digested with the cocktail of collagenase IV and hyaluronidase for 30 min under incubation, and CAFs were isolated by gravity sedimentation, as described above. CAFs were further enriched by differential trypsinization two times. After isolation, MMFs and CAFs were maintained in DMEM/F-12 media supplemented with insulin, hydrocortisone, epidermal growth factor, and 10% FBS (Sigma Aldrich). Fibroblast media was exchanged every 2 days during culture leading up to seeding. Fibroblasts were used in experiments at low passage numbers (2–4) to minimize potential cellular changes associated with extended culture of harvested primary cells.

Immunofluorescence

Isolated CAFs were seeded into 4-well chamber slides (Thermo Scientific) at a concentration of 1.0×10^5 cells/ml. After 24 h, cells were fixed with 4% (w/v) paraformaldehyde (PFA, Sigma-Aldrich) for 15 min at room temperature (RT), and subsequently permeabilized with 0.1% Triton X-100 (Sigma-Aldrich) for 5 min at RT. After washing with 1X PBS, cells were blocked with 5% BSA in 1X PBS for 1 h at RT. Subsequently, primary antibodies were added to wells and incubated overnight at 4°C: CXCL12 antibody at 12.5 μg/ml concentration (R&D Systems, MAB350), PDGFR-α antibody at 1:1000 dilution (CST, 3174), and Nidogen-2 at 1:400 dilution (Abcam, ab14513). After aspiration and extensive washing with 1X PBS, secondary antibodies were added and incubated for 1 h at RT: AF-594 anti-rabbit and AF-488 anti-mouse (1:1000 dilution, Invitrogen). The slide was washed with 1X PBS, and the coverslip was mounted with DAPI-containing mounting medium (Vector Laboratories). The slide was stored at 4°C until imaging. Fluorescence images were acquired on a Nikon A1R confocal microscope: representative images were taken at ×40 magnification, and quantification of PDGFR-α and Nidogen-2 was performed on ×10 images. For quantification, mean pixel intensity was quantified by NIH ImageJ software and normalized by dividing by total cell count ($n \geq 150$ cells) to obtain intensity per cell in arbitrary units (AU).

Western blotting

Western blot analysis was performed as previously described (Anand et al., 2013; Garg et al., 2019; Charan et al., 2020). Briefly, the cells were lysed using RIPA buffer (Thermo Scientific) supplemented with proteases and phosphatase inhibitors. Total protein was estimated with Bradford protein assay, per manufacturer's instructions (Bio-Rad). Subsequently, 40 μg of protein was loaded on 4–12% gradient SDS–polyacrylamide gel (Invitrogen) under reducing conditions, transferred to nitrocellulose membrane, and blocked with 5% non-fat dry milk (NFDM) in Tris-buffered saline with 0.1% Tween 20 (TBST). The membrane was incubated overnight with anti-CXCR4 primary antibody (Santa Cruz, sc-53534) at a 1:200 dilution, washed 3 times with TBST, and incubated for 1 h at RT with horseradish peroxidase-conjugated secondary antibody (1:10,000) in blocking buffer. Membranes were washed and developed by using an enhanced chemiluminescence (ECL) system (Thermo Scientific) and

immediately exposed to autoradiography film (GeneMate). Δ/Δ; PyT CAFs from Cxcl12$^{\Delta/\Delta}$; PyT mice were unavailable for the Western blot.

Microfluidic microtissue analogue

The microtissue analogue system, was fabricated using soft lithography of poly (dimethylsiloxane) (PDMS) as previously reported (Chang et al., 2020). This configuration enabled us to create laterally adjacent stromal and endothelial compartments to mimic the *in vivo* conditions for fibroblast and EC interactions within the tumor stroma. Briefly, the base and curing agent of PDMS were mixed at a ratio of 10:1, respectively, and poured onto a patterned silicon wafer. After curing for at least 2 h at 65°C, the PDMS layer was subsequently bonded to a glass slide by oxygen plasma treatment. Type I collagen (Corning) sourced from rat tail tendon was pipetted into the central ECM compartment of the device at a concentration of 6 mg ml^{-1} and incubated for at least 30 min at 37°C to polymerize. For experimental co-culture conditions, CAFs were added to the collagen matrix at a density of 6×10^3 cells per µl prior to polymerization and pipetted into the stromal compartment of the device in a similar fashion. Lateral microchannels were coated with fibronectin (100 mg ml^{-1}) at least 30 min prior to cell seeding to improve cellular attachment and biocompatibility of the device. Upon seeding, mouse embryonic endothelial cells (MEECs) lined the lateral channels to form *in vitro* microvessel analogues within a microtissue system.

Apparent vascular permeability

Collagen hydrogel was added to the central ECM compartment of the device at a concentration of 6 mg ml^{-1} to minimize spontaneous sprouting. Previously, we confirmed using confocal microscopy that in the microtissue system endothelial cells form a confluent monolayer at the endothelial cell/ECM interface (Chang et al., 2020). MEECs were cultured in the microtissue system for 3 days prior to permeability measurements: 24 h with control media and the subsequent 48 h with the respective media, conditioned or otherwise. Endothelial media was added to T-75 culture flasks with CAFs at approximately 90% confluency and incubated for 24 h to generate conditioned media. Conditioned media was freshly prepared for each experimental run. A volume of 2 µl of 70 kDa Texas-Red-conjugated Dextran was passively loaded into one of the MEEC-lined microchannels as a fluorescent tracer at a concentration of 0.05 mM. Dye diffusion across the interface of the vessel microchannel into the collagen ECM channel was detected using time-lapse epifluorescent microscopy (TS-100, Nikon) over the course of 3 hours under temperature-controlled incubator conditions. Changes in fluorescence intensity within the adjacent ECM region were quantified using NIH ImageJ software to define apparent vascular permeability. Apparent permeability, P_{App}, was calculated using Eq. 1:

$$P_{App} = \left(\frac{1}{\Delta I}\right) \times \left(\frac{dI}{dt}\right) \times \left(\frac{V_v}{S_v}\right) \quad (1)$$

where ΔI is the initial source intensity in the vessel channel immediately proximate to each aperture, dI/dt is the change in intensity over time in the adjacent ECM region, and V_v/S_v is the volume-to-surface area ratio of the dye-loading microvessel analogue channel (Chang et al., 2020).

Collagen gel contraction assay

The contractility of fibroblasts was measured to quantify the physical remodeling of fibroblast-laden collagen gels (Ren et al., 2019; Zhang et al., 2019). Collagen gels were prepared by adding fibroblasts suspended in cell media at a density of 1.0×10^6 cells/ml to a type I collagen solution (Corning) at a concentration of 1 mg/ml. A total volume of 500 µl was cast into each well of a 24-well plate with four replicates per condition. Collagen gels polymerized for 30 min at 37°C and 5% CO_2 in a humidified incubator. Following polymerization, an additional 500 µl of fibroblast media was added to each well. AMD3100 (Tocris) was reconstituted to a concentration of 10 µM in fibroblast media to passively diffuse into collagen hydrogels for experimental conditions involving the CXCR4-blocking agent. Images of gels were taken with a stereo microscope (Nikon, SMZ18) across 3 days. The surface area of the gels was quantified by NIH ImageJ software at each time point. The percent contraction was determined by Eq. 2:

$$Contraction\ percentage\ (\%) = \frac{A_{well} - A_{gel}}{A_{well}} \times 100 \quad (2)$$

where A_{well} and A_{gel} are the surface area of the well and fibroblast-embedded collagen gel, respectively.

Statistical analysis

Each experimental condition was conducted at least in triplicate. Reported values represent the mean ± standard deviation. Ordinary one-way analysis of variance (ANOVA) was carried out for apparent permeability data with Dunnett's multiple comparisons test to identify statistical significance compared to control. Two-way ANOVA was performed for analysis of contraction assay with Tukey's multiple comparisons test to compare between groups. Post hoc unpaired, two-tailed Student *t*-tests were performed, as

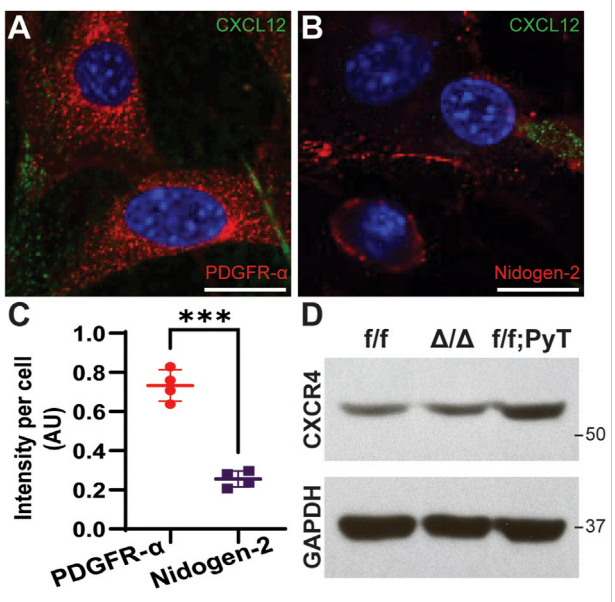

FIGURE 1
Molecular characterization of fibroblasts isolated from mouse mammary glands. **(A,B)** Representative confocal images of cancer-associated fibroblasts (CAFs) by immunofluorescence (IF) staining of CXCL12 (green) and PDGFR-α (red for **A**) and Nidogen-2 (red for **B**). Nuclei (blue) were counterstained with DAPI. Scale bars are 20 μm. **(C)** Quantification of fluorescence intensity of PDGFR-α and Nidogen-2 per cell from confocal IF images. Values represent the mean ± standard deviation, with n = 4 technical replicates: $^{*}p \leq 0.05$, $^{**}p \leq 0.01$, $^{***}p < 0.001$ from unpaired t-test. **(D)** Western blot analysis of CXCR4 from fibroblast lysates derived from mouse mammary glands. f/f: floxed control allele MMFs, Δ/Δ: CXCL12-knockout MMFs, f/f; PyT: CAFs from tumor-bearing mammary glands of Cxcl12$^{f/f}$;PyT mice. CXCR4 expression is preserved in the CXCL12 genetically ablated fibroblasts and robust in CAFs.

necessary. Data were analyzed using GraphPad Prism 9 (GraphPad Software), and statistical significance was set to α = 0.05: $^{*}p \leq 0.05$, $^{**}p \leq 0.01$, $^{***}p < 0.001$.

Results and discussion

Subclasses of cancer-associated fibroblasts and CXCR4 expression

Subpopulations of breast cancer-associated fibroblasts have been previously reported by interrogating the transcriptome of isolated murine CAFs using single-cell RNA-sequencing (scRNA-seq) (Bartoschek et al., 2018). The proposed taxonomy of CAFs in breast cancer defined discrete subtypes by their gene expression profiles. Among the subclasses, vascular CAFs (vCAFs) and matrix CAFs (mCAFs) play important roles in breast tumorigenesis and were of particular interest given the context of our microfluidic model, which is constituted by matrix-embedded CAFs in proximity to microvessel analogues. To better characterize our f/f; PyT CAFs at the molecular level, we performed immunofluorescence (IF) on isolated cells to stain for the vCAF marker Nidogen-2, and the mCAF marker PDGFR-α (Figures 1A,B). We found both Nidogen-2-positive vCAFs and PDGFR-α-positive mCAFs; however, the fluorescence intensity of PDGFR-α was nearly 3-fold higher than that of Nidogen-2, suggesting a greater subpopulation of mCAFs than vCAFs (Figure 1C). Furthermore, each subclass of CAFs is attributable to a putative origin (Bartoschek et al., 2018): vCAFs derive from perivascular cells that invade the tumor stroma, and mCAFs originate from co-opted resident fibroblasts. Thus, we conclude that we had a greater preponderance of mCAFs originating from local fibroblasts that had been co-opted by the breast tumor. The higher PDGFR-α signal exhibited by our f/f; PyT CAFs harvested from 8-week-old mice is also in agreement with Bartoschek et al. (2018) who reported that PDGFR-α-positive mCAFs from the MMTV-PyMT tumor mouse model were most prevalent at 8 weeks and decreased during tumor progression through 15 weeks.

We next examined the relative basal levels of CXCR4 protein expression among the fibroblasts *via* Western blot analysis. Floxed control allele MMFs (f/f), CXCL12-knockout MMFs (Δ/Δ), and CAFs from tumor-bearing Cxcl12$^{f/f}$;PyT mice (f/f; PyT) were isolated from mouse mammary glands and included for analysis. The fibroblast-specific gene deletion of CXCL12 did not have a significant effect on CXCR4 expression evidenced by comparing Δ/Δ fibroblasts to their wild-type counterparts (f/f) (Figure 1D). Moreover, the receptor CXCR4 is robustly expressed in f/f; PyT CAFs and qualitatively higher compared to MMFs. Taken together, we conclude that CXCR4 expression is preserved in the CXCL12 genetically ablated fibroblasts, and that disruption of CXCL12 signaling *via* competition with AMD3100 to CXCR4 is possible in each of the fibroblast cell lines.

Fibroblast-derived CXCL12 is a major driver of vessel permeability

Our microtissue analogue device was employed to investigate the role of soluble fibroblast-derived CXCL12 on endothelial vessel function (Chang et al., 2020). MEECs lined one microchannel of the device, which laterally interfaced with an adjacent stromal compartment containing a 3-D hydrogel of type I collagen (Figures 2A,B). Texas Red-conjugated Dextran (MW ~70 kDa) dissolved in media served as a fluorescent tracer. Changes in fluorescence intensity within the stromal compartment were used to calculate apparent vascular permeability (Figure 2C). These measurements were obtained for MEEC microvessel analogues in the presence of conditioned media (CM) collected from respective CAFs or from co-culture models in which CAFs were embedded within the collagen gel matrix in the central

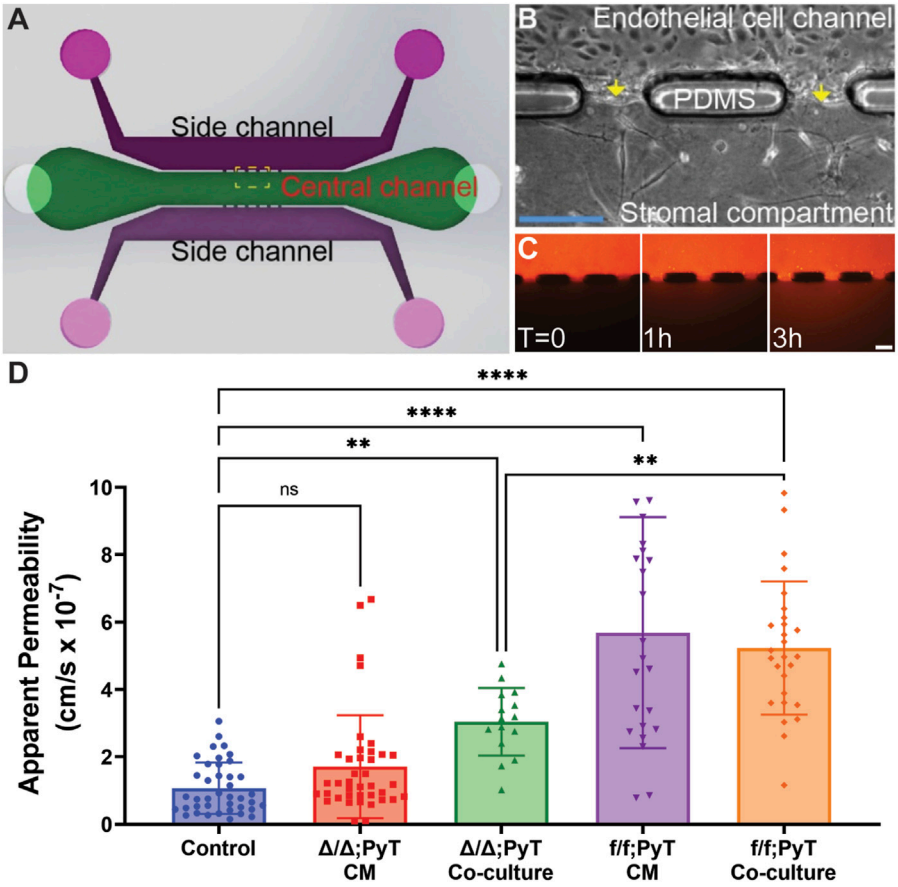

FIGURE 2
Compartmentalized microfluidic device for vascular permeability measurements. **(A)** Schematic of microtissue analogue microfluidic device. **(B)** Dashed boxed region in **(A)** depicting endothelial cell-lined microchannel laterally adjacent to a central stromal compartment containing fibroblasts embedded in a 3-D type I collagen gel. Arrows depict the endothelial-stromal compartment interface. **(C)** Texas Red-conjugated Dextran (70 kDa) dissolved in media served as a fluorescent tracer and was introduced into the MEEC-lined channel. The fluorescent tracer passes through the endothelial monolayer of the microvessel analogue and enters the stromal compartment by diffusion. Scale bars are 50 μm. **(D)** Changes in fluorescence intensity within the stromal compartment were used to calculate apparent vascular permeability of vessels in the presence of conditioned media (CM) or co-cultured with CAFs—with and without Cxcl12 gene deletion. Reported values represent the mean ± standard deviation, with $n \geq 3$ biological replicates and at least 15 apertures analyzed for each condition: $^{*}p \leq 0.05$, $^{**}p \leq 0.01$, $^{***}p < 0.001$.

compartment. As a control condition, the apparent permeability of MEEC-lined channels was measured using normal endothelial culture media in the absence of fibroblasts.

The presence of the chemokine CXCL12 from f/f; PyT CAFs significantly increased the vascular permeability of endothelial microvessel analogues approximately 5-fold in both conditioned media and the co-culture model: means of 5.7 and 5.2 × 10^{-7} cm/s, respectively, compared to the control arm of 1.1 × 10^{-7} cm/s (Figure 2D). Given that the values from CM and co-culture models were not significantly different from each other, the presence of CAFs and soluble CXCL12 did not appear to have an additive effect on permeability. In the absence of CXCL12 from CAFs with the fibroblast-specific CXCL12 deletion (Δ/Δ; PyT), conditioned media did not have a significant effect on vessel permeability compared to control. Notably, conditioned media from CAFs contains a vast myriad of growth factors, cytokines, and other extracellular matrix protein constituents of the CAF secretome. Therefore, the principal difference between Δ/Δ; PyT conditioned media and f/f; PyT conditioned media is the absence of fibroblast-derived CXCL12. Consequently, soluble CXCL12 can be attributed as a primary driver of this observed rise in vascular permeability operating through a paracrine signaling axis between CAFs and nearby endothelia.

Interestingly, apparent permeability significantly increased approximately 3-fold in the CXCL12-depleted CAF co-culture model (Δ/Δ; PyT), with a mean of 3.0 × 10^{-7} cm/s, compared to control. This suggests that despite the absence of soluble CXCL12, CAFs are capable of augmenting vessel permeability within the local tumor microenvironment through other means,

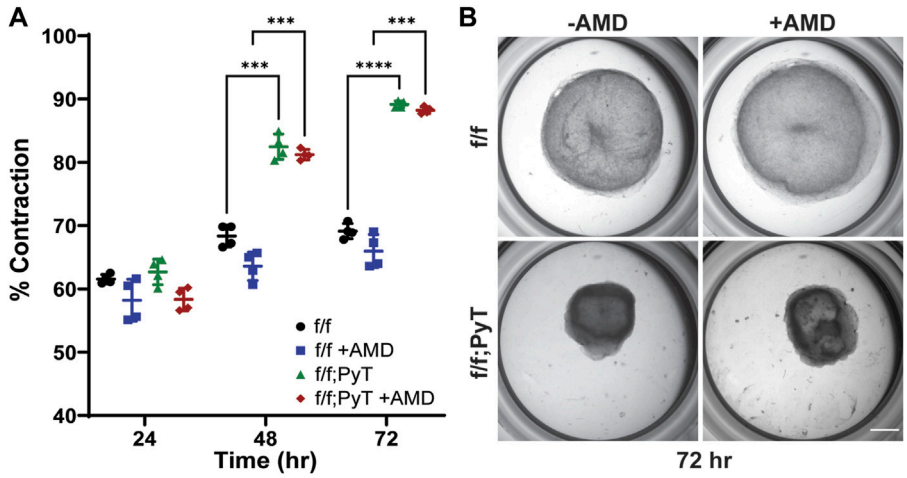

FIGURE 3
Collagen gel contraction assay to determine fibroblast contractility. **(A)** Percent contraction of normal mouse mammary gland fibroblasts (f/f) and CAFs (f/f; PyT) harvested from PyT tumor-induced mice, with and without the pharmacological CXCR4 inhibitor, AMD3100 (AMD). CAFs exhibit greater contractility compared to their normal counterparts by 48 h. AMD did not have a statistically significant effect on fibroblast contraction, although a slight reduction in mean contraction is observed for both cell lines. Reported values represent the mean ± standard deviation, with $n = 4$ technical replicates for each condition: $*p \leq 0.05$, $**p \leq 0.01$, $***p < 0.001$. **(B)** Representative images of fibroblast-laden collagen gels under stereo microscope after 72 h of contraction. Scale bar is 2 mm.

for example, indirectly through ECM remodeling or TME reprogramming. Of note, CAFs are known to produce excess collagen leading to increased matrix density, desmoplasia, and tissue stiffness (Mouw et al., 2014; Shen et al., 2020). A highly fibrotic tumor can also cause immunosuppression by excluding T lymphocytes through various mechanisms, and thus promotes tumor survival (Chen et al., 2019). In addition, tissue stiffness has been shown to promote a leakier tumor-like vasculature and angiogenesis (Bordeleau et al., 2017), thereby suggesting an interplay between fibroblast contractility, matrix stiffness, and an altered vascular phenotype. These findings prompted us to investigate the autocrine signaling effect of CXCL12 on fibroblasts' ability to remodel the ECM. Namely, the contractility of fibroblasts—both CAFs and mouse mammary fibroblasts (MMF) from normal glands—on type I collagen was investigated (Figure 3).

CXCL12-mediated fibroblast remodeling of the ECM

In vitro collagen gel contraction assays were performed for MMFs and CAFs harvested from their respective mice models in the presence and absence of AMD3100 (AMD). AMD3100, a pharmaceutical also known as plerixafor, is a highly selective antagonist to the CXCR4 receptor, thus, it directly competes with endogenous CXCL12. The pharmacological blocking of soluble CXCL12 was used to disrupt the autocrine signaling axis of CXCL12 secreted by both normal fibroblasts and CAFs. Collagen hydrogels contracted more than 55% after 24 h for both CAF and MMF conditions confirming the ability of these fibroblasts to contract ECM *in vitro* (Figure 3A). While contractility increased for all four conditions over 3 days, CAFs exhibited significantly greater contractility compared to their normal counterparts by Day 2 lasting through the duration of the assay (Figure 3B). By Day 3, mean contraction for CAF-laden gels had reached 88 and 89%, with and without AMD, respectively. By contrast, normal mammary fibroblasts contracted 66 and 69%, with and without AMD, respectively. Overall, AMD3100 did not have a statistically significant effect on fibroblast contraction, although, a modest drop in mean contraction was observed for both cell lines. As a result, the antagonistic blocking of autocrine CXCL12 by AMD3100 does not significantly affect fibroblasts' ability to remodel the local ECM. The primary upstream trigger of CAF contractility is likely not CXCL12, such that autocrine effects of CXCL12 are probably not responsible for making fibroblasts substantially more contractile. Taken together, CXCL12 from CAFs increases the permeability of surrounding microvessel analogues—which has implications for tumor intravasation and metastasis—however, CXCL12 does not seem to play a major role in the ECM remodeling of CAFs by autocrine control.

Conclusion

Stromal CXCL12 secreted by CAFs has a potent effect on increasing the vascular permeability of local blood microvessels through paracrine signaling of the chemokine. A leakier

endothelium is of particular importance given its role in angiogenesis and intravasation by tumor cells within the broader context of the metastatic cascade. Furthermore, co-culture with CAFs that had a CXCL12-specific genetic ablation resulted in a reduction of vascular permeability compared to CXCL12-secreting CAFs—presumably through indirect matrix remodeling. Despite CAF-secreted CXCL12 promoting tumor-like vasculature, CXCL12 does not appear to control fibroblast contractility through upstream autocrine signaling mechanisms.

Data availability statement

The raw data supporting the conclusion of this article will be made available by the authors, without undue reservation.

Author contributions

Design and conceptualization of the study: JCH, C-WC, AA, DKA, RKG, and JWS. Methodology: JCH, C-WC, AA, AAG, AKV, MC, and DKA. Data curation: JCH, C-WC, AA, AKV, MC, and DKA. Writing–Original Draft Preparation: JCH and DKA. Writing–Review and Editing: JCH, C-WC, AA, AAG, AKV, MC, DKA, RKG, and JWS. Project Administration and Funding Acquisition: DKA, RKG, and JWS.

Funding

This work was supported by the funding awarded to JS from an NSF CAREER Award (CBET-1752106) and to RG from NIH (CA109527). One of the authors (JH) gratefully acknowledges funding from a Graduate Diversity Supplement to NHLBI grant R01HL141941. Two of the authors (C-WC and AA) gratefully acknowledge funding from the Pelotonia Graduate Fellowship Program. One of the authors (AV) gratefully acknowledges funding from the Postdoctoral Candidate Pelotonia Fellowship Program. One of the authors (AG) gratefully acknowledges support as a FAST (Future Academic Scholars Training) Scholar from the Department of Mechanical and Aerospace Engineering at The Ohio State University. Confocal microscopy images presented in this report were generated using instruments and services at the Campus Microscopy and Imaging Facility (CMIF), The Ohio State University. This facility is supported in part by grant P30 CA016058, National Cancer Institute.

Conflict of interest

The authors declare that the research was conducted in the absence of any commercial or financial relationships that could be construed as a potential conflict of interest.

Publisher's note

All claims expressed in this article are solely those of the authors and do not necessarily represent those of their affiliated organizations, or those of the publisher, the editors and the reviewers. Any product that may be evaluated in this article, or claim that may be made by its manufacturer, is not guaranteed or endorsed by the publisher.

References

Ahirwar, D. K., Nasser, M. W., Ouseph, M. M., Elbaz, M., Cuitino, M. C., Kladney, R. D., et al. (2018). Fibroblast-derived CXCL12 promotes breast cancer metastasis by facilitating tumor cell intravasation. *Oncogene* 37, 4428–4442. doi:10.1038/s41388-018-0263-7

Anand, A. R., Zhao, H., Nagaraja, T., Robinson, L. A., and Ganju, R. K. (2013). N-terminal Slit2 inhibits HIV-1 replication by regulating the actin cytoskeleton. *Retrovirology* 10, 2. doi:10.1186/1742-4690-10-2

Bartoschek, M., Oskolkov, N., Bocci, M., Lovrot, J., Larsson, C., Sommarin, M., et al. (2018). Spatially and functionally distinct subclasses of breast cancer-associated fibroblasts revealed by single cell RNA sequencing. *Nat. Commun.* 9, 5150. doi:10.1038/s41467-018-07582-3

Bordeleau, F., Mason, B. N., Lollis, E. M., Mazzola, M., Zanotelli, M. R., Somasegar, S., et al. (2017). Matrix stiffening promotes a tumor vasculature phenotype. *Proc. Natl. Acad. Sci. U. S. A.* 114, 492–497. doi:10.1073/pnas.1613855114

Chang, C. W., Seibel, A. J., Avendano, A., Cortes-Medina, M. G., and Song, J. W. (2020). Distinguishing specific CXCL12 isoforms on their angiogenesis and vascular permeability promoting properties. *Adv. Healthc. Mat.* 9, e1901399. doi:10.1002/adhm.201901399

Charan, M., Das, S., Mishra, S., Chatterjee, N., Varikuti, S., Kaul, K., et al. (2020). Macrophage migration inhibitory factor inhibition as a novel therapeutic approach against triple-negative breast cancer. *Cell Death Dis.* 11, 774. doi:10.1038/s41419-020-02992-y

Chen, I. X., Chauhan, V. P., Posada, J., Ng, M. R., Wu, M. W., Adstamongkonkul, P., et al. (2019). Blocking CXCR4 alleviates desmoplasia, increases T-lymphocyte infiltration, and improves immunotherapy in metastatic breast cancer. *Proc. Natl. Acad. Sci. U. S. A.* 116, 4558–4566. doi:10.1073/pnas.1815515116

Finak, G., Bertos, N., Pepin, F., Sadekova, S., Souleimanova, M., Zhao, H., et al. (2008). Stromal gene expression predicts clinical outcome in breast cancer. *Nat. Med.* 14, 518–527. doi:10.1038/nm1764

Garg, A. A., Jones, T. H., Moss, S. M., Mishra, S., Kaul, K., Ahirwar, D. K., et al. (2019). Electromagnetic fields alter the motility of metastatic breast cancer cells. *Commun. Biol.* 2, 303. doi:10.1038/s42003-019-0550-z

Hanahan, D. (2022). Hallmarks of cancer: New dimensions. *Cancer Discov.* 12, 31–46. doi:10.1158/2159-8290.cd-21-1059

Hanahan, D., and Weinberg, R. A. (2011). Hallmarks of cancer: The next generation. *Cell* 144, 646–674. doi:10.1016/j.cell.2011.02.013

Houthuijzen, J. M., and Jonkers, J. (2018). Cancer-associated fibroblasts as key regulators of the breast cancer tumor microenvironment. *Cancer Metastasis Rev.* 37, 577–597. doi:10.1007/s10555-018-9768-3

Jin, M. Z., and Jin, W. L. (2020). The updated landscape of tumor microenvironment and drug repurposing. *Signal Transduct. Target. Ther.* 5, 166. doi:10.1038/s41392-020-00280-x

Kalluri, R. (2016). The biology and function of fibroblasts in cancer. *Nat. Rev. Cancer* 16, 582–598. doi:10.1038/nrc.2016.73

Kojima, Y., Acar, A., Eaton, E. N., Mellody, K. T., Scheel, C., Ben-Porath, I., et al. (2020). Autocrine TGF-beta and stromal cell-derived factor-1 (SDF-1) signaling drives the evolution of tumor-promoting mammary stromal myofibroblasts. *Proc. Natl. Acad. Sci. U. S. A.* 107, 20009–20014. doi:10.1073/pnas.1013805107

Littlepage, L. E., Egeblad, M., and Werb, Z. (2005). Coevolution of cancer and stromal cellular responses. *Cancer Cell* 7, 499–500. doi:10.1016/j.ccr.2005.05.019

Luker, K. E., Lewin, S. A., Mihalko, L. A., Schmidt, B. T., Winkler, J. S., Coggins, N. L., et al. (2012). Scavenging of CXCL12 by CXCR7 promotes tumor growth and metastasis of CXCR4-positive breast cancer cells. *Oncogene* 31, 4750–4758. doi:10.1038/onc.2011.633

Maller, O., Drain, A. P., Barrett, A. S., Borgquist, S., Ruffell, B., Zakharevich, I., et al. (2021). Tumour-associated macrophages drive stromal cell-dependent collagen crosslinking and stiffening to promote breast cancer aggression. *Nat. Mat.* 20, 548–559. doi:10.1038/s41563-020-00849-5

Mouw, J. K., Yui, Y., Damiano, L., Bainer, R. O., Lakins, J. N., Acerbi, I., et al. (2014). Tissue mechanics modulate microRNA-dependent PTEN expression to regulate malignant progression. *Nat. Med.* 20, 360–367. doi:10.1038/nm.3497

Müller, A., Homey, B., Soto, H., Ge, N., Catron, D., Buchanan, M. E., et al. (2001). Involvement of chemokine receptors in breast cancer metastasis. *Nature* 410, 50–56. doi:10.1038/35065016

Nair, N., Calle, A. S., Zahra, M. H., Prieto-Vila, M., Oo, A. K. K., Hurley, L., et al. (2017). A cancer stem cell model as the point of origin of cancer-associated fibroblasts in tumor microenvironment. *Sci. Rep.* 7, 6838. doi:10.1038/s41598-017-07144-5

Orimo, A., Gupta, P. B., Sgroi, D. C., Arenzana-Seisdedos, F., Delaunay, T., Naeem, R., et al. (2005). Stromal fibroblasts present in invasive human breast carcinomas promote tumor growth and angiogenesis through elevated SDF-1/CXCL12 secretion. *Cell* 121, 335–348. doi:10.1016/j.cell.2005.02.034

Park, C. Y., Min, K. N., Son, J. Y., Park, S. Y., Nam, J. S., Kim, D. K., et al. (2014). An novel inhibitor of TGF-beta type I receptor, IN-1130, blocks breast cancer lung metastasis through inhibition of epithelial-mesenchymal transition. *Cancer Lett.* 351, 72–80. doi:10.1016/j.canlet.2014.05.006

Ren, J., Smid, M., Iaria, J., Salvatori, D. C. F., Van Dam, H., Zhu, H. J., et al. (2019). Cancer-associated fibroblast-derived Gremlin 1 promotes breast cancer progression. *Breast Cancer Res.* 21, 109. doi:10.1186/s13058-019-1194-0

Shen, Y., Wang, X., Lu, J., Salfenmoser, M., Wirsik, N. M., Schleussner, N., et al. (2020). Reduction of liver metastasis stiffness improves response to bevacizumab in metastatic colorectal cancer. *Cancer Cell* 37, 800–817.e7. e807. doi:10.1016/j.ccell.2020.05.005

Shiga, K., Hara, M., Nagasaki, T., Sato, T., Takahashi, H., Takeyama, H., et al. (2015). Cancer-associated fibroblasts: Their characteristics and their roles in tumor growth. *Cancers (Basel)* 7, 2443–2458. doi:10.3390/cancers7040902

Trimboli, A. J., Cantemir-Stone, C. Z., Li, F., Wallace, J. A., Merchant, A., Creasap, N., et al. (2009). Pten in stromal fibroblasts suppresses mammary epithelial tumours. *Nature* 461, 1084–1091. doi:10.1038/nature08486

Valkenburg, K. C., De Groot, A. E., and Pienta, K. J. (2018). Targeting the tumour stroma to improve cancer therapy. *Nat. Rev. Clin. Oncol.* 15, 366–381. doi:10.1038/s41571-018-0007-1

Wiseman, B. S., and Werb, Z. (2002). Stromal effects on mammary gland development and breast cancer. *Science* 296, 1046–1049. doi:10.1126/science.1067431

Zhang, T., Day, J. H., Su, X., Guadarrama, A. G., Sandbo, N. K., Esnault, S., et al. (2019). Investigating fibroblast-induced collagen gel contraction using a dynamic microscale platform. *Front. Bioeng. Biotechnol.* 7, 196. doi:10.3389/fbioe.2019.00196

frontiers | Frontiers in Bioengineering and Biotechnology

TYPE Original Research
PUBLISHED 09 December 2022
DOI 10.3389/fbioe.2022.1008481

OPEN ACCESS

EDITED BY
Jonathan W. Song,
The Ohio State University, United States

REVIEWED BY
Vanessa Coelho-Santos,
Seattle Children's Research Institute, United States
Bingmei M. Fu,
City College of New York (CUNY), United States

*CORRESPONDENCE
John C. Chappell,
jchappell@vtc.vt.edu

SPECIALTY SECTION
This article was submitted to Tissue Engineering and Regenerative Medicine, a section of the journal Frontiers in Bioengineering and Biotechnology

RECEIVED 31 July 2022
ACCEPTED 23 November 2022
PUBLISHED 09 December 2022

CITATION
Willi CE, Abdelazim H and Chappell JC (2022), Evaluating cell viability, capillary perfusion, and collateral tortuosity in an ex vivo mouse intestine fluidics model. *Front. Bioeng. Biotechnol.* 10:1008481. doi: 10.3389/fbioe.2022.1008481

Evaluating cell viability, capillary perfusion, and collateral tortuosity in an ex vivo mouse intestine fluidics model

Caroline E. Willi[1,2], Hanaa Abdelazim[1,2] and John C. Chappell [1,2,3,4]*

[1]Fralin Biomedical Research Institute (FBRI) at Virginia Tech-Carilion (VTC), Roanoke, VA, United States, [2]FBRI Center for Vascular and Heart Research, Roanoke, VA, United States, [3]Department of Biomedical Engineering and Mechanics, Virginia Tech, Blacksburg, VA, United States, [4]Department of Basic Science Education, Virginia Tech Carilion School of Medicine, Roanoke, VA, United States

Numerous disease conditions involve the sudden or progressive loss of blood flow. Perfusion restoration is vital for returning affected organs to full health. While a range of clinical interventions can successfully restore flow to downstream tissues, the microvascular responses after a loss-of-flow event can vary over time and may involve substantial microvessel instability. Increased insight into perfusion-mediated capillary stability and access-to-flow is therefore essential for advancing therapeutic reperfusion strategies and improving patient outcomes. To that end, we developed a tissue-based microvascular fluidics model to better understand (i) microvascular stability and access-to-flow over an acute time course post-ischemia, and (ii) collateral flow in vessels neighboring an occlusion site. We utilized murine intestinal tissue regions by catheterizing a feeder artery and introducing perfusate at physiologically comparable flow-rates. The cannulated vessel as well as a portion of the downstream vessels and associated intestinal tissue were cultured while constant perfusion conditions were maintained. An occlusion was introduced in a selected arterial segment, and changes in perfusion within areas receiving varying degrees of collateral flow were observed over time. To observe the microvascular response to perfusion changes, we incorporated (i) tissues harboring cell-reporter constructs, specifically *Ng2-DsRed* labeling of intestinal pericytes, and (ii) different types of fluorescent perfusates to quantify capillary access-to-flow at discrete time points. In our model, we found that perfusion tracers could enter capillaries within regions downstream of an occlusion upon the initial introduction of perfusion, but at 24 h tissue perfusion was severely decreased. However, live/dead cell discrimination revealed that the tissue overall did not experience significant cell death, including that of microvascular pericytes, even after 48 h. Our findings suggest that altered flow conditions may rapidly initiate cellular responses that reduce capillary access-to-flow, even in the absence of cellular deterioration or hypoxia. Overall, this *ex vivo* tissue-based microfluidics model may serve as a platform upon which a variety of follow-on studies may be conducted. It will thus enhance our understanding of microvessel stability and access-to-flow during an occlusive event and the role of collateral flow during normal and disrupted perfusion.

KEYWORDS
pericytes, vascular stability, reperfusion injury, collateral flow, microfluidic models

Introduction

Blood vessels facilitate nutrient exchange and waste removal to sustain the health of all tissues. When these essential conduits become obstructed such as in stroke, myocardial infarction, or acute intestinal ischemia (e.g., in necrotizing enterocolitis), it is critical to re-establish perfusion and restore organ homeostasis (Nowicki, 2005; Moskowitz et al., 2010). Clinical treatments for stroke, for instance, include rapid infusion of tissue plasminogen activator (tPA, chemical thrombus disaggregation) within 4 h last-known-well, or catheter-based mechanical thrombectomy (MT, surgical clot removal) in the hyper-acute phase between 4 h and recently-extended 24 h last-known-well (Powers et al., 2018). Similar approaches are employed in other acute ischemia scenarios such as myocardial infarction, but tissue reperfusion outcomes can vary widely and suffer from the "no-reflow" phenomenon, that is, the incomplete restoration of blood flow to all capillary beds (Eeckhout and Kern, 2001; Ito, 2006). A more complete understanding of the mechanisms that limit reperfusion will therefore inspire the development of next-generation therapies that can achieve better recovery endpoints.

Blood vessels are known to experience reperfusion injury when flow is reintroduced to vasculature following static conditions. This complex scenario involves the convergence of mechanical and signaling mechanisms that yield a range of consequences including increased leukocyte recruitment, disrupted vasomotion, and microvessel obstruction and instability (Heusch, 2020). Circulating thrombi may lodge within microvascular networks and reduce blood flow to capillary beds (Bray et al., 2020), and reactive oxygen species induce cellular damage, dysfunction, and death (Granger and Kvietys, 2015). It has also been proposed that vascular pericytes in the heart and brain may constrict capillaries during ischemia and die in this constricted state, resulting in permanently occluded microvessels (Yemisci et al., 2009; Hall et al., 2014; O'Farrell and Attwell, 2014; O'Farrell et al., 2017). Recent observations have questioned the extent to which dead pericytes may remain intact and are able to sustain capillary occlusion (Hoque et al., 2021), but pericyte loss from the vessel wall is likely a key component of microvessel instability that may limit tissue reperfusion. While our knowledge of the underlying causes for inadequate perfusion after recanalization continues to expand, many open questions remain regarding post-ischemia capillary access-to-flow and stability. These gaps in knowledge highlight the need for additional experimental models that might help dissect molecular and biophysical factors contributing to restricted blood flow distribution following therapeutic intervention.

A range of experimental models have been developed to gain insight into specific aspects of tissue ischemia and reperfusion injury responses. *In vivo* models frequently involve vessel occlusion by ligation or clamp for a short period of time and then removing the occlusion to reestablish blood flow to the downstream tissue (Gonzalez et al., 2015). These models capture inherent biological complexities within the ischemia-reperfusion setting including the cellular, biochemical, and mechanical components of blood as well as the effects of hypoxia, among other factors (Heusch, 2020). Conversely, these complexities can pose challenges with interpreting results, especially when overlaid on other variables that are altered due to the experimental approach e.g., surgical intervention causing systemic immune activation and anesthesia altering cardiovascular physiology (Luo et al., 2007). *In vivo* models are also restricted temporally, not easily facilitating experiments that correspond to the timing of ischemia onset and clinical intervention.

In contrast, cell-based microfluidic models allow for flexibility in cell type selection to mirror specific vasculature of interest such as the blood-brain barrier (BBB) (Bang et al., 2017), placental exchange (Haase et al., 2019), or the tumor microenvironment (Phan et al., 2017). These models often incorporate primary cells e.g., human umbilical vein endothelial cells (HUVECs) or differentiated stem cells (embryonic or induced pluripotent), and can achieve expression of vascular markers and comparable physiological behaviors (Song and Munn, 2011; Akbari et al., 2017). Nevertheless, they often lack important blood-derived inputs such as key fluid mechanics and circulating hormonal signals as well as the complexity of a tissue-specific microenvironment i.e., adjacent cell types and extracellular matrix (ECM) components. These experimental platforms are also often limited by (i) a paucity of vessels that remain capillary size (i.e., diameters less than 10 μm) and (ii) heterogeneous mural cell incorporation such as by pericytes and/or smooth muscle cells (Hesh et al., 2019). To bridge *in vivo* and *in vitro* models, *ex vivo* models have been developed as an intermediate approach for retaining many important biological features while allowing greater experimental control and more rigorous assessment, though with inherent limitations as well.

Tissue-based *ex vivo* models typically involve the extraction of an organ of interest and preparing it to be cultured in conditions that sustain cellular health and minimize deviation from the *in vivo* scenario. New insights into the dynamics of vascular remodeling and barrier function have been gleaned from *ex vivo* models of retinal (Sawamiphak et al., 2010), mesenteric (Azimi et al., 2017; Suarez-Martinez et al., 2018), lung (Sava et al., 2017), and dermal (Payne et al., 2021) microcirculatory networks, though fluid transit was absent in these models. To capture the effects of intraluminal forces on the vessel wall, a subset of tissue-based models have incorporated pressurization

of the vasculature as an orthogonal approach to better understand vasomotor responses to tissue activities and behavior (Hall et al., 2014). Recently, a number of perfused *ex vivo* models have been developed to recapitulate aspects of fluid mechanics on blood vessel physiology (Goeden and Bonnin, 2013; Motherwell et al., 2019; Gonzales et al., 2020). Although these models lack key features such as the viscosity and cellular or biochemical components of blood, they retain critical aspects of vessel wall structure and composition (e.g., ECM components) in addition to the intrinsic architecture and hierarchy of *in vivo* vascular networks.

In the current study, we sought to develop an *ex vivo* fluidics platform utilizing the mouse intestinal vasculature, inspired by recently developed approches involving rat mesentery (Motherwell et al., 2019). We sought to address the question of why capillary perfusion may become restricted in vessel occlusion and ischemia-reperfusion scenarios. Our specific focus was on the influence of cell viability and fluid mechanics on flow through capillary networks. As such, we established culture conditions that sustained tissue viability and allowed a closed-loop perfusion of intestinal vessels for up to 48 h. To model ischemic injury, a vessel blockage was simulated by an occlusion of an arterial branch downstream of the catheterization point. We verified that perfusate could access intestinal capillaries within 1 h of experimental set up, including those downstream of the occlusion. Nevertheless, after 24 h and 48 h of sustained fluid flow *ex vivo*, the microvasculature lacked perfusion when assessed by FITC-Dextran-mediated fluorescence angiography. We also found that secondary intestinal arteries displayed a higher degree of tortuosity at both time points, suggesting these vessels experienced higher intraluminal pressures that could not be resolved by fluid flow through downstream capillary networks. Overall, our results suggest that restricted capillary perfusion may be less affected by microvessel stability than previously thought, as cell viability, specifically that of the pericytes, was largely maintained, and yet microvessel fluid flow rapidly decreased. Our study also reinforces the potential utility of *ex vivo* fluidics platforms in addressing open questions regarding the microvascular response to changes in tissue perfusion.

Materials and methods

Animal use

All animal experiments were conducted with review and approval from Virginia Tech Institutional Animal Care and Use Committee (IACUC), which reviewed and approved all protocols. The Virginia Tech NIH/PHS Animal Welfare Assurance Number is A-32081–01 (expires 31 July 2025). To view pericytes on intestinal capillaries, mice expressing the red fluorescent protein variant (DsRed.T1) under control of the mouse NG2 (*Ng2/Cspg4*) promoter/enhancer [i.e., *Ng2:DsRed* mice–NG2DsRedBAC, Stock name Tg (Cspg4-DsRed.T1) 1Akik/J, #008241, The Jackson Laboratory] were utilized between the ages of 6 and 12 months old. Wild type mice were also used, specifically C57BL/6 mice (Stock name C57BL/6J, #000664, Jackson Laboratory) within the same age range (see Supplementary Material for more details).

Perfused ex vivo intestial tissue preparation

Murine intestinal tissue was excised and transferred to a tissue culture dish. The incision points were sutured and cleared of debris. The area of interest was established by identifying a section with (i) a relatively large artery to ease needle insertion, and (ii) downstream branching that allows for the introduction of an occlusion to a central branch while neighboring branches could remain non-occluded and sustain flow. Sutures were made at the occlusion site, around neighboring, non-catheterized arteries, and on the intestines at either end of the area of interest. The catheter was introduced by making an incision in the feeder artery and gently advancing a 33G needle connected to silicone tubing into the vessel. The connection was secured with tissue adhesive, and the tissue was transferred to an incubator. The catheter was connected to a peristaltic pump, which administered pulsatile flow (1 ml/min–1.5 ml/min flow rate). The peristaltic pump functions by alternating between compressing and decompressing flexible tubing containing fluid as the rotor rotates. This motion creates pockets of fluid that quickly form as the rotor position moves from compressing to releasing. This quick fluid motion/tubing expansion creates a pulse. To establish a closed-loop system, the same solution acting as the perfusate was also used as tissue culture media. Perfusate solution/media is Minimum Essential Medium (Thermo Fisher catalog #11095080) with 1% penicillin streptomycin and fetal bovine serum (see Supplemental Material). The incubation media volume was controlled by a secondary pump that removed excess volume and deposited it back into the reservoir for reperfusion. Controlled flow was maintained throughout the duration of tissue culture.

Sample immunostaining, imaging, and analysis

Experiments were completed over 1 h, 24 h, and 48 h to assess the tissue and vascular responses at these time points. Immediately following the cessation of pump-administered controlled flow, the tissue was perfused with a FITC-Dextran solution and imaged using a Zeiss Discovery dissection microscope. The tissue was then moved to a Zeiss Epi-Fluorescent microscope to image vessel tortuosity. Finally, the

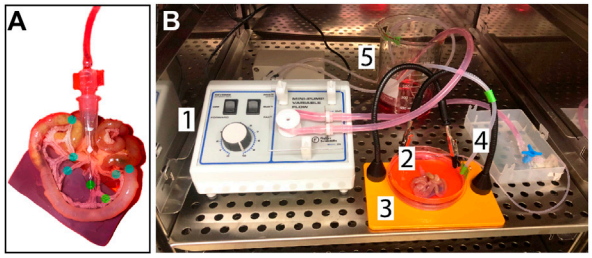

FIGURE 1
Experimental Design and Setup Schematics. **(A)** Close-up of the catheter insertion point and suture points: The green dots label the needle insertion point, which is secured with tissue adhesive, and the occlusion suture. The blue dots label sutures made on neighboring, non-catheterized arteries and on the intestine on either end of the area of interest. These sutures serve to emulate the resistance that would be present *in-vivo* from blood flow. **(B)** Set up of the controlled-flow tissue culture environment: 1. The peristaltic pump provides controlled flow of the perfusate (MEM with 1% penicillin-streptomycin and 10% fetal bovine serum) at a flow-rate of 1 ml/min *via* an arterial catheter, 2. 3. The tissue is kept in the same media solution acting as the perfusate to create a closed circuit where the media volume in the dish is controlled by a secondary pump, 4, and deposited back into the reservoir to be cycled again, 5. All components are maintained at 37°C and 5% CO_2.

tissue was stained unfixed using the live-dead stain DRAQ7 with subsequent labeling by DAPI or Hoechst to detect cell nuclei and imaged on a Zeiss LSM 880 confocal microscope.

All image quantification was conducted using ImageJ/FIJI software (Rasband, 1997; Schindelin et al., 2012), and, aside from the pericyte viability assay, biological replicates for each experiment were at a minimum of $n = 3$. Cell viability was quantified as the percentage of DRAQ7+ and DAPI+ or Hoechst+ cells relative to the total number of DAPI+ or Hoechst+ cell nuclei. Positivity for DRAQ7 is indicative of permeable cells that are non-viable due to apoptosis or necrosis. Integrated density measurements of FITC-Dextran (measurement area x mean of gray values) was captured at three locations in each of the five distinct areas relative to the occluded area, as well as a background value for each image. The background value was subtracted from each metric to account for differences in imaging parameters, yielding the relative integrated density value. The distance-metric tortuosity was quantified by (i) measuring the displacement distance from vessel end-points, and (ii) dividing that value by the direct-line distance. Tortuosity was measured for vessels classified by diameter as "primary" (greater than 45 µm in diameter) and secondary (less than 45 µm in diameter).

Statistical analysis

Statistical analysis was performed in GraphPad Prism 8 software. For all measurements, we applied an ordinary one-way Analysis of Variance (ANOVA) test followed by Tukey's multiple comparisons test to analyze differences between each experiment group and/or classification. Statistical significance was achieved when $p \leq 0.05$. Again, all experiments were conducted with an $n = 3$ or more for biological replicates (with a biological replicate being one individual animal), and technical replicate measurements were taken per each biological replicate.

Results

Mouse intestinal vasculature can be excised and cultured while being perfused

In an effort to develop an intermediate platform bridging *in vitro* microfluidic approaches and *in vivo* experimental models, we drew from previous studies suggesting the mouse intestinal vasculature as an organ system that could be excised and cultured *ex vivo* similar to rat-based models (Azimi et al., 2017; Suarez-Martinez et al., 2018; Motherwell et al., 2019). We found vessel segments downstream of the superior mesenteric artery to be accessible *via* a 33G needle after minimal resection of adipose and connective tissue (Figure 1). Initial attempts at perfusion revealed the necessity for occlusion of non-catheterized arteries in flanking regions to simulate intraluminal fluid pressure and prevent retrograde flow back up these vessels. This configuration resulted in (i) fluid flow largely, though not completely, out of veins, and (ii) post-transit perfusate contributing to the media surrounding the isolated tissue. To achieve a closed-loop system, culture media was pumped into the perfusion reservoir that continuously flowed through the intestinal vasculature *via* peristaltic pump (Figure 1). The entire platform was placed in an incubator to maintain temperature (37°C), humidity, and an appropriate gas environment (5% CO_2) for the media selected.

One primary goal in developing this system was to model fluid flow through capillary networks (i.e., vessel diameter less than 10 um, pericytes present, established ECM basement membrane, etc.), as this remains elusive in the design of microfluidic platforms (Hesh et al., 2019). We perfused PBS systemically *via* an intracardiac catheter following euthanasia to limit thrombi formation that might prevent flow through the intestinal microcirculation. We avoided reintroducing flow abruptly following artery cannulation to reduce the likelihood and/or severity of reactive vasoconstriction that might also restrict perfusion within the microvasculature. To confirm that these approaches were useful in maintaining capillary access to fluid flow, we introduced green fluorescent microspheres with 1 µm diameters (FluoSpheres™) into the perfusate. We then used live imaging to capture their transit through microvessels surrounded by *Ng2:DsRed*+ pericytes (Figure 2). Microspheres rapidly flowing through intestinal vessels appeared as streaks of light indicating their path of travel through vessel networks. We noted numerous instances of microspheres passing through capillary-sized vessels clearly associated with *Ng2:DsRed*+ pericytes (Figure 2). Further

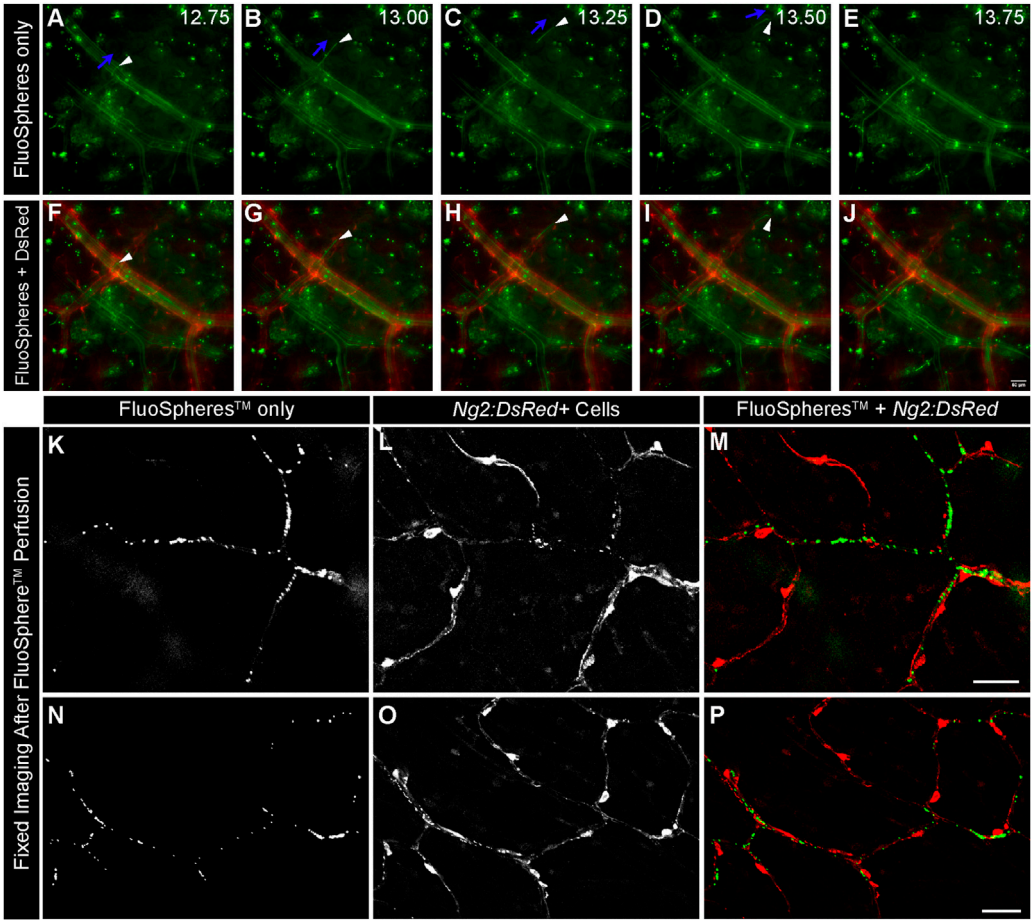

FIGURE 2
Green FluoSpheres™ Perfuse *Ng2:DsRed*-labeled Intestinal Capillaries. Representative time-lapse images of fluorescent green microspheres [green in **(A–J)**, 1 μm in diameter] suspended in PBS traveling through the intestinal vasculature *via* feeder artery catheterization in an *Ng2:DsRed* reporter mouse [red, in **(F–J)**]. An artery-vein pair is shown, in which the vessels are distinguished by the presence of DsRed in the NG2+ smooth muscle cells wrapped around the artery **(F–J)**. Green microspheres are observed traveling through both the artery and the vein, validating that the spheres are advancing down to the microvasculature. The directionality of one sphere is labeled with blue arrows, and the sphere is indicated by a white arrowhead in panels **(A–D)**. Capturing the phenomenon of a single 1 μm sphere flowing through a smaller-order vessel further supports the idea that our mechanism of providing flow is able to advance to the microvascular level. Time is shown in seconds **(A–E)**. Scale bar in **(J)** is 50 μm. Representative confocal images of fluorescent microspheres [**(K,N)** green in **(M,P)**] adjacent to *Ng2:DsRed+* pericytes [**(L,O)** red in **(M,P)**] after perfusion through the intestinal capillaries. Scale bars in **(M,P)** are 50 μm.

evidence of capillary transit was observed in high-power confocal images acquired after microsphere perfusion in which FluoSpheres™ were found intraluminally adjacent to *Ng2:DsRed+* pericytes (Figure 2) and not outside of the vessel wall. Taken together, this data instills confidence that capillary perfusion was maintained during experimental set up.

Static and controlled flow ex vivo culture conditions maintain tissue viability over 24 h and 48 h time courses

Previous studies have suggested that the viability of cells within the microcirculation plays a critical role in vessel stability and in turn perfusion of microvascular networks (Galiuto et al., 2000). Specifically, pericytes have been described as severely narrowing capillary diameters and dying in this constricted state, thereby limiting downstream blood flow and exacerbating the no-reflow phenomenon (Yemisci et al., 2009; Hall et al., 2014; O'Farrell et al., 2017). Therefore, a critical aspect in developing this experimental setup was establishing the appropriate culture conditions that maintained tissue viability over an extended period without activating cells (i.e., inducing proliferation, etc.). We tested a range of concentrations for fetal bovine serum (FBS) under static conditions and found that 1% and 5% were insufficient in limiting cell death. Specifically, we detected a relatively high number of cells labeled by DRAQ7, which was used to identify permeabilized, non-viable cells due to

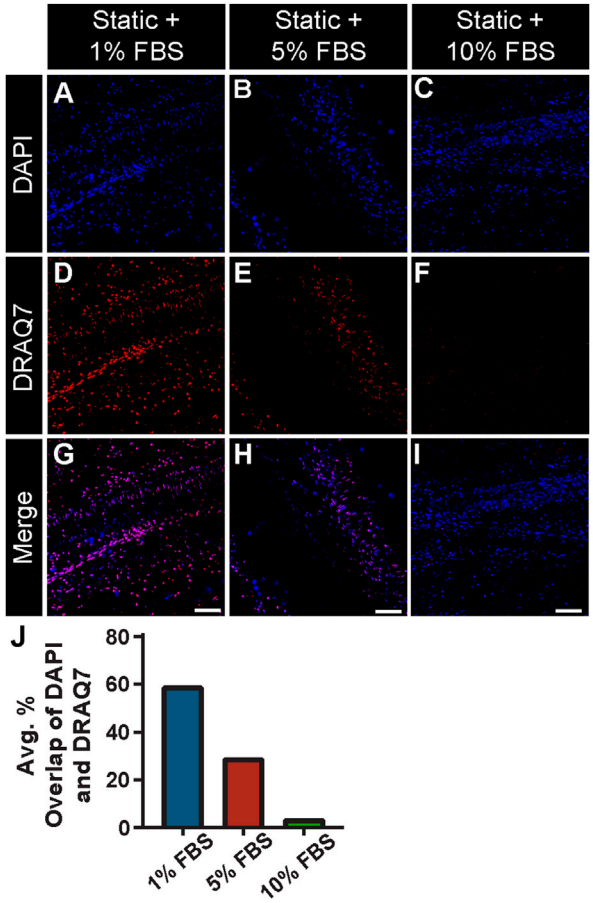

FIGURE 3
FBS Concentration Assessment with a Cell Viability Assay under Static Conditions. Representative images of DAPI-labeled cell nuclei [blue in **(A–C)** and **(G–I)**] relative to compromised cell nuclei labeled with DRAQ7 [red in **(D–I)**] in a 48 h static tissue culture of intestinal sections with 1% **(A,D,G)** 5% **(B,E,H)** and 10% FBS **(C,F,I)** in media. Note, 10% FBS showed a significant reduction of cell death compared to 5% and 1%, with the percent overlap of DAPI and DRAQ7 found to be 54.58%, 15.60%, and 1.82% for 1%, 5%, and 10% FBS concentrations, respectively. Therefore, 10% FBS was used in the experimental setup with controlled flow. Scale Bars in **(G,H,I)** are 100 μm. **(J)** Average percent overlap of DAPI and DRAQ7 signals across the intestinal tissue area under static conditions with 1% FBS (blue bar), 5% FBS (red bar), and 10% FBS (green bar).

the ability of this dye to only access the nuclei of dying cells (Figure 3). We suspect cell death was largely due to necrosis, though apoptotsis may also be occurring. In contrast, 10% FBS significantly lowered the presence of DRAQ7+ cells, suggesting that while some cell death was occurring in these intestine preparations, a higher concentration of serum was capable of minimizing cell loss and tissue degradation.

While 10% FBS in the culture media appeared sufficient in limiting cell death and tissue degradation during static conditions, we sought to address the question of maintaining cell viability under flow conditions and over an extended culture time course. After 24 h and 48 h of culture with flow maintained at physiologically relevant levels, we assessed intestinal tissue viability by incubating with DRAQ7, again a dye that should not label cell DNA extensively unless the nuclear envelope is compromised, potentially indicative of progression towards cell death. At 24 h, we found on average approximately 2.6% of all cells positive for DRAQ7, with only a slight increase to 3.5% at the 48 h time point (Figure 4). We also noted that vascular cell types such as pericytes were sustained by this approach because we observed very little, if any, overlap in the *Ng2:DsRed+* signals and DRAQ7 labeling (Figure 4) nor did we find gross changes in microvessel morphology (see Supplementary Figure S1). Some disruption in the continuity of the DsRed signal was noted, which may be attributable to early stages of cell degeneration but also to stability dynamics for this particular fluorescent reporter (Sacchetti et al., 2002). These data suggest that flow conditions did not severely diminish cell viability at the time points observed, suggesting further that the media circulating within and around isolated tissues was able to sustain a relatively high level of cell and tissue viability over the experimental time course.

Perfusion of intestinal capillary networks was limited after 24 h and 48 h despite lack of tissue degradation

As an orthogonal approach to flowing fluorescent microspheres to verify capillary perfusion after experimental set up, we conducted separate experiments in which we exposed tissues to flow conditions for 1 h and then introduced FITC-Dextran to the perfusate. In all regions within these tissue preparations, we found the FITC-Dextran capable of filling capillary networks (Figure 5). We even detected this dye in regions downstream of the occluded vessel, suggesting collateral channels were capable of facilitating perfusion into regions no longer supplied by direct fluid flow. Nevertheless, after 24 h of culture under flow conditions, perfusion of intestinal capillary networks was severely limited (Figure 5), even though tissue viability was largely maintained. This decrease in microvascular perfusion and capillary access to fluid flow was even more notable at the 48 h time point, despite the lack of significant tissue degradation found by the specific quantifications applied to these tissues.

Throughout these experiments, we observed changes in the morphology of collateral vessels bridging adjacent regions across the isolated tissues. Specifically, the curvature of these collateral vessels appeared to increase, which has been described in previous studies as a change in vessel tortuosity (Han, 2012; Chong et al., 2017). Increased tortuosity of blood vessels is often associated with increased intraluminal pressures and found in the context of vascular occlusive events (Hutchins et al., 1978;

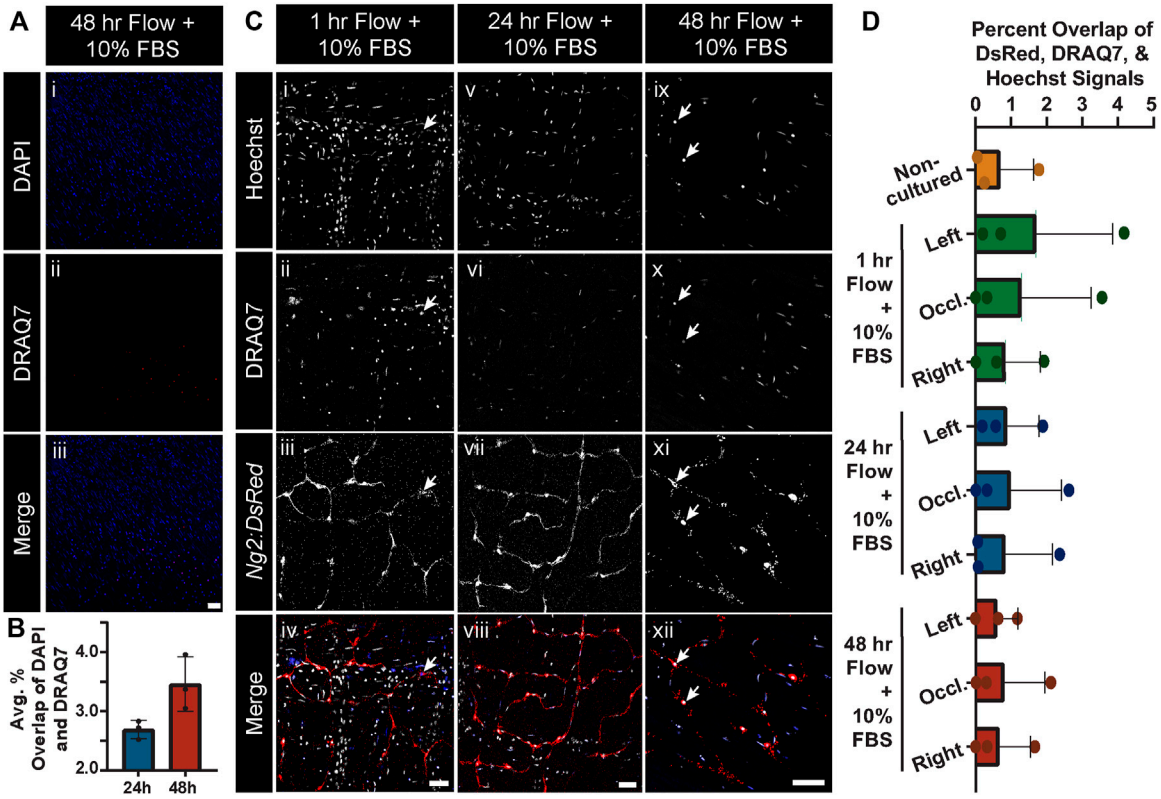

FIGURE 4
Global and *Ng2:DsRed+* Cell Viability Remains Unchanged after Culture in Controlled Flow Conditions. **(A)** Representative images of general cell viability as gauged by DAPI-labeled cell nuclei (blue in i and iii) relative to compromised cell nuclei labeled with DRAQ7 (red in ii and iii) in a 48 h tissue culture with 10% FBS and controlled flow. Scale bar in iii is 50 μm. **(B)** Average percent overlap of DAPI and DRAQ7 signals across the intestinal tissue area at 24 h (blue bar) and 48 h (red bar) where controlled flow was supplied (note, *y*-axis range is from 2% to 4.5%). Error bars represent ± standard deviation. Note, the live-dead staining with DRAQ7 revealed that there was not extensive cell death under the controlled flow and tissue culture conditions at 24 h or 48 h, despite the lack of flow access to most smaller-order vessels. Biological replicates for this experiment were at a minimum of $n = 3$. **(C)** Representative images of Hoechst-labeled cell nuclei (i, v, ix; white in iv, viii, xii), DRAQ7-labeled cell nuclei (ii, vi, x; blue in iv, viii, xii), and *Ng2:DsRed*-labeled pericytes (iii, vii, xi; red in iv, viii, xii) in the occluded areas of 1 h (i-iv), 24 h (v-viii), and 48 h (ix-xii) cultures with controlled flow. Scale bars in (iv), (viii), (xii) are 50 μm. Note, live-dead staining with DRAQ7 revealed no notable pericyte death, even in the occluded area. Additionally, no abnormal pericyte morphology was observed. **(D)** Average percent overlap of DsRed, DRAQ7, and Hoechst signals across intestinal tissues not cultured (orange bar and circles) and cultured in controlled flow conditions for 1 h (green bars and circles), 24 h (blue bars and circles), and 48 h (red bars and circles). Error bars represent standard deviation.

Jackson et al., 2005). This feature may represent a mechanism whereby intrinsic vessel geometry compensates for intraluminal pressure changes and shields the microcirculation from these changes that might otherwise damage capillaries. We therefore measured the tortuosity of primary and secondary arteries as a proxy for intraluminal pressure, asking if this pressure might decrease over time with increasing capillary access-to-flow i.e., *via* reduced resistance to flow through capillary networks. Consistent with the lack of FITC-Dextran detected in flow cultured tissues, we found a high degree of tortuosity for secondary vessels relative to primary vessels at both the 24 h and 48 h time points (Figure 6). Secondary vessel tortuosity was also fairly consistent across regions, though vessels in closer proximity to the occlusion site were slightly more tortuous at 48 h (Figure 6). By qualitative assessment, primary vessels appeared more linear, whereas secondary collaterals displayed a higher degree of inflection as a feature of their tortuosity (Sun et al., 2022). From initial observations of tortuous vessels, the flow-rate was lowered from 1.5 ml/min to 1 ml/min, but the tortuous vessels remained. Overall, these data support the idea that tissue viability was maintained in flow cultured conditions such that mechanisms (i) restricting capillary perfusion and (ii) sustaining elevated intraluminal pressure in collateral vessels remained intact over the experimental time course.

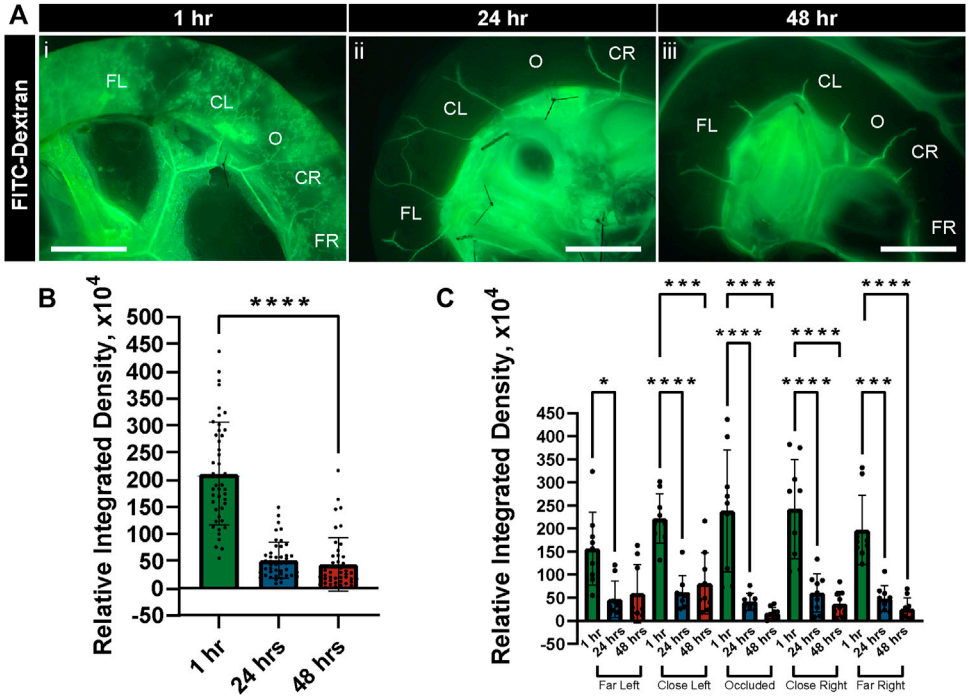

FIGURE 5
FITC-Dextran Perfusion in Intestinal Vasculature Decreases after Culture in Controlled Flow Conditions. **(A)** Representative images of FITC-Dextran (green in i-iii) following perfusion through the intestinal vasculature after 1 h (i), 24 h (ii), and 48 h (iii) of tissue culture with controlled flow. Regions are labeled as to their location relative to the occlusion site (O), with more distal areas labeled as Far Left (FL) and Far Right (FR) and more proximal areas as Close Left (CL) and Close Right (CR). Scale bars in each image (i-iii) are 1 cm. **(B)** Relative integrated densities of FITC-Dextran quantified in tissue after 1 h (green bar), 24 h (blue bar), and 48 h (red bar) of culture with controlled flow. Error bars represent ± standard deviation. ****$p \leq 0.0001$ for 1 h vs. 24 h and 48 h. **(C)** Relative integrated densities of FITC-Dextran quantified in tissue after 1 h (green bars), 24 h (blue bars), and 48 h (red bars) of culture with controlled flow, disaggregated by region. Error bars represent ± standard deviation. *$p \leq 0.05$, ***$p \leq 0.001$, and ****$p \leq 0.0001$ for the comparisons denoted. Biological replicates for this experiment were at a minimum of $n = 3$, and data points shown are from technical replicates across all experiments.

Discussion

Tissue reperfusion outcomes vary widely following therapeutic intervention, largely due to an incomplete understanding of the underlying causes. Microvessel instability for example has been proposed as a contributing factor, with capillary-associated pericytes potentially fueling microvascular dysfunction during ischemia (Yemisci et al., 2009; Hall et al., 2014; O'Farrell et al., 2017). A broader range of experimental models are therefore necessary to identify specific factors that may limit reperfusion and in turn address important gaps in our knowledge of the "no-reflow" phenomenon (Eeckhout and Kern, 2001; Ito, 2006). To that end, we developed an *ex vivo* tissue culture model in which vessel perfusion was maintained *via* cannulation of an upstream feeder artery. We established appropriate culture conditions for this closed-loop system and verified that, following experimental set up, perfusate access to capillary beds was feasible. Tissue viability was sustained over the experimental time course, as was the stability of the microvasculature and associated pericytes. In spite of these relatively stable microcirculatory networks, perfusion rapidly became limited to larger collateral vessels, which exhibited hallmarks of a sustained elevation in intraluminal pressure, specifically an increase in their tortuosity. Taken together, our data demonstrate that, despite the lack of overt cell death and tissue or vessel degradation by the measurements applied, capillary access-to-flow was severely reduced regardless of vascular integrity (as assessed by lectin-labeling vascular networks immediately preceding flow-controlled culture, then imaging post-culture *via* confocal microscopy (See Supplemental Materials) or proximity to a primary occlusion. Though we fully acknowledge that we did not formally measure the full range of vascular integrity indicators (e.g., small molecular weight tracer leakage or tight/adherens junction assessment). The current study also highlights the utility of tissue-based platforms to complement *in vitro* and *in vivo* approaches to isolate and explore the crosstalk between cellular responses and perturbations to fluid flow conditions.

Changes in blood flow within a tissue can lead to a wide range of consequences. For instance, limited or absent perfusion results

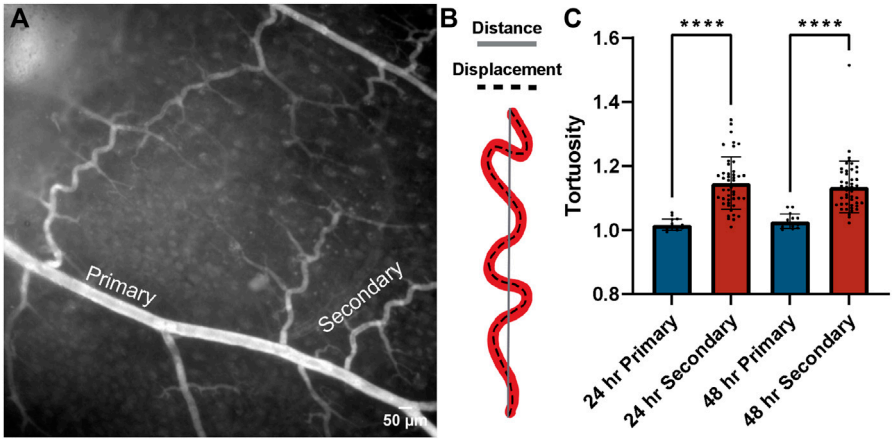

FIGURE 6
Collateral tortuosity remained increased during intestinal tissue culture in controlled flow conditions. **(A)** Representative image of intestinal tissue cultured under controlled flow conditions with primary and secondary collateral vessels denoted. Scale bar is 50 µm. **(B)** Schematic illustrating distance-metric tortuosity measurement of vessel (red) distance from end-point to end-point (solid gray line) and displacement (dashed black line). **(C)** Distance-metric tortuosity was measured at 24 h (blue bars) and 48 h (red bars) in primary (> 45 um) and secondary (< 45 um) vessels across all regions relative to the area downstream of the occlusion. ****$p \leq 0.0001$ for the comparisons denoted. Tortuosity was consistently lower in primary vessels than in secondary vessels across regions after both 24 h and 48 h of tissue culture with controlled flow. Biological replicates for this experiment were at a minimum of $n = 3$, and data points shown are from technical replicates across all experiments.

in ischemic conditions including hypoxia, and disrupts nutrient/waste exchange as well as the biophysical forces on vessel walls (Hademenos and Massoud, 1997). The duration of the ischemic event also dictates the nature of cellular responses. Hypoxic conditions, both acute and chronic, have been suggested to induce microvascular instability (Schoch et al., 2002) *via* cell death and disengagement and in turn limit the capacity for reperfusion (Galiuto et al., 2000). Pericytes for example have been described as contracting and dying in this constricted state, thereby causing regional blood flow deficits following ischemia (Yemisci et al., 2009; Hall et al., 2014; O'Farrell and Attwell, 2014; O'Farrell et al., 2017). This phenomenon may be tissue- and/or time-dependent, as our data suggest that restricted flow may occur (i) more upstream of the capillary beds where pericytes are most abundant, and (ii) independent of overt pericyte death or detachment. While pericytes may be indirectly involved in the mechanisms that limit reperfusion, we did not find extensive cell death at the 24 h or 48 h time points observed, though we did not use live imaging to establish the exact time course for these changes. Furthermore, we cannot rule out the possibility that pericytes may communicate paracrine or intracellular signals to upstream cells that may be more directly involved in vasoconstriction and limiting capillary access to flow. But we did not observe widespread pericyte death in flow-restricted regions that would suggest their involvement in reduced fluid transit. Nevertheless, future studies will be needed to build upon these observations to further elucidate the potential roles of microvascular pericytes in limiting capillary perfusion in the context of tissue ischemia and reperfusion.

An additional outcome of altered blood flow is often morphological adaptation of affected vessels. For example, in the current study, we observed fluid transit primarily through collateral channels over an acute time course. We found that these tortuous vessels were consistently present throughout the entire region receiving controlled flow, even after adjusting the flow-rate in an attempt to relieve excessive shear stress on the vessel walls. Though we did not quantify features such as bending length and inflection points (Sun et al., 2022), measuring vessel tortuosity revealed that secondary, smaller-order vessels, such as the collaterals bridging adjacent territories, saw the highest degree of tortuosity. Two possible interpretations seem to emerge from this observation. First, the increased vessel tortuosity may reflect a temporary "morphological response" to altered flow patterns, that is, an adaptation based on inherent vessel geometry as opposed to structural remodeling that likely occurs over a more extended period of time (Chappell et al., 2008; Song and Munn, 2011; Chong et al., 2017). Vessel curvature may in fact reflect a means by which higher intraluminal pressure is dissipated, such as in scenarios where flows must be reduced for functional reasons e.g., uterine spiral arteries (Osol and Moore, 2014). In our study, the degree of tortuosity being generally lower at the 48 h time-point compared to 24 h suggests that perhaps vessel tortuosity changes are an acute, functional adaptation to abnormal flow rather than a permanent, negative consequence of it. Second, the degree of tortuosity in secondary vessels being higher at 48 h only in the occluded area suggests that these vessels may be facilitating larger flow volumes than their distal counterparts (Han, 2012). These secondary collaterals may

need to adapt *via* tortuosity changes more substantially as compared to non-occluded areas, which is consistent with the idea that neighboring vessels may be actively shunting flow to the occluded area as a means to sustain tissue health. Overall, vessel tortuosity observed experimentally, or perhaps even clinically, may be a useful indicator of vessel adaptations to altered blood flow states and the relative efficiency of perfusion within downstream tissues.

In addition to the data and interpretations discussed above, the work presented herein aimed to highlight the utility of *ex vivo* tissue explant platforms as complementary approaches to *in vitro* microfluidics models and *in vivo* experimentation. Vascular-focused microfluidics models (Song and Munn, 2011; Sobrino et al., 2016; Phan et al., 2017; Haase et al., 2019) are moving towards, but have yet to achieve, recapitulation of key microcirculation features including: (i) sustained capillary diameters of 10 microns or less, (ii) appropriate deposition of ECM components within the vascular basement membrane, (iii) inclusion of microvascular pericytes exhibiting *in vivo* morphologies, and (iv) network architecture and hierarchy reflecting those found in specific tissues (Hesh et al., 2019). While *in vivo* experimental models can more accurately capture the complex biological response to altered blood flow (Gonzalez et al., 2015), that complexity can make it difficult to isolate and understand the individual components involved. Activation of the inflammatory cascade (Nowicki, 2005), for example, can create challenges in understanding contributions of recruited immune cells relative to local cellular constituents. *In vivo* models are also limited with respect to the time-course of experimental interventions, as applying multiple, acute manipulations in an animal model is incredibly difficult without compromising the health and wellbeing of the subject. These models are further complicated by the broad effects that anesthesia (Luo et al., 2007), pain management (Peterson et al., 2017), and surgical intervention have on the cardiovascular and immune systems as well as on overall animal physiology. While the experimental model presented in the current study has certain limitations, this *ex vivo* tissue perfusion system may offer an intermediate approach to bridge the gap between *in vitro* and *in vivo* applications.

As with all studies, it is critical to acknowledge the limitations of our model and approaches as well as possible alternative interpretations. While *Ng2:DsRed* was used in conjuction with vessel and cellular morphology to identify pericytes, we fully acknowledge that *Ng2/Cspg4* is expressed by other cell types including other mural cells such as vascular smooth muscle cells. Another important limitation in the interpretation of our findings is that the intestinal tissue studied herein is relatively thin and may be able to absorb nutrients/oxygen from the superfusate, while tissues such as the brain are much thicker and likely be precluded from use in our experimental setup. Furthermore, interrogating potential molecular mechanisms involved in our observations was beyond the scope of the current study but will be a goal moving forward. This work provides a foundation for using this *ex vivo* tissue-based fluidics platform to transcriptionally profile vascular cell types in regions experiencing variable levels of fluid flow and mechanical stress (Culver and Dickinson, 2010). Regarding specifics for our model, it is possible that our observations may depend on the viscosity of the perfusate, which was selected to promote tissue viability but not necessarily to reflect specific characteristics of blood. Though we were able to achieve flow and intraluminal pressurization, the fluid itself may have lacked key mechanical and/or chemical properties to prevent persistent vaso-occlusion and restricted access to capillary networks. Another consideration for future studies might be the rate at which flow was reintroduced into our system. Major vessel occlusions are rapidly removed clinically to restore blood flow to downstream tissues, but we sought to reintroduce fluid flow into the cannulated tissues more moderately. Perhaps an even more gradual increase in reperfusion may limit or prevent any reactive myogenic vasoconstriction that might occur due to the increased intraluminal pressure. These and other alternative approaches and interpretations offer numerous opportunities for follow-on studies to further understand the molecular and mechanical cues that contribute to vascular adaptation to altered flow conditions and perhaps to persistent vasoconstriction events seen clinically.

Data availability statement

The raw data supporting the conclusion of this article will be made available by the authors, without undue reservation.

Ethics statement

The animal study was reviewed and approved by Institutional Animal Care and Use Committee (IACUC), Virginia Tech.

Author contributions

CW and JC contributed to conception and design of the study. CW performed the statistical analysis. JC wrote the first draft of the manuscript sections: Introduction, Results, and Discussion. CW wrote the Methods section of the manuscript. All authors contributed to manuscript revision, read, and approved the submitted version.

Funding

This work was supported in part by funding from the National Science Foundation (CAREER Award 1752339 to

JC). The funder provided financial resources to conduct this research. No funds were received for open access publication.

Acknowledgments

We would like to thank all of the Chappell lab members for their support and valued assistance on this project.

Conflict of interest

The authors declare that the research was conducted in the absence of any commercial or financial relationships that could be construed as a potential conflict of interest.

Publisher's note

All claims expressed in this article are solely those of the authors and do not necessarily represent those of their affiliated organizations, or those of the publisher, the editors and the reviewers. Any product that may be evaluated in this article, or claim that may be made by its manufacturer, is not guaranteed or endorsed by the publisher.

Supplementary material

The Supplementary Material for this article can be found online at: https://www.frontiersin.org/articles/10.3389/fbioe.2022.1008481/full#supplementary-material

References

Akbari, E., Spychalski, G. B., and Song, J. W. (2017). Microfluidic approaches to the study of angiogenesis and the microcirculation. *Microcirculation* 24 (5). doi:10.1111/micc.12363

Azimi, M. S., Motherwell, J. M., and Murfee, W. L. (2017). An *ex vivo* method for time-lapse imaging of cultured rat mesenteric microvascular networks. *J. Vis. Exp.* 120, 55183. doi:10.3791/55183

Bang, S., Lee, S. R., Ko, J., Son, K., Tahk, D., Ahn, J., et al. (2017). A low permeability microfluidic blood-brain barrier platform with direct contact between perfusable vascular network and astrocytes. *Sci. Rep.* 7 (1), 8083. doi:10.1038/s41598-017-07416-0

Bray, M. A., Sartain, S. E., Gollamudi, J., and Rumbaut, R. E. (2020). Microvascular thrombosis: Experimental and clinical implications. *Transl. Res.* 225, 105–130. doi:10.1016/j.trsl.2020.05.006

Chappell, J. C., Song, J., Klibanov, A. L., and Price, R. J. (2008). Ultrasonic microbubble destruction stimulates therapeutic arteriogenesis via the CD18-dependent recruitment of bone marrow-derived cells. *Arterioscler. Thromb. Vasc. Biol.* 28 (6), 1117–1122. doi:10.1161/atvbaha.108.165589

Chong, D. C., Yu, Z., Brighton, H. E., Bear, J. E., and Bautch, V. L. (2017). Tortuous microvessels contribute to wound healing via sprouting angiogenesis. *Arterioscler. Thromb. Vasc. Biol.* 37 (10), 1903–1912. doi:10.1161/ATVBAHA.117.309993

Culver, J. C., and Dickinson, M. E. (2010). The effects of hemodynamic force on embryonic development. *Microcirculation* 17 (3), 164–178. doi:10.1111/j.1549-8719.2010.00025.x

Eeckhout, E., and Kern, M. J. (2001). The coronary no-reflow phenomenon: A review of mechanisms and therapies. *Eur. Heart J.* 22 (9), 729–739. doi:10.1053/euhj.2000.2172

Galiuto, L., DeMaria, A. N., del Balzo, U., May-Newman, K., Flaim, S. F., Wolf, P. L., et al. (2000). Ischemia-reperfusion injury at the microvascular level: Treatment by endothelin A-selective antagonist and evaluation by myocardial contrast echocardiography. *Circulation* 102 (25), 3111–3116. doi:10.1161/01.cir.102.25.3111

Goeden, N., and Bonnin, A. (2013). *Ex vivo* perfusion of mid-to-late-gestation mouse placenta for maternal-fetal interaction studies during pregnancy. *Nat. Protoc.* 8 (1), 66–74. doi:10.1038/nprot.2012.144

Gonzales, A. L., Klug, N. R., Moshkforoush, A., Lee, J. C., Lee, F. K., Shui, B., et al. (2020). Contractile pericytes determine the direction of blood flow at capillary junctions. *Proc. Natl. Acad. Sci. U. S. A.* 117 (43), 27022–27033. doi:10.1073/pnas.1922755117

Gonzalez, L. M., Moeser, A. J., and Blikslager, A. T. (2015). Animal models of ischemia-reperfusion-induced intestinal injury: Progress and promise for translational research. *Am. J. Physiology-Gastrointestinal Liver Physiology* 308 (2), G63–G75. doi:10.1152/ajpgi.00112.2013

Granger, D. N., and Kvietys, P. R. (2015). Reperfusion injury and reactive oxygen species: The evolution of a concept. *Redox Biol.* 6, 524–551. doi:10.1016/j.redox.2015.08.020

Haase, K., Gillrie, M. R., Hajal, C., and Kamm, R. D. (2019). Pericytes contribute to dysfunction in a human 3D model of placental microvasculature through VEGF-ang-tie2 signaling. *Adv. Sci.* 6 (23), 1900878. doi:10.1002/advs.201900878

Hademenos, G. J., and Massoud, T. F. (1997). Biophysical mechanisms of stroke. *Stroke* 28 (10), 2067–2077. doi:10.1161/01.str.28.10.2067

Hall, C. N., Reynell, C., Gesslein, B., Hamilton, N. B., Mishra, A., Sutherland, B. A., et al. (2014). Capillary pericytes regulate cerebral blood flow in health and disease. *Nature* 508 (7494), 55–60. doi:10.1038/nature13165

Han, H. C. (2012). Twisted blood vessels: Symptoms, etiology and biomechanical mechanisms. *J. Vasc. Res.* 49 (3), 185–197. doi:10.1159/000335123

Hesh, C. A., Qiu, Y., and Lam, W. A. (2019). Vascularized microfluidics and the blood-endothelium interface. *Micromachines (Basel)* 11 (1), 18. doi:10.3390/mi11010018

Heusch, G. (2020). Myocardial ischaemia-reperfusion injury and cardioprotection in perspective. *Nat. Rev. Cardiol.* 17 (12), 773–789. doi:10.1038/s41569-020-0403-y

Hoque, M. M., Abdelazim, H., Jenkins-Houk, C., Wright, D., Patel, B. M., and Chappell, J. C. (2021). The cerebral microvasculature: Basic and clinical perspectives on stroke and glioma. *Microcirculation* 28 (3), e12671. doi:10.1111/micc.12671

Hutchins, G. M., Miner, M. M., and Bulkley, B. H. (1978). Tortuosity as an index of the age and diameter increase of coronary collateral vessels in patients after acute myocardial infarction. *Am. J. Cardiol.* 41 (2), 210–215. doi:10.1016/0002-9149(78)90158-3

Ito, H. (2006). No-reflow phenomenon and prognosis in patients with acute myocardial infarction. *Nat. Rev. Cardiol.* 3 (9), 499–506. doi:10.1038/ncpcardio0632

Jackson, Z. S., Dajnowiec, D., Gotlieb, A. I., and Langille, B. L. (2005). Partial off-loading of longitudinal tension induces arterial tortuosity. *Arterioscler. Thromb. Vasc. Biol.* 25 (5), 957–962. doi:10.1161/01.ATV.0000161277.46464.11

Luo, F., Li, Z., Treistman, S. N., Kim, Y. R., King, J. A., Fox, G. B., et al. (2007). Confounding effects of volatile anesthesia on CBV assessment in rodent forebrain following ethanol challenge. *J. Magn. Reson. Imaging* 26 (3), 557–563. doi:10.1002/jmri.21083

Moskowitz, M. A., Lo, E. H., and Iadecola, C. (2010). The science of stroke: Mechanisms in search of treatments. *Neuron* 67 (2), 181–198. doi:10.1016/j.neuron.2010.07.002

Motherwell, J. M., Rozenblum, M., Katakam, P. V. G., and Murfee, W. L. (2019). Bioreactor system to Perfuse mesentery microvascular networks and study flow effects during angiogenesis. *Tissue Eng. Part C. Methods* 25 (8), 447–458. doi:10.1089/ten.TEC.2019.0119

Nowicki, P. T. (2005). Ischemia and necrotizing enterocolitis: Where, when, and how. *Seminars Pediatr. Surg.* 14 (3), 152–158. doi:10.1053/j.sempedsurg.2005.05.003

O'Farrell, F. M., and Attwell, D. (2014). A role for pericytes in coronary no-reflow. *Nat. Rev. Cardiol.* 11 (7), 427–432. doi:10.1038/nrcardio.2014.58

O'Farrell, F. M., Mastitskaya, S., Hammond-Haley, M., Freitas, F., Wah, W. R., and Attwell, D. (2017). Capillary pericytes mediate coronary no-reflow after myocardial ischaemia. *Elife* 6, e29280. doi:10.7554/eLife.29280

Osol, G., and Moore, L. G. (2014). Maternal uterine vascular remodeling during pregnancy. *Microcirculation* 21 (1), 38–47. doi:10.1111/micc.12080

Payne, L. B., Darden, J., Suarez-Martinez, A. D., Zhao, H., Hendricks, A., Hartland, C., et al. (2021). Pericyte migration and proliferation are tightly synchronized to endothelial cell sprouting dynamics. *Integr. Biol. (Camb)* 13 (2), 31–43. doi:10.1093/intbio/zyaa027

Peterson, N. C., Nunamaker, E. A., and Turner, P. V. (2017). To treat or not to treat: The effects of pain on experimental parameters. *Comp. Med.* 67 (6), 469–482.

Phan, D. T. T., Wang, X., Craver, B. M., Sobrino, A., Zhao, D., Chen, J. C., et al. (2017). A vascularized and perfused organ-on-a-chip platform for large-scale drug screening applications. *Lab. Chip* 17 (3), 511–520. doi:10.1039/c6lc01422d

Powers, W. J., Rabinstein, A. A., Ackerson, T., Adeoye, O. M., Bambakidis, N. C., Becker, K., et al. (2018). 2018 guidelines for the early management of patients with acute ischemic stroke: A guideline for healthcare professionals from the American heart association/American stroke association. *Stroke* 49 (3), e46–e110. doi:10.1161/STR.0000000000000158

Rasband, W. S. (1997). *ImageJ*. Bethesda, Maryland, USA: U.S. National Institutes of Health.

Sacchetti, A., Subramaniam, V., Jovin, T. M., and Alberti, S. (2002). Oligomerization of DsRed is required for the generation of a functional red fluorescent chromophore. *FEBS Lett.* 525 (1-3), 13–19. doi:10.1016/s0014-5793(02)02874-0

Sava, P., Ramanathan, A., Dobronyi, A., Peng, X., Sun, H., Ledesma-Mendoza, A., et al. (2017). Human pericytes adopt myofibroblast properties in the microenvironment of the IPF lung. *JCI Insight* 2 (24), e96352. doi:10.1172/jci.insight.96352

Sawamiphak, S., Ritter, M., and Acker-Palmer, A. (2010). Preparation of retinal explant cultures to study *ex vivo* tip endothelial cell responses. *Nat. Protoc.* 5 (10), 1659–1665. doi:10.1038/nprot.2010.130

Schindelin, J., Arganda-Carreras, I., Frise, E., Kaynig, V., Longair, M., Pietzsch, T., et al. (2012). Fiji: An open-source platform for biological-image analysis. *Nat. Methods* 9 (7), 676–682. doi:10.1038/nmeth.2019

Schoch, H. J., Fischer, S., and Marti, H. H. (2002). Hypoxia-induced vascular endothelial growth factor expression causes vascular leakage in the brain. *Brain* 125, 2549–2557. doi:10.1093/brain/awf257

Sobrino, A., Phan, D. T., Datta, R., Wang, X., Hachey, S. J., Romero-Lopez, M., et al. (2016). 3D microtumors *in vitro* supported by perfused vascular networks. *Sci. Rep.* 6, 31589. doi:10.1038/srep31589

Song, J. W., and Munn, L. L. (2011). Fluid forces control endothelial sprouting. *Proc. Natl. Acad. Sci. U. S. A.* 108 (37), 15342–15347. doi:10.1073/pnas.1105316108

Suarez-Martinez, A. D., Bierschenk, S., Huang, K., Kaplan, D., Bayer, C. L., Meadows, S. M., et al. (2018). A novel *ex vivo* mouse mesometrium culture model for investigating angiogenesis in microvascular networks. *J. Vasc. Res.* 55 (3), 125–135. doi:10.1159/000489102

Sun, Z., Jiang, D., Liu, P., Muccio, M., Li, C., Cao, Y., et al. (2022). Age-related tortuosity of carotid and vertebral arteries: Quantitative evaluation with MR angiography. *Front. Neurol.* 13, 858805. doi:10.3389/fneur.2022.858805

Yemisci, M., Gursoy-Ozdemir, Y., Vural, A., Can, A., Topalkara, K., and Dalkara, T. (2009). Pericyte contraction induced by oxidative-nitrative stress impairs capillary reflow despite successful opening of an occluded cerebral artery. *Nat. Med.* 15 (9), 1031–1037. doi:10.1038/nm.2022

Frontiers in
Bioengineering and Biotechnology

Accelerates the development of therapies, devices, and technologies to improve our lives

A multidisciplinary journal that accelerates the development of biological therapies, devices, processes and technologies to improve our lives by bridging the gap between discoveries and their application.

Discover the latest Research Topics

See more →

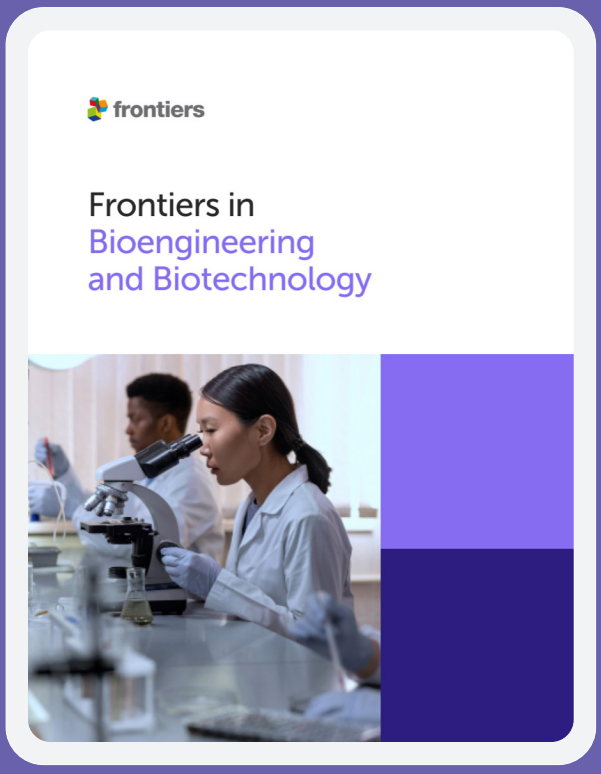

Frontiers

Avenue du Tribunal-Fédéral 34
1005 Lausanne, Switzerland
frontiersin.org

Contact us

+41 (0)21 510 17 00
frontiersin.org/about/contact